



**EVOLUTION OF COMPLEX
VERTICAL SUCCESSIONS OF
FLUID VENTING SYSTEMS
DURING CONTINENTAL MARGIN
SEDIMENTATION**

SUTIENG HO

**Submitted in partial fulfilment of the requirements
for the degree of Ph.D.**

Cardiff University

September 2013

DECLARATION OF WORK

This work has not been submitted in substance for any other degree or award at this or any other university or place of learning, nor is being submitted concurrently in candidature for any degree or other award.

Signed SUTIEUG HO (candidate)

Date30 September 2013.....

STATEMENT 1

This thesis is being submitted in partial fulfillment of the requirements for the degree ofPhD.....(insert MCh, MD, MPhil, PhD etc, as appropriate)

Signed SUTIEUG HO (candidate)

Date30 September 2013.....

STATEMENT 2

This thesis is the result of my own independent work/investigation, except where otherwise stated.

Other sources are acknowledged by explicit references. The views expressed are my own.

Signed SUTIEUG HO (candidate)

Date30 September 2013.....

STATEMENT 3

I hereby give consent for my thesis, if accepted, to be available for photocopying and for inter-library loan, and for the title and summary to be made available to outside organisations.

Signed SUTIEUG HO (candidate)

Date30 September 2013.....

STATEMENT 4: PREVIOUSLY APPROVED BAR ON ACCESS

I hereby give consent for my thesis, if accepted, to be available for photocopying and for inter-library loans **after expiry of a bar on access previously approved by the Academic Standards & Quality Committee.**

Signed SUTIEUG HO (candidate)

Date30 September 2013.....

Author note and status of publications

- At the time of thesis submission Chapter 4 has been published as Ho, S., Cartwright, J. A., & Imbert, P. (2012); “*Vertical evolution of fluid venting structures in relation to gas flux, in the Neogene-Quaternary of the Lower Congo Basin, Offshore Angola*” in the journal of Marine Geology.
- A poster has been presented in 2012 AAPG Annual Convention and Exhibition and published as Ho, S., Imbert, P., & Cartwright, J. A. (2012); “*Fluid Venting Structures of the Lower Congo Basin on 3-D Seismic: Gas Flux Variations Recorded by the Vertical Evolution of Pockmarks and Associated Amplitudes Anomalies*” in AAPG Search and Discovery Article.
- Additional work on data calibration to support the research result in Chapter 4 has been presented as an oral presentation on 30th IAS Meeting of Sedimentology 2013 September as “*Patchy high-amplitude seismic anomalies in the Lower Congo Basin: an insight into their subsurface morphology from analogue outcrops of SE France*”.
- At the time of thesis submission parts of Chapter 5 have been presented in 2012 AAPG Annual Convention and Exhibition, and published as Ho, S., Cartwright, J., & Imbert, P. (2012); “*The Formation of Advancing Pockmarks Arrays: An Interplay between Hydrocarbon Leakage and Slope Sedimentation*” in AAPG Search and Discovery Article.
- At the time of thesis submission parts of Chapter 6 has been presented in 75th EAGE Conference & Exhibition incorporating SPE EUROPEC 2013, and has been published as extend abstract as Ho, S., Carruthers, T. D., Imbert, P., & Cartwright, J. (2013); “*Spatial Variations in Geometries of Polygonal Faults Due to Stress Perturbations & Interplay with Fluid Venting Features*” in EarthDoc of EAGE. An oral presentation has also been given as “*A case study of fluid venting structures and amplitude anomalies as indicators hydrocarbon leakage in interplay with basin configuration: reconstruction of fluid migration history of Neogen-Quaternary in Lower Congo-Angola basin*” in 11th Conference of Gas in Marine Sediments 2012.

Acknowledgements

I would like to acknowledge Cardiff University and Total S.A. for funding the project Total S.A. for supplying seismic data and for allowing its publication.

I would also like to thank my academic supervisor Joe Cartwright who provided me the opportunity to undertake this PhD research project and who provided lots of useful comments and advice. I am also grateful to my industrial supervisor, Patrice Imbert (Total) for his years of tuition in sedimentology and geophysics, and thanks for his enormous support, guidance, patience and important discussions. Special thanks for my academic monitor Dan Carruthers (previously affiliated Cardiff University, currently in University of Texas at Austin) for his incredible job for being my teacher and best friend, who gets me through all of the hardest times along my PhD. I would like to thank Benoit Paternoster (Total) for sharing his geophysics knowledge, for his supervision and his precious advice.

I am grateful for the constructive discussions and positive interaction with Eric Cauquil (Total). I would also like to thank Jean-Philippe Blouet (Total) for technical support and lab assistance. Furthermore I would like to acknowledge the rest of Total home team; Firdarus Tampilang and Jose Podia for providing data and support, Ka Hoe Chee and Pierre Thore for geophysics support, Patrick Simone, Domnique Beziat and Edmond Poyol for sedimentology lab-work assistances and lastly Didier Cave for printing publication materials.

At Cardiff University I would like to thank Gwen Pettigrew for technical support and other members of the 3D Lab with particular thanks to Gordon Lawrence for his guidance, Ian Clark, Jennifer Moss, Iqbal Muhammad and Ben Manton for their positive effect and interactions. I am grateful for the useful and interactive discussions with the geological team in Total, Johnathan Pelletier, Romain Bibonne, Michal Wardynski, Jean-Noël Ferry, Remi Castilla, Quentine Soulas, and Anne B., Corrine, B., for their administration assistances.

I would like to acknowledge important educations in sedimentology provided by professors and lectures in the geology department at the University of Western Brittany, who provided a crucial foundation in scientific research. I would like to thank my Godfather Dr. François Michaud (University of Brest) for educating me in science and life, my sister Ian Ho (Museu das Comunicações de Macau) for her useful discussions and experience sharing in physical sciences.

Finally and most of all, I am forever grateful to my parents, family and friends for the enormous amount of support and love they have given me.

Table of contents

Abstract	1
CHAPTER 1	4
1.0 Introduction	5
1.1 Rationale	5
1.2. Overview	7
1.2.1. Focused vertical fluid venting systems in fine-grained sediments	7
1.2.2. Vertical fluid conduit: chimney or pipe structures	9
1.2.2.1. Seismic expressions of vertical gas chimneys and ground truth outcrops	20
.....	22
1.2.3. Pockmarks	25
1.2.3.1. Environment for pockmark and chimney formations	28
1.2.3.2. Vertical evolution of pockmarks	29
1.2.4. Methane-related carbonates	31
1.2.4.1. Depth of occurrence of methane derived authigenic carbonate occurrence vs. relative fluid flux	33
1.2.4.2. $\delta^{13}\text{C}$ isotopic signature	35
1.2.4.3. Expression of methane-related carbonates in seismic and their ground truth calibration	35
.....	
1.2.5. Model for the vertical evolution of methane-related carbonates and their genetic relationship with pockmarks and gas chimneys	36
1.2.6. Relationship between fluid flux and development of venting structures	47
.....	50
1.3. The motivation and aim of the thesis.....	50
1.3.1. Thesis layout.....	53
CHAPTER 2	54
2.0 Methodology	55
2.1. Introduction	55
2.2. Seismic data.....	55
2.2.1 The science of 3D seismic data	55
2.2.1.1. Amplitude and colour convention	58
2.2.1.2. Vertical resolution and impact of thickness variations on amplitudes	58
2.2.1.3. Horizontal resolution	60
2.2.2. Location, parameters of 3D exploration seismic data	61
2.2.3. 3D seismic interpretation techniques.....	63
2.2.3.1. 3D seismic interpretation software	63
2.2.3.2. Seismic attributes.....	64
2.2.3.3. Technique on interpretation of fluid venting structures on 3D seismic	66
2.2.3.3.1. Detection and visualizing of fluid venting structures.....	66
2.2.3.3.2. Recognition of fluid venting structures base on seismic wave lobes	67
2.3. Limitations and potential solutions	69
2.3.1. Seismic resolution	69
2.3.2. Calibration of positive high amplitude anomalies on seismic and ground truth	71
2.4. Age of seismic stratigraphic units	71
CHAPTER 3	72
3.0. Geological setting	73
3.1. Introduction	73
3.2. Regional geological setting	73
3.3. Stratigraphy of the study area.....	76
3.4. Local structural geology of the study area.....	78

3.5. Regional ocean currents.....	86
CHAPTER 4	91
4.0. Vertical evolution of fluid venting structures in relation to gas flux, in the Neogene-Quaternary of the Lower Congo Basin, Offshore Angola	92
4.1. Abstract.....	92
4.2. Introduction	93
4.3. Data and methods	95
4.4. Regional geological setting	96
4.5. Seismic expression and interpretation of fluid venting structures.....	96
4.5.1. Types of fluid venting structures	96
4.5.2. Positive high amplitude anomalies (PHAAs).....	96
4.5.2.1. Definition and description of sub-circular PHAAs.....	98
4.5.2.2. Definition and description of linear PHAAs.....	100
4.5.3. Fluid venting structures with associated PHAAs	102
4.5.3.1. Linear conduits in seismic	102
4.5.3.2. Vertical succession of the two types of PHAAs.....	104
4.5.3.3. Interpretation of ‘Polyphased pockmarks’ and their associated PHAA	104
4.5.3.3.1. Internal structures associated with PHAAs in 3-D views.....	107
4.6. Discussion.....	108
4.6.1. Relationship between methane flux and positive amplitudes variations	108
4.6.1.1. Methane-related carbonates in Offshore Congo–Angola	109
4.6.1.2. Timing of venting at the palaeo-seabed.....	110
4.6.1.3. Genetic model.....	111
4.6.2. Methane fluxes and their subsurface expression	112
4.6.2.1. Relationship between sub-circular PHAAs and pockmarks.....	112
4.6.2.2. Linear conduits and PHAA without pockmark	113
4.6.2.3. The origin of linear conduit geometries	114
4.6.3. Conceptual model for the formation of ‘Polyphased pockmarks’	115
4.7. Conclusion.....	119
CHAPTER 5	123
5.0. The formation of two new types of pockmarks - Advancing pockmarks arrays and Nested pockmarks: an interplay between hydrocarbon leakage and slope sedimentation	124
5.1. Abstract.....	124
5.2. Introduction	125
5.3. Seismic data and methodology	127
5.3.1. Seismic data.....	127
5.3.2. Methodology.....	127
5.4. The local structure and stratigraphy	128
5.5. Results and seismic interpretation	129
5.5.1. Definition and structure of ‘Advancing pockmark arrays’	130
5.5.1.1. Basal craters / earliest pockmarks of the arrays	137
5.5.1.2. Stacked advancing pockmark arrays	138
5.5.2. Definition of “Nested pockmarks”	141
5.5.3. Stratigraphic position of pockmarks arrays	148
5.5.4. Chronology of different generations of infill within pockmarks systems	149
5.5.5. Heights of pockmarks arrays and the distances of horizontal offsets between apices	149
5.5.6. Regional distribution of the pockmarks and associated regional features.....	150
5.5.7. Association with other types of fluid flow structures.....	154
5.6. Discussion.....	166
5.6.1. Role of hydrocarbons	166
5.6.2. Role of sedimentation and bottom currents.....	167

5.6.3. Correlations between topography and spatial distribution of pockmarks	171
5.6.4. Mechanisms of pockmarks formation	173
5.6.4.1. Advancing pockmarks	173
5.6.4.1.1. The ruptured surfaces on downstream side wall	173
5.6.4.1.2. Formation model of advancing pockmarks	174
5.6.4.2. Nested pockmarks	177
5.6.4.2.1. Progradational infill in interaction with topography and potential bottom currents	177
5.6.4.2.2. Formation model of nested pockmarks	178
5.6.4.2.3. Positive high amplitude mounds above nested pockmarks	182
5.6.4.2.4. The limitation for studying the pockmark depositional model in seismic	183
5.6.4.3. Origin of the earliest pockmarks and fluid migration regime	188
5.6.4.3.1. Zigzag pockmark trail 2 above channel complex 2.....	188
5.6.4.3.2. Regular linear pockmark trail 1 above channel complex 1	191
5.6.5. Summary for the chronology of pockmarks formation	194
5.6.6. Implication for petroleum exploration.....	196
5.7. Conclusion	197
CHAPTER 6	201
6.0. Focus fluid flow systems in interplay with geological setting, tectonic structures and stress fields	202
6.1. Abstract.....	202
6.2. Introduction	203
6.2.1. Filamental and linear positive high amplitude anomalies (PHAAs).....	206
6.2.2. Distinction between shallow flat-bottomed depressions and conical pockmarks	207
6.3. Seismic data and methodology	208
6.3.1. Statistic of linear seismic chimneys at different position along polygonal faults	208
6.3.2. Measurements of the depths and diameters of pockmarks and calculation of sidewall inclinations	209
6.4. Structural geology of the study area	209
6.4.1. Report of local geological structures in the studied surveys	209
6.5. Results and interpretations	212
6.5.1. Description and seismic interpretation of fluid venting structures.....	212
6.5.1.1. Linear chimneys and associated high amplitude anomalies (HAAs).....	212
6.5.1.2. Pockmarks	215
6.5.1.3. Distributions of fluid venting structures across different geological settings	217
6.5.1.3.1. Salt-withdrawal Syncline 3 (in hanging wall domain)	217
.....	221
6.5.1.3.2. Salt-withdrawal Syncline 2 (in hanging wall area)	221
.....	225
6.5.1.3.3. Above palaeo-channel complexes and salt-withdrawal Syncline 1 (in hanging wall area)	227
6.5.1.3.4. Normal fault set in the footwall domain.....	230
6.5.1.3.5. Complex evolution of a local fluid venting systems above Syncline 0.....	238
6.5.1.3.6. Honeycomb pockmarks within polygonal fault tier-1	248
.....	250
6.6. Interpretations and discussions.....	251
6.5.1. Significance of linear chimneys within polygonal fault tier-2	251
6.5.1.1. Formation of linear chimneys at polygonal fault locations	251
6.5.1.2. Gas accumulations in the lowest part of polygonal fault footwall	254
6.5.1.3. Propagation of linear hydraulic fracture in hanging wall domain	261
6.5.1.4. Orientation of linear hydraulic fractures in polygonal fault tiers	262
6.5.1.5. Concentrically aligned PHAAs around pockmarks.....	264

6.5.1.6. Influence of stress regime on geometry and alignment of venting features.....	265
6.5.1.7. Additional evidence for the timing of polygonal faulting, linear fractures and fluid venting	266
6.5.2. Relationship between the distribution and orientation of linear venting structures and local tectonic settings	269
6.5.2.1. Fluid migration pathways in the three salt-withdrawal synclines and in the footwall domain	269
6.5.2.2. Linear venting structures in paralleling to first order anisotropic polygonal faults ..	271
6.5.2.3. Linear PHAAs around tectonic faults location in footwall domain	271
6.5.2.4. Occurrences of sub-circular pockmarks and carbonate mounds at tectonic faults in the footwall domain.....	272
6.5.2.5. Orientation of linear fractures above the salt-withdrawal synclines	273
6.5.3. Evolution of a network of linear venting structures to pockmarks fields and the role of varying host lithology.....	274
6.5.3.1. Interpretation of linear fracture networks in hemipelagic-1 unit.....	274
6.5.3.2. Influence of lithology on the different types of fluid venting features.....	277
6.5.3.2.1. Mechanism of linear fracturing in fine-grained sediments.....	277
6.5.3.2.2. Fluid migrations and hydraulic fracturing within debris flow and MTCs.....	278
6.5.3.2.3. Rheology of debris flows and MTC in the study area and the behaviour of hydraulic fractures	279
6.5.3.2.4. Formations of pockmarks at the top surface of MTC-1b and 2.....	285
6.5.3.2.5. Pockmarks in the hemipelagic unit above the MTC sequence.....	285
6.5.3.3. The origin of Honeycomb pockmarks	286
6.6. Conclusions	287
CHAPTER 7	293
7.0. Discussion	294
7. 1. Introduction	294
7.2. Summary on discussed topics.....	294
7.3. Spatial and temporal evolution of fluid venting structures across different geological settings.....	294
7.3.1 Slow to moderate seepage in Middle Miocene above syncline 0.....	295
7.3.2. Moderate to fast seepages between 6.05H–6.25H within the Late Miocene hemipelagic sediments of PF tier-1.....	302
7.3.3. Moderate venting at 5.5H above Anticline 1 and 2.....	304
7.3.4. Moderate to fast venting at 5.3Ma above Anticline 1 and 2	306
7.3.5. Fast vents at the end of Messinian above palaeo channel complex 1, 2 and in Syncline 3	306
7.3.6. Alternation of slow, and moderate to fast venting regime during Pliocene above channel complex 1 and 2.....	308
7.3.7. Slow or moderate venting during Quaternary above channel complex 1 and 2.....	311
7.3.8. A regional slow venting event at the transition period from the Late Pliocene to Early Quaternary above synclines 1, 2, 3 and in the footwall domain.....	314
7.3.9. Slow to moderate seepage during the Quaternary and Holocene above tectonic faults in the footwall domain.....	317
7.4. Implications	318
7.4.1. Origin of gas: biogenic or thermogenic.....	319
7.4.2. Triggering cause of local or regional fluid venting events	321
7.5. Research limitations	323
7.6. Future work	324
7.6.1. Classification of fluid venting structures with ground truthed flux.....	325
7.6.2. Analogue modelling on hydraulic fracturing in different sedimentary prosperities ...	325
7.6.3. Numerical record of analogue model compare to seismic modelling	326

	CHAPTER 8	327
8.0. Conclusions		328
8.1. Chapter 4 conclusion		328
8.2. Chapter 5 conclusion		329
8.3. Chapter 6 conclusion		330
	REFERENCE	332
	Appendix I.....	354
	Appendix II	358
	Appendix III.....	361

List of Abbreviations

AMO	Anaerobic Methane Oxidation
A	Anticline
AAIW	Atlantic Intermediate Water
AUV	Autonomous Underwater Vehicle
BGHSZ	Base Of Gas Hydrate Stability Zone
BC	Benguela Current
BSR	Bottom-Simulating Reflector
CMP	Common Mid-Point
CS	Channel - South
CN	Channel - North
DF	Debris Flow
D	Diapir
EUC	Equatorial Under Current
GHSZ	Gas Hydrate Stability Zone
HD	Hemipelagic Sediments
HAA	High Amplitude Anomaly
H	Horizon
MTC	Mass Transport Complex
MTD	Mass Transport Deposit
MDAC	Methane Derived Authigenic Carbonate
NADW	North Atlantic Deep Water
NHAA	Negative High Amplitude Anomaly
PF	Polygonal Fault
PHAA	Positive High Amplitude Anomaly
ROV	Remotely Operated Vehicle
RMS	Root Mean Square Amplitude
SEG	Society Of Exploration Geophysicists
SECC	South Equatorial Counter Current
SMTZ	Sulphate-Methane Transition Zone
S	Syncline
TS	Turbidite Systems
TWT	Two-Way Travel Time

List of Figures

Chapter 1

Figure 1.1. The three main types of fluid venting structures observed in the study area. They are respectively pockmark (a), chimney (b) and methane-related carbonate (c). These venting structures are illustrated respectively on seismic section (images on left side), two-way-time map (images in middle) and truth grounds (images on right side) from different areas.

10

Figure 1.2. Conceptual model of Foucher et al. (2009) illustrating the internal structure of a seismic-scale gas chimney and the free gas migration inside the chimney. The main chimney is composed by a coalescence of smaller fractures and gas vents.

11

Figure 1.3. Illustration of vertical chimney formation by Løseth et al. (2011). a) Propagation of hydraulic fracture once fluid pressure exceeds the vertical stress plus the tensile strength of overburden sediment. b) The fracture reaches the seabed, resulting in high speed fluid venting. c) A crater forms above the fracture due to high speed fluid expulsion.

13

Figure 1.4. Conceptual model of vertical chimneys and its later development by Moss and Cartwright (2010a). a) Initiation of hydraulic fractures which causes cap rock failure. b) The hydraulic fracture connects to seabed where overburden pressure declines and induces brutal fluid eruption to form a seabed crater. c) Eruptional craters are sealed by sediment depositions, and by repeating stage (b) new generations of craters are formed above the first crater (b).

14

Figure 1.5. Schematic model of gas chimney in association with multiple seabed craters. a) Gas (light grey) below its cap rock (dark grey). b) Once fluid overpressure breaks the cap rock, hydraulic fractures form and allow fluid migration. When gas-filled fractures reach about half way to the seabed, pockmarks start to form on the seabed. c) The closer the hydraulic fracture reaching to the seafloor, the more the pockmarks form. d) Final fluid eruption causes a major crater above the fractured zone once the fractures reach the seafloor.

16

Figure 1.6. Numerical model of fluid migration in two types of sediments by Jain and Juanes (2009). a) Model of fracture opening in fine-grained sediment ($<1\mu\text{m}$); fracture propagation in fine-grained sediment is done by pushing matrix grains apart. b) Fluid migration in coarser-

grained sediment (= 1mm); fluid migrations are mainly done by capillary invasion and no fractures are formed in this case. Blue dots: gas; Brown lines: compressive strengths between each grain; Pink line: locations of grain boundaries collapsing.

17

Figure 1.7. Tensile stresses at fracture (bubble) tips increase with the rise of methane bubble lengths. A conceptual model proposed by Algar et al. (2011). a) Initiation of hydraulic fracturing by bubble rise: difference in tensile stress at the tip and the tail of the bubble is negligible with respect to the internal bubble pressure, the tensile stress can be considered constant along the length of the fracture (bubble). b) As the bubble grows and changes form, the difference of tensile pressure becomes greater between the top and bottom of bubble. c) When the bubble becomes teardrop-shape the tensile stress concentrates at the fracture (bubble) tip, while the tensile stress drops to zero at the fracture (bubble) tail, and compressive stress around the fracture (bubble) trail closes the trail. Red arrows: tensile stress; Blue arrows; compressive stress.

19

Figure 1.8. Chimneys are expressed by narrow vertical zones of seismic pull-up (convex) reflections on profile; taken from Horosal et al. (2009).

21

Figure 1.9. Chimney is expressed by a vertical narrow zone of seismic push down (concave) reflections on profile. Free gas is indicated by letter “G”. Image taken from Hovland et al. (1985).

22

Figure 1.10. Chimneys are characterized by columnar acoustic turbidity zones on seismic; taken from Wood et al. (2002).

23

Figure 1.11. Chimneys are characterized by bright and dim amplitude columns with polarity inversions and high amplitude topmost terminations; taken from Løseth et al. (2010).

24

Figure 1.12. Methane-derived authigenic carbonate (MDAC) chimneys outcrop in Black Sea seafloor. Screen capture from video of “Microbial reefs in the Black Sea”, HERMES project (<http://www.eu-hermes.net/intro.html>) (<http://www.youtube.com/watch?v=P6tORN44X58>). Notice that methane bubbles are coming out from the MDAC chimneys.

26

Figure 1.13. The first reported pockmarks in LaHaye Basin by King and MacLean (1970). a) Pockmark on a 2D seismic profile. b) Plan view of pockmarks (red ellipses) seen on a side-scan sonar backscatter image. Images taken from King and MacLean (1978).

27

Figure 1.14. Conceptual model of a pockmark at different development stages (modified after Hovland, 1982). a) Early stage: fluid migrates potentially via shear strain fissures and induces brutal fluid eruption at the seabed. b) Mature stage: sediment slumping occurred on the pockmark sidewall. c) Final stage: pockmark is buried by sediments and associated with an underlying columnar disturbance.

30

Figure 1.15. The first conceptual model for the vertical evolution of a pockmark succession by Cifci et al. (2002). a) Formation of a first pockmark on the seafloor. b) Sediment fills the pockmark. c) A new pockmark occurred in sediment above the sealed pockmark.

32

Figure 1.16. Illustration shows the depth of sulphate-methane transition zone (SMTZ) as a function of methane flux; modified after Paull and Ussler III (2008). The base of the SMTZ has been pushed upward to the seafloor at the location of high methane flux. Chemosynthetic communities and methane-derived authigenic carbonates developed around the fast seep at the seafloor and in sediment right below. Moving away from the rapid seeping point, methane flux decreases and surface expression of venting disappears. In addition, the amounts of MDAC decline as the depth of SMTZ increases.

34

Figure 1.17. The first calibration between positive high amplitude anomalies on 3D seismic and methane-related carbonates, as illustrated in Cauquil and Adamy (2008). The reported seabed depression occurs in offshore Nigeria and shows a positive high-amplitude anomaly. A survey by ROV indicated that the positive high-amplitude anomalies correspond to chemosynthetic communities living on the hard ground of methane-derived authigenic carbonates. (a) The reported fluid-related depression on a seismic profile. (b) Superposition of amplitude of the depression and seabed dip map. (c) ROV image showing chemosynthetic communities growing on underlying carbonate hard grounds. Images taken from Cauquil and Adamy (2008).

37

Figure 1.18. The first published cartoon that shows a succession of vertically stacked reefs by Hovland (1989). (a) Emplacement of a hydrocarbon-related reef above fluid conduits. (b)

Development of a second generation of reefs above the first one. (c) Burial of the reef succession and infill by hydrocarbons once the overburden is thick enough not being breached.

38

Figure 1.19. The first published conceptual model for the formation of methane-derived authigenic carbonate (MDAC) in association with a pockmark, by Hovland (1987). (a) Methane migration induces shallow depression at the seabed and MDAC precipitation in the sulfate-methane transition zone (SMTZ). (b) Fluid pressure builds up and fractures the MDAC, followed by brutal fluid eruption and generation of a pockmark crater on the seabed. (c) The pockmark becomes buried once fluid venting becomes less intense.

40

Figure 1.20. Schematic model for the formation of methane-related carbonate on the seabed by Mazzini et al. (2006). (a) Slow hydrocarbon seepage initiated the formation of methane-related carbonate on the seafloor. (b) The carbonate grew over time with lateral extensions. (c) Expulsion of overpressured fluid from gas pockets underneath deformed the carbonate slabs.

41

Figure 1.21. Schematic evolutionary model of methane-derived authigenic carbonate (MDAC) formation at the seabed in a pockmark by Mazzini et al. (2006). (a) A pockmark formed by fluid expulsion on the seafloor. (b) Precipitation of MDAC at water-sediment interface, with chemosynthetic organisms developed on it. (c) The MDAC became thicker over time, fluid bypassed the impermeable carbonate, enhancing the lateral growth of the carbonate; as a result the carbonate grows not only vertically but preferentially laterally.

42

Figure 1.22. Diagram showing the relationship between backscatter reflectivity and different types of methane-related carbonates and fauna; modified after Gay et al. (2007).

43

Figure 1.23. Conceptual model on the genetic relationship between gas chimneys, pockmarks, and methane-derived authigenic carbonate (MDAC) by Plaza-Faverola et al. (2011). (a) Genetic relation between gas chimneys and MDAC: i) initiation of a gas chimney above a free gas-bearing layer, in which free gas migrates underneath the base of gas hydrate stability zone (BGHS); ii) a MDAC occurs above the chimney; iii) the carbonate is buried and a new chimney forms above it by step (i). b) Genetic relationship between gas chimneys, pockmarks and MDAC: i) MDAC precipitated at methane seep above a gas chimney; ii) Sediment around the seep was eroded by fluid expulsion and bottom current; a pockmark was formed around the MDAC; iii) The pockmarks and MDAC were buried afterward by overburden sediment; a

new chimney formed above with emplacement of a new pockmark and MDAC at the top by steps (i) and (ii).

44

Figure 1.24. A conceptual model for the formation of an outcrop fossil pockmark and its associated methane-derived authigenic carbonate (MDAC) by Agirrezabala et al. (2013). a) A MDAC was formed by methane oxidation/sulfate reduction at the seep location. A depression i.e. a pockmark is formed by methane seep and by the weight of the MDAC body which induces subsidence in sediment. b) A sandy turbidite is deposited inside the pockmark and the MDAC continues to grow. c) Turbidites are deposited in the pockmark in alternation with clayey drapes; step (b) is repeated until methane migration is deactivated, and the MDAC is sealed by sediment drape.

46

Figure 1.25. Classification of fluid venting structures base on the qualitative fluid flux rate as observed at the seafloor by ROV (Roberts, 2001; Roberts et al., 2006). Key principles of this classification are in accordance with those suggested by other authors in literature.

48

Figure 1.26. Conceptual diagram of this thesis research. The scope of the thesis is defined by the overlap of three principal areas: expression of fluid expulsion, impact of topography, influence of tectonic stress field.

51

Figure 1.27. Block diagram representing the spatial distributions of fluid venting structures in the Neogene-Quaternary interval of the studied seismic block. The themes covered in the core chapters of this thesis are placed in the context of this conceptual framework. These core themes interact at the local and basinal scale are interlinking the research presented in the core chapters.

52

Chapter 2

Figure 2.1. Seismic horizontal resolution. a) Lateral sampling of seismic traces as a function of spacing of hydrophones. b) Fresnel zone A-A' for an energy pulse created at the sea surface (x) and striking a horizontal geological interface at depth Z_0 . c) Reduction in the width of the Fresnel zone after the (post-) migration of seismic data. Modified after Sheriff (2001). The post migration Fresnel zone is one quarter of the dominant wavelength.

56

Figure 2.2. SEG colour convention for the display of seismic traces. Positive impedance contrasts are shown in red. Negative impedance contrasts are shown in black.

59

Figure 2.3. Seismic spectrum of the studied seismic data sets. a) The dominant frequency of the main survey is about 55 – 60Hz in the first second TWT below the seabed. b) The dominant frequency of a high resolution survey is about 70 – 80 Hz in the first second TWT below the seabed.

62

Chapter 3

Figure 3.1. Location of the study area on the Angolan Margin as defined by the two 3D seismic surveys red filled and outlined boxes respectively. The white dashed line defines the outer extremities of the Zaire Fan.

74

Figure 3.2. Regional dip line showing the main structural domains (see coloured bars at base of the figure) and tectono-stratigraphic units on the Angolan margin. The position of the study area with respect to the slope is shown by the red arrow at the top of the Figure.

75

Figure 3.3. Representative seismic section from the 3-D survey (location see Figure. 1) tied to the local stratigraphy (see panels to right of seismic section). The panel at the far right of the Figure shows the vertical distribution of different fluid venting structures. HD: hemipelagic deposits; TS: turbiditic system; SB: sequence boundary; MFS: maximum flooding surface.

77

Figure 3.4. 3D map and map view domain of the study area. Horizon shown is 5.3Ma. White dash-dotted lines show positions of seismic sections shown in Figure 3.5 and 3.6. The red dashed line demarcates the hanging wall-footwall domain boundary.

80

Figure 3.5. Morphology of syncline 0. a) 3D isochron map of horizon 20Ma with dip attributes superimposed. b) Cross section showing the structure of Syncline 0 and surrounding Anticline 1 and Diapir 1. c) Instantaneous phase map of 6H showing a debris flow which is distinguished from background sediments of End Miocene at the location of syncline 0.

81

Figure 3.6. Regional cross sections across salt-related synclines 1, 2 and 3. a) Profile across the footwall domain and the NW corner of the survey, syncline 1 and anticline 1. b) Profile

across the footwall domain, syncline 2, anticline 1 and 2. c) Profile across the hanging wall domain, syncline 3, anticline 2.

82-84

Figure 3.7. Present day ocean current patterns along the Western coast of Africa (modified after Van Bennekom and Berger (1984), Jansen et al. (1984) and Licari and Mackensen (2005)). Topography map of Africa sourced from NASA.

87

Figure 3.8. Ocean water circulation in the Atlantic Ocean and the distribution of water salinity. Values along contour line are salinity with unit in per mille. Modified after Tchernia (1980) in Berger et al. (2002).

89

Chapter 4

Figure 4. 1. Distribution of PHAAs in the study area around Syncline 2 and Diapir 1. a) A 20 ms TWT thick amplitude window above the top boundary of polygonal fault tier shows two types of PHAA: sub-circular and linear. Notice that linear PHAAs follow the trend of polygonal faults. b) A dip horizon shows the locations of the two types of PHAAs coincide with the polygonal fault network and regional faults.

97

Figure 4. 2. Vertical succession of sub-circular PHAAs. a) Cross-section through a “column” of amplitude anomalies, including PHAAs of various morphologies (e.g. reflection 8 & 9, sub-horizontal; reflection 4, mounded; reflection 3, pockmark-like). Its location is depicted on horizon 1 in b) by a green dotted line A. Note also the pockmark at the base (near 6.25 H). The succession is subdivided by a low-reflectivity interval between 5.5 H and 5.2 H. b) 3-D rendering of individual amplitude anomalies within the column (numbered in a)). These high amplitude reflections show: sub-circular depressions associated with PHAAs (horizon 3, 5 to 9); the base of the high amplitude sequence (horizon 1 & 2) is affected by a linear fault, along which PHAAs occur. The stacked, sub-circular depressions (horizon 3 to 5) host sub-circular PHAAs with a central prominent relief, which corresponds to the interpreted vertical zone that is deformed by faults or fractures (represented in dash on a)) in the central of the vertical succession; a mounded PHAA is likely crossed by the interpreted vertical deformed zone (horizon 4).

99

Figure 4.3. Seismic profiles and amplitude maps of numbered horizons showing a single linear conduit originating from the lower tip of a graben in the polygonal fault tier. a) Profiles i and ii are arbitrary lines across and along the axis of the linear anomaly, respectively, and are located in b) with yellow dashed line. The shallow v-shaped and curved reflections 4 correspond to a linear PHAA on horizon 4 in B. b) Horizons of positive reflections that cross the pipe within the polygonal faulting interval (numbered on A): Horizon 1 shows the pull up zone corresponding to the linear lower amplitude area on the base of the polygonal fault tier. Horizon 2 shows that the linear shape is consistent up to (horizon 3) the top of the fault tier; Horizon 4 shows the linear conduit terminates upward into a high amplitude v-shaped reflection with a linear planform. Horizon 5 shows sub-circular furrows at the present day seabed, above the pipes and at the same location (the undulating lines running WSW–ENE are processing artifacts).

101

Figure 4.4. Composite linear PHAAs on profile and amplitude maps. a) linear PHAAs link together above two linear acoustic pipes due to their proximity. Its location is depicted on horizons in b) by blue dotted lines A. b) Horizons that cross the high amplitude reflector above the acoustic pipes, show linear PHAAs (reference points are red tacks): Horizon 1 shows the high amplitude elongate-ring shapes surround the central seep points of linear conduits. Horizons 2, 3, 5 show the disrupted reflections with elongated gaps, and horizon 4 & 6 above which composite linear PHAAs occur with shallow/or no negative relief.

103

Figure 4.5. Stacked up PHAAs below an advancing pockmark, and above the turbidite surface. a) Seismic profile. Its location is showed on horizon 3 in b) by a green dotted line. b) Horizons 1 & 2 (numbered on a) of the high amplitude reflections show a smaller linear PHAA with two segments. These linear PHAAs are stacked below a sub-circular PHAA on horizon 3, which is limited inside a sub-circular depression.

105

Figure 4.6. A polyphased pockmark. a) Profiles i and ii are arbitrary lines across and along the pockmark axis. Note that the incomplete dome-shape in profile i, at reflection 3B is still linked partly with its original reflection, but disconnected on profile ii. b) Amplitude maps of the numbered horizons. Horizon 1 shows an elliptical PHAA which is delimited by two small amplitude dim points in both ends; Horizon 2 shows an elliptical PHAA surrounded by a horseshoe-shaped PHAA; Note that the seep point 1 is still observed with a small dim zone. Horizon 3 shows a hoof-shaped PHAA above the edge of underlying elliptical PHAAs; Horizon 3B shows a dome structure at the pockmark base, with a long gap along its edge from

N to W. Horizon 4 shows a crescentic shaped PHAA above the edge of the dome structure and a surrounding sub-elliptical truncation zone. Horizon 5 shows an asymmetric circular dim zone. Horizon 6 shows an 'almost circular' dim zone. Note the lower amplitude ring shaped feature in the middle of the crater. Horizon 7 shows the sediment cover subsiding asymmetrically above the first seep point location, with a small dim zone in the center. Horizon 8 shows the sediment subsiding asymmetrically.

106

Figure 4.7. Theoretical model for step-wise genesis of polyphased pockmarks (see also Fig. 4. 6a for the numbering scheme of reflections). a) Slow methane seep is expressed by the small methane-related carbonate patches at the site. Fluid escape then bypassed the central carbonate seal and created two seep points (1 and 2 in red). b) The elliptical carbonate patch continued to develop at the central seep. Slow fluid flux at seep 2 bypassed the sealed locations, and fed the new carbonates surrounding the central patch. The small depression at seep point 1 suggests a relatively faster flux. c) Low fluid flux at seep point 2 bypassed the carbonate patches of reflection 1 and 2 and escaped, to form a hoof-shaped PHAA/carbonate above the edge of previous carbonate. d) A less permeable layer, an interpreted carbonate dome, was deposited and covered the seep site during the lower fluid flux period. Overpressure fluid inside the carbonate dome breached the NW internal edge of the dome. e) Fast flux concentrated at seep point 0 where carbonate was unable to form. Fluid at seep 2 continued to by-pass the sealed location and migrated upward to form a crescentic PHAA (horizon 4; Fig. 4. 6b) above the edge of the previous carbonate. f) Sediment deposited above the seepage, during the fluid less active period. Slow methane flux is suggested to interact with the later sedimentation within GSHZ. Gas hydrates veins or layers were formed within the sediment layers, above the seep point and within an elliptical perimeter. g) Horizontal deposits (before their deformation) at reflection 6 suggest a fluid inactive period. Gas hydrate dissociation is probably induced by sealevel fluctuations or erosional event, which is indicated by truncation surface (reflection 6; Fig. 4. 6a). Over pressured, liquefied sediment below the reflection 6 escaped to surface by cutting a crescentic window (horizon 6; Fig. 4. 6b). h) Sediment cover collapsed. Vertical movement of liquefied sediment (brown arrow) left the trace as a dim ring in the center of crater (horizon 6; Fig. 4. 6a). Notice that, the expulsive focus of this pockmark shifted from NW to SE, from above the gap of the dome to above the seep point 0. It is confirmed by the moderate-amplitude ring shape within the crater and above the seep point 0. i) Later sedimentation sealed the whole crater as the fluid flux waned and died. It is suggested by the geometries of horizon 7 and 8.

116-117

Figure 4.8. A hypothetical combined vertical succession for the evolution of different venting structures, depending on the dynamics of venting. a) Slow seeps at fault locations are characterized by linear PHAAs (interpreted carbonates). b) Slow to moderate seeps are characterized by sub-circular PHAAs. C1) Moderated seeps often generate sub-circular like depressions with gently dipping base. C2) Fast seeps are represented by circular crater or characterized by absences of PHAAs. d) Constant but less active fluids interact with later sedimentation to form hydrate within sediment layers in GHSZ. Finally, e) gas hydrate dissociations induce sediment liquefactions and f) expulsion to create collapsed depressions.

120

Chapter 5

Figure 5.1. Evolution of palaeo channel complex across the different structural domains of the study area. The upstream side of the channel complex (opaque green color) is defined as the segment located above syncline 1 in the upper part of the hanging wall domain of the major growth fault. The lower part of channel complex located above the anticline and on the slope to the SW is defined as the downstream part. See location in fig. 5.5.

129

Figure 5.2. Vertically stacked pockmark arrays. a) The two arrays (P1) occur above a basal/earliest pockmark (P0) with negative high amplitude. b) Amplitude map of Lower Pliocene across the base of vertically stacked pockmark (P1) and the top of earliest pockmarks (P0).

131

Figure. 5.3. Advancing pockmark arrays. a) Section view of advancing pockmark arrays, which occur above the earliest pockmarks P0, P1 and channel complex 1. Individual layers within the arrays that have been mapped were labelled as "h" followed by a number. Their 3D map views are shown in fig. 5.6. b) Illuminated TWT map of horizon 5.3Ma showing pockmark trail 1; location of the advancing pockmark array mapped on fig. 5.6 is indicated by a red arrow. Red dots indicate the centre of each crater.

132

Figure 5.4. Nested pockmark. a) and b) are arbitrary lines along and across major axis of the pockmark. c) Two-way time map of the initial crater (basal pockmark) at 5.3Ma. d) Dip map of the top of a nested pockmark infill showing a combination of radial and concentric patterns. e) Two-way time map of the convex positive high amplitude reflection at the top of the pockmark.

Figure 5.5. Structural maps showing the main geological features of the study area. a) Key horizon 5.3 Ma shows two pockmark trails and the distribution of different types of pockmarks. Two-way time map is overlain by semi-transparent dip map. The direction of pockmark infill migration is indicated by symbols on this map. b) Two-way time map of horizon of 6 H with dip overlain. It shows the two channel complexes underlying the two pockmark trails. A: Anticline; D: Diapir; S: Syncline; C N: North Channel; C S: South Channel.

Figure 5.6. Two-way time maps of individual layers within the advancing pockmark array in fig. 5.3. They are labelled as "h" followed by a number. The apex of each layer is aligned with its position on the seismic section.

Figure 5.7. Pockmark trail 1 above channel complex 1. This pockmark trail is composed by vertically stacked pockmark arrays and advancing pockmark arrays lined up along the axis of the underlying channel. a) Advancing pockmark trail in the downstream side of this channel complex. b) Vertically stacked pockmarks arrays above sedimentary undulations in the upstream side of the channel complex. Notice that the major growth faults are located in the right hand side of this profile. Black arrows indicate high-amplitude bright spot chimneys; each undulation is labelled with a number. c) Seismic section parallel to the axis of the channel complex, intersecting the edge of pockmark trail 1; it shows sedimentary undulations above the buried channel. The numbers label each undulation, like in 5.7.b above. d) Block diagrams showing the geometry of individual sedimentary undulations (not scaled).

Figure 5.8. Advancing pockmark array composed by three smaller-scale arrays. a) Section along the direction of infill migrations; blue dots indicate the lowest and topmost apexes of each secondary array. b) Seabed dip map showing that the topmost depression of the array is expressed by a small shallow depression at the present day seabed. c) Amplitude map of 5.3 Ma showing the topmost depression in the lowest array.

Figure 5.9. Elongate morphology of the basal craters of nested pockmarks with major axis parallel to bathymetric contours on the flanks of the syncline. a) Amplitude map of horizon 5.5 H superposed with its bathymetric contours. This horizon is located between the top surface of channel complex 2 and horizon 5.3 Ma which is truncated by nested pockmarks. It runs across the middle level of nested pockmarks and shows the elongate geometry of the

basal craters. b) Superposition of two-way time map and dip map of 5.3 Ma (grey to pale yellow background), and the first infill layer of nested pockmarks. This infill layer shows a preferential orientation toward the syncline. For the stratigraphic location of this layer see fig. 5.11a.

143-144

Figure 5.10. Vertical organisation and age of nested pockmark infill. a) Arbitrary line across the pockmark of fig. 5.4, oblique to the one that is already figured. The first infill layer extends in far field on the syncline flank, towards syncline 1. b) Correlation between the infill of basal craters (earliest pockmarks) underneath nested pockmarks (left) and advancing pockmark arrays (right and extreme left).

145

Figure 5.11. Pockmark trail 2 above channel complex 2, composed by nested pockmarks in the upstream side and advancing pockmark arrays in the downstream side. Channel complex 2 results from the convergence of two individual channels, the north channel (CN) and the south channel (CS). a) Nested pockmarks are located above CN and above tectonic (compensation) faults at anticline 1. b) Chimney structure expressed by vertically stacked seismic amplitude anomalies on the far upstream side of the channel complex. c) Advancing pockmark arrays above CS on hanging wall slope.

146-147

Figure 5.12. Cross-plot of height versus total migration distance for advancing pockmark arrays.

151

Figure 5.13. Sketch showing the regional topography and the location of two pockmark trails in and around syncline 1; this is a schematic interpretation of fig. 5.5. Vertically stacked pockmark arrays are lined up above channel complex 1 in the upper part of the hanging wall domain. Nested pockmarks are located above the levees the south channel (CS), which joins the north channel (CN) on the hanging wall slope. Advancing pockmark alignments are found above both channel complexes on the hanging wall slope.

152

Figure. 5.14. Negative high amplitude anomalies at 5.3 Ma located above patches of reversed polarity at the top of channel complex 1. a) A cross section in the downstream side of channel complex 1 showing negative high amplitude anomalies (NHAAs) and polarity reversal above and at the channel surface (horizon 6H). b) Negative high amplitude anomalies showing elongate and rounded shapes on the amplitude map of horizon 5.3 Ma (indicated by warm colours). Blue contours indicate the location of polarity reversals below the NHAAs. c) Areas

of polarity reversal correspond to the black patches on this amplitude map of horizon 6H, they also show elongate and rounded shapes.

155

Figure 5.15. Interpreted gas chimneys rooting into the levees of channel complex 2. a) Amplitude map of the present day seabed. Two chimneys terminate upward into shallow depressions at the present day seabed. These shallow depressions show linear and circular shapes and are associated with positive high amplitude anomalies which have been interpreted previously as methane-related carbonates or possibly in association with gas hydrate. b) A chimney above a levee terminating up into a depressed elongate positive high amplitude anomaly.

156

Figure 5.16. Bottom-simulating reflector (BSR, blue dot line) above sedimentary undulations and above the upstream side of channel complex 1. The BSR marks the top of a series of negative high amplitude reflections underneath, and cuts across the lowest part of vertically stacked pockmark arrays.

157

Figure 5.17. Mounded reflection with positive high amplitude at the top of a chimney that crosses the margin of a nested pockmark. Cross sections in (a) and (b) show that this mounded structure is associated with a shallow depression at the present day seabed, and (c) its top partly crops out on the bottom of the shallow depression. This positive high amplitude mound shows an elongate shape on the amplitude map of horizon 2.5 Ma (d); it has been interpreted as methanogenic carbonate mound (Chapter 4). (e) Two-way time map of horizon 5.3Ma with dip overlain. It shows the morphology of basal crater (earliest pockmark) of the nested pockmark.

158

Figure 5.18. Set of seismic attribute maps in the syncline 1 area, showing different fluid-related effects that occur at different stratigraphic levels i.e. above and underneath the two pockmark trails. a) instantaneous phase map of the two channel complexes showing different dominant phases of maximum amplitude energy. The phase rotation are indicated by the colour on the map; white: $\pm 180^\circ$; red: -90° ; blue: 0° ; green: 90° (for interpretation see section 5.6.1); white areas on the map have been clipped and do not indicate any instantaneous phase values. b) Dip map of horizon 5.3 Ma showing the basal craters/earliest pockmarks of the different pockmark arrays. c) Amplitude map of 2.5 Ma zoomed on the upstream area of the two channel complexes (location indicated by red boxes on (b) and (d)). This map shows positive high amplitude anomalies above the pockmarks. d) Seabed

amplitude map with the dip overlain. Positive high amplitude anomalies are observed at about the same locations as on horizon 2.5 Ma, above pockmarks in the upstream side of the two channel complexes. e) Instantaneous phase map of the two channel complexes in superposition with dip map of 5.3 Ma.

159-161

Figure 5.19. Zoon in of seismic attribute maps in figure 5.18; close-up view of channel complex 2. a) Seismic attribute map of instantaneous phase of channel complex 2 (individual channel N and S) shows different dominant phases of maximum amplitude energy. b) Dip map of 5.3 Ma shows the basal craters/earliest pockmarks of the pockmark trail 2. c) Seismic attribute map of instantaneous phases of the channel complex 2 in superposition with dip map of 5.3 Ma. d) Positive high amplitude anomalies with negative reliefs above the nested pockmarks in the upstream side of channel S. Top left corner: zoon in of amplitude map of 2.5 Ma of fig. 5.18c; Background: shallow depressions in associated with positive high amplitude anomalies which stack vertically with these ones of 2.5Ma and above nested pockmarks in upstream side.

163-164

Figure 5.20. Conceptual diagram showing the morphology of pockmark arrays as a function of the energy of bottom currents and the sedimentation rate. The regional dip of the strata in areas where pockmarks occur is indicated.

172

Figure 5.21. Model for the development of advancing pockmarks. a) First phase of infill above the last earliest pockmark P1. b) Resuspension of fine-grained sediment on the downstream pockmarks sidewall by vortex and seepage. A horseshoe-shaped truncated area is formed. c) Infill phase during time of reduced bottom-water current activity, horseshoe-shaped erosional patch is filled by the new deposits. d) a new layer is deposited and followed by a truncation episode. e) Lateral migration by the creation of reactivation pockmarks which truncate the downslope flank of the preceding infill sequence.

176

Figure 5.22. Model for the development of nested pockmarks. In the first step, sediment is deposited by the secondary branch of currents (cavity flows) which is separated from the main branch. Two possible flow models for the secondary currents, which are suggest to deposit sediment in the initial depression (earliest pockmarks): the first one is depression-parallel streaming (a) and the second one is vortex flow (b) Infill sediment was either transported by (a) the laminar, depression-parallel flow from the upstream side of the pockmark, or by (b) vortex and backward flow from the downstream margin of the pockmark; the coarser

sediment grains are deposited first at the bottom of the depression. c) During periods of reduced bottom current activity, finer-grained sediment settles from suspension draping the previous infill deposition by hemipelagites. d) Stage (a) repeated after a new layer is deposited. e) Stage (b) repeated. f) Regardless of the depositional process in the previous stage (d or e), the outcome for the infill structure is suggested to be the same. g) During periods of increased bottom current activity, vortices form on the downstream slope of pockmark, inducing erosion. This is evidenced by reflections truncation on the downstream sidewall of nested pockmarks, as shown in figure 5.4. During the erosional event, unconsolidated fine-grained sediment was likely re-suspended by vortices; stage (c) repeated when the bottom current became less active. The pockmark continued to fill (i) and (j) by the same process as in stage (d) and (e) and (c) until all accommodation space was finally be used up. k) The nested pockmark was thus formed, and was sealed by hemipelagic deposits; it showed erosional characters on certain infill layers in the downstream sidewall. l) Formation of methane-related carbonate patches with convex structure which is possibly formed directly above the nested pockmark at the seabed. Hemipelagites deposited only around the methane ebullition. j) The whole pockmark system was buried by hemipelagic sediment afterward.

179-180

Figure 5.23 Alternative interpretations for the development of the top reflection of nested pockmarks. Notice that hemipelagites deposited also in the far field area of the nested pockmark during bottom current less active period. Steps (a, b, d, e, f) are the same as in fig. 5.22. Steps (c, g, h, i, j, k) with hemipelagites drapped in the far field surrounding the pockmark. (l) Formation of the methane-related diagenetic carbonate patches with convex structure which cross cuts the top of infill sequence and the coeval hemipelagites.

185-186

Figure 5.24. Conceptual model for hydrocarbon migration along channel complex 2 and timing of pockmark formation; line drawing of the seismic section in fig. 5.9. a) Nested pockmarks above the north channel (CN) in syncline 1. b) Advancing pockmark arrays located above the individual south channel (CS) on the hanging wall slope. Interpreted fluid migration pathways are indicated by red arrows. Sediment thickness within the interval hosting the earliest pockmarks (basal craters) is indicated on the interpreted sections.

187

Figure 5.25. Timing of occurrences of vertically stacked fluid venting structures along the upstream side of channel complex 2 (north channel) and further to the NE. a) Up: correlation between nested pockmarks, chimneys and the associated positive high amplitude anomalies (interpreted methane-related carbonates); Down: Stratigraphic distribution of these venting

structures along the section in fig. 5.11. b) Summary of the interpreted variations of fluid venting intensity over time, as suggested by the different types of venting structures.

189

Figure 5.26. Timing for the formation of different types of fluid venting structures along channel complex 1; interpretation of seismic section in fig. 5.1 and fig. 5.7. Interpreted fluid migration pathways are indicated by red arrows. Thickness of sediment within the host interval of earliest pockmarks (basal craters), between horizon 5.3 Ma and top surface of channels are indicated on the interpreted section.

192

Chapter 6

Figure 6.1. Distribution of fluid venting structures within the interval of Holocene and End Miocene in the 3D seismic survey. Each studied fluid venting structures are represented by a symbol and are shown on the key horizon of 5.2Ma dip map. S: Syncline; A: Anticline, D: Diapir.

211

Figure 6.2. Examples of chimneys intersecting and emanating different parts of PF's. The plan for dimensions of the chimney are shown on maps below each section. a) Zoomed seismic sections intersecting the short (left panel) and long (right panel) axis of linear chimneys. Note that the chimney intersects the apex of the underlying PF graben as illustrated in cartoon below. Horizons labelled 1-5 are amplitude and dip maps showing the plan form geometry of the chimney at different stratigraphic levels (see labelled on sections in a). b) Seismic section showing chimney intersecting the basal portion of a conjugate PF. Zoomed seismic sections below intersect the long axis of chimneys 1 and 2 in b. c) Zoomed seismic section showing linear chimney emanating from basal tip of single PF (see underlying map for location). d) Zoomed seismic section showing bright amplitude column intersecting centre of conjugate PF graben. e) Zoomed seismic section showing chimney intersecting PF horst block. f) Zoomed seismic section showing chimney intersecting the centre of a rotated fault block. g) Zoomed seismic section showing chimney terminating abruptly upwards against a PF plane. h) Zoomed seismic section showing chimney intersecting middle portion of PF plane. i) Zoomed seismic section showing chimney emanating from a deep-seated tectonic fault.

213-214

Figure 6.3. Pie charts showing the percentage of chimneys intersecting or emanating from different parts of fault planes or adjacent fault blocks. a) Percentages based on all 209 chimneys identified within PF tier 2 (statistic including chimneys intersected PFs that were linked with underneath tectonic faults). b) Percentages based on all chimneys identified in PF tier 2 which intersect PFs only (sample number = 171) and which were not connecting with any underlying tectonic fault. The position of the chimney-fault intersection are illustrated with cartoons in each pie segment. The type chimney in each case is shown by combination pattern of red and black bold lines (see key at the bottom middle of figure).

216

Figure 6.4. Distribution and alignment of fluid venting structures and high amplitude anomalies in withdrawal syncline 3. a) Dip and amplitude attribute map of the basal surface of PF tier 2 showing the preferential alignment of linear chimneys parallel to the strikes of aligned PF arrays above withdrawal syncline 3. Pink arrows indicate chimneys that have been shown in fig. 6.2c, g and f.. b) Amplitude map of Horizon 6.27H c. 100 ms below the basal surface of Tier 2 showing preferred orientations of linear chimneys which are parallel to the strikes of extensional concentric faults (tectonic and PFs) around withdrawal syncline 3. c) Zoomed seismic section showing emanating from the tectonic concentric faults on the western flank of withdrawal syncline 3 (see red dotted line on maps a and b for location). d) Amplitude extraction of a window between top and base of PF tier 2 showing kilometre scale accumulations of negative high-amplitudes within withdrawal syncline 3. The region of negative high amplitudes are bound by tectonic concentric faults intersecting the edge of the withdrawal syncline as shown by green dot and dashed lines. Also note the presence of several pocks as denoted by black arrows. e) Zoom of negative high-amplitude accumulation on the eastern flank of withdrawal syncline (see light blue box on map d). f) Zoomed seismic section across PF tier 2 showing negative high amplitude accumulations (see location on map in e). g) Dip map of the sea bed showing circular and elongate shallow depressions above the region of negative high amplitude shown on map d. Locations of depressions are denoted by white arrows. Some depressions occur above advancing pockmarks (see green arrow and compare with section in h). h) N-S Seismic section intersecting withdrawal Syncline 3 showing advancing pocks within PF tier 2. Location of shallow sea bed depression is shown by the green arrow. Stratigraphy dip and thicken toward the centre of the withdrawal syncline.

218-219

Figure 6.5. Maps showing the relationship and alignment of linear chimneys parallel to polygonal faults in withdrawal syncline 2. a) Amplitude extraction of a window in the upper portion of PF tier 2 showing linear PHAAs (red = positive amplitude). b) Seismic section

intersecting linear chimneys showing predominantly containing positive bright spots at the top and negative bright spots at the bottom. Amplitude windows in a and c are indicated by brackets at the left of the section. c) Amplitude extraction of a window in the lower portion of PF tier 2 extracted onto a dip map of the basal tier surface showing negative amplitude anomalies associated with chimneys (red = negative amplitude).

222

Figure 6.6. a) Coherence attribute extracted onto the basal surface of PF tier 2 showing the geometry and preferential alignment of PF's in withdrawal syncline 2 and around Diapirs 1 and 2. b-d) Zooms of map in (a). Locations of maps are shown by color squares.

223

Figure 6.7. a) Amplitude map of horizon 5.5H c. 40 ms beneath PF tier 2 showing shallow elongate depressions parallel to extensional faults in withdrawal syncline 2. b) Seismic sections I-III intersecting shallow elongate depressions, linear chimneys and PHAAs (line locations annotated on map in (a); green arrow indicates the location of an overlying linear PHAA; pink arrow indicates the possible downward termination of the chimney. Lines IV and V are zooms of the shallow depressions on 5.5H. Note that PHAAs, linear chimneys and shallow depressions are stacked vertically on lines I and III. Also note that the basal tips of PFs on line V terminate at above the edge of shallow depressions on 5.5H. c) Dip map of the basal tier surface of PF tier 2 overlain on the amplitude map of horizon 5.5H. d) Dip map of basal tier surface of PF tier 2 draped onto the amplitude map of horizon 2.5H c. 10 ms above tier 2. Only high dip values are shown on the overlay maps in b and c in order to illustrate the PF pattern. Note that the shallow depression on 5.5H are bound by PF cells and that linear PHAAs which occur directly above them are parallel to PF strikes (see green arrow on map d). e) Dip map of the sea bed showing shallow elongate depressions above linear PHAAs which are denoted by orange dashed lines.

225

Figure 6.8. Maps showing variations in the aspect ratio of shallow depressions with respect to proximity to salt diapirs and withdrawal basins. a) Amplitude of horizon 5.5H showing circular shallow depressions above Anticline 2 as denoted by black arrows. Strikes of normal faults in the anticline crest indicate the orientation of the fold axis. b) Amplitude map of horizon 5.5H c. 40 ms beneath PF tier 2, c) Zoom of map in map a centred on the SW flank of Diapir 2 showing linear shallow depressions between radial faults.

226

Figure 6.9 Relationship and geometry between linear PHAAs and chimneys, pockmarks and concentric faults. a) Amplitude extraction from a window of the lower part of PF tier 2. b)

Amplitude extraction from a window of the upper part of PF tier 2 (interval used for amplitude extractions are shown on underlying seismic sections d and e). c) Amplitude map of horizon 2.5H, d-e) Zoomed seismic sections across and around the edge of the pockmark craters respectively and showing overlying PHAAs and chimneys. Line locations are shown on map (a) and (b). Cartoon between (d) and (e) shows a simplified cross section and map interpretation showing the concentric alignment of PHAAs parallel to concentrically aligned PF around and above a pockmark crater. f) Zoomed seismic section across linear PHAAs branching away from the pockmark edge. g) 3D view of a dip map of the basal tier surface of Tier 2 (horizon 5.3H). Superimposed are the 3D accumulations of high amplitudes from the pockmark fill sequence and overlying chimneys. h) Plan form view of 3D map in (g). Chimneys defined by regions of high dip show that they are aligned parallel to PHAAs. i) High amplitudes (red patches) from the seabed horizon draped on a dip map of the sea bed. j) Dip map of the sea bed with high amplitudes (red patches) from horizon 5.5H and high dip values (short blue lineaments) from horizon 5.3 H draped on top. Note that PHAAs have the same plan form geometry as overlying shallow depressions.

228-229

Figure 6.10. Seismic attribute maps showing the spatial distribution of different types of fluid venting structures in the northern corner of the footwall domain (see Fig 6.1 for location of footwall domain). a) Amplitude extraction from a window in the upper part of PF tier 2. The traces of tectonic faults which intersect the interval are shown by light blue dashed lines. b) Amplitude extraction from a window between the seabed to 40 ms below. Red circles show the locations of vertically stacked pockmarks and/or depressions. c) Amplitude map of horizon 2.5H. d) Dip map of the seabed showing shallow depressions above the upper tips of tectonics faults which tip out close to the seafloor.

231

Figure 6.11. a) Seismic section showing vertically stacked pockmarks and depressions in the footwall domain (see line and map location on Figure 6.10b). b) Dip map of horizon 2.5H at the top of PF tier 2.

232

Figure 6.12. Association of linear PHAAs with tectonic faults in the footwall domain. a) Amplitude extraction from a window between the seabed and the top surface of PF tier 2. The zoomed map shows hook-shaped PHAAs in the hangingwall of a tectonic fault “X”. Note that the anomalies have an orthogonal intersection with the tectonic fault. b) Dip map of the top surface of PF tier 2, c) High amplitude from the amplitude window in a draped over the dip map in b showing PFs and PHAAs perpendicular to a tectonic fault cutting the PF tier (see

zoomed map to the right of the figure). The transparent green area on maps in b and c denotes a region of isotropic arrangements of PFs. d) Seismic section intersecting polygonal faults which are in the hangingwall of and orthogonal to a deep-seated tectonic fault. The location of the line is denoted by the red dashed line on maps a-c. The planes of tectonic faults and polygonal faults are interpreted with a light blue dashed line on the section in d. The intersection of the tectonic fault with basal surface of Tier 2 is shown by a dark blue filled circle on map a-d. Vertical blue arrows show the location of PHAAs. The inset and zoomed seismic section shows a PHAA above the graben of a conjugate PF pair. e) Seismic section showing a positive high-amplitude carbonate mound above the upper tip of a deep-seated tectonic fault. f) Dip-amplitude overlay map of the sea bed showing shallow depressions on the sea floor. Some of these depressions occur above PHAAs hosted in the immediately underlying Quaternary sediments (compare maps a and f). g) Amplitude map of horizon 6.27H showing the relationship between burial turbidites and shallow seabed depressions (brown dot contours). h) Elongate zone of coalescence depressions. Maps i & ii are zooms of map f. Cross sections iii – v intersect the seabed depressions and PHAAs and show that they occur above a deep-seated tectonic fault (see line locations on maps i & ii. i) Seismic section across sea bed depressions shown on map f. Note that seabed depressions occur above chimneys which emanate from the upper tips of tectonics faults.

233-235

Figure 6.13. Association of carbonate mounds with deep-seated tectonic faults in the NE part of the footwall domain. a) Seismic section showing positive high-amplitude mounds above deep-seated tectonic faults. Mounds are shown by blue arrows. The pink arrows show the location of a shallow seabed depression above a deep-seated tectonic fault. b) Amplitude extraction of the Quaternary sediments showing the distribution of PHAAs. The high amplitude area to the right of the map as defined by the white opaque area is a result of local erosion of a footwall block rather than being related to fluid flow. c) Dip map of the sea bed showing shallow seabed depressions. Note they occur directly above carbonate mounds as indicated by blue arrows. Depressions on the upthrown blocks are indicated by orange arrows and associated with deep root faults. d) High amplitudes from map in (b) draped over the dip map in (c).

237

Figure 6.14. Complex venting systems in Syncline 0. a) Seismic section intersecting the West flank of Diapir 1 and Syncline 0 showing vertically stacked pockmarks and shallow depressions (see green arrows). The stacked pockmarks and depressions occur above a kilometre scale negative high amplitude accumulation (see MTC0a). b) Seismic section

orthogonal to the stacked pockmark system labelled by the green arrow 3 on section a. The negative high-amplitude anomaly on section b is shown by the blue arrow and is high lined by green dot line. c) Seismic section showing negative reliefs below positive high amplitude shallow depressions; the negative reliefs are surrounding by black dot line.. The location of the line can be found on Figure 6.15e.

239

Figure 6.15. Amplitude maps showing variations in the evolution in the distribution and geometry of fluid venting structures during the 5.75H – 12Ma the Late Miocene. a) Deepest linear negative high amplitude accumulation. b) Grooves on the top of MTC0b. c) PHAA linear network within the hemipelagic unit-1. d) PHAA linear network at the top of hemipelagic unit-1. e) Elongate-to-oval shaped anomalies in the Debris Flow 1a and quasi absent of linear anomalies. f) Quasi absent of high amplitude anomalies at the base of MTC 1b. g) Elongate depressions and few circular craters on the top surface of MTC 1b. h) Circular craters at the top surface of MTC2. i) Honeycomb pockmark field on the basal horizon of PF tier-1, and zone in of the pockmarks. j) The only pockmark remain at the top horizon of PF tier-1. k) The debris flow in End Miocene hemipelagites in syncline 0. Note changes in amplitude polarity on colour scales across figs (a), (c) and (h). The dote line with NE-SW direction on each map indicates the location of the seismic section in fig. 6.14.

240

Figure 6.16. Relationship between dominant seismic facies and the geometry of a network of linear high amplitude anomalies in syncline 0. a) Dip map of horizon 11.2H showing morphology of a network of linear anomalies. b) Amplitude map of horizon 11.2H. c) Instantaneous phase map of horizon 11.2H. The map show the degrees of the dominant phase of maximum amplitudes. Different phases correspond to different magnitudes of seismic hardness of the sediments. The blue and red regions on the instantaneous phase map are directly above the deepest and earliest negative high-amplitude accumulations located at horizon MTC0a (primary axis is denoted with a dashed black line).

242

Figure 6.17. Relationship between dominant seismic facies and the geometry of a network of linear high amplitude anomalies in syncline 0. a) Dip map of horizon 10.55 H showing morphology of a network of linear anomalies. b) Amplitude map of horizon 10.55H. c) Instantaneous phase map of horizon 10.55H. The map show the degrees of the dominant phase of maximum amplitudes. Different phases correspond to different magnitudes of seismic hardness of the sediments. The blue and red regions on the instantaneous phase map

are directly above the deepest and earliest negative high-amplitude accumulations located at horizon MTC0a (primary axis is denoted with a dashed black line).

244

Figure 6.18. Elongate-to-oval depressions occur above linear high amplitude network and are observed in DF-1a in location of syncline 0. a) Dip and amplitude overlay map of horizon Debris Flow-1a showing the morphology of shallow depressions which are indicated by green arrows. The depressions occur above the network of linear anomalies which are hosted in the units beneath horizon hemipelagic 1. b) Zoom section of map in a showing morphology of elongate to oval shaped amplitude anomalies.

245

Figure 6.19. Relationship between dominant seismic facies and the distribution of honeycomb pockmarks in syncline 0. a-c) Amplitude, instantaneous phase and dip map of horizon 6.25H respectively. Note that the area containing honeycomb pockmarks corresponds to a red area on the instantaneous phase map which equals -90 degrees. This equates to soft phased horizons. The location of the zoomed inset map on (c) is denoted by the blue box.

247

Figure 6.20. Statistical analysis of pockmark dimensions, crater depth and flank inclination. a) Aspect ratio of honeycomb pockmarks (blue square) and sub-circular pockmark depressions (pink square) on horizon 6.25H near the base of PF tier 1. b) Graph showing the relationship between the depth and sidewall inclination of pockmark craters and depressions. Note that honeycomb pockmarks and sub-circular pockmarks fall into two distinct groups.

250

Figure 6.21. A model of fluid migration within polygonal fault tier base on the interpretation of seismic images. Fluid migration via vertical fractures which initiated in the lower part of PF footwall and propagated in PF hanging wall. Cartoon not to scale.

253

Figure 6.22. a) Diagram showing the magnitude of shear straining of the rocks around a normal fault (taken from Welch et al, 2009). b) Displacement of horizontal beds by a normal fault (figure taken from Barnett et al., 1987). c) Regions of relative extension and compression of the rocks around a normal fault (figure taken from Barnett et al., 1987).

256

Figure 6.23. Conceptual mode for the migration of free-gas into the permeable layer at the bottom of polygonal fault tier 2. Cartoon not to scale.

257

Figure 6.24 Conceptual model illustrating possible mechanism to allow gas migration into an intra-tier permeable bed from an underlying carrier bed. Note that there is an impermeable layer in the PF graben and also that the certain parts of the PF plane are impermeable as shown by the bold blue tracing on the fault plane. a-b) Cases where the carrier bed occurs at the base of a polygonal fault tier. In (a) gas migrates into the overlying permeable layer when it is juxtaposed against the carrier bed. In (b) gas migrated into the permeable layer via a permeable polygonal fault plane. c) Case where the carrier bed occurs beneath the basal tier surface of the PF tier. In C first-order PF's (i.e. those which have propagated under the influence of tectonic stresses) have propagated beneath the regional tier surface and have intersected the carrier bed. d) In the last stage the overpressure increases enough to breach the seal provided by the overlying impermeable layer and gas migrates vertically upward out of the top of the conjugate PF graben.

260

Figure 6.25. Conceptual model showing the migration pathway of methane gas along deep-seated tectonic faults into a shallow interval deformed by a polygonal fault system. Notice that negative bright spots are confined to the interval beneath the Intra-Pliocene horizon and that PHAAs generally occur above the top surface of the polygonal tier. Cartoon not to scale.

270

Figure 6.26. Cartoon summarising the evolution of complex venting systems in syncline 0. a is the oldest stage and f is the most recent stage. a) Formation of linear negative high amplitude accumulation. b) Formation of linear PHAA network. c) Development of linear PHAA network. d) Formation of elongate-oval shaped depressions. e) Formation of vertically stacked craters. f) Formation of honeycomb pockmark.

275

Figure 6.27. Plan form evolution of small linear depressions above fractures (stage 1) to larger hybrid linear-elongate depressions during lateral expansion of fluid, which is indicated by black arrows (stage 2). Following this fluid continued to migrate vertically (stage 3). An elongate shallow depression formed when fluid pressure was strong enough to induce fluid expulsion at the surface of the debris flow (stage 4).

282

Figure 6.28. Conceptual model for the fluid migration pathway or fracturing within an MTC unit. Fractures or pathways are strongly influenced by clasts and grains. Note that fractures deviated around or stop at grain contacts.

284

Chapitre 7

Figure 7.1. Block diagram of the study area showing the situation at the end of the middle Miocene, with the two turbidite channel complexes deposited during the early and middle Miocene (20 to 12 Ma).

296

Figure 7.2. Fluid venting structures and venting intensities on the palaeo seafloor at the end of the middle Miocene.

297

Figure 7.3. Fluid venting structures and venting intensities on the palaeo seafloor at the beginning of the late Miocene.

299

Figure 7.4. Fluid venting structures and venting intensities on the palaeo seafloor of the middle Messinian.

301

Figure 7.5. Fluid venting structures and venting intensities on the palaeo seafloor at the beginning of the late Messinian.

303

Figure 7.6. Fluid venting structures and venting intensities on the palaeo seafloor in the latest Messinian.

305

Figure 7.7. Fluid venting structures and venting intensities on the palaeo seafloor at the end of the Messinian.

307

Figure 7.8. Fluid venting structures and venting intensities on the palaeo seafloor during Early to Middle Pliocene.

309

Figure 7.9. Fluid venting structures and venting intensities on the palaeo seafloor during Middle to Late Pliocene.

312

Figure 7.10. Fluid venting structures and venting intensities on the palaeo seafloor during Early Quaternary.

313

Figure 7.11. Fluid venting structures and venting intensities on the palaeo seafloor in Intra-Quaternary.

315

Lists of Tables

Table	Description	Page
Table 3.1.	Subdivision of sediment units in the study interval.	79
Table 5.1.	Different types of crater and their signification toward fluid flow. Interpreted fluid venting intensity in terms of the size and depth of fluid expulsion crater.	193
Table 6.1.	Stratigraphic distributions of fluid venting structures in different geological settings.	210

Appendix Tables

Table	Description	Page
Table A2.1	Geometrical parameters of earliest pockmarks (basal craters). Yellow filled boxes indicate Advancing pockmarks, Pale yellow boxes indicate Nesting pockmarks. White filled boxes indicate normal pockmarks. In the location column S = Syncline, C = Channel complex, D = Diapir, TSE = Topographic high in SE.	359-360
Table A3.1	Measurements of the aspect ratio (column 5) and inclinations of honeycomb pockmark or circular pockmark sidewalls along short (Columns 6-9) and long (columns 10-12) plan form axes. Blue filled boxes indicate circular pockmarks L_s = Short axis, L_L = Long axis. The inclination measurements were based on 3 different velocity values as indicated in row 2. LD = Linear Depression	362
Table A3.2	Number of chimneys which emanate or intersect different parts of polygonal and tectonic faults in different parts of the study area.	363

Appendix Figures

Figure	Description	Page
Figure A1.1.	A PHAA that has been drilled through shows high gamma ray value and low rate of penetration. Sediment from this interval of borehole correspond alternation of shale layers and methane-derived carbonate layers.	353
Figure A.1.2.	Comparison of lithology between the interval of PHAA in the well log and a seep carbonate outcrop in SE France.	353

Abstract

Fluid venting structures are used to evaluate fluid migration in the subsurface and vertical changes in their morphology reflect variations in the intensity of fluid leakage through time. This research uses high-resolution 3D seismic data from the Lower Congo Basin offshore Angola to analyse complex assemblages of vertically-stacked fluid venting systems in the Middle Miocene to Holocene succession.

Individual fluid-venting structures that form part of vertical venting systems include conical pockmarks, fluid related shallow depressions with flat bottom, chimney structures and positive high amplitude anomalies (PHAAs). Detailed seismic interpretation reveals for the first time that chimneys and PHAAs have a variety of plan form geometries (circular through to linear) within a given vertical succession of fluid venting structures. Linear chimneys are often associated with PHAAs which are interpreted as deposits of methane-related carbonate. The geometry and depth of depressions associated with fluid venting structures are used to infer relative rates of fluid flux or intensity of the fluid eruption. This classification scheme is as follows; linear PHAAs and conduits (slow fluid venting), sub-circular PHAAs and shallow depressions (slow to moderate rates of venting), pockmarks (fast rates of fluid venting).

Two new types of pockmarks are identified based on the architecture of the sediments which infill them. They include advancing pockmark arrays and nested pockmarks. In contrast to normal pockmarks which are stacked vertically, successions of nested pockmarks and advancing pockmark arrays are laterally offset and migrate laterally, typically downslope. The reactivated craters of advancing pockmarks erode the downstream margin of preceding and underlying infill sequences whilst the infill sequence of nested pockmarks migrate gently downslope but without eroding the underlying and preceding infill sequence. Nested pockmarks and advancing pockmark arrays are confined to inclined surfaces. Downslope migration is a product of the interplay between slope inclination, sedimentation rate and bottom current activity. The trails of nested pockmarks and advancing pockmarks cluster above the axis of gas-bearing turbidite channels. PHAAs, chimneys, a present day bottom simulating reflector and negative high amplitude pockmark infills also occur in these areas and pockmarks occur above crestal faults which root in underlying rollover anticline. This implies the fluid source was derived from depth in the turtle anticline structure. The presence of negative, high-amplitude pockmark infills may suggest the fluid source was gas.

A detailed spatial analysis and characterization of fluid venting structures on successive horizons in the middle Miocene to Holocene succession indicates that their distribution and type are affected by tectonic structures and vertical changes in the nature of the host sediments. Linear chimneys occur vertically below Linear PHAAs. The former occur within the polygonally faulted interval whilst the later occur at the top of above the polygonally faulted interval. They tend to cluster in parts of the basin where the orientations of polygonal faults are strongly perturbed such as around salt diapirs and in salt-withdrawal synclines. Both linear venting structures are interpreted to post-date polygonal fault growth. Linear chimneys and linear PHAAs both have a close spatial and geometric relationship with PFs and deeper extending salt-related faults. The parallel relationship between linear venting structures and adjacent faults (salt or compaction related) are attributed to development and alignment of vertical hydraulic fractures (vertical conduits for linear chimneys) in the local fault induced stress field which subsequently provides fluid migration pathways. A model of vertical fluid migration through the polygonally faulted interval is proposed it involved initial fault-bound trapping, sealing and overpressure beneath an impermeable horizon in the lower part of the PF tier in the early stages, and vertical breaching, hydraulic fracturing and vertical fluid rise through the upper part of the tier in the later stages.

Vertical changes in the morphology and type of fluid venting structures occur across small vertical transitions which reflect changes in gross lithology from fine-grained hemipelagites to chaotic and heterogeneous mass transport deposits (MTDs). A linear zone of positive high amplitude anomalies, referred to as a linear venting network, transitions to an array of elongate-to-sub circular shallow depressions with flat bases or conical pockmarks at the upper surface of MTDs. Further changes occur above MTDs where honeycomb pockmarks, so-called based on their hexagonal-shaped perimeter which coincides with polygonal fault intersections, exist. In these cases vertical changes in the type of fluid venting structures are attributed to contrasting patterns of mechanical failure in different sediment when subject to fluid overpressure.

Although individual linear chimneys and PHAAs post-dating polygonal growth are strongly affected by the location and orientation of PFs those which precede polygonal fault growth such as pockmarks can affect the orientation of PFs. For example deep pockmark craters with the steepest sidewall inclinations coincide with overlying concentrically aligned PFs yet those which are shallower and have gently dipping sidewalls coincide with more isotropic PF patterns. This suggests that the topographic relief of pockmark craters or compaction above craters of certain depths perturb the stress state within sediments where polygonal faults form.

Abstract

This thesis has demonstrated that seismic interpretation of vertical successions of different types of fluid venting structures can be used to reconstruct spatial variations in the intensity of fluid flow at different stages in the evolution of basins.

CHAPTER 1

INTRODUCTION

1.0 Introduction

1.1 Rationale

Fluid venting structures on the seafloor or in the shallow sub seafloor are commonly interpreted as expressions of hydrocarbon migration in the subsurface (Roberts, 2001; Van Rensbergen et al., 2003; Ligtenberg, 2005). They generally result from the leakage of overpressure fluid from buried hydrocarbon accumulations. They are associated with 1) physical processes such as sedimentary deformation, hydraulic fracturing or development of depressions or conical craters; 2) thermodynamic processes e.g. gas hydrate formation or oil and gas ebullition; 3) chemical processes e.g. seep carbonate precipitation; and 4) biological processes as in the development of chemosynthetic communities. Fluid seepages and the associated venting structures lead to localized sedimentary anomalies. They occur mainly in marine or lacustrine sedimentary environments, commonly above underlying oil and gas accumulations (Hovland and Judd, 1988).

Fluid venting structures are present extensively in sedimentary basins worldwide. They are valuable tools for tracking petroleum generating systems, hydrocarbon leakage locations and can also be used to assess geohazards. Studies of fluid venting structures have a wide range of applications in industrial or scientific research domains, such as in petroleum exploration (Heggland, 2005), tracking of present and past fluid migration pathways (Heggland 1988); dating periods of leakage at the palaeo seabed (Hovland and Judd, 1987); CO₂ storage (Chadwich et al., 2009); planning of undersea infrastructure construction (Cathles et al., 2010); geohazard (Connolly and Aminzadeh, 2003); estimation of past greenhouse gas release to the seabed (Karisiddaiah and Veerayya, 1994; Kelley et al., 1994). Sites of seafloor seep are also the ideal location for studying the impact of thermal anomalies for the development of chemosynthetic communities (Sibuet and Olu, 1998).

Reflection seismic data indicate that individual fluid venting structures at the seabed or in the vicinity of the shallow sub-seafloor frequently stack vertically to form focused vertical venting pathways (cf. Moss and Cartwright, 2010a, b). The vertical successions of fluid venting structures record the history of fluid leakage at the seabed (Judd and Hovland, 2007), and indirectly thereby the evolution of pressure regimes in the subsurface. Each type of venting structure is considered to represent different dynamic degrees of leakage (Roberts, 2001; Roberts et al., 2006). Thus each evolutionary stage of morphology of vertical venting sequences can provide information on the leakages intensity at the moment when the venting

structure form (Roberts, 2001; Roberts et al., 2006). However, the significance of fluid venting structures for the assessment of intensity for paleo fluid leakage on the seabed has not received much attention, nor has their vertical evolution over time been studied in detail since the first description of such features, i.e. pockmarks (King and MacLean, 1970). The relationship between the morphology of venting structures and the fluid flux responsible for their formation is a new topic which has only been investigated by Roberts (2001), and Roberts et al. (2006). A classification for fluid flux that is represented by individual venting structures has been pioneered by Roberts (2001). Moreover, the use of venting structures to assess leakage intensity to assess has never been taken into consideration for the reconstruction of a basin's fluid flow history. Recent publications (cf. Andresen and Huuse, 2011; Andresen, 2012) have demonstrated the applications of fluid venting structures for tracing the palaeo fluid migration pathways and tackling leakage locations, but the temporal variations of venting dynamic and morphological evolutions of leakage sites during basin fluid flow histories have not been investigated. Thus, using vertical successions of fluid venting structures to reconstruct the dynamic of seepage over geological time is a novel direction in fluid flow research.

Fluid venting in relationship with geological structures, tectonic faults or basin setting have been discussed in many locations worldwide (cf. Eichhubil et al., 2000; Dupré et al., 2007; DiLeonardo et al., 2002; Moore et al., 2007), but the geometries of fluid expulsion structures that form under the influence of tectonic structures stress fields are not well known, apart from sand injectities. There are only a few studies on this topic have been carried out and include for example: the geometrical evolution of outcropped Miocene sand injectities in relationship with stress around tectonic structures in South California (Boehm and Moore et al., 2002); the relationship between state of stress and the geometry of sand injectities in Gulf of Mexico (Moore et al., 2007); elongate and linear gas chimneys affected by the stress field of deep faults in the margins of mid-Norway and in offshore Namibia, respectively by Hustoft et al. (2010) and by Moss (2011).

Research on how stress field of geological structures impact the temporal-geometric evolution of vertical stacked venting structures e.g. conical pockmarks, fluid-related depressions, venting pipes and the associated methane-related carbonates has never been investigated in literatures. The development of different types of fluid venting structures is profoundly affected by the nature of the sediments in which they form (cf. Hovland and Judd, 1988; Judd and Hovland, 2007; Jain and Juanes, 2009). The way in which changes in rheology or other physical properties of sediments and rocks impact fluid migration pathways (e.g. directions of hydraulic fracturing) is a topic that has been studied in detail at the

microscopic scale (cf. Jain and Juanes, 2009; Boudreau, 2012). But direction of fluid fractures affected by changes of nature of sediment depositions at basin scale is a topic that has not been investigated using 3D seismic primarily at the scale of seismic resolution (i.e. > 8 m). This thesis focuses on these interactions. The morphology of fluid venting structures potentially indicates the variation of seepage dynamics, and the vertical evolution of these structures potentially reflects changes of leakage intensity overtime. This research is thus centred on the use of the geometries and vertical successions of fluid venting structures to reconstruct the variation of flux at different locations. Besides fluid flux, vertical evolution of venting structures is also affected by basin sedimentations. Exploring the interaction between the vertical evolution of fluid flow features, fluid flux and geological setting is the key objective of this research.

1.2. Overview

The aims of this introductory chapter are:

- 1) To introduce gas chimneys, pockmarks and methane-related carbonates in relation with fluid migration;
- 2) To provide an overview of the current theory on the formation of these three types of fluid venting structure;
- 3) To outline the current state of knowledge regarding the vertical evolution and the genetic relationship of the three types of fluid venting structures; and
- 4) To document what work has been done on the relationship between the morphology / type of fluid expulsion features and fluid flux.

1.2.1. Focused vertical fluid venting systems in fine-grained sediments

This section gives a brief introduction on the genesis and the known processes of formation and vertical evolution of pockmarks, gas chimneys and methane-related carbonates. It is not a comprehensive description of the processes involved nor does it discuss any of the research in this thesis.

Vertical fluid venting systems can be composed of one or several types of fluid venting structures stacked vertically. In some cases they are associated with active or passive focused hydrocarbon seepage from buried reservoirs or oil gas accumulations. Fluid venting structures are the product of focused fluid flow as opposed to more distributed flow regimes often invoked in basin scale hydrogeological models. The initiation of focused fluid expulsion usually involves localized pressure increase through one of the processes described by Swarbrick and Osborne (1998). Overpressure in turn results in caprock failure when it exceeds the fracturing pressure of the overburden (Løseth et al., 2011). Overpressure fluids then escape through reactivation of this weakened zone or via newly created fractures (Zhang and Jeffrey, 2006; Sathar et al., 2012).

Most fluid venting structures are developed in muddy sediments (Judd and Hovland, 2007), due to the low permeability and unconsolidated fine-grained sediments often act as a seal for underlying fluid accumulations (Hovland and Judd 1988; Gay et al., 2006b). The process for triggering fluid venting structures in fine-grained sediments is that, pressures of upward migrating fluid build up preferentially beneath the less permeable sediments until they exceed the tensile strength of the overlying fine-grained sediments (cf. Roberts and Nunn, 1995), followed by hydraulic fractures propagation and fluid expulsion through the fine-grained sediments above.

On the other hand, because of the cohesive character of fine-grained sediment, which are able to preserve the trace of fluid expulsion (Hovland and Judd, 1988), while fluid migration in coarser grained unconsolidated sediment occurs by advection through the porous network and does not leave any trace (Judd and Hovland, 2007). Fluid leakage is commonly focused by discontinuities like faults, or guided to the surface by local thinning of the overburden like slump scars, glacial scours or even anthropogenic activities like seabed trawling. The thinning leads to the reduction of lithostatic pressure by diminution of overlying sediment thickness (Pilcher and Argent, 2007).

Variations of fluid venting intensity in a given environment under constant sedimentation and tectonically stable conditions result in different types of venting structures (Roberts, 2001). Episodic seepages at a given location engender intermittent venting structures, and produces vertical sequences of venting structures. The evolution of type, size and morphology of individual venting structures within a vertical succession, reflects changes in the intensity of fluid venting over time. One of the most common combinations of fluid venting structures in stacked systems consists of successions of gas chimneys, pockmarks, flat-bottomed depressions and positive high amplitude anomalies or mound structures. The

vertical succession reflects the variation of seepage intensity over time. The fluid venting structures that are studied in this thesis fall into the sub-group of ‘gas chimneys’, ‘pockmarks’, ‘methane-related carbonate’ whose geometries are illustrated in Figure 1.1. Each of these venting structures has been given a separate brief review on their mechanism of formation in following sections, and all existing conceptual models for the developments of these venting structures are also summarised at the end of each section.

1.2.2. Vertical fluid conduit: chimney or pipe structures

Vertical fluid conduits in sedimentary environment are expressed by narrow zones that vertically cut through stratigraphic layer and interrupt continuous strata irrespective of their scale (cf. De Boever et al., 2006; Heggland, 1998; Løseth et al., 2011; Moss and Cartwright, 2011a). They are interpreted as a result of hydraulic fracturing in sediments (cf. Løseth et al., 2011; Moss and Cartwright, 2011a, b; Davies et al., 2012), which serve as vertical fluid pathways and can be a kilometer long, and terminate upward into shallow depressions hundreds of meters in diameter (cf. Løseth et al., 2001; 2011; Moss and Cartwright, 2011a, b). In the literature, there is no standard scientific term for describing the vertical fluid conduit neither on seismic nor for outcrop samples, and they have been termed in most of study as: chimneys (cf. Heggland, 1998; Meldahl et al., 2001; Aminzadeh et al., 2002; Ligtenbert, 2003; Gay et al., 2003; De Boever et al., 2006; Arntsen et al., 2007; Hustoft et al., 2010; Petersen et al., 2010; Cathles et al., 2010) or pipes (cf. Berndt et al., 2005; Løseth et al., 2011; Moss and Cartwright, 2011a; Planke et al., 2011) regardless to their scales.

Centimetre- to metre-scale fossil chimney structures in outcrops have been observed to aggregate together and form very localized zone of “chimney concretions” (Ewen, 2009; Blouet et al., 2012), and which have been thought to compose the infill of chimney in seismic-scale. Such as the conceptual model proposed by Foucher et al. (2009) that seismic-scale gas chimney is composed by multiple elementary fractures and gas veins (fig. 1.2). In this section, I will extend this notion to the microscopic scale.

Examples include seismic chimneys of hundred meters-scale have been well documented in the literature (cf. Hovland and Judd, 1988; Heggland, 1998; Løseth et al., 2001; Petersen et al., 2010; Moss and Cartwright, 2011a). Centimetric- to metric-scale fossil chimneys in outcrops (e.g. Aiello et al., 2001; Lein et al., 2004; Clari et al., 2004; Barbieri and Cavalazzi, 2005; De Boever et al., 2006; Ewen, 2009), and millimetric- to centimetric-

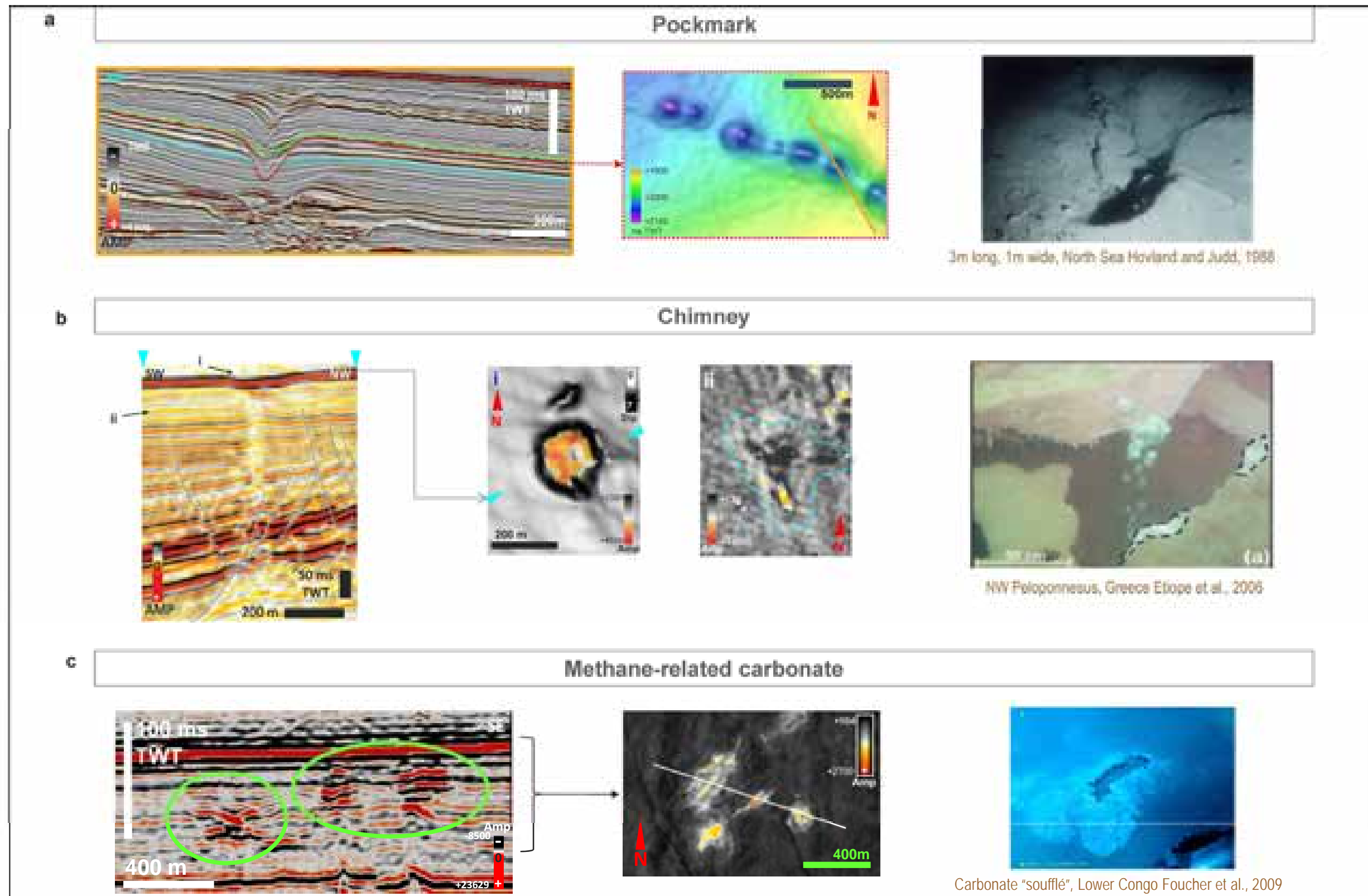


Figure 1.1. The three main types of fluid venting structures observed in the study area. They are respectively pockmark (a), chimney (b) and methane-related carbonate (c). These venting structures are illustrated respectively on seismic section (images on left side), two-way-time map (images in middle) and truth grounds (images on right side) from different areas.

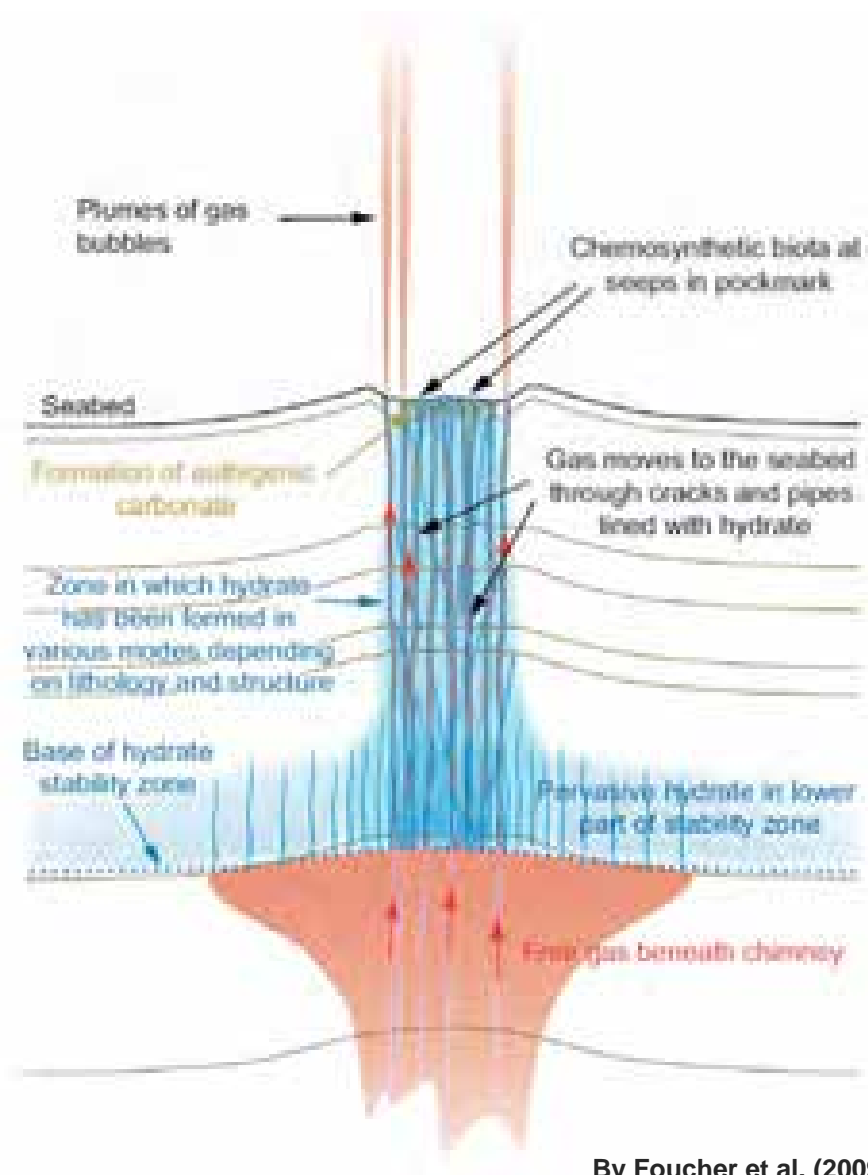


Figure 1.2. Conceptual model of Foucher et al. (2009) illustrating the internal structure of a seismic-scale gas chimney and the free gas migration inside the chimney. The main chimney is composed by a coalescence of smaller fractures and gas vents.

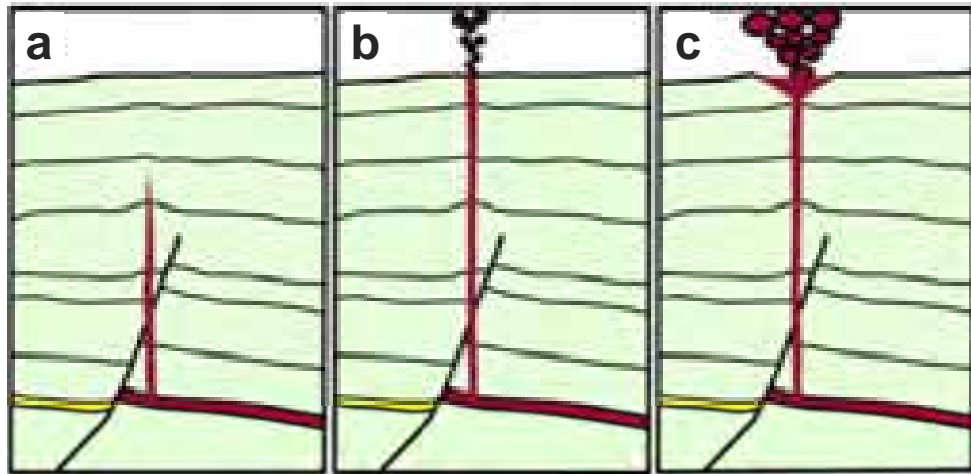
scale artificial gas chimneys in analogue models (Gay et al., 2012) have also been well studied and investigated.

Two recent studies have attempted to compare seismic chimneys with suitable outcrop exposures. These include a study by Løseth et al. (2001) who compared chimney structures outcropping in Rhodes to those in the Niger Delta and more recently by Ho et al. (2012) who compared outcrops of fossil pipe concretions in the Vocontian basin in SE France with those offshore Angola. However, given that there is still some debate on what a seismic pipe is composed of it is difficult to know what comprises a suitable outcrop for analysis.

In active hydrocarbon migration systems, seal analysis is of primary importance for oil and gas exploration (Ligtenberg and Connolly, 2003). Breaking of cap rock and hydrocarbon leakages in subsurface can be detected by seismic chimneys on seismic data (Aminzadeh et al., 2002; Ligtenberg, 2005; Heggland, 2005), and which are practical tools to evaluate the underground plumbing system as well helping to understand the leakage processes (Meldahl et al., 2001; Ligtenberg, 2003; Løseth et al., 2009). Fluid leakage through hydraulic fractures/gas chimneys could be episodic or continuous (Løseth et al., 2009; Cartwright et al., 2007). Hydraulic fractures will become hydraulically close once fluid pressures decrease and are as a function of pressure variations in underneath fluid accumulations or reservoirs (c.f. Pedersen and Bjorlykke, 1994).

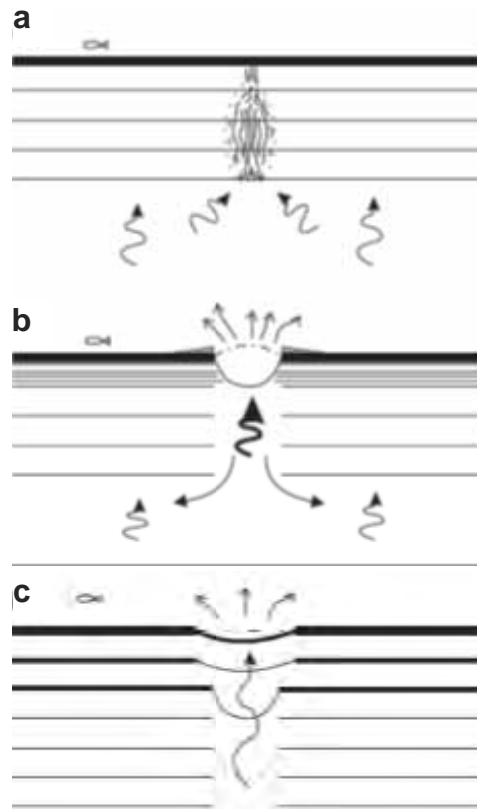
Formation of vertical gas chimneys by hydraulic fracturing at five different scales, have been investigated by researchers in different geosciences disciplines such as: petroleum geology, physics of sediment, geomechanics, geochemistry. **The five scales** in which hydraulic fractures formed have been examined in: seismic scale (one), outcrop scale (two), analogue model scale (three), microporo-scale (four) and molecular-scale (five). Researchers from these scientific domains are interested in the same phenomenon but in different scale and for different purposes. Researchers in each of these disciplines can help remediate the limitations of the others, and are useful for acquiring a more comprehensive vision on the formation of gas chimneys.

Representative conceptual models for the formation and evolution of vertical chimneys in fine-grained sediments at seismic scale have been proposed by Løseth et al. (2011) (fig. 1.3) and Moss and Cartwright (2010a) (fig. 1.4). These models suggest gas chimneys develop when the pore pressure exceeds the sum of the minimum lateral stress and the tensile strength of the overburden (Løseth et al., 2011; Moss and Cartwright, 2010a). This



By Løseth et al. (2011)

Figure 1.3. Illustration of vertical chimney formation by Løseth et al. (2011). a) Propagation of hydraulic fracture once fluid pressure exceeds the vertical stress plus the tensile strength of overburden sediment. b) The fracture reaches the seabed, resulting in high speed fluid venting. c) A crater forms above the fracture due to high speed fluid expulsion.

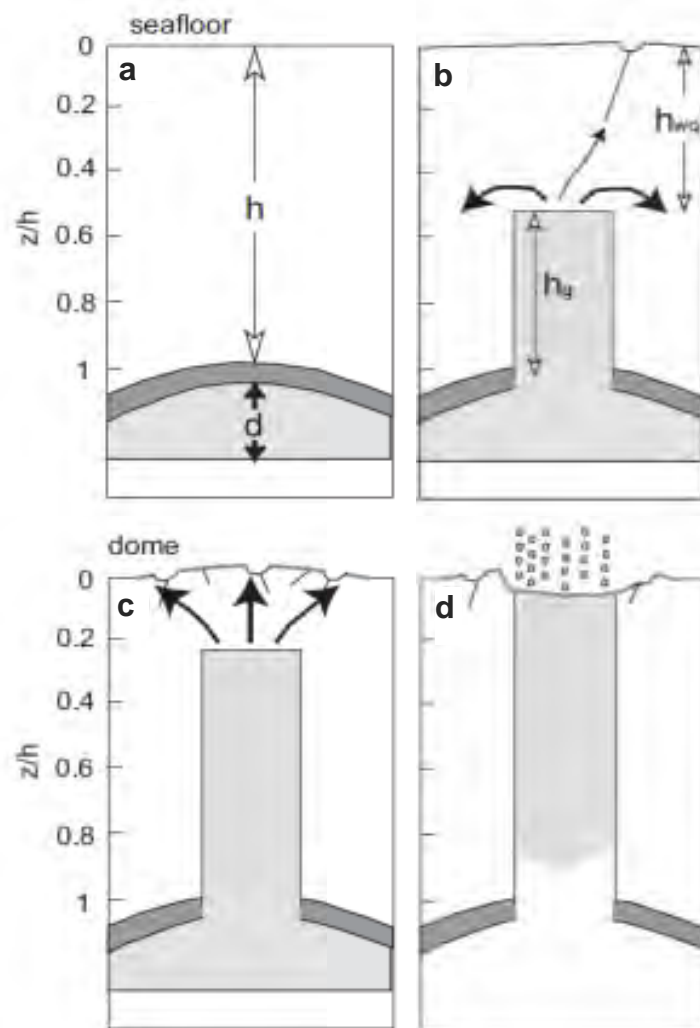


By Moss and Cartwright (2010a)

Figure 1.4. Conceptual model of vertical chimneys and its later development by Moss and Cartwright (2010a). a) Initiation of hydraulic fractures which causes cap rock failure. b) The hydraulic fracture connects to seabed where overburden pressure declines and induces brutal fluid eruption to form a seabed crater. c) Eruptive craters are sealed by sediment depositions, and by repeating stage (b) new generations of craters are formed above the first crater (b).

initiation is followed by the propagation of hydraulic fractures upward through the overlying sediment (fig.1.3.a, fig.1.4.b) perpendicular to the direction of the least principal stress (Phillips, 1972; Cosgrove, 1995; Løseth et al., 2009; 2011; Moss and Cartwright, 2010a). Hydraulic fractures can evolve afterward into either seepage pipes (fig. 1.3b) or blowout pipes (fig. 1.3c), as classified by Cartwright et al. (2007). If overpressured fluid flows out rapidly from the fracture, circular depressions or pockmarks may develop on the seabed (fig. 1.3c; fig. 1.4b, c) (cf. Roberts, 2001; Løseth et al., 2011; Moss and Cartwright, 2010a, b), then forming blow out pipes (Cartwright et al., 2007). Episodic fluid expulsion can be expressed by vertical stacked craters above the same location (fig. 1.4c). The last stage of blow out pipe has been simulated in numerical model by Cathles et al. (2010) (fig. 1.5). Their model is based uniquely on the buoyancy of fluid ascension in shallow sediment, and assumes that the permeability and density of shallow sediment are constant. Cathles et al. (2010) make the simple approximation that the difference between gas and water densities (ca. 0.3 and 1.0 kg/m³ respectively) is similar to that between water and shallow sediment (1.0 and ca. 1.7). Under this configuration (fig. 1.5a), a continuous gas column breaches its overburden once its thickness reaches the half height of the overburden (Cathles et al., 2010), and followed by occurrences of smaller fractures above the gas column which extend to the seafloor and create a first pockmark (fig. 1.5b) (Cathles et al., 2010). More craters will be formed afterwards with the growth of chimney (fig. 1.5c) and these craters will then merge together by a final big crater which issued from the final dramatic eruption (fig. 1.5d) (Cathles et al., 2010).

Analogue experiments on the formation of chimneys by Gay et al. (2012) agree with the hypotheses of Løseth et al. (2011) and Moss and Cartwright (2010a), and reveal a detail that; during gas bubble growth and rise toward the surfaces, shear deformations occurs along fractures by fluid ascension which fluidize the sidewalls of fractures (Gay et al., 2012). The occurrence of shear structures thus provides a clue for the potential sediment remobilization within hydraulic fractures during the latter's propagation in fine-grained sediments. Mechanisms of micropore-scale fracturing in homogenous sediment environment have been simulated numerically by Jain and Juanes (2009) (fig. 1.6). Who demonstrated the deformation in fine grained sediment by fluid migration is done by breaking cohesive bonds between grains. In other words, matrix grains have been forced apart (fig. 1.6a), as the surface tension that induced by cohesion strength between fine grains (< 1µm) is small because of the small grain size (Shin and Santamarina, 2010) in comparison to the case of coarser grains (= 1mm) in which gas invasion occurs by buoyancy exceeding capillary entry pressure (fig. 1.6b) (Jain and Juanes, 2009). However, the hypotheses above do not answer how overpressured fluid migrates in shallow unconsolidated fine-grained sediments. This question is important to



By Cathles et al. (2010)

Figure 1.5. Schematic model of gas chimney in association with multiple seabed craters. a) Gas (light grey) below its cap rock (dark grey). b) Once fluid overpressure breaks the cap rock, hydraulic fractures form and allow fluid migration. When gas-filled fractures reach about half way to the seabed, pockmarks start to form on the seabed. c) The closer the hydraulic fracture reaching to the seafloor, the more the pockmarks form. d) Final fluid eruption causes a major crater above the fractured zone once the fractures reach the seafloor.

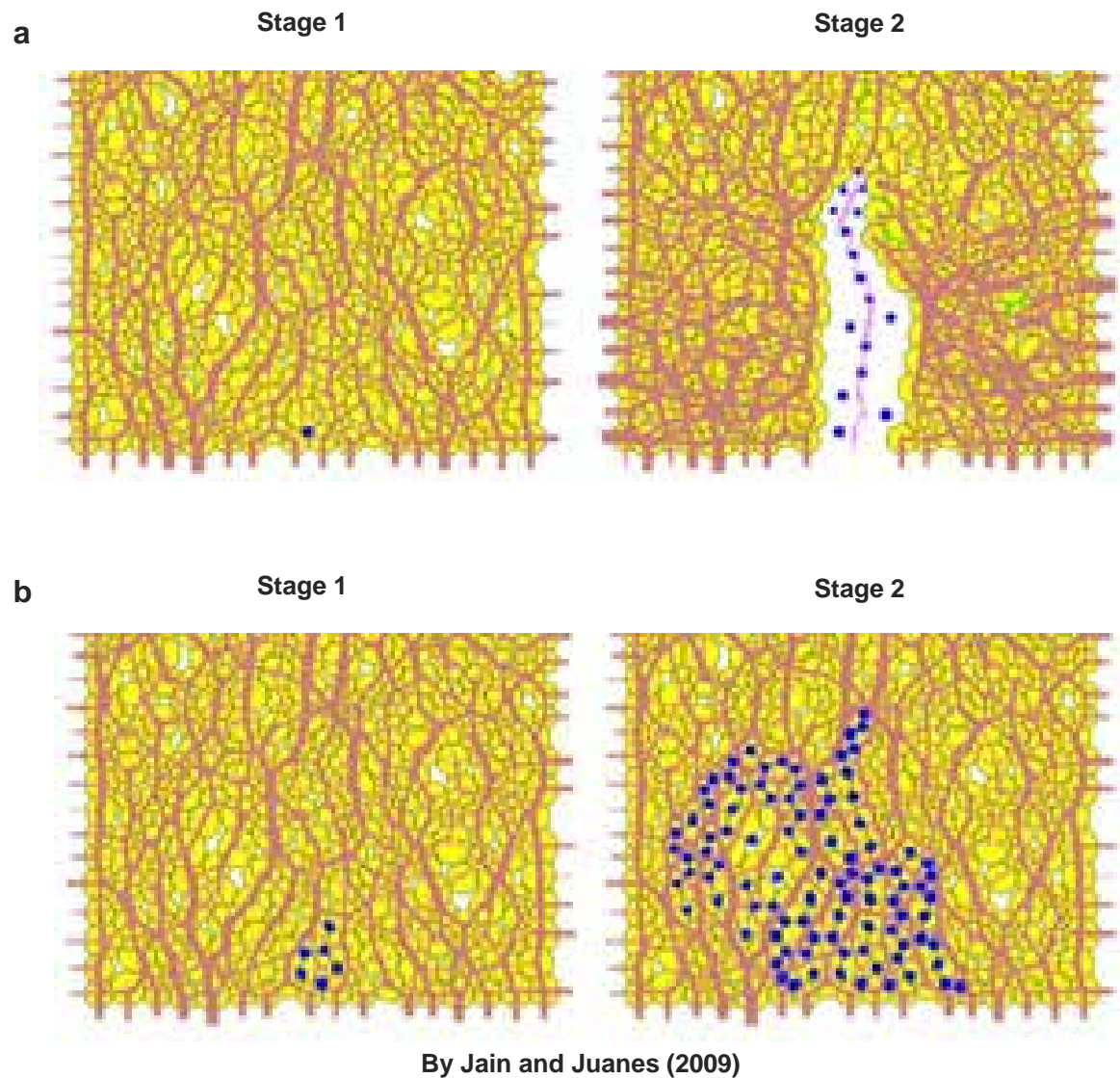
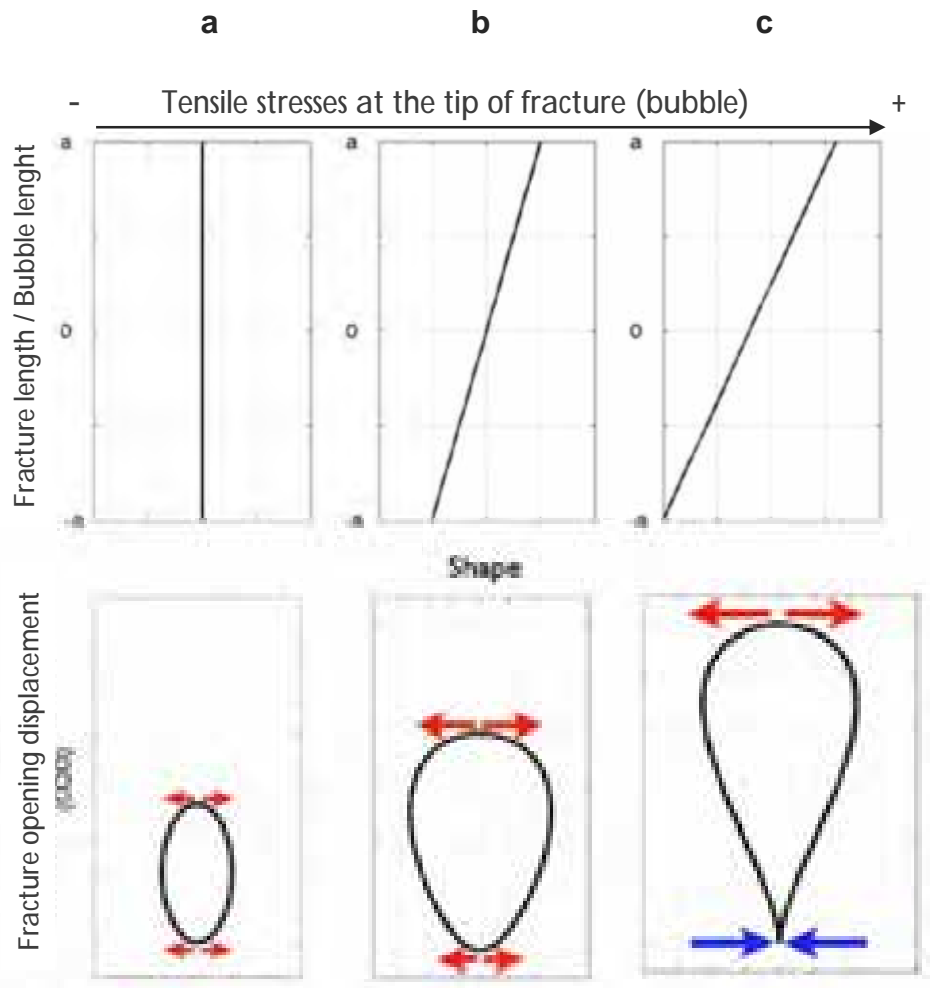


Figure 1.6. Numerical model of fluid migration in two types of sediments by Jain and Juanes (2009). a) Model of fracture opening in fine-grained sediment ($<1\mu\text{m}$); fracture propagation in fine-grained sediment is done by pushing matrix grains apart. b) Fluid migration in coarser-grained sediment ($=1\text{mm}$); fluid migrations are mainly done by capillary invasion and no fractures are formed in this case. Blue dots: gas; Brown lines: compressive strengths between each grain; Pink line: locations of grain boundaries collapsing.

this research because fluid venting structures are principally occurred in fine grained hemipelagites in the studied area. Moreover, the mechanism of formation for chimneys in seismic, in outcrop or in microporo-scale are rarely associated and are often addressed separately. A brief review is given below for the formation of hydraulic fractures at microporescale.

Methane gas migration in cohesive shallow sediment (< 100 m) (Boudreau, 2012) is strongly governed by rising bubbles (Algar and Boudreau 2009; Barry et al., 2010; Algar et al., 2011; Boudreau, 2012). The mechanisms of rising gas bubbles and hydraulic fracturing are caused by the density contrast between bubbles and the sediment matrices which engender a vertical movement of gas bubbles (fig. 1.7) (Nunn and Meulbroek, 2002; De Vries et al., 2007b; Algar et al., 2011; Boudreau, 2012). The ascension of a methane bubble through the sediment column is accompanied by the bubble growth (Algar et al., 2011). Once the gas bubbles reach a critical size, they will push aside fine grains matrix and create fractures in sediments (Boudreau et al., 2005; Barry et al., 2010; Algar et al., 2011). It is different from fluid migration in coarser sediments where fluids will invade the sediment by capillary pressure (Jain and Juanes, 2009). In addition, by the differential of lithostatic pressure between the top end and the lower end of the growing bubble (Algar et al., 2011), tensile stress (bubble internal pressure) at the bubble head becomes more important than at the bubble end and it makes the fractures open always above the upper tip of bubble (Boudreau, 2012). Therefore the fracture by fluid will always propagate upward (Algar et al., 2011; Boudreau, 2012).

Small-scale heterogeneities of sediment will cause some changes in fracture propagation behaviour (Arch et al., 1988; Johnson et al., 2012) which influences bubble shapes and internal pressures (Barry et al., 2010). Gas bubbles do not necessarily create their own fractures or rise perfectly vertically (Boudreau, 2012). In some cases, bubbles will fill and expand the pre-existing sub-vertical cracks (van Kessel and van Kesteren, 2002; van Kesteren and van Kessel, 2002; Boudreau, 2012), as this is easier than creating new fractures (Delaney, 1986). It is found also that the opening direction of fractures can be deviated towards that of the perpendicular to the minimum principal stress (Watanabe et al., 2002; De Vries et al., 2007b) as shown by the analogue model of Watanabe et al. (2002). On the other hand, fluid can repeatedly utilize the same fracture as migration path to flow to more shallow depths (Boudreau, 2012). The tensile strength in fractured cohesive sediments needs time to re-establish, which favours re-opening of the weakened path by subsequent bubbles (Boudreau, 2012).



By Algar et al. (2011)

Figure 1.7. Tensile stresses at fracture (bubble) tips increase with the rise of methane bubble lengths. A conceptual model proposed by Algar et al. (2011). a) Initiation of hydraulic fracturing by bubble rise: difference in tensile stress at the tip and the tail of the bubble is negligible with respect to the internal bubble pressure, the tensile stress can be considered constant along the length of the fracture (bubble). b) As the bubble grows and changes form, the difference of tensile pressure becomes greater between the top and bottom of bubble. c) When the bubble becomes teardrop-shape the tensile stress concentrates at the fracture (bubble) tip, while the tensile stress drops to zero at the fracture (bubble) tail, and compressive stress around the fracture (bubble) trail closes the trail. Red arrows: tensile stress; Blue arrows; compressive stress.

Furthermore, vertical migration of methane gas bubbles will change into lateral when the gas encounters a zone where lateral fracture toughness of sediment is lower (De Vries et al. 2009; Mazzini et al., 2008; Boudreau, 2012). Gas bubbles start to accumulate in the zone of lower lateral strength (Boudreau, 2012; Barry et al., 2012), and raise the sediment cover and create a dome structure under the seafloor (Boudreau, 2012). Doming induced by overpressured fluid in unconsolidated sediment has also been simulated by analogue modelling by Mazzini et al. (2008) and Gay et al. (2012). The dome structure will be fractured when the accumulated gas exceeds the tensile strength of sediment cover, which may result in the formation of a seabed crater or pockmarks (Mazzini et al., 2008; De Vries et al., 2007b).

1.2.2.1. Seismic expressions of vertical gas chimneys and ground truth outcrops

As already discussed by Moss (2011); there is no standard scientific term for describing the seismic expression of potential vertical fluid conduits. So in general, columnar acoustic perturbations in seismic are also named as chimneys or pipes in the literature (Moss, 2011; Davies et al., 2012), and hereafter, all of these vertical acoustic anomalies in seismic will be called fluid chimneys.

Active vertical gas chimneys are represented by columnar acoustic disturbance zones, when detectable on seismic. These acoustic anomalies are due to seismic energy being absorbed or dispersed by free gas accumulations, by gas hydrate, by carbonates during seismic acquisitions (Wood et al., 2002), or by strata interruption breached by vertical fluid flow (Bouriak et al., 2000; Berndt et al., 2003; Gay et al., 2007; Hustoft et al., 2007). In literature, the seismic expressions of vertical gas chimneys include: 1) seismic reflection pull up, which is characterised by convex-up reflections and is generated by high velocity material (fig. 1.8) (Coffeen, 1986), 2) seismic reflection push downs (fig. 1.9), which is expressed by convex reflections and is caused by low velocity material (Coffeen, 1986), 3) seismic acoustic turbidity zone (fig. 1.10), 4) seismic bright amplitude column with a high negative or a high positive polarity at the topmost terminations (fig. 1.11).

The internal structures within the seismic disturbance zones are still under discussion. Løseth et al. (2011) demonstrated that seismic chimneys which are characterised by pull-up reflections, their internal structure is seismically structureless according to seismic modelling results. However, the outcrop observations of Løseth et al. (2011) in Rhodes do reveal the

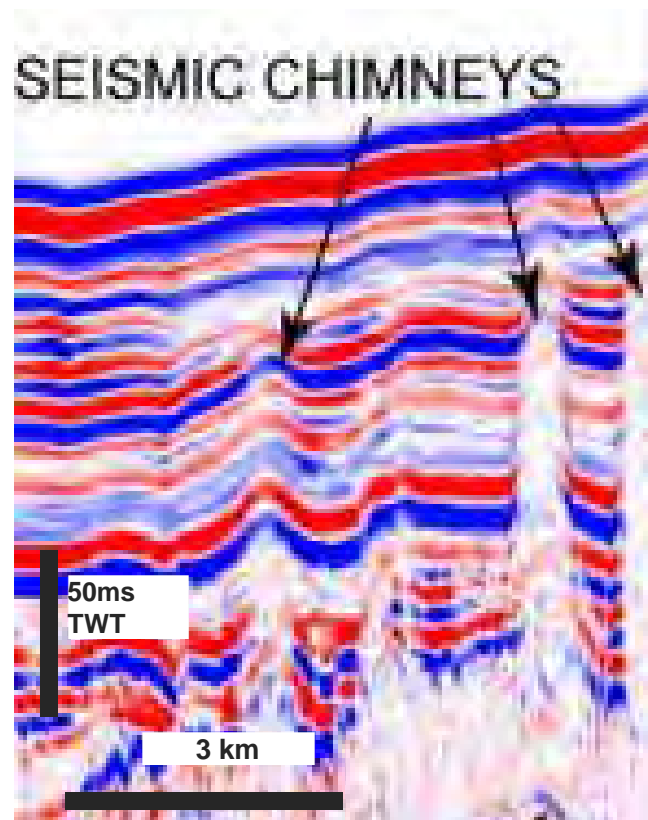


Figure 1.8. Chimneys are expressed by narrow vertical zones of seismic pull-up (convex) reflections on profile; taken from Horosal et al. (2009).

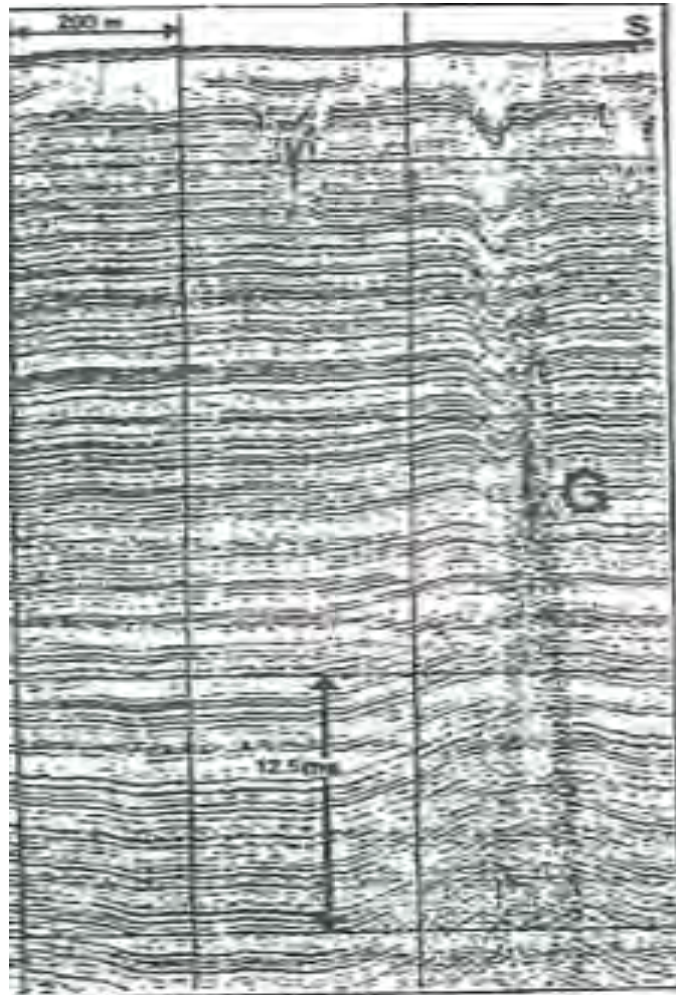


Figure 1.9. Chimney is expressed by a vertical narrow zone of seismic push down (concave) reflections on profile. Free gas is indicated by letter "G". Image taken from Hovland et al. (1985).

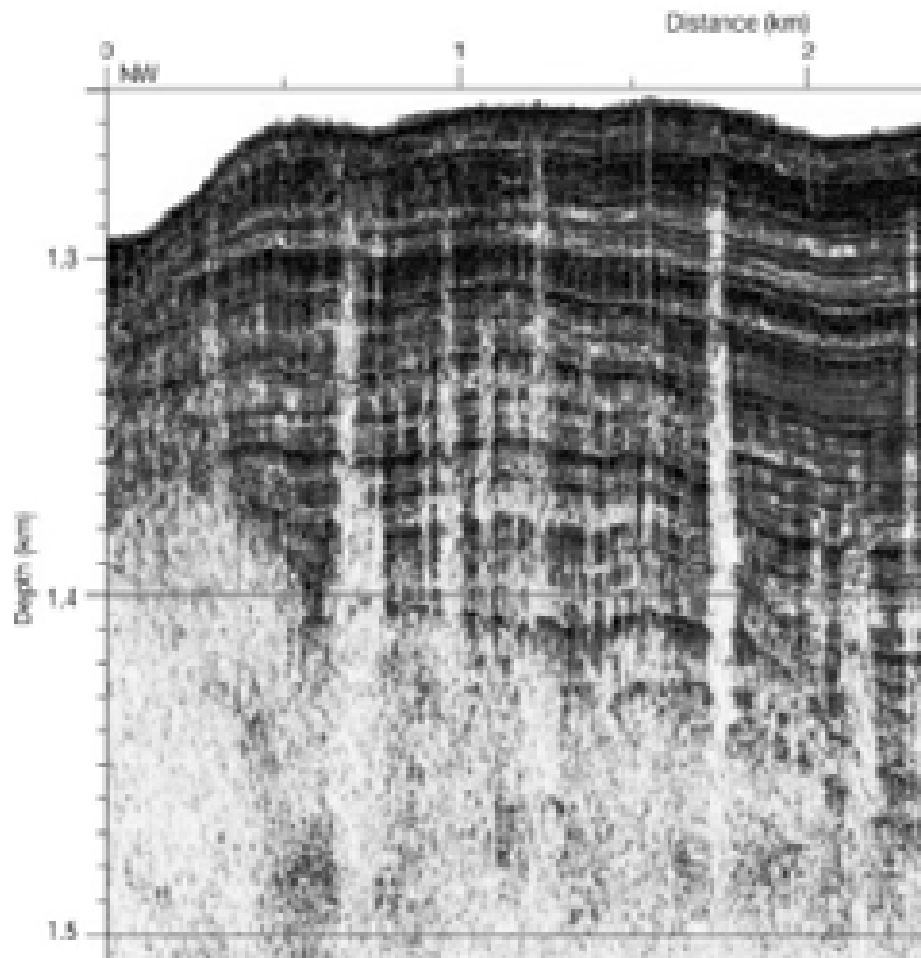


Figure 1.10. Chimneys are characterized by columnar acoustic turbidity zones on seismic; taken from Wood et al. (2002).

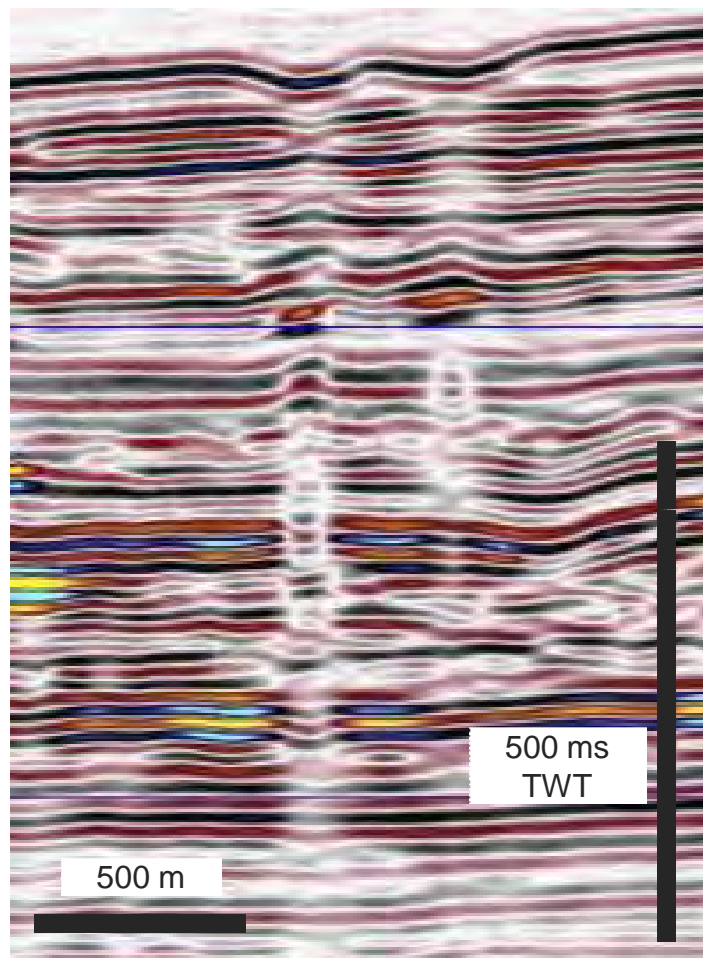


Figure 1.11. Chimneys are characterized by bright and dim amplitude columns with polarity inversions and high amplitude topmost terminations; taken from Løseth et al. (2010).

metric-scaled, abnormal columnar zones within clastic lithologies contain brecciated sediments and fracture networks. On the other hand, chimneys in seismic-scale are believed to be composed by the coalescence of small chimneys (Løseth et al., 2009; Foucher et al., 2009; Van de Streen et al., 2002; Eichhubl and Aydin, 2003; Davies et al., 2012). Centimetric- to metric-scale, onshore outcropping fossil chimneys in the Northern Apennines of Italy (Barbieri and Cavalazzi, 2005), Santa Cruz in California (Aiello et al., 2001), the Vocontian basin (Blouet et al., 2012), Varna in NE Bulgaria (De Boever et al., 2006), the east coast basin of New Zealand (Ewen, 2009) have been observed to be cemented and filled by methane-related carbonate. Whilst a live undersea outcrop of methane-related carbonated chimneys in Black sea, has been observed to emit methane streaming and bubble on the seafloor (see video of Microbial reefs in the Black Sea, HERMES project in <http://www.eu-hermes.net/intro.html>) (fig. 1.12).

1.2.3. Pockmarks

Pockmarks are tightly linked with gas chimneys because of their genetic relationship as what has been mentioned in the previous section 1.2.2, and they often represent the last stage of evolution of a gas chimney. The term “Pockmark” is applied to concave, craterlike depressions that occur in profusion on muddy sediment bottoms (King and Maclean, 1970). They were first noted as V-shaped notches (fig. 1.13) along the sediment-water interface on echograms of the Scotian Shelf (King and Maclean, 1970; fig. 1.13). In the 1970s, V-shaped anomalies on 2D seismic data were commonly interpreted as fluvial (subaerial) channels, tidal channels on the continental shelf, or erosional turbidite channels in the deep sea (e.g. Exon and Willcox, 1978).

In 1965 the first identified pockmark was revealed by a side scan survey which has recorded an acoustic pattern of an isolated conical depression with well defined bottom apexes (King and Maclean, 1970). Early investigations documented that pockmarks are close to circular in map view and that their size may vary significantly both between areas and within an individual area (Hovland and Judd, 1988). Some have smooth and relatively flat bottoms while in other cases the bottom is mounded (cf. Judd and Hovland, 2007). Pockmarks occur world-wide in unconsolidated fine-grained sediments (Hovland and Judd, 1988; Gay et al., 2006b; Pilcher and Argent, 2007). They are frequently seen in areas where petroleum source rocks exist (Loncke et al., 2004). Pockmark fields can extend over an area of a few



Figure 1.12. Methane-derived authigenic carbonate (MDAC) chimneys outcrop in Black Sea seafloor. Screen capture from video of “Microbial reefs in the Black Sea”, HERMES project (<http://www.eu-hermes.net/intro.html>) (<http://www.youtube.com/watch?v=P6tORN44X58>). Notice that methane bubbles are coming out from the MDAC chimneys.

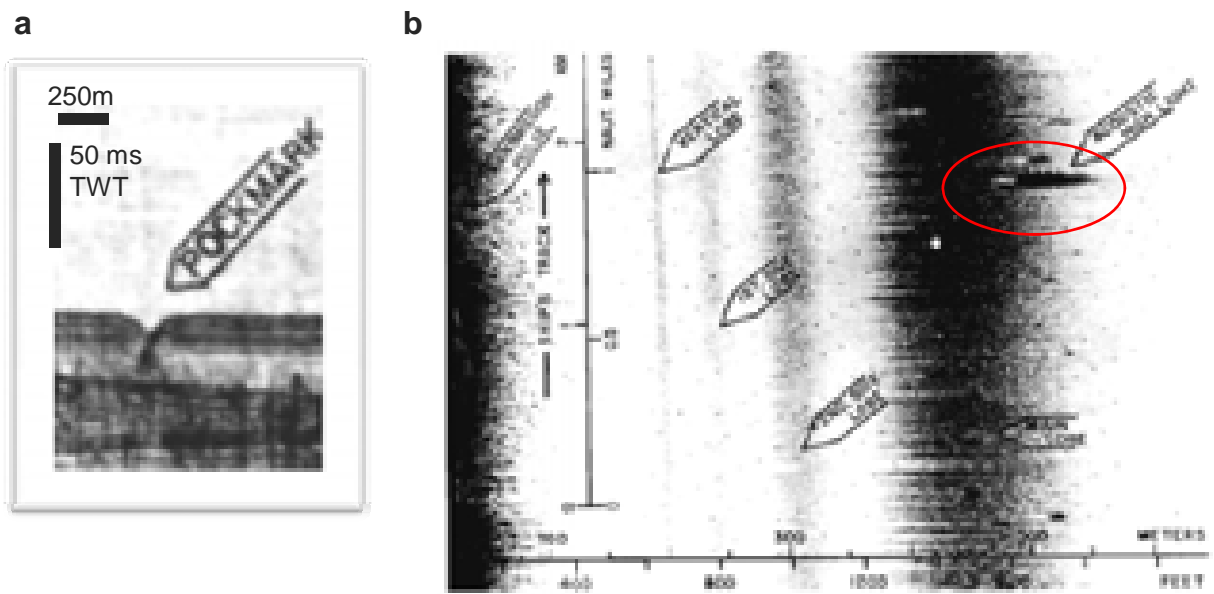


Figure 1.13. The first reported pockmarks in LaHaye Basin by King and MacLean (1970). a) Pockmark on a 2D seismic profile. b) Plan view of pockmarks (red ellipses) seen on a side-scan sonar backscatter image. Images taken from King and MacLean (1978).

square kilometres in which pockmarks occur individually or in clusters (Van Rensbergen et al., 2003).

The first pockmark known to be continuously emanating gas bubbles was found in the North Sea (Hovland and Sommerville, 1985). Pockmarks are considered as significant indicators for subsurface hydraulic activities and the possibility of slope failure and seabed instability (Hovland et al., 2002). They are regarded as evidence of focused fluid flow and as recorders of past and present seepages on the seabed (Hovland et al., 2002). In the 1980's the most plausible theory for the formation of pockmarks was that they are caused by efflux of liquids or gas through the seafloor (Josenhans et al., 1978; Newton et al., 1980; Hovland, 1982; Hovland and Gudmestad, 1984; Nelson et al., 1979; Hovland, 1985). Formation processes of pockmarks as final stage of chimneys evolution have been detailed in the previous section already, in a further section only vertical evolution processes of pockmarks is reviewed.

1.2.3.1. Environment for pockmark and chimney formations

Pockmarks and chimneys are commonly found in geological environments such as: (1) Petroleum-generating regions (Ellis and McGuinness 1986; Hovland et al. 1984; Josenhans et al. 1978; Maisey et al. 1980; Newton et al. 1980; Rise et al. 1999; Hovland et al., 2002); (2) Above active faults (Dimitrov and Woodside, 2003; Fader, 1991; Soter, 1999; Syvitski and Praeg, 1989; Pilcher and Argent, 2007), or associated with underneath fault zones (Gay et al., 2003; Gay et al., 2006a) so that linear arrangements of pockmarks are aligned along the strike of a deeper fault (Plicher et al., 2007); (3) Regions underlain by crystalline bedrock (Flodén & Söderberg 1988; Papatheodorou et al. 2001; Hovland et al., 2002); (4) In association with mud diapirs and mud volcanoes (Dimitrov and Woodside Woodside, 2003; Hovland, 1992; Hovland and Judd, 1988; Pilcher and Argent, 2007); (5) Above buried channels (e.g. Haskell et al., 1997; Gay et al., 2006a). (6) associated with submarine slumps (Dimitrov and Woodside, 2003; Foland et al., 1999; Schwab and Lee, 1988; Pilcher and Argent, 2007) occur on shelf slopes (Hovland et al., 2002); (7) Associated with a (Bottom Simulating Reflector) BSR (e.g. Mienert et al., 1998; Bouiak et al., 2000; Bünz et al., 2003; Mazzini et al., 2006; and Gay et al., 2003; 2006).

Pockmarks and pipes are known to occur in a variety of marine environments from estuarine to marine shelf, slope and abyssal plain settings and have been recorded at all water

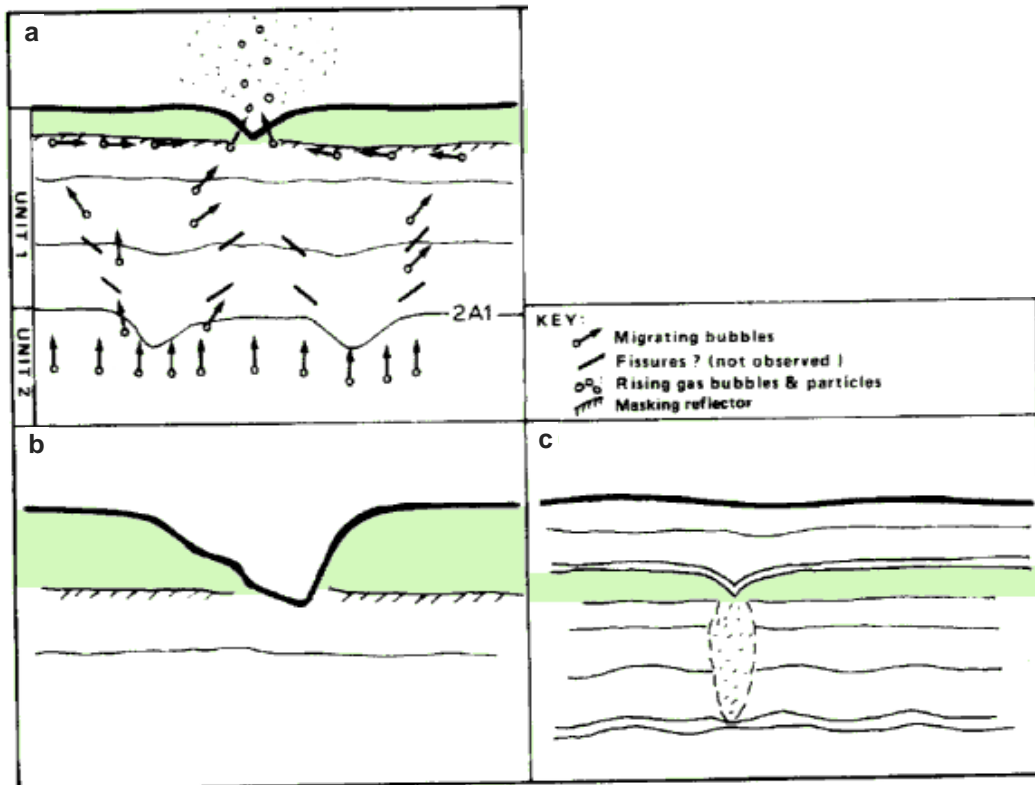
depths from ~10 m to ~5000 m (Hovland and Judd, 1988; Pilcher and Argent, 2007; Garcia-Garcia et al. 1999; Hill et al. 1992; Kelley et al. 1994; Scanlon and Knebel 1989; Taylor 1992; etc, Hovland et al., 2002). In addition to estuaries and coastal areas pockmarks have also been found in lacustrine environments (Hovland and Judd, 1988; Pickrill, 1993; Pilcher and Argent, 2007), in environments with or without hydrothermal activity (Pickrill 1993; Hovland et al., 2002), and in areas of groundwater flow (Bussmann and Suess 1994; Hovland et al., 2002). Pockmarks have also been considered to be formed as a result of seabed disturbance by grounded, moving icebergs (Fader, 1991). It has been suggested that this relates to iceberg movements removing certain quantities of overburden sediment and making fluid escape more easy (Judd and Hovland, 2007).

1.2.3.2. Vertical evolution of pockmarks

Pockmarks indicate the timing of fluid eruptions on the (palaeo) seabed as gas chimneys do. Truncations of underlying stratigraphic interval by fluid eruptions are widely recognized as markers for time of fluid explosion (Judd and Hovland, 2007). Therefore, multiple generations of pockmarks at the same vertical spatial location, can give information on the timing of activation and deactivation of the underlying fluid system at a focused leakage point (cf. Cifci et al., 2003; Plaza-Faverola et al., 2011).

The first two conceptual models published for the vertical evolution of pockmarks are based on two case studies: pockmarks in the central Norwegian Trench (Hovland, 1982) and pockmarks on the Turkish shelf (Cifci et al., 2003). Hovland's model (1982) that is based on pockmarks in central Norwegian Trench, proposes pockmarks formation is likely due to migration of overpressured methane along vertical shear strain fissures that are engendered by differential compaction above an irregular surface (fig. 1.14a). The mature stage of pockmarks is characterized by slump inside the pockmark (fig. 1.14b) and coalescence of individual pockmarks to form a final large pockmark (Hovland, 1982). The last stage is represented by sedimentary units draping the uppermost erosional surface (fig. 1.14.c) (Hovland, 1982).

This concept of unit pockmarks merging into a single big pockmark has been reprinted by Cathles et al. (2010). In Cathles et al.'s model (2010), it suggests that the coalescence is due to the large gas chimney finally reaching the seabed with a considered volume of fluid,



By Hovland, 1982

Figure 1.14. Conceptual model of a pockmark at different development stages (modified after Hovland, 1982). a) Early stage: fluid migrates potentially via shear strain fissures and induces brutal fluid eruption at the seabed. b) Mature stage: sediment slumping occurred on the pockmark sidewall. c) Final stage: pockmark is buried by sediments and associated with an underlying columnar disturbance.

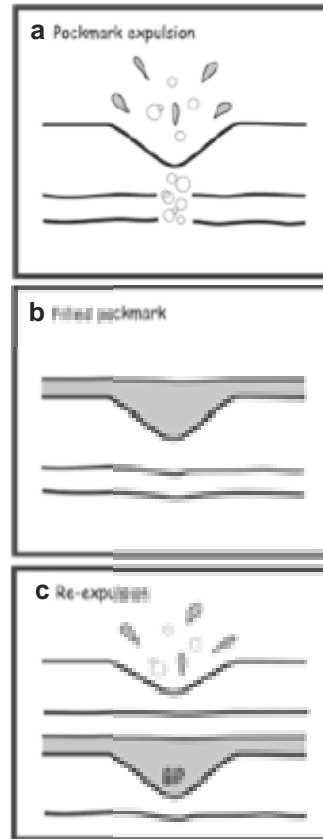
which undergo depressurization and induce a bigger eruptional crater that superposed onto the old unit pockmarks. On the other hand, big pockmarks that coalesce into a giant pockmark have been observed in sonar side surveys (e.g. Solheim and Elverhøi, 1985; van Rensbergen, 2003; Gay et al., 2006b) and in 3D seismic (Cifci et al., 2003; Cartwright et al., 2003; Imbert et al., 2011). Moss et al. (2012) also proposed a model with seismic observation on the unit pockmarks that are formed above infills of larger pre-existing pockmarks.

The first conceptual model for the vertical evolution of a pockmark succession has been well illustrated by Cifci et al. (2003). The authors show an initial pockmark sealed by sediment (fig. 1.15a, b), with a second generation developing after some drape of the first one. (fig. 1.15c) (Cifci et al., 2003). This model has been integrated afterward with combination of timing of polygonal fault formations by Andresen and Huuse (2011). However, these models have not integrated the changes of geometry, nor have they taken into consideration long-term fluid flux variations.

1.2.4. Methane-related carbonates

Methane-related carbonates regroup chemosynthetic benthic and methane-derived authigenic carbonates (MDAC). They are also called methanogenic carbonates (Hovland and Irwin, 1992). They have been reported worldwide in seep locations. Methane-related carbonates are often associated with seeps, pockmarks, chimneys or gas hydrates (cf. Judd and Hovland, 2007), and are characterized by depletion of carbon isotope $\delta^{13}\text{C}$ in the carbonate fraction (Ritger et al., 1987). Isotope analysis is beyond the scope of this thesis and is only discussed here to give context to further work in chapters 4-6.

MDAC were first identified by isotopic analysis in 1968 on the continental margin of the north-eastern United States by Hathaway and Degens, who named them Methane-Derived Marine Carbonates (Hathaway and Degens, 1968). Since the 1980's, they are more commonly known as Methane-Derived Authigenic Carbonates (Ritger et al., 1987) or authigenic carbonates (Hein et al., 1979). In 1983; MDAC were discovered in North Sea pockmarks and seeps by a remotely operated vehicle (ROV) (Hovland and Sommerville, 1985; Hovland et al., 1987; Hovland and Judd, 1988; Hovland and Thomsen, 1989; Judd and Hovland, 2007). They were investigated later by Hovland and his co-workers in 1987 (Hovland et al., 1987; Hovland and Judd, 1988).



By Cifci et al., 2002

Figure 1.15. The first conceptual model for the vertical evolution of a pockmark succession by Cifci et al. (2002). a) Formation of a first pockmark on the seafloor. b) Sediment fills the pockmark. c) A new pockmark occurred in sediment above the sealed pockmark.

Since the discovery of methane-related carbonate in cold seep locations, they have been extensively reported and studied by scientists worldwide (Hovland, 1982; Ritger et al., 1987; Aiello et al., 2001; Paull and Ussler III, 2008; Mazzini et al., 2006; Gay et al., 2006b; De Boever et al., 2006; Olu et al., 2007; Ewen, 2009; Naudts et al., 2010). Methane-related carbonates are potentially useful for detecting variations of methane flux in episodic or continuous hydrocarbon seepage sites (Roberts et al., 2006), but they are also “fossils of green house gas” which are produced by anaerobic methane oxidation (AMO) and calcite precipitation in seabed or shallow subseabed sediments. In other words, before methane escapes to the water column, part of it is retained in sediment and reacted with sulfate to produce water, hydrosulphide ion and bicarbonate ion (see reaction 1 below). The latter in turn reacts with calcium ion and precipitate calcium carbonates to form MDAC (see reaction 2 below).



1.2.4.1. Depth of occurrence of methane derived authigenic carbonate occurrence vs. relative fluid flux

AMO takes place in the sulphate–methane transition zone (SMTZ) (fig. 1.16), which generally occur from the seafloor to a depth of a few tens or a hundred of meters (Ritger et al., 1987; Judd and Hovland, 2007). Paull and Ussler III (2008) proposed a model to account for the relationship between production of MDAC, the methane flux and depth of SMTZ. Notice that the term “fluid flux” is generally used qualitatively to compare the intensity of fluid expulsion at different locations in the same setting (Roberts, 2001). It is used for distinguishing the relative speed of hydrocarbon delivery to the ocean floor (cf. Roberts, 2001), instead of using for qualifying the volume of expelled fluid (Moss, 2011). Introduction on a spectrum of fluid flux is given in a further section 1.2.6.

According to the model of Paull and Ussler III (2008), relatively intense methane flux consumes all sulphate in the SMTZ and produce MDAC (fig. 1.16). As a result, the excess volume of methane gas escapes into seawater as bubbles, pushing upward the SMTZ to the water-sediment interface (Paull and Ussler III, 2008). In the adjacent area of the venting exit where the methane flux is less intense, the SMTZ is located in sediment directly beneath water-sediment interface (fig. 1.16). Relatively stable venting environment allow AMO

Productions of methane-related carbonate vary according to methane flux rate

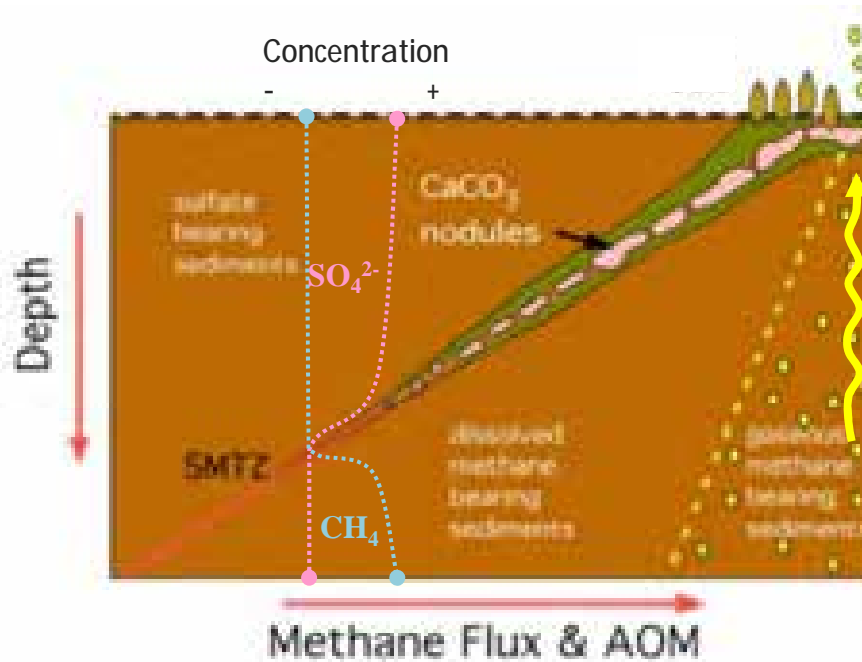


Figure 1.16. Illustration shows the depth of sulphate-methane transition zone (SMTZ) as a function of methane flux; modified after Paull and Ussler III (2008). The base of the SMTZ has been pushed upward to the seafloor at the location of high methane flux. Chemosynthetic communities and methane-derived authigenic carbonates developed around the fast seep at the seafloor and in sediment right below. Moving away from the rapid seeping point, methane flux decreases and surface expression of venting disappears. In addition, the amounts of MDAC decline as the depth of SMTZ increases.

reactions and the calcite precipitations (Paull and Ussler III, 2008), and favours the development of chemosynthetic fauna on the seabed above the MDAC (Paull and Ussler III, 2008). Further away from the major seep point, the depth of SMTZ becomes deeper with the decrease of methane flux (fig.1.16), and the production of MDAC declines while the chemosynthetic fauna absent on the seabed (Paull and Ussler III, 2008).

In conclusion, methane-related carbonates are formed either at the seafloor or in the sulfate methane transition zone (SMTZ) (Hovland, 1984; Ritger et al., 1987; Mazzini et al., 2006). Below the seafloor, they mostly result from anaerobic oxidation of methane (AOM), while at the seafloor they may result from AOM or from the development of chemosynthetic communities.

1.2.4.2. $\delta^{13}\text{C}$ isotopic signature

Methane-related carbonates have an isotopic signature depleted in $\delta^{13}\text{C}$, compared with normal marine carbonate. This is due to the different intra-molecular isotopic distribution and the different isotopic composition of carbonate sources (Durant, 1980). Carbonate precipitations or shells/skeletons of marine fauna use bicarbonate from seawater whose isotopic composition $\delta^{13}\text{C}$ is around 0 (Wood, 1991). Whereas, formation of methane-related carbonate or development of chemosynthetic fauna use the carbonate molecule of methane which is depleted in $\delta^{13}\text{C}$ with negative value of tens order (cf. Judd and Hovland, 2007). Notice that it does not exist a fix range of $\delta^{13}\text{C}$ isotopic value for distinguishing carbonates with biogenesis and thermogenesis origin and which should be interpreted with considering the “geological field association” as stated by Judd and Hovland (2007). Eventhough, the distinction between methane-related carbonates and typical marine carbonate or fauna is mainly based on isotopic analysis.

1.2.4.3. Expression of methane-related carbonates in seismic and their ground truth calibration

Methane-related carbonates are represented by patches of high backscatter (strong acoustic pulses) in side scan sonar records (Orange et al., 2002; Johnson et al., 2003; Sahling et al., 2008; Naudts et al., 2010) and generally by localized positive high amplitude anomalies

(PHAAs) in exploration seismic surveys (Roberts, 2001; Roberts et al., 2006; Cauquil et al., 2003; Cauquil and Adamy, 2008). Both backscatter and PHAAs are caused by the high sonic velocity and high density of carbonate that induce a strong impedance contrast with the soft background (fine-grained) sediment, which have lower density and velocity. A framework on backscatter intensities of a wide range of fluid venting structures at the present day seabed has been established by Roberts (2001), whilst different intensities of backscatter have been correlated with the productivity of chemosynthetic fauna from an active pockmark on the present day seabed by Gay et al. (2006b; 2007). In Gay et al.'s (2006b; 2007) synthetic schema of backscatter intensities, the highest backscatter reflections corresponds to carbonate crusts and domes that concentrate in the pockmarks centre (Gay et al., 2006b; 2007). Medium and low backscatter reflections are respectively caused by chemosynthetic fauna on pockmarks sidewall and hemipelagic sediments in the vicinity (Gay et al., 2006b; 2007).

In 3D seismic, PHAAs are characterized by a positive high amplitude seismic wavelet overlying a negative one and are associated with seismic pull up in some cases (Anstey 1981; Coffeen, 1986; Sheriff, 1978). However, the only published calibration of a PHAA observed on 3D seismic is of several present day seabed pockmarks and depressions by Cauquil et al. (2003) and Cauquil and Adamy (2008) (fig. 1.17).

The previous work of Cauquil et al. (2003) and Cauquil and Adamy (2008) on the calibration along with this thesis are the first steps for understanding the relationship between fossil methane seeps and palaeo fluid venting intensity.

1.2.5. Model for the vertical evolution of methane-related carbonates and their genetic relationship with pockmarks and gas chimneys

This section reviews all published conceptual models on the evolution over time of methane-related carbonate and the related fluid venting structures.

The first conceptual model on the vertical evolution of methane-related carbonate was proposed by Hovland (1989). Succession of vertically stacked methane related carbonate is formed by secondary chemosynthetic reefs that occur above the buried one due to episodic methane seepage (fig. 1.18) (Holvand, 1989).

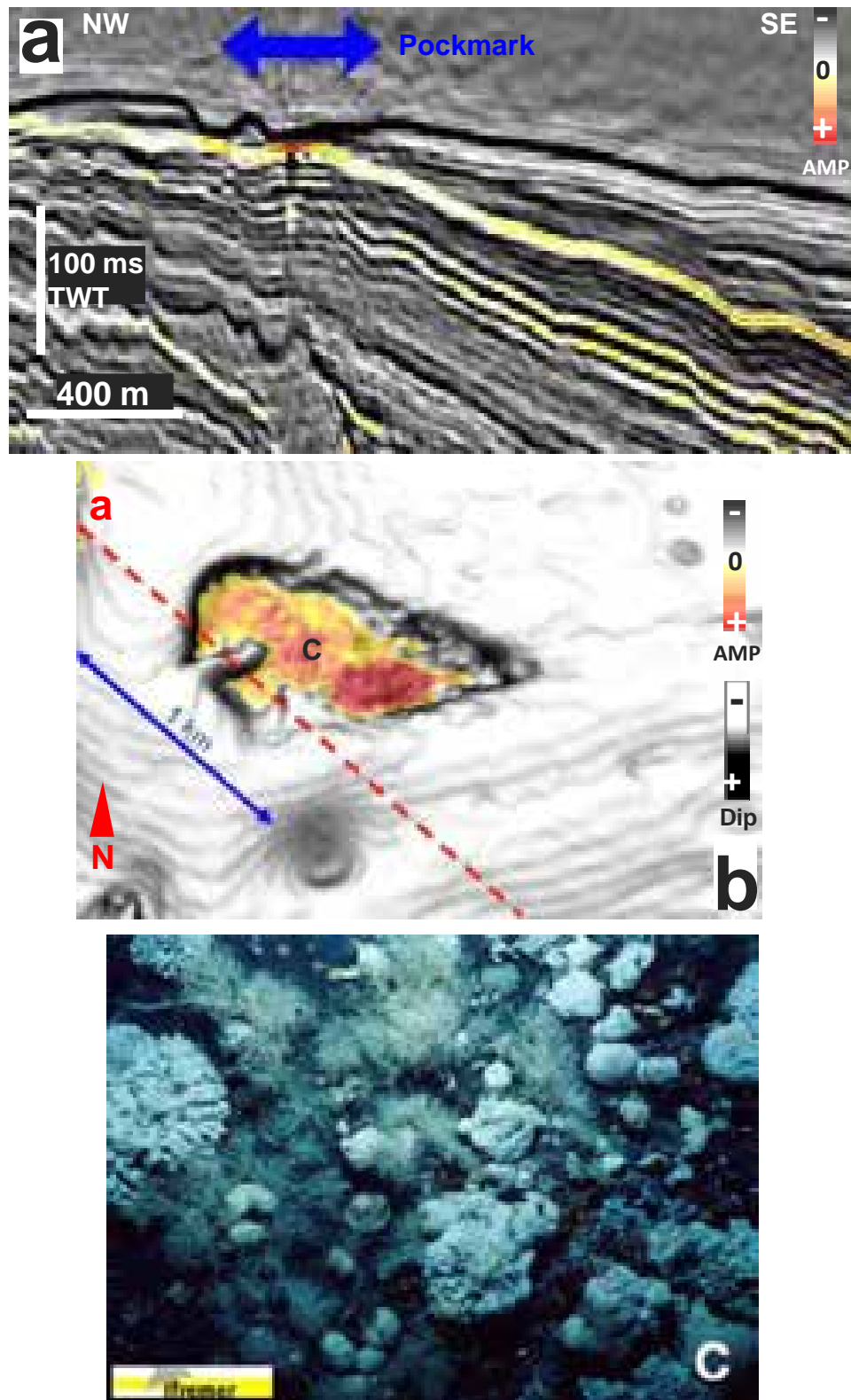
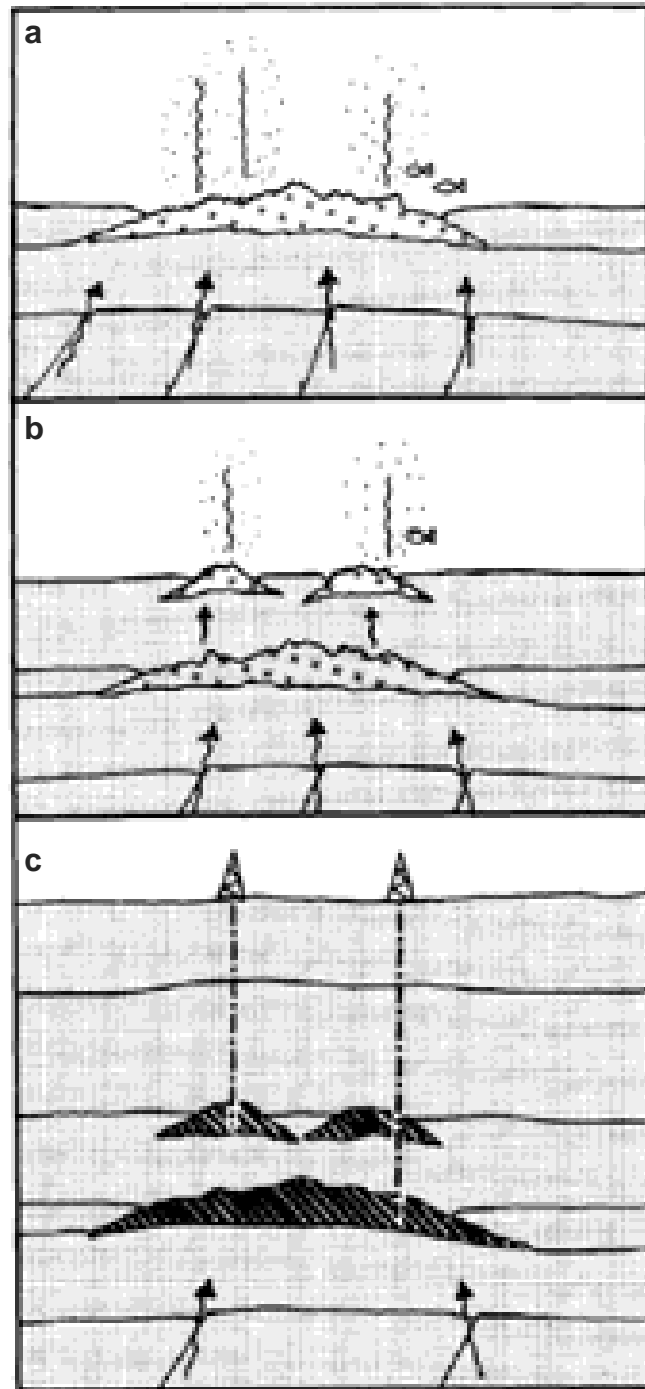


Figure 1.17. The first calibration between positive high amplitude anomalies on 3D seismic and methane-related carbonates, as illustrated in Cauquil and Adamy (2008). The reported seabed depression occurs in offshore Nigeria and shows a positive high-amplitude anomaly. A survey by ROV indicated that the positive high-amplitude anomalies correspond to chemosynthetic communities living on the hard ground of methane-derived authigenic carbonates. (a) The reported fluid-related depression on a seismic profile. (b) Superposition of amplitude of the depression and seabed dip map. (c) ROV image showing chemosynthetic communities growing on underlying carbonate hard grounds. Images taken from Cauquil and Adamy (2008).



By Hovland, 1989

Figure 1.18. The first published cartoon that shows a succession of vertically stacked reefs by Hovland (1989). (a) Emplacement of a hydrocarbon-related reef above fluid conduits. (b) Development of a second generation of reefs above the first one. (c) Burial of the reef succession and infill by hydrocarbons once the overburden is thick enough not being breached.

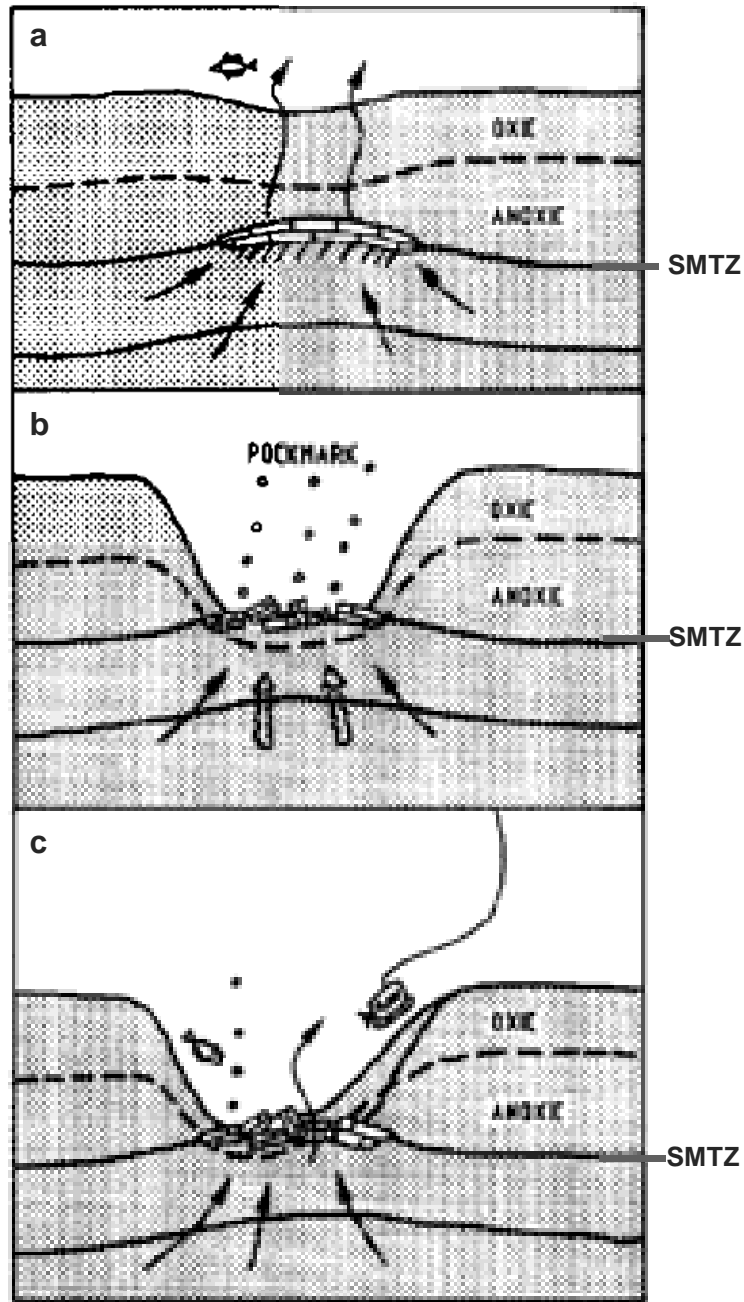
MDAC development in association with a pockmark crater was first proposed by Hovland in 1987 with a case study from the Viking Graben (Hovland, 1982). In Hovland's (1987) model, MDAC initially formed a few meters below the seabed is then fractured by the accumulation of overpressure fluid underneath the MDAC (fig. 1.19) (Hovland, 1987). Overpressure fluid explosion creates a pockmark and deforms the MDAC (fig.1.20b); it then starts to be buried once the methane flux decreases (fig.1.20c) (Hovland, 1987). This is a first conceptual model on the genetic relation between the formations of MDAC, evolution of fluid flux and subsequent fluid venting structures.

The depth of MDAC pavement that is fractured by overpressured methane gas in a pockmark example of Nyegga was discussed by Mazzini et al. (2006). Differing from Hovland's (1987) model, Mazzini et al. (2006) suggest two solutions for the depth of MDAC's formation such that MDAC could be formed actually on the seabed (fig. 1.20) or a few centimetres below (fig. 1.21).

In the second model of Mazzini et al. (2006) (fig. 1.21), pockmark is suggested to form first (fig. 1.21a) while MDAC and chemosynthetic fauna develop afterward inside the pockmark (fig. 1.21b) (Mazzini, et al., 2006). The MDAC grows over time to eventually become a carbonate mound which fills the whole pockmark (fig. 1.21c) (Mazzini et al., 2006). The two models of Mazzini et al. (2006) focus principally on the dynamics of the precipitation of carbonates and other mineral phases (see Mazzini et al., 2006), instead of centering on the interaction between venting structure and fluid flux.

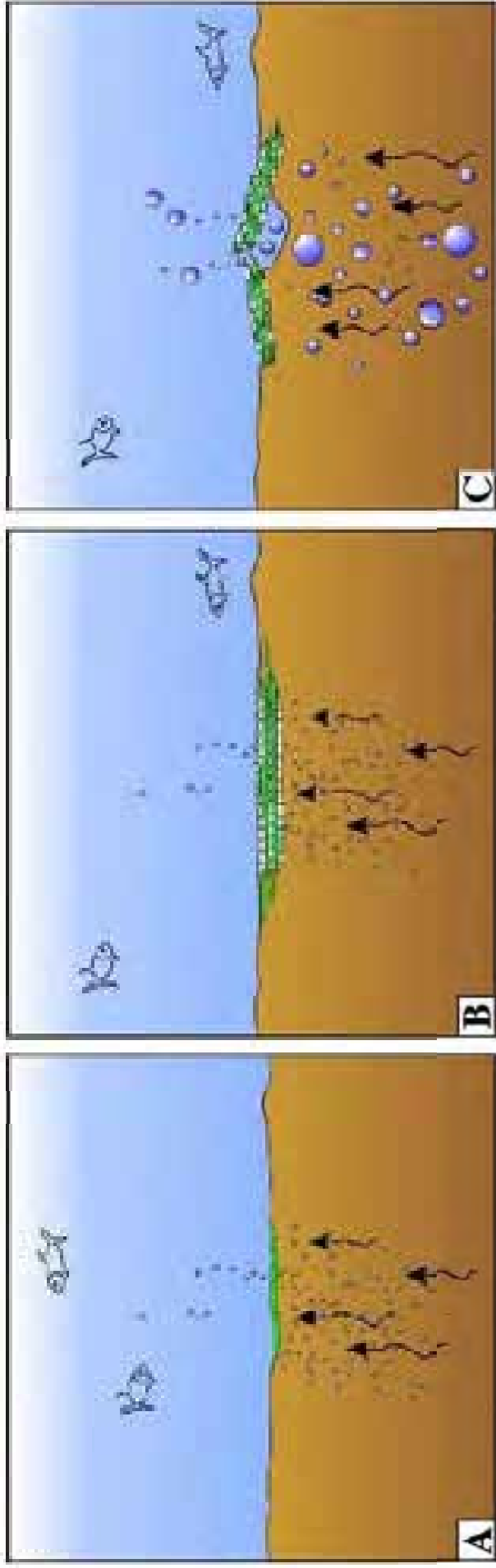
A concept on the vertical evolution of cold-seep carbonates and their associated communities at methane venting locations has been proposed by Gay et al. (2007). The conceptual diagram of Gay et al. (2007) suggests 1) the production of the cold-seep carbonate and communities at the seafloor vary overtime (fig. 1.22) is a function of methane supply variance; 2) different evolutionary phases of these cold-seep assemblages given different responses in backscatter intensity. However Gay et al.'s (2007) diagrams only focus on variations of backscatter intensity induced by different evolutionary phases of the cold-seep assemblages. The impacts of temporal variations of methane venting intensity on the size and geometric of surface areas of cold-seep assemblage have not been investigated (fig. 1.22).

The genetic relation between the timing and type of fluid venting structure has been studied by Plaza-Faverola et al. (2011). In a case study of fluid venting structures in Offshore Norway, Plaza-Faverola et al. (2011) describe how a fluid conduit is formed and promotes methane migration to the seabed (fig. 1.23.a-i), while a MDAC mound forms afterward (fig. 1.23.a-ii) (Plaza-Faverola et al., 2011). This MDAC mound in Plaza-Faverola et al.'s (2011) study was buried by hemipelagic deposition when the seepage was deactivated, then was



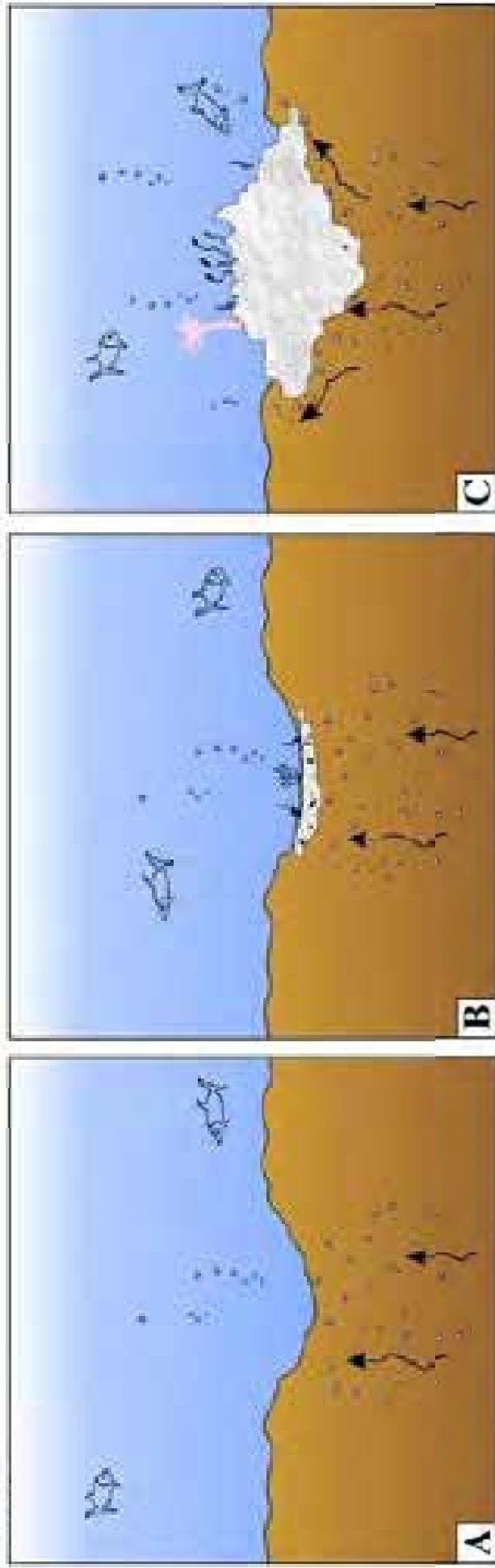
By Hovland, 1987

Figure 1.19. The first published conceptual model for the formation of methane-derived authigenic carbonate (MDAC) in association with a pockmark, by Hovland (1987). (a) Methane migration induces shallow depression at the seabed and MDAC precipitation in the sulfate-methane transition zone (SMTZ). (b) Fluid pressure builds up and fractures the MDAC, followed by brutal fluid eruption and generation of a pockmark crater on the seabed. (c) The pockmark becomes buried once fluid venting becomes less intense.



By Mazzini et al. (2006)

Figure 1.20. Schematic model for the formation of methane-related carbonate on the seabed by Mazzini et al. (2006). (a) Slow hydrocarbon seepage initiated the formation of methane-related carbonate on the seafloor. (b) The carbonate grew over time with lateral extensions. (c) Expulsion of overpressured fluid from gas pockets underneath deformed the carbonate slabs.



By Mazzini et al. (2006)

Figure 1.21. Schematic evolutionary model of methane-derived authigenic carbonate (MDAC) formation at the seabed in a pockmark by Mazzini et al. (2006). (a) A pockmark formed by fluid expulsion on the seafloor. (b) Precipitation of MDAC at water-sediment interface, with chemosynthetic organisms developed on it. (c) The MDAC became thicker over time, fluid bypassed the impermeable carbonate, enhancing the lateral growth of the carbonate; as a result the carbonate grows not only vertically but preferentially laterally.

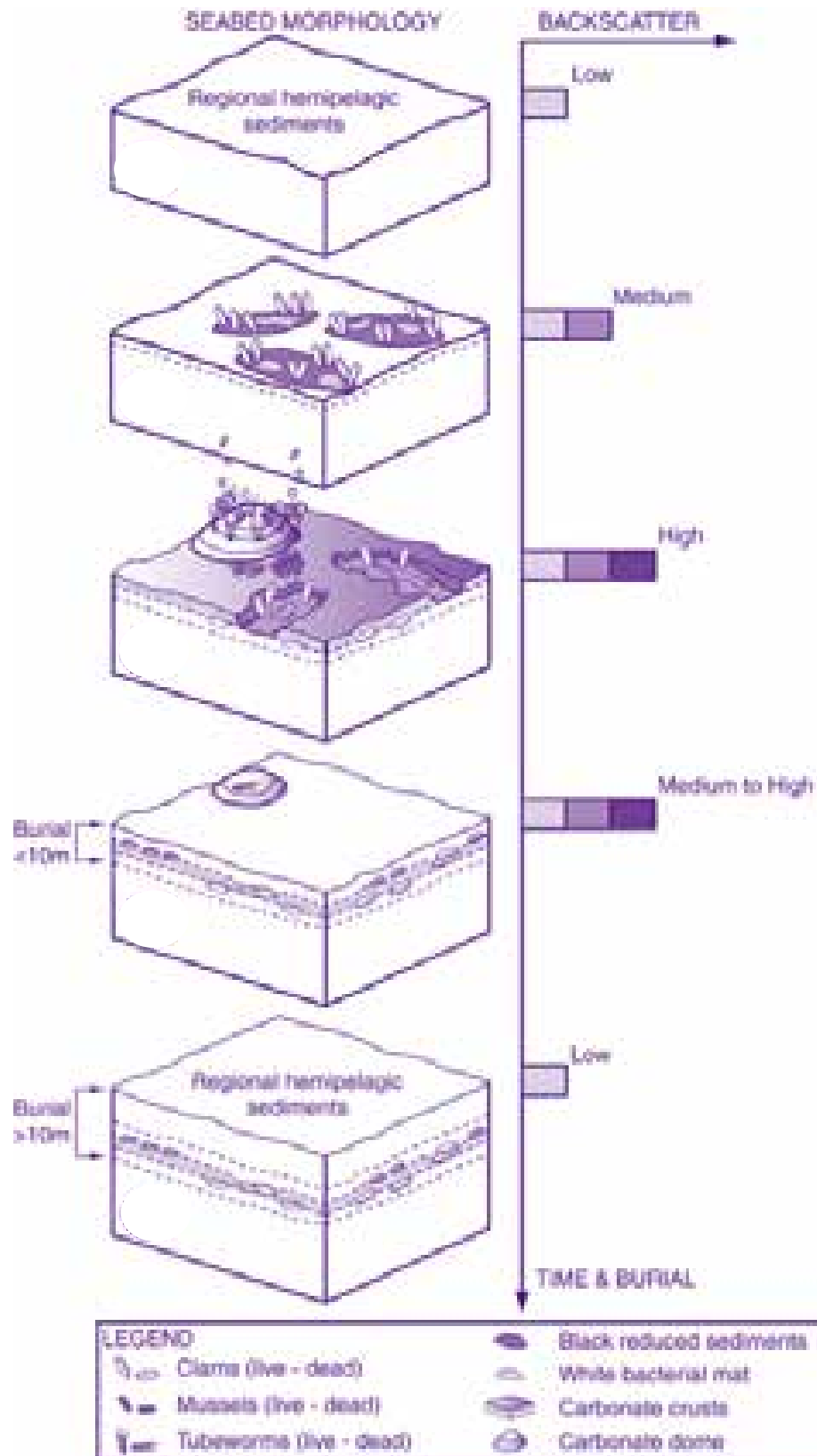
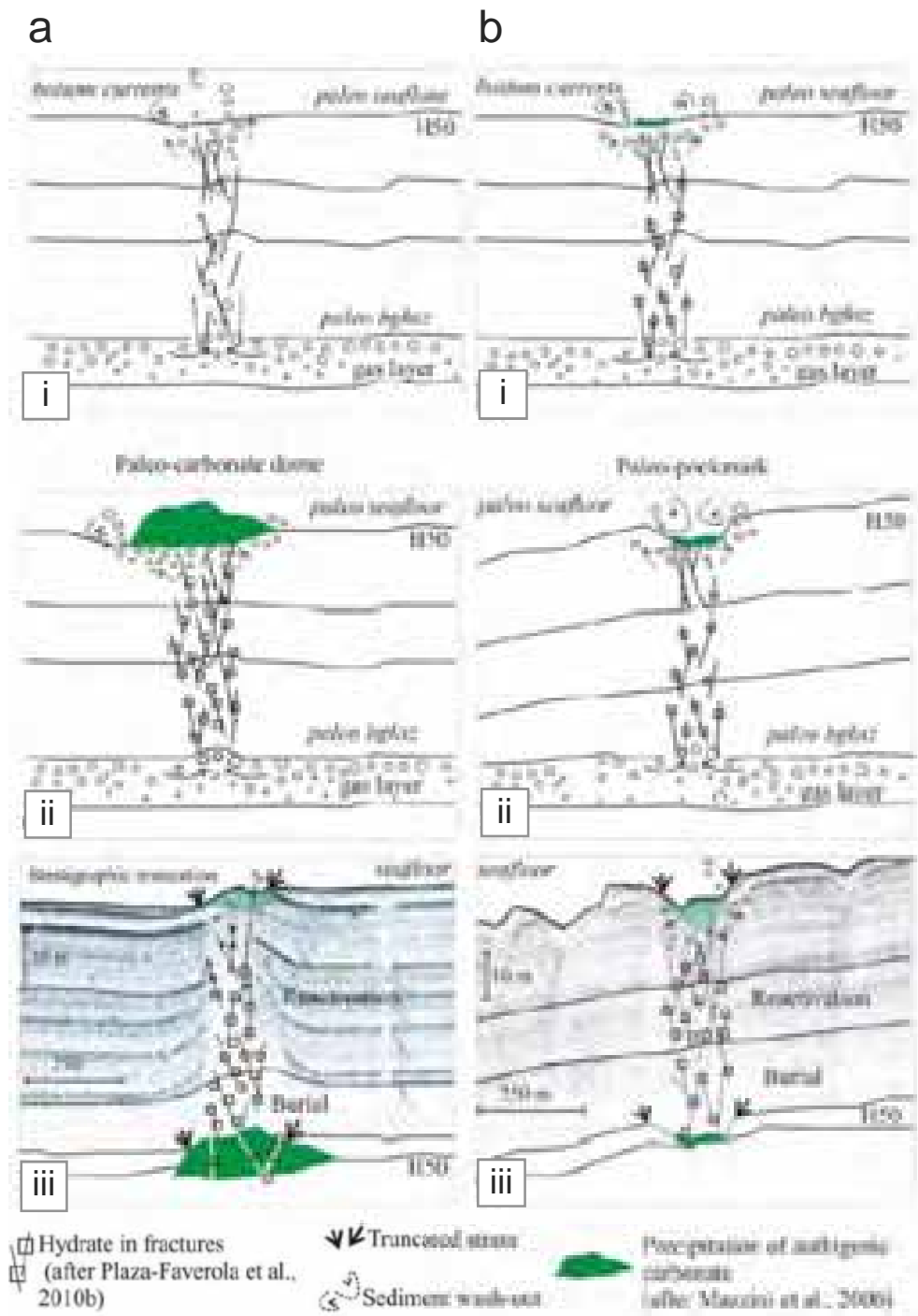


Figure 1.22. Diagram showing the relationship between backscatter reflectivity and different types of methane-related carbonates and fauna; modified after Gay et al. (2007).



By Plaza-Faverola et al. (2011)

Figure 1.23. Conceptual model on the genetic relationship between gas chimneys, pockmarks, and methane-derived authigenic carbonate (MDAC) by Plaza-Faverola et al. (2011). (a) Genetic relation between gas chimneys and MDAC: i) initiation of a gas chimney above a free gas-bearing layer, in which free gas migrates underneath the base of gas hydrate stability zone (BGHS); ii) a MDAC occurs above the chimney; iii) the carbonate is buried and a new chimney forms above it by step (i). b) Genetic relationship between gas chimneys, pockmarks and MDAC: i) MDAC precipitated at methane seep above a gas chimney; ii) Sediment around the seep was eroded by fluid expulsion and bottom current; a pockmark was formed around the MDAC; iii) The pockmarks and MDAC were buried afterward by overburden sediment; a new chimney formed above with emplacement of a new pockmark and MDAC at the top by steps (i) and (ii).

deformed afterward by upward propagations of hydraulic fractures following the reactivation of the seepage (fig. 1.23a-iii) (Plaza-Faverola et al., 2011). A new generation of MDAC mound is formed on the seabed above the newly propagated fractures and the previous MDAC, hence forming a vertical stack (fig. 1.23a-iii) (Plaza-Faverola et al., 2011).

A more complex genetic relationship between pockmarks, gas chimneys and MDACs is discussed in a second conceptual model of Plaza-Faverola et al. (2011). A MDAC is formed at seep point where methane ebullition and bottom currents prevent sedimentation (fig. 1.23.Ib-i). The latter process induces a pockmarks characterized by a hard bottom made of MDAC (fig. 1.23b-ii) (Plaza-Faverola et al., 2011). This MDAC-associated pockmark is buried during a phase of inactivity of the seep (fig. 1.23b-iii) (Plaza-Faverola et al., 2011). Once the seepage is reactivated, the cycle of overpressure fluid fracturing; methane gas migration; MDAC formation; sedimentation; pockmark formation restarts, thus forming a vertical succession of fluid venting structures (fig.1.24b-iii) (Plaza-Faverola et al., 2011).

However, in Plaza-Faverola et al.'s (2011) conceptual model focused on the timing of formation of fluid venting structures but the influence varying methane venting intensity on different types of venting structures at seeping locations was not investigated.

A first outcrop of methane-related carbonate in association with a pockmark has been discovered along the northwest coast of Spain by Agirrezabala et al. (2013). According to the Agirrezabala et al.'s (2013) outcrop study, pockmark and methane-related carbonates are interpreted to form by methane seepages with the carbonate growing through vertical overlying strata at the seep location (Agirrezabala et al., 2013). The volume of carbonate is suggested to increase over time so as to eventually induce local subsidence at seep location, thereby initiating a pockmark in the conceptual model of Agirrezabala et al. (2013) (fig. 1.24a). Turbidites are observed alternating with hemipelagites inside the pockmark in which they are cemented by seep carbonate each time after their deposition (fig. 1.24b, c) (Agirrezabala et al., 2013).

In comparison with seismic-scale pockmarks (depth more than several tens meters; diameters more than a hundred meter) that are commonly reported in literature (e.g. Hovland and Judd; 1988; Pilcher and Argent ; 2007; Gay et al., 2006b; Judd and Hovland 2007; Olu et al., 2009), the outcropped pockmarks in Agirrezabala et al. (2013) do not show any truncation of underlying strata or v-shaped, but simply parallel bedding inside shallow depressions (depth < 40 centimeters, diameter < 25 meters). So the “pockmarks” that studied by Agirrezabala et al. (2003) may possibly correspond in a strict sense to cold seeps rather than a

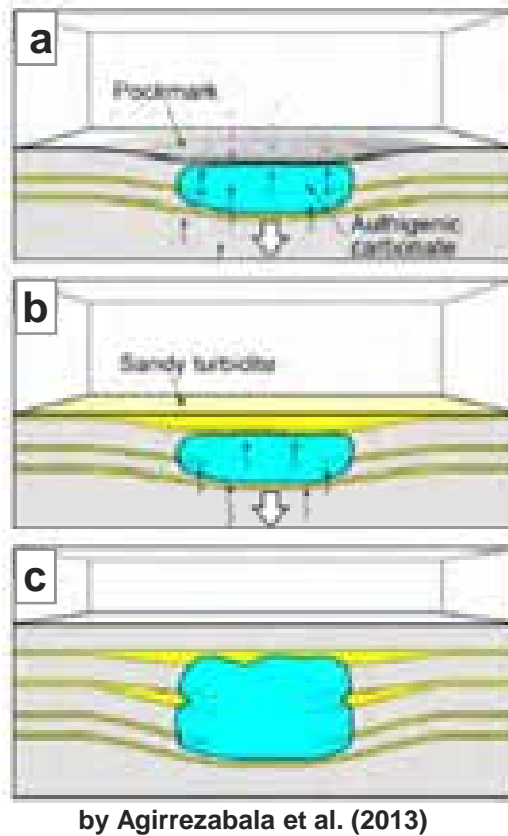


Figure 1.24. A conceptual model for the formation of an outcrop fossil pockmark and its associated methane-derived authigenic carbonate (MDAC) by Agirrezabala et al. (2013). a) A MDAC was formed by methane oxidation/sulfate reduction at the seep location. A depression i.e. a pockmark is formed by methane seep and by the weight of the MDAC body which induces subsidence in sediment. b) A sandy turbidite is deposited inside the pockmark and the MDAC continues to grow. c) Turbidites are deposited in the pockmark in alternation with clayey drapes; step (b) is repeated until methane migration is deactivated, and the MDAC is sealed by sediment drape.

common reported (v-shaped) pockmarks (cf. King and Maclean, 1970; Hovland and Judd; 1988; Pilcher and Argent ; 2007; Judd and Hovland 2007; Olu et al., 2009).

Agirrezabala et al.'s (2013) model suggests a new process for the formation of methane-related depressions by subsidence rather than by fluid expulsion or by starvation of sediment due to fluid vents. Their study provides some more accurate information on seep carbonate formational environment. Their reported outcrop is a first genetic vertical sequence of methane-related depressions and MDAC that has been observed in the field worldwide.

Unfortunately, the duration of MDAC successive depositional events could not be dated in the outcrop studied by Agirrezabala et al.'s (2013) because the duration of the MDAC precipitation event was lower than the temporal resolution of the radiometric or biostratigraphic dating. Thus, the timing between the formation of pockmark and carbonate remains unclear and fluid flux during each evolutionary stage could not be assessed.

1.2.6. Relationship between fluid flux and development of venting structures

A qualitative spectrum of fluid flux has been established by Roberts (2001), Roberts et al. (2006). It is based on a decade of studies and direct observations on seepages activities of different types of venting structures by remote control submersible at the seabed in Gulf of Mexico by Roberts (2001), and leads to the notion that morphological developments of fluid venting structures are directly linked with intensities of fluid expulsions. Roberts (2001) and Roberts et al. (2006) have classified fluid venting structures and the associated chemosynthetic organisms according to whose representing fluid flux (fig. 1.25). The key findings of this classification are in agreement with the research results of other researchers such as; Torres et al. (2002), Cartwright et al. (2007), Gay et al. (2007), Naudts et al. (2010).

The term “fluid flux” in this classification is refers to: “*Qualitative expressions of comparative rates at which hydrocarbons, fluidized sediment, and other carrier fluids are delivered to the modern slope surface*” Roberts (2001). The sediment response of fluid seepages cannot be quantified by a direct numerical relationship (cf. Roberts, 2001; Moss, 2011), and there does not exist an exact scientific term to describe the degree of fluid expulsion in literature. Therefore, in this thesis, the terms “flux” or “intensity” of fluid venting/seepages are used to describe degrees of fluid expulsions, and which are relative character obtained based on the comparison of fluid venting structures morphology and is not

Methane seepages and seabed responses

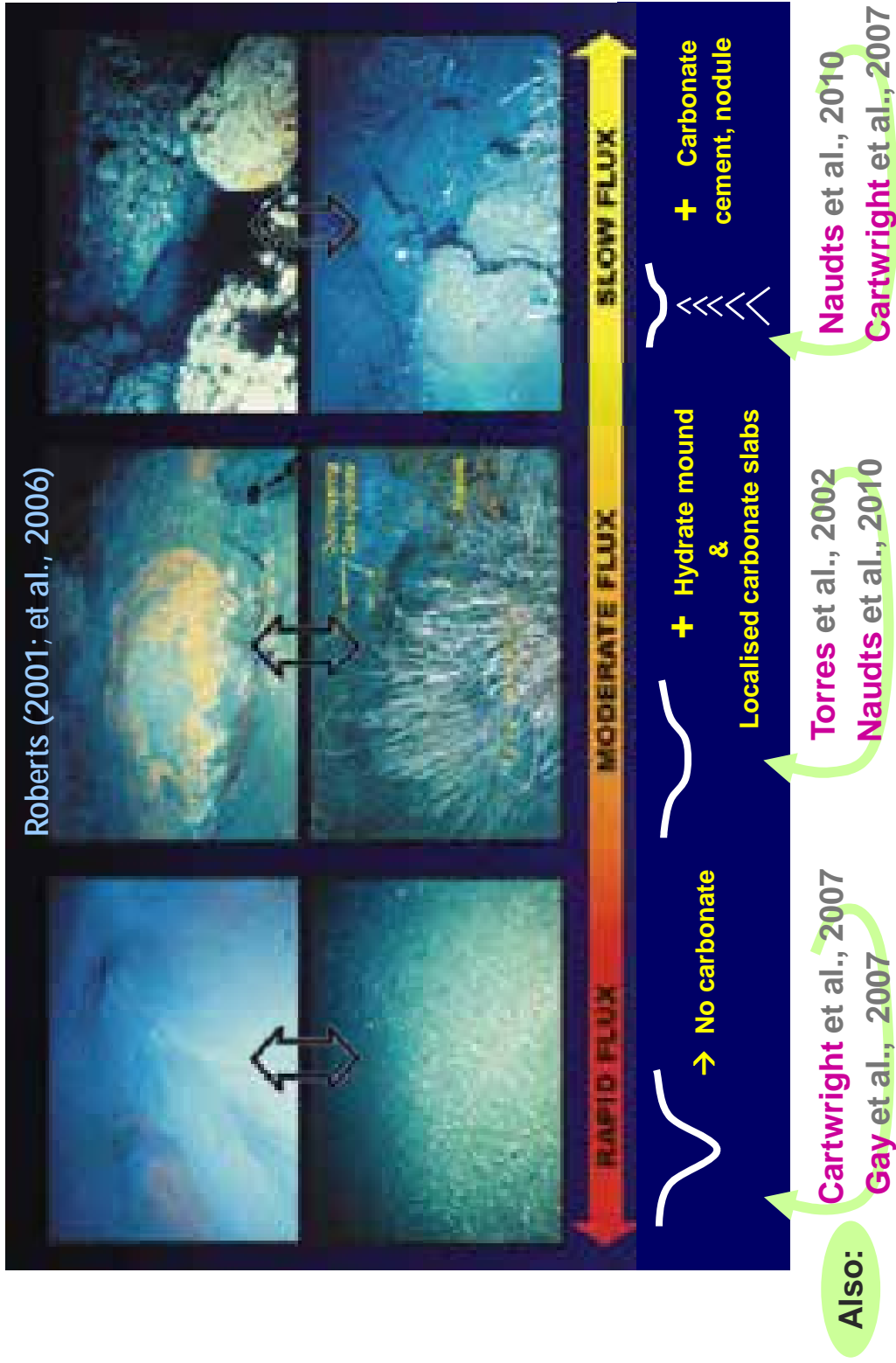


Figure 1.25. Classification of fluid venting structures base on the qualitative fluid flux rate as observed at the seafloor by ROV (Roberts, 2001; Roberts et al., 2006). Key principles of this classification are in accordance with those suggested by other authors in literature.

quantitative. As the absolute value on fluid flux cannot be determined on different type of venting structures, thus fluid venting structures in this thesis are classified into types based on relative fluid expulsion intensity.

The main principles of the classification of Roberts et al. (2006) can be summarized as follows:

a) Slow flux (fig. 1.25) is characterized by mineralized gas chimneys (Roberts, 2001; Roberts et al., 2006; Cartwright et al., 2007; Naudts et al., 2010), MDAC nodules and very localized bacterial mats or chemosynthetic clams (Roberts, 2001; Roberts et al., 2006; Naudts et al., 2010). The slow delivery and the insufficient quantities of hydrocarbons in the ocean floor do not allow the development of chemosynthetic macroorganisms above slow seeps (Roberts, 2001; Torres et al., 2002; Roberts et al., 2006).

b) Moderate or intermediate flux (fig. 1.25) is represented by small-scale gas expulsion features i.e. non conical pockmarks (Roberts, 2001; Roberts et al., 2006); gas hydrate mounds; abundant complex chemosynthetic communities associated with isolate carbonate slabs; massive authigenic carbonate rocks and low relief carbonate mounds (Roberts, 2001; Roberts et al., 2006; Torres et al., 2002; Naudts et al., 2010). The intermediate flux provides a more stable hydrodynamic environment at venting exit and provides sufficient methane flux for precipitation of MDAC or solid gas hydrate which serves as hard substratum for the development of benthic chemosynthetic fauna (Roberts, 2001; Roberts et al., 2006).

c) Rapid flux (fig.1.25) is indicated by circular expulsion centres (Roberts, 2001; Roberts et al., 2006; Gay et al., 2007), or mud-prone features or mud volcano with quasi absence of macro faunal communities and MDAC at the vent (Roberts, 2001; Roberts et al., 2006). It is principally due to fast seepage that does not allow the emplacement of any stable substratum for the development of chemosynthetic communities nor the precipitation of MDAC (Roberts, 2001; Torres et al., 2002; Roberts et al., 2006).

In summary, present or past fluid leakage occur at the seabed can be indicated by the presence of chimneys, pockmarks and also methane-related carbonatemethane-related carbonates. Among these indicators only methane-related carbonates are diagnostic of methane gas. The fact that methane-related carbonates are formed on the seabed or in sediment close to the seafloor (within the limits of SMTZ) suggests that vertical successions of methane-related carbonates can reflect the variations over time of fluid leakages at given seep points. The size, number and morphology of methane-related carbonates are interpreted

to reflect approximately the relative flux of escaped methane. In combination with the presence of pockmarks and chimneys associated with vertical successions of PHAA (interpreted methane-related carbonates) on seismic, the dynamics of fluid expulsion and the variation of flux over time can be estimated qualitatively.

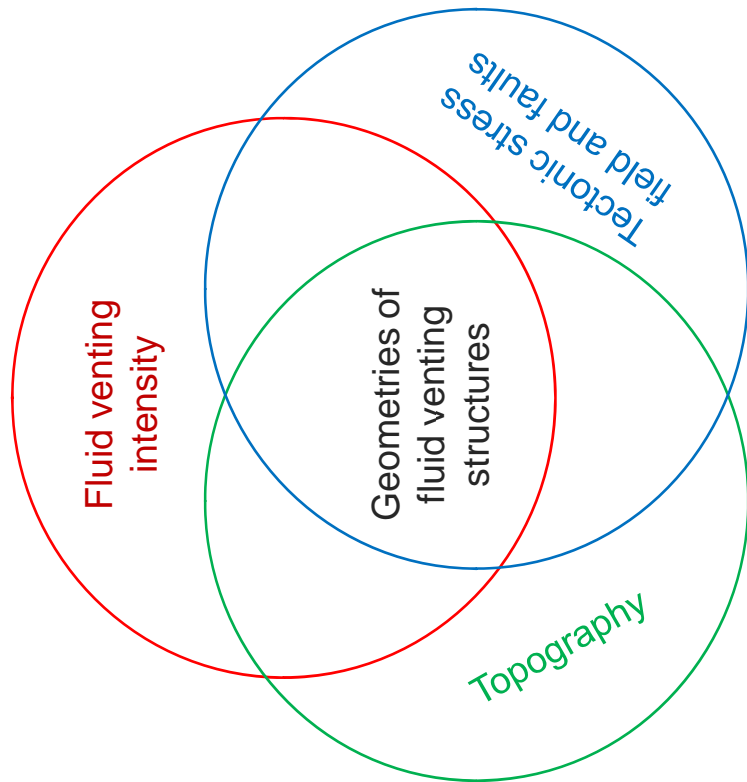
1.3. The motivation and aim of the thesis

This thesis aims to fill gaps identified in the research fields of subsurface fluid flow science. These were outlined in the preceding sections. Each of the objectives below provides a platform for addressing the overriding theme of the thesis which is to explore the interactions between the evolution of fluid venting structures and fluid leakage intensity (fig. 1.26), as well as to establish how the structural and stratigraphic evolution of a basin affects fluid venting structures (fig. 1.27). The aims and objectives are:

1. To investigate positive high amplitude anomalies (PHAAs) in a 3D seismic data set from the Lower Congo Basin and to establish/determine their origin (Chapter 4).
 - To analyse in detail the geophysical character and geometry of PHAAs.
 - To investigate the relationship between PHAAs and other venting structures.
2. To put forward a method by using seismic expressions of methane-related carbonate to find out the timing and duration of seepages at the seabed over geological time (Chapter 4).
 - To identify methane--related carbonates on seismic data.
 - To investigate their areal and stratigraphic distribution.
3. To study new types or variety of fluid venting structures on 3D seismic and study their genetic relationships, as well as their implications as regards fluid flow: linear fluid conduits (Chapter 4), linear PHAAs and the networks they define (Chapter 4, 6), vertical successions of sub-circular PHAAs (Chapter 4), polyphased pockmarks (Chapter 4), nested pockmarks (Chapter 5), advancing pockmarks (Chapter 5), honeycomb pockmarks (Chapter 6).
 - To analyse the size, geometry and complexity of each individual venting structure.
 - To identify the geometry of all fluid venting structure present in this study area.
 - To extend the classification of Roberts (2001) and Roberts et al. (2006) and integrate the key findings of other researchers on this topic (Chapter 4).

Geological responses for different degrees of fluid seepages

Chapter 4



Chapter 5

Influences of topography on geometrical evolution of fluid venting structure

Chapter 6

Interplay between tectonic settings and distributions of fluid venting structures

Figure 1.26. Conceptual diagram of this thesis research. The scope of the thesis is defined by the overlap of three principal areas: expression of fluid expulsion, impact of topography, influence of tectonic stress field.

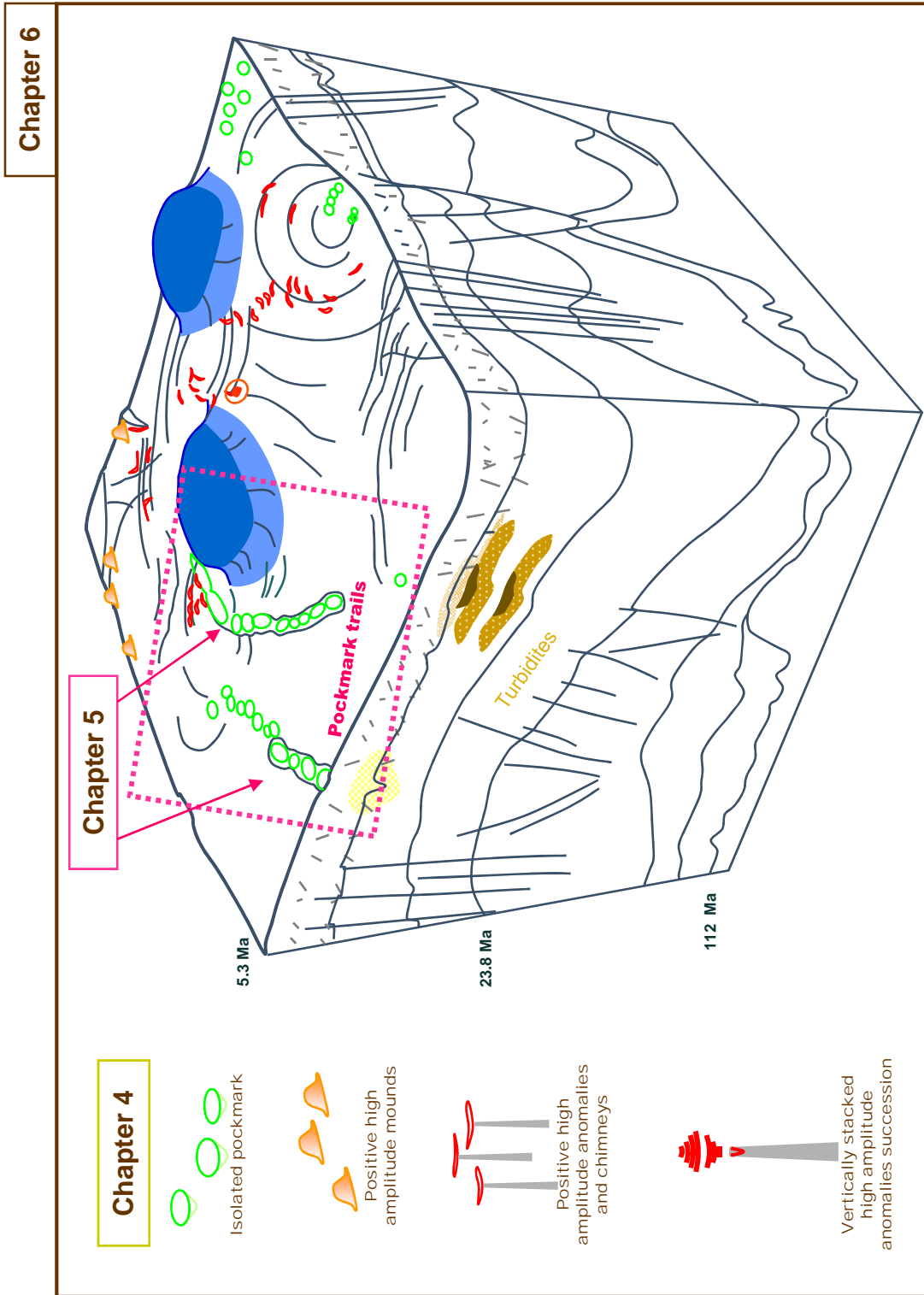


Figure 1.27. Block diagram representing the spatial distributions of fluid venting structures in the Neogene-Quaternary interval of the studied seismic block. The themes covered in the core chapters of this thesis are placed in the context of this conceptual framework. These core themes interact at the local and basinal scale are interlinking the research presented in the core chapters.

- To establish a new categorization with more details on the evolution of gas chimneys, methane-related carbonates, shallow fluid-related depressions and pockmarks (Chapter 4).
4. To propose a new methodology and demonstrate how to use vertical successions of fluid venting structures to determine variations in the intensity of focused seepage over time (Chapter 4).
- To identify, classify and date each type of fluid venting structure in the succession.
 - To use the morphology and stratigraphic infill of venting structures to determine the intensity of fluid venting (Chapter 4).
5. To understand the interrelationship between fluid seepage dynamics and such control factors, i.e. as the regional topography and geological setting (Chapter 5), the development of tectonic structures and variations in the style of sediment depositions during basin evolution (Chapter 6). To integrate all these elements into a historical reconstruction of fluid seepage intensity in the study area (Chapters 6, 7).
- To map the spatial and temporal distributions of fluid venting structures across the study area in the studied stratigraphic interval.
 - To investigate the tectonic history of the study area.

1.3.1. Thesis layout

An introduction and overview of the research topic covered in this thesis have been presented in the preceding sections of this Chapter 1. An introduction of the data used, a brief review on the common methods used in all results chapters, and the limitations to the research project are presented in Chapter 2. An overview on the geological setting of in the Lower Congo Basin is given in Chapter 3. The research results are presented in core-chapters 4 to 6. A discussion of this thesis research and implications are provided in Chapter 7. The conclusion of the research is presented in Chapter 8. Complementary data of each core chapter are attached as appendices.

CHAPTER 2

METHODOLOGY

2.0 Methodology

2.1. Introduction

The research results presented in this thesis are based on the observation, interpretation and detailed analysis of fluid venting structures visible on 3D seismic data. The aim of this methodology chapter is to 1) give a brief overview on the reflection seismic method; 2) outline the seismic surveys used in this thesis and describe their parameters; 3) present an overview of the methods that were used to interpret and analyse fluid venting structures; and finally, 4) describe the limitations induced by the data and a strategy to find solutions.

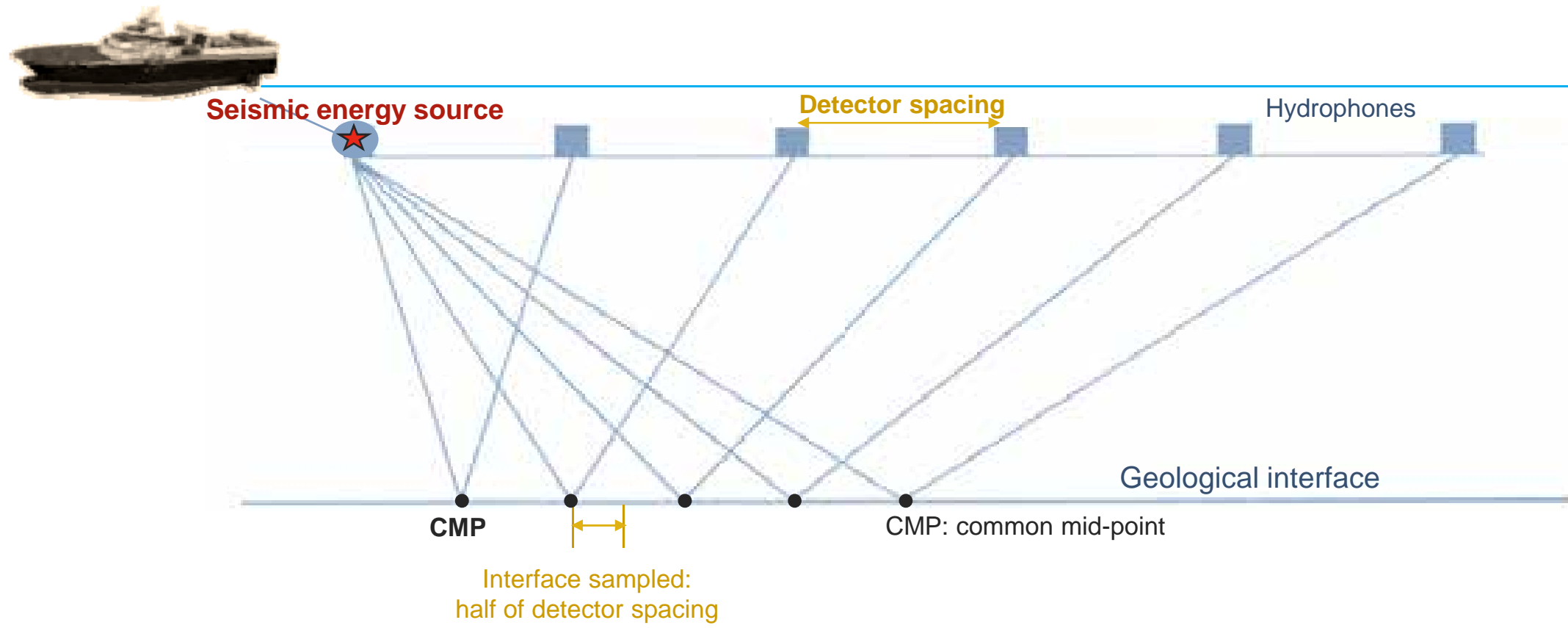
2.2. Seismic data

This thesis on fluid venting structures of Offshore Angola is based on two 3D seismic surveys. The research presented in Chapter 4 is based on a high resolution delineation 3D volume in the transitional zone of Offshore Angola. Chapters 5 and 6 are based on the same 3D volume in addition to a regional 3D exploration volume which covers the compressional to transitional zones of Offshore Angola.

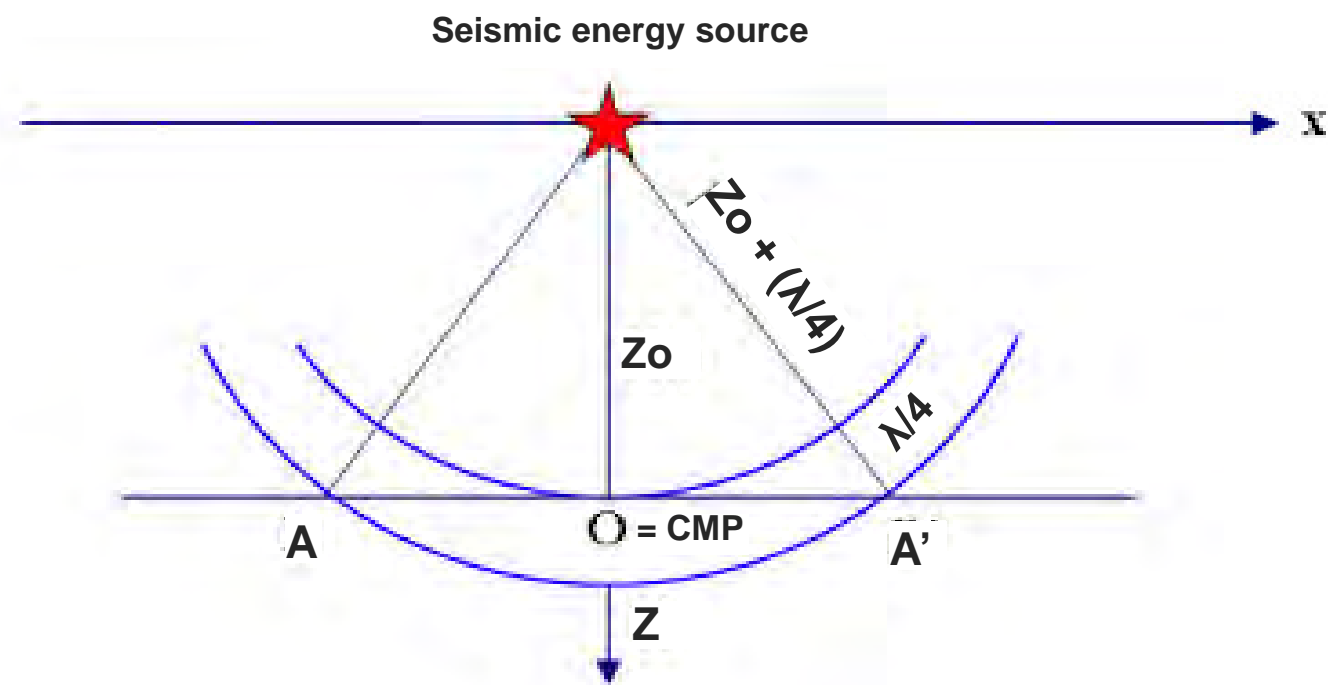
2.2.1 The science of 3D seismic data

Reflection seismology is a geophysical technique for imaging basins. Acquisition of marine seismic reflection data consists in the recording of the wave field generated by an impulsive pressure source, the airgun (Bacon et al., 2003). The recording sensors are hydrophones and are embedded in a streamer towed by a boat and submerged close to the surface of the sea (fig. 2.1a). The source, considered as punctual, consists of a cluster of chambers which release high pressure air into the water close to sea surface at regular time intervals. It creates a pressure pulse or a seismic wave which propagates in all directions (Anstey, 1977). Seismic waves penetrate into the subsurface and are reflected back at low

a



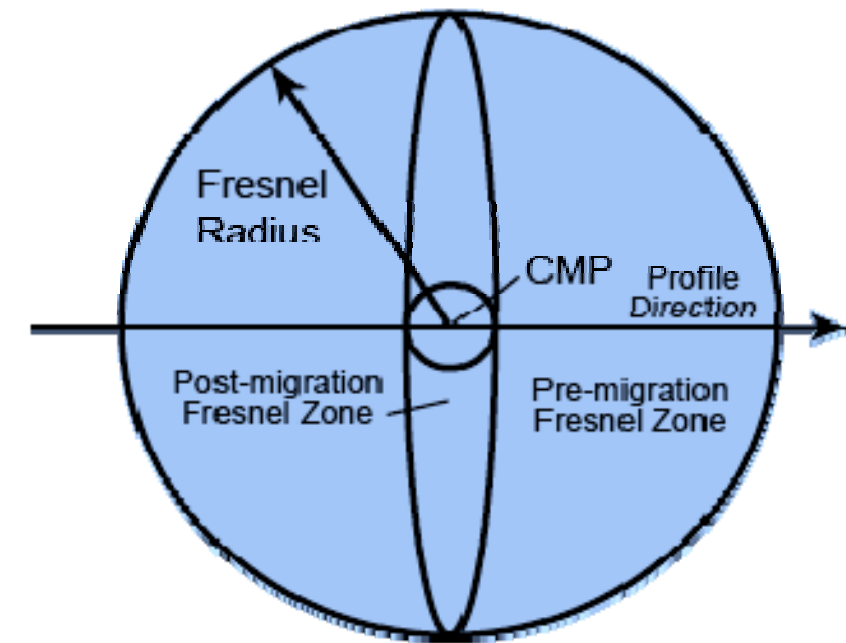
b



Dominant frequency: λ

Rayleigh limit of vertical resolution: $\frac{1}{4} \lambda$

c



CMP: common mid-point

Figure 2.1. Seismic horizontal resolution. a) Lateral sampling of seismic traces as a function of spacing of hydrophones. b) Fresnel zone A-A' for an energy pulse created at the sea surface (x) and striking a horizontal geological interface at depth Z_0 . c) Reduction in the width of the Fresnel zone after the (post-) migration of seismic data. Modified after Sheriff (2001). The post migration Fresnel zone is one quarter of the dominant wavelength.

angle of incidence by interfaces with acoustic impedance contrasts across them and return to the recording streamer (Sheriff, 1992). Any single airgun shot is recorded by all of the hydrophones located in the streamer. All of these data are processed together in order to 1) shape the propagating source wavelet into a simple symmetric shape (deconvolution) (cf. Bacon et al., 2003), 2) enhance the signal reflected once off any subsurface interface (demultiple and stacking) (cf. Bacon et al., 2003), 3) locate the reflected energy at the right place allowing for the propagation velocity structure (migration) (cf. Bacon et al., 2003). The result of seismic processing forms a volume of data showing reflection interfaces of different intensity and shape located at different times. This time depends on the vertical time it would take the source pulse to travel from surface to the interface and back (two-way travel time). The succession of such reflections on a vertical time (or depth) axis forms what is called a seismic trace (cf. Coffeen, 1986; Brown, 2004).

The visibility of interfaces in seismic traces depends on a principal parameter: the acoustic impedance contrast. It corresponds to the product of the acoustic velocity and density of the medium through which the source pulse have propagated. More precisely, reflection intensities (R) relate to the relative difference in acoustic impedance between successive geological layers. For more detail see Anstey (1977).

The depth of penetration of such a compressive wave and clarity of interfaces depends not only on the frequency content of the initial source but also on the absorption properties of the medium which will filter out higher frequencies (cf. Anstey, 1977; Sheriff, 1992; Brown, 2004). As a result, the seismic energy will lose its strength when travelling downward. Only a part of the seismic energy of lower frequencies will be reflected from the deeper subsurface back to the sea surface (Sheriff, 1992). Hence image qualities of deeper interfaces will be decreased.

In general, the higher the initial emitted frequencies are, the lower is depth penetration but the higher is resolution for seismic reflections in the shallower interval (Brown, 2004). Inversely, the lower the initial frequencies are, the lower is the resolution of seismic reflections but the deeper is the penetration. A full explanation on seismic acquisition and signal processing can be found in e.g. Bacon et al. (2003).

2.2.1.1. Amplitude and colour convention

Amplitude values of seismic reflections are generated by geologic layers which have difference sonic velocity and density (Anstey, 1977). When the seismic wave propagates through the succession of geological layers, it meets layers of different acoustic impedances. A downward increase in impedance will result in a positive reflection (Coffeen, 1978), whereas a decrease of impedance downward will produce a negative one (Coffeen, 1978). The stronger the contrast, the higher will be the amplitude of the seismic reflection will be (see Anstey, 1977; Sheriff, 1978; Beck, 1981).

In the studied surveys, the seismic data have been processed in such a way that the seismic response of a single isolated interface with positive reflectivity corresponds to a symmetrical pulse with a positive amplitude. Such a wavelet is called zero-phase.

The colour convention for amplitude display on seismic sections in this thesis is red-yellow-white-black (fig. 2.2) and is followed the colour scheme of SEG (Society of Exploration Geophysicists). The most intense reds correspond to the strongest positive reflections. Yellow represents intermediate positive amplitudes whereas white colour refers to zero-crossing and black indicates a negative reflectivity.

2.2.1.2. Vertical resolution and impact of thickness variations on amplitudes

Vertical resolution determines how detailed a stratigraphic layer can be imaged on seismic. The vertical resolution in reflection seismic data is determined by the shortest wavelength of the seismic wavelet. It is a function of the emitted frequencies and velocities of geological formations, as well frequency-dependent attenuation and processing.

The true thickness of geological features cannot be represented correctly by seismic data if the feature is below the 'tuning thickness' (vertical seismic resolution) (Widess, 1973). This phenomenon will be generated if the basic seismic response of the two reflections which define the top and base of a thin layer are spaced by less than one quarter of the wavelength, then their side lobes merge and generate the composite waveform (see Brown, 2004).

A thin geological layer will be represented by two seismic reflections whose total thickness is seismically thicker than the real geological layer. This is because of the two main wave lobes, which compose the reflections and represent the top and bottom of the geologic

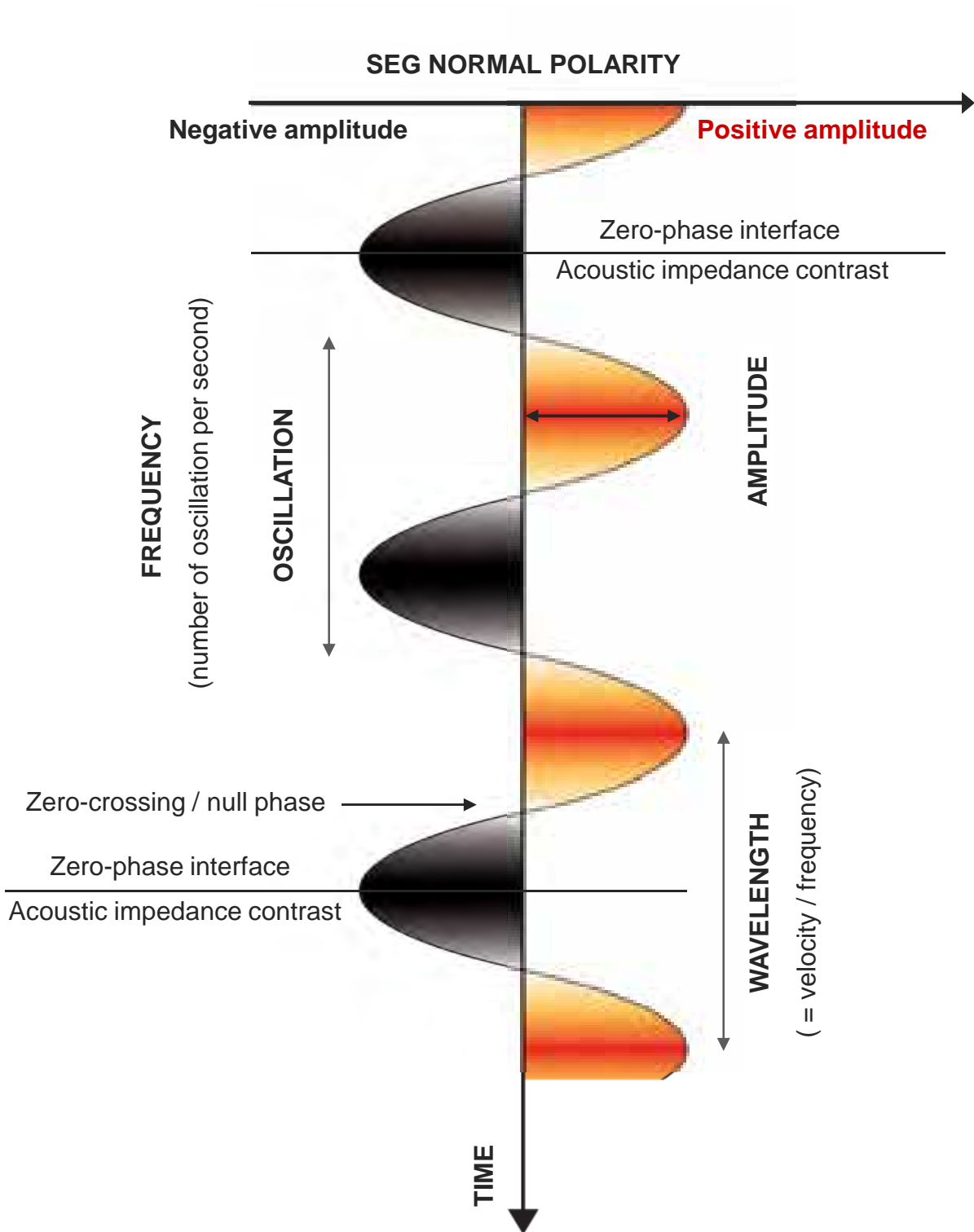


Figure 2.2. SEG colour convention for the display of seismic traces. Positive impedance contrasts are shown in red. Negative impedance contrasts are shown in black.

layer, have a minimum wavelength to respect (minimum thickness of reflections) in a given interval, and their wavelength cannot be less than the minimum value that are defined by the seismic frequencies since the data acquisition (see Brown, 2004).

Beside the thickness of tuned reflections, the second concern is the amplitude response displayed by the reflections. Depending on the true thickness of layers relative to the wavelength of the propagating wavelet, the amplitude of the composite waveform varies. At 'tuning thickness', it is the sum of the maximum amplitude of the central peak and that of the adjacent side lobe of the propagating wavelet and then decreases nonlinearly to zero as the layer pinches out (fig. 8 in Kallweit and Wood, 1982). The composite wavelet also keeps the same apparent wavelength while its amplitude decreases from the possible maximum value to zero (Brown, 2004).

2.2.1.3. Horizontal resolution

Horizontal seismic resolution is the width of a surface that can be covered by seismic wave fronts emitted during each emission of pressure pulse. It determines how much detail can be imaged between the centre reflection points of each neighbour surface on seismic horizons. The horizontal resolution (planar view) in 3D seismic data is controlled by mainly two parameters, the size of First Fresnel Zone and the lateral sampling of data that is controlled by the spacing of hydrophones (fig. 2.1a). The First Fresnel zone is the seismic energy that returns to the receiver within the half cycle of the first reflection during the travel of compressive wave (Lindsey, 1989). In other words, the area that is covered by Fresnel zone can be imaged on seismic. The vertical thickness of the Fresnel zone that can be recorded by seismic signal is conditioned by an interval, which defined by two wavefronts separated by a quarter wavelength with one of them tangential to an interface (Sheriff, 1978) (fig. 2.1b). The First Fresnel zone can be estimated by simple geometry (fig. 2.1b, c). Its size varies with the emitted frequencies (Sheriff, 1996). Objects with a lateral extension larger than the Fresnel zone will be visible (Brown, 2004) but becomes a single point of reflection when they are smaller than the Fresnel zone (Sheriff, 1978).

Horizontal resolution can be impacted during seismic processing by lateral sampling. The number of seismic traces that can be sampled depends on the initial spacing of the hydrophone layout (both inline - along the shooting direction - and crossline) during seismic

acquisition. The spacing of hydrophones has influence on horizontal resolution, only if the following equation is not respected (see Ashton et al., 1994):

$$\text{Bin size} < V_{\text{rms}} / (4f_{\text{max}} \sin \Theta)$$

Bin size: The horizontal distance between each seismic trace which passes vertically through the common mid-point (CMP) in a migrated 3-D seismic data volume.

V_{rms} : is the root mean square average of velocities down to the target

f_{max} : is the maximum nonaliased frequency required to resolve the target

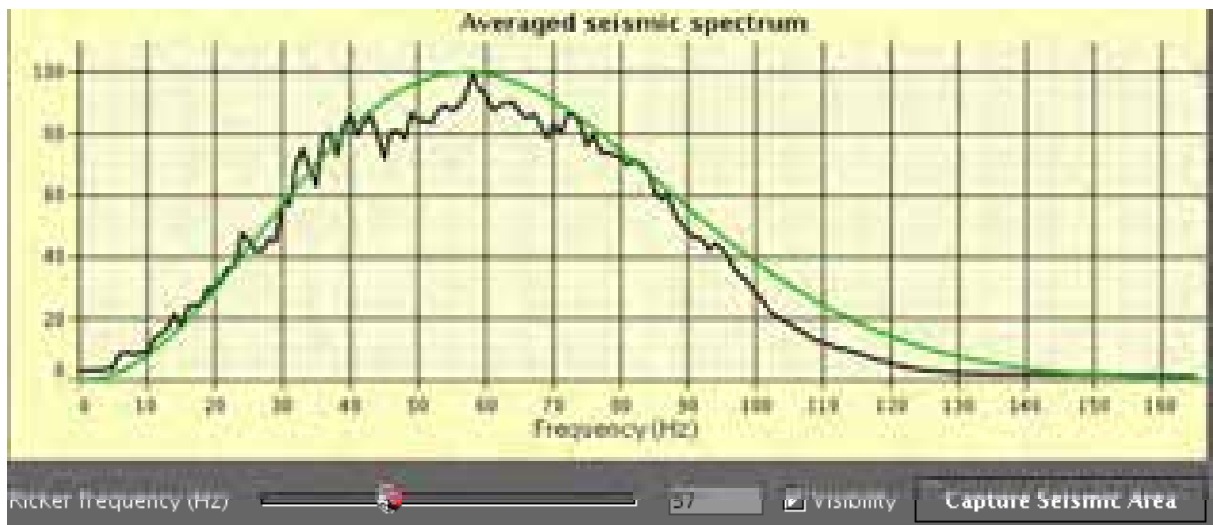
Θ : is slope dip

Restriction of vertical resolution limits also the image's lateral resolution (Robein, 2003). However this is out of the scope of this thesis, so I summarise briefly the explanation given in Robein (2003): "The image of an isolated point inevitably appears as a smeared spot whose size will be linked to the effective frequency band of the emitted signal and the imaging aperture used. During the calculation of all the image points for the trace along a given diffraction (D) point's vertical, it does not result in a single point, instead the signal making up the diffraction point is spread throughout depth. On the other hand, Due to a seismic signal's limited frequency bandwidth (has non-zero duration), but also because of the limited aperture of the acquisition array, summation of return seismic signals along the emitted wavefronts will give non-zero values for points adjacent to point D; the image of D is smeared laterally, effectively limiting the seismic image's lateral resolution." For more detail, please refer to Robein (2003).

2.2.2. Location, parameters of 3D exploration seismic data

The 3D seismic reflection data used for this study were acquired on the outer continental shelf of the Angola margin (fig. 3.1) on 2006, in water depths of 800 to 1300 meters. The near-seabed velocity is approximately 1700m/s (Total internal report). The study survey is composed by two seismic surveys shot at the same location: 1) the main survey consists of an area of 1310 km². It has a dominant frequency of about 55 – 60Hz with a main vertical resolution of about 7 m for the first second two-way travel time (TWT) below the seabed (fig. 2.3a). This survey extends from the seafloor to basement with a depth of 4.5 second (TWT). Its inline direction runs from NNW to SSE; 2). A higher resolution survey within the main survey covers hydrocarbon fields with a smaller area of 530 km². Its

a



b

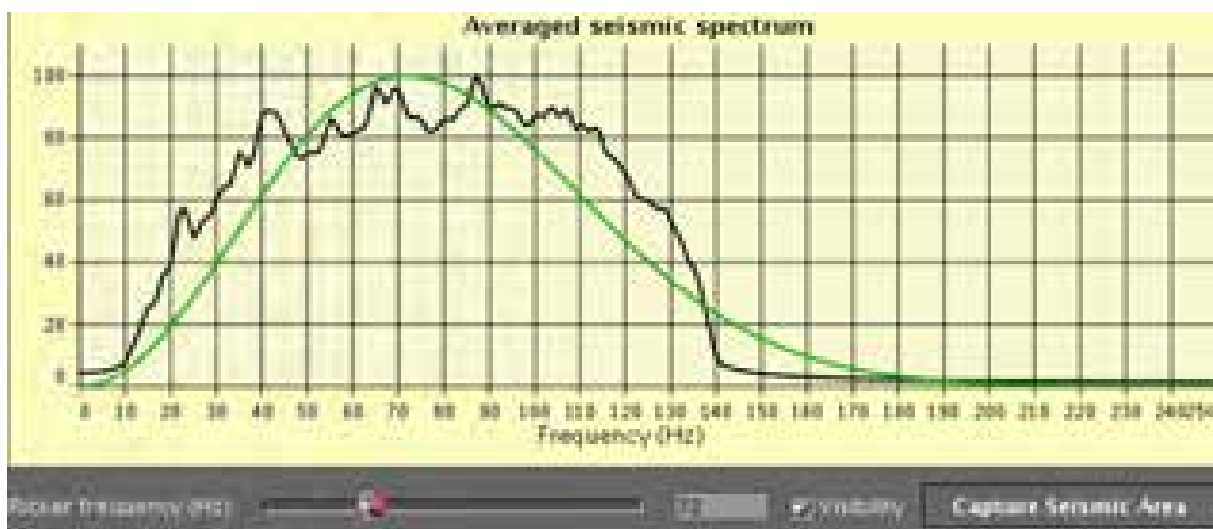


Figure 2.3. Seismic spectrum of the studied seismic data sets. a) The dominant frequency of the main survey is about 55 – 60Hz in the first second TWT below the seabed. b) The dominant frequency of a high resolution survey is about 70 – 80 Hz in the first second TWT below the seabed.

dominant frequency is about 70 – 80Hz (fig. 2.3b), and vertical resolution is about 5 m for the first second TWT below the seabed. Its depth from the seafloor down to the base is 5.2 s TWT and the inline acquisition direction is NNE to SSW.

The two 3D cubes have a bin size 6.25 x 6.25 m yielding a horizontal resolution of 6.25 m. Both seismic dataset are poststack migrated and has been zero phased. The downward increase of acoustic impedance is represented by positive amplitude value, i.e. SEG normal polarity (fig. 2.2).

Differently processed cubes of the same seismic surveys are available: near, middle and far offset. They represent sample reflectivities obtained at different angles of incidence.

This thesis research is based on studying the near offset seismic volume as it has the best resolution. Rock physical analysis of the seismic data was beyond the scope of this study. The higher resolution survey has been used in Chapters 4 to 7, and the main survey has been used in Chapters 5 to 7.

2.2.3. 3D seismic interpretation techniques

2.2.3.1. 3D seismic interpretation software

Seismic interpretation is the main approach in this thesis study and allows image analysis of fluid venting structures in the sub-surface beneath seabed. Seismic data interpretation was undertaken in Cardiff University and at Total's France office due to the availability of data and as this project is based in two research institutes. Interpretation results of the seismic data were undertaken under Linux operating system on IESX GeoFrame© 4.0 software developed by Schlumberger and on the Sismage© software developed by Total for its internal use.

Mapping horizons was carried out by manual picking along reflections on different 3D seismic sections. Orbital line, inline and crossline were all used for reflection picking and the choice was made depending on the complexity and lateral continuity of reflections. Line spacing for mapping was no more than 500m. Reflections were first picked along a primary grid which served as seeds for automatic horizon propagation and infill in intermediate areas.

2.2.3.2. Seismic attributes

In this thesis, a range of seismic attributes have been computed in order to strengthen the different characteristics of geological structures of interest. A seismic attribute is a measurement of a specific aspect of seismic data (McQuillin et al., 1984). Stratigraphic interpretation and study of fluid flow features require detailed visualizations of the local shape of seismic data (Sheriff, 1996). Seismic attributes are useful to see where waveshape changes occur (Quillin et al., 1984), hence providing indicators for the spatial variations of geological formations.

The primary purpose of attribute analysis is to enhance subtle features which otherwise might be neglected. Different aspects of the data with different displays are valuable in making features perceptible to interpreters who might not notice the importance of such features in interpretation (Quillin et al., 1984).

Several seismic attributes that have been particularly used for assisting this studied is listed as follows:

Time horizon and amplitude

The most basic of all seismic attributes is the time at which a given event occurs. A time structure horizon map (TWT) is constructed by picking at consistent part of the reflection loop at every location. Time horizon mapping at amplitude maxima or minima allows the extraction and mapping of the seismic amplitude at this same time value.

Mapping of amplitude anomalies is the key tool for recognizing fluid flow features such as gas chimneys, hydrocarbon accumulations, and methane-related carbonates.

Root mean square amplitude (RMS)

RMS Amplitude attribute corresponds to the square root of the sum of squared amplitudes divided by the number of samples inside the selected time window. This attribute is linked to the relative variations of acoustic impedance across a defined interval. It is a layer attribute and allows a quick characterization across intervals which can be quite large whereas amplitude along horizon is a local measurement.

This is useful for visualizing high amplitude anomalies such as carbonates, coarser sand, clastic blocks, hydrocarbon filled reservoirs, within given intervals.

Dip

The dip attribute is the magnitude of the slope of the local topography that is calculated at each grid point of a time horizon given as input. This attribute is particularly efficient for visualizing microrelief of fluid venting structures, tectonic structures and topographies.

Coherence

Coherence is a measurement of discontinuity between neighbouring seismic traces (Bahorich and Farmer, 1995).

Reflections from faulted or deformed area have different seismic characters compared to continuous areas. The former show low coherence values. Coherence is often used to visualize faults or discontinuities on horizons. It offers an alternative approach for identifying strata that cut through by gas chimneys or deformed by pockmarks.

Instantaneous phase and envelope of maximum energy

Instantaneous phase (Sheriff, 1987) is one type of single analysis obtained by representing seismic data in the time domain as a simple cosine function whose phase angle rotates with time and which is modulated by a slowly varying positive function: the trace envelope. The instantaneous phase allows tracking fine details of the wavelet shape as its value indicates the singular situations of minimum, maximum or zero-crossing of the original seismic trace. Its variation through time gives an instantaneous frequency. The envelope represents the strength of the reflections, irrespective of their polarity and shape. In fact, the term “phase” can also be used to describe a global rotation value applied to the instantaneous phase function of a seismic trace or wavelet.

To obtain these representations, seismic traces will be transformed by mathematical equations (Barnes et al., 1998). During constant phase rotations, the maximum amplitude values at wave crests that occur along the rotated seismic trace is regarded as the envelope of

maximum energy and so called instantaneous amplitude or reflection strength. The phase value at the time of maximum energy will be isolated and displayed by different colours depend on the angle of phase rotations (cf. Paternoster et al., 2011a, b). This dominant phase attribute that I used in Sismage© can be used for detecting the dominant polarities of several stacked-up reflections which show lateral amplitude variations and tracking lateral changes of lithology. It is related to a specific horizon surface since it is an extraction at the precise time at which the maximum of envelop occurs closest to the interpreted time. Hence it is useful for distinguishing reflections originating from a single geological interface or from an isolated thin layer. Its value can indicate whether the thin layer is acoustically 'hard' or 'soft' thus helping with the identification of carbonate, water, oil or gas bearing sands layers etc.

Values of computed phases are comprised between -180° to 180° and are expressed by a colour wheel (Taner et al., 1979). With the conventions used in Sismage© and for the polarity of the seismic data that were used in the project, the significations of the phases are as follows (cf. Brown, 2004; Paternoster et al., 2011a, b): phases of -90° are represented by red and can be interpreted in this study context as free gas; 0° phase are indicated by blue and indicated hard lithology i.e. sand; 90° phases are represented medium hard lithology such as thin carbonate or brine; and finally 180° or -180° phases are indicated by white colour and stand for soft formations i.e. silt.

2.2.3.3. Technique on interpretation of fluid venting structures on 3D seismic

This section provides a brief review on the methodology and steps for detecting and recognising fluid venting structures.

2.2.3.3.1. Detection and visualizing of fluid venting structures

In general fluid venting structures are expressed as seismic amplitude anomalies in seismic as described in the chapter of introduction. Their occurrences in different stratigraphic intervals have been detected principally by dip or amplitude horizons.

Fluid venting structures have been recognized on plan view were based on, first, their distribution as isolated, ten- to hundred-meter scale high amplitude objects; and second, based

on their geometries such as round-shapes or elongate for pockmarks and methane-related carbonates.

Once potential venting structures were identified, they were examined in all directions by different arbitrarily oriented seismic profiles. For validating the authenticity of fluid venting structure occurrences and for avoiding pitfall in seismic interpretation i.e. seismic artefacts, further checking on far, middle and near seismic volumes was made. Comparison with acquisition directions, bathymetric contour lines and verifying the local geological context has also been undertaken.

If the fluid venting structure intersects more than one horizon, other horizons that intersect the venting structure would be mapped. Mapping the intersected horizons not only allows visualizing the internal morphology of the fluid venting structures, but also helps distinguish the chronological relationship for fluid venting structures which are likely to have occurred in more than one generation episode.

Small sizes of fluid venting structures were most of the time close to seismic resolution, so in order to obtain the most accurate morphological maps, manual mapping in pixel scale was carried out in combination or not with automatic horizon propagation.

For several generations of venting structures that cross cut horizons within the given interval, and if the area is too broad or if reflections are too discontinuous across most of the survey; then set of (sub) parallel RMS map with equal or proportional vertical distance within the given interval will be calculated, and this technique is called iso-proportional layering. RMS attribute maps allow examining the spatial distribution of fluid venting structures over time, and make high amplitude events, which otherwise cannot be easily seen on seismic sections, become more obvious.

2.2.3.3.2. Recognition of fluid venting structures base on seismic wave lobes

In this research, methods that were employed for interpreting fluid venting structures on seismic data, are based on basic principles of geophysics.

On seismic sections fluid venting structures have been distinguished through analyzing reflection continuity, amplitude and polarities of wavelets. As described in the introduction chapter, conical pockmarks on section view can be recognized based on the discontinuity of reflections that truncate laterally both sides of v-shape structures (fig. 2.2).

Fluid or gas chimneys are identified by the occurrences of columnar acoustic perturbation zone (Heggland, 1997; Løseth, 2001; Moss and Cartwright, 2011a, b) that disrupted horizontal continuities of strata, or by the presences of vertically stacked up bright-spots. Depending on the type of acoustic perturbations e.g. acoustic turbidite zone, push down and pull up, the seismic hardness of geological objects that overlying or associating with chimneys can be distinguished (cf. Heggland, 1998; Løseth et al., 2001; Petersen et al., 2010). A detailed interpretation on seismic chimneys is given in Chapter 4.

Recognition of gas or carbonate formation on seismic sections is based on the polarity of high amplitude anomalies which stand up from the background (cf. Coffeen, 1986), along with the associated acoustic perturbations.

Gas accumulation or presence of free gas that are characterised by low velocity and low density (Anstey, 1977; Coffeen, 1986), are identified according to occurrences of polarity reversal of seismic reflection, negative high amplitude anomalies, push down and acoustic turbidite zone.

Given that the study area is dominated by fine-grained sediments and carbonates, and which are characterised by high impedances on seismic (Coffeen, 1986; Hustoft et al., 2007; Westbrook et al., 2008). Hence carbonates are recognized by positive polarities of high amplitude anomalies (positive high amplitude wavelet overlying the negative one) (fig. 2.1), as well according to underlying seismic pull up vertical zone.

The generation of seismic pull up is depended on the quantity of carbonates or degree of cementation, and association with free gas or not which may decrease the total velocity (Coffeen, 1986). Whilst the association with gas hydrate in gas hydrate stabilization zone would likely increase the overall velocity (Coffeen, 1986). A detailed discussion on this topic is given in Chapter 4.

Distinction of carbonate with methane-related origin or not on seismic, is made according to the distribution of carbonates and their associated seepage environments. Methane-related carbonates are often associated with pockmarks and show isolated circular form (cf. Hovland, 1987), they are also frequently associated with faults or hydraulic fractures (chimneys) (Judd and Hovland, 2007).

The vertical organisation of carbonate, i.e. stacking up vertically above faults, chimneys, or below pockmarks is another observational constraint that is used for interpreting the methanogenic origin of carbonates. A detailed discussion for distinction of carbonate origin is given in Chapter 4.

In order to distinguish carbonate or gas from each other in more complicated high amplitude events i.e. to different positive and negative high amplitude anomalies within double (or triple) high amplitude reflections, which have progressive, lateral amplitude variations. In this case seismic attribute of instantaneous phases were calculated (see Section 2.2.3.2) for displaying dominant polarities on map view.

2.3. Limitations and potential solutions

This section presents the major limitations that were encountered during the seismic interpretation, and the measurements and strategies that have been taken in this research to address these.

In this thesis, 3D seismic reflection data provide the basic support material for studying fluid venting structures. All observations and interpretations are based on seismic image analysis. Seismic resolution however is limited by acquisition parameters, signal processing, heterogeneity or anisotropy of medium (Robein, 2003) and noise from various sources. The second issue is the lack of well data for seismic calibration.

2.3.1. Seismic resolution

The resolution issue is the greatest limitation encountered when examining fluid venting structures.

One of the biggest difficulties is first, to determine the morphology and size of fluid venting structures. When the diameter of the object of interest is several times bigger than the horizontal bin size, the surface of the object can be approximately outlined by time horizon mapping but the lateral boundary will never be accurately imaged on seismic data. However, if the fluid venting structure has a size smaller than the bin size, or even if there are more than one structure at the same location, it will only be recorded as a single reflection event without any precise planar form on seismic horizons. Errors in diameter measurement in this case will be highly proportional to the object's real size. This is a common problem but unavoidable in any seismic interpretation. These points have been taken into consideration together with the geological context during the data interpretation in this thesis.

The issue of horizontal resolution is especially concerned when dealing with positive high amplitude anomalies (e.g. interpreted carbonates), as these are “morphologically shapeless in seismic”, their geometry cannot be visualized by time horizon but only amplitude maps. Even then, the lateral extension and boundary of amplitude anomalies are not easily determined, neither any of their internal structures can be imaged. When the amplitude anomalies occur within pockmarks or depressions or associated with special geological structures, their shapes can be deduced or interpreted in combination with the dip maps of their associated time structure map. Demonstrations and detailed discussions are given in Chapter 4. Nevertheless, amplitude anomalies showing as isolated features along individual reflection without association with any visible geological structures will have a more uncertainty attached to their morphology. In such cases, the second major difficulty will be the issue of vertical resolution. As the geological objects of interest and is expressed by high amplitude anomalies at reflections may have a geological thickness close to or below the limit of vertical resolution of seismic reflections in the studied survey, so local tuning is probable (see section 2.2.1.2 in this chapter).

For these two major issues of geometry and thickness of the real geological object, the maximum envelope is a helpful attribute to illustrate the most reflective areas, and thus assists to determine the lateral boundary and shape of anomalies (cf. Paternoster et al., 2011a, b). The instantaneous phase attribute is useful for distinguishing frontiers between different adjacent lithologies along a given horizon, and the geometry of high amplitude anomalies can thus be outlined (Paternoster, 2011a, b). This method has been used in Chapter 5 and 6 for resolving the horizontal boundary distinction of high amplitude anomalies generated by different lithologies.

Acoustic distortions that are associated with lateral seismic velocity variations such as pull up, push down of deeper seismic reflections or acoustic turbidites, perturb the seismic imaging and mask the geological formations on seismic profiles. In the case of gas chimneys, these seismic perturbations prevent identifying the lower termination of the chimneys. The phenomenon of seismic disturbances is unavoidable in seismic interpretation when using P-wave data (Hustoft et al., 2007). This is another type of resolution issue that affects the determination of the exact contact position between the bottom ending of gas chimneys and polygonal faults. Imaging and delineation of gas chimneys is discussed in details in Chapters 4 and 6.

2.3.2. Calibration of positive high amplitude anomalies on seismic and ground truth

The second major limitation that encountered in this research was that the interpretation of positive high amplitude anomalies was entirely based on geophysical aspects and on comparison with previous studies. The opportunity of relating seismic amplitude anomalies with ground truth, has been provided by calibration with cutting samples of a well only at the very late stage of this research, immediately before the submission of this thesis. Therefore, the results of the preliminary studies performed on these cuttings will only be available for presentation as conference abstract (see Appendix I) and without being integrated into the core chapters of this thesis. However, the results of drilling and isotopic analysis have confirmed my interpretation of PHAAs as caused by the presence of methane-related carbonates.

2.4. Age of seismic stratigraphic units

Confidential well data, mud logs and formation picks were used to calibrate seismic horizons with the regional stratigraphy. Ages for each of these units and their bounding surfaces have been obtained by standard biostratigraphic dating techniques such as identification of specific assemblages of foraminifera (Berggren et al., 1995). Well data and age constraints are sparse and generally lacking in the shallowest section (Pliocene-Quaternary units). Ages of horizons within these units were estimated by assuming a uniform sedimentation rate at a location where tectonic activity ceased and were stable during Neogene-Quaternary, and then by extrapolating ages from known surfaces based on interval thickness. Given that the Pliocene-Quaternary section is largely composed of hemipelagic sediments, the sedimentation rate at the tectonically stable location would not be expected to change to significantly. Thus, I consider the estimations of ages for horizons in this interval as fairly close to their true age.

CHAPTER 3

GEOLOGICAL SETTING

3.0. Geological setting

3.1. Introduction

The aims of this chapter are to; (1) provide an brief overview of the tectonic-stratigraphic evolution of the Lower Congo Basin, (2) detailed stratigraphic framework of the Neogene and Quaternary succession which is the focus of this thesis and (3) to summarize the structural elements of the study area.

3.2. Regional geological setting

The Lower Congo Basin, offshore Angola forms the study area in this research project (fig. 3.1). The Lower Congo Basin like the other basins along the passive continental margins of Western Africa and SE Brazil formed as a result of the break-up of Gondwana and opening of the South Atlantic in the Early Cretaceous (Masche and Phillips, 1972; Larson and Ladd, 1973). This led to the development of Late Cretaceous grabens and half grabens. The syn-rift sequence is overlain by a succession of evaporites of Aptian age. Overlying the evaporites is a thick succession of Albian carbonates and Cenozoic clastic sediments (Liro and Dawson, 2000; Lavier et al., 2001; Séranne and Anka, 2005). They are deformed by salt-related extensional faults and salt structures which formed during gravity-driven thin-skinned extension (Duval et al., 1992) (fig. 3.2).

Major uplift of the hinterland occurred during the Late Oligocene/ Early Miocene (Walgenwitz et al., 1990), exposed the shelf and led to redistribution of sediment into deeper parts of basin (Broucke et al., 2004) in the form of turbidites and debris flow deposits (Droz et al., 1996; Anderson et al., 2000; Cramez and Jackson, 2000; Anka and Séranne, 2004; Anka et al., 2009; Savoye et al., 2009). Abundant channel-levee systems transported coarser clastic sediments across the upper slope region of the margin during Early and Late Miocene (Anderson et al., 2000) which are interbedded with hemipelagites and mass transport deposits (Anderson et al., 2000; Broucke et al., 2004).

At the end of the Miocene and early Pliocene rates of basin margin uplift accelerated (Frerichs and Shive, 1971; Lavier et al., 2001). The superposition of basin margin uplift and

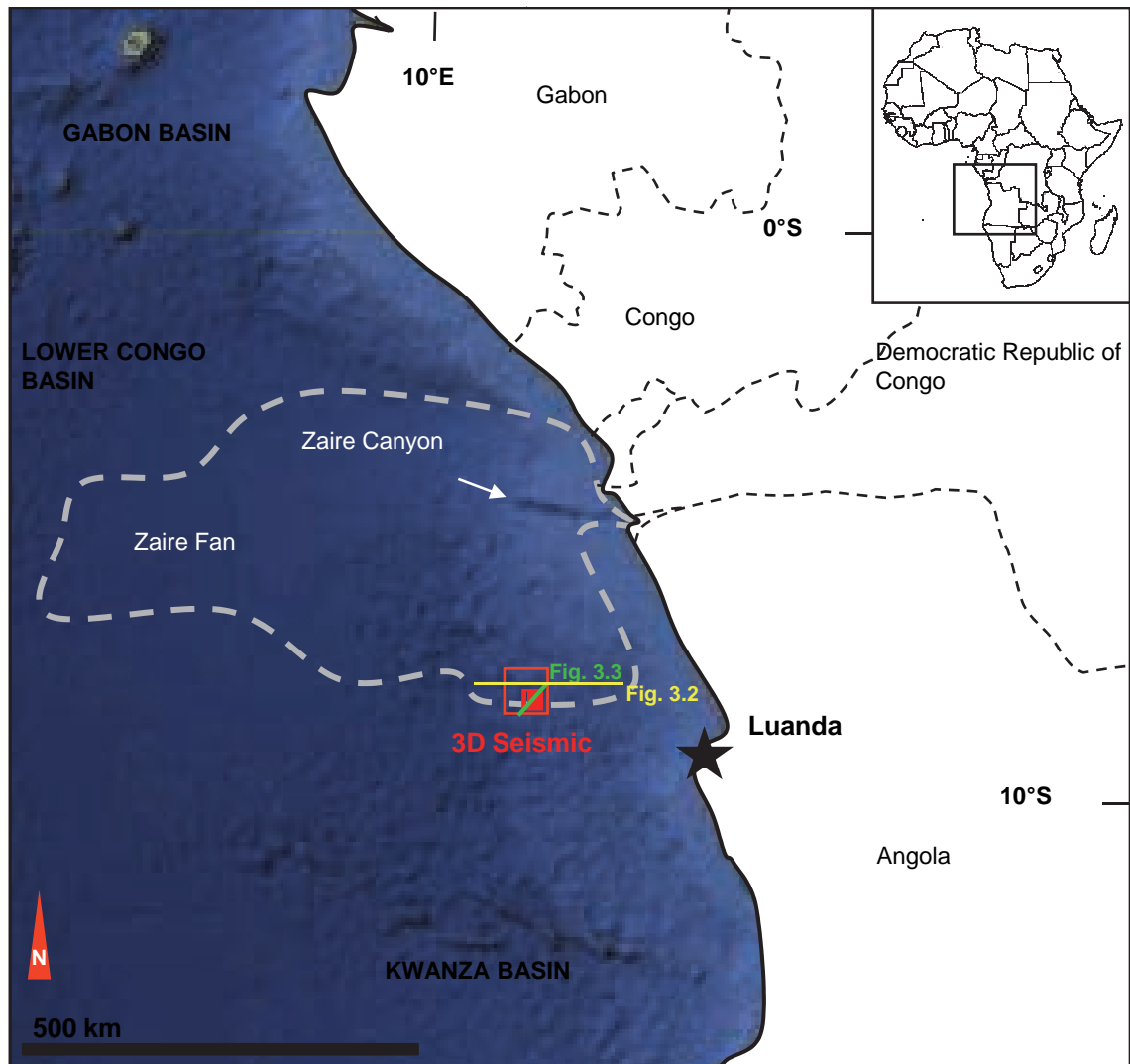


Figure 3.1. Location of the study area on the Angolan Margin as defined by the two 3D seismic surveys red filled and outlined boxes respectively. The white dashed line defines the outer extremities of the Zaire Fan.

Figure 3.2

**THIS PAGE HAS BEEN BLANKED
OUT FOR COPY RIGHT REASON**

gravitational instability of the Aptian evaporite units and the overburden led to the incision of the Congo Canyon which in turn restricted turbidite deposits to the lower slope and abyssal plain (Anka and Séranne, 2004; Anka et al., 2009) while the shelf and upper slope above salt were bypassed. As a result sedimentation on the outer shelf and slope was dominated by hemipelagic deposition which is still ongoing (Anka et al., 2009).

3.3. Stratigraphy of the study area

The study area is located in offshore Angola, in water depths from 800m to 1300 m. The stratigraphic interval of interest is the Quaternary-Neogene hemipelagic sediments, which comprise the most shallow kilometer of the basin fill (Total internal report, Vignau et al., 2000) (fig. 3.3).

The Neogene-Quaternary sequence in this survey is dominated by hemipelagic sediments (Broucke et al., 2004; Total internal report, Vignau et al., 2000). Turbidite channel complexes occur between the well-bedded hemipelagic units (Broucke et al., 2004; Total internal report, Vignau et al., 2000). Gravity-driven salt tectonics heavily deformed the Upper Cretaceous and Cenozoic strata (Liro and Dawson, 2000; Lavier et al., 2001). As a result the Miocene turbidite channel reservoirs and silty, clay-dominated seals were intersected by salt-related faults. Polygonal faults (*sensu* Cartwright and Dewhurst, 1998) were observed in two tiers, one within the Upper Miocene, and the other covering the whole Pliocene interval (Gay et al., 2006a). The studied pockmarks mainly occur within the latter.

The Neogene-Quaternary sections was calibrated by biostratigraphy, seismic horizons were given a name reflecting their age according to the Berggren chart (Berggren et al., 1995; Total internal report, Vignau et al., 2000). Horizons without age calibration were named with the letter “H” after the digit (e.g. 6 H, 6.3 H) to reflect the interpolated age estimated using averaged sedimentation rates between the calibrated horizons (see Chapter 2 Methodology, section 2.4).

The studied interval is subdivided into several units based on the occurrence of two main seismic facies (Brouck et al., 2004): (1) moderate amplitude, parallel, continuous reflections interpreted as hemipelagic sediments (HD4, 3, 2) (Broucke et al., 2004); and (2) high-amplitude, lower continuity packages encased in low-amplitude intervals interpreted as turbidite systems (TS4, 3) in association with massive transport deposits (MTDs) in some cases (fig. 3.3) (Broucke et al., 2004).

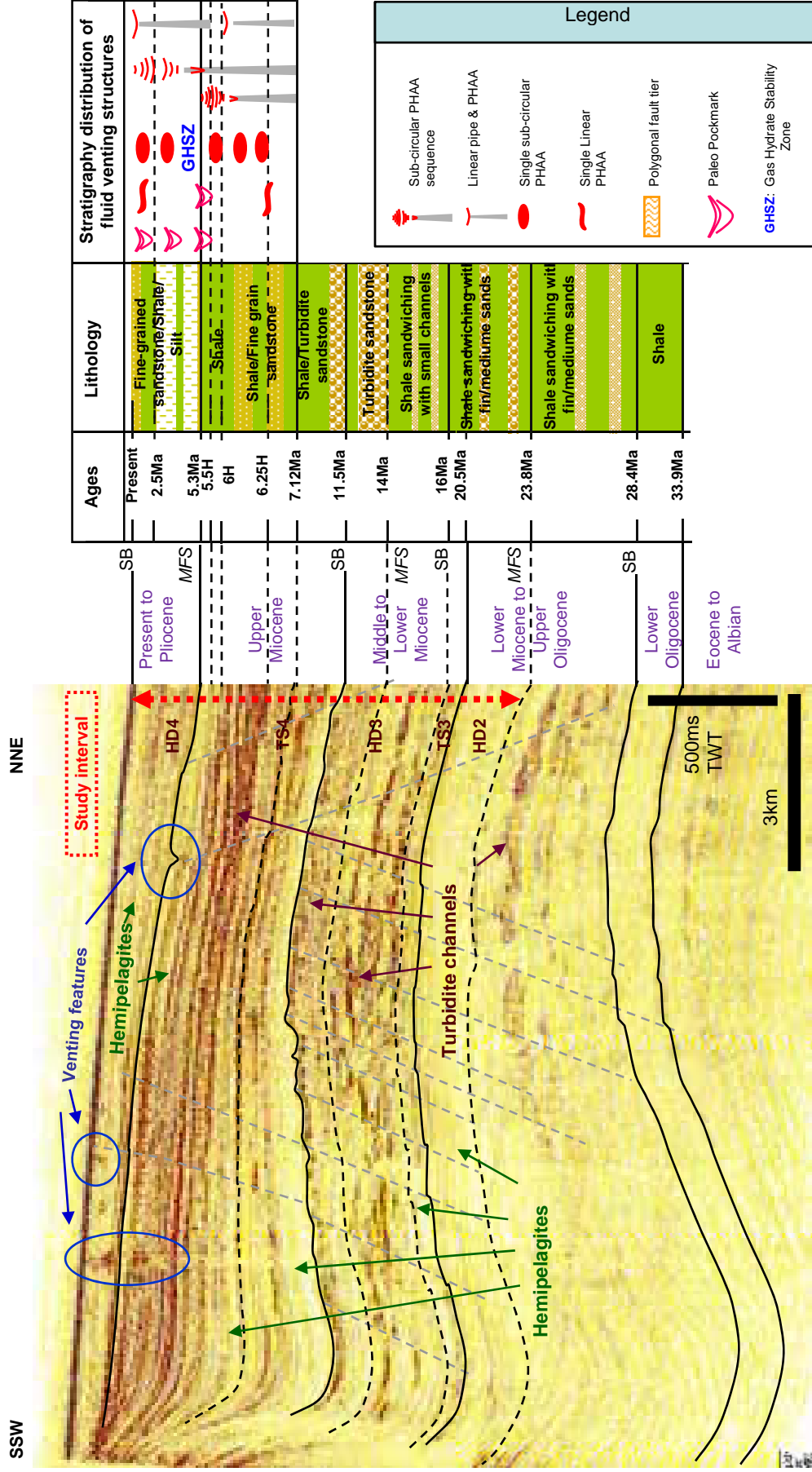


Figure 3.3. Representative seismic section from the 3-D survey (location see Figure. 1) tied to the local stratigraphy (see panels to right of seismic section). The panel at the far right of the Figure shows the vertical distribution of different fluid venting structures. HD: hemipelagic deposits; TS: turbiditic system; SB: sequence boundary; MFS: maximum flooding surface.

Even most of massive transport deposits and their complexes are observed with the TS interval, but in some case they can also be observed within the hemipelagic sequences of the Paleogene-Upper Miocene (6H).

The detailed lithostratigraphy for the Neogene is based on Vignau et al. (2000). The studied interval is subdivided as follows in Table 3.1.

3.4. Local structural geology of the study area

**THIS PAGE HAS BEEN BLANKED
OUT FOR COPY RIGHT REASON**

Ages	Division of sediment intervals (Brouck et al., 2004)	Characteristic of sub-divide units
		Two sub units have been distinguished.
0 Ma – 5.3 Ma	HD4	The upper unit of the interval occurs within sediment of 0 to 2.5 Ma age, and contains continuous internal reflections with low-to-moderate acoustic amplitudes. The lower unit is bounded by horizon of 2.5 Ma and 5.3 Ma. Sediments within this lower unit deformed. The interval has been reported to comprise hemipelagites (Vignau et al., 2000) until the base of the unit which occurs at the top of a polygonal fault tier as defined by Cartwright and Dewhurst (1998). The base of gas hydrate stability zone (GHSZ) observed “locally” in the area approximately coincides with the base of the polygonal fault tier, at a horizon dated as the Base Pliocene (5.3 Ma).
5.3 Ma – 11.5 Ma	TS4	This unit was subdivided into three sub units: a) 5.3 Ma – 6 H (H: Horizon with interpolated age but no age calibration) very continuous clay-rich sediments, b) 6 H – 6.25 H deeper level polygonal fault tier composed of claystones/fine-grained sandstones interval which overlays locally fine-grained turbidites, c) 6.25 H – 11.5 Ma silty claystone units containing coarse-sand bodies.
11.5 Ma – 16 Ma	HD3	Strongly layered claystone/fine-grained sandstone beds Interbedded with fine to medium turbidites interbedded with.
16 Ma – 20.5 Ma	TS3	Well bedded fine-grained sandstone alternating with Claystone.
20.5 Ma – 23.8 Ma	HD2	Claystone and well bedded fine-grained sandstone.

Table 3.1. Subdivision of sediment units in the study interval.

Figure 3.4

**THIS PAGE HAS BEEN BLANKED
OUT FOR COPY RIGHT REASON**

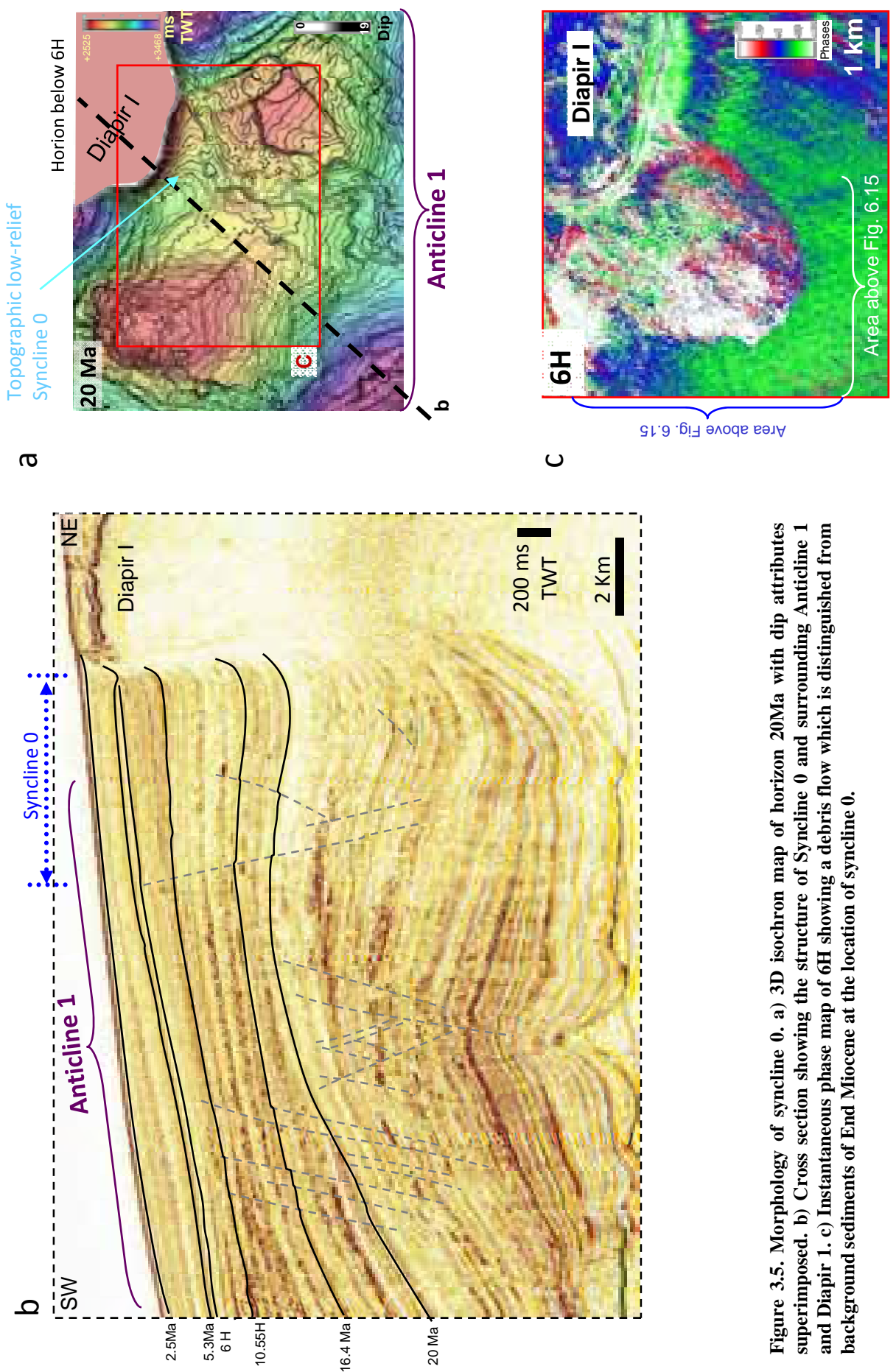


Figure 3.5. Morphology of syncline 0. a) 3D isochron map of horizon 20Ma with dip attributes superimposed. b) Cross section showing the structure of Syncline 0 and surrounding Anticline 1 and Diapir 1. c) Instantaneous phase map of 6H showing a debris flow which is distinguished from background sediments of End Miocene at the location of syncline 0.

Figure 3.6

**THIS PAGE HAS BEEN BLANKED
OUT FOR COPY RIGHT REASON**

Figure 3.6

**THIS PAGE HAS BEEN BLANKED
OUT FOR COPY RIGHT REASON**

Figure 3.6

**THIS PAGE HAS BEEN BLANKED
OUT FOR COPY RIGHT REASON**

**THIS PAGE HAS BEEN BLANKED
OUT FOR COPY RIGHT REASON**

THIS PAGE HAS BEEN BLANKED OUT FOR COPY RIGHT REASON

3.5. Regional ocean currents

In order to know what type of currents could affect the study area during the interval of interest, I reviewed the available literature on present-day currents. Although information on the Neogene ocean current circulation in the study area is unavailable, reviewing present-day situation can be regarded as a first approximation for a better understanding of this question in the absence of precise data about the stratigraphic interval of interest.

Lots of questions still exist about the bottom currents in water depths ranging from 500 to 1500 m (upslope domain) along the Angola margin (Séranne and Nzé-Abeigne, 1999). The ocean surface circulations off Western Africa from 10°S further to the north is complex (Séranne & Nzé-Abeigne, 1999), several types of currents interact at the ocean surface, in subsurface and under the Congo River water plume: the Equatorial current, the South Equatorial Counter Current (SECC), and the Equatorial Under Current (EUC; Jansen, 1990). The interactions of these currents generate not only multiple patterns of water current fronts, but also gyres and domes (Van Bennekom and Berger, 1984) (fig. 3.7).

The SECC transports water from deeper interval (> 150 m deep) up to the sea surface at about 10°S and 5°S, (fig. 3.7), and then separates into two branches near the African coast (Van Bennekom and Berger, 1984). This separation forms the southward-flowing Angola current and the northward-flowing Benguela current. The latter mixes with the coastal branch of the Benguela Current (BC) from the south west (fig. 3.7) (Van Bennekom and Berger, 1984). The main branch of the Benguela Current orientates to northwest at 20°S (fig. 3.7), while the coastal branch continues to stream northward along the coast up to 13 – 15°S (Van Bennekom and Berger, 1984). Further to the north of the SECC, the EUC flows toward the

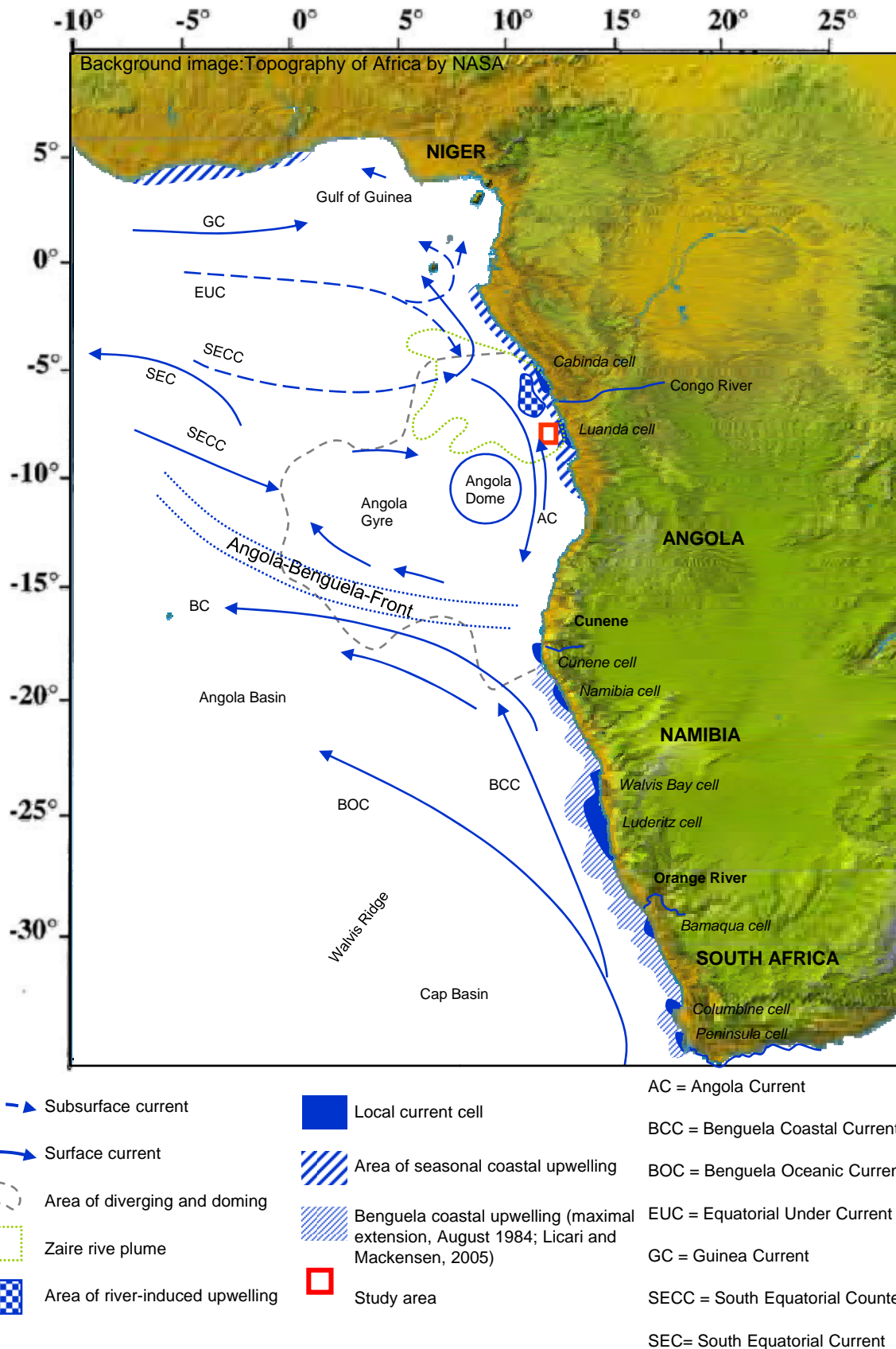


Figure 3.7. Present day ocean current patterns along the Western coast of Africa (modified after Van Bennekom and Berger (1984), Jansen et al. (1984) and Licari and Mackensen (2005)). Topography map of Africa sourced from NASA.

West Africa coast at depths between 50 – 100 m and also splits into two branches when it gets close to the coast at about 5°E (fig. 3.7) (Van Bennekom and Berger, 1984).

The sub surface water (> 150 m) along the Western Africa coast between Cap Lopez and the north of Cabo de Santa Maria (fig. 3.7), where the studied survey is located, is interpreted to originate from the EUC or Lomonosov Current and is carry on to flow toward the south east (Wauthy, 1977).

At the mouth of the Congo River and below the river water plume, EUC, BC SECC water masses are involved at 30 – 70 m in the turbulent region (Van Bennekom and Berger, 1984). The vertical boundary between EUC and BC water off the river mouth is fuzzed by mixing with fresh water from the Congo River, and it engenders upwelling and vertical mixing in subsurface (Van Bennekom and Berger, 1984).

Apart from these currents themselves, the Angola Benguela Front that results from the convergence of the Angola Current and the colder northward streaming Benguela Current can be observed at 14 -17°S (fig. 3.7) (Licari and Mackensen, 2005).

Another feature such as the Angola Dome occurs seasonally due the fact that water at 20 m depth in the southwest area of the Zaire River mouth has a lower temperature than the surrounding water of 20°C (Mazeika, 1967).

The deep waters in Angola Basin are composed mainly by the dominant North Atlantic Deep Water (NADW) and 20 – 30% of Atlantic Intermediate Water (AAIW) (fig. 3.8) (Van Bennekom and Berger, 1984). The Angola basin is characterized by the quasi absence of Antarctic Bottom Water (AABW) (Jansen, 1990), which is blocked by the Walvis Ridge but only enters the basin through the Romanche Trench near the equator where the AABW mixes with the NADW (fig. 3.7) (Berger and Richer, 2002). Antarctic Intermediate Water circulates northward along the Western Angola margin (Boersma, 1984). It flows at a mean depth of 700 – 800 m and above 1500 m (Shannon, 2009). The vertical mixing zone between AAIW and the top boundary of NADW is located at 1100 – 1400 m (fig. 3.7) (Berger et al., 2002). Below that depth, the water mass is dominated by NADW (fig. 3.7) (Berger et al., 2002). The study area is therefore located in the transitional zone between AAIW and NADW.

Coastal upwelling is estimated to have started during the latest Miocene just before 6 Ma (Berger et al., 2002) and occurs at a depth around 200 m along the coast of Western Africa (c.f. Jansen et al., 1984). The upwelled water that migrates from 100 to 200 m depth to the surface is suggested to be provided by the northward-flowing AAIW (Séranne and Nzé

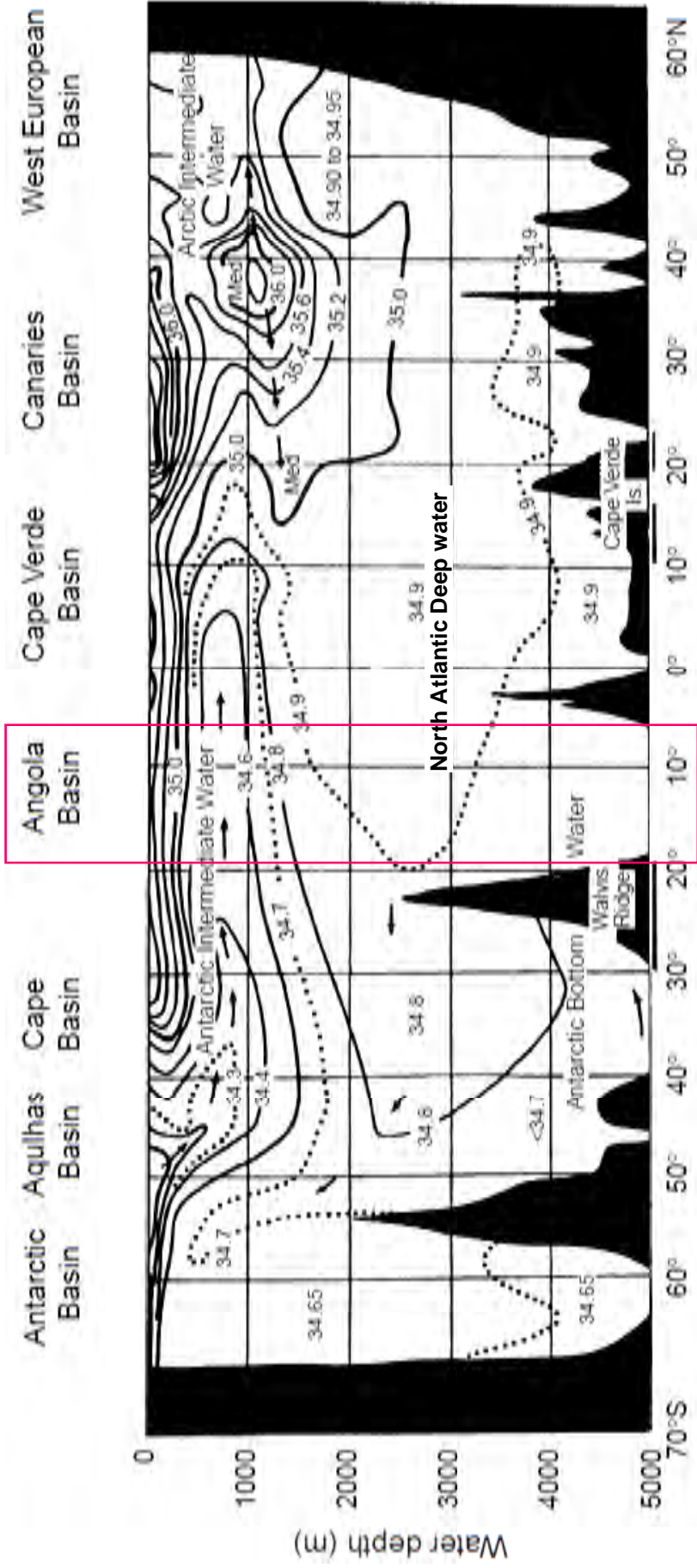


Figure 3.8. Ocean water circulation in the Atlantic Ocean and the distribution of water salinity. Values along contour line are salinity with unit in per mille. Modified after Tchernia (1980) in Berger et al. (2002).

Abeigne, 1999). The closest upwelling cells to the study area (the southern edge of the Congo River water plume), have been identified in the north and south of the Congo river mouth located at about 5°S and about 7°S (Lutjeharms and Meeuwis, 1987).

Deep erosional channels with a depth of several hundred meters, originating on the upper slope around -500 m and ending mid-slope around -1500 m have been described Offshore Congo by Séranne and Nzé-Abeigne (1999). They grew with the aggradation of the slope over the whole Miocene interval and show unidirectional northward migration over that span of time. They were interpreted by Séranne and Nzé Abeigne to result from upwelling. This is the only published indication about Miocene currents in the studied basin, but ca. 200 km to the north of this study area where no such channels could be observed in seismic.

To summarize, the present-day current pattern in the area is complex, but provides ample evidence for the existence of surface and bottom-currents. The existence of bottom currents in the Miocene when the coastal morphology was similar to the present-day one is therefore taken as a plausible working hypothesis.

However no documentation is available for the origin of bottom current waters in this part of study area located to the south of the river plume. So hereafter, I simply use the term of “local bottom current” to describe the water mass at the bottom of this study area.

CHAPTER 4

**VERTICAL EVOLUTION OF FLUID VENTING
STRUCTURES IN RELATION TO GAS FLUX, IN
THE NEOGENE-QUATERNARY OF THE LOWER
CONGO BASIN, OFFSHORE ANGOLA**

4.0. Vertical evolution of fluid venting structures in relation to gas flux, in the Neogene-Quaternary of the Lower Congo Basin, Offshore Angola

4.1. Abstract

The processes preceding the genesis of pockmarks and their subsequent evolution has been rarely studied since pockmarks were discovered in 1970 (King and McLean, 1970). A high-resolution 3-D seismic survey from the continental slope of the Lower Congo basin allows us to study in detail the structures that developed before the formation of pockmarks, as well as their subsequent geometric evolution. This chapter aims at reporting new type of fluid-related structures that relate to pockmarks. The objective of this research is to understand: 1) the evolution of these structures and their genetic relationship with pock-marks, and 2) how their morphologies may be influenced by changes in venting intensity over time. Pockmark and chimney structures in this survey are hosted within Late Miocene to Quaternary hemipelagites, above clastic reservoirs in a petroliferous basin. They are all associated with positive high amplitude anomalies (PHAAs) on seismic data. PHAAs are interpreted from their dramatically higher acoustic impedance relative to the background sedimentary values of the host units, and by their association with seismic pull-up effects. From their planforms and cross-sectional geometry, PHAAs are primarily interpreted as being due to the development of methane-related carbonates but they may be associated with gas hydrates in one or two examples. Methane-related carbonates form either by authigenic accumulation or by anaerobic methane oxidation (AMO) once upwardly migrating methane enters the sulfate-methane transition zone (SMTZ), typically within the first few tens of meters below the seabed. Therefore, vertical accumulations of PHAAS are interpreted to reflect the temporal evolution of methane flux migrating upward to reach the palaeo-seabed or SMTZ. Timing of local scale fluid leakage can therefore be diagnosed by analyzing PHAAs at seep locations that occur in association with pockmark/chimney structures. A conceptual model for the evolution of different fluid venting structures is proposed here, and is based on

the analysis of venting structures that I expressed by 3-D seismic reflections . In this model the main features are linked into a process-based sequence, culminating in the in fill and termination of the pockmarks as fluid venting sites. This model summarizes different rhythms of venting which are expressed by different types of PHAAs along with venting structures. Linear PHAAs and conduits inferred slow seeps. They can be succeeded by sub-circular PHAAs and shallow depressions which inferred slow to moderate seeps. Then the seep can become either a fast vent and terminated into a pockmark crater; or it can become less active and be sealed afterwards. Subsurface sediment fluidizations and remobilizations are likely to happen in the last case and are probably caused by hydrate dissociations.

4.2. Introduction

Pockmarks, chimney structures and interpreted methane-related carbonates have been observed in the Late Neogene/Quaternary interval of the Lower Congo Basin (Gay, 2002; Charlou et al., 2004; Olu-Le Roy et al., 2007; Pierre and Fouquet, 2007). These types of structure represent different degrees of fluid flux, and provide general indications of fluid migration pathways in the subsurface (Hovland and Judd, 1988; Berndt, 2005; Gay et al., 2003; Cartwright et al., 2007; Andresen et al., 2011), hence cap rock leakage or underlying reservoir locations can be detected (Hegglund, 1997; Gay et al., 2003).

Once hydrocarbons breach a cap rock, they can leave behind trails that relate to the mode of expulsion at the time of fluid escape. However, the question of how the fluid migration phenomena evolve both at the seabed and the immediate sub-surface over time, has only rarely been addressed. The geometrical evolution of venting structures may potentially reflect the longer term dynamics of fluid leakage, because each fluid expulsion episode creates recognizable and characteristic topographic features at seep locations, thereby affecting later sediment accumulation. Thus overpressured fluid expulsion events can be reconstructed at least qualitatively by analyzing in detail the architectures of each venting structure. For this purpose, a basic framework for surface and subsurface expressions of fluid expulsion has been presented by Roberts (2001) and Roberts et al. (2006). The general framework for classifying surface expressions of fluid dynamics according to variations in gas flux of Roberts (2001) and Roberts et al. (2006) will be used as a starting point for this study.

Subsurface expressions of fluid escape in this study survey are found principally in the Late Neogene/Quaternary interval in the Lower Congo Basin. The following fluid escape

features are recognized: (1) seismic chimneys (cf. Løseth et al., 2001; 2011; Moss and Cartwright, 2010a, b) are considered to be an indicator of gas seepage from deeper reservoirs (Hegglund, 1997) and defined as a specific class of seal bypass system by Cartwright et al. (2007); (2) pockmarks (cf. Hovland, 1981b; Gay et al., 2003), they exhibit more elaborated internal organizations than the simple v-shape pockmarks of King and MacLean (1970) in this survey; (3) Positive high amplitude anomalies: the interpreted methane-related carbonates in this survey, they occur at pockmarks or seismic chimneys locations.

The relationship of hydrocarbon leakage flux to different leakage indicators and sedimentary structures, has become an increasingly popular research theme in the last two decades (cf. Hovland, 1981b; Hegglund, 1997; Roberts, 2001; Gay et al., 2003; Cartwright et al., 2007). Methane-related carbonates (and fauna) at cold seep sites have also been intensely studied since the eighties (cf. Hovland et al., 1984; Campbell and Bottjer, 1993; Roberts, 2001; Aiello, 2005; De Boever et al., 2006; Mazzini et al., 2008). The build-up of carbonate-rich benthic chemosynthetic communities are manifestations of active fluid migration near the seabed (Hovland, 2008), and the quantity of carbonate in the buried seepages reflects the intensity of fluid flux (Gay et al., 2007; Naudts et al., 2010). Cold seep carbonates on pockmark floors were first studied in the 1980's in the North Sea, where they appear as highly reflective patches on side-scan sonar (Hovland and Judd, 1988). The first pockmarks associated with methane-related carbonate were discovered in the North Sea in 1981 by side scan sonar (Hovland, 1985; Hovland, et al., 1987), and by a remote-operated vehicle in 1983 (Hovland and Sommerville, 1985; Hovland et al., 1987; Hovland and Judd, 1988; Hovland and Thomsen, 1989; Judd and Hovland, 2007).

Both methane-related carbonates and gas hydrates are high velocity materials (Ecker et al., 1998; Hustoft et al., 2007; Westbrook et al., 2008; Chand et al., 2009; Petersen et al., 2010). They create strong acoustic impedance contrasts at their interface with the surrounding/overlying softer layer, and result in positive high amplitude anomalies (PHAAs) on reflection seismic data. PHAAs have been reported in a number of recent publications, as high amplitudes (reflections) or anomalies in the diverse settings: (1) within craters (Hegglund, 1998); (2) at a pockmark bottom (Cauquil et al., 2003), (3) at the sea floor above pipe structures (Hustoft et al., 2007); (4) in the deeper lunate part or in the central elevation of a pockmark (Andresen et al., 2008); (5) on the seabed along a pockmark fringes (Chand et al., 2009); (6) immediately adjacent to or within pipes (Moss and Cartwright, 2010a, b); and (7) at the top of pipes (Petersen et al., 2010).

However, the detailed geometry of PHAA has barely been discussed: their evolution at seep locations has not previously been analyzed using seismic data, nor has their specific spatio-temporal relationship with pockmarks or other venting structures been examined.

I will demonstrate in this paper, the vertical occurrence of PHAAs within venting systems has considerable value for determining the timing at which fluids reach the near seabed. I will propose in the conclusion, a conceptual model that exhibit the genetic relationships and the evolutionary sequence, which are suggested by the geometric complexity and the vertical position of PHAAs within different venting systems.

Therefore in this chapter I aim to: 1) determine the role of PHAAs during the evolution of venting structures; 2) reconstruct qualitatively the steps that comprise the basic process of how a pockmark grows from low flux seepage, by integrating the geometrical development of PHAAs over time; 3) try to re-establish the relationships between flux rates and the types of venting features and to develop a theoretical sequence for the evolution of venting structures.

4.3. Data and methods

A high-resolution 3-D seismic survey was provided by Total S.A. The 3-D dataset covers an area of 425 km² in water depths of ca. 1150–1540 m with a bin size of 6.25×6.25 m. The acquisition direction (NNW–SSE) is not aligned with the long axis of any studied fluid venting structures, so there are no spatial aliasing problems with the imaging of shallow features.

For the target interval of this study the average peak to trough distance is about 7–8 ms TWT. This corresponds to a vertical resolution approximately 3–4 m at a near-seabed velocity of 1700 ms⁻¹.

Mapping of all fluid-related structures was carried out manually on a line-by-line basis, to ensure the maximum resolution of the finer structure and amplitude variation. These structures were examined in arbitrary line transects in a full 360 degree pattern centered on the fluid related structures using differently processed cubes of the seismic volume (near, middle and far offset cubes). Seismic attributes such as the dip of picked horizons, RMS amplitude, and minimum and maximum amplitude within specific two-way time windows from a mapped horizon were calculated and were used in my interpretations. Interpretation of

windowed amplitude maps was undertaken with careful calibration with the seismic data to ensure that tuning effects were correctly identified (Widess, 1973; Kallweit and Wood, 1982).

4.4. Regional geological setting

The study area is located offshore Angola, in the Lower Congo Basin (fig. 3.1, Chapter 3). This basin results from the opening of the South Atlantic in the Early Cretaceous (Masle and Phillips, 1972; Larson and Ladd, 1973). The interval of interest i.e. the Cenozoic succession, is dominated by extensional gravity tectonics over the mobile salt (Duval et al., 1992), and is constituted mainly by siliclastic deposits (Liro and Dawson, 2000; Lavier et al., 2001; Séranne and Anka, 2005).

The fluid venting structures of interest occur in Neogene Quaternary interval, which is dominated by hemipelagite deposition until the present time (Anka et al., 2009).

Details of geological context and lithology are given in Chapter 3 Geological setting.

4.5. Seismic expression and interpretation of fluid venting structures

4.5.1. Types of fluid venting structures

All the fluid venting structures in this part of the Lower Congo Basin are hosted in hemipelagic sediments of Late Miocene to Recent age. They principally occur above or within the interval affected by polygonal faults. Based on the morphology and seismic characteristics of these structures, I have grouped them into three families: 1) positive high amplitude anomalies (PHAAs), 2) seismic pipes and 3) pockmarks. PHAAs were observed to always be associated with the last two features.

4.5.2. Positive high amplitude anomalies (PHAAs)

Two main types of PHAAs were distinguished on the basis of their planforms: sub-circular and linear (fig. 4.1a). They appear on amplitude maps as strong, sharply bounded

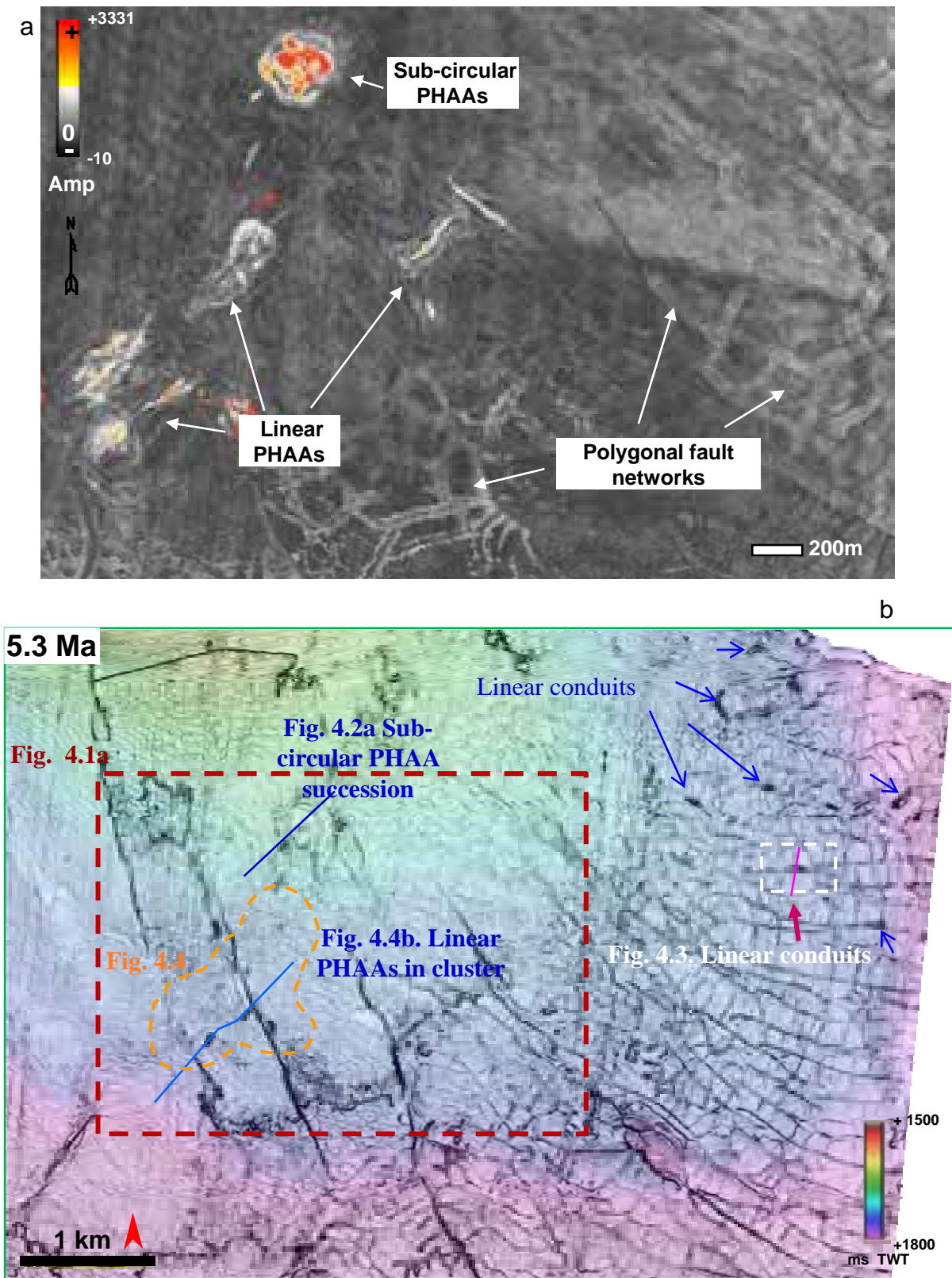


Figure 4.1. Distribution of PHAAs in the study area around Syncline 2 and Diapir 1. a) A 20 ms TWT thick amplitude window above the top boundary of polygonal fault tier shows two types of PHAA: sub-circular and linear. Notice that linear PHAAs follow the trend of polygonal faults. b) A dip horizon shows the locations of the two types of PHAAs coincide with the polygonal fault network and regional faults.

high amplitude regions in a generally low background amplitude value. Both sub-circular PHAAs and linear PHAAs are mainly observed within the interval from the 7.3 Ma marker to the seabed. Linear PHAAs usually occur at a single high amplitude reflection in seismic sections and are associated with acoustic pipes.

The dip horizon of Base Pliocene (TS4; fig. 4.1b) shows the PHAAs are distributed parallel to or along the strike of polygonal faults, or in some cases coincide with the positions of deeper-seated tectonic faults, in contrast to the context for chimneys reported by Gay et al. (2004). However, no venting structures in the study area were observed to lie above the triple junction of polygonal cells (Gay et al., 2004).

4.5.2.1. Definition and description of sub-circular PHAAs

Sub-circular PHAAs can be regular or irregular, nearly circular or elliptical in planform. They can be morphologically flat but most of the time they are associated with near-circular depressions.

A representative example of a series of sub-circular PHAAs stacked up vertically to form a high amplitude sequence is presented in Figure 4.2. Stacked amplitude anomalies seen on seismic profiles (e.g. fig. 4.2a) are observed to consist of sub-circular to elliptical planforms in the set of amplitude maps from this example (fig. 4.2b). This stack of amplitude anomalies is located at the top of deep-seated normal faults which are larger than polygonal faults and which intersect the upper and lower boundary of the polygonal fault tier. The larger faults are regarded as being tectonic in origin as vertical extent and displacement cannot be explained by the layer-bound compaction which formed the polygonal faults. The anomalies terminate upwards in a circular depression 200 m in diameter at the present day seabed. The anomalies are also associated with a pockmark below with a chaotic infill, and are interpreted to produce an acoustic wipe-out zone below.

The size and diameter of sub-circular PHAAs vary from a few tens of meters up to 100 m, and are often limited within the area of sub-circular depressions, whose diameter ranges from 100 to 200 m, with depth of concave relief ranging from 5 to 10 m. These sub-circular depressions are expressed by gently curved/concave upwards reflections, which are offset slightly from the laterally correlative reflections (e.g. reflection 3, 4; fig. 4.2A). Polarity reversals were observed in some cases within the high amplitude succession.

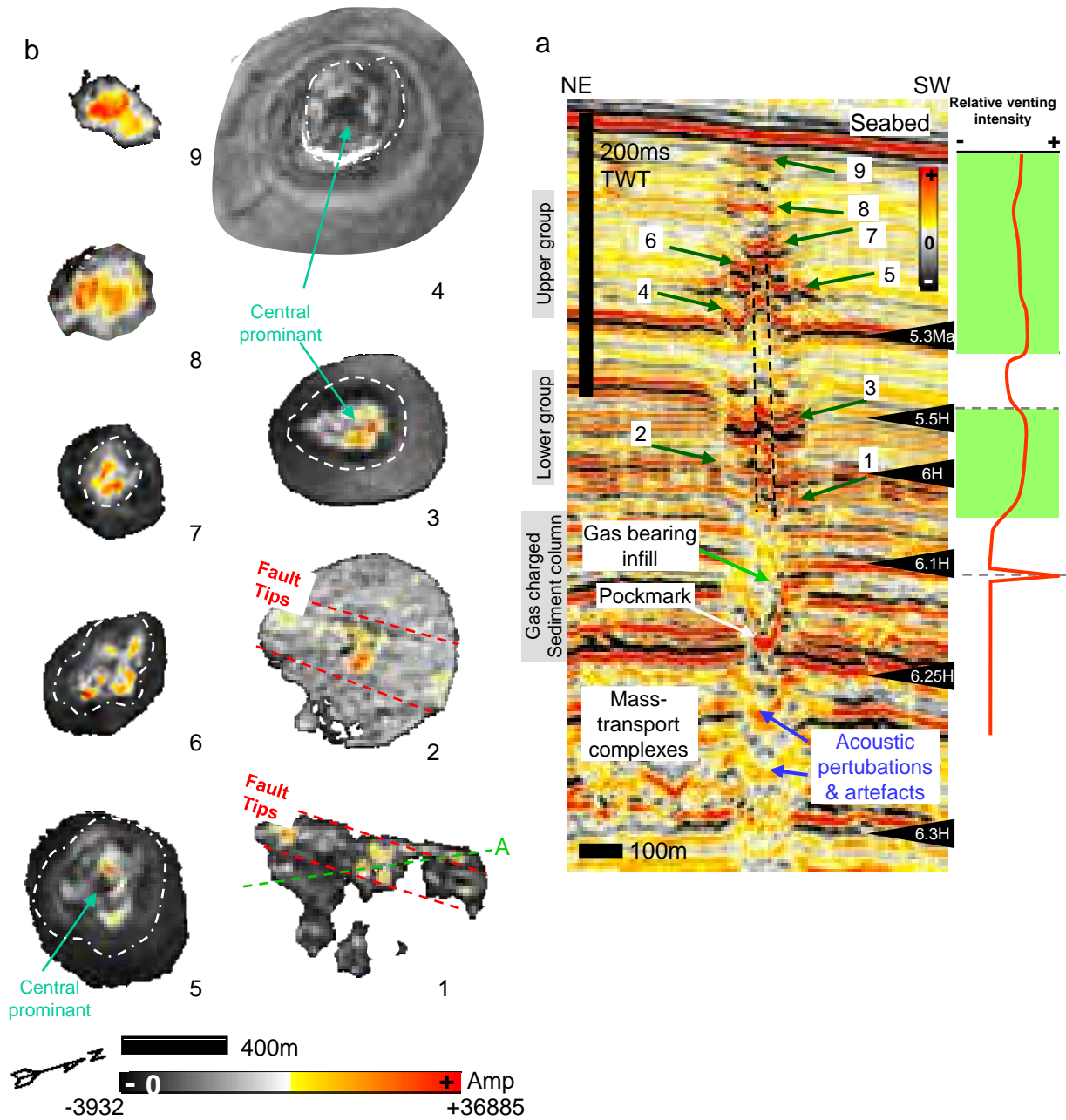


Figure 4.2. Vertical succession of sub-circular PHAAs. a) Cross-section through a “column” of amplitude anomalies, including PHAAs of various morphologies (e.g. reflection 8 & 9, sub-horizontal; reflection 4, mounded; reflection 3, pockmark-like). Its location is depicted on horizon 1 in b) by a green dotted line A. Note also the pockmark at the base (near 6.25 H). The succession is subdivided by a low-reflectivity interval between 5.5 H and 5.2 H. b) 3-D rendering of individual amplitude anomalies within the column (numbered in a)). These high amplitude reflections show: sub-circular depressions associated with PHAAs (horizon 3, 5 to 9); the base of the high amplitude sequence (horizon 1 & 2) is affected by a linear fault, along which PHAAs occur. The stacked, sub-circular depressions (horizon 3 to 5) host sub-circular PHAAs with a central prominent relief, which corresponds to the interpreted vertical zone that is deformed by faults or fractures (represented in dash on a)) in the central of the vertical succession; a mounded PHAA is likely crossed by the interpreted vertical deformed zone (horizon 4).

This high amplitude series is divided vertically into an upper and lower group (fig. 4.2A). The diameter of sub-circular PHAAs within the lower group increases upward, while those in the upper group decrease upward (reflection 4–7; fig. 4.2b), then increase again close to the seabed (reflection 8–9; fig. 4.2b). In addition, the PHAA associated depressions mirror these size changes.

The two groups of amplitude anomalies are separated by a low amplitude interval where reflections become disorganized (between horizons 5.5 and 5.2). The upper group occurs within the gas hydrate stability zone (GHSZ), as identified by a discontinuous bottom simulating reflector (BSR). The high amplitude reflections within the lower group appear to sag downward around the central axis, and exhibit raised flanks. This central axis corresponds to a narrow vertical, faulted zone which exhibits minor reverse faulting. It appears in 3-D view as central uplift inside depressions (e.g. reflection 3 & 5; fig. 4.2b), and goes up through a mounded PHAA at horizon 5.2 Ma (reflection 4; fig. 4.2a & b).

The central prominent part located in the bottom of the lower group (reflection 5 & 6; fig. 4.2a) shows continuous, linear positive relief in planform (horizon 5 & 6; fig. 4.2b) and is linearly aligned with the main fault beneath. The first PHAAs that appear at bottom of this group are small sub-circular PHAAs that align along the linear positive reliefs (horizon 5 & 6; fig. 4.2b) and are not limited by depressions.

4.5.2.2. Definition and description of linear PHAAs

Linear PHAAs are characterized by their long but narrow shape on amplitude maps with aspect ratios of more 5, and ranges from ten(s) to hundred(s) of meters in length with widths less than 50 m. Linear PHAAs are associated with furrow-like shallow negative relief up to 2 m deep. These reflections are often horizontally discontinuous with their laterally correlative reflections (fig. 4.3a), and with minor disruption of continuity beneath. All linear PHAAs are associated with chimney structures that are invariably affected by pull-up effects in this seismic survey.

Two types of linear PHAAs are observed lying above isolate linear conduits or clustered linear conduits: individual and composite. They occur within well-bedded sediments that overly the polygonal fault tier, immediately below the seabed (reflection 3; fig. 4.3a). They have the same orientation as the polygonal faults below, and are often associated with

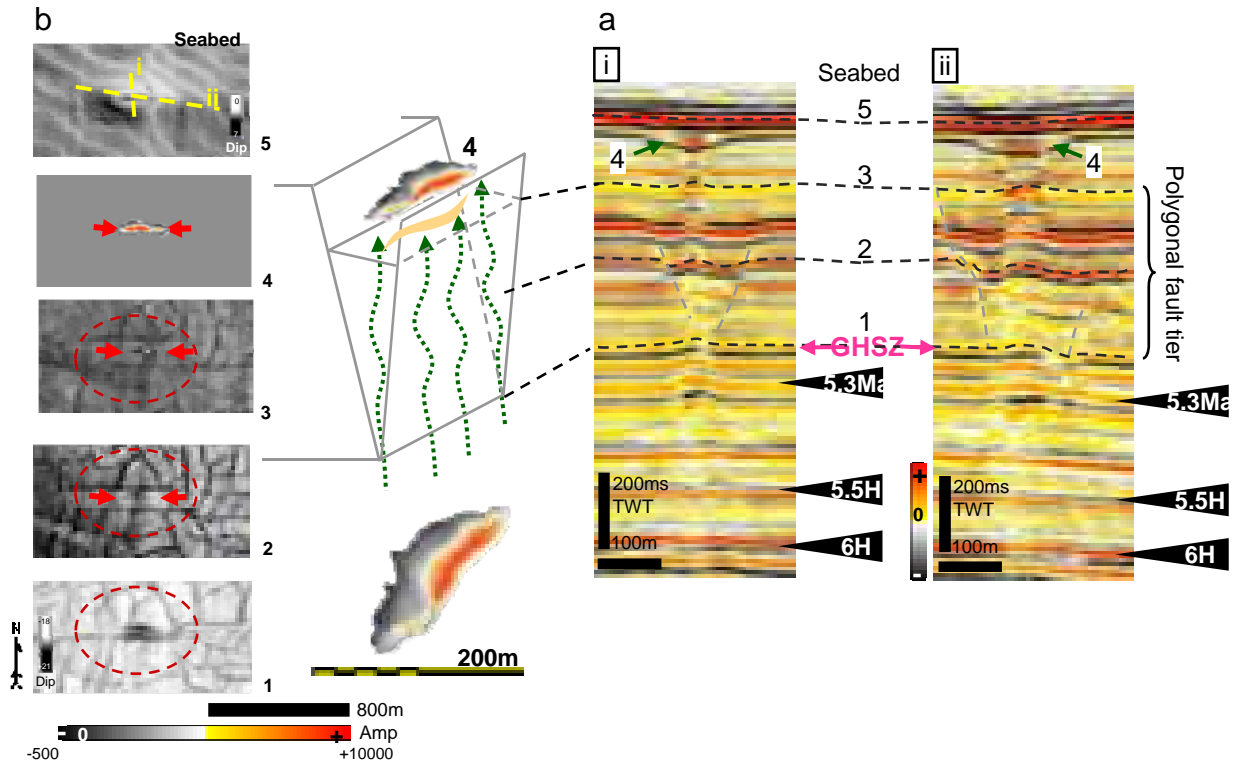


Figure 4.3. Seismic profiles and amplitude maps of numbered horizons showing a single linear conduit originating from the lower tip of a graben in the polygonal fault tier. a) Profiles i and ii are arbitrary lines across and along the axis of the linear anomaly, respectively, and are located in b) with yellow dashed line. The shallow v-shaped and curved reflections 4 correspond to a linear PHAA on horizon 4 in B. b) Horizons of positive reflections that cross the pipe within the polygonal faulting interval (numbered on A): Horizon 1 shows the pull up zone corresponding to the linear lower amplitude area on the base of the polygonal fault tier. Horizon 2 shows that the linear shape is consistent up to (horizon 3) the top of the fault tier; Horizon 4 shows the linear conduit terminates upward into a high amplitude v-shaped reflection with a linear planform. Horizon 5 shows sub-circular furrows at the present day seabed, above the pipes and at the same location (the undulating lines running WSW–ENE are processing artifacts).

elliptical depressions at the seabed. These elliptical depressions have maximum diameters ranging from 200 to 300 m.

(1) The Individual linear PHAAs (Horizon 4; fig. 4.3b) are expressed by a single high amplitude reflection with shallow negative relief on seismic sections (reflections 4; fig. 4.3A). Their length ranges from 100 to 350 m. Individual linear PHAAs have the same trends as polygonal faults below, and frequently have similar orientations to tectonic faults to which they are often linked.

(2) The composite linear PHAAs, are the second type of linear PHAAs, and are found as positive high amplitude vertically stacked reflections. They are characterized by several individual linear patterns that link or group together. They are associated with linear conduits beneath that are adjacent to each other (fig. 4.4a). The composite linear PHAAs have the same character as the individual linear PHAAs but are geometrically more complex. In plan view their length varies greatly between a few tens to several hundreds of meters.

Figure 4b shows in plan view that the shapes and lengths of these linear PHAAs vary within the vertical succession. The lowest PHAAs exhibit elongate ring shapes and progressively change upwards into composite linear PHAAs (horizons 4 & 6; fig. 4.4b). Discontinuous areas are observed below the linear PHAAs in certain locations (horizon 2, 3, 5; fig. 4.4b), and are represented by disrupted reflections in seismic sections.

4.5.3. Fluid venting structures with associated PHAAs

4.5.3.1. Linear conduits in seismic

Linear conduits are interpreted as being represented by linear low amplitude zones (dimming) that contrast strongly with the positive background amplitude of the horizons (e.g. horizon 1; fig. 4.3b). The low amplitude zones in plan view have lengths (a hundred to several hundred meters) larger than their widths (less than 50 m). They usually have the same sizes and orientations as the associated PHAAs at their top.

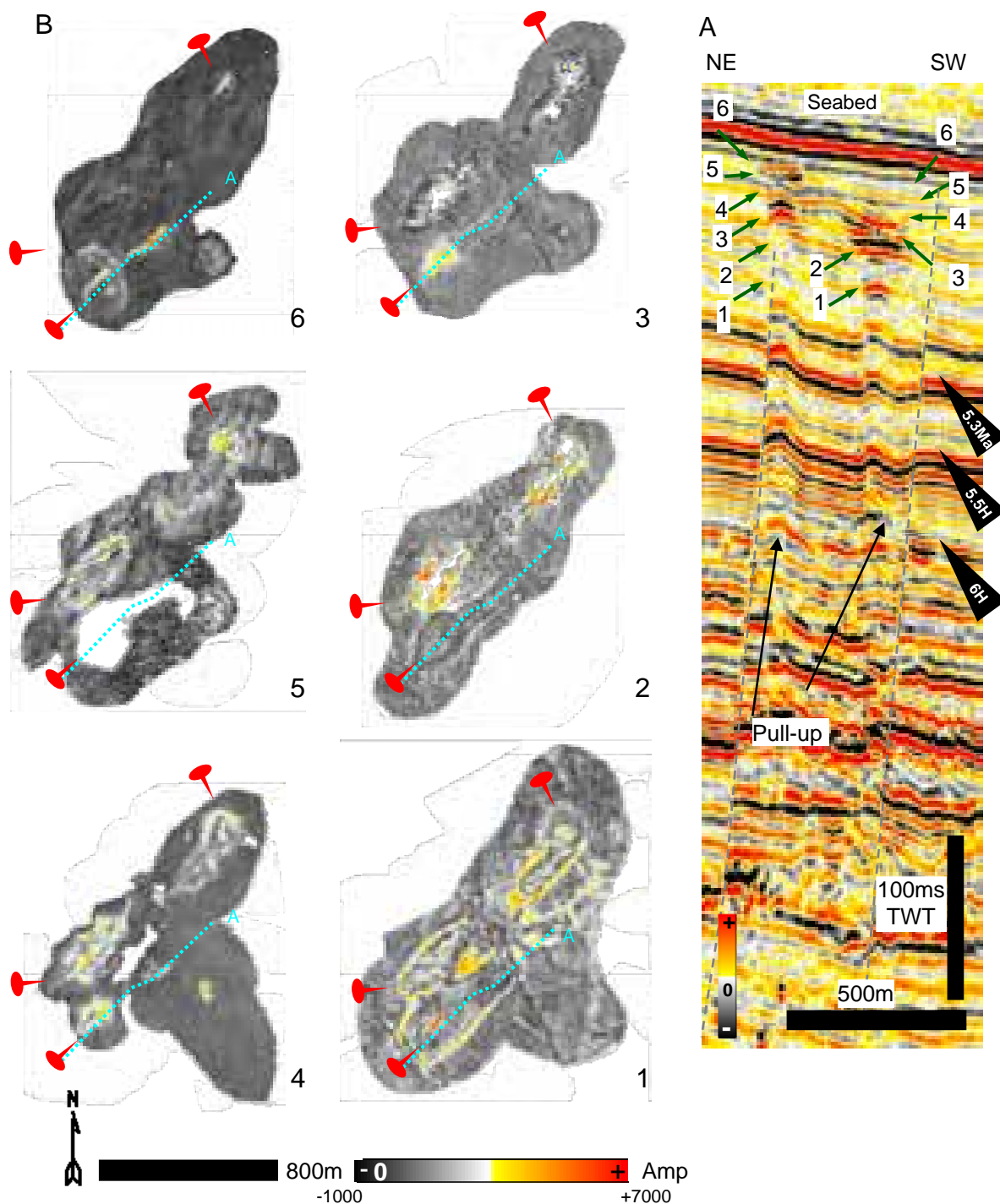


Figure 4.4. Composite linear PHAAs on profile and amplitude maps. a) linear PHAAs link together above two linear acoustic pipes due to their proximity. Its location is depicted on horizons in b) by blue dotted lines A. b) Horizons that cross the high amplitude reflector above the acoustic pipes, show linear PHAAs (reference points are red tacks): Horizon 1 shows the high amplitude elongate-ring shapes surround the central seep points of linear conduits. Horizons 2, 3, 5 show the disrupted reflections with elongated gaps, and horizon 4 & 6 above which composite linear PHAAs occur with shallow/or no negative relief.

In this survey, the seismic disturbance columns narrow upward (depth ~350 ms TWT), and inside these zones internal reflections are affected by pull-up effects (5–10 ms TWT). Polarity reversals are observed at the top of disturbance zones in some cases. Linear conduits are interpreted within the polygonal fault tier (figs. 3a; 4a), and terminate into positive high amplitude reflections / packages at the top of the polygonal fault tier. Elongated shallow pockmarks were frequently observed at the present day seabed where they are seen to lie directly above linear PHAAs and pipes (horizon 5; fig. 4.3b). The deeper limits of the linear conduits are apparently rooted into debris flows of marker horizon 6 H or in tectonic fault zones.

Horizons 1 to 4 in fig. 4.3b illustrate that the disturbed columns intersect with the bottom of polygonal faults and go up through the central axis of grabens within the polygonal fault network.

4.5.3.2. Vertical succession of the two types of PHAAs

Linear PHAAs have been observed to be succeeded vertically by a circular PHAA under the base of an “advancing” pockmark (Chapter 5). They are expressed by several high amplitude reflections within a turbiditic unit (fig. 4.5a). The oldest PHAA is labelled as reflection 1 (horizon 1; fig. 4.5b), shows a linear PHAA (diameter ~200 m) in plan view, and is overlain by a longer linear PHAA (diameter 300 m) at reflection 2 (fig. 4.5b). The dish-like high amplitude reflection (label 3) cuts through the surface of the turbidite deposit, and has a diameter of 400 m. It appears as a sub-circular PHAA in plan view (horizon 3; fig. 4.5b), and is directly overlain by a pockmark. This vertical succession is suggestive of an evolutionary signature of the high amplitude anomalies in which PHAAs size increasing with time and vertically in space, up to the base of this pockmark.

4.5.3.3. Interpretation of ‘Polyphased pockmarks’ and their associated PHAA

Vertically stacked elliptical PHAAs with complex internal structures were observed either at the base of or surrounding the lower part of pockmarks. These pockmarks are characterized by dome-shaped reflections (3b; fig. 4.6a) below the craters. Their sidewalls are defined by the terminations of truncated reflections in seismic sections (fig. 4.6a). The

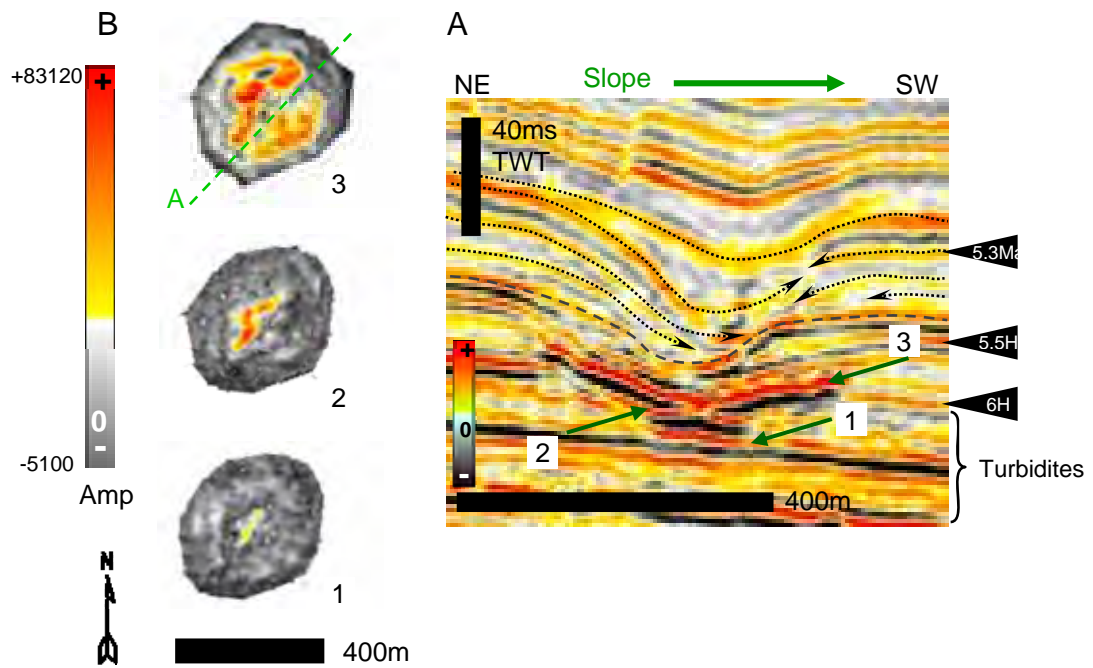


Figure 4.5. Stacked up PHAAs below an advancing pockmark, and above the turbidite surface. a) Seismic profile. Its location is showed on horizon 3 in b) by a green dotted line A. b) Horizons 1 & 2 (numbered on A) of the high amplitude reflections show a smaller linear PHAA with two segments. These linear PHAAs are stacked below a sub-circular PHAA on horizon 3, which is limited inside a sub-circular depression.

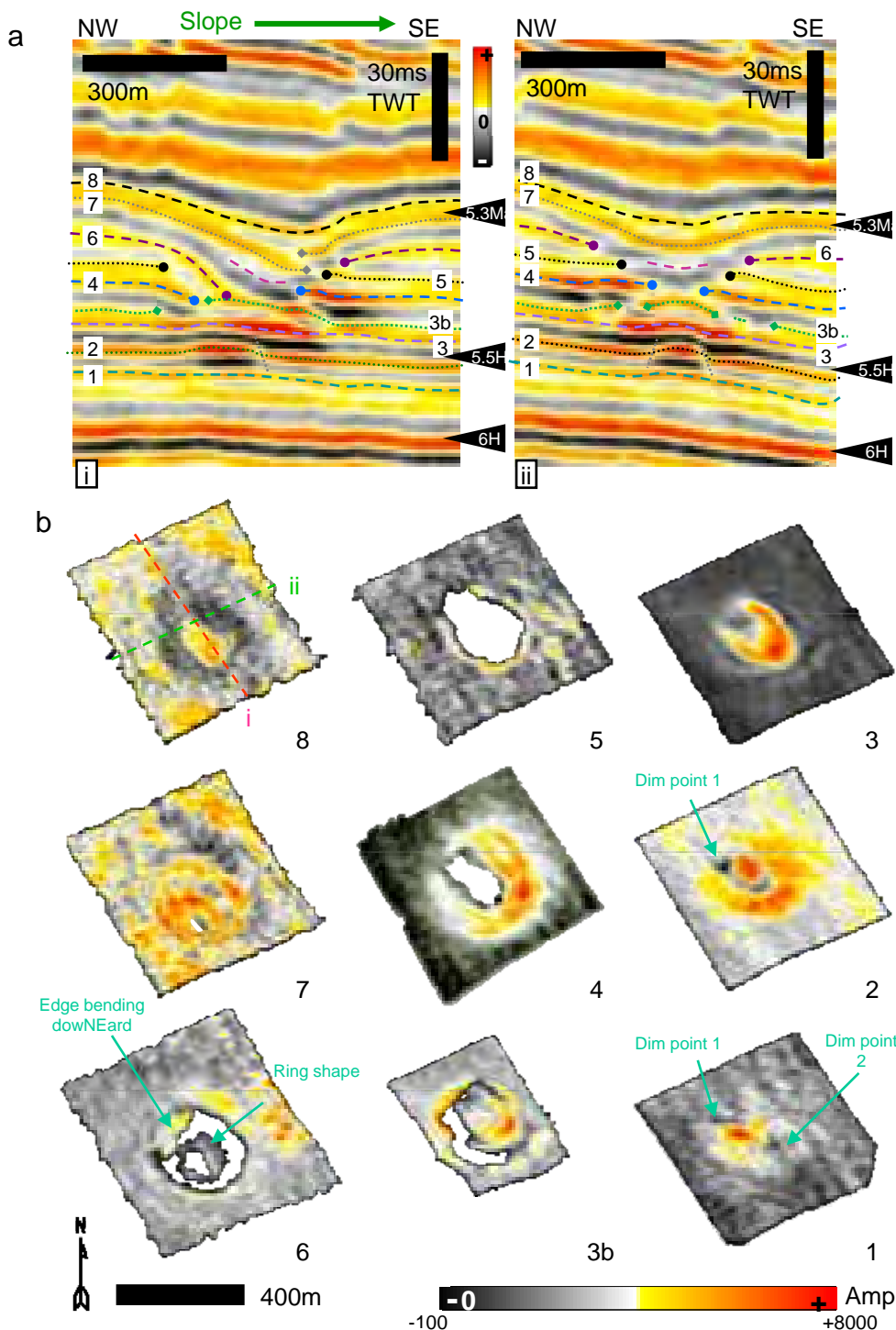


Figure 4.6. A polyphased pockmark. a) Profiles i and ii are arbitrary lines across and along the pockmark axis. Note that the incomplete dome-shape in profile i, at reflection 3B is still linked partly with its original reflection, but disconnected on profile ii. b) Amplitude maps of the numbered horizons. Horizon 1 shows an elliptical PHAA which is delimited by two small amplitude dim points in both ends; Horizon 2 shows an elliptical PHAA surrounded by a horseshoe-shaped PHAA; Note that the seep point 1 is still observed with a small dim zone. Horizon 3 shows a hoof-shaped PHAA above the edge of underlying elliptical PHAAs; Horizon 3B shows a dome structure at the pockmark base, with a long gap along its edge from N to W. Horizon 4 shows a crescentic shaped PHAA above the edge of the dome structure and a surrounding sub-elliptical truncation zone. Horizon 5 shows an asymmetric circular dim zone. Horizon 6 shows an ‘almost circular’ dim zone. Note the lower amplitude ring shaped feature in the middle of the crater. Horizon 7 shows the sediment cover subsiding asymmetrically above the first seep point location, with a small dim zone in the center. Horizon 8 shows the sediment subsiding asymmetrically.

pockmark sidewalls are partly covered by a downward-bending reflection in the northwest (reflection 6; fig. 4.6a, left), which is the uppermost reflection of the v-shaped crater. The downward bending reflection is disrupted in SW but can be followed continuously from the NE far field into the pockmark. This type of pockmarks exhibits different sizes and forms of circular amplitude dim zones on horizons which stack vertically (3D horizon 4 to 6; fig. 4.6b). The immediate sedimentary infill of the pockmarks consists of two reflections which sag asymmetrically downward (e.g. reflection 7, 8; fig. 4.6a, left), whereas the lowest reflection 7 is disrupted at the inflexion point. These reflection configurations suggest that the pockmarks have gone through different stages of evolution, therefore they are called “Polyphased pockmarks”.

Polyphased pockmarks occur within clay-dominated intervals, in the stratigraphic interval between 5.5 Ma and 5.3 Ma, i.e. between the two polygonal fault tiers. Their circular shapes in plan view measure approximately 150 m to 200 m, and the measured relief on seismic sections is less than 50 ms TWT.

4.5.3.3.1. Internal structures associated with PHAAs in 3-D views

The lowest elliptical PHAA with NW–SE orientation on horizon 1 and below the polyphased pockmark represented in fig. 4.6 is associated with two small lower amplitude depressions at its two ends (horizon 1; fig. 4.6b).

A bigger elliptical PHAA on horizon 2 is located in the northwest of this region where a small depression is observed (at dim point 1), and is surrounded by a ‘horseshoe’ shaped PHAA (horizon 2; fig. 4. 8B). Above the same location on horizon 3, a ‘hoof’ shaped PHAA (horizon 3; fig. 4.6B) with the same orientation is observed. A structure comprising a dome is found at reflection 3b (fig. 4.6A). Similar features characterize the base of all polyphased pockmarks in this survey. This dome is associated with a crescentic-shaped PHAA in the SE (horizon 3B; fig. 4.6B). A long gap is found along the NW side of the dome feature and corresponds to the disruptions of reflection 3B (fig. 4.6A). An elongated discontinuous zone and an asymmetric circular discontinuous zone oriented NW–SZ are observed on horizons 4 and 5 (fig. 4.6B). They cross the middle of pockmark and are located above the dome feature. A crescentic-shaped PHAA surrounds the elongated dim zone on horizon 4. The asymmetric dim zone on horizon 5 is larger along the SE side. Reflection 6 (fig. 4.6A) crosses the topmost part of the v-shaped crater and continues laterally into the pockmark in the NW, appearing as a circular dim zone with extended edge depressions in SE

in 3-D view (horizon 6; fig. 4.6B). The sediments (reflection 7, 8) which cover the v-shaped crater and sagged downward, show the asymmetrical depression centers in three dimensional views (horizon 7 & 8; fig. 4.6B). The disruption at the inflexion point of reflection 7, corresponds to a small circular dim zone in the depression (horizon 7; fig. 4.6B).

4.6. Discussion

No direct lithological calibration of PHAAs is available in this shallow section. PHAAs were not sampled in the area, none of the available wells were penetrated the PHAAs. As a result, their interpretation has to rely on their acoustic expression, their geometry, and on indirect evidence from regional constraints on sedimentation in the area, from comparison with interpretation analogues of pockmarks at the sea floor in the study area and elsewhere.

4.6.1. Relationship between methane flux and positive amplitudes variations

Positive high amplitudes correspond to a downward increase of acoustic impedance, and could indicate (1) a single 'hard' layer, or (2) a (set of) thin hard layer under a seismic resolution (Widess, 1973).

In the context of the Neogene of this study area, lithologies that could account for the patches of high acoustic impedance within the high continuity seismic facies (clay rich hemipelagites with soft impedance), are most likely to be hard carbonates or carbonate-cemented layers because of their high interval velocity (Hanneman et al., 1994; Westbrook et al., 2008) and resultant localized velocity pull-up effects (Woods, 1991).

Gas hydrates (hosting sediment) are another high impedance material which could explain the high positive amplitudes, because they have high interval velocity compared to claystones (Westbrook et al., 2008) and are observed to generate pull-up effects (Hustoft et al., 2007). However they can only be present in the GHSZ. Only a small number of reliably interpreted occurrences of hydrates were observed in this area (250–275 mbsf, at the lower polygonal fault boundary of HD4).

The possibility that the PHAAs result from sand injection or silica diagenesis was also considered. Sand intrusions can exhibit a variety of geometries, but none of the published examples of sandstone intrusions exhibit the three-dimensional geometry shown here for

the PHAAs (see reviews in Hurst and Cartwright, 2007). Many circular or sub-circular sandstone intrusions have a conical geometry with distinctive, discordant margins dipping about 15° to 25°. In marked contrast, PHAAs are flat-lying to gently mounded.

Silica diagenetic transformation from opal A-CT and opal CT-quartz occurs in formations rich in depositional amorphous silica (Kastner et al., 1977). The transformations result in increases in acoustic impedance, and a strong positive reflection at the phase boundary (e.g. Davies and Cartwright, 2002), commonly extending over many thousands of square kilometers. Localized anomalies due to silica diagenesis have been reported from northern Norway (Ireland et al., 2011) in association with a regionally extensive opal-A to CT phase boundary reflection. However, these have a contrasting three-dimensional geometry to the PHAAs as described here, and furthermore, there is no evidence in the study area of a regional phase boundary reflection. Although ODP bore-holes drilled in this region have documented that the interval contains siliceous sediments (Wefer et al., 1998), reports state that their concentration never reaches very high values (Wefer et al., 1998). Therefore, I suggest this would not result in a major diagenetic transformation zone, so that would be visible in seismic data, and any seismic anomalies in this interval must have another origin. Thus, I think it highly unlikely that PHAAs are related to silica diagenesis.

The systematic restricted distribution of PHAAs below palaeo-pockmarks suggests a genetic relationship between the PHAAs and the pockmarks, and points to an interpretation of a fluid-related origin (i.e. methanogenic) for PHAAs. The geometry of the amplitude anomalies does not resemble any known depositional carbonate sedimentary features at this scale. Velocity pull-ups are most frequently observed beneath isolated PHAA: this phenomenon occurs especially within the GHSZ. In contrast, the vertically stacked PHAAs at the base of palaeo pockmarks below the BSR, are not associated with any velocity pull up. This suggests that the single PHAA occurring above a BSR may well be associated with gas hydrates.

4.6.1.1. Methane-related carbonates in Offshore Congo–Angola

According to previous studies of this basin (e.g. Gay, 2002; Charlou et al., 2004; Olu-Le Roy et al., 2007; Pierre and Fouquet, 2007), the documented methane-related carbonates include principally four main types of carbonates: authigenic carbonate pavements, cemented clastic rocks or nodules, and cold seep carbonate communities (e.g. Hovland and Judd, 1988).

Therefore I use the term methane-related carbonates to describe all of these methane-related carbonates.

Methane-related carbonates without seismic calibration are reported in a drill location in this survey, and are found in clay rich facies (hemipelagite or muddy turbidite deposits). They have a low isotopic $\delta^{13}\text{C}$ value (-34.4‰ ; Total internal report; Vignau et al., 2000) which is suggestive of methane as a carbon source (Hovland et al., 1985). The measured $\delta^{18}\text{O}$ value (3.9‰) indicates that the temperature at which the carbonate formed was $5\text{--}10\text{ }^{\circ}\text{C}$ and implies that these carbonates would have precipitated very early and close to the sediment-water column interface (Vignau et al., 2000).

Cold seep communities and gas hydrates with methane-rich plumes are associated with active pockmarks on the Congo–Angola margin (Gay, 2002; Charlou et al., 2004; Olu-Le Roy et al., 2007; Pierre and Fouquet, 2007). Floating gas hydrates from the interface between massive carbonate crusts and reduced sediments were also observed by remote-operated vehicle inside a giant pockmark in the same region (Charlou et al., 2004).

Methane-related carbonates form at, or close to the seabed through the production of cold seep communities or/and Anaerobic Methane Oxidation (Hovland et al., 1987; Judd and Hovland, 2007). This oxidation can only be completed within the first tens of meters of burial within the sulfate-methane transition zone (SMTZ) (e.g. Borowski et al., 1996; Snyder et al., 2007), which is $10\text{--}50$ mbsf depth at present in this region (Wefer et al., 1998). Below the sea floor, methane-related carbonates result from anaerobic oxidation of methane (AOM; Hovland et al., 1987), while at the seabed they result from the development of chemosynthetic communities (Bayon et al., 2007) and AOM (Mazzini et al., 2006).

Therefore, I suggest that the horizons at which methane-related carbonates are inferred to occur, represent a shallow burial diagenetic ‘datum’ near the palaeo-seabed or palaeo water-sediment interface.

4.6.1.2. Timing of venting at the palaeo-seabed

It is propose that the timing of methane flow at the palaeo-seabed can be approximated by the stratigraphic age of the horizons in which PHAAs occur when they are associated with pockmarks or depressions. The interpreted carbonates are associated with topographic depressions that can only be produced by moderate to fast methane flux, and one that would be able to elevate the base of SMTZ to within a few meters of the seabed (Hovland

et al., 1987). Accumulation of chemosynthetic faunas occurs within the seep depression at the seabed (Hovland et al., 1987). The coincidence of a depression and a PHAA argues strongly that the SMTZ was very close to the seafloor, well within the resolution of the available seismic. The approximate timing of methane flow at the seabed would in this case be indicated by the stratigraphic position of methane-related carbonates (PHAAs).

The duration of methane venting is suggested here to be reflected in the thickness of methane-related carbonate (PHAAs), which cannot be assessed in detail without direct borehole calibration. PHAAs that are not associated with pockmarks/depressions, are suggested to have formed deeper below the seabed at different levels within the SMTZ (Regnier et al., 2011).

We distinguish fossil methane-related carbonates from the actively forming systems, based on the fact that the fossil ones are buried by continued deposition and are thus moved below the SMTZ. Therefore, methane-related carbonates (expressed by PHAAs here) that are found beyond the sulfate reduction zone, are interpreted as fossil seeps (cf. Paull et al., 1995).

4.6.1.3. Genetic model

The framework that I adopt here to interpret the significance of PHAAs within different types of venting sites is based on a model proposed by Roberts (2001) and Roberts et al. (2006). This model states that the variation in quantity and in morphology of authigenic and chemoherm carbonates (or PHAAs in my interpretation) is related to the dynamics of methane seepage. The model is in good agreement with measurements of measured methane fluxes and with the types of associated methane-derived formations at different venting sites reported by other authors (e.g. Torres et al., 2002; Gay et al., 2006b; Naudts et al., 2010).

The following classification is proposed by Roberts (2001) and Roberts et al. (2006):

- Slow methane flux is principally characterized by chimneys (Roberts, 2001; Cartwright et al., 2007), as well as carbonate cemented hardgrounds or mounds (Roberts, 2001), and bacterial mats with near total absence of macrofauna (Roberts, 2001; Naudts et al., 2010);
- Moderate flux is expressed by small fluid expulsion features (Roberts, 2001; Roberts et al., 2006), which could be a pipe with a crater above (Løseth et al., 2001; Cartwright et al., 2007; Moss and Cartwright, 2010a, b), isolated authigenic carbonates pavements, gas hydrate mounds and dense chemosynthetic communities (Roberts, 2001; Torres et al., 2002; Naudts et al., 2010);

- High flux is associated with conical structures (pockmarks) which are considered as the result of dramatic and strong fluid releases (Pantin, 1980; Hovland, 1981b; Roberts et al., 2006; Cartwright et al., 2007), and absence of chemosynthetic carbonates (Roberts, 2001; Gay et al., 2007). This model is used to interpret the various types of venting structures observed in this study.

4.6.2. Methane fluxes and their subsurface expression

4.6.2.1. Relationship between sub-circular PHAAs and pockmarks

Sub-circular PHAAs associated with a series of vertically stacked shallow depressions (fig. 4.2A) are interpreted to be the result of moderate methane flux, since the formation of methane-related carbonate is not favored at a rapid seep site (Roberts et al., 2006; Naudts et al., 2010). Although the sub-circular, concave depressions exhibit a degree of fluid venting dynamics, the overlying configuration suggests that the flux is modest enough to inhibit crater development but dynamic enough to create shallow, sea floor depressions. These depressions created by fluid expulsions can nonetheless be regarded as pockmarks (Judd and Hovland, 2007).

The shallow pockmarks (e.g. reflection 3, 5; fig. 4.2A & B) have prominent centers and I interpret these as cylindrical zones of fracturing (black dot lines in fig. 4.2A), which most likely acted as conduits to feed the youngest pockmarks. This central zone or conduit is interpreted to grow from a sub-vertical fault below, which was masked by the seismic distortions. The upper tip of this fault is visible in deeper amplitude maps (reflection 1 & 2; fig. 4.2A & B).

We interpret the formation of this high amplitude succession as due to gas leaking from the reservoirs below horizon 6.25 H (H: Horizon with interpolated age but no age calibration), and the gas expulsion at the palaeo-seabed (6.1 H) is expressed by the gas-charged infilled pockmark (fig. 4.2A). The lower amplitude interval above with low continuous reflections suggested fluid flow decreased between 6 H to 6.1 H (fig. 4.2A). The widths of PHAAs progressively increase upwards (fig. 4.2) indicating that fluid flow was progressively reactivated at horizon 6 H. The occurrence of horizontal deposits between horizon 5.5 H and 5.2 Ma suggests that fluid venting stopped during this period. The mound shaped carbonate (PHAA) at 5.2 Ma indicates that seepage restarted at the palaeo-sea floor

with a relatively moderate flux rate. The PHAAs associated with pockmarks which occurred later decrease in size upwards (reflection 8, 9; fig. 4.2A), suggesting that the fluid expulsions decreased gradually and the methane flux slowed down progressively (fig. 2A).

The PHAAs associated with pockmarks become bigger and flatter at 50 ms TWT below the seabed, which likely indicates that the fluid flow increased but remained in a relatively moderate state of flux, because of the observed flat morphologies and the absence of craters. Finally, this high amplitude series terminated upward into a gently dipping pockmark at the current seabed, implying the seep site is still active.

4.6.2.2. Linear conduits and PHAA without pockmark

Acoustic pipes or columnar seismic disturbance zones are widely recognized as gas conduits (Hegglund, 1997; Løseth et al., 2001; Bünz et al., 2003; Hustoft et al., 2007; Moss and Cartwright, 2010a, b). Linear conduits associated with linear PHAAs are quite different from the sub-circular PHAAs sequence, as no obvious pockmarks or expulsion craters were observed within the vertical succession. So the linear conduits are interpreted as a type of slow fluid venting feature, the so-called ‘seepage-pipe’ (Cartwright et al., 2007).

The upwards bending of reflections commonly observed in pipes are believed in some cases to represent the deformation of sedimentary strata due to vertical fluid movement or episodic blow out events (Bouriak et al., 2000; Løseth et al., 2001; Berndt et al., 2003; Gay et al., 2007; Hustoft et al., 2007). An alternative interpretation is that these upward bending zones are velocity pull-up anomalies due to the presence of high velocity material within the pipe above (Ecker et al., 1998; Holbrook et al., 2002; Hustoft et al., 2007; Chand et al., 2009; Hustoft et al., 2010). This material could be carbonates (Hustoft et al., 2007; Westbrook et al., 2008) or gas hydrates within or directly above the pipes (Ecker et al., 1998; Hustoft et al., 2007). Forward seismic modelling of Løseth et al. (2011) demonstrated that the ‘local anticline’ or the pull-up structures within the pipes in the offshore Nigeria, are most likely geophysical artifacts related to imaging complexity. Løseth et al. (2011) also argued that hydraulic fractures should be present inside the seismically disturbed zone of the pipes.

The pipes identified in the study area most likely represent highly focused palaeo-fluid-migration paths, and this inference is supported by the occurrence of linear PHAAs at the top of pipes above the polygonal fault tier. These are interpreted as methane-related carbonates fed by the methane that migrated through linear conduits which were guided by

polygonal faults beneath. The occurrences of pockmarks (shallow depression on horizon 5; fig. 4.3B) at the current seabed indicate that the pipe conduits are still active, or were active very recently.

4.6.2.3. The origin of linear conduit geometries

The geometry of these linear conduits is interpreted to result from the deformational exploitation by the overpressured fluid of pre-existing fracture networks. The basal apex of polygonal fault graben is likely to be the first weak zone that the fluid encountered. The dim zones on the horizons that cross the seismic chimney (fig. 4.3) are compatible with the propagation of linear fractures upward through the central axis of the graben from the base, since they have the same length and orientation as the polygonal fault planes (figs. 4.3b; horizon 2 & 3).

Normal faulting in the polygonal fault system corresponds to an extensional regime, with σ_1 (stress 1) vertical and σ_2 and σ_3 identical ($\sigma_2 = \sigma_3 = \sigma_H$) regionally, with local modifications around fault nucleation points. Along a given fault, σ_3 is horizontal and perpendicular to the fault strike whereas σ_2 aligns with the fault strike. If fluid pressure exceeds σ_3 , hydraulic fracture would occur perpendicular to σ_3 , i.e. in the vertical plane following the axis of the graben defined by a point of conjugate faults in a polygon (fig. 4.3).

Slow to moderate fluid flux was suggested to be transported by the linear conduit and allowed the development of linear accumulation of methane-related carbonates above, as seen on the seismic data as linear PHAAs occurring above the polygonal fault tier (fig. 4.3).

Concentrated fluid leakage at multiple fault locations, is suggested to allow the linear PHAAs to develop in clusters (fig. 4.4), as the lateral terminations of linear PHAAs extended until they connected to each other.

The example shown in fig. 4.5 demonstrates that linear PHAAs below pockmarks can grow upwards and evolve into sub-circular PHAAs, and then terminate upwards into a pockmark crater. Such a model of methane-related carbonates occurring prior to the formation of eruption craters has previously been documented by Hovland et al. (1987). My preferred interpretation of the vertical succession of PHAAs is that they represent an increase of flux over time, from slow to moderate flux, followed by the rupture of sediment by an overpressured fluid eruption that generated the initial pockmark crater (cf. some early examples in Worzel and Watkins, 1974; Sieck, 1975; Hovland and Judd, 1988) (Hovland,

1982; 1989; Judd and Hovland, 2007; Cathles et al., 2010). My interpretation is thus fully in agreement with the model proposed by Hovland et al. (1987) in which the formation of methane-related carbonates is prior to the seal failure. Examples presented here show how one type of PHAA can grade into another over time.

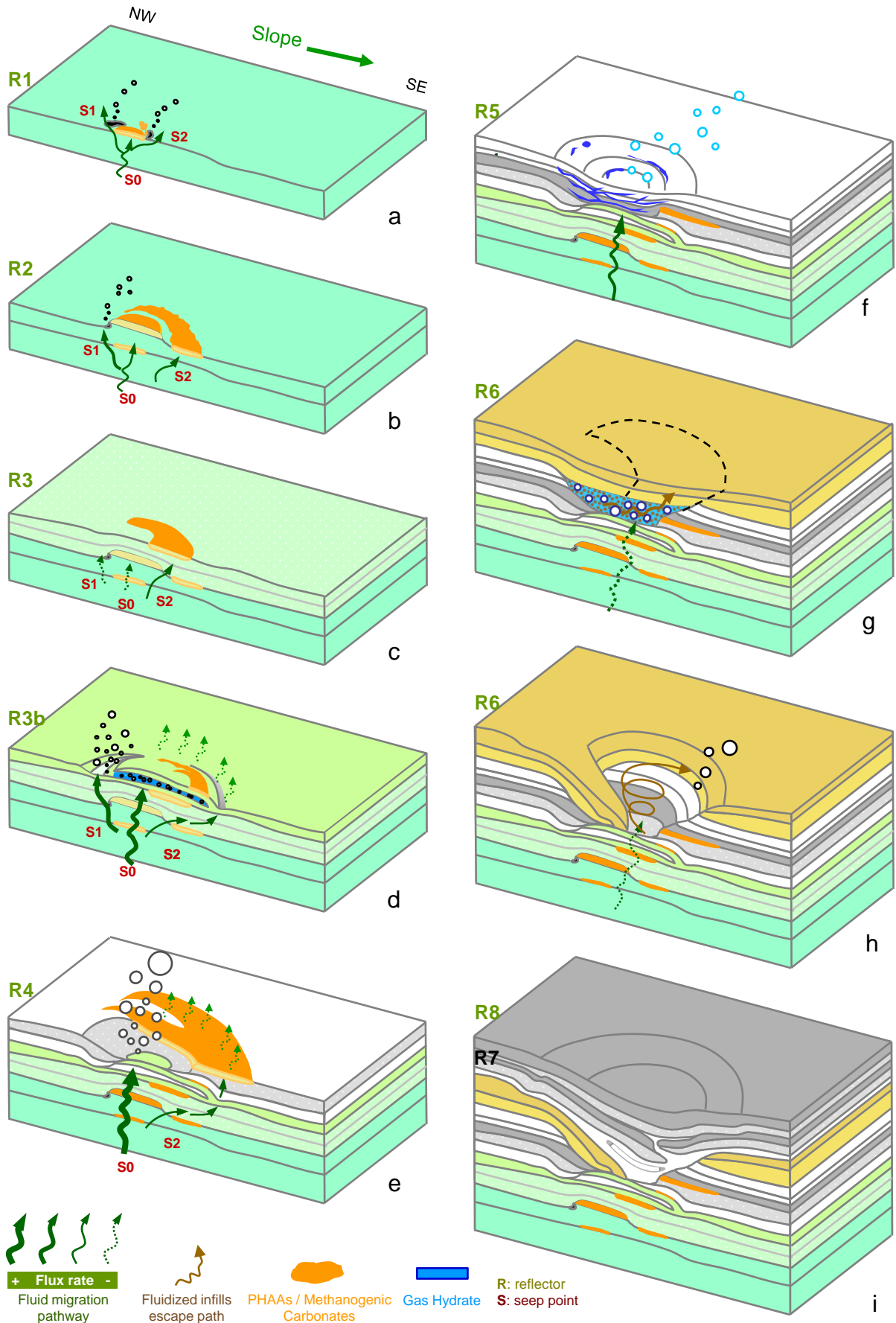
4.6.3. Conceptual model for the formation of ‘Polyphased pockmarks’

The internal structures of polyphased pockmarks suggest the fluid expulsion responsible for their genesis was episodic (cf. Hovland et al., 2005; Hovland and Svensen, 2006; Andresen and Huuse, 2011). An evolutionary sequence for polyphased pockmarks in this study area is proposed in fig. 4.7A, where the uppermost horizons represent the surfaces that occurred at or close to the palaeo-seabed, and where methane-related carbonates developed. The evolutionary stages in this model are as follows:

- (1) The occurrence of a near-elliptical PHAA on horizon 1 & 2 (figs. 4.6b & 4.7b), below the pockmark (at seep point S0; fig. 4.7a & b) and without eruptional crater, suggests that the seepage started with a slow flux. The small lower amplitude depressions (point 1 & 2) on horizon 1 & 2 (fig. 4.6b), are interpreted as palaeo-seepage points (as S1 & S2; fig. 4.7a & b) left by small scale vents.
- (2) The occurrence of crescentic methane-related carbonates (PHAA) surrounding the elliptic one (horizon 2; fig. 4.6b) most likely results from fluid at seep point 2 bypassing the newly formed top seals (PHAA) above S0 and escaping via their outer boundary (horizon 2; fig. 4.7b), while S1 is deactivated. Just above, methane-related carbonates were fed and developed as open circular shapes.
- (3) The carbonates continued to develop above the seal breach at the edge of the previous carbonate zone, and moderate fluid escape from the only active seep point 2 formed a hoof-shaped PHAA (horizon 3; figs. 6b & 7c). Levin (2005) observed a similar shape of cold seep carbonate with smaller size (1 m diameter) outcropped in the Monterey Bay bottom, and was called ‘seep-ring’.

The positive dome-shaped reflection (horizon 3b; fig. 4.6a) shows a localized PHAA in plan view, and appears as a dome in 3D view (horizon 3b; fig. 4.6b). It is interpreted as a dome-shaped carbonate pavement. Alternatively, this dome-shaped structure could be a less permeable layer which was domed upwards by the overpressured fluid beneath, and its sidewalls were sufficiently strong to maintain the structural form, possibly because it was

Figure 4.7. Theoretical model for step-wise genesis of polyphased pockmarks (see also Fig. 4. 6a for the numbering scheme of reflections). a) Slow methane seep is expressed by the small methane-related carbonate patches at the site. Fluid escape then bypassed the central carbonate seal and created two seep points (1 and 2 in red). b) The elliptical carbonate patch continued to develop at the central seep. Slow fluid flux at seep 2 bypassed the sealed locations, and fed the new carbonates surrounding the central patch. The small depression at seep point 1 suggests a relatively faster flux. c) Low fluid flux at seep point 2 bypassed the carbonate patches of reflection 1 and 2 and escaped, to form a hoof-shaped PHAA/carbonate above the edge of previous carbonate. d) A less permeable layer, an interpreted carbonate dome, was deposited and covered the seep site during the lower fluid flux period. Overpressure fluid inside the carbonate dome breached the NW internal edge of the dome. e) Fast flux concentrated at seep point 0 where carbonate was unable to form. Fluid at seep 2 continued to by-pass the sealed location and migrated upward to form a crescentic PHAA (horizon 4; Fig. 4. 6b) above the edge of the previous carbonate. f) Sediment deposited above the seepage, during the fluid less active period. Slow methane flux is suggested to interact with the later sedimentation within GSHZ. Gas hydrates veins or layers were formed within the sediment layers, above the seep point and within an elliptical perimeter. g) Horizontal deposits (before their deformation) at reflection 6 suggest a fluid inactive period. Gas hydrate dissociation is probably induced by sealevel fluctuations or erosional event, which is indicated by truncation surface (reflection 6; Fig. 4. 6a). Over pressured, liquefied sediment below the reflection 6 escaped to surface by cutting a crescentic window (horizon 6; Fig. 4. 6b). h) Sediment cover collapsed. Vertical movement of liquefied sediment (brown arrow) left the trace as a dimpling in the center of crater (horizon 6; Fig. 4. 6a). Notice that, the expulsive focus of this pockmark shifted from NW to SE, from above the gap of the dome to above the seep point 0. It is confirmed by the moderate-amplitude ring shape within the crater and above the seep point 0. i) Later sedimentation sealed the whole crater as the fluid flux waned and died. It is suggested by the geometries of horizon 7 and 8.



preferentially cemented by carbonate deposits (Mazzini et al., 2008). Under the assumption that the pockmark was located at the palaeo-seabed and within GHSZ, at the moment of its formation (the present day depth of GHSZ is 200 ms TWT, approximately 180 mbsf). It is possible that the material that accumulated inside the carbonate dome was gas hydrate by analogy with the case of a hydrate dome covered by pelagic sediment in the Gulf of Mexico (Fisher, 1997; in Penn State website <http://www.science.psu.edu/news-and-events/1997-news/iceworms.htm>).

The hydrate dissociated afterwards: this may have been caused by the pressure reduction at the palaeo-seabed, and was probably due to contemporary sea level fluctuations. As a result, the overpressured fluid breached the lateral zone (along NW side) of the less permeable dome structure, and a long fracture was observed (horizon 3b; fig. 4.6b). New sediments were deposited above the deformed dome-shape (fig. 4.9e), whilst the seep point 1 became inactive and seep point 0 reactivated with a strong flux. This would explain the occurrence of carbonate developed above the edge of the dome and surrounding the strong venting point which formed a shallow elliptical crater (horizon 4; figs. 4.6b & 4.7e). Then fluid flow declined to the point where sediment could drape the shallow crater beneath, and any subsequent flux may have led to hydrate formation within later sediment deposits once again (horizon 5; fig. 4.7f).

The drape unit at reflection 6 is suggested to be deposited during the period of fluid deactivation (fig. 4.7g). Hydrate dissociation under reflection 6 would induce liquefaction of host sediment (Riedel et al., 2006), during probably the events of contemporary sea level fluctuation. Sediments would be fluidized by the liberated methane becoming overpressured below the sedimentary cover (reflection 6), and created a circular crater on horizon 5 (fig. 4.6b). We suggest that liquefied sediment along with the gas would have escaped through the margins of the crater where the seal has been breached (fig. 4.7h). Therefore, a crater was developed at the surface due to the volume loss in the underlying subsurface, and it is expressed by the bending downward reflection 6 on NW sidewall (fig. 4.6A).

I caution that, the origin cause for the deformation of the sedimentary cover represented by reflection 6 could be a modified hemipelagic draping by bottom current or originate from deposition by bottom current effects. But the clear circular edge of the crater at reflection 6 (fig. 4.6), suggests that it can only be created by the fluid expulsion rather than by the local current activity. Likewise, the collapsed feature within individual v-shaped circular craters has been observed in different locations of this survey, and it supports this model. Equally, fossil pockmarks associated with collapse features induced by subsurface material

removal has been reported firstly by Imbert et al. (2008), who interpreted their origin to be related to hydrate dissociation. Actual lenticular gas hydrate inside an active Nigerian pockmark was detected by an Autonomous Underwater Vehicle (AUV) seismic survey (Tony-George and Cauquil, 2007). The model of collapse within a pockmark, has been tested on the same Nigerian pockmark through numerical modelling by Sultan et al. (2010), and supports the explanation of hydrate dissociation. In this study area, it is plausible that hydrate dissociation could have led to collapsed pockmark formation, since there is clear evidence for the position of the GHSZ at the present day.

Finally, the vertical movements of fluidized sediment inside the depression continued intermittently until final termination of the venting site (fig. 4.7i).

Moreover, all polyphased pockmarks are sealed at 5.3 Ma, at the End Miocene/Early Pliocene and it is interesting that this coincides with a eustatic sea level rise (Haq et al., 1987). It is suggested that this may have stabilized the subsurface fluid pressure regime and deactivated the fluid venting episode.

4.7. Conclusion

A conceptual model of a combination of vertical succession for fluid venting structures summarizes my hypothesis (fig. 4.8). The uppermost horizons representing the surface close to or at the palaeo-seabed, are viewed here as the positions where methane-related carbonates resulted from AOM or activity of chemosynthetic communities. Because of the vertical seismic resolution limits of this survey, and the close vertical separation between the PHAAs at the seabed and below, I interpret these to be expressed by a single reflection. The genetic relationship between all these fluid venting features is found through the geometric and morphologic analyses on seismic, coupled with the interpretation of amplitude variations. The conclusions for this study are:

1. The order of occurrence for methane-related carbonates, pockmarks or chimney structures within vertical successions, is dependent on the fluid flux of episodic vents.
2. PHAAs are always associated with fluid flow structures, e.g. pockmarks, chimney structures.
3. PHAAs occur within GHZS are often associated with seismic structures that are affected by pull-up effects.
4. PHAAs correspond to high impedance and material with high interval velocity.

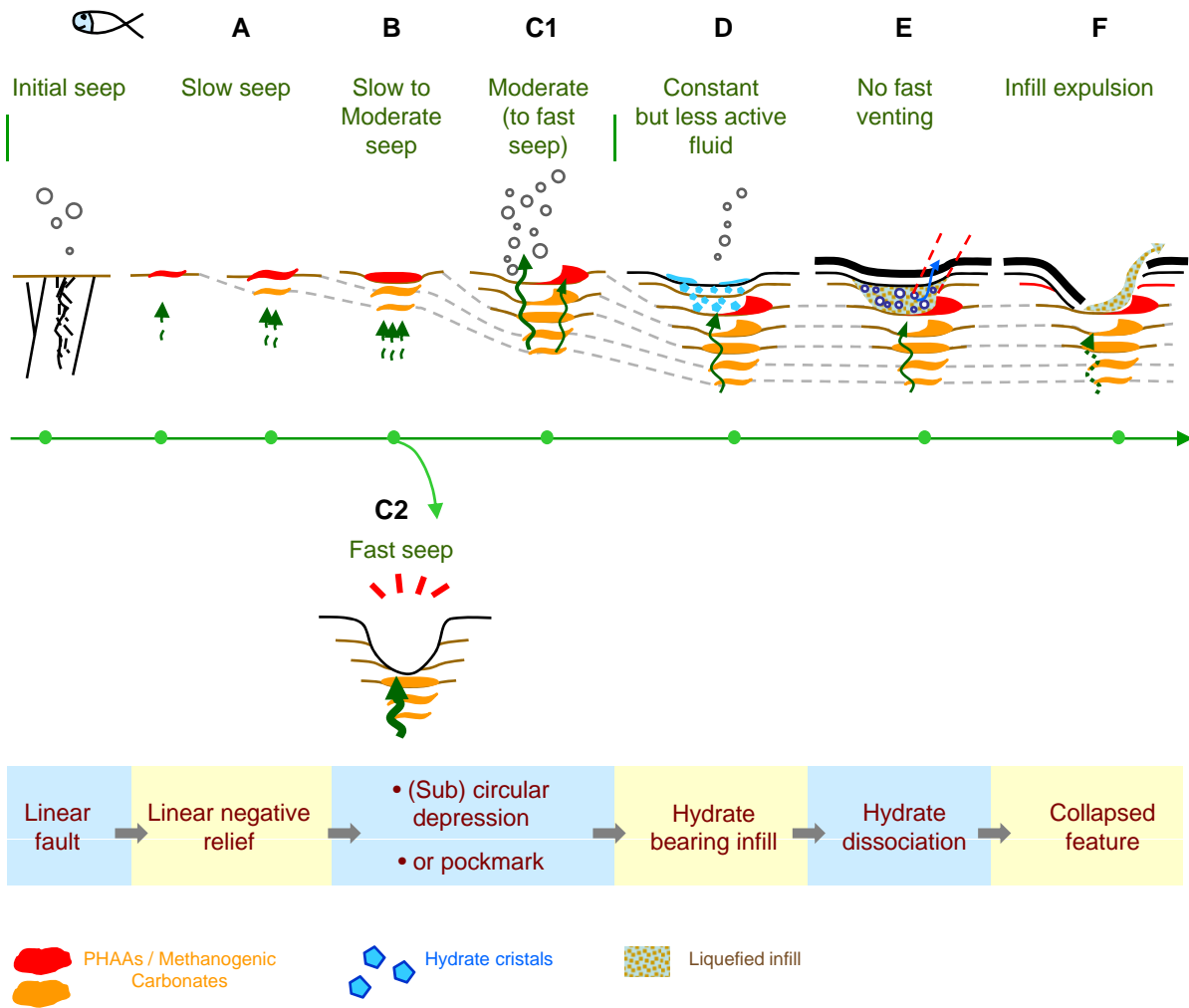


Figure 4.8. A hypothetical combined vertical succession for the evolution of different venting structures, depending on the dynamics of venting. a) Slow seeps at fault locations are characterized by linear PHAAs (interpreted carbonates). b) Slow to moderate seeps are characterized by sub-circular PHAAs. (C1) Moderated seeps often generate sub-circular like depressions with gently dipping base. (C2) Fast seeps are represented by circular crater or characterized by absences of PHAAs. (d) Constant but less active fluids interact with later sedimentation to form hydrate within sediment layers in GHSZ. Finally, (e) gas hydrate dissociations induce sediment liquefactions and (f) expulsion to create collapsed depressions.

5. PHAAs are isolated and very localized features.
 - a. They have two main forms, circular and linear, and are associated with shallow, linear or circular depressions of 5 to 7 ms TWT depth (2 m depth).
 - b. Their sizes vary from few tens to few hundred meters.
6. PHAAs are sited above tectonic faults and this implies that gas migrated from deeper sources.
7. Linear PHAAs follow always trends of polygonal faults or regional faults underneath.
8. PHAAs are interpreted here as methane-related carbonates and/or gas hydrate in an acoustically soft host lithology (hemipelagite).
9. Methane-related carbonates formed either at the seabed by chemosynthesis communities, or in the very shallow seabed by AOM, at the first tens meters below the sea floor in the SMTZ.
10. PHAAs indicate the location of where methane was released at the palaeo-seabed or within the shallow subsurface as methane-related carbonates (PHAAs) form within the SMTZ which is close to or at the sea bed.
11. The dynamics of fluid expulsion is expressed by the venting structures and by the geometries of associated PHAAs.
12. Linear PHAAs with associated linear shallow depressions are interpreted as slow seep.
13. Sub-circular PHAAs with associated sub-circular depressions are interpreted as moderate seep.
14. Sub-circular PHAAs within shallow depressions are potentially the stage before proceeding into pockmarks, during an overall increases of seepage rate.
15. PHAAs which terminate into pockmarks and craters, suggest the increase of methane flux over time and changes from moderate to a fast venting model (fig. 4.5).
16. Vertical successions of PHAAs recorded the local fluid leakages, by studying these successions, histories of fluid migration in basins can be reconstructed.
17. Polyphased pockmarks are characterized by several generations of PHAAs at their basements which are overlain by fluid expulsion craters with collapsing structures above. They are formed by the major steps as following:
 - a. Their formations are initiated by slow to moderate seepages which favor the formation of methane-related carbonates (PHAAs) at their basement.
 - b. Slow methane flux in GHSZ induces gas hydrate formation within sediment above the seep point.

- c. Methane disassociation occurred under overburden sediments, was likely liquefied the hosted sediment of gas hydrate.
- d. Liquefied sediment was expelled by overpressured methane gas under the overburden sediments and a collapsed crater was formed.

CHAPTER 5

**THE FORMATION OF TWO NEW TYPES OF
POCKMARKS - ADVANCING POCKMARKS
ARRAYS AND NESTED POCKMARKS: AN
INTERPLAY BETWEEN HYDROCARBON
LEAKAGE AND SLOPE SEDIMENTATION**

5.0. The formation of two new types of pockmarks - Advancing pockmarks arrays and Nested pockmarks: an interplay between hydrocarbon leakage and slope sedimentation

5.1. Abstract

Two new types of pockmark arrays have been observed aligning above turbidite channels in Offshore Angola. They are characterized by the geometry of their infill that shows a combination of draping and gentle downslope migration. They commonly show successive phases of infill and reactivation. In the first type, each new pockmark cross-cuts the downslope margin of the previous one; in the second, new pockmarks fit within the depression created by the previous episode of depressional infill without being truncated by further fluid eruptions, but with a slight downslope shift of the apex.

These pockmarks develop within the Pliocene-Quaternary interval affected by polygonal faults, and often align into trails above buried gas-bearing turbidite channel reservoirs or deep-seated extensional faults. Pockmarks of the first type (erosive reactivation) are named “advancing pockmarks”, those of the second type (non-erosive reactivation) are called “nested pockmarks”. The apices of advancing pockmark arrays are offset by several hundreds of meters downslope while those of nested pockmarks migrate by a few tens to a hundred of meters, rarely more. Migration of the infill of advancing pockmarks occurs systematically in the same direction over the evolution of the pockmark array. “Normal” or “common” vertically stacked pockmarks on the contrary show vertically stacked successive episodes of individual pockmark formation.

The genesis mechanism of these two new types of pockmarks has never been investigated. The objectives of this chapter are establishing what factors control the development of advancing pockmarks and nested pockmarks, and to define their implications on the interpretation of the hydrocarbon migration system.

In the area of interest, pockmarks occur in different geological settings. “Normal” pockmarks occur on relatively flat topography and above the troughs of sediment undulations

that are confined by a channel. On the other hand, “advancing” and “nested” pockmarks are located on inclined topographies above buried turbidite channels. The infills of the two new types of pockmark migrates downslope implying that local bottom currents and slopes play an important role in the migration process.

A bottom-simulating reflector (BSR) was observed above a turbidite channel and underlying the vertically stacked pockmark arrays on the study seismic dataset. The BSR is restricted to channel area and is interpreted to reflect the presence of gas hydrates. Chimneys are observed to emanate from high negative amplitude reflections which occur inside the basal craters of the pockmark arrays and are capped by the overlying BSR, thereby suggesting the presence of free gas at the location of the pockmarks along the channel. The spatial-distribution of these fluid-related structures strongly recommended that gas played a significant role in the origin of the pockmarks overlying channels.

To conclude, internal structures of advancing pockmarks and nested pockmarks indicate they are affected by interactions between hydrocarbon migrations, bottom currents and topographies. The intensity of hydrocarbon leakage from the plumbing system underneath over time can be reconstructed by studying the geometric evolution of pockmarks, and their associated chimneys and methane-related carbonates.

5.2. Introduction

Pockmarks have been interpreted as consequences of gas eruptions (Josenhans et al., 1978; Hovland, 1981; Judd, 1981) since they were discovered by McLean & King (1970).

Classic examples of present day or buried pockmarks in literature often appear as simple v-shaped craters with a simple draping or aggrading infill (c.f. Hovland and Judd, 1989; Kelley et al., 1994; Judd and Hovland, 2007; Jobe et al., 2011). A high resolution, three-dimensional seismic survey acquired in 2006 offshore Angola in the Lower Congo Basin illustrates in detail a series of pockmarks with complex internal organisation. These pockmarks migrate laterally during their development, with their infill showing progressive downslope migration along the axis of underlying turbidite channels. This phenomenon has rarely been described. In contrast, most pockmark successions described so far show vertical stacking, commonly with variable diameter or depth, but in pure aggradation. In this configuration, the apices of successive pockmarks are stacked vertically; they have been interpreted to record a succession of fluid eruptions above the same vertical position over time

(c.f. Hovland, 1981, Cifçi et al., 2003; Moss and Cartwright, 2010a, b). Pockmarks whose infill or reactivation episodes progressively migrating downslope are interesting for fluid flow studies, as they may have different significations as regards fluid flow. Their restricted geological distribution (e.g. confined above buried channels on the slope) could provide wider information on fluid migration on inclined topography and its interaction with underlying plumbing systems.

Pockmarks aligned above buried channels have previously been reported by Haskell et al. (1997) in the West African slope; by Davies (2003) who observed a series of conical fluidization structures associated with a subsurface channel in the Niger Delta; Gay et al. (2002; 2003) investigated a sinuous pockmark belt above a buried turbidite channel in the Lower Congo Basin; Cauquil et al. (2003) reported pockmarks associated with a meandering buried channel in Nigeria; Cotterill et al. (2005) reported pockmark trails in the Gulf of Guinea; Pilcher and Argent (2007) studied linear pockmark trains located above listric slump faults, initiated on the steepest slopes of the West African continental margin; Jobe et al. (2011) focused on the pockmarks that developed above submarine canyons in the Rio Muni Basin of West Africa. Among these authors, Gay et al. (2002; 2003) and Cauquil et al. (2003) showed pockmarks following the geometry of sinuous to meandering underlying channels.

However, none of these pockmarks clearly records obvious multi-phased formation in seismic, apart from those shown by Heinio and Davies (2007); these authors described aligned depressions with a non-hydrocarbon origin which contained laterally migrating infill sequences. They proposed that the migrating infill sequences were induced by the activity of bottom currents (Heinio and Davies, 2007).

The explanation proposed for the formation of pockmarks aligned above channels is that they are caused by lateral fluid drainage within the underlying turbidite channel (Gay et al., 2002; 2003; Cauquil et al., 2003) and subsequent escape of overpressured pore fluids upward along the margins of the channels (cf. Davies, 2003; Pilcher and Argent, 2007; Jobe et al., 2011). While Gay et al. (2002; 2003) argued that the principal cause of the pore pressure excess within the channel is an increased fluid supply from deeper reservoirs.

In this chapter my objective is to report and interpret this new type of pockmarks. My aim to find out the relationship between fluid leakage and infill processes in relation with the depositional setting and its morphology. Conceptual models for the formation of advancing pockmarks arrays and nested pockmarks are proposed in this study, based on the geometries that shown on seismic sections and 3D horizons.

5.3. Seismic data and methodology

5.3.1. Seismic data

The data volume used in this chapter study consists of one main seismic survey (1310 km²) and a higher resolution one (530 km²) in the Lower Congo basin offshore Angola. Their locations and data details are given in Chapter 2, Methodology.

5.3.2. Methodology

Pockmarks trail 1 is covered by both seismic surveys; the detailed mapping of individual reflection of pockmark infill has been carried out on the higher resolution survey. Pockmarks trail 2 is covered by the main survey only. Individual horizons of pockmarks infill in trail 1 have been mapped manually and examined under a 3D viewer. In pockmarks trail 2, the geometry of the infill of the pockmarks can be well illustrated on seismic sections but the layers can not be distinguished or mapped precisely in 3 dimensions as those of pockmarks trail 1 due to lower seismic resolution. This difference in resolution however does not affect the geometrical distinction of different types of pockmarks in the two trails, as the geometric differences are obvious. Comparison of the seismic character and geometries of some pockmarks and other type of venting structures has been carried out where they are covered by both surveys. The result of this comparison is that, apart from vertical resolution, no geometric differences were found for the same fluid venting structures covered by both surveys. In addition, pockmarks in both pockmarks trails and other fluid venting structures have been examined in 360° on seismic, even though the 3D horizon of pockmark infills of pockmark trail 2 cannot be completed.

Bathymetric contours and dip attribute have been calculated for visualizing the topography of horizons of interest.

In order to distinguish all high amplitude facies and to target the negative high amplitude anomalies, which are the expression of potential free gas accumulations (Coffeen, 1986), phase extraction from the maximum energy envelope of reflections with maximum strength (Partyka, 1998) have been calculated (see Chapter 2 Methodology).

5.4. The local structure and stratigraphy

The study area is located across the limit between the extensional zone and transitional domains (fig. 3.3, Chapter 3). The water depth ranges from 810 m to 1662 m. The study area is cut by a major growth fault, which defines a footwall domain and a hanging wall domain in the study area (fig. 3.5a, Chapter 3; fig. 5.1). The growth fault was active during the late Miocene and is sealed by Pliocene deposits. The footwall domain has been deformed extensively by normal faults (fig. 3.5, Chapter 3), while the hanging wall has a rollover morphology (fig. 3.5a, Chapter 3). Two diapirs rose along the growth fault (fig. 3.5, Chapter 3). The main diapir (D1) located in the middle part of the growth fault, and the other one (D2) located in the SE side. A more detailed geological setting is given in Chapter 3.

The interval of interest where fluid venting structures and pockmarks of interest occur is comprised between top middle Miocene and the seabed. The Neogene-Quaternary sequence in this survey is dominated by hemipelagic sediments (Broucke et al., 2004; Total internal report, Vignau et al., 2000). Turbidite channel complexes occur within the well-bedded hemipelagic units (Broucke et al., 2004; Total internal report, Vignau et al., 2000). Two turbidite channel complexes cross the area of interest in the Upper Miocene interval, they locate in 60 meter or directly below the pockmarks of interest. These channels are oriented NE-SW and cross the growth fault. In this study, the side of channel complexes in the upper part of the hanging wall domain is referred as the upstream side, while the side on the hanging wall slope is referred as the downstream side. Gravity-driven salt tectonics heavily deformed the Upper Cretaceous and Cenozoic strata (Liro and Dawson, 2000; Lavier et al., 2001); as a result the Miocene turbidite channel reservoirs and silty, clay-dominated seals were intersected by salt-related faults.

Polygonal faults were observed in two tiers, one within the Upper Miocene, and the other covering the whole Pliocene interval (fig. 3.3, Chapter 3). The studied pockmarks mainly occur within the latter.

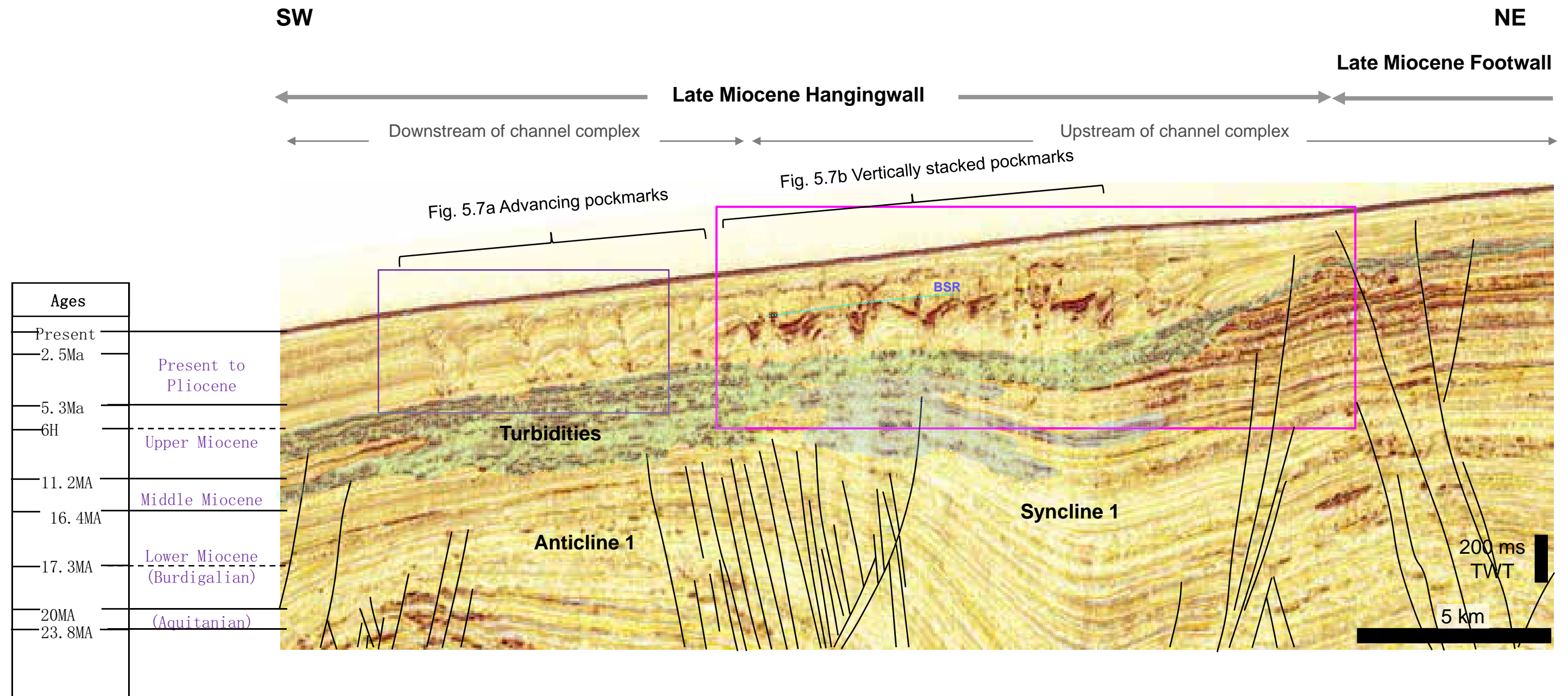


Figure 5.1. Evolution of palaeo channel complex across the different structural domains of the study area. The upstream side of the channel complex (opaque green color) is defined as the segment located above syncline 1 in the upper part of the hanging wall domain of the major growth fault. The lower part of channel complex located above the anticline and on the slope to the SW is defined as the downstream part. See location in fig. 5.5.

5.5. Results and seismic interpretation

Three main types of pockmarks have been observed in this survey. They have been classified according to the organisation of their infill and the evolution of their apexes within the arrays. The three types of pockmarks are: 1) pockmarks with draping infill layers that stack up vertically on seismic sections and are laterally continuous in far field (fig. 5.2), 2) pockmarks with infill sequences show downslope shifting over time on seismic sections, the infill layers are laterally continuous in the far field but are truncated intermittently by subsequent craters within the arrays (fig. 5.3), 3) pockmarks with infill sequences grade over of the basal craters (i.e. do not extend laterally into the far field) and slight migrate downslope (fig. 5.4). The first type of pockmarks is the most common and has already been widely investigated by other researchers (c.f. Hovland, 1981; Cifçi et al., 2003; Moss and Cartwright 2010a), so we are not going to discuss it in this study. The two other types of pockmarks have never been reported in literature, nor has any formation process been proposed so far for them. Thus, in the section below I examine in detail the structures and morphology of the pockmark arrays that show oblique or prograding migration on seismic sections. The mechanism of the pockmark formations will be discussed in further sections.

5.5.1. Definition and structure of ‘Advancing pockmark arrays’

An “advancing pockmark array” is defined as a stack of individual pockmarks that progressively migrating downslope, with younger pockmarks truncating both the downstream margin of older pockmarks and their infill sequences (fig. 5.3a).

In the study area, they are observed in the Pliocene hemipelagic interval. The horizontal distance of migration of the individual arrays ranges from 60 to 650 m. The infill of individual pockmarks in the arrays has a dominantly draping character, in continuity with the far field interval: it is thus identified as dominated by hemipelagites (Sangree et al., 1978). As shown on fig. 5.3.a, it also shows some downslope migration (fig. 5.3.a), indicating an additional depositional process to pure settling from suspension. The diameters of individual pockmark craters generally vary from 300 to 600 meters (fig. 5.3b), and their depths are less than 50 ms TWT. The height of advancing pockmarks arrays in the study survey is ca. 150 meters on average; the arrays are often limited by the top and base boundaries of the polygonal fault tier (fig. 5.3a). The upslope part of individual pockmarks is draped in

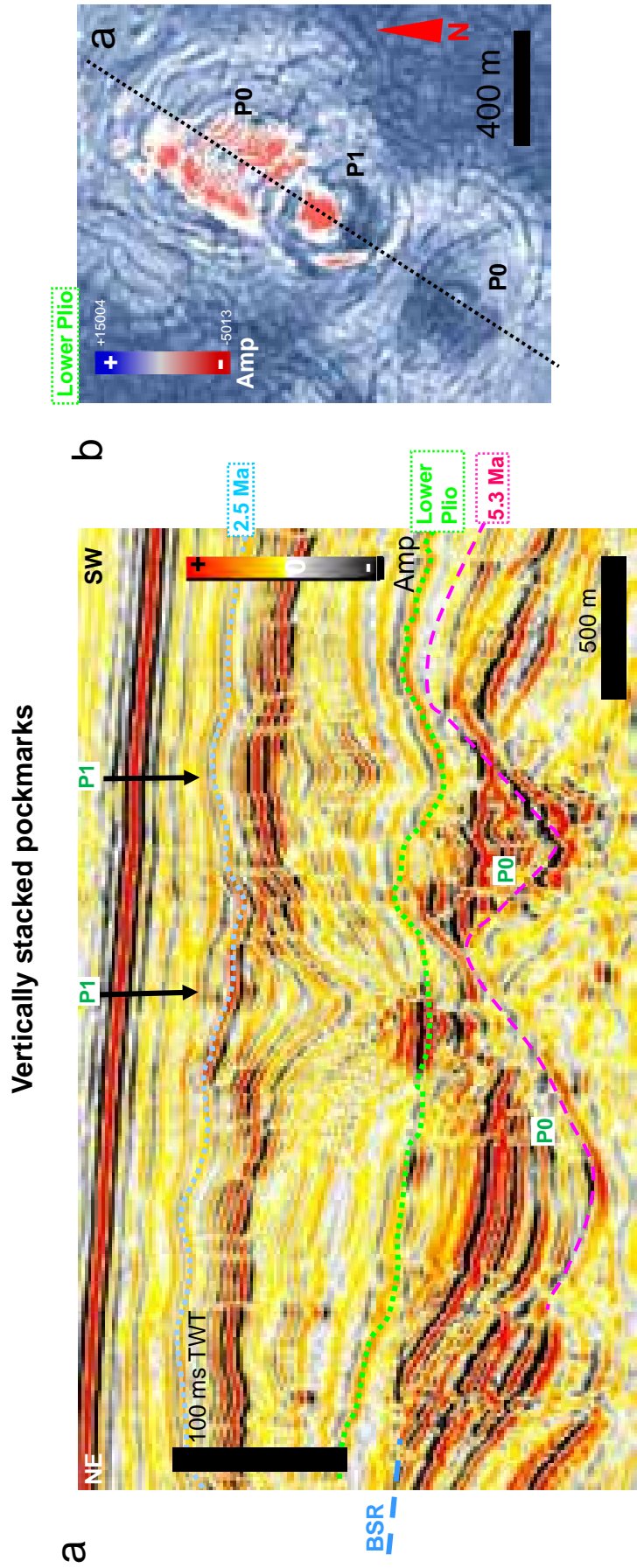


Figure 5.2. Vertically stacked pockmark arrays. a) The two arrays (P1) occur above a basal/earliest pockmark (P0) with negative high amplitude. b) Amplitude map of Lower Pliocene across the base of vertically stacked pockmark (P1) and the top of earliest pockmarks (P0).

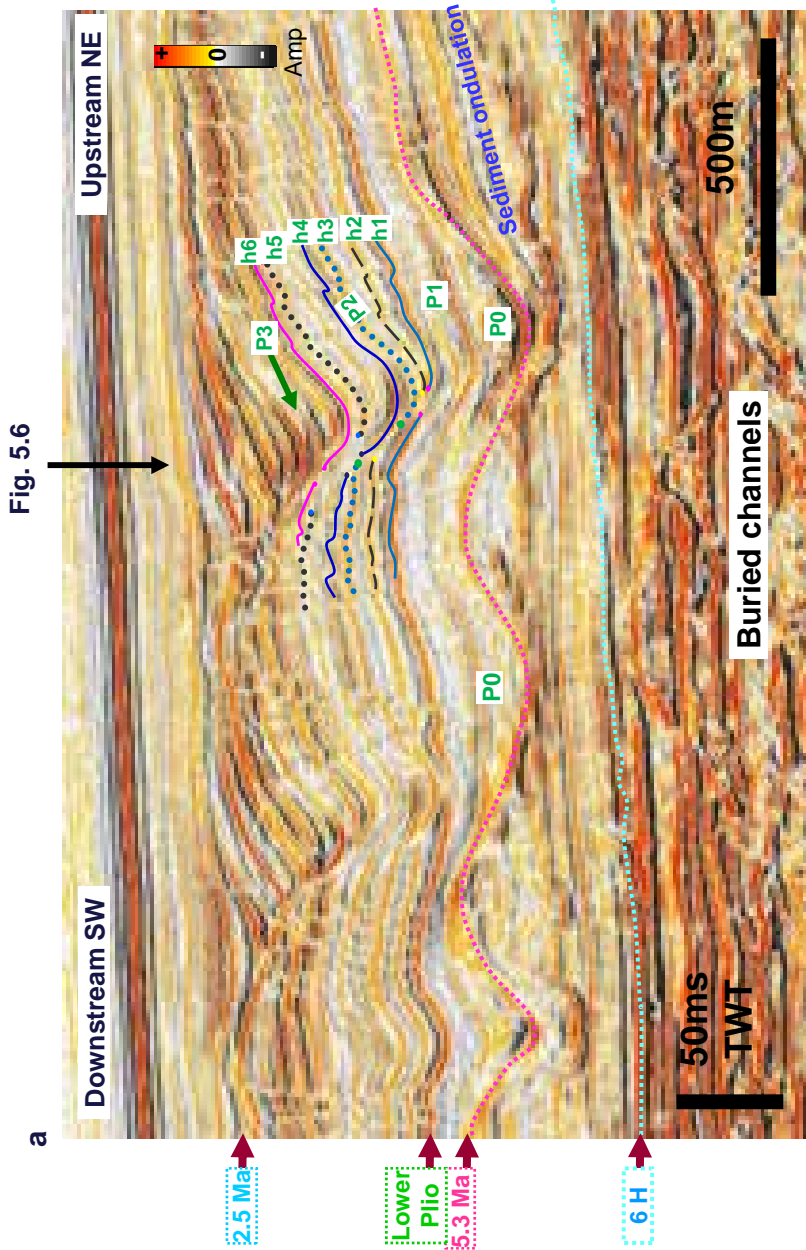


Fig. 5.6

Figure. 5.3. Advancing pockmark arrays. a) Section view of advancing pockmark arrays, which occur above the earliest pockmarks P0, P1 and channel complex 1. Individual layers within the arrays that have been mapped were labelled as "h" followed by a number. Their 3D map views are shown in fig. 5.6. b) Illuminated TWT map of horizon 5.3Ma showing pockmark trail 1; location of the advancing pockmark array mapped on fig. 5.6 is indicated by a red arrow. Red dots indicate the centre of each crater.

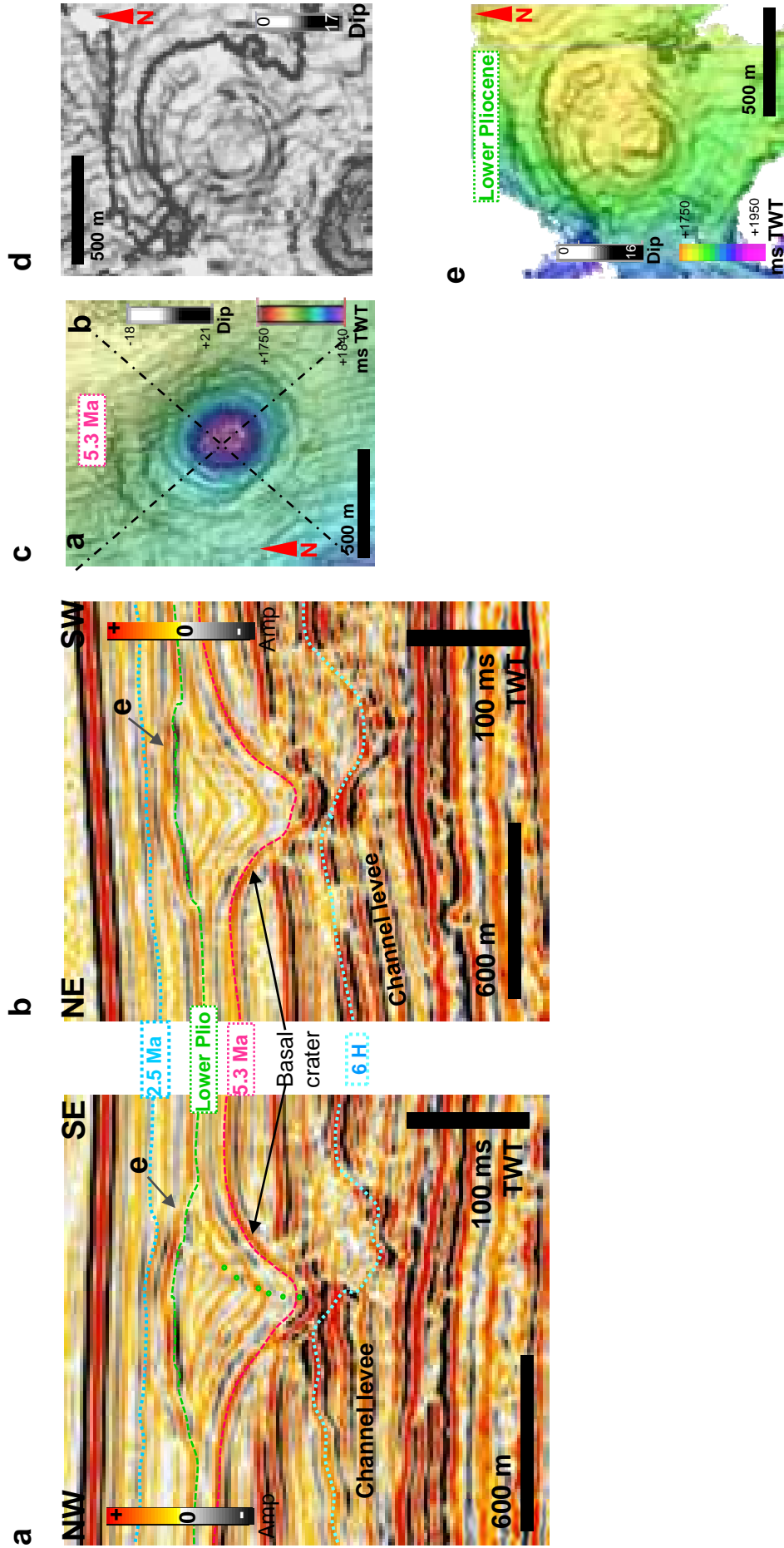


Figure 5.4. Nested pockmark. a) and b) are arbitrary lines along and across major axis of the pockmark. c) Two-way time map of the initial crater (basal pockmark) at 5.3Ma. d) Dip map of the top of a nested pockmark infill showing a combination of radial and concentric patterns. e) Two-way time map of the convex positive high amplitude reflection at the top of the pockmark.

continuity with far field reflections, while their downslope sidewall is interrupted along the trend of the turbidite channels underneath (fig. 5.3a, b).

Advancing pockmark arrays are principally found above turbidite channels and line up with their axis, and form pockmark trails (fig. 5.3b; pockmark trails 1 and 2 above channel complexes 1 and 2, in fig. 5.5a and 5b). Two pockmark trails are observed in this study area and are described in section 5.5.6.

Two main features within advancing pockmarks arrays have been observed through detailed horizon mapping. These are 1) the downslope shift of the apex of the infill sequences; 2) the downslope migration of successive pockmark craters.

1) Downslope migration of infill sequence: The seismic section along the axis of a palaeo channel complex on Figure 5.3a illustrates the infill sequence of two pockmarks advancing in the downslope direction (e.g. h1-3; fig. 5.3a; fig. 5.6). Reflection discontinuities observed on the downstream sidewall of pockmark arrays exhibit a horse-shoe shape in plan view (h1-3; fig. 5.6) and are lined up along the strike of buried channels. The tips of these disrupted reflections (are indicated by colour points on fig. 5.6) onlap against the inclined downstream sidewall, whilst reflections surround the pockmark array onlap against the secondary or subsequent craters that truncated the older infill in the downstream side.

These inclined onlap terminations against the inclined surface of the downstream pockmark sidewall, form what appears to be a migrating or advancing pockmark (fig. 5.3a). However, this is simply the influence of pockmark slope and locally depressed bathymetry (pockmark crater) on sediment deposition within the pockmark. Distinctively the upstream sidewalls are continuous and show parallel stratal geometries within the array (fig. 5.3a).

2) Lateral migration of pockmark craters: pockmark development in the arrays is multi-phased, i.e. new and younger pockmarks (e.g. p3 in fig. 5.3a and fig. 5.6) intermittently develop on or above the downslope margin of the previous one (h4; fig. 5.6), thereby truncating the previous infill sequence. This means that the centre of the new pockmark erodes the downslope flank of preceding infill sequence (h4 in fig. 5.3a and fig. 5.6; see also arrays in left hand side in fig. 5.3a). Towards the top of the arrays, these younger pockmarks become shallower while their apical angles increase. The accommodation provided by these late craters thus progressively reduces upward, until the depressions become almost filled and are sealed by Quaternary sediments.

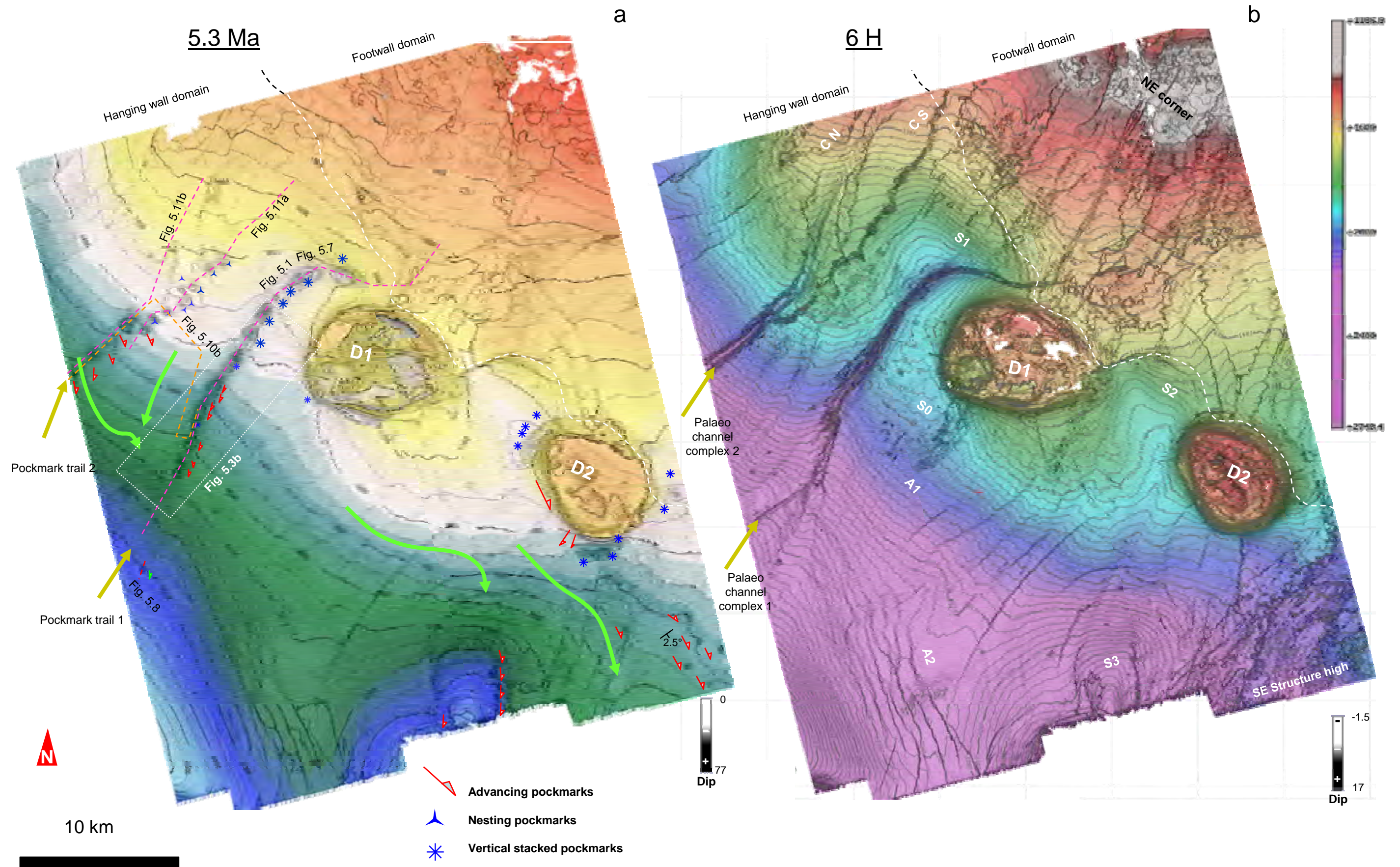


Figure 5.5. Structural maps showing the main geological features of the study area. a) Key horizon 5.3 Ma shows two pockmark trails and the distribution of different types of pockmarks. Two-way time map is overlain by semi-transparent dip map. The direction of pockmark infill migration is indicated by symbols on this map. b) Two-way time map of horizon of 6 H with dip overlain. It shows the two channel complexes underlying the two pockmark trails. A: Anticline; D: Diapir; S: Syncline; C N: North Channel; C S: South Channel.

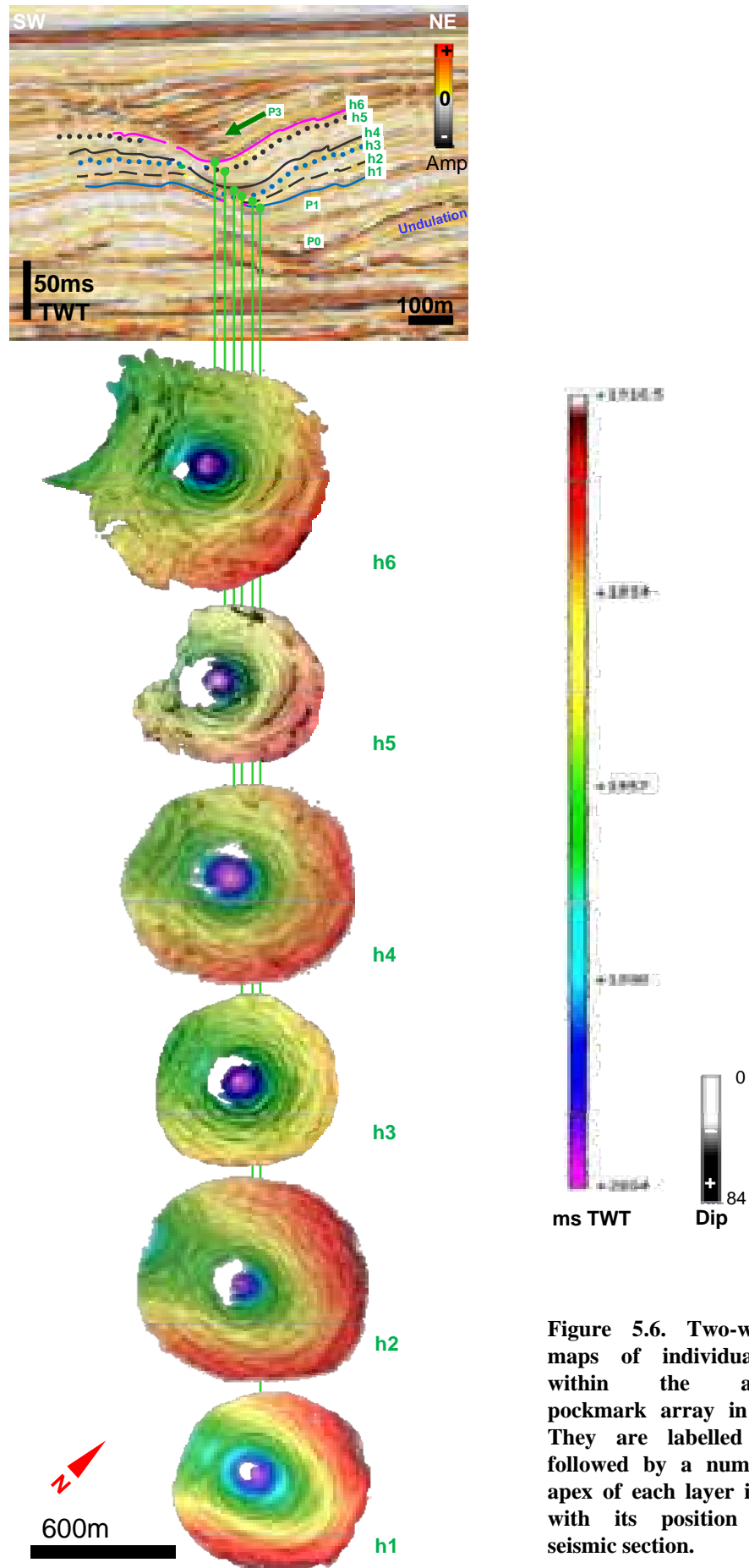


Figure 5.6. Two-way time maps of individual layers within the advancing pockmark array in fig. 5.3. They are labelled as "h" followed by a number. The apex of each layer is aligned with its position on the seismic section.

These younger pockmarks are likely represented different episode of fluid expulsions, so hereby they are termed “reactivation craters” or “reactivation pockmarks”.

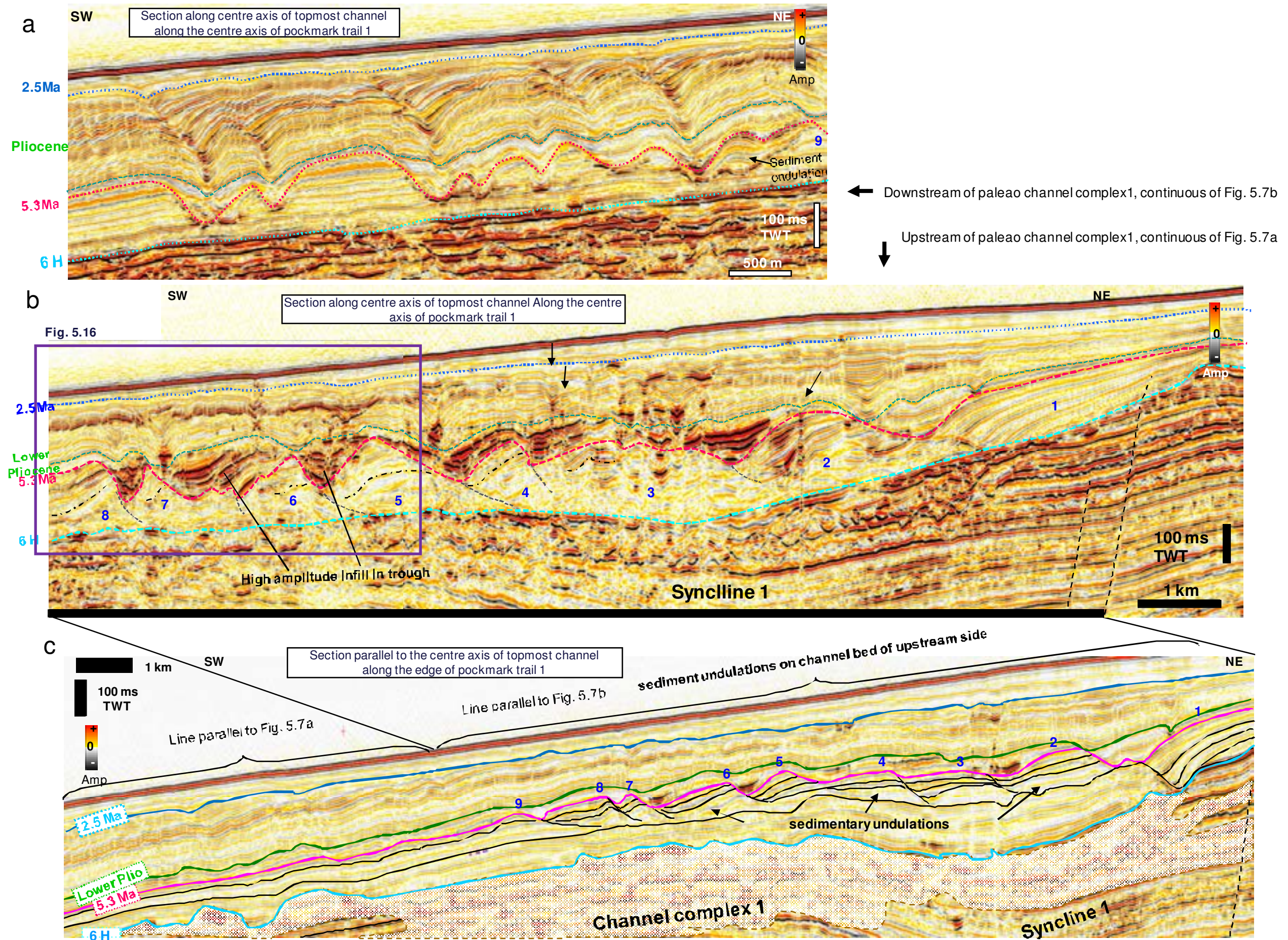
5.5.1.1. Basal craters / earliest pockmarks of the arrays

Advancing pockmarks arrays and vertically stacked pockmarks arrays have been observed to develop above a basal circular crater (P0; fig. 5.3a). The two types of pockmark arrays are observed to occur either above the centre of the basal craters (in right, in fig. 5.3a) or above whose downslope margin (in left, in fig. 5.3a). These basal craters are interpreted as the earliest pockmarks underneath the pockmark arrays. They were often bigger than the individual ones within the pockmark arrays above. These earliest pockmarks have diameters ranging from 300 to more than 1000 meters with depths varying from 50 to 100 ms TWT. They occur in an interval of 30 – 100 ms TWT above the palaeo channel surfaces (fig. 5.7a, b), and are organised as a chain of depressions above buried channels (fig. 5.3b).

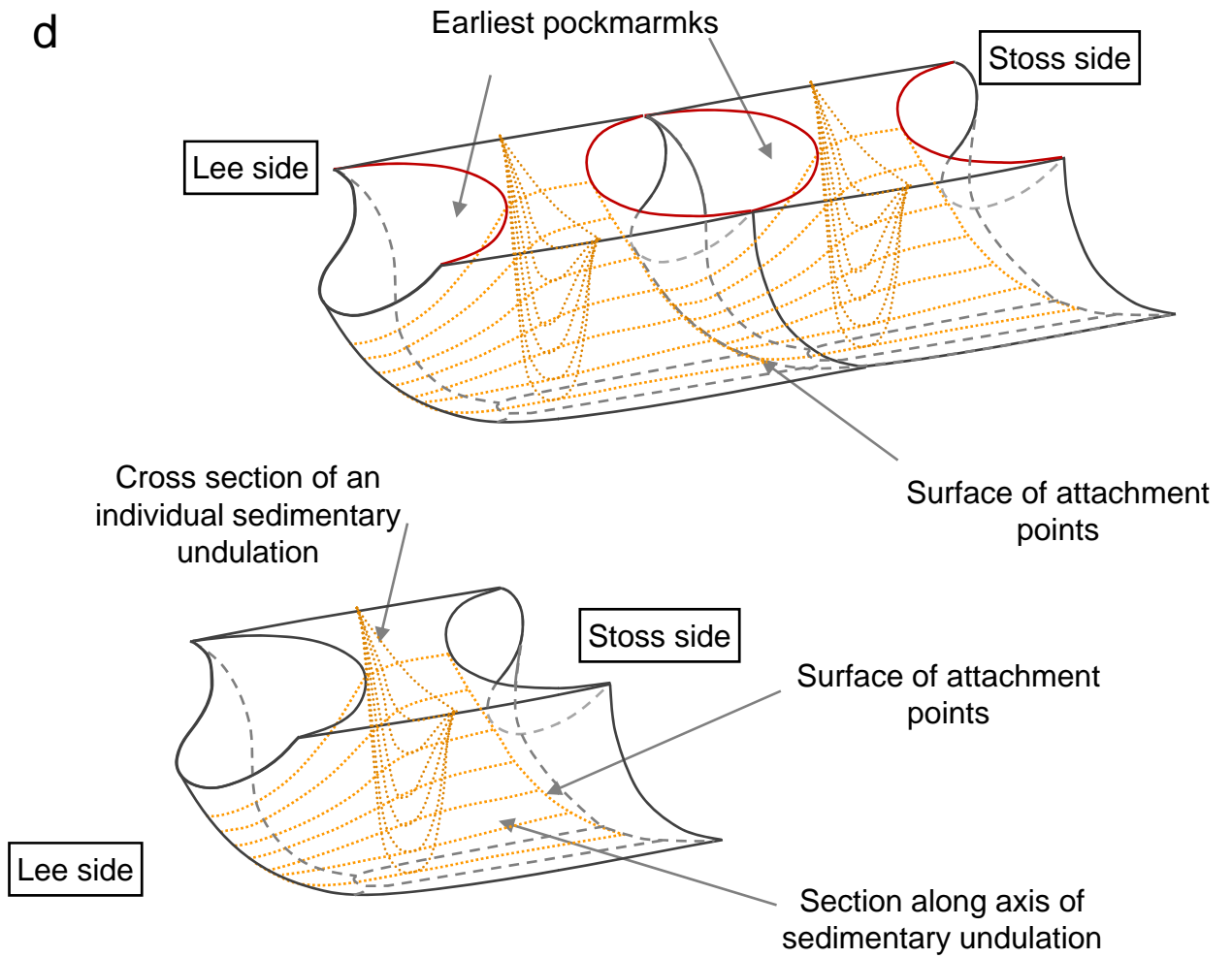
These earliest pockmarks are principally circular in plan view (fig. 5.3b), some of them can connect with the neighbour ones and merge to form elongated shapes (red dots in fig. 5.3b). Some individual craters which are originally elongated can be observed above the crest of sediment undulations in the upstream part of the underlying channel (fig. 5.7b). The earliest pockmarks truncated the lee and stoss side of the undulation (e.g. between undulation 5 and 6 in fig. 5.7b), and sediments in lee sides were better conserved in some cases (fig. 5.7c, d). Infill inside the earliest pockmarks are parallel and overlapped against the sidewalls i.e. lee and stoss sides of the undulations (fig. 5.3a; fig. 5.7a, b).

Another generation of earliest pockmark can be found in some case within these overlapped infill (e.g. P1 in fig. 5.3a). These craters are likely provided an irregular topography for initiation of advancing pockmarks arrays, and are thus interpreted as the basement of pockmarks arrays. In addition, the vertically stacked pockmarks that occur above the upstream location of this channel complex, their basal craters are likely developed above the surface of attachment points of the sediment undulations (fig. 5.7b, c, d). The infill of these basal craters is expressed by high amplitude reflections.

Figure 5.7. Pockmark trail 1 above channel complex 1. This pockmark trail is composed by vertically stacked pockmark arrays and advancing pockmark arrays lined up along the axis of the underlying channel. a) Advancing pockmark trail in the downstream side of this channel complex. b) Vertically stacked pockmarks arrays above sedimentary undulations in the upstream side of the channel complex. Notice that the major growth faults are located in the right hand side of this profile. Black arrows indicate high-amplitude bright spot chimneys; each undulation is labelled with a number. c) Seismic section parallel to the axis of the channel complex, intersecting the edge of pockmark trail 1; it shows sedimentary undulations above the buried channel. The numbers label each undulation, like in 5.7.b above. d) Block diagrams showing the geometry of individual sedimentary undulations (not scaled).



d



5.5.1.2. Stacked advancing pockmark arrays

Stacked advancing pockmark arrays, each developing above the downstream margin of the previous generation have been observed within the Neogene-Quaternary interval (fig. 5.8a). These successions of pockmarks arrays were not associated with a basal crater at their base. The depressional bathymetry of infill within the topmost arrays can still be observed on the present day seabed, and show a shallow small depression (fig. 5.8b). The horizontal distance between the bottom apexes of the topmost crater, and the one of the lowest arrays is illustrated on the seabed dip map and the amplitude map of 5.3Ma in Figure 5.8b and c.

5.5.2. Definition of “Nested pockmarks”

Another type of pockmarks is observed in the interval between *the top Miocene and intra-lower Pliocene*, (fig. 5.4). These pockmarks are characterised by a series of conical stacked infill layers that do not extend in the far field (fig. 5.4a, b, c), and the successive apexes of their infill prograde slightly downslope by a distance of 40 – 160 m. On seismic sections, the volumes of the crater infill decay up sequence and toward up the top of arrays. The tops and bottoms of each unit are defined and are limited by the previous infill topographies. The result of this mode of deposition in the pockmark crater means multi-layered infill sequences appear as concentric layers in plan view (fig. 5.4d, e). The structure of this type of pockmark arrays can be thus compared to nested bowl sets, and we term it ‘nested pockmark’ here. In this study area, the diameters of this type of pockmark craters vary from > 300 to 600 meters, with depths ranging from 90 to 150 ms TWT. The initial craters of this type of pockmarks are rather elongate (fig. 5.9a) with their long axis parallel to bathymetry contours (fig. 5.9b).

Like advancing pockmarks arrays, pockmarks of this type are aligned along a channel complex underneath (fig. 5.10; fig. 5.11, pockmark trail 2 and channel complex 2 in fig. 5.5a and b). The main difference between this type of pockmarks arrays and advancing pockmark arrays is that they show only one episode of eruptional event.

Infill reflections inside the initial craters of nested pockmarks prograde from the upstream margin of the underneath crater and migrate gently toward the downstream sidewall (fig. 5.4a; fig. 5.10a). They show updip terminations which onlap onto the margin or sidewall of the underneath depression (fig. 5.4a; fig. 5.10a). The uppermost part of the infill sequences

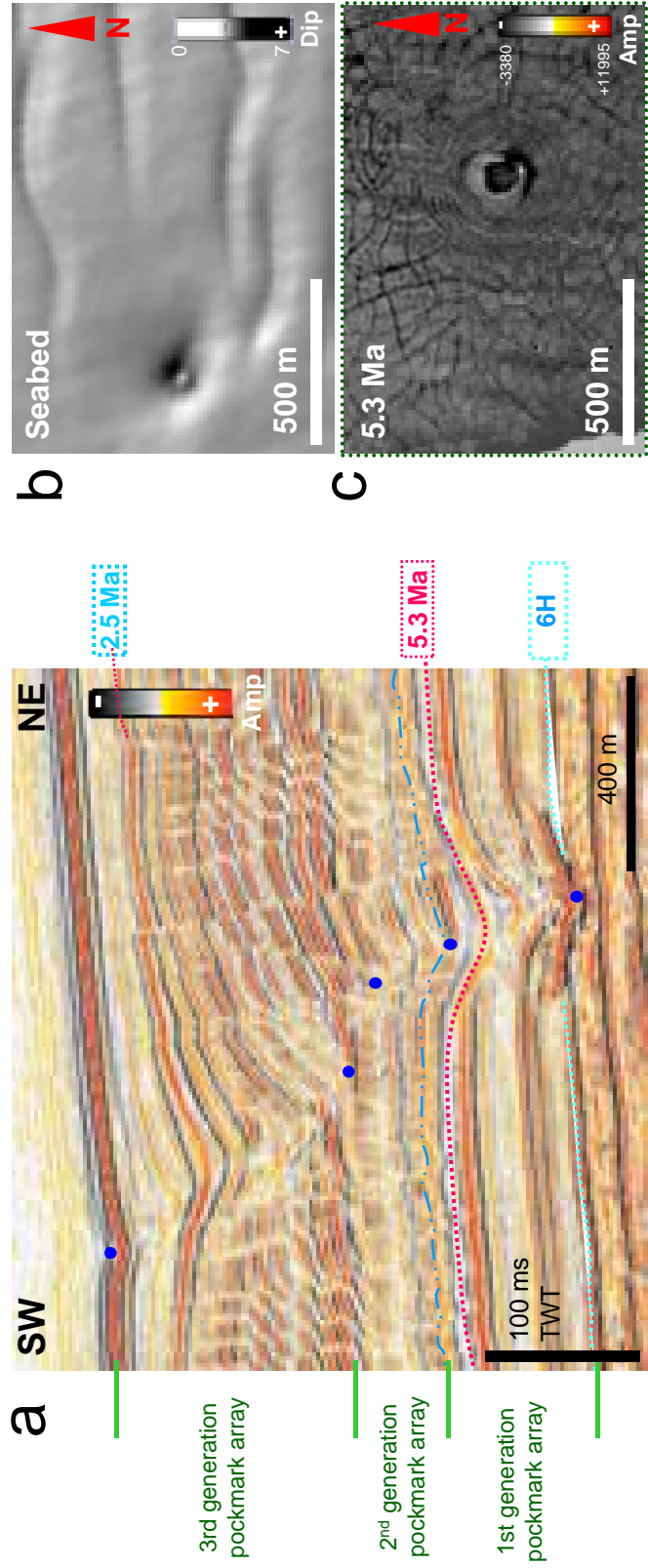
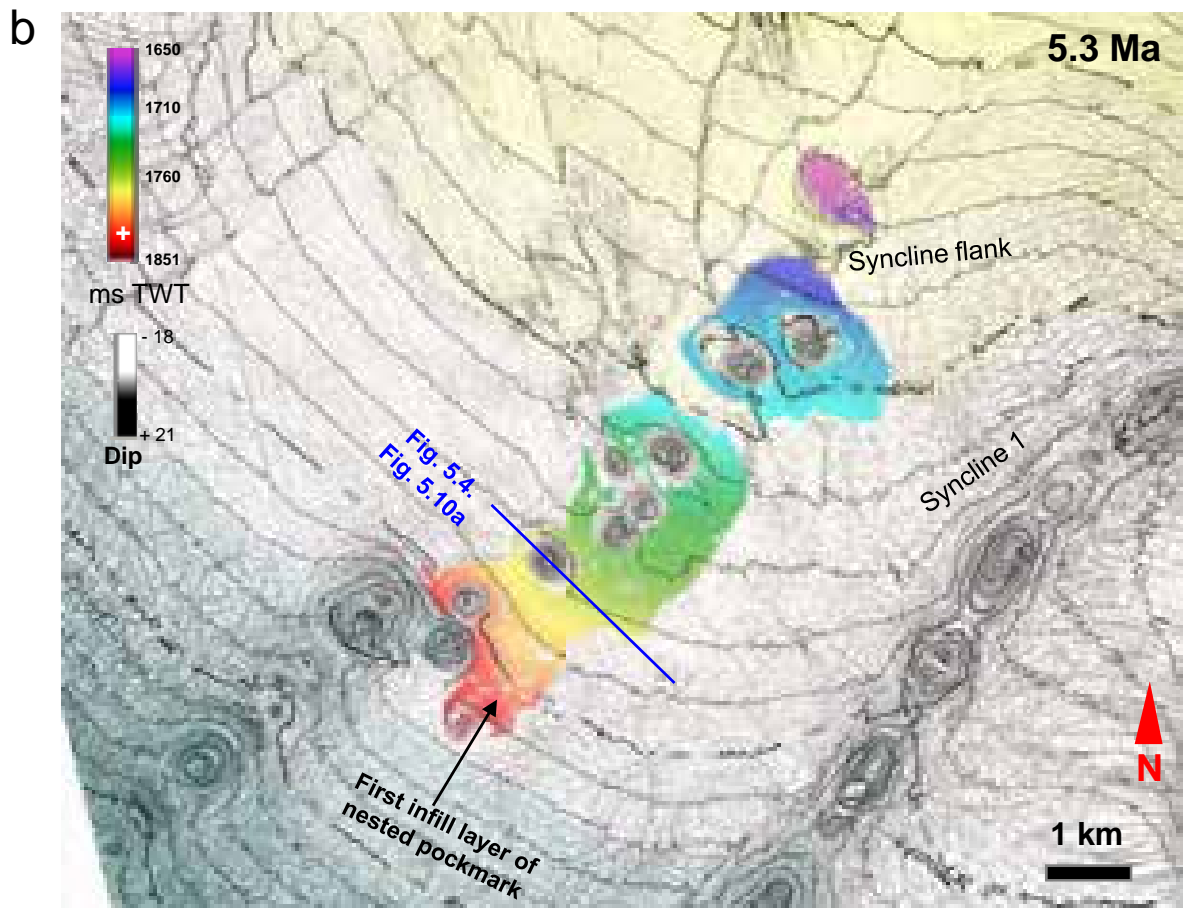
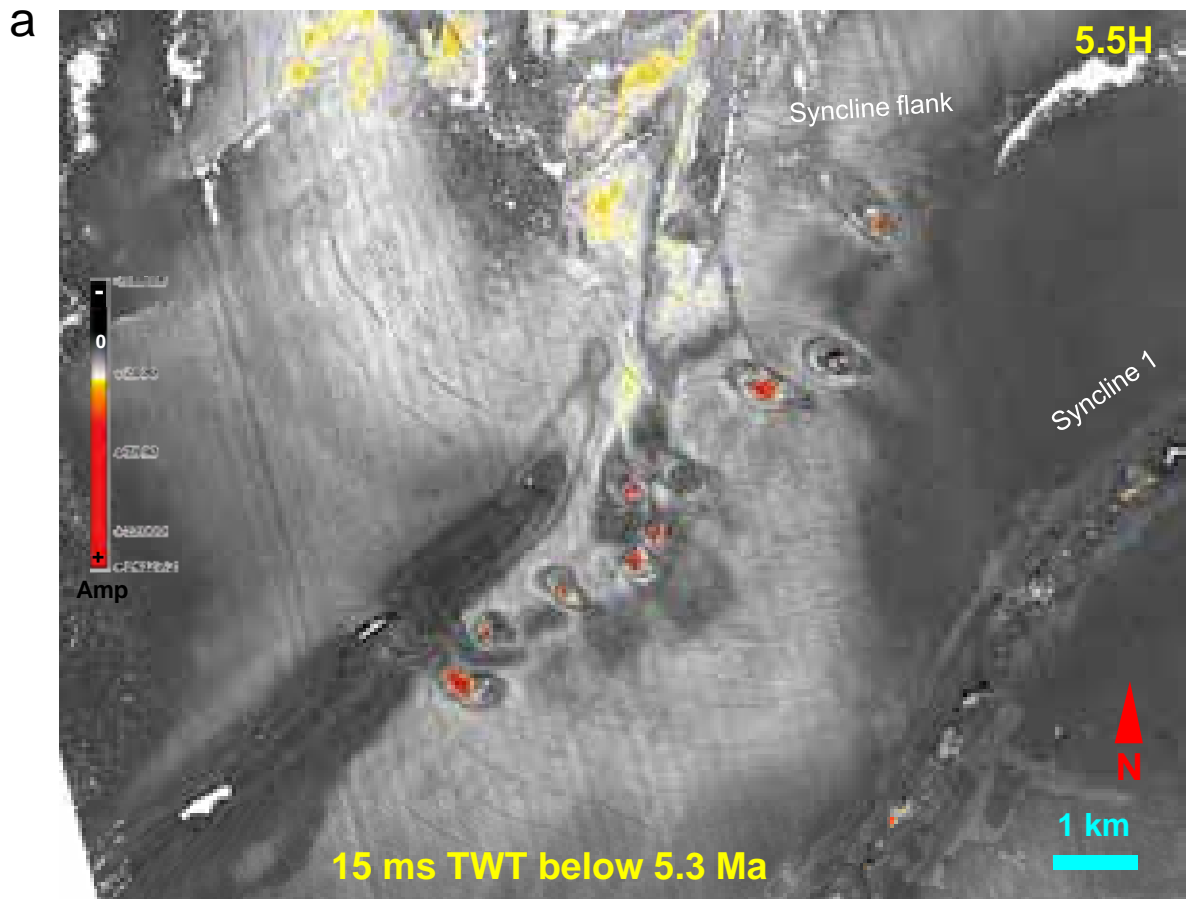


Figure 5.8. Advancing pockmark array composed by three smaller-scale arrays. a) Section along the direction of infill migrations; blue dots indicate the lowest and topmost apexes of each secondary array. b) Seabed dip map showing that the topmost depression of the array is expressed by a small shallow depression at the present day seabed. c) Amplitude map of 5.3 Ma showing the topmost depression in the lowest array.

Figure 5.9. Elongate morphology of the basal craters of nested pockmarks with major axis parallel to bathymetric contours on the flanks of the syncline. a) Amplitude map of horizon 5.5 H superposed with its bathymetric contours. This horizon is located between the top surface of channel complex 2 and horizon 5.3 Ma which is truncated by nested pockmarks. It runs across the middle level of nested pockmarks and shows the elongate geometry of the basal craters. b) Superposition of two-way time map and dip map of 5.3 Ma (grey to pale yellow background), and the first infill layer of nested pockmarks. This infill layer shows a preferential orientation toward the syncline. For the stratigraphic location of this layer see fig. 5.11a.



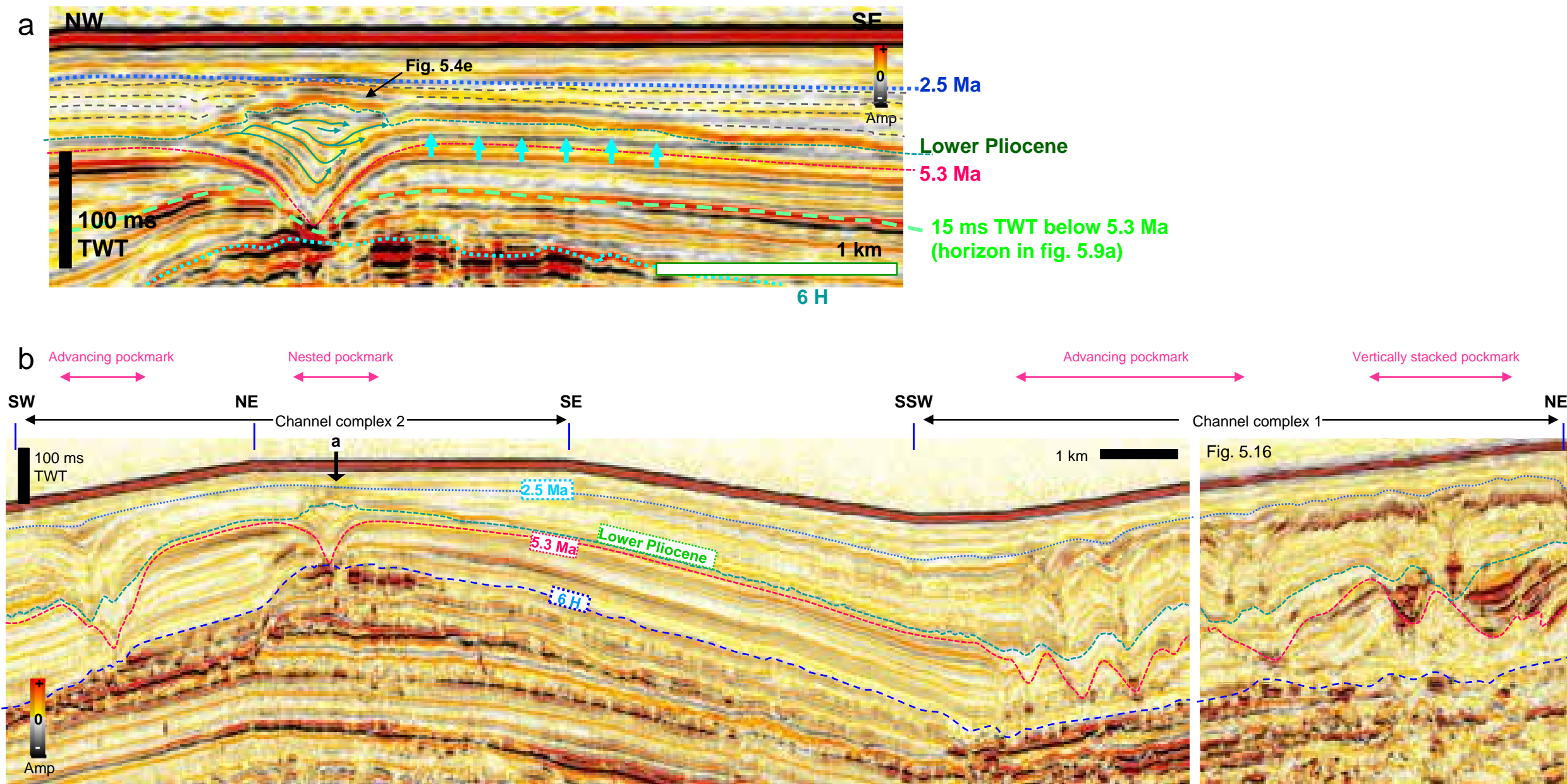
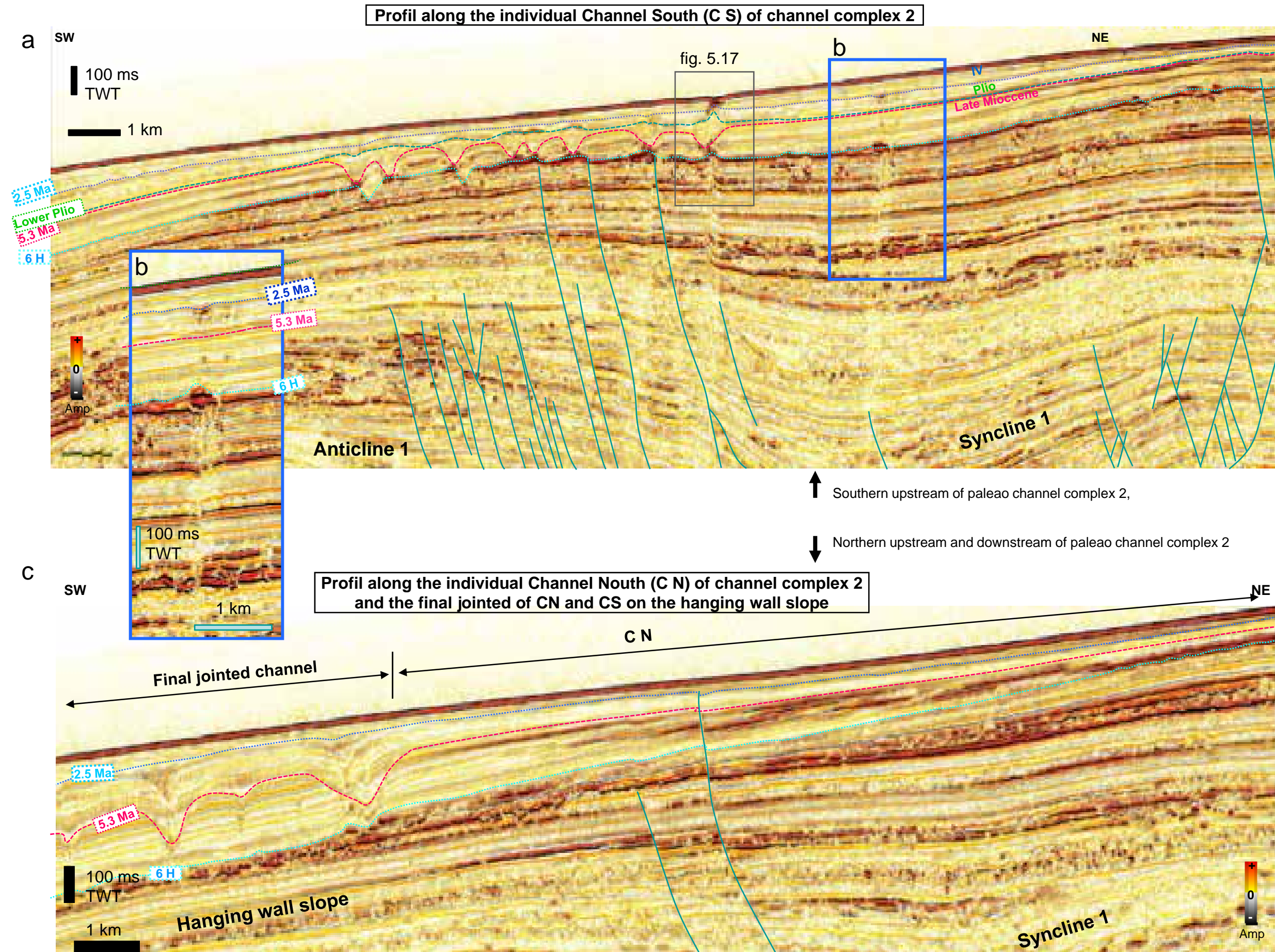


Figure 5.10. Vertical organisation and age of nested pockmark infill. a) Arbitrary line across the pockmark of fig. 5.4, oblique to the one that is already figured. The first infill layer extends in far field on the syncline flank, towards syncline 1. b) Correlation between the infill of basal craters (earliest pockmarks) underneath nested pockmarks (left) and advancing pockmark arrays (right and extreme left).

Figure 5.11. Pockmark trail 2 above channel complex 2, composed by nested pockmarks in the upstream side and advancing pockmark arrays in the downstream side. Channel complex 2 results from the convergence of two individual channels, the north channel (CN) and the south channel (CS). a) Nested pockmarks are located above CN and above tectonic (compensation) faults at anticline 1. b) Chimney structure expressed by vertically stacked seismic amplitude anomalies on the far upstream side of the channel complex. c) Advancing pockmark arrays above CS on hanging wall slope.



(the trough between the lee and stoss side) is filled by sub-horizontal onlapping deposits. The layers inside the crater are thicker on the lee side and thinning toward the stoss side of the slope (fig. 5.4a; fig. 5.10a). The sediment infills of the neseted pockmarks are restricted inside the accommodation space that is created by the initial crater. The one exception is the first layer that drapes across the whole crater and extends only to downslope far field area toward the syncline of the depression (blue arrows; fig. 5.10a; fig. 5.9b). The direction of infill migration is aligned with the long axis of the initial craters, parallel to the bathymetric contours (fig. 5.9b).

In contrast to advancing pockmark arrays, the infill sequences of this type of pockmarks were deposited directly on the earliest and largest craters rather than on their sediment infill. The horizons that define the top and base of the infill of these nested pockmark correlate to the top and bottom of the infill inside the basal craters underneath advancing pockmark arrays and vertically stacked pockmark arrays (fig. 5.10b).

The package of reflections that represent the thickness of infill inside nested pockmarks reflect the sedimentation rate which is more important than time equivalent units inside the lower craters of advancing pockmarks arrays (fig. 5.10b).

Additionally, the top of each array is marked by a mounded strong positive reflection (fig. 5.4a, d; fig. 5.10a). This mounded reflection in some cases appears to cross-cut background horizons and onlapped by sounding strata (fig. 5.4; fig. 5.10a), which raises the issue of its origin. This question will be dealt with in section 5.6.4.2.3 hereafter.

5.5.3. Stratigraphic position of pockmarks arrays

The first generations of pockmark craters below the previously described arrays occur in sediment between *the top Miocene and intra-lower Pliocene*, and right below the Pliocene polygonal fault tier as nested pockmarks do (fig. 5.10b). While the advancing pockmark arrays and vertically stacked pockmarks occur mainly within the Pliocene polygonal fault tier. Some successions of advancing pockmark arrays can extend upward and develop in the Quaternary, even up to the seafloor (fig. 5.7a; fig. 5.8a). Overall, the infill of advancing pockmark arrays occurs within the same stratigraphic interval above the two channel complex are all Pliocene age (fig. 5.10b). In detail, however, several factors make it difficult to correlate individual episodes of reactivation or infill between neighbouring advancing pockmarks: 1) the close distance between advancing pockmarks makes them intersect with

each other in some cases; 2) reactivation craters interrupt strata continuity of the infill and 3) polygonal faulting deforms far field sediments in the Pliocene interval.

5.5.4. Chronology of different generations of infill within pockmarks systems

The timing of infill depositions within different types of pockmarks is quite different. The infill of nested pockmark is synchronous with the infill of earliest craters at the base of advancing pockmarks and vertically stacked pockmarks (fig. 5.10b). But they did not synchronize with the infill of advancing pockmark arrays neither the one of vertically stacked-up pockmarks, as most of nested pockmarks were sealed before the advancing pockmarks sequences started to develop in the Early Pliocene (fig. 5.10b).

The phases of infill and reactivation that made the advancing pockmark arrays occur throughout the Pliocene interval, but reactivation craters within advancing pockmark arrays at the two channel complexes locations or at rest of the study area were not synchronous. Most of the reactivation craters were sealed by Quaternary sediments, but few of them were still active and continued to provide a nucleation point for the subsequent sediment layer to prograde downslope (e.g. fig. 5.8a). These “remained active” younger craters can be traced at the present day seabed by tracking the shallow depressions at the already-known location of advancing pockmarks arrays (e.g. fig. 5.8b).

5.5.5. Heights of pockmarks arrays and the distances of horizontal offsets between apexes

Arrays heights and distances of lateral migration have been measured for 67 pockmarks arrays (see section below). Twenty-seven of the 67 pockmarks arrays are of the “advancing” type; 9 are “nested pockmark arrays”; 28 are vertically stacked. The measurements have been taken for each array along the direction of its maximum lateral migration. The height of a pockmark array is defined as the vertical distance between the lowermost apex and the topmost margin of the array. It ranges from 20 to several hundred ms TWT as follows:

- 1) 100 to 300 ms TWT for advancing pockmarks arrays above turbidite channels;

- 50 to 100 ms TWT for these ones in the Southern of the hanging wall domain;
- 2) 90 to 150 ms TWT for nested pockmarks ;
- 3) 20 to 180 ms TWT for vertically stacked pockmarks arrays.

The distances of horizontal offsets between the topmost and lowermost apex within pockmarks arrays are as follows:

- 1) 80 m to 650 m for advancing pockmarks arrays above turbidite channels,
 - 60 to 350 m for the rest of the locations in the South of hanging wall slope;
- 2) 100 and 160 m for nested pockmark;
- 3) Almost no lateral migration for the infill of vertically stacked pockmarks.

Advancing pockmark arrays are in general higher than the other types and their infill migrating further downslope. My observations and measurements lead us to the general conclusion that the higher the arrays, the longer the lateral migrations distance (fig. 5.12).

5.5.6. Regional distribution of the pockmarks and associated regional features

The area in which the two pockmark trails and their associated turbidite channels occur can be subdivided structurally into three zones (fig. 5.13): zone 1 is the rim Syncline 1 of diapir D1; zone 2 is the NW margin of the syncline; zone 3 is the open slope to the SW side of the syncline, on the hanging wall of the main growth fault affecting the area. In zone 1, i.e. in the axis of the rim Syncline 1 through which channel complex 1 runs, vertically stacked pockmarks arrays are observed (fig. 5.13; fig. 5.7b). In zone 2 and above turbidite channel complex 2, the infill of nested pockmarks progrades in a direction oblique to the maximum slope, i.e. toward the axis of the rim syncline (fig. 5.13; fig. 5.11a). In zone 3, advancing pockmarks arrays develop above both channel complexes (fig. 5.13; fig. 5.7a, 5.11b). The average dip of these zones was measured on seismic sections close to the channel axes but avoiding the pockmarks to ease the evaluation. The basinward dip in the axis of the rim syncline is about 1.5° , the dip of zone 2 is about 2° , while the dip of zone 3 exceeds 3° .

Advancing pockmarks arrays in this survey have been observed to associate with special geological structures (fig. 5.5a): (1) palaeo channels complexes, (2) concentric

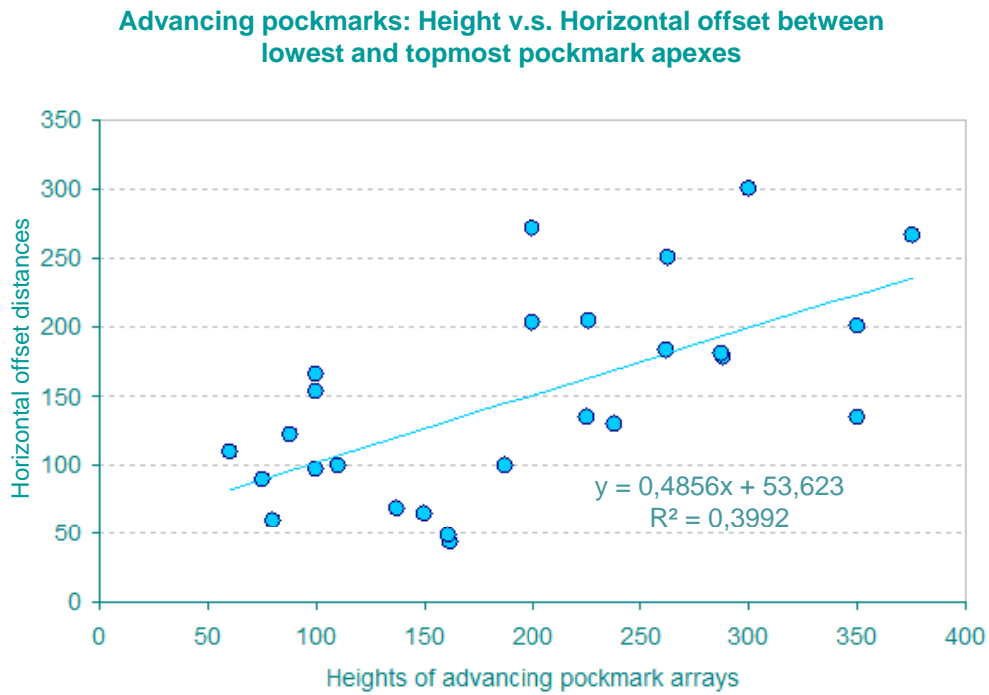


Figure 5.12. Cross-plot of height versus total migration distance for advancing pockmark arrays.

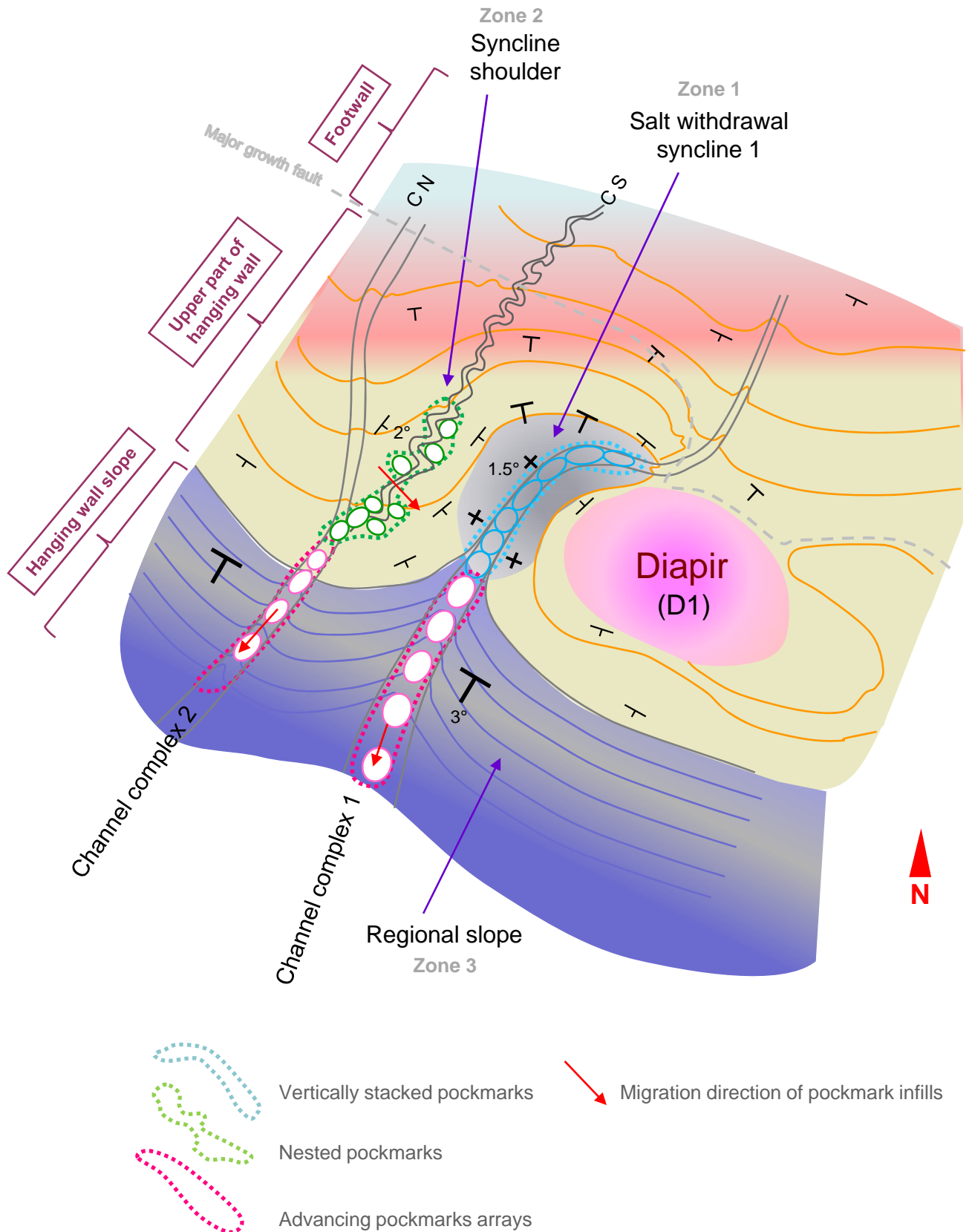


Figure 5.13. Sketch showing the regional topography and the location of two pockmark trails in and around syncline 1; this is a schematic interpretation of fig. 5.5. Vertically stacked pockmark arrays are lined up above channel complex 1 in the upper part of the hanging wall domain. Nested pockmarks are located above the levees the south channel (CS), which joins the north channel (CN) on the hanging wall slope. Advancing pockmark alignments are found above both channel complexes on the hanging wall slope.

extensional faults around diapir D2 (3) the local slope in the SSE corner and (4) diapir flanks. Other types of pockmarks can also be observed at the aforementioned locations, except in the location above the southern syncline and in the SSE corner of the survey.

1) Above buried channel complexes

The three types of pockmark arrays described above are organized in two trails (fig. 5.5b). Pockmark trail 1 is quite regular (fig. 5.3b), while pockmark trail 2 is more erratic with a zig-zag pattern (fig. 5.9b). These two pockmarks trails are occurred above two turbidite channel complexes (fig. 5.5), which bypass the Diapir 1 and cross over the location above the anticline.

Channel complex 1 (underneath pockmark trail 1) (fig. 5.5b) flowed from the NE side of footwall domain and across the growth fault into its hangingwall. It then bypassed the NW flank of the diapir 1 and flowed toward the SW. This channel complex developed throughout the Upper Miocene, and has a thickness about 500 ms TWT.

Pockmarks trail 1 is composed of advancing pockmark arrays and vertically stacked pockmark arrays above the downstream side (fig. 5.7a) and upstream side (fig. 5.7b) of channel complex 1 respectively. The upstream side of channel complex 1 corresponds to zone 1, while the downstream side is located on zone 3 (fig. 5.13).

Channel complex 2 is associated with the zigzag pockmarks trail (fig. 5.5b). It is composed of two sets of channels, Channel North (CN) and Channel South (CS) (fig. 5.5; fig. 5.11; fig. 5.13), that come from different locations and merge on the hangingwall slope of the study area. Channel South is meandering and Channel North is more rectilinear (fig. 5.5b). The final channel of this complex is rather meandering in the upstream and more regular in the downstream (fig. 5.5b; fig. 5.13). It occurs within the Upper Miocene interval on NW of syncline flank (zone 2) and its thicknesses varies from 100 to 200 ms TWT (fig. 5.10b).

All nested pockmarks arrays of this survey are located in the upstream part of the Channel South (CS) in the hanging wall domain (fig. 5.11a). While several advancing pockmarks arrays are observed to locate above the downstream part of jointed channels on the hanging wall slope (fig. 5.5; fig. 5.11c). Nested pockmarks arrays develop above the crest of the rollover anticline that makes the upper part of the hanging wall domain (fig. 5.11a); this crest is affected by normal extensional faults. Nested pockmarks arrays occur above the tips of these normal faults. These pockmarks arrays are located right above the levees of the topmost individual channel of the complex underneath (fig. 5.11a). Figure 5.5b shows that

this topmost channel is meandering. The zigzag pattern of nested pockmarks arrays can be seen to follow the meanders of the channel underneath (fig. 5.5; fig. 5.9).

2) Normal faults of salt-withdrawal Syncline 3

Another set of advancing pockmarks is observed above a concentric normal fault system associated with Syncline 3 in the south of this survey (fig. 5.5) (Chapter 3). The direction of the infill sequences of these pockmarks arrays was pointing toward the south (green arrows in fig. 5.5a) i.e. the centre of the syncline 3 instead of aligning with the one of regional slope (dipping toward SW).

3) Local slope in the SSE corner

Another sets of pockmark arrays develops in the SE corner of the survey, close to Diapir 2. (fig. 5.5a, b). In this location, the height of pockmark arrays is shorter and the lateral migration distances of infill are smaller according to the statistic (fig. 5.12; see section 5.5.5; table A3.1 in appendix III).

4) At SW flanks of Diapir 2

Some pockmark arrays have been found around the salt walls or on the edges of the lateral synclines / depressions flanks (fig. 5.5a). However, only 3 advancing pockmarks arrays have been observed on the SW flanks of Diapir 2, at the upper edge of hanging wall slope (D2 in fig. 5.5a).

5.5.7. Association with other types of fluid flow structures

Fluid migration-related seismic features other than pockmarks have been observed in the subsurface where along the turbidite channel complexes, and some of them are even cropped out at the seabed. They are as follows: 1) negative high amplitude anomalies (fig. 5.14a, b) and polarity reversals (fig. 5.14c), 2) seismic chimneys (fig. 5.15; fig. 5.16), 3) BSR (bottom simulating reflector) associated with high amplitude reflections inside the underneath basal craters (fig. 5.16), 4) positive high amplitude mounds (fig. 5.17). These fluid migration-related features often stack up at the same location to form vertical successions. For instance negative high amplitude anomalies (fig. 5.18a) are commonly observed below pockmark

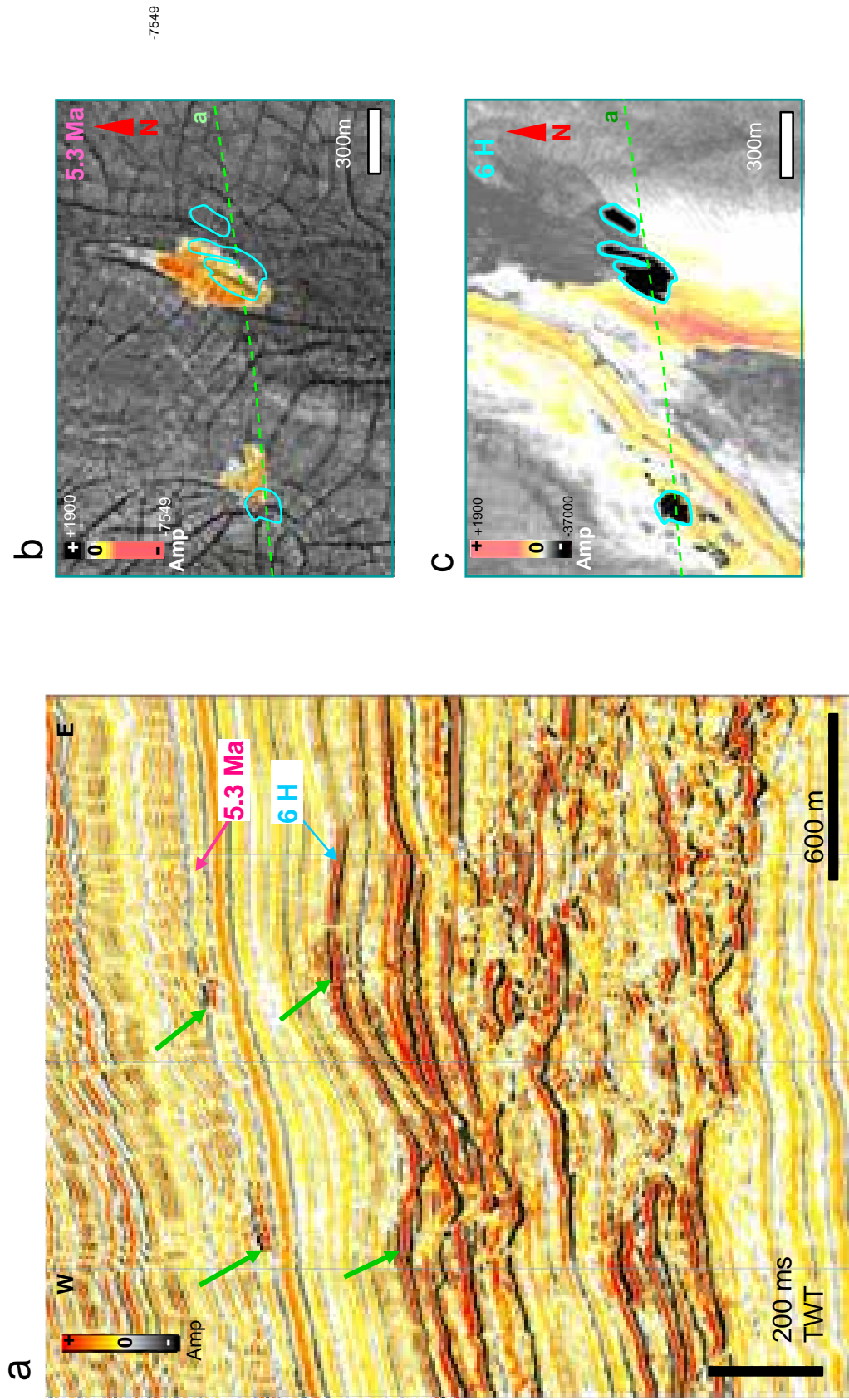


Figure. 5.14. Negative high amplitude anomalies at 5.3 Ma located above patches of reversed polarity at the top of channel complex 1. a) A cross section in the downstream side of channel complex 1 showing negative high amplitude anomalies (NHAAAs) and polarity reversal above and at the channel surface (horizon 6H). b) Negative high amplitude anomalies showing elongate and rounded shapes on the amplitude map of horizon 5.3 Ma (indicated by warm colours). Blue contours indicate the location of polarity reversals below the NHAAAs. c) Areas of polarity reversal correspond to the black patches on this amplitude map of horizon 6H, they also show elongate and rounded shapes.

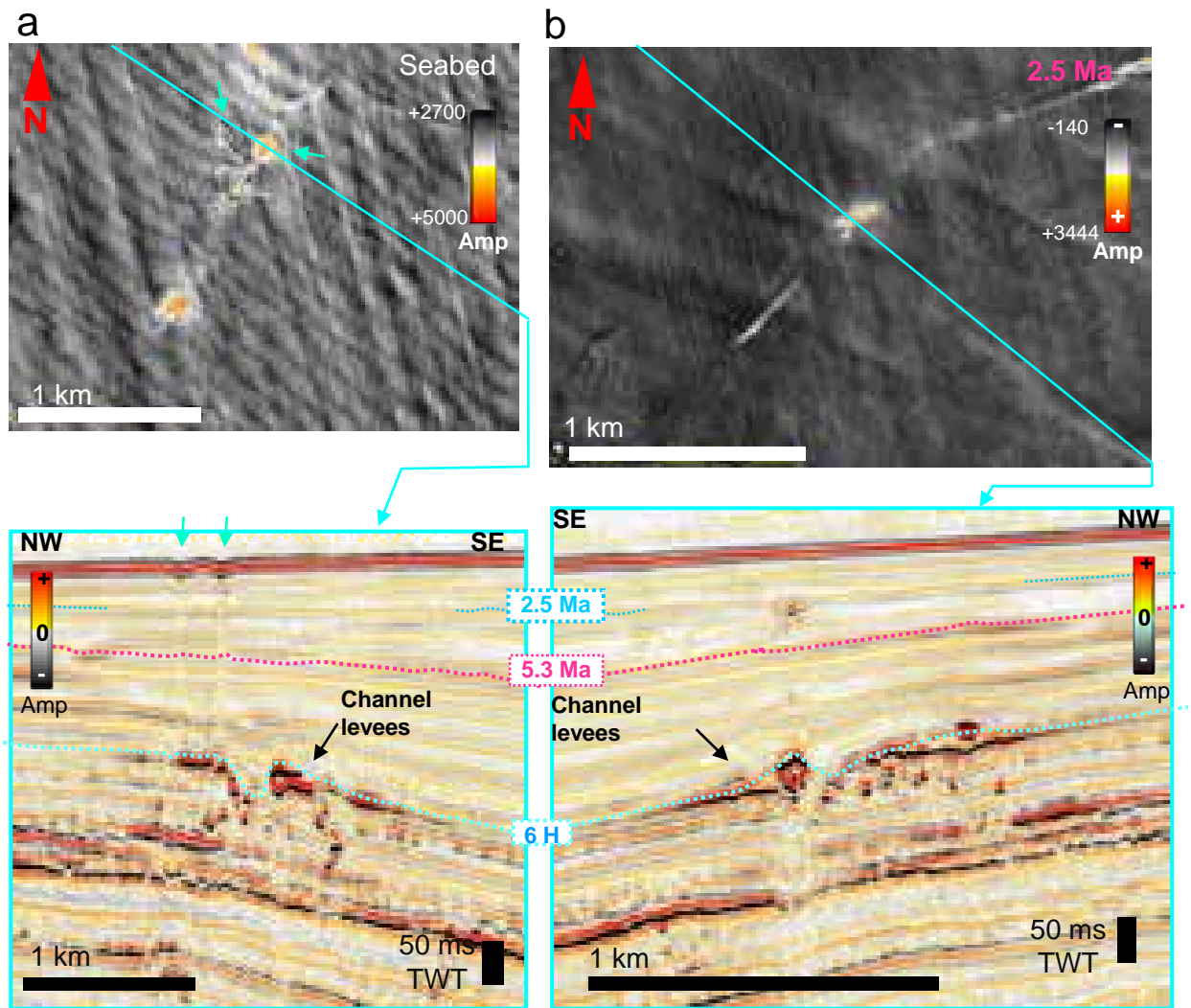


Figure 5.15. Interpreted gas chimneys rooting into the levees of channel complex 2. a) Amplitude map of the present day seabed. Two chimneys terminate upward into shallow depressions at the present day seabed. These shallow depressions show linear and circular shapes and are associated with positive high amplitude anomalies which have been interpreted previously as methane-related carbonates or possibly in association with gas hydrate. b) A chimney above a levee terminating up into a depressed elongate positive high amplitude anomaly.

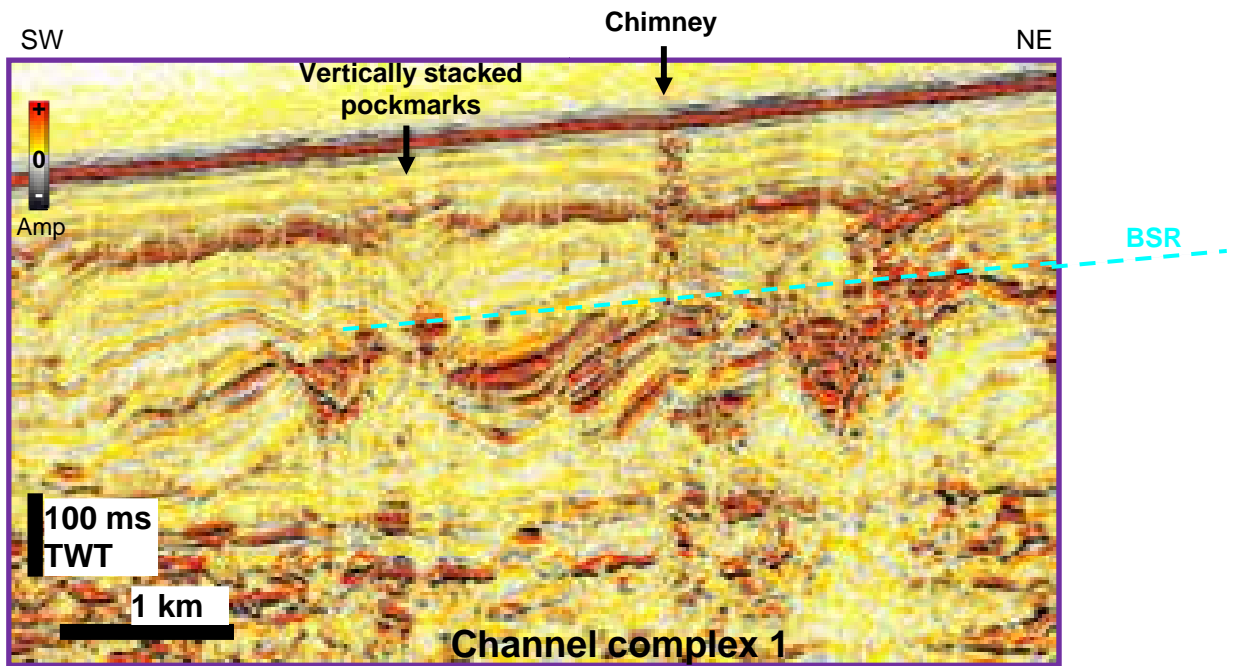


Figure 5.16. Bottom-simulating reflector (BSR, blue dot line) above sedimentary undulations and above the upstream side of channel complex 1. The BSR marks the top of a series of negative high amplitude reflections underneath, and cuts across the lowest part of vertically stacked pockmark arrays.

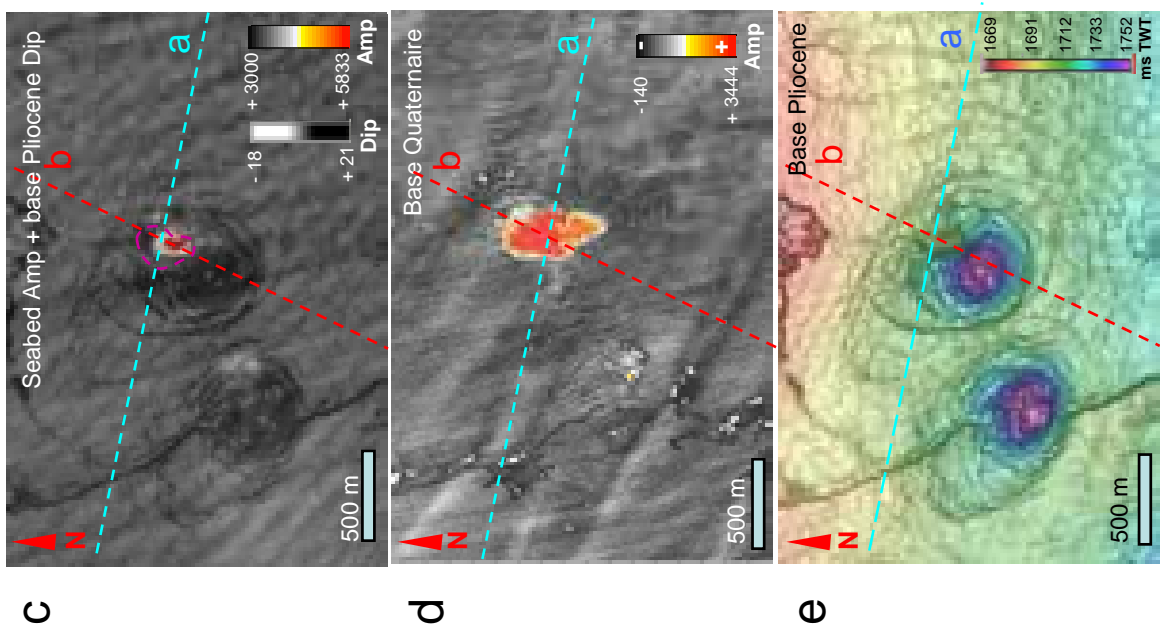
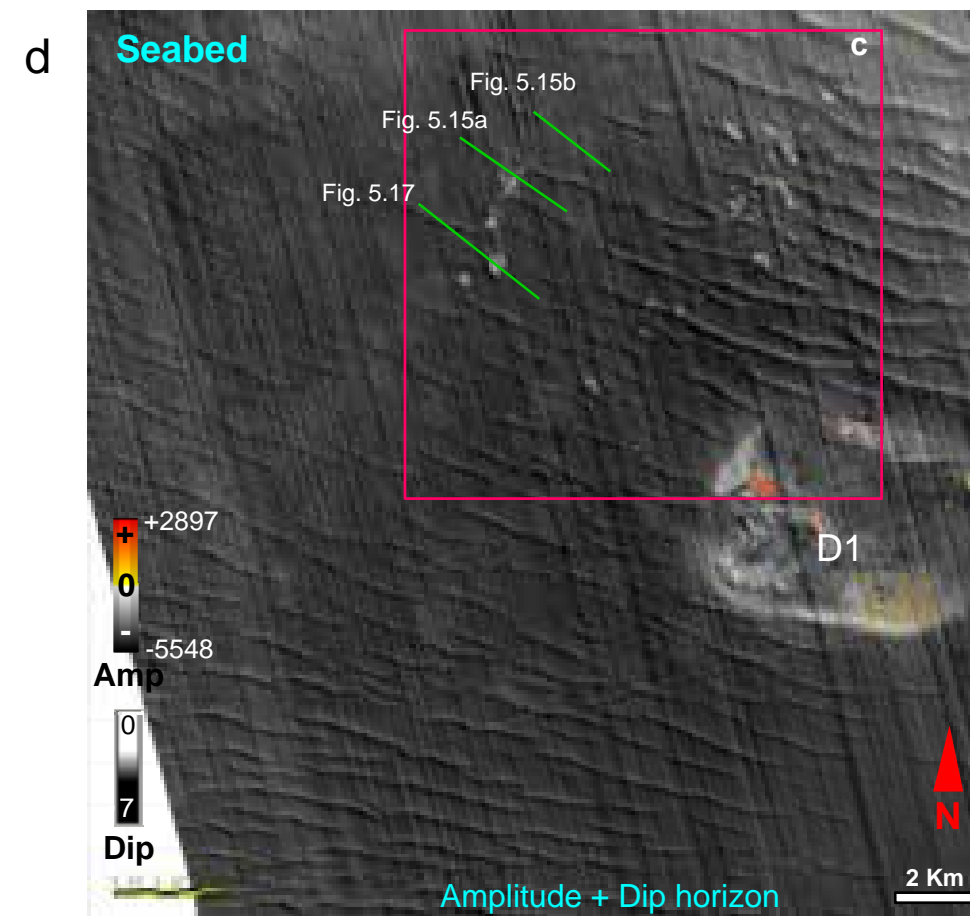
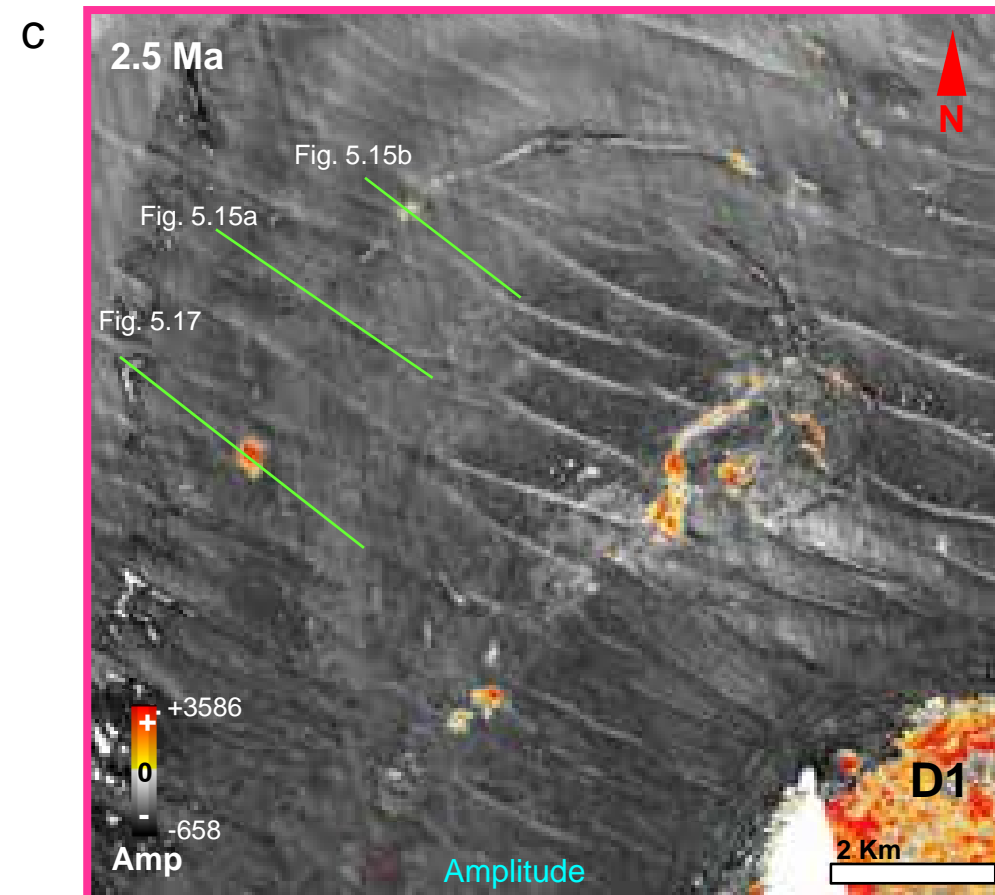
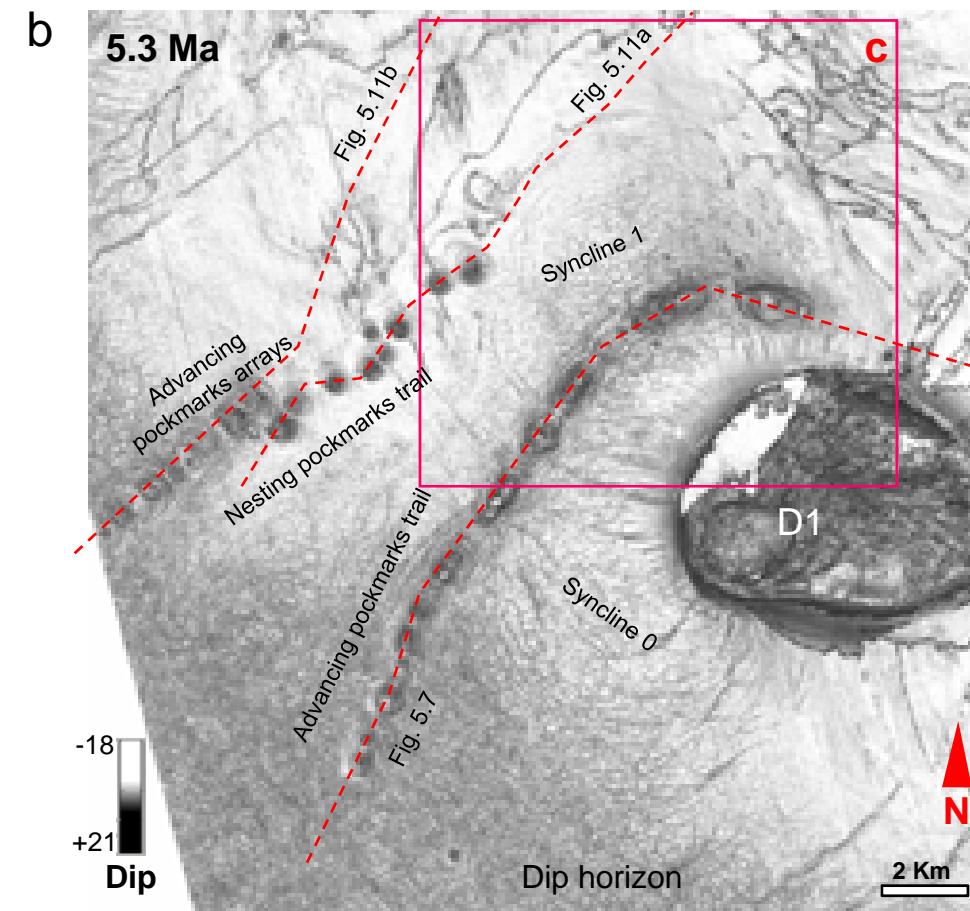
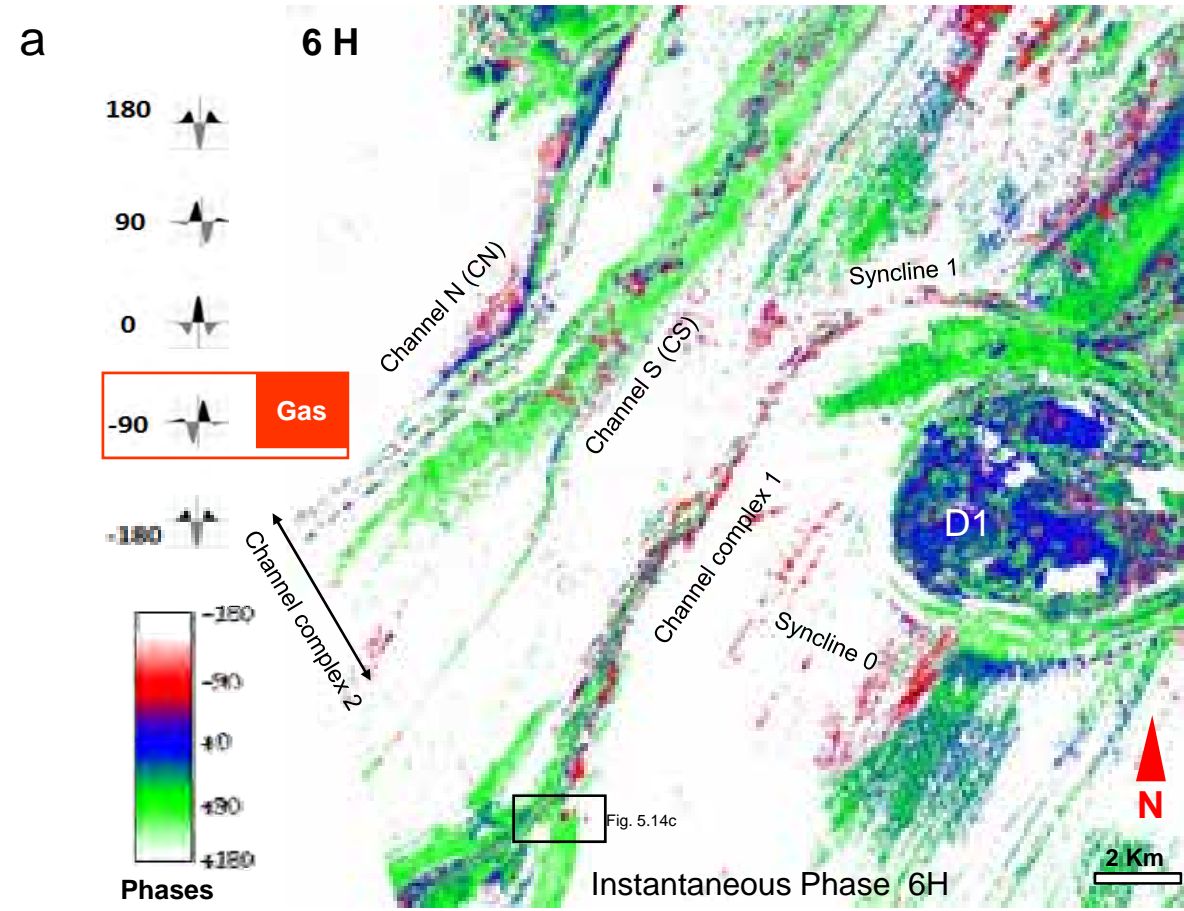
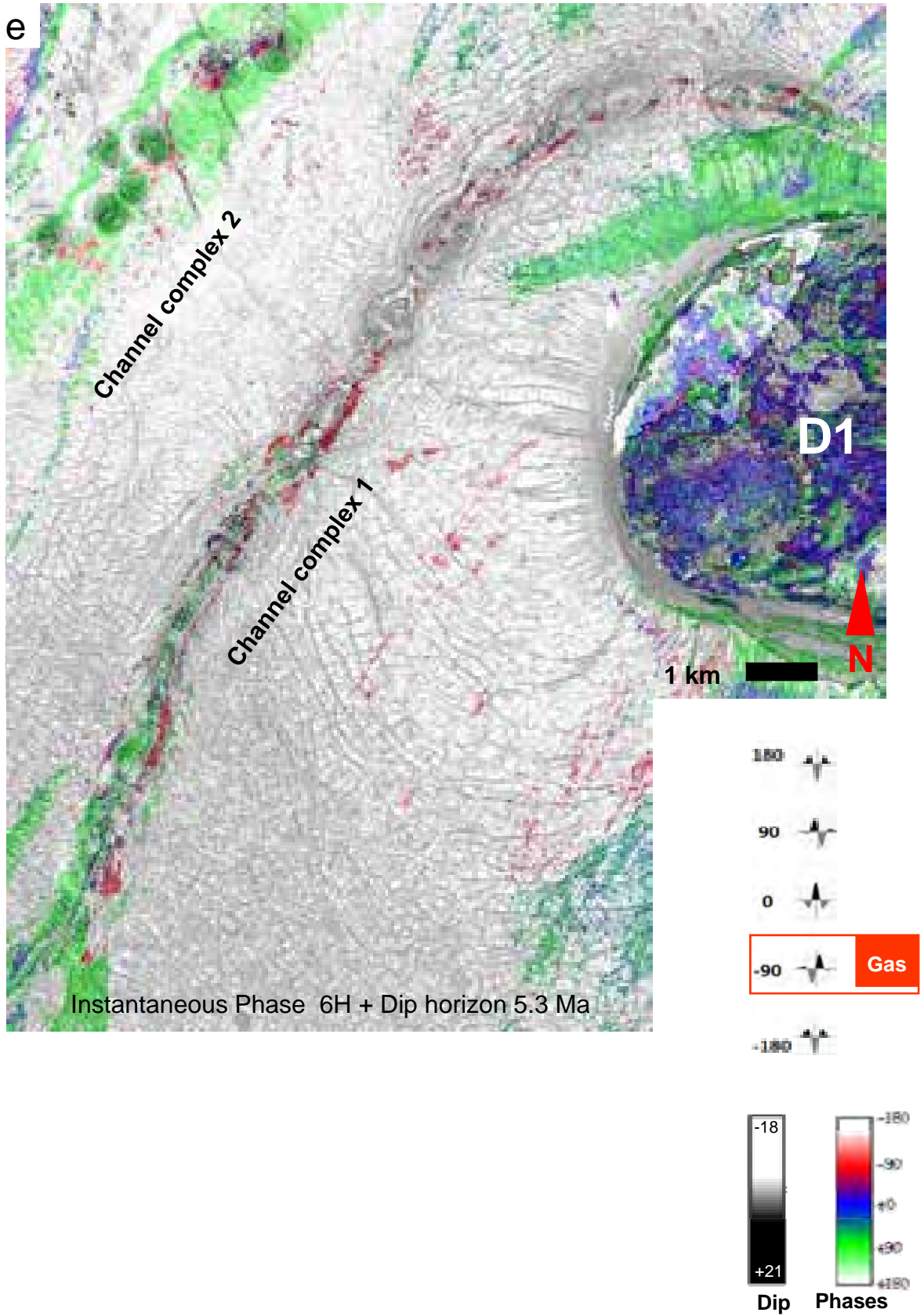


Figure 5.17. Mounded reflection with positive high amplitude at the top of a chimney that crosses the margin of a nested pockmark. Cross sections in (a) and (b) show that this mounded structure is associated with a shallow depression at the present day seabed, and (c) its top partly crops out on the bottom of the shallow depression. This positive high amplitude mound shows an elongate shape on the amplitude map of horizon 2.5 Ma (d); it has been interpreted as methanogenic carbonate mound (Chapter 4). (e) Two-way time map of horizon 5.3Ma with dip overlain. It shows the morphology of basal crater (earliest pockmark) of the nested pockmark.

Figure 5.18. Set of seismic attribute maps in the syncline 1 area, showing different fluid-related effects that occur at different stratigraphic levels i.e. above and underneath the two pockmark trails. a) instantaneous phase map of the two channel complexes showing different dominant phases of maximum amplitude energy . The phase rotation are indicated by the colour on the map; white: +/- 180°; red: -90°; blue: 0°; green: 90° (for interpretation see section 5.6.1); white areas on the map have been clipped and do not indicate any instantaneous phase values. b) Dip map of horizon 5.3 Ma showing the basal craters/earliest pockmarks of the different pockmark arrays. c) Amplitude map of 2.5 Ma zoomed on the upstream area of the two channel complexes (location indicated by red boxes on (b) and (d)). This map shows positive high amplitude anomalies above the pockmarks. d) Seabed amplitude map with the dip overlain. Positive high amplitude anomalies are observed at about the same locations as on horizon 2.5 Ma, above pockmarks in the upstream side of the two channel complexes. e) Instantaneous phase map of the two channel complexes in superposition with dip map of 5.3 Ma.





arrays (fig. 5.18b) and are overlain by positive high amplitude anomalies (fig. 5.18c) and shallow depressions (fig. 5.18d). This phenomenon occurs all along the two channel complexes and is particularly visible when superposing attribute maps of different horizons (fig. 5.18e; fig. 5.19a-c).

1) Seismic amplitude anomalies were observed at two levels above the channels: at the base of the polygonal fault tier (5.3 Ma) and at the top of channel-levee complexes 1 and 2 (6 H). At the latter level, these anomalies develop at both the top of the channel and at the crest of the levees of channel complex 2.

At the downstream end of pockmarks trail 1, local polarity inversions have been found at the top surface of the underlying channel complex 1 (fig. 5.14a, c) and ca. 300 ms above at the base of polygonal fault tier (fig. 5.14b). The areas of polarity inversions and negative high amplitude anomalies on the map view show rounded-to-elongate shapes (fig. 5.14b, c).

Figure 5.18c shows turbidite channels immediately below the two pockmark trails (fig. 5.18b) are associated with high-amplitude facies which have different rotational degrees. The dominant phases represent geological formations with different seismic hardnesses and can be distinguished as follows (cf. Brown, 2004; Paternoster et al., 2011a, b) (see Chapter 2): phase red for -90° which indicate the presence of free gas in the context of this study; blue for 0° representing hard lithologies (e.g. sand or carbonate crust); green for $+90^\circ$ representing medium-hard lithologies (e.g. brine or thin carbonate cement) and white for $-/+180^\circ$ indicating soft formations (e.g. silty-shale or shale). In order to obtain the best visualisation for the dominant phases of high amplitude facies only the dominant phases of high amplitudes are isolated and displayed, while phases of $-/+180^\circ$ have been excluded. White areas on the map indicate areas where the map has been clipped around high-amplitude facies and thus do not indicate any instantaneous phase values. Phases of -90° (red) are observed mainly within the channel bed of complex 1 (fig. 5.18e), and at the levees of channel complex 2 (fig 19a).

2) Seismic chimneys were also observed within the shallow interval above both channel complexes. Seismic chimneys are vertically stacked seismic anomalies (as stated in Chapter 1 Introduction). At the location of nested pockmark trail (fig. 5.19c), chimneys occur above the seismically soft facies at the levee crests (fig. 5.19b, c) and are likely rooted in these soft facies (fig. 5.15a, b; fig. 5.19d). Chimneys in the study area often terminate upward into linear or elongate positive high amplitude anomalies with shallower depressions (ca. 2ms TWT), either in shallow subseafloor (fig. 5.15b; fig. 5.7b) or up to the seabed (fig. 5.18c, d;

Figure 5.19. Zoon in of seismic attribute maps in figure 5.18; close-up view of channel complex 2. a) Seismic attribute map of instantaneous phase of channel complex 2 (individual channel N and S) shows different dominant phases of maximum amplitude energy. b) Dip map of 5.3 Ma shows the basal craters/earliest pockmarks of the pockmark trail 2. c) Seismic attribute map of instantaneous phases of the channel complex 2 in superposition with dip map of 5.3 Ma. d) Positive high amplitude anomalies with negative reliefs above the nested pockmarks in the upstream side of channel S. Top left corner: zoon in of amplitude map of 2.5 Ma of figure 5.18c; Background: shallow depressions in associated with positive high amplitude anomalies which stack vertically with these ones of 2.5Ma and above nested pockmarks in upstream side.

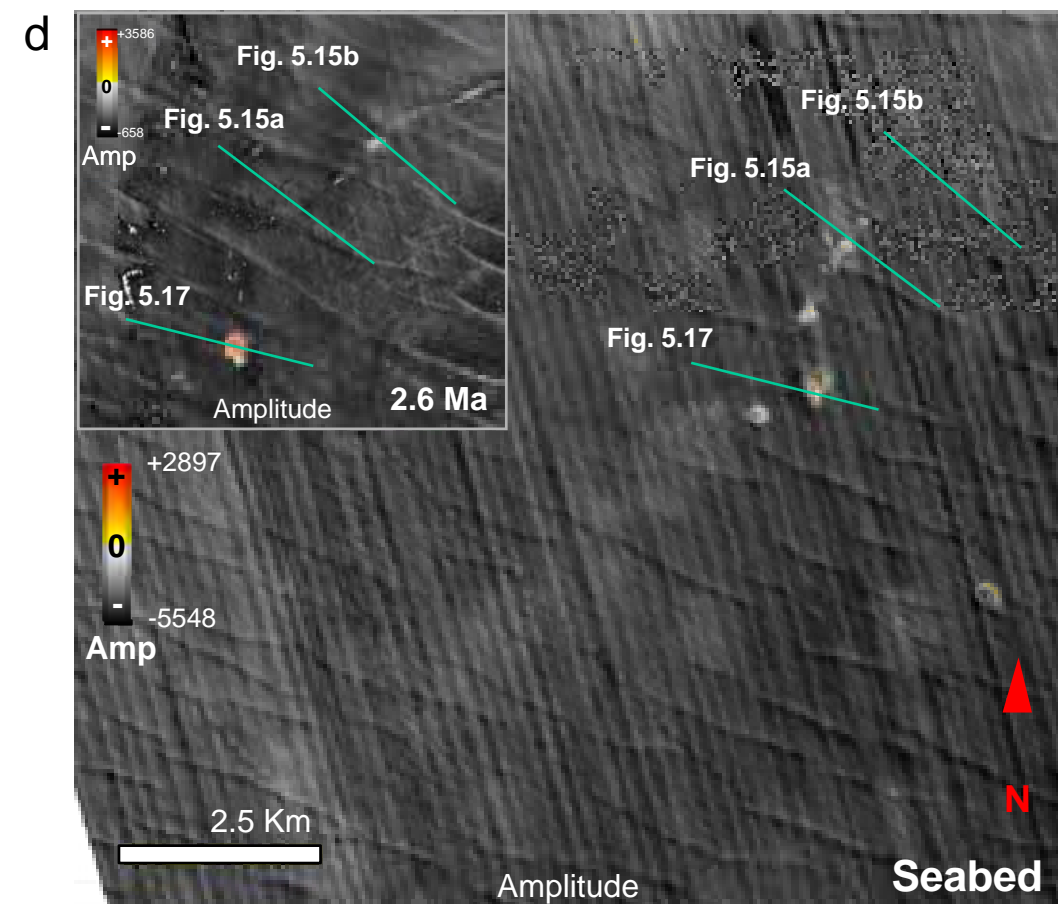
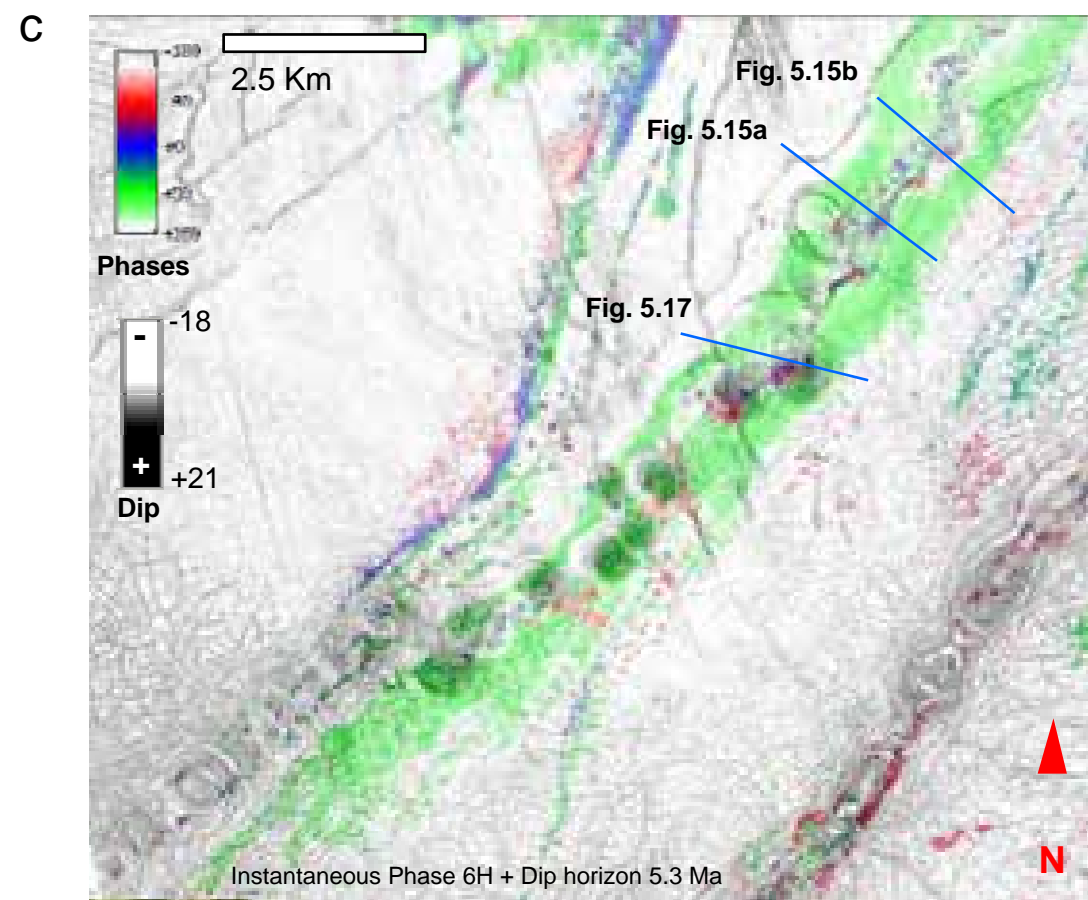
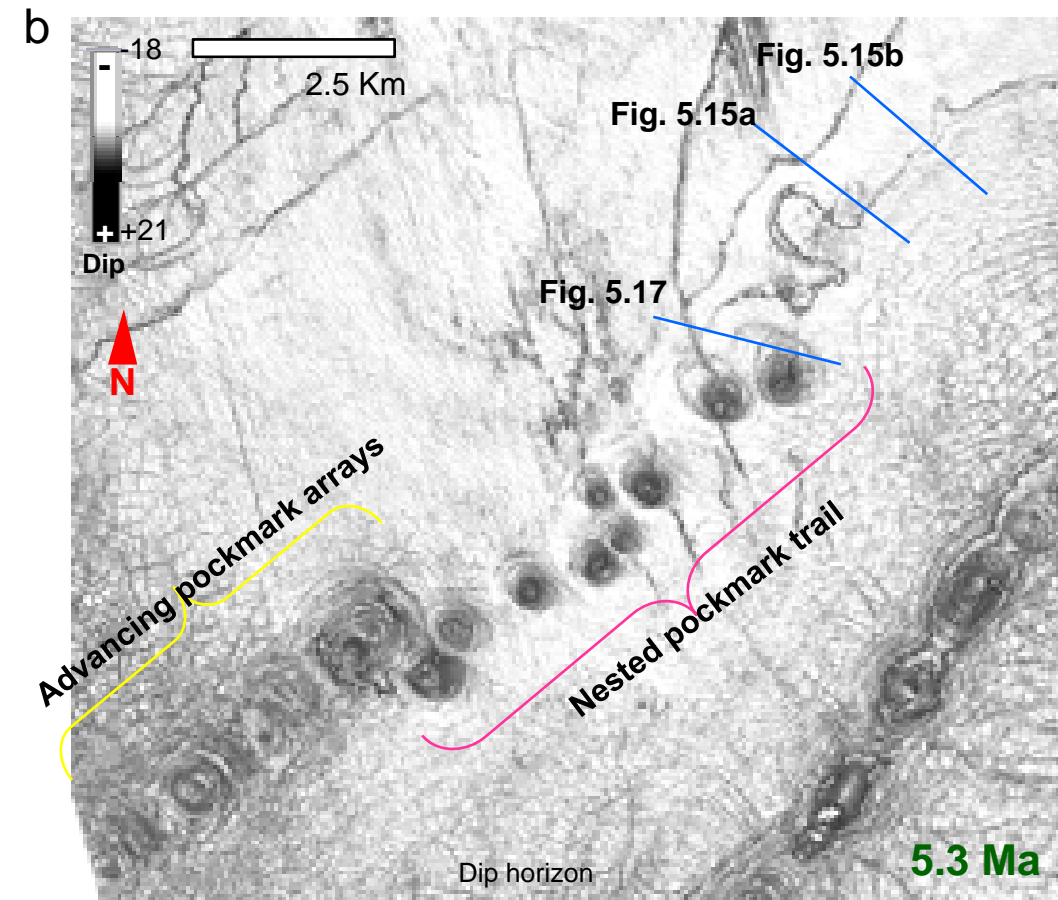
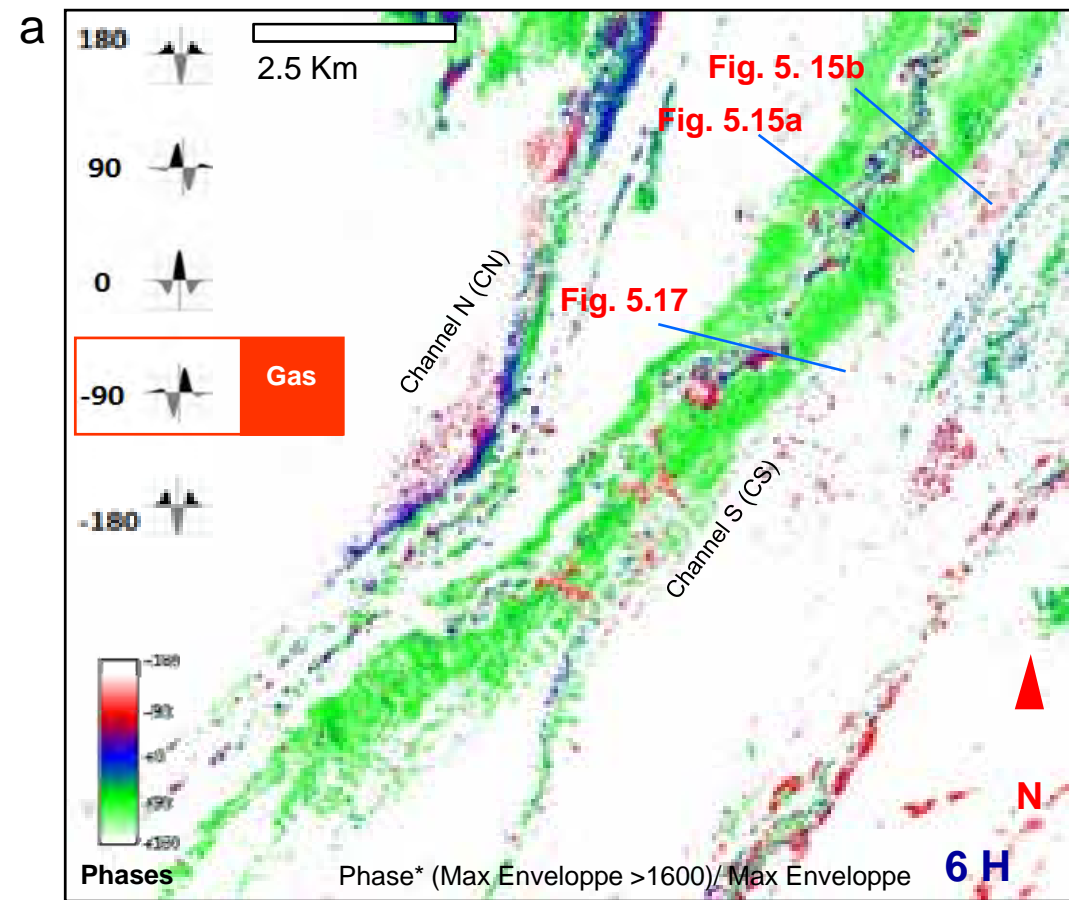


fig. 5.19d). Along the advancing pockmark trail, chimneys have been observed to go through vertically the whole pockmarks system and emanated from the high amplitude pockmark infill underlying a BSR (fig. 5.16). The roots of these chimneys on seismic data can be traced down to the underneath channels (black arrows in fig. 5.7b).

3) A BSR associated with seismic chimneys has been observed above the upstream part of channel complex 1. It is expressed by a strong negative reflection parallel to the seabed (fig. 5.16; fig. 5.7b). It interrupts the reflections it crosses, and cuts across the base of vertically stacked pockmarks arrays in the upstream part (fig. 5.16; fig. 5.7b).

This BSR which occurs above the high amplitude infill of earliest pockmark craters are overlying the sediment undulations (fig. 5.7b; fig. 5.16). Most of the vertically stacked pockmarks along the same trend are associated with high amplitude events. Narrow seismic acoustic perturbation zones underneath the BSR terminate upward into these high amplitude events (fig. 5.7b; fig. 5.16). Some high amplitude chimneys are observed to emanate from the underlying channel complex or from the high amplitude infill of earliest pockmark, then intersect vertically the BSR and terminate upward into stacked shallow depressions (fig. 5.7b).

In addition, the BSR, high amplitude events and chimneys are located above channel complex 1 in Syncline 1 and above the compensation fault sets of anticline 1 (fig. 5.1 and fig. 5.16; fig. 3.6b in Chapter 3).

4) Mound-shaped positive high amplitude reflections were observed above pockmark margins in several locations in the upstream part of channel complexes. These mounds are associated with shallow depressions on the seabed and underlying seismic pull-up chimneys. fig. 5.17a and b is the best image to show a mound above the margin of a nested pockmark, and which associate stacked vertically with a shallow depression above it and a seismic chimney below it (fig. 5.17c, d, e). It has a diameter of about 300 m and a height of 30 ms TWT. This carbonate mound outcrops partly on the floor of the associated depression on the seabed (fig. 5.17c), and is expressed as a positive high amplitude patch. According to the geophysical characters of the mounds, they are interpreted as methane-related carbonate (Chapter 4).

5.6. Discussion

5.6.1. Role of hydrocarbons

Methane fluid-escape features on seismic have been widely used for tracking hydrocarbon leakage and possible associated accumulations (Heggland, 1997; Van Rensbergen et al., 2003; León et al., 2007; Andresen, 2012). This section will examine how the various features described in the previous chapters help tracking hydrocarbon migration through geological times in the study area.

Among the various fluid flow features that were described in the previous section, the presence of a BSR at a depth compatible with the stability domain of methane hydrates indicates that methane gas is very likely being supplied by the hydrocarbon plumbing system, or at least was supplied in a very recent past (a few hundred years, cf. Sultan et al., 2004). Evidence for fluid migration through the channels is supported by the negative, high-amplitude reflections inside the earliest pockmarks which sit beneath the BSR (fig. 5.7b). These negative, high amplitude anomalies are interpreted as free gas accumulations (Coffeen, 1986; Sheriff, 1978). In addition, the “high-amplitude bright spot” chimneys with negative polarity at their tops which emanate from the earliest gas-bearing pockmarks or from the underlying channel (black arrows; fig. 5.7b) have been interpreted as methane gas conduits (Hustoft et al., 2007; Petersen et al., 2010; Andresen and Huuse, 2011). These fluid-related features provide evidence for the presence of free gas in the system where they occur. They may be associated with ongoing migration or be relict from older episodes of gas migration. Moreover, the presence of gas is supported by the phase reversal which locally occurs in local culminations of the levees of channel complex 2 (fig. 5.14a). The patches showing phase reversal are thus interpreted as shallow gas pockets. Figure 14c shows the areas of phase reversal as elongate patches on both sides of the channel. On the other hand, the negative high amplitude anomalies that occur at the base of the polygonal fault tier 200 ms TWT above these reversed phase patches (fig. 5.14) are interpreted to indicate that gas already migrated vertically from the channels underneath up into the pockmarks when they were emplaced, i.e. that gas migration had already started at that time.

Other features, i.e. pockmarks and positive high-amplitude reflections likely mark past events of gas escape (cf. Brendt, 2005; Hustoft et al., 2007; Plaza-Faverola et al., 2010; Petersen et al., 2010). The occurrence of all these in vertical stacks above turbidite channel complexes suggests that gas has been escaping upward from the channel reservoirs

underneath. However, the most receivable evidence for the free gas migrating from gas-bearing channel complexes is provided by the map of instantaneous seismic phase. Gas accumulations lead to a -90° phase rotation (coded in red on the instantaneous phase maps like fig. 5.10a). Such anomalies occur in the channel below the linear pockmarks trail 1 and in the levees below the zigzag pockmarks trail 2. The distribution of free gas shown on the maps indicates a close relationship between pockmark formation and gas migrations from these channel complexes. Chimneys which terminate upward into positive high amplitude patches with shallow depressions have been observed above channel complex 1 and the levees of complex 2 (fig. 5.15; fig. 5.16; fig. 5.18d; fig. 5.19d). These amplitude patches are interpreted as methane-related carbonates, or as an association of such carbonates and gas hydrates when they occur inside the gas hydrate stability zone (cf. Ecker et al., 1998; Hustoft et al., 2007; Westbrook et al., 2008; Chand et al., 2009; Petersen et al., 2010) (Chapter 4). This association is thus interpreted as a result of episodic gas venting from the gas-bearing levees and channel complexes via the vertical chimneys.

In conclusion, there is converging evidence that gas has been actively migrating upward from the buried channels up into their overburden since shortly after burial, and that the methane migration system is still active today. In addition, many of the escape conduits are long-lived with episodic fluctuations and reactivation episodes.

5.6.2. Role of sedimentation and bottom currents

Seismic reflection patterns i.e. the seismic-scale geometry of sediments reflects sedimentary processes and the energy of depositional environments (Mitchum et al., 1977). In the same manner, the geometry of the infill of pockmarks can provide information on the mode of sediment transport and deposition, and can be used as an indicator for the direction of bottom currents at the time of their emplacement, as shown for instance by Cattaneo et al. (2004). In order to examine models of sediment deposition related to different types of currents or processes, the section below will compare the infill structure of the earliest pockmarks, vertically stacked pockmark arrays, advancing pockmark arrays and nested pockmark arrays.

Over the study area and in the interval of interest, the dominant seismic facies is sheet-drape (cf. Sangree et al., 1978; Mitchum et al., 1977; Sangree and Widmier, 1978). Outside

advancing pockmark arrays and nested pockmarks, individual seismic reflections can be followed across a widely extended area and the packages they define show limited variations in thickness. This draping character indicates that deposition depends neither on the location with respect to turbidite fairways (lows) nor on the local topography of the sea bottom. Draping thus indicates settling from suspension, i.e. hemipelagic deposition. Consequently, any departure from this stationary character indicates influence from other sedimentary agents, bottom currents in the local context. The infill of nested pockmarks and earliest pockmarks in particular is marked by local variations in thickness with respect to far field values. These local variations will be used to infer the role of bottom currents in the development of the studied pockmark types.

a) Infill of vertically stacked pockmark arrays showing sheet-drape structures. Vertically stacked pockmarks and depressions occur in the Pliocene interval of Syncline 1. Their infill layers are purely draping and remain isopach all over the area of interest, inside and outside the pockmarks. This character indicated settling from suspension, i.e. hemipelagic deposition. This type of pockmarks has been previously studied in detail by e.g. Moss and Cartwright (2010a); the authors interpreted this character as indicating hemipelagic drape above the initial pockmark depression. In addition, the parallel draping character are extended widely over the whole basin during the Pliocene (Broucke et al., 2004; Gay et al., 2006a; Andresen and Huuse, 2011).

b) Infill of advancing pockmark arrays. The infill of advancing pockmark arrays does not show onlap terminations or thickness variations, although it is disrupted on the downstream sidewall. Most of the time, it can be followed approximately in the far field as parallel layers which mimic the morphology of underlying individual depressions. Their infill layers are sheet draped and isopach inside and outside the pockmarks, and suggest that sedimentation was likely constant within advancing pockmark arrays during Pliocene. As described in section 5.5.1. above, reactivation craters in the downstream side of advancing pockmark arrays provided accommodation space further downstream for sediment deposition at each reactivation episode. The downslope migration of reactivated craters over time leads to pockmark infill sequence being deposited progressively further downstream and thus causing downslope migration of the pockmark. Therefore, the infill of advancing pockmark arrays is unlikely to result from bottom currents only.

Detailed discussion for the mechanism of formation for advancing pockmark arrays is given in section 5.6.4.1 below.

c) Comparison between infill of vertically stacked pockmark arrays and advancing pockmark arrays. The reflections that extend from the upstream side of the advancing pockmarks arrays to their far field can be correlated with those within the vertically stacked pockmark arrays (fig. 5.10b). Reflections of each individual infill layer within these pockmark arrays are sheet-draped structures (Sangree et al., 1978) i.e. parallel to each other and to underlying craters and do not show thickness variations above the channel complexes. If the sediment was deposited by bottom currents, there would be a very little opportunity for sediment infill sequences to develop a sheet-drape architecture across a wide extended area in the Lower Congo basin (cf. Gay et al., 2003; 2004; 2006a). As these infill layers can be traced from the vertically stacked pockmarks down to the advancing pockmarks, it is difficult to explain why the sediment drape is present locally in the upper part of channel complex 1 but not in the lower part. Thus, it strongly suggested that sediments were deposited by hemipelagic draping rather than by unidirectional bottom currents on the regional slope and within Syncline 1. The conservation of adjacent reflections within vertically stacked pockmark arrays and advancing pockmark arrays indicate that hemipelagic infill sequences were deposited during a period when the bottom currents were less active.

d) Earliest pockmarks of vertically stacked pockmark arrays and of advancing pockmarks arrays. They are filled by reflections that are continuous, parallel and onlapping onto the pockmark sidewall (fig. 5.7a, b). This last character, with deposition restricted to the lows indicates that sedimentation was likely dominated by turbidity currents (Mitchum et al., 1977; Sangree et al., 1978; Sinclair, 2000; Cattaneo et al., 2004; McCaffrey and Kneller, 2001; Hamlin, 2009).

On the other hand, the infill of the earliest pockmarks in the trough of sediment undulation in the centre of Syncline 1 is apparently thicker than on the hanging wall slope (fig. 5.7b). This may be because of the earliest pockmarks were filled during the reactivation of Syncline 1 (5.3Ma to 6H) (Chapter 3), and the subsidence provided more accommodation space for sediment deposition.

The existence of bottom currents at the location of channel complex 1 could be demonstrated by the occurrence of undulations in the syncline center (fig. 5.7b). These undulations were formed within the interval between 5.3Ma – 6H when Syncline 1 was

reactivated. Thicker and larger sediment undulations occurred mainly in the syncline centre and become shorter in length and height in a downslope direction (fig. 5.7c). This may be because of more sedimentations are favoured by increase of accommodation space created by sag, and the reactivation of subsidence might perturb the bottom current in this location at the moment when these undulations formed.

Undulations 1, 2, 5, 6 in Figure 5.7b and 1-3, 5-7 in Figure 5.7c show sigmoid progradational structures with generally the lee side thicker than stoss side. Even though the stoss sides were truncated by the formation of the earliest pockmarks, they can still be fairly well illustrated at certain locations. The geometries of these undulations are similar to the sedimentary drift of type between A and B in the classification of Jopling and Walker's (1968) for ripple-drift, and type B2 in the classification of Allen's (1970) for cross-laminated deposits. In both classifications, sigmoid or oblique aggradations with incline attachment plan dipping upslope, indicate bottom currents flowing toward downslope (Jopling and Walker, 1968; Allen, 1970).

Nevertheless, the migration direction of these sediment undulations is uncertain, in the lack of oceanographic data, reconstruction for the direction of a flow from only the morphology and the orientation of the undulation proves difficult. The formational processes of deep sea sediment undulations are still in highly debate (Cattaneo et al., 2004) and are not the focus of this study, so I am not going into further discussion in here.

e) The shapes of the basal craters of nested pockmarks are elliptical on plan view (fig. 5.10a). Nested pockmarks have their major axis parallel to the bathymetric contours of the NW flank of Syncline 1 (fig. 5.10b). As demonstrated by Bøe et al. (1988), Josenhans et al. (1978), Judd and Hovland (2007), the elongate plan form of pockmarks can be used to indicate the direction of bottom currents. Thus, it suggested that the basal craters were probably modified into elliptic shapes by a contour current (sensu Heezen et al., 1966) that flowed towards SE along the flank of the syncline.

The existence of the contour-parallel current is also evidenced by the progradational infill in the basal craters of nested pockmarks (fig. 5.4; fig. 5.10a). This infill is most of time not continuous in far field and is thicker than sediment drape in far field. Progradation occurred towards the SE, also parallel to the contour lines of the syncline flanks (fig. 5.5a). Progradation infills have been interpreted to deposit by low-energy turbidity currents (Sangree et al., 1978; Sangree and Widmier, 1978) and lower sediment supply (Michum et al., 1977; Sangree and Widmier, 1978). In addition, the sediment transport direction is likely indicated

by the first infill layer of the nested pockmarks, which extends preferentially on the SE side of syncline flank (fig. 5.10b), and deposited in the same direction as the infill progradation.

In comparison to the earliest pockmarks underneath vertically stacked and advancing pockmarks arrays, onlap infills within these earliest pockmarks are some time continuous and across horizontally several craters (fig. 5.7a). This suggests that more sediment might be retained in syncline depressions than on the syncline slope. It is possible that once sediment was deposited inside the basal craters on the SE syncline flank, the rest of sediment bypassed the more inclined syncline slope. If the assumption above was valid, it may explain why, under the same regime of current activity i.e. low-energy turbidity currents, how deposits of sediment evolved into different patterns. As a result, the sedimentation at the beginning of Pliocene in nested pockmarks (in the upstream of channel complex 2) and earliest pockmarks (in the upstream of channel complex 1) were different.

Sedimentation rate in each type of pockmark versus the energy of potential bottom or turbidity currents is summarised in a conceptual diagram (fig. 5.20).

5.6.3. Correlations between topography and spatial distribution of pockmarks

Results of pockmark mapping (fig. 5.5a) reveal that pockmarks with progradational infill mainly occur on inclined topography. As demonstrated by the two-way time map of horizon 5.3 Ma, advancing pockmarks are located above channels on the hanging wall slope (dipping at c. 3°), on the slope in SE corner of the survey (dipping at c. 2.5°) and on the NW-SE flank of Diapir 2. Then, nested pockmarks arrays which do not show strong infill migration are located on the flanks of Syncline 1 which dip at approximately 2° . Finally, vertically stacked pockmarks arrays occur only on flat-lying areas (with dip c. 1.5°) such as the centre of Syncline 1 and in the least inclined regions of the survey (fig. 5.5a).

As demonstrated by the directions of migrated infill strata which are aligned with the local slope, the geometries of pockmark infill were likely related with the local topography. This could be especially supported by the geometries of nested pockmark basal craters, which have their long axis oriented along the bathymetry contours. Moreover, the difference in sediment accumulation rates from upslope to downslope of nested pockmarks sidewall suggests that the depositional processes occurred in a regime dominated by currents impinging on the seafloor and affected by the pre-existing local topographies that could

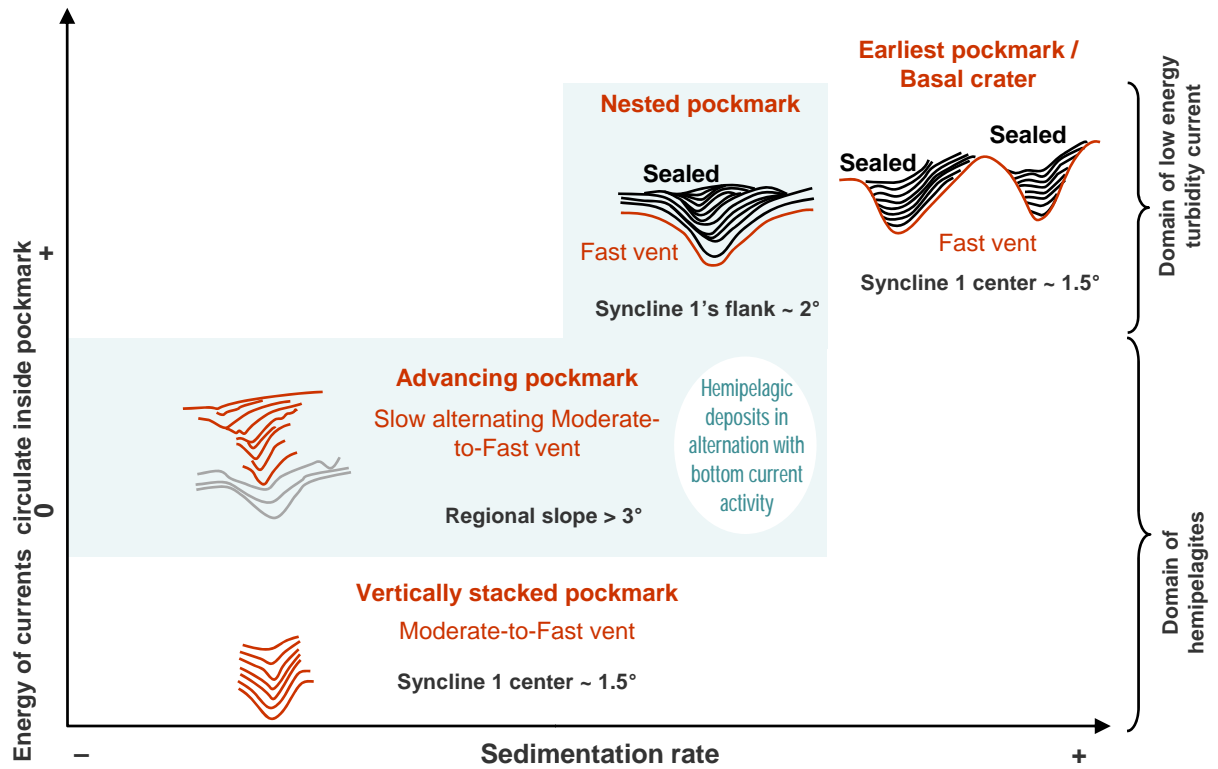


Figure 5.20. Conceptual diagram showing the morphology of pockmark arrays as a function of the energy of bottom currents and the sedimentation rate. The regional dip of the strata in areas where pockmarks occur is indicated.

explain the lateral changes in sediment accumulation rates (cf. Cattaneo et al., 2004). Therefore, the geological configurations and current circulations in the Angola margin likely influenced the development of different types of pockmarks.

5.6.4. Mechanisms of pockmarks formation

In this section, models for the genesis of advancing pockmarks and nested pockmarks are proposed based on the geometries of their infill on seismic.

5.6.4.1. Advancing pockmarks

5.6.4.1.1. The ruptured surfaces on downstream side wall

Several observations indicate that the formation of advancing pockmarks arrays is multi-phased. The reactivation craters (e.g. P3, h6 in fig. 5.6) and the crescent-shaped disruption on the downstream side of advancing pockmarks arrays (e.g. horizon h1 - h5 in fig. 5.6) are the main indications for successive episodes in their development, and are the key features to understand their evolution over time. It is therefore important to figure out the origin of these two features.

For the disruption of reflections on the downstream pockmark side wall, we acknowledge that the disruption of reflections on the downstream side of advancing pockmark could have different causes, one of which could be seismic resolution. The disappearance of a reflection can correspond either to the real disappearance of the corresponding sedimentary layer(s), or to thinning below seismic resolution. These cashew-shaped disrupted areas occur only on the downstream sidewall of pockmarks, in the same trend as the channels beneath. This strongly suggests that reflections disruption could originate from sidewall thinning by starvation or erosion, both due to bottom currents trending along the channel direction. In a recent pockmark study in Burlington Bay, Manley et al. (2004) and Watzin et al. (2004) showed that starvation or erosions on pockmark sidewall by fluid seepage and vortexes are both possible during and after sediment deposition within pockmarks. In addition, starvation or erosion on pockmarks sidewall induced by fluid seepage has also been demonstrated by the analogue model of De Vries et al. (2007a).

Vortexes of cavity flow which is refereeing to flow circulating around pit depressions or pockmarks are well studied for research in environment of benthos habitats (Nowell and Jumars, 1984; Yager et al., 1993; Abelson and Denny, 1997; Manley et al., 2004; Watzin et al., 2004). Vortexes have been identified being an important factor to resuspend fine-grained sediments on depression side walls (Nowell and Jumars, 1984; Yager et al., 1993; Abelson and Denny, 1997; Manley et al., 2004; Watzin et al., 2004). Most studies dealing with cavity flow demonstrate that vortexes are the dominant pattern and are issued from flow separation over a negative topography (Takematsu, 1965; Taneda, 1979; Sinha et al., 1981; Higdon, 1985; Fang et al., 1999; Rowley et al., 2002; Zdanski et al., 2003; Camacho and Barbosa, 2005; Podvin et al., 2006; Brè and Colonius, 2007; Dudley and Ukeiley, 2011). Given that infill disruptions within advancing pockmarks occur only on the downstream side of their infill, and vortexes are formed by rapid downward current on the same side and where shear stress is the highest within depressional area (Sinha et al., 1981; Webster et al., 2004; Haigermoser et al., 2007), therefore sediment in the stoss side of pockmarks are suggested to be eroded or resuspended. Moreover, basing on the intermittent presence of crescent-shaped disrupted surface and reactivation craters in the downstream side of advancing pockmark arrays, I suggest that there is an alternation between the fluid eruptions or seepages and erosion caused by vortexes in the downstream side.

In the following section, I am going to discuss the model of infill depositions within advancing pockmark arrays.

5.6.4.1.2. Formation model of advancing pockmarks

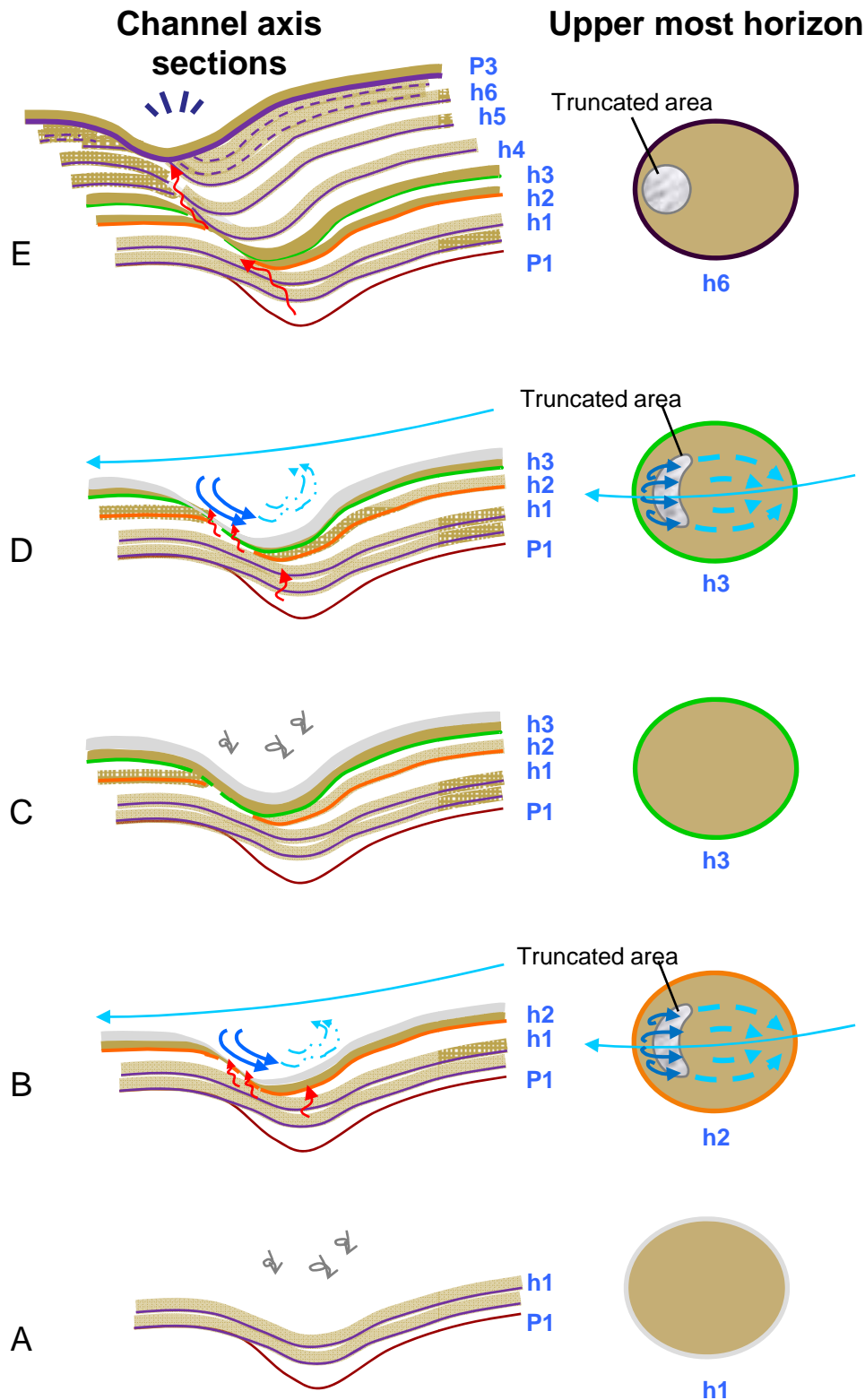
A model for the development of advancing pockmark arrays is proposed, based on 1) the nucleation site and migration of pockmark craters, 2) the stratal geometries within the pockmark crater, and 3) their association with gas accumulations in the channel complex underneath (fig. 5.18e).

Phase 1) Generation of initial depression: fluid was expelled from the underlying channel creating the earliest pockmark (P0 in fig. 5.3a). Later eruptions occurred through the seal of this pockmark, creating another depression (P1 in fig. 5.3a). The last depression of this series provided the nucleation point for the subsequent development of advancing pockmarks.

Phase 2) Cycle of sedimentation and deformation: Once a depression was created the first phase of infill occurred, hemipelagic deposits draped this depression (h1-2 in fig. 5.3a and in fig. 5.21a). The infill phase may have occurred during times of reduced bottom water current activity. On the other hand, the seismic discontinuity of the reflections within the pockmark (h1-2; fig. 5.3a) could occur either through erosion (actual removal of sediment, real discontinuity) or reduced sediment deposition (thinning of the corresponding interval below seismic resolution). These could result attenuations of seismic reflections because beds thin to below the vertical resolution. Vortex is most likely the origin of erosion (fig. 5.21b). It is generated close to the downstream pockmark sidewall, by the separation of unidirectional flow upslope (Brothers et al., 2011; Fang et al., 1999; Clarence et al., 2002; Zdanski et al., 2003; Camacho and Barbosa, 2005; Bré and Colonius, 2007; Dudley and Ukeiley, 2011). The vortex formed due to the flow separation above the upcurrent rim of the pockmark (Abelson and Denny, 1997; Clarence et al., 2002; Manley et al., 2004; Povin et al., 2006). Unconsolidated fine-grained sediments on the downstream sidewall, were then resuspended by the vortex (Abelson and Denny, 1997; Manley et al., 2004). Reduced sediment deposition during episodes of fluid venting on the sidewall (De Vries et al., 2007a; Manley et al., 2004; Watzin et al., 2004) is proposed as an extra cause for local thinning. The reduction in lithostatic pressure due to erosion caused by the activity of bottom water currents, could have promoted fluid escape.

Phase 3) Downslope migration and deposition of permeable stringers: Later phases of sedimentation resulted in a draping of the initial depression (fig. 5.21c). Throughout the lateral advancement of the pockmark, sediments filled the horseshoe-shaped area left by sediment starvation or by erosion (fig. 5.21c). During phases of seepage and/or increased bottom current activity these draped sequences were periodically eroded (fig. 5.21d). The combination of these two processes formed the infill geometries observed on fig 1a (h1 – h3). Fluid flow pathways were created along the downstream pockmark sidewall through the vertical connection of permeable, fine-grained sand stringers (fig. 5.21d). The top of the migration path is interpreted as the bathymetry of the contemporaneous seabed, and is located at the downstream flank of the uppermost depression.

Phase 4) formation of reactivation crater: Episodes of low sea level stand, by reducing pressure on the seabed (i.e. lithostatic pressure) while fluid pressure remained unchanged in closed reservoirs may have triggered fluid expulsion from deeper sources. They overall favoured the preferential migration of gas along the vertically connected permeable pathway in the downstream side of pockmark arrays. This architecture of deposits thus controlled the site where a new eruption crater would be formed (fig. 5.21e). Repetition of preferential



Cycle: a → b → c → d → e → a → b → ...

Figure 5.21. Model for the development of advancing pockmarks. a) First phase of infill above the last earliest pockmark P1. b) Resuspension of fine-grained sediment on the downstream pockmarks sidewall by vortex and seepage. A horseshoe-shaped truncated area is formed. c) Infill phase during time of reduced bottom-water current activity, horseshoe-shaped erosional patch is filled by the new deposits. d) a new layer is deposited and followed by a truncation episode. e) Lateral migration by the creation of reactivation pockmarks which truncate the downslope flank of the preceding infill sequence.

erosion/starving, overpressure and crater formation downslope from the previous one results in a lateral migration of the pockmark infill (fig. 5.21e).

Phase 5) Sealing: The lateral migration of the pockmark terminates when fluid venting ceases. Once fluid venting stops, reactivation craters cease to form and are buried by subsequent sedimentation.

5.6.4.2. Nested pockmarks

5.6.4.2.1. Progradational infill in interaction with topography and potential bottom currents

The formation of nested pockmark is similar to that of advancing pockmarks. In both cases, conical infill progressively reduces accommodation upwards. The main difference is that no reactivation phase was observed for nested pockmarks.

The infill models for these two types of pockmarks are different. In the case of nested pockmarks, their infill was most likely deposited mainly by bottom currents instead of draping (see section 5.5.2). According to the indications on the migration directions of infill that are provided by the geometries nested pockmarks: 1) the infill of nested pockmarks migrates toward the centre of Syncline 1 (fig. 5.5a), 2) the long axes of the basal craters of nested pockmarks are oriented parallel to the bathymetric contours and pointing toward the syncline (fig. 5.9); 3) The first infill layer of nested pockmarks preferentially extends on the slope of the syncline flanks, along the bathymetry contours (fig. 5.7a). The depositional direction of this first infill layer is the same as the migration direction of nested pockmark infill. These elements suggest the probable presence at the time of early infill of a bottom current that streamed parallel to the bathymetry and interacted with the local topography (the syncline slope), by flowing into the irregular topographies (earliest pockmarks) and depositing sediment on them. This migration is potentially related to contour-parallel bottom currents (cf. Heezen et al, 1966; Cattaneo et al., 2004) in this study area. The degree of migration shows a regional organization, pockmarks locate on upslope are more aggrading while those locate on syncline flank and on regional slope have highest rate of migration.

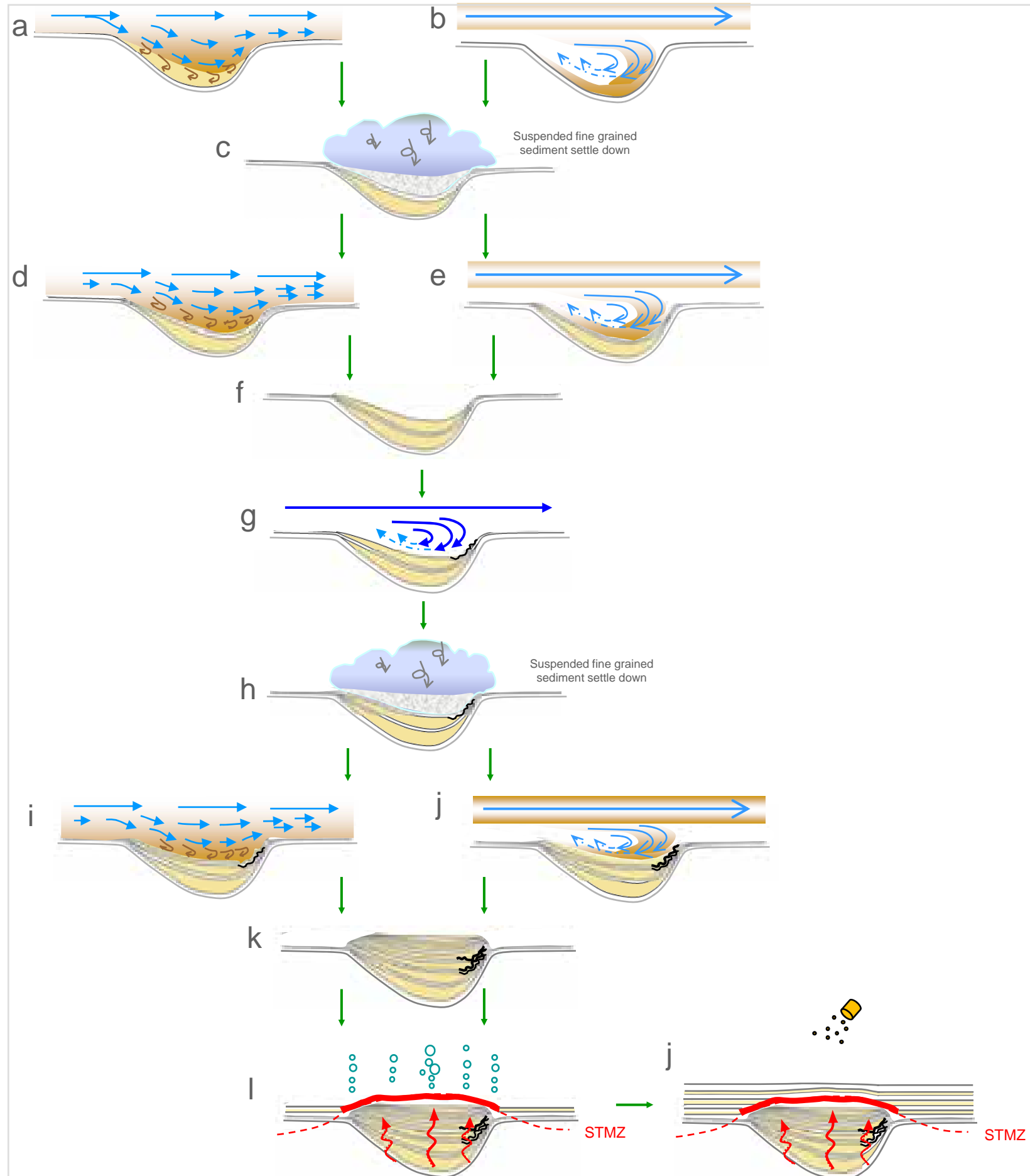
5.6.4.2.2. Formation model of nested pockmarks

The model proposed for the formation of nested pockmark is deduced from the geometry of their infill sequences and is based on the aforementioned observation, as follows: Fine-grained sediments could be transported by different type of bottom currents (turbidity currents or nepheloids, both flowing downslope, or contour currents flowing along the slope). Bottom currents are suggested to undergo flow separation at the upstream rim of pockmark rims and transformed to cavity flow when the currents flowed over the basal craters (Taneda, 1979; Fang et al., 1999; Yao et al., 2000; Brès and Golonius, 2007; Dudley and Ukeiley, 2011). The main branch of the current with higher velocity (Clarence et al., 2002; Zdanski et al., 2003; Camacho and Barbosa, 2005; Brè and Colonius, 2007; Brothers et al., 2011) continued to flow towards the SE while the secondary branch with lower velocity sank into the pockmark (Sinha et al., 1981; Camacho and Barbose, 2005; Podvin et al., 2006). As suggested by the geometries of nested pockmark infill (fig. 5.4a), sediments transported by the secondary branch were apparently deposited on the lee side of nested pockmarks, where the pockmark slopes were more gentle (5° - 10°), while less deposition occurred on the steeper stoss side (10° - 15°).

The curved geometry of nested pockmark infill could result from different flow model of the secondary current inside pockmarks. Depending on the aspect ratio of the basal craters/earliest pockmarks and Reynolds number (defined by velocity, density and travel distance of fluid) (Reynolds, 1883) of the main currents (e.g. Fang et al., 1999; Zdanski et al., 2003), the secondary currents that flowed into the basal crater could be transformed to: 1) stream lines parallel to the pockmarks topography (fig. 5.22a, c, d, f, g, h, i, k) (Fang et al., 1999; Zdanski et al., 2003; Hammer et al., 2009) and 2) vortex flow (fig. 5.22b, c, e, f, g, h, j, k) (Sinha et al., 1981; Higdon, 1985; Fang et al., 1999; Clarence et al., 2002; Zdanski et al., 2003; Camacho and Barbosa, 2005; Podvin et al., 2006; Brè and Colonius, 2007; Dudley and Ukeiley, 2011). Both possibilities have been demonstrated in the numerical modelling results of e.g. Fang et al. (1999) and Zdanski et al. (2003). However, due to lack of oceanographic data and physical parameters, the flow model of current within pockmarks can not be verified. Therefore, two possible flow styles have been proposed below.

For case 1) when a dense, sediment-laden fluid layer flows over the depression, the secondary branch of the currents with lower velocity sinks into the crater along its lee side slope and stream in paralleling to the topography of the crater (Fang et al., 1999; Zdanski et

Figure 5.22. Model for the development of nested pockmarks. In the first step, sediment is deposited by the secondary branch of currents (cavity flows) which is separated from the main branch. Two possible flow models for the secondary currents, which are suggest to deposit sediment in the initial depression (earliest pockmarks): the first one is depression-parallel streaming (a) and the second one is vortex flow (b) Infill sediment was either transported by (a) the laminar, depression-parallel flow from the upstream side of the pockmark, or by (b) vortex and backward flow from the downstream margin of the pockmark; the coarser sediment grains are deposited first at the bottom of the depression. c) During periods of reduced bottom current activity, finer-grained sediment settles from suspension draping the previous infill deposition by hemipelagites. d) Stage (a) repeated after a new layer is deposited. e) Stage (b) repeated. f) Regardless of the depositional process in the previous stage (d or e), the outcome for the infill structure is suggested to be the same. g) During periods of increased bottom current activity, vortices form on the downstream slope of pockmark, inducing erosion. This is evidenced by reflections truncation on the downstream sidewall of nested pockmarks, as shown in figure 5.4. During the erosional event, unconsolidated fine-grained sediment was likely re-suspended by vortices; stage (c) repeated when the bottom current became less active . The pockmark continued to fill (i) and (j) by the same process as in stage (d) and (e) and (c) until all accommodation space was finally be used up. k) The nested pockmark was thus formed, and was sealed by hemipelagic deposits; it showed erosional characters on certain infill layers in the downstream sidewall. l) Formation of methane-related carbonate patches with convex structure which is possibly formed directly above the nested pockmark at the seabed. Hemipelagites deposited only around the methan ebullition. j) The whole pockmark system was buried by hemipelagic sediment afterward.



al., 2003) (fig. 5.22a). According to the numerical experiments of Fang et al. (1999) and Zdanski et al. (2003) this can only happen if the aspect ratio is relatively high (Zdanski et al., 2003) or the Reynolds number is relatively low (Fang et al., 1999). It is suggested that the reduction in current velocity which is induced by separation of bottom current, engenders loss of particles transport capacity which is caused by a small discontinuity in a streambed (Allen, 1970). It would suffice to entrap and deposit (the heavier) particles carried along the vortex current fronts along a streambed (Jopling, 1964; Allen, 1970; Manley et al., 2004). The secondary currents thus likely left deposits on the upstream slope (lee side) of crater (fig. 5.22a, d, i). The bigger, heavier grains e.g. silts could be as a result deposited firstly on the lee side, while the smaller size grains e.g. clay particles were still in suspension within the depression. Deposits are thinner on the downstream side of nested pockmarks (fig. 5.4a; fig. 5.10a). This indicates that the secondary currents had likely lost velocity while flowing up the downstream sidewall, so that less sediment was deposited on the downstream slope of the pockmarks. The infill reflections within nested pockmarks vary in thickness and alternate between negative and positive polarity. It is likely indicated that during periods of lesser activity of the bottom currents, the smaller size grains e.g. mud in suspension draped the layer that was previously deposited by the secondary branch current (fig. 5.22c, h),

Layers on the downstream side wall occasionally appear to be truncated (fig. 5.4a; fig. 5.10a). This indicates that deformation probably happened after the sediment was deposited inside the crater on the stoss side wall (fig. 5.22g). The deformation is suggested to be caused by vortexes that are generated by descents of secondary currents along the downstream pockmark slope (fig. 5.22g). In addition, the episodic appearance of truncation surfaces of downstream depositional sequence suggests the dynamic of bottom currents or activities of fluid seepages vary over the time of deposition.

2) Alternatively, sedimentation may occur inside the pockmark craters directly by reverse flows i.e. vortexes in the negative topography (fig. 5.22b, e, g). Vortexes are engendered by rapid downward flowing water at the downstream edge of negative depressions (Yager et al., 1993; Dudley and Ukeiley, 2011; Kulsri et al., 2007; Fang et al., 1999). Shear stresses induced by friction between backward moving currents and the side wall of the depression sidewall are higher relative to (Sinha et al., 1981; Webster et al., 2004; Haigermoser et al., 2007) the lee side where current flows out (Nowell and Jumars, 1984; Albelson and Denny, 1997; Dudley and Ukeiley, 2011). The reduction in shear stress on the lee side of the depression enhances sediment deposition in the depression (Nowell and Jumars, 1984) while erosion will most likely occur on the stoss side.

The truncations could not be observed every time on the downstream side of infill layers, which suggested that erosion by vortices did not happen during each deposition event that was represented by a single reflection. Thus I think that the infill geometries were either caused by process (1) or by a combination of the two processes (1) and (2), which might co-exist and alternate over time depending on current intensity. As mentioned above, the flow type of the secondary current was likely controlled by Reynolds number of the initial current before it flowed into the depressions. However, in the absence of oceanographic data in this study area, the distinction for the two flow models is impossible.

The lack of reactivation crater in the nested pockmarks did not allow the creation of extra accommodation space as in the case of advancing pockmark arrays, and no cross cutting erosions were observed on the margin of nested pockmarks. After all accommodation space of the initial craters (earliest pockmarks) was filled (fig. 5.22k), the top surface of the pockmark infill outcropped on the palaeo seafloor (fig. 5.4d). This surface shows an annular structure (fig. 5.4d, e). This concentric structure is caused by different generations of depressional infill inside the nested pockmarks.

5.6.4.2.3. Positive high amplitude mounds above nested pockmarks

The positive high amplitude mounds above the nested pockmarks appear to be overlapped by surrounding parallel strata. The top of the mound appears to truncate the underlying infill sequence of the nested pockmark (fig. 5.10a; fig. 5.11a). They have been interpreted as methane-related carbonate mound based on their seismic character (Chapter 4). In the majority of cases positive high amplitude events have a convex morphology (fig. 5.4e) above seeps i.e. nested pockmarks. Hemipelagites do not drape directly over them so it could be interpreted as a diagenetic front at the methane-sulphate transition in sediments close to the seabed. This methane-sulphate transition zone may be pushed upward by the stronger methane flux coming from the middle of the nested pockmarks. By anaerobic methane oxidation coupled with sulphate reduction (see Chapter 1) methane-related carbonates are likely formed along this diagenetic front and which are thus fossilised by the carbonates (fig. 5.22i). This hypothesis could explain the apparent truncations at the top of nested pockmarks, and the overlying reflections onlap on the mounds. However, the seismic resolutions do not allow a further geometric analysis on detailed sedimentary architecture at the location of nested pockmarks, so I am not going to develop more in here.

5.6.4.2.4. The limitation for studying the pockmark depositional model in seismic

Assuming that the hypothesis above is valid, then the formational depth of these interpreted methane-related carbonate mounds raise an issue for the sediment depositional model within and around nested pockmarks. There are two possible interpretations of the timing of the carbonate mound based on how the seismic expression is interpreted. The termination of the parallel horizons against the carbonate mound could be interpreted as onlap and thus date the formation of the creation of positive relief of the carbonate mound.

Alternatively, the inclined edge of the carbonate mound may not be a time horizon of a specific age but rather a local diagenetic front which cross cuts stratigraphy. If this is true then it means the parallel horizons surrounding the carbonate mound are lateral and time equivalents of the infill sequence within the pockmark.

Because the present day SMTZ which controls the formational depth of carbonate mound occurs at less than 50 mbsf in the Lower Congo Basin (Wefer et al., 1998), there is a possibility that the carbonate mound formed on the palaeo seafloor or in sediments immediately below (see Chapter 4). The formational depth of the carbonate mound is determined for the depositional model of nested pockmark infills. If these mounded structures formed on the seabed, and if the flux of methane ebullitions were sufficiently high, then hemipelagites would not be able to drape over the carbonate mound but settle around it forming parallel layers which would onlap against the carbonate mound (fig. 5.22i). Once the methane seepage deactivated the whole venting system was sealed by hemipelagites (fig. 5.22j) as shown by the parallel continuous horizons in the Quaternary interval. However, deposition of mound-shaped progradational infill sequences within the depression has never been reported before and their mechanism of formation remains unclear. This is because of the multiple possible interpretations of the carbonate mound's expression in seismic data and that the vertical resolution prevents the most accurate interpretation.

Alternatively, it is possible that the carbonate mound formed during the Quaternary by which time the nested pockmark had been sealed. The carbonate mound would have formed during deposition of sediments which occur 50 m above its present day top surface. The mound is not formed at the present day because the carbonate mounds occur beyond the present day SMTZ. If it is the case, then the apparent truncations at the top of nested pockmarks could be interpreted as a local diagenetic front related to the SMTZ which now cross cuts the overlying strata. It means the parallel strata surrounding the carbonate mounds

were deposited at the same time as the infill of nested pockmarks (fig. 5.23). However, given the limitations of vertical seismic resolution (~8 m), it is difficult to correlate the surrounding parallel strata above the nested pockmarks with the infill sequence inside the pockmarks (fig. 5.4; fig. 5.11).

Due to the lack of chemical data and the limit of vertical seismic resolution to give a conclusive interpretation on whether the carbonate mound pre-or-post-dates the parallel strata which terminate at its inclined edge. Chemical or core data are probably required to deduce which of these is more likely.

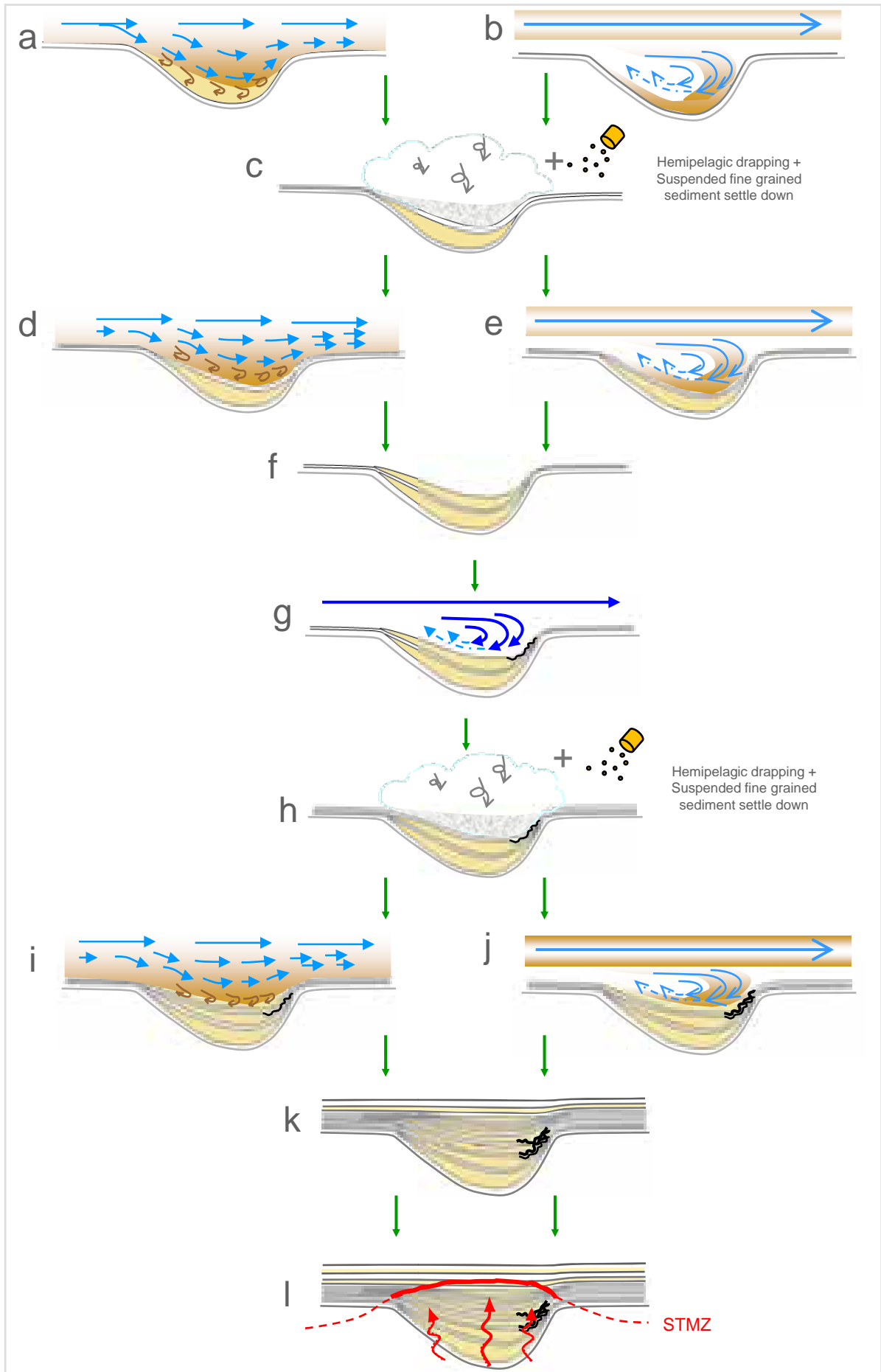
5.6.4.3. Origin of the earliest pockmarks and fluid migration regime

Fluid expulsions above channel complexes and resulting pockmark formation have been discussed in the previous sections. Degassing played an important role in the emplacement of pockmark arrays. Pockmark alignments are suggested to be controlled by the organisation and location of underlying channels. The deflection of the channels around Diapir 1 suggests diapir growth induced positive relief at the sea floor as illustrated by the map of the 6 H horizon (fig. 5.5b; fig. 5.18a). This is also evidenced by the local thinning of the channel units against sediments which overlie the top of the diapir (fig. 3.3 in Chapter 3). Apart from pockmarks, other types of fluid-related structures i.e. gas chimneys, positive high amplitude anomalies also occur along the axis of channel complexes. In the sections below, we are going to discuss the regime of fluid leakage of the channels which are likely indicated by the geometries and the stratigraphic position of these fluid related structures.

5.6.4.3.1. Zigzag pockmark trail 2 above channel complex 2

The earliest craters of the nested pockmark arrays were formed around 5.3 Ma. They are about 80 m deep (5.3Ma) (fig. 5.24) and occur above the faulted crest of the rollover anticline (fig. 5.11). No pockmarks are observed further to the NE along channel complex 2, although the burial of the channel at 5.3 Ma was similar to that of the previous area, around 80 m (fig. 5.24). The main difference between these two locations is that the pockmark-bearing zone overlies a faulted zone while the area devoid of pockmarks is devoid of seismically visible faults. Moreover, several individual pockmark arrays appear to be rooted at the tip of deeper crestal faults. The fact that nested pockmarks occur at the upper tips of

Figure 5.23 Alternative interpretations for the development of the top reflection of nested pockmarks. Notice that hemipelagites deposited also in the far field area of the nested pockmark during bottom current less active period. Steps (a, b, d, e, f) are the same as in Figure 5.22. Steps (c, g, h, i, j, k) with hemipelagites drapped in the far field surrounding the pockmark. (l) Formation of the methane-related diagenetic carbonate patches with convex structure which cross cuts the top of infill sequence and the coeval hemipelagites.



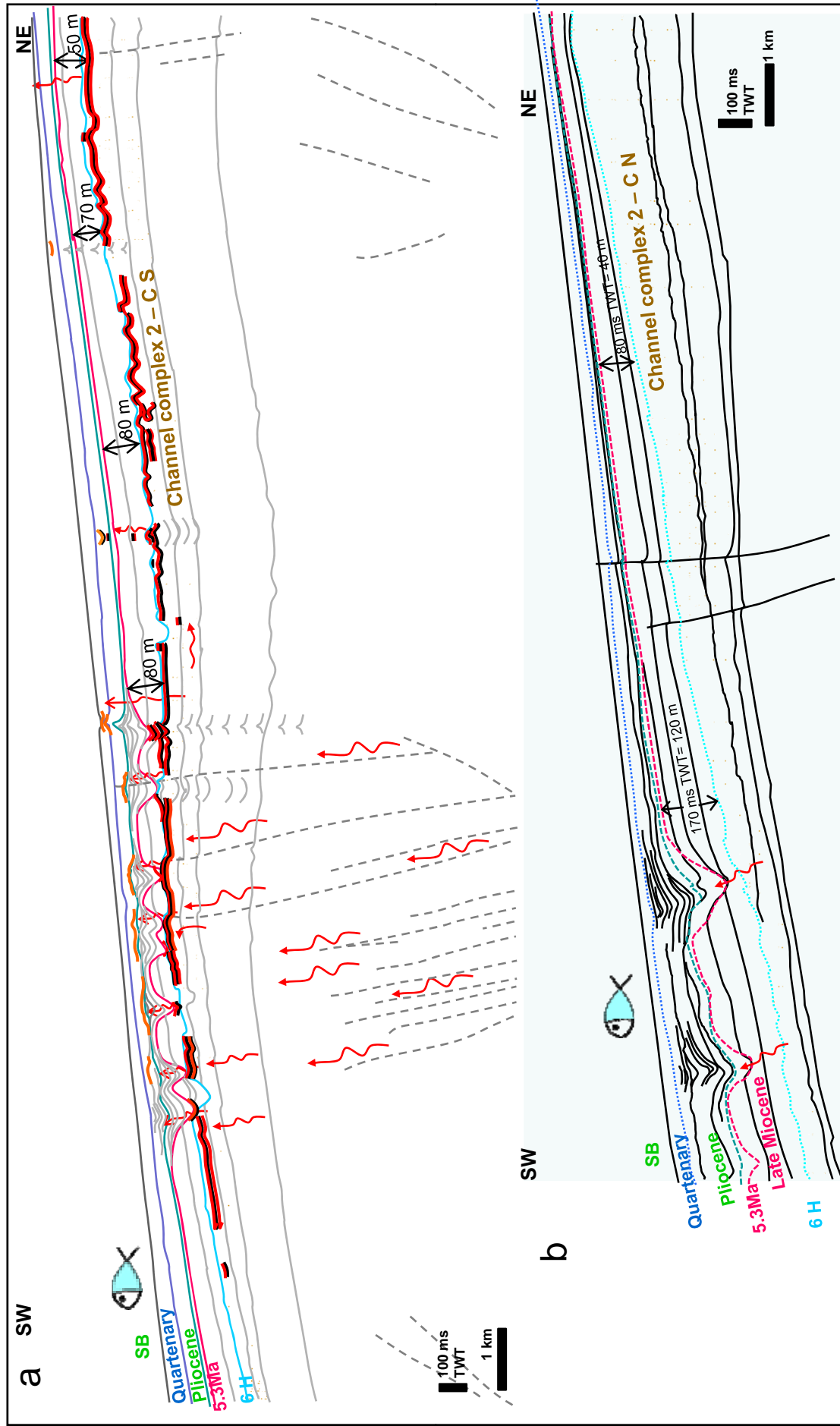


Figure 5.24. Conceptual model for hydrocarbon migration along channel complex 2 and timing of pockmark formation; line drawing of the seismic section in fig. 5.9. a) Nested pockmarks above the north channel (CN) in syncline 1. b) Advancing pockmark arrays located above the individual south channel (CS) on the hanging wall slope. Interpreted fluid migration pathways are indicated by red arrows. Sediment thickness within the interval hosting the earliest pockmarks (basal craters) is indicated on the interpreted sections.

crestal faults of the Anticline 1 and above gas-bearing levees, suggest that gas migrated along the faults up into the levees (fig. 5.19c; fig. 5.24).

The nested pockmark trail that occurs above channel complex 2 was all initiated at the same time. A slow pressure disequilibrium would likely result in the emplacement of one fluid outlet at the weakest point. Instead of that, we observe about 10 pockmarks erupting at the same time along the trail. This is interpreted to indicate that pressure buildup was too sudden for fluid to escape through one single point. Triggering by eustatic change therefore seems unlikely, and a tectonic origin is more plausible. A tectonic pulse is recorded around that time by differential subsidence between Syncline 1 and its margins (see Chapter 3). Seismicity associated with this reactivation and the corresponding activity of the crestal faults is a likely candidate for this trigger, inasmuch as pockmarks develop right above the tips of crestal faults, indicating a likely genetic relationship.

On the NE side of the channel where pockmarks are absent, several chimneys associated with PHAA (interpreted methane-related carbonates) and shallow depressions have been observed above the levees, respectively in the *Pliocene and Quaternary intervals* (fig. 5.24a; fig. 5.25a). Given that, the shallow depressions which occur at the top of these chimneys are linear (fig. 5.15b; fig. 5.18c) instead of circular or conical, they were unlikely induced by intense gas eruption (see Chapter 4) and are thus interpreted as the expression of slow seepages at the seabed. These indicate that slow gas leakages likely happened during the Pliocene and Quaternary in the NE area that is devoid of obvious deep fluid conduits (fig. 5.24a).

The nested pockmark trail ends where the underlying individual channel CS merges downslope into channel complex CN underneath (fig. 5.19a, b, c). It is followed downslope by a trail of advancing pockmarks above the merged channel complex 2 (fig. 5.19a, b, c). The earliest craters of the advancing pockmarks alignment were likely formed within sediment of more than 170 ms TWT (about 120 m) below the palaeo seafloor (fig. 5.24b), and above an individual channel of complex 2 (fig. 5.19a, b, c). The sediment in the host interval of the pockmark arrays becomes thinner and pinches out toward the upstream side of the individual channel CS (fig. 5.24b). No fluid-related features were observed in this interval (Late Miocene) where sediment is thinner than 170 ms TWT.

These may imply that gas seepage was absent from the NE part of this individual channel. Alternatively, 120 m might be a critical thickness for vertical fluid venting. One reason might be that sediment in the latter case had started to be consolidated, with a decline of permeability as proposed by Osborne and Swarbrick (1997). As a result fluid was probably become imprisoned in pores, and pore pressures rise up in the sediment (of > 120 m) until the

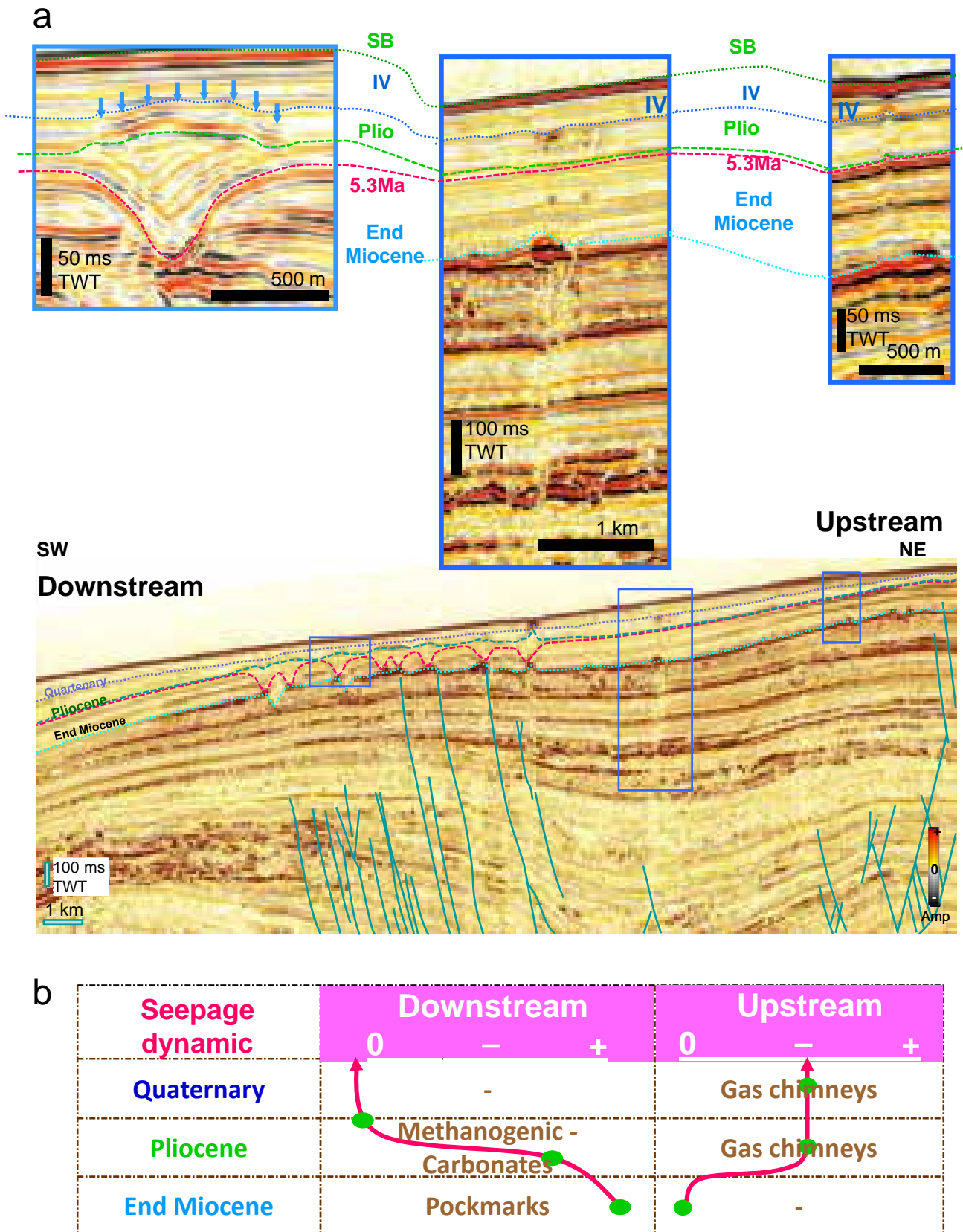


Figure 5.25. Timing of occurrences of vertically stacked fluid venting structures along the upstream side of channel complex 2 (north channel) and further to the NE. a) Up: correlation between nested pockmarks, chimneys and the associated positive high amplitude anomalies (interpreted methane-related carbonates); Down: Stratigraphic distribution of these venting structures along the section in fig. 5.11. b) Summary of the interpreted variations of fluid venting intensity over time, as suggested by the different types of venting structures.

fluid pressure became strong enough to create tensile strength in the sediments (Osborne and Swarbrick, 1997) then induced eruptional craters. It may explain why earliest craters are formed only in the first 120 meters sediment below the palaeo seabed.

The Pliocene

In the Pliocene, seepage is expressed by 1) positive high amplitude mound (interpreted methane-related carbonate) overlying the top of nested pockmarks (fig. 5.2c, 6a) and 2) linear chimneys systems above the levees (fig. 5.11b; fig. 5.15b). Following the interpretation by Roberts (2001) and Roberts et al. (2006) and as explanations given in Chapter 4, these are interpreted to reflect slow or slow-to-moderate fluid venting.

The morphology of carbonate patches mimics the topography of top nested pockmarks (fig. 5.4d), suggested that fluid migrated from the whole pockmark underneath the patches. This may explain the presence of gas chimneys further upstream where were no pre-existing fluid conduits. In the upstream side, fluid was suggested to have accumulated in the levees since at least the late Miocene before it became overpressured. Once fluid pressure overcame the tensile strength of cover sediment, fluids would create their own migration path way (Cosgrove, 1997) i.e. gas chimneys. As stated before, “the final products” of gas vent at the palaeo seabed are linear shallow depression and PHAAs (interpreted carbonates) above gas chimneys rather than circular craters, so the intensity of venting is suggested being slow in the further upstream side of channel complex (fig. 5.25b).

Meanwhile, the advancing pockmarks alignment further downstream in the thicker Pliocene interval show episodic eruptional craters within their arrays (fig. 5.11c; fig. 5.24b). The dynamic of fluid venting was probably higher at locations of advancing pockmarks than in nested pockmarks during the Pliocene, as no circular craters were found above nested pockmarks but methane-related carbonates (PHAAs patches instead).

The Quaternary

In the Quaternary, there are no venting structures above the advancing pockmark alignment and nested pockmark trail in downstream of channel complexes, but there are high-amplitude patches interpreted as methane-related carbonates above the gas chimneys in the upstream areas (fig. 5.15d; fig. 5.18c). Fluid venting was likely deactivated in the downstream

side of channel complex 2 but remained active in the upstream side (fig. 5.25d). The occurrence of interpreted methane-related carbonates in the Quaternary, above the margin of a nested pockmark suggests moderate fluid venting was active at this pockmark location. These quaternary chimneys and this carbonate mound are associated with shallow depressions at the present day seabed (fig. 5.15a; fig. 5.18d; fig. 5.19d), indicating that fluid migration was still going on at these locations.

5.6.4.3.2. Regular linear pockmark trail 1 above channel complex 1

The earliest craters of pockmark arrays are observed within the *upper Miocene* interval along turbidite channel complex 1 (fig. 5.7; fig. 5.26). The earliest craters in the upstream part of channel complex 1 occur in the troughs of sediment undulations (fig. 5.7b, c). Given that, only gas bearing infill are found above the surfaces of attachment points in the “pockmark-trough”, and the surfaces are directly connected to the underlying channel complex. This suggests that gas in the underlying channel might use the surface of attachment as migration paths, which determined the location of earliest pockmarks. Alternatively, the earliest pockmarks may preferentially occur in the trough of undulations because of the smaller thickness of the cover resulting in smaller overburden pressure.

Further downstream, the earliest pockmarks occur almost directly some ca. 50 ms TWT above the channel complex (fig. 5.7; fig. 5.26). It is suggested that fluids migrated directly from the channels below, in contrast to the upstream location. In addition, extensional faults at the crest of Anticline 1 are observed right below channel complex 1 and below several sediment undulations; some of them even intersect the channel complex (fig. 5.1). Methane accumulated inside the channels may have migrated along these faults from the deeper part of the anticline into the turbidite channels which stream through the syncline and the anticline (fig. 5.26).

In the upstream area and close to the location of the major growth fault (fig. 5.7b; fig. 5.26), the thickness of channel complex decreases dynamically while the number of pockmarks decline to zero. A similar situation is likely to happen also in the downstream side, where channel complex becomes thinner below the end of pockmark trail 1 (fig. 5.1). These observations suggested a close relationship between the channel thickness and the distribution of earliest pockmarks. Moreover, the last earliest pockmark in the upstream side above the wedge of channel complex 1 (fig. 5.7b; fig. 5.26), is not associated with negative high amplitude (gas bearing) infill and this location is poor in venting structures. These likely

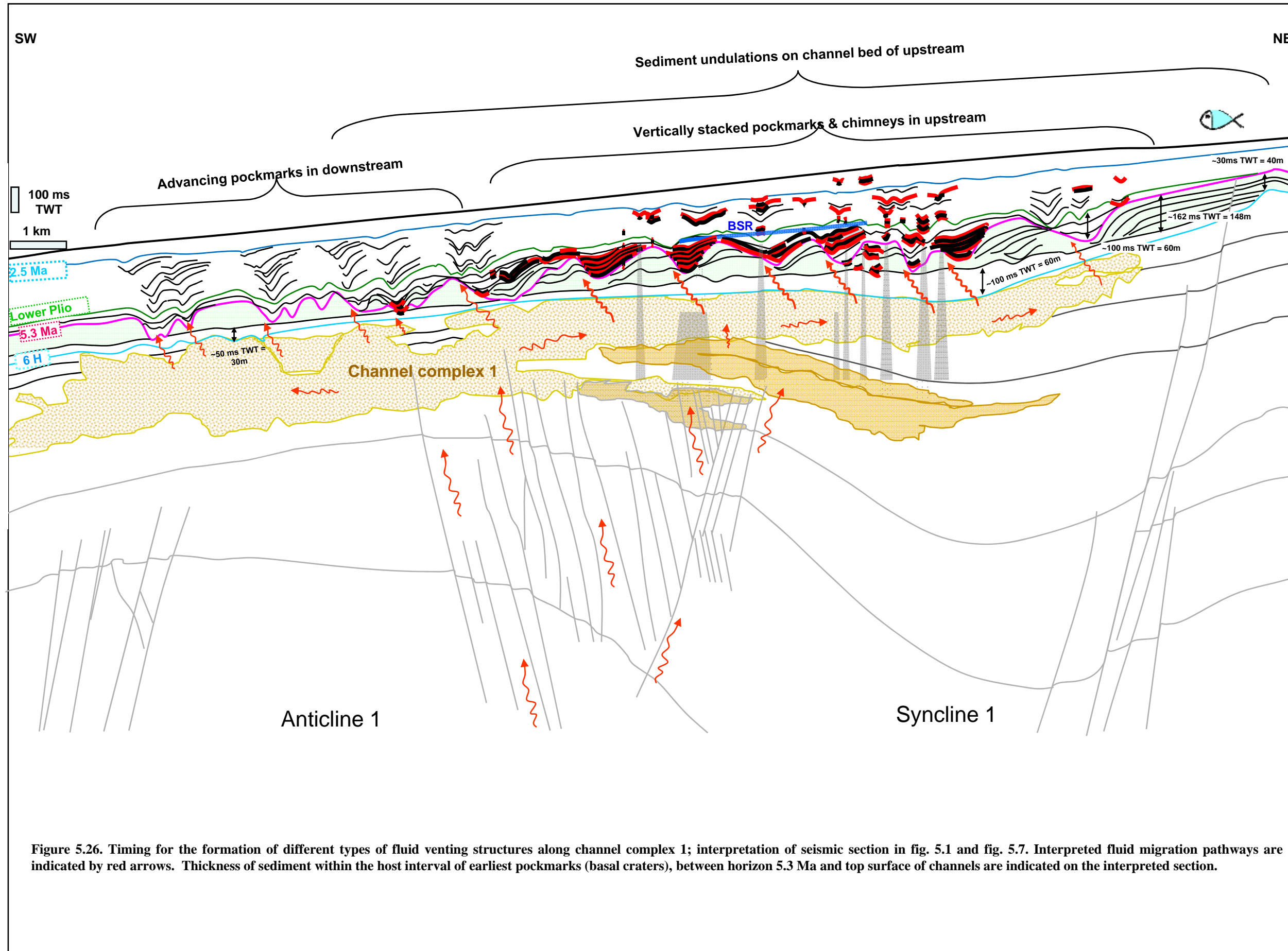


Figure 5.26. Timing for the formation of different types of fluid venting structures along channel complex 1; interpretation of seismic section in fig. 5.1 and fig. 5.7. Interpreted fluid migration pathways are indicated by red arrows. Thickness of sediment within the host interval of earliest pockmarks (basal craters), between horizon 5.3 Ma and top surface of channels are indicated on the interpreted section.

indicate a lower gas column in the upstream part of the channels than in the downstream part. These elements imply that, the thicker the channel complex, the higher gas column and supplies for pockmark formations.

The Pliocene

Vertically stacked and advancing pockmark arrays both developed in the Pliocene.

Vertically stacked pockmarks or shallow depressions associated with chimneys are occurred mainly above the interpreted gas-bearing infill (negative high amplitude reflections) of earliest pockmarks/trough of sediment undulations. Given that vertically stacked pockmarks are smaller (diameter from 200 – 400 meters, with depth < 50 TWT) than the earliest pockmarks (diameter from > 300 to 600 meters, with depth > 100 ms TWT), they are likely to be created by less intense fluid eruptions than earliest pockmarks. So, instead of being induced by rapid fluid expulsion (Hovland and Judd, 1988; Roberts et al., 2006) as the bigger earliest pockmarks, these they are interpreted as the results of episodic moderate-to-fast venting events in this study. Shallow depressions (with diameters < 200 meters and depth < 20 ms TWT) are linear or elongate in plan form indicating slow and slow-to-moderate fluid venting (Chapter 4) (Table 5.1). According to the vertical locations of these venting structures as discussed before (section 5.5.7), especially for chimneys that emanated apparently from the sediment undulations or underlying channels, overpressured fluid likely migrated from the earliest pockmarks or from the underlying channel complex (fig. 5.26).

<i>Types of crater</i>	<i>Diameter (meter)</i>	<i>Depth (ms TWT)</i>	<i>Intensity of venting</i>
Earliest pockmark	> 300 – 600	> 100	Fast
Small pockmark (vertically stacked)	200 - 400	< 50	Moderate-to-fast
Shallow depression	< 200	< 20	Slow-to-moderate
Shallow depression	< 200	< 11	Slow

Table 5.1. Different types of crater and their signification toward fluid flow. Interpreted fluid venting intensity in terms of the size and depth of fluid expulsion crater.

In the downstream side, the alternation between pockmarks reactivation, and sediment drape which composes advancing pockmark arrays indicates episodic rapid fluid expulsion events. The instantaneous phase map of fig. 5.18a indicates the presence of free gas in channel complex 1. The fluid is thus interpreted to come from the channels underneath via the earliest pockmarks. The genesis of advancing pockmarks is discussed in section 5.6.4.1.

The Quaternary

During the Quaternary up to the present day, the combination of a BSR, chimneys and PHAAs (interpreted methane-related carbonates) above the upstream side of buried channel complexes (fig. 5.18c, d) is interpreted to indicate slow seepage.

Negative high amplitudes indicate gas-charged sediment within the earliest craters; in addition, the present day BSR above the sediment undulations (fig. 5.7b; fig. 5.16c) implied that the permeable pathways, the surface of attachment points, are still active at present. The BSR is suggested to be fed by gas migrating from the reservoir underneath via the surface of attachment points. Fluid is likely to be transported upward to the earliest pockmarks and then be trapped underneath the BSR. This could explain why the BSR occurs only above the sediment undulations but nowhere else.

Moreover, shallow elongate depressions observed at the present day seabed above chimneys and vertically stacked venting structures (fig. 5.18d), likely indicate that these venting locations are still active. The situation of channels complex 1 during the Quaternary is very similar to that of channel complex 2, as both are associated with the same types of venting structures in the same intervals. Thus, the upstream sides of channel complex 1 and 2 is likely characterised by slow and slow-to-moderate fluid vents during the Quaternary.

5.6.5. Summary for the chronology of pockmarks formation

In previous sections, we have examined the potential factors (topography, bottom current, fluid vents) which could affect sedimentation within pockmarks. The spatial distributions of different types of pockmarks have been correlated with differences in topography, and the directions of infill migrations are found to correspond to the dipping directions of incline topographies. The relationship above pointed out that interaction between

topography and sediment transport played a crucial role on the geometric development of pockmarks. In the following, a summary is given for the timing of pockmark formation, interactions between pockmark infill, topography and bottom currents.

At the end of the Miocene, earliest pockmarks craters (diameter 300 – 600m; depth 90 – 150 ms TWT) were formed above the two channel complexes of Syncline 1, in the Syncline 3, in the SE corner of hanging wall. The earliest pockmarks provided initial depressional topographies for nucleation of pockmarks arrays. Within the interval between *the top Miocene and intra-lower Pliocene*, sediment infill within the basal craters (earliest pockmarks) of the vertically stacked pockmarks and advancing pockmarks arrays onlap onto the sidewall above channel complex 1 and individual channel CN. Meanwhile the infill sequences of nested pockmarks above channel complex 2 show a slight progradation (fig. 5.2c, 6a). According to the onlap terminations of reflections in the basal craters of vertically stacked pockmarks and advancing pockmarks arrays, sediments were likely deposited in the first place in the craters by low-energy turbidity current (Sangree et al., 1978), and the rest was likely carried out by channel-confined bottom currents toward more distal areas.

In the interval between the *intra-lower Pliocene and the base Quaternary*, advancing pockmark arrays started to develop above the downstream part of both channel complexes on the hanging wall slope (fig. 5.5a, 6b) and right after the demise of nested pockmarks (fig. 5.8). It is proposed that fluids escaped from the underlying gas-bearing channels, through the permeable pathway on the downstream sidewall of advancing pockmarks arrays. The crescentic ruptured area and reactivated craters in the downstream side of advancing pockmark arrays are likely indicated alternation between slow venting and moderate-to-fast venting. Meanwhile, pockmarks were stacking vertically in the upstream area of the first channel complex (fig. 5.5b). As the same time, on the Syncline 1's flanks, slow fluid seepage likely occurred at the contemporary seabed above the top of nested pockmarks. Fluid likely migrated via the whole pockmarks and induced precipitations of mound-shaped methane-related carbonates (convex positive high amplitude reflections) which covered entirely the top of the pockmarks (fig. 5.4a, b). Slow venting also likely happened in the syncline depression above the sediment undulations, as indicated by the gas chimneys which terminated upward into linear or elongate shallow depressions (fig. 5.13). Moderate fluid eruptions indicated by the smaller pockmarks (diameters 200 – 400 m; depth < 50 TWT) with vertically stacked infill (fig. 5.5b) also occurred in the same location. In addition, the vertical aggradation of infill within vertically stacked pockmarks or depressions likely indicate the velocity of bottom

currents at this location was not high enough to modify the geometry of hemipelagic draping as on the slope locations.

Within the Quaternary, deposits above the pockmarks show horizontal bedding and almost all pockmark systems are sealed (fig. 5.5, 6), except in a few locations above the upstream side of channels and at the seabed, where shallow depressions with high amplitude anomalies (interpreted methane-related carbonates) above the vertically stacked pockmarks or depressions. The seabed depressions likely indicate that fluid venting is still active above these pockmark successions (fig. 5.2c, 6a). The well bedded hemipelagites and the absence of particular stratal patterns suggests that bottom currents were relatively calm in the whole study area, and fluid migration was nearly deactivated at most of pockmarks locations.

5.6.6. Implication for petroleum exploration

In the absence of wells or seabed geochemistry data, fluid venting structures can be used for identifying the timing and location of fluid release to the seafloor. As fluid venting structures fossilize the fluid exit at the seabed, their vertical succession records the evolution of leakage pathways over time.

The interpreted gas chimneys on seismic in association with methane-related carbonates (PHAAs) have been shown to be associated with present day hydrocarbon accumulations (e.g. at the levees of channel complex 2 in this survey, and in the upstream side of the two channels complexes). In addition, the evolution of the relative intensity of fluid venting during the formation of a pockmark array can be estimated by the occurrence of methane-related carbonates, gas chimneys and morphology of pockmarks (cf. Roberts, 2001; Roberts et al., 2006). Moreover, the erosions or deformations of infill layers within the vertical successions of venting structures could help to investigate the intensity and recurrence time of fluid venting events at the leakages location (e.g. infill sequences eroded by s and crescentic erosional surfaces point out that the formation of advancing pockmark arrays was multi-phased and caused by episodic venting). Finally, it is important to investigate the infill geometry of venting structures and the possibility of associated permeable stringers. These could act as preferential fluid migration pathways and determine the future emplacement of subsequent venting structures (e.g. the permeable pathways in the downstream sidewall of

advancing pockmarks, and the surface of attachment points of sediment undulations, both of which are interpreted to determine the location of fluid eruption).

5.7. Conclusion

The results of this chapter point out that pockmarks trails are not simply indicating the location of fluid leakage, but their geometry also reflects the interaction between topography and fluid vents. The relationship between fluid venting, topography and geological setting is demonstrated by comparing the mechanism of formation of different pockmark systems. The conclusions for this chapter are the following:

1. Two new types of pockmarks have been described and studied: "Advancing pockmark arrays" and "nested pockmarks".
2. Advancing pockmark arrays are characterised by downslope progradation resulting from asymmetry of the infill on the one hand with thicker deposits on the upslope than on the downslope side, and from the presence of reactivation pockmarks on the other.
 - a. The reactivation pockmarks truncate the downslope margin of underlying infill sequence.
 - b. Distance of horizontal offset between topmost and lowest pockmark apexes is on the order of a few hundred meters.
 - c. Individual pockmark have diameters that vary from 300 to 600 meters, and depth of several tens of ms TWT.
 - d. Advancing pockmark arrays occur mainly within PF tier and the parallel horizontal bedding within PF tier.
 - e. Heights of advancing pockmark arrays ranges from 130 to 350 ms TWT.
 - f. Some advancing pockmarks develop through Quaternary sediment up to the present day seabed.
 - g. Advancing pockmarks occur only on the slope and above palaeo channel complexes 1 and 2.
3. Nested pockmarks are an intermediate form between advancing pockmarks and vertically stacked pockmarks.

- a. They are characterized by a series of conical infill layers which fit inside the basal craters and have apexes slightly prograding along the slope of Syncline 1.
 - b. The infill layers are not laterally continuous into the far field and often onlap against the basal crater margin or against the sidewall.
 - c. The basal craters have diameters ranging from about 300 to 600 meters.
 - d. The height of nested pockmarks ranges from 40 to 160 ms TWT.
 - e. Nested pockmarks occur on the syncline shoulder and develop above the levees of channel complex 2.
4. Advancing pockmarks, nested pockmarks and vertically stacked pockmarks form two pockmark trails above the two channel complexes 1 and 2.
 - a. Vertically stacked pockmarks line up above the upstream part of channel complex 1 above the center of the syncline where the topography is relatively flat (dip $< 1.5^\circ$).
 - b. Vertically stacked pockmark arrays develop above the syncline, above the troughs of sediment undulations confined by a channel.
 - c. Nested pockmarks occur above a channel levee overlying tectonic faults in the upstream part of channel complex 2. Channel complex 2 is stream along the shoulder of synclines (inclination about 2°).
 - d. Advancing pockmarks occur along the downstream part of channel complexes 1 and 2 on the regional slope (inclination about 3°).
 5. The morphology of the hanging wall slope in combination with the depressional topography of earliest pockmarks has an important local impact on the bottom currents flow model.
 6. Fluid eruption controls the creation of pre-existing pockmark topography on seabed which in turn controls the location of sediment accumulation.
 7. The lateral migration of pockmarks results from the interplay between fluid venting and generation of local depressions in the sediment surface, and the perturbation of bottom-water currents within the depression.
 8. Bottom current dynamics and seepage within pockmarks in addition with topographic depressions modified sediment deposition. They had a direct impact on the vertical communication of different layers in pockmark systems as the varying degree of grain size was likely to control permeability.
 9. The infill sequences of nested pockmarks resulted mainly from the interaction between bottom currents and depressions at the seafloor. The geometry of pockmarks is

interpreted to have caused flow separation at the upcurrent margin of each pockmark, resulting in the emplacement of vortex in the pockmark.

10. Advancing pockmark arrays record the palaeo-activity of fluid movements, which in this study is envisaged as a combination of bottom currents and subsurface seepage at the palaeo-seabed.
 - a. Episodic venting is reflected by successive generations of reactivated advancing pockmark craters. Fluid venting is interpreted to cause discontinuities of pockmark infill.
11. Fluids in deeper interval were likely remobilized along tectonic faults during tectonic pulses and accumulated in channel complex 1 and the levees of channel complex 2.
12. Buried channels and tectonic faults are suggested to act as conduits for fluid flow.
13. Hydrocarbon leakage occurred above the two palaeo-channel complexes as indicated by the occurrences of two pockmark trails.
 - a. Basal crater/earliest pockmarks developed above the troughs of sediment undulations developed above turbidite channel complex 1.
 - b. High amplitude reflections within primary pockmark craters above the troughs of sediment wave, are capped by a BSR, and are interpreted as gas bearing.
 - c. Gas-bearing levees in the upstream location of channel complex 2, and underneath nested pockmarks, are cut by tectonic faults suggesting that these promoted gas migration from deeper down.
 - d. Advancing pockmarks occur above the channel bed in the downstream part of both channels complexes, suggested overpressured fluid originated from the underlying sandy channel fill.
14. Degassing occurred along the two channel complexes was likely during the reactivation of Syncline 1 round 5.3 Ma (Messinian), which resulted in the formation of earliest pockmarks craters (diameter 300 – 600m; depth 90 – 150 ms TWT).
15. At the beginning of Pliocene, infill event in basal craters/earliest pockmark along two channel complexes, and nested pockmarks were formed.
16. During the Pliocene, in the center of Syncline 1 and in upstream part of channel complex 1, pockmarks with vertically stacked infill occurred above earliest pockmarks and sediment undulations. These vertically stacked pockmarks have smaller diameters (200 – 400 m; and depth < 50 ms TWT) and are interpreted as the expression of moderate-to-fast venting.
 - a. The sediment undulations likely acted as fluid migration pathways. This interpretation is suggested by the present day BSR and negative high amplitude infill, which are

interpreted as gas-bearing infill underneath the BSR and occur only above the surface of attachment points of the sedimentary structures.

- b. Fluid migrated slowly with occasional slow-to-moderate episodes of fluid expulsion, as indicated by the gas chimneys which terminate upward into interpreted methane-related carbonate mounds and elongate shallow depressions.
 - c. At the same location and above the second channel complex, fluid continued to migrate very slowly through nested pockmarks from the underlying turbidite channels, as suggested by the methane-related carbonate patches at the top of nested pockmarks.
 - d. On the hanging wall slope, slow and moderate-to-rapid fluid eruptions occurred occasionally in the downstream sidewall of advancing pockmarks arrays. It is indicated by the crescent-shaped erosions and reactivation craters within the arrays above the two channel complexes.
17. During the Quaternary, fluids continued to migrate slowly in the upstream part of both channel complexes, through the gas chimneys that terminate upward into shallow linear or elongate depressions within the Quaternary interval or at the seabed.

CHAPTER 6

FOCUS FLUID FLOW SYSTEMS IN INTERPLAY WITH GEOLOGICAL SETTING, TECTONIC STRUCTURES AND STRESS FIELDS

**DIVERSITY AND MORPHOLOGY OF FLUID VENTING
FEATURES IMPACTED BY ARCHITECTURE OF CENOZOIC
SEDIMENTS ON THE ANGOLA MARGIN**

6.0. Focus fluid flow systems in interplay with geological setting, tectonic structures and stress fields

Diversity and Morphologies of fluid venting features impacted by architecture of Cenozoic sediment on the Angola margin

6.1. Abstract

This study has investigated the role that; 1) tectonic structures and the surrounding stress field, and 2) variations in petrophysical properties of sediments have on fluid flow in subsurface. High resolution 3-D seismic data from the Lower Congo Basin, Offshore Angola provided the main data source for this study. The seismic data reveal that fluid venting structures in the Neogene-Quaternary stratigraphy are associated with particular types of geological structures. In particular, linear chimneys and linear positive high-amplitude anomalies (PHAAs) which are interpreted as methane-related carbonates occur in regions deformed by salt-withdrawal and where polygonal faults (PFs) are anisotropic rather than isotropic as is typical. A complex network of linear PHAA's hosted within a hemipelagic unit evolved upward into shallow depressions and pockmarks within mass transport complexes (MTCs). Pockmarks that grew from beneath MTC's and developed within the overlying polygonally faulted intervals have a polygonal planform geometry rather than circular.

Linear chimneys which are aligned parallel to the strikes of preferentially aligned PFs nucleated at their basal tip or along the lower part of the polygonal fault and propagated vertically upward through their hanging walls. The fluid pressure is thus interpreted to have been strong enough to only open the lower part of the PF and not the entire fault plane. Free gas accumulated in a fault bound trap in the lower part of the polygonal fault footwall. Overpressure attributed to gas accumulation caused fluid leakage and nucleation of hydraulic fractures in such locations. Therefore, polygonal faults define locations of overpressure and fluid leakage. I argue that fractures probably propagated vertically in the hanging wall and laterally parallel to the strike of the adjacent polygonal fault. The parallel alignments of these

fractures with respect to adjacent 'anisotropic' polygonal faults and tectonic faults suggest their geometry was controlled by a perturbation in the regional stress state. Perturbations of the regional state of stress were probably controlled by local tectonic stresses associated with salt withdrawal and salt diapirism. As a result, the plan form geometry of these fractures were linear and aligned parallel to the intermediate principal stress of the local and regional anisotropic stress field.

Methane gas preferentially migrated along linear fractures within the hemipelagic units. The change from fine-grained sediment to more heterogeneous MTCs affected the style, rate and direction of fluid flow. This changed the style of fluid invasion from vertical fracturing in fine-grained matrices into collapsing of weakness planes or defects in the anisotropic fabric environment within MTCs.

Edges of pockmarks and depressions less than 12ms TWT deep and with slope dipping less than 4.6° from horizontal are intersected by isotopically arranged PFs. Pockmarks with greater depths and slope inclinations are sub-circular in shape and are not deformed by PFs but rather surrounded by curving, anisotropic PFs. These indicate the state of stress anisotropy in sediments of deep pockmarks was strongly perturbed from the regional stress state than shallower pockmarks. The strikes of PFs were perturbed by this local stress anisotropy forming aligned fault arrays. The studied results suggest that pockmarks greater than 12 ms and with slopes inclinations greater than 4.6 degrees is the sufficient threshold value to induce enough stress anisotropy to preferentially align polygonal faults.

6.2. Introduction

The use of fluid flow features as indicators of fluid migration pathways, reservoirs, and timing of leakage have been widely recognized and investigated worldwide (cf. Hovland and Judd, 1988; Heggland, 1997; Judd and Hovland, 2007). The morphology and size of fluid flow features have been used to infer the intensity of fluid expulsion on the palaeo-seafloor (Robert 2001; Roberts et al., 2006). The study of fluid venting structures in 3D seismic can provide a powerful tool for making preliminary risk evaluations for leakage sites in future exploration areas. In addition, frequency of hydrocarbon leakage from buried reservoirs has been inferred from vertical successions of venting structures (Roberts and Carney, 1997). Thus, the dynamics of fluid expulsion and variations in flux rates over time can be determined by studying the expression of fluid flow.

Thrasher et al. (1996), Andersen et al. (2011), Andresen et al. (2012), Macelloni et al. (2012) and Ilg et al. (2012) have recently demonstrated the potential of venting structures in reconstructing fluid migration pathways in sedimentary basins. However, variations in seepage intensity over time were not considered. Studies focusing on the spatial relationship between the formation of specific types of venting structures and their distribution above specific geological features are lacking. Numerous publications have reported that the leakage of fluid from the subsurface and development of subsequent venting structures are associated with or controlled by tectonic structures such as faults (Robert and Carney, 1997; Gay, 2006; Løseth et al., 2009; Plaza-Faverola et al., 2012), polygonal faults (Gay, 2006; Løseth et al., 2009; Plaza-Faverola, 2012), rotated blocks (Løseth et al., 2009; Hustoft et al. 2010; Plaza-Faverola, 2012), triple junction of faults (Gartrell et al. 2004), crestal faults above diapirs (Macelloni et al., 2013), salt structures (Robert and Carney, 1997; Thrasher et al., 1996; Gay, 2006), folds (Eichhubl, 2000), accretionary prisms (Moore et al., 1990), basin edges (Thrasher et al., 1996), the edge of continental margins (Hill and Driscoll, 2004), and sedimentary features such as; deep buried channels (Gay, 2006; Naudts et al., 2006; Pilcher and Argent, 2007), contourite mounds (Hustoft et al. 2010), crests of sedimentary ridges (Naudts et al., 2006), sedimentary wedges (Hjelstuen et al., 2009). Nevertheless, the geometrical variations, evolutions and development of fluid venting structures have not been integrated with fluid flow histories.

Two types of fluid flow features cross-cut stratigraphy and occur at the present day seafloor. These include sand injectites and extrudites and seismic chimneys. Both have been discussed previously by Moore et al. (2007), Hustoft et al. (2010) and Moss (2011). Moore et al. (2007) suggested that the local stress states induced by the formation of geological structures can affect the geometry and orientation of sandstone injectites. Just as some fault sets can be used to infer the palaeo state of stress, the studies discussed above suggest that fluid venting structures may also be used as palaeo-stress indicators. Hustoft et al. (2010) and Moss (2011) were the first studies to comment on the aspect ratio of a seismic chimney's plan form and suggested that high aspect ratios were related to the local stress field of deeper tectonic structures. Furthermore, Hustoft et al., (2010) suggested that preferred orientations of the long axis through an elongate chimney's plan form were caused by local stress perturbations associated with of tectonic structures.

On the other hand, Roberts and Carney (1997) were pioneers in bringing the association of fluid flux rates of modern seepages, which were expressed by different venting structures (Roberts, 2001; Robert et al., 2006), with specific tectonic settings (Roberts and Carney, 1997). However, these aforementioned case studies remain the studies of fluid flow

structures only at the present-day-seabed and today no studies have applied these same analyses on buried fluid venting structures. This is probably due to the limited seismic coverage and quality of data. Furthermore, there are no studies which have attempted to; 1) reconstruct temporal and spatial variations in the rate and style of fluid venting and 2) understand how lateral and vertical variations in sedimentary units, tectonic structures and the local stress state influence fluid migration. For the first time, we undertake an integrated analysis of fluid migration with incorporation of all elements mentioned above. Previous works of Roberts and Carney (1997), Roberts (2001), and Roberts et al. (2006) provide a platform for this chapter in which we establish if palaeo fluid flow structures can be used to reconstruct spatial and temporal variation in the intensity of fluid venting in the Lower Congo Basin. In this study area we observed that each specific type of venting structures occurred as local populations above particular geological structures. This implies that the local geological setting plays a role in the history of fluid venting.

It has been noticed that active or buried fluid venting structures i.e. seismic chimneys, conical pockmarks, circular depressions, seismic expressions of methane-related carbonates and anisotropically arranged polygonal faults in this surveys were aligned parallel to underlying and surrounding geological structures. The parallelism between different fluid venting features and the geological structures, especially anisotropically arranged polygonal faults implies that geological structures and their associated stress field play an important role in fluid flow and the development fluid venting structures. Halokinesis (salt flow) has strongly impacted the sedimentary architecture of the study area (Total internal reports; Phillippe, 1999; 2000; Grauls, 2000) with the development of salt withdrawal basins and domes which affected sediment accommodation space. Salt diapir rise and fall which caused extensional faulting. In this study we find evidence that the local stress field attributed to salt movement played an important role on the 3D geometry of fluid venting structures.

Linear fluid venting structures that occur within fine-grained hemipelagic units have also been observed to be disrupted by mass transport deposits (MTDs). They evolved into shallow pockmarks/depressions within the interval of mass transport complexes (MTCs).

In this chapter I demonstrate also how variations in sediment deposition (Robert and Casery, 1997), changes in lithology, physical behaviour and rheology of sediments impact fluid migration (Jain and Juanes, 2009) and pathways (Robert and Casery, 1997). This topic is going to be discussed in detail with a new example.

The aims of this study are; 1) to report and describe new types of fluid venting structures which we call “filamental / linear” positive high amplitude anomaly (networks) and “honeycomb pockmarks” that are linked to the spatial-temporal distribution of polygonal

faults, 2) illustrate that the local tectonic and sedimentary setting has affected the geometry of fluid venting structures, 3) to introduce a new method to reconstruct the dynamics of fluid leakage at the palaeo-seabed during the basin evolution by using different type of venting structures as indicators of fluid venting intensity, 4) to integrate the classification of venting structures established previously by Robert (2001) and Robert et al. (2006) into this research and develop a new one based on the venting structures occurring in this study area.

6.2.1. Filamental and linear positive high amplitude anomalies (PHAAs)

Seismic chimneys or acoustic pipes are commonly characterised by amplitude dim-zones on seismic horizons (Ligtenberg, 2005; Heggland, 2005; Hustoft et al., 2007 and 2010; Petersen et al., 2010; Løseth et al., 2009 and 2011; Moss and Cartwright, 2010a, b; Ilg et al., 2012). They exhibit circular- to sub-circular plan form geometries (Hustoft et al., 2007 and 2010; Petersen et al., 2010; Løseth et al., 2009 and 2011; Moss and Cartwright, 2010a, b). Vertical seismic chimneys which have linear-shaped dim zones on horizons and which are aligned parallel to strikes of polygonal faults were first reported and interpreted as linear fluid conduits (see Chapter 4). The morphology of seismic chimneys play an important role on fluid flow studies as they indicate how fluid invades their host rock and where it breaches a seal.

Filament-like, clustered or individual linear PHAAs with negative depressions which have developed along the strike of PFs were first reported and were interpreted as methane-related carbonate in this thesis (see Chapter 4). They were found in a Neogene-Quaternary aged interval containing fine grained sediments in the Lower Congo Basin. Similar types of linear, positive high-amplitude anomalies hosted within a Miocene aged interval of fine-grained sediments were documented in an earlier internal study of Total S.A. by Cartwright and Huuse (2006) who found that the anomalies cluster and define broad networks. These networks are composed of interconnecting-to-individual, linear anomalies with high positive amplitudes or are linked with sub-circular-to-elongate anomalies in some cases. They have been termed “filamental anomalies” (Cartwright and Huuse, 2006). Because of the morphological and geophysical similarity between these filamental anomalies (Cartwright and Huuse, 2006) and linear anomalies (Chapter 4) they are re-examined in detail in this study. Both types of anomalies have the same range of depths and dimensions. They are often developed above or along extensional faults (either tectonic or compaction in origin) and are

typically elongated parallel to fault strike. “Filamental anomalies” observed by Cartwright and Huuse (2006) are same as the “linear PHAAs” studied in Chapter 4. Unlike the non-published study of Cartwright and Huuse (2006) the linear PHAAs in this study are not restricted to the Miocene strata but in strata of various ages and can be found at depths as shallow as few milliseconds beneath the present sea floor. Therefore, we strongly suggest that regardless of the ages of intervals in which positive high amplitude anomalies occur, if they have similar geometrical, morphological and geophysical characters such as: 1) filamental or linear shapes (with aspect ratios of 1:4), 2) exhibit negative relieves, 3) expressed as positive, high-amplitude reflections and 4) are associated with faults; then these anomalies are correspond to the “filamental” and “linear PHAAs” as termed by Cartwright and Huuse (2006) and in Chapter 4.

6.2.2. Distinction between shallow flat-bottomed depressions and conical pockmarks

Venting structures typically exhibit a range of aspect ratios in their plan-form dimensions which range from circular (aspect ratios of 1), elongate (aspect ratios of 1:2) and linear (aspect ratios of 1:4). Fluid venting features that display elongate, oval or sub-circular planar forms have been classified into two types of depressions: 1) flat-bottomed which are often shallow; and 2) conical. Fluid venting structures with depressions which have flat bases are typically 5 to 11 ms (TWT) deep. This range of depths are close the limit of vertical resolution of seismic reflections. The significance of these shallow depressions for fluid venting are interpreted to reflect a seepage spectrum between slow and moderate seepage rates (Roberts 2001a, b, Roberts et al., 2006).

Conical depressions are so called V-shaped pockmarks based on their downward-conical geometry in cross section (King and Maclean, 1970). Their depths are typically more than 12 ms TWT in this study area and are not comparable with flat-bottomed depressions. In general, two sub-types of pockmarks are distinguished in this survey based on their range of depression depths. Pockmarks with depths less than 25 ms TWT usually have diameters less than 250 m while pockmarks with depths of several tens meters are often larger than 250 m in diameter. They are interpreted to have formed by moderate-to-fast and fast fluid venting rates respectively (cf. King and Maclean, 1970; Pantin, 1980; Hovland and Judd, 1988; Hovland and Judd, 2007).

A vertically stacked succession of amplitude anomalies with negative reliefs can comprise conical pockmarks and shallow flat-bottom depressions. Such depressions are observed in the footwall domain and in a polygonally faulted (PFs) interval within the hangingwall domain which I describe in section 6.5.13.4 and 6.5.13.6. In order to facilitate the description of different types of circular depressions which occur within the same vertical succession on seismic sections but are not distinguishable on same horizons, I simplify the nomenclature in the following sections and term all fluid venting structures with circular-shaped depressions as pockmarks.

6.3. Seismic data and methodology

The two seismic surveys of Offshore Angola that are discussed in Chapter 2 are used in this chapter. The biggest survey covers 1310 km² and envelops the smaller one of 530 km². Methods relating to seismic attribute analysis of constituent reflections of fluid venting structures, on whose seismic characters and shape can be found in Chapter 2.

All polyphased or multiphased fluid venting structures with complex organisations are all located within the seismic survey with the higher resolution and have been mapped manually. They have been examined in both seismic surveys in 360° on seismic sections. Some fluid venting structures without complex geometries i.e. vertically stacked pockmarks and seismic chimneys were not covered by the higher resolution survey. Since these venting structures have a simple morphology which can thus be compared with those in the higher resolution survey, and the display of their geometry on seismic sections, their interpretation and visualisations have not been affected due to the coverage by different seismic surveys. Both seismic surveys have a similar range of dominant frequency i.e. 55 – 60Hz for the higher resolution one and 70 – 80Hz for the main one.

6.3.1. Statistic of linear seismic chimneys at different position along polygonal faults

Vertical seismic chimneys are referred to columnar acoustic disturbed zones on seismic sections and have been counted manually. Their downward terminations emanated from different positions along polygonal fault plane were examined one by one on inline and crossline seismic sections of chimneys. The number of different positions at which chimneys

are terminated downward at polygonal faults have been analysed by plotting graph using Microsoft Excel.

6.3.2. Measurements of the depths and diameters of pockmarks and calculation of sidewall inclinations

The diameter and depth of all pockmarks in a selected pockmark field have been measured and mapped. The inclination of pockmarks sidewalls in seismic data can only be obtained by indirect method as the studied survey is in time and has not been processed into depth. As the seismic survey is in time, the velocity model for conversion of data from time to depth has an impact on the dip calculations. Therefore, in order to ensure correct values for sidewall inclinations are obtained a series of velocity values for depth conversions have been used. The calculated results have been controlled by comparing each series. The sidewall inclination of pockmark craters have been calculated from their radius and depths by an equation of tangent trigonometric function:

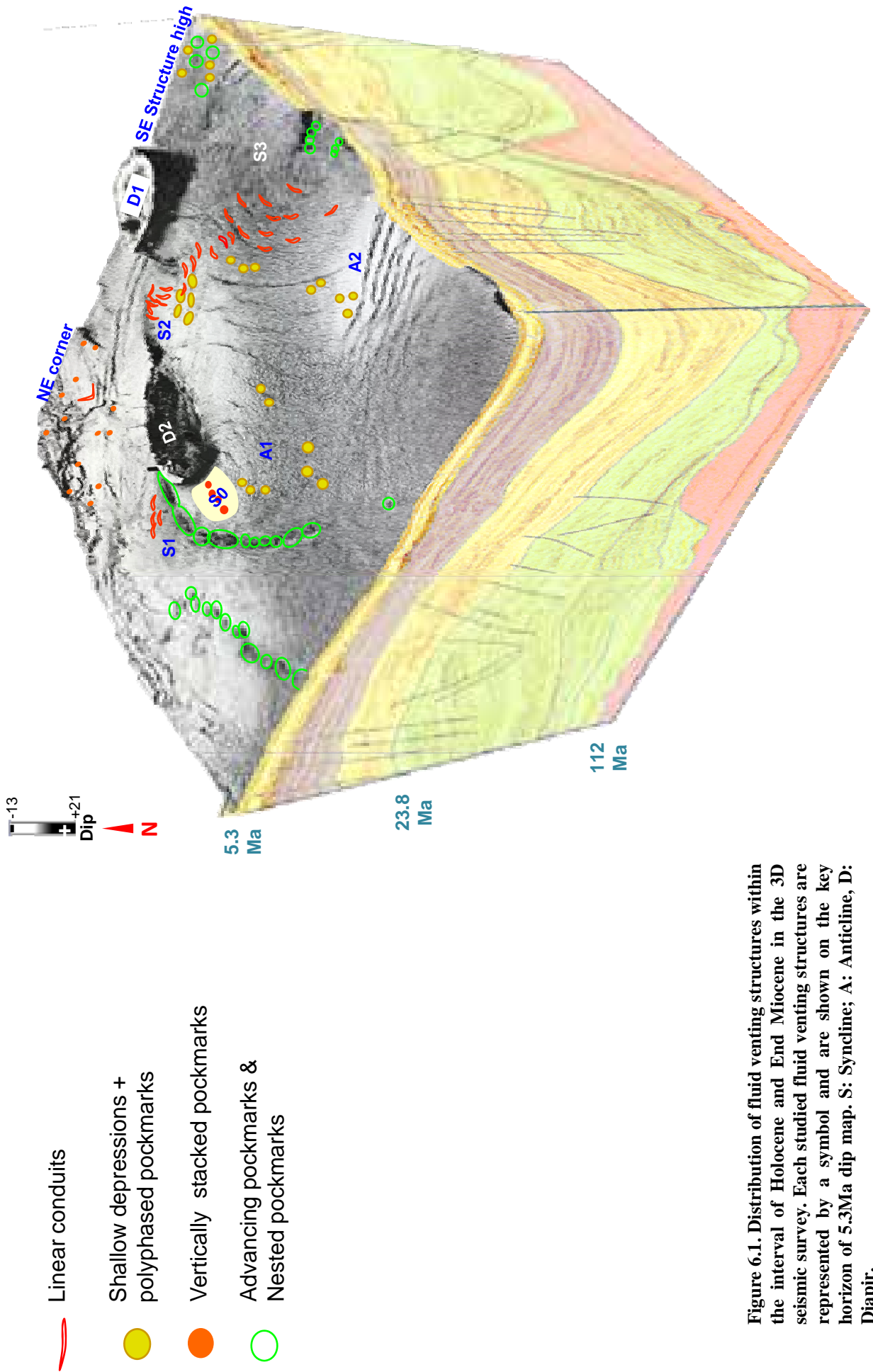
$$90^\circ - \{[\text{ATAN} * (\text{radius in meter} / \text{depth in meter})] * 180/\text{PI}\}$$

In order to obtain the most accurate dip values for sub-circular craters, the longest and shortest axis of pockmarks have been measured and used to calculate the sidewalls dip. To validate the results, inclination values of sidewalls have been double checked on the seismic data which has been converted afterward into depth with only one velocity model, by using a digital function of manual dip measurement. Finally, ellipticity indices of these studied pockmarks have also been calculated as the ratio $L_{\text{axis}}/S_{\text{axis}}$ between the shortest axis (S_{axis}) and the longest axis (L_{axis}).

6.4. Structural geology of the study area

6.4.1. Report of local geological structures in the studied surveys

The geological context and lithology of the study area is given in Chapter 3. The main tectonic structural and fluid venting structures distribution in the studied area is summarized








-  Linear conduits
-  Shallow depressions + polyphased pockmarks
-  Vertically stacked pockmarks
-  Advancing pockmarks & Nested pockmarks
-  Nested pockmarks

Figure 6.1. Distribution of fluid venting structures within the interval of Holocene and End Miocene in the 3D seismic survey. Each studied fluid venting structures are represented by a symbol and are shown on the key horizon of 5.3Ma dip map. S: Syncline; A: Anticline, D: Diapir.

6.5. Results and interpretations

Different types of fluid venting structures in the study area are summarized in Table 6.1 which shows their relationship with the geological setting in which they developed. There are three groups of venting structures which possess sub-circular to linear plan form geometries namely; 1) linear chimneys and linear PHAAs, 2) sub-circular/elongate pockmarks or shallow depressions and 3) carbonate mounds. Given that carbonate mounds have already been widely studied they are not the focus of this study.

6.5.1. Description and seismic interpretation of fluid venting structures

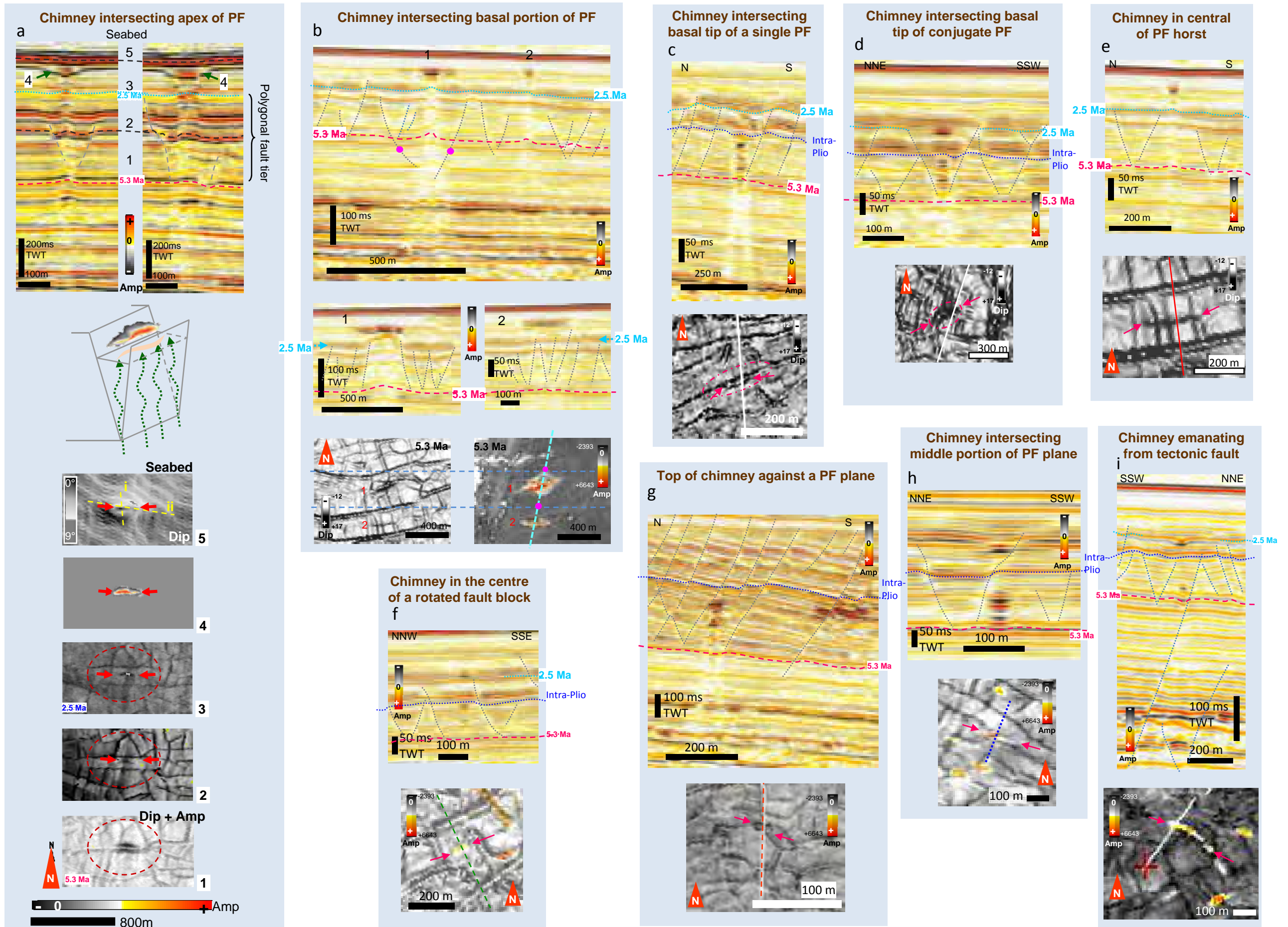
6.5.1.1. Linear chimneys and associated high amplitude anomalies (HAAs)

All linear fluid venting structures in this survey are parallel to strikes of normal faults or follow major trends of anisotropically arranged polygonal fault networks (PFs). For the most part linear venting structures they occur in the polygonally faulted intervals, however a network of linear anomalies have been observed in the Middle Miocene aged fine grained units which are devoid of polygonal faults. Linear chimneys (see Chapter 4) are usually expressed as columnar zones of acoustic perturbation in seismic data and linear low-amplitude zones of several tens-to-hundred meters on horizon attribute maps. They often terminate upward into: 1) linear PHAAs with shallow negative reliefs of about 3 – 5 ms TWT and have similar lengths (hundred meters) as linear conduits do (Chapter 4); or 2) negative high amplitude accumulations.

The first type of linear conduits are characterised by pull-up seismic effects. The linear conduits terminate upward into linear PHAAs. These linear PHAAs are composed by one or several vertically stacked seismic wave lobes of peak over trough. They are interpreted as methane-related carbonates potentially in association with gas hydrates when located within gas hydrate stabilization zones (Chapter 4). The linear chimney and linear PHAA form a vertical linear venting system (cf. fig. 6.2a) (Chapter 4).

The second type of linear conduits that are characterised by negative, high amplitude columns or bright spot are often associated with push-down seismic effects (fig. 6.2c) and are

Figure 6.2. Examples of chimneys intersecting and emanating different parts of PF's. The plan for dimensions of the chimney are shown on maps below each section. a) Zoomed seismic sections intersecting the short (left panel) and long (right panel) axis of linear chimneys. Note that the chimney intersects the apex of the underlying PF graben as illustrated in cartoon below. Horizons labelled 1-5 are amplitude and dip maps showing the plan form geometry of the chimney at different stratigraphic levels (see labelled on sections in a). b) Seismic section showing chimney intersecting the basal portion of a conjugate PF. Zoomed seismic sections below intersect the long axis of chimneys 1 and 2 in b. c) Zoomed seismic section showing linear chimney emanating from basal tip of single PF (see underlying map for location). d) Zoomed seismic section showing bright amplitude column intersecting centre of conjugate PF graben. e) Zoomed seismic section showing chimney intersecting PF horst block. f) Zoomed seismic section showing chimney intersecting the centre of a rotated fault block. g) Zoomed seismic section showing chimney terminating abruptly upwards against a PF plane. h) Zoomed seismic section showing chimney intersecting middle portion of PF plane. i) Zoomed seismic section showing chimney emanating from a deep-seated tectonic fault.



interpreted as conduits that contain free gas (cf. Coffeen, 1986). 209 linear seismic chimneys have been identified in the polygonally faulted interval. Many of these chimneys intersect polygonal faults but can be divided into different groups based on their position. These intersection positions include 1) intersection between conjugate PFs (Chapter 4), 2) the lower part to the base of a conjugate PF (fig. 6.2b), 3) the bottom of a single PF (fig. 6.2c), 4) the centre of the horst or rotated blocks (fig. 6.2 d, e, f), 5) those bound by the plane of the polygonal fault (fig. 6.2g), 6) those cross cutting the polygonal fault plane (fig. 6.2h), and 7) those which emanate from tectonic faults (fig. 6.2i). A pie chart was constructed to show the number of chimneys which have downward termination at these different positions (fig. 6.3).

We suggest that the linear morphology and narrow widths of the conduits reflect a slower intensity of fluid venting (Chapter 4) compared with those structures which develop in the circular craters (cf. Roberts et al., 2006; Cartwright et al, 2007; Gay et al., 2007). In this research I expand the investigation of the previous Chapters to study what conditions and geological environments favour the development of linear venting systems. Five types of geological structures in this survey have been observed to associate with linear venting systems. (fig. 6.1):

- i. Polygonal fault tier above salt withdrawal synclines
- ii. Diapir related radial faults
- iii. Concentric polygonal faults around pockmarks above a palaeo-channel complex
- iv. Normal faults in the foot wall domain
- v. Hemipelagic unit overlying MTCs

6.5.1.2. Pockmarks

Pockmarks (King and McLean, 1970) are widely present in the study area and are often located above faults tips and turbidites systems. Their conical morphology indicates the intensity of fluid migration was high, resulting from violent eruptions (cf. Hovland and Judd, 1988; Roberts 2001; Roberts et al., 2006; Gay et al., 2007; Cartwright et al., 2007). Four types of pockmarks exist in the study area namely; “polyphased pockmarks” (Chapter 4), “advancing pockmarks” (Chapter 4), “nesting pockmarks” (Chapter 5) and ”vertically stacked

Position of downward termination of chimneys at polygonal fault

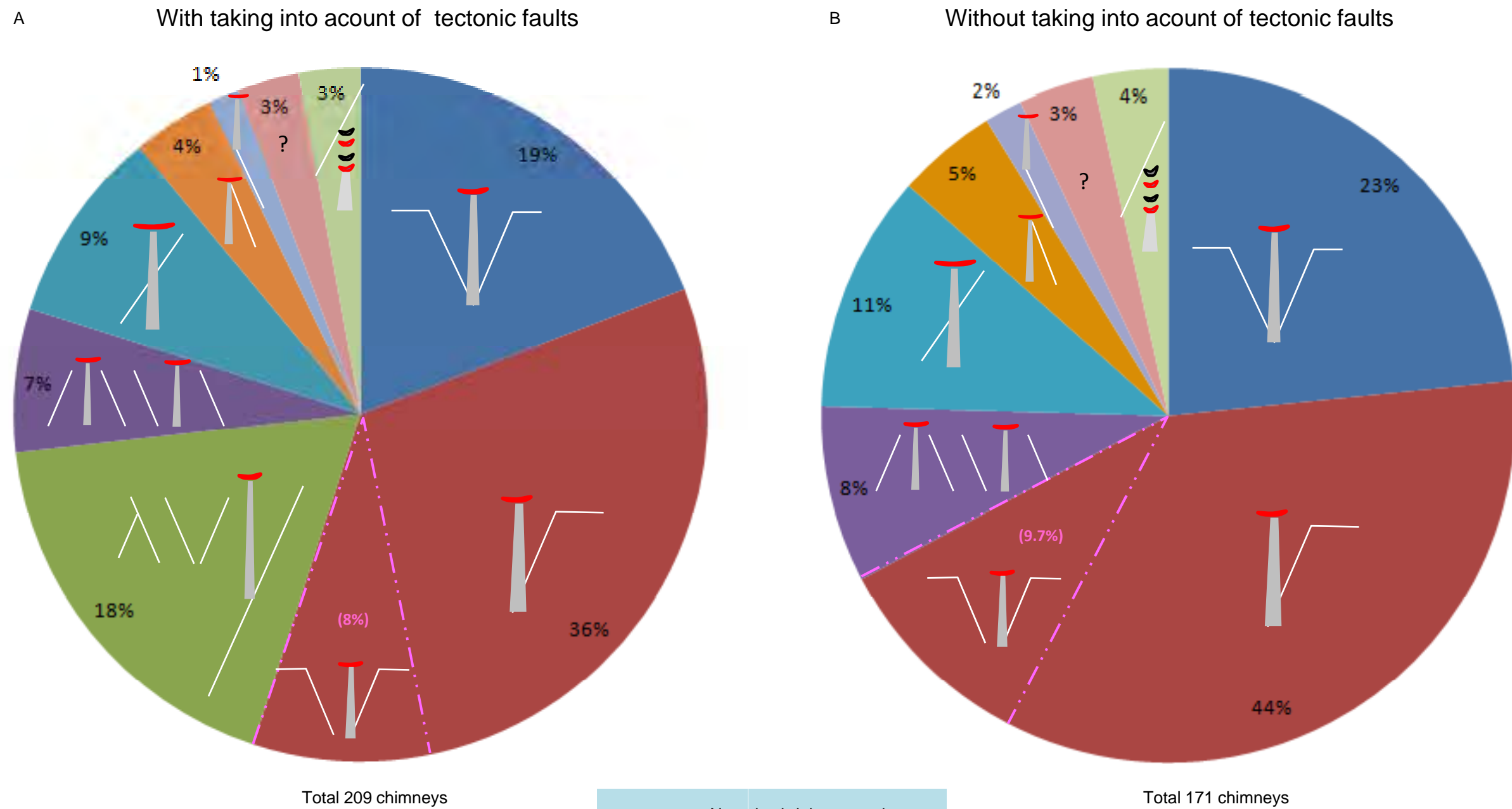


Figure 6.3. Pie charts showing the percentage of chimneys intersecting or emanating from different parts of fault planes or adjacent fault blocks. a) Percentages based on all 209 chimneys identified within PF tier 2 (statistic including chimneys intersected PFs that were linked with underneath tectonic faults). b) Percentages based on all chimneys identified in PF tier 2 which intersect PFs only (sample number = 171) and which were not connecting with any underlying tectonic fault. The position of the chimney-fault intersection are illustrated with cartoons in each pie segment. The type chimney in each case is shown by combination pattern of red and black bold lines (see key at the bottom middle of figure).

pockmarks” (cf. Cifci et al., 2003; Gay et al., 2003). Besides vertically stacked pockmarks which have already been extensively studied (cf. Cifci et al., 2003; Gay et al., 2003; Moss and Cartwright, 2011a, b), the other three types of pockmarks are all fairly new, being described for the first time in detail in Chapters 4 and 5. Because their genesis and evolution was discussed in Chapters 4 and 5 the main aim of this chapter is to understand what causes their distribution, for example their relationship to specific tectonic and sedimentary structures. Moreover, I aim to understand how regional fluid venting is affected by the geological configuration of the study area.

In this study area pockmarks are associated with the following geological structures (fig. 6.1):

- i. Concentric extensional faults in salt withdrawal synclines
- ii. Elongate pockmarks beneath salt diapir-related radial faults
- iii. Pockmarks trails associated with palaeo-channel complexes
- iv. Normal faults of graben on the foot wall domain
- v. Polygonal fault tier above MTCs

6.5.1.3. Distributions of fluid venting structures across different geological settings

Different types of fluid venting structures have been observed to occur above different geological structures across the study survey and which have been described in Chapter 3, as well their distributions are illustrated in Figure 6.1. In the following sections, the seismic characters of each population of venting structures are described together with their associated geological structures.

6.5.1.3.1. Salt-withdrawal Syncline 3 (in hanging wall domain)

Linear chimneys are aligned parallel to and located adjacent to the longest (first-order) polygonal fault segments (fig. 6.4a-c). These first-order PFs typically have lengths several

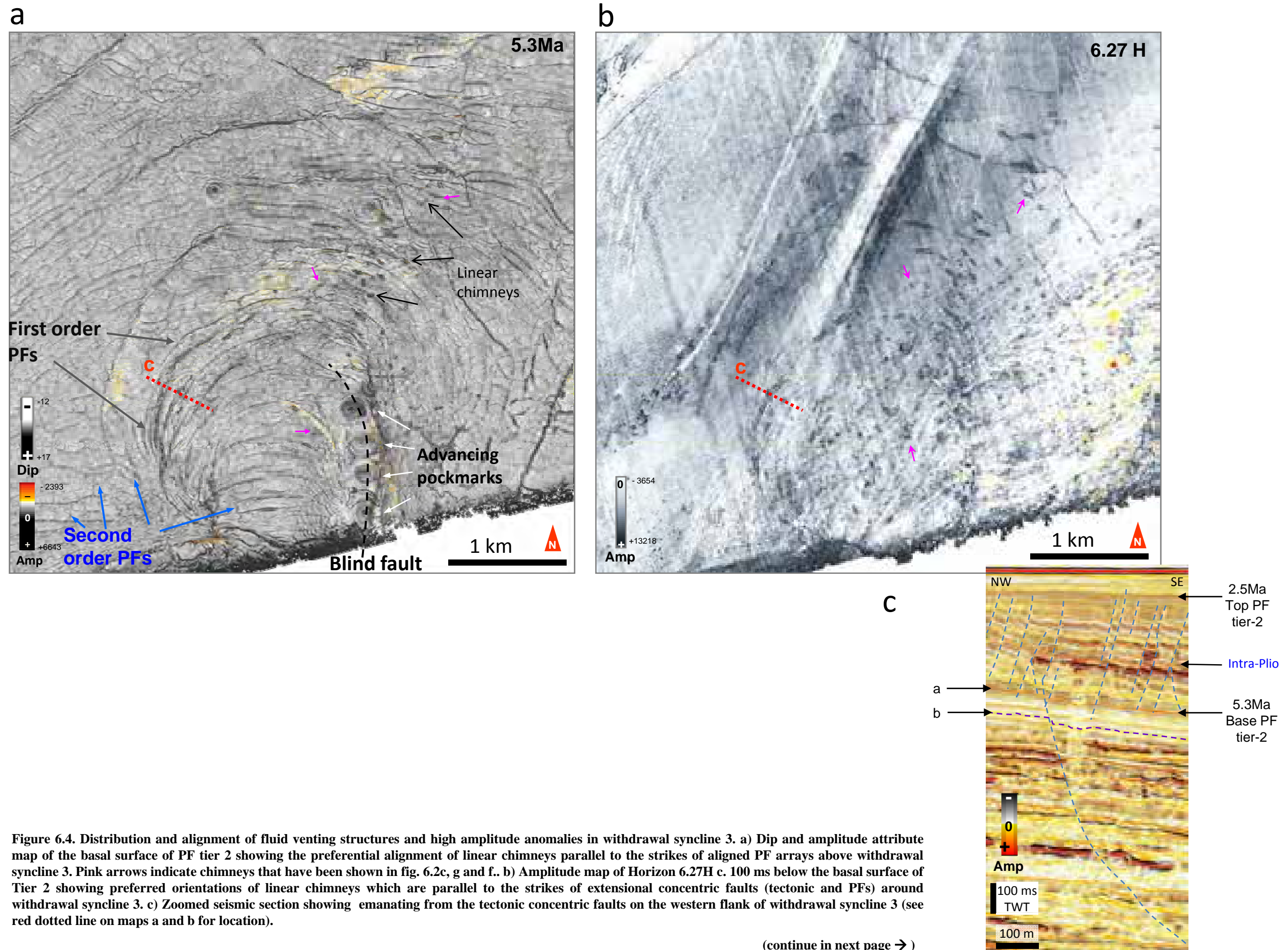
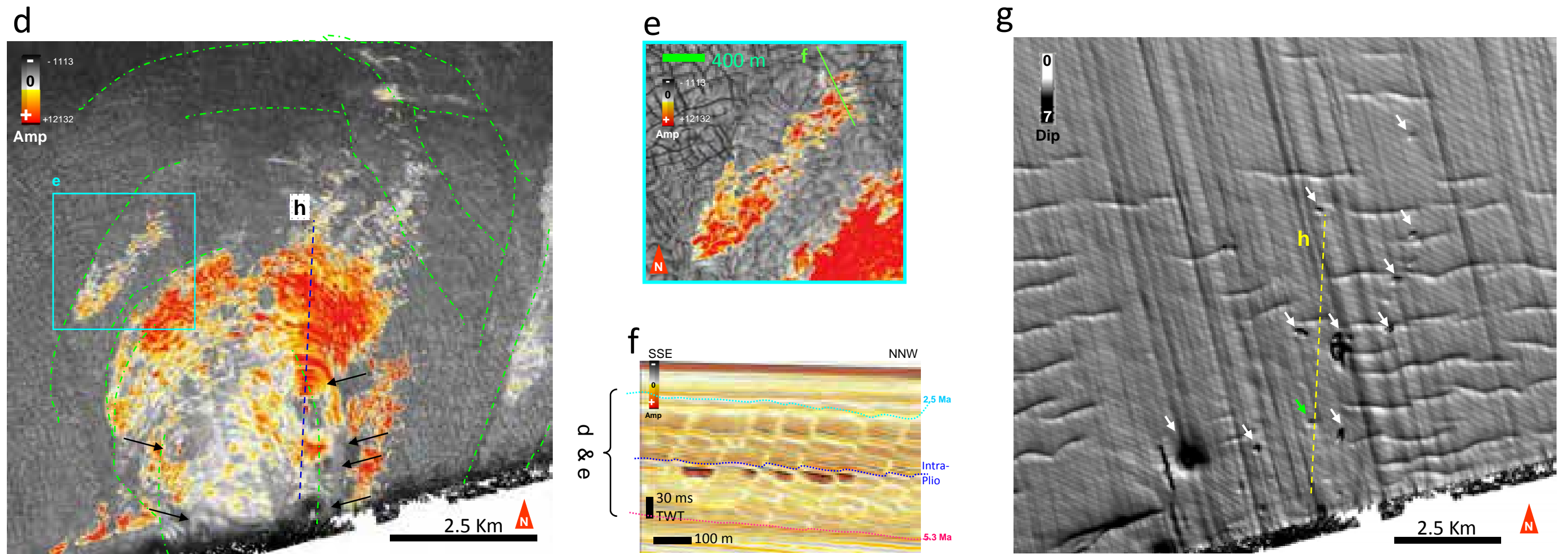


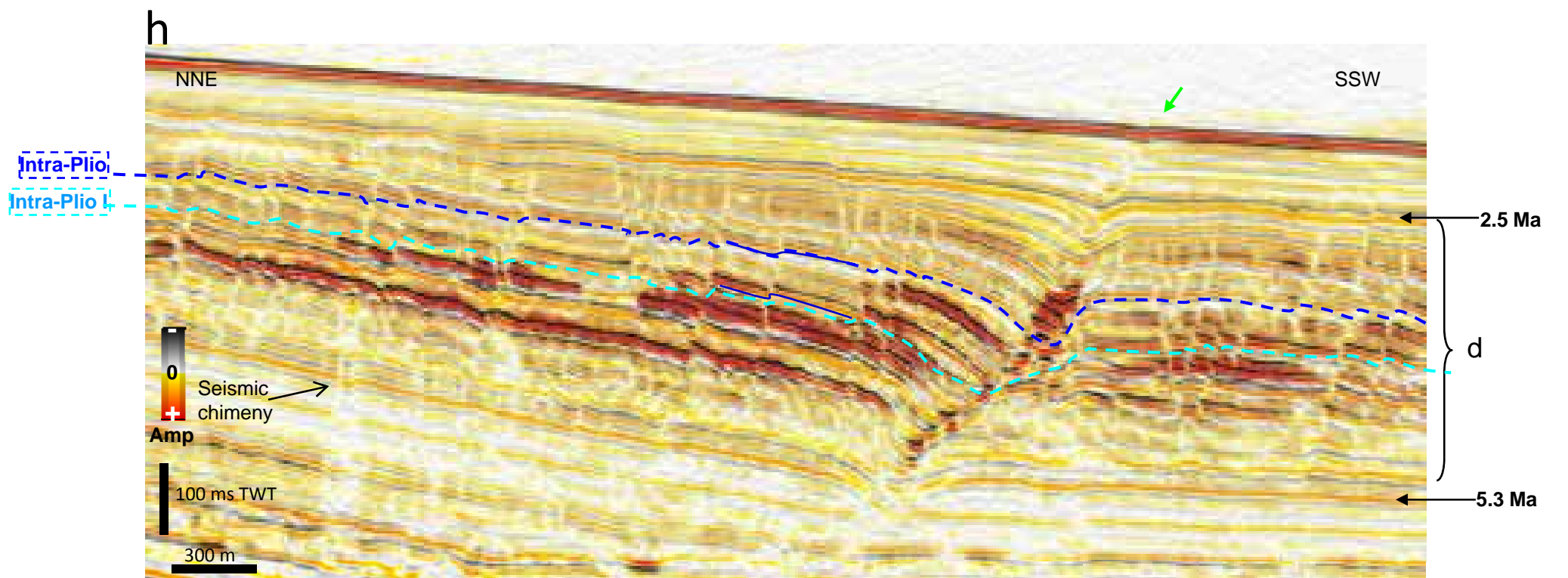
Figure 6.4. Distribution and alignment of fluid venting structures and high amplitude anomalies in withdrawal syncline 3. a) Dip and amplitude attribute map of the basal surface of PF tier 2 showing the preferential alignment of linear chimneys parallel to the strikes of aligned PF arrays above withdrawal syncline 3. Pink arrows indicate chimneys that have been shown in fig. 6.2c, g and f.. b) Amplitude map of Horizon 6.27H c. 100 ms below the basal surface of Tier 2 showing preferred orientations of linear chimneys which are parallel to the strikes of extensional concentric faults (tectonic and PFs) around withdrawal syncline 3. c) Zoomed seismic section showing emanating from the tectonic concentric faults on the western flank of withdrawal syncline 3 (see red dotted line on maps a and b for location).

(continue in next page →)



(← continuous of the previous page)

d) Amplitude extraction of a window between top and base of PF tier 2 showing kilometre scale accumulations of negative high-amplitudes within withdrawal syncline 3. The region of negative high amplitudes are bound by tectonic concentric faults intersecting the edge of the withdrawal syncline as shown by green dot and dashed lines. Also note the presence of several pocks as denoted by black arrows. e) Zoom of negative high-amplitude accumulation on the eastern flank of withdrawal syncline (see light blue box on map d). f) Zoomed seismic section across PF tier 2 showing negative high amplitude accumulations (see location on map in e). g) Dip map of the sea bed showing circular and elongate shallow depressions above the region of negative high amplitude shown on map d. Locations of depressions are denoted by white arrows. Some depressions occur above advancing pockmarks (see green arrow and compare with section in h). h) N-S Seismic section intersecting withdrawal Syncline 3 showing advancing pocks within PF tier 2. Location of shallow sea bed depression is shown by the green arrow. Stratigraphy dip and thicken toward the centre of the withdrawal syncline.



times longer than the second-order PFs or the average length of PF segments in isotropic PF networks. The anisotropic polygonal fault network occurs in a salt withdrawal syncline between the two salt diapirs in the study area. First-order polygonal faults are aligned roughly parallel to the perimeter of the syncline presenting in a concentric pattern. Larger and deeper cutting extensional faults with the same orientation are considered to be tectonic in origin and formed in response to salt-withdrawal. Linear chimneys are also located adjacent to and are parallel to these extensional collapse faults (fig. 6.4b).

The topmost termination of linear chimneys consisting of columns of stacked bright spots are characterised by a trough over peaks (fig. 6.2g; fig.6.4c) and often have inversed polarities along the column. These chimneys that are constituted of negative bright spots occur primarily in the lower part of PF tier-2 (fig. 6.2c, f; fig.6.4c), and are often associated with underlying acoustic wipe-out zones or push downs (fig. 6.2c, f; fig. 6.4c). Most of the chimneys in this location terminate upward into km-scale negative high amplitude accumulations (fig. 6.4d-f), linear shallow depressions at the present day seabed (fig. 6.4g) or even circular depressions in a few cases. The chimneys are characterized by columns of stacked negative bright spots which often terminate beneath the Intra-Plio horizon (e.g. fig. 6.2c, f; fig. 6.4c). In some cases the chimneys are bounded by PFs planes underneath the Intra-Plio level (e.g. fig. 6.2g).

The km-scale high negative amplitude accumulations located above the linear chimneys (fig. 6.4h) and within polygonal fault tier-2 are distributed across the entire salt withdrawal syncline (fig. 6.4d). Their distribution is limited laterally by the extensional collapse faults. Their vertical distribution is restricted to the interval between the horizon of Base-Plio and Intra-Plio or Intra-Plio I. (fig. 6.4f, h).

Patches of high negative amplitudes are bounded by polygonal faults segments suggesting there is a relationship between fluid migration and polygonal fault distributions. The map in Figures 6.4e and d shows crude polygonal networks of linear amplitude anomalies reminiscent of polygonal fault patterns.

Advancing pockmarks (fig. 6.4h) (Chapter 5) in this location are inside the area of negative high amplitudes (fig. 6.4d, h) and are associated with a deep-seated tectonic faults (fig. 6.4d). Advancing pockmarks are primarily present within the polygonally faulted Pliocene interval (Chapter 5). However, some of them are developed through whole the Quaternary interval till the present day seabed and where the upper-most circular depression of an advancing pockmark array can be observed (fig. 6.4g).

6.5.1.3.2. Salt-withdrawal Syncline 2 and radial faults (in hanging wall area)

Linear venting systems are also observed within polygonal fault tier-2 in the salt withdrawal basin 2 that is developed between the two salt diapirs in the study area (fig. 6.1) (fig. 6.5a). The topmost termination of linear conduits which occur above the center of the Syncline-2 are often characterised by linear PHAAs (fig. 6.5b; fig. 6.2i) rather than terminating upwards into negative, high-amplitude accumulations as those which occur above salt-withdrawal Syncline-3. The downward terminations of the most linear systems in this area are expressed as negative bright spots in the lower part of PF tier-2 (fig. 6.5b; fig. 6.2i) and have linear plan form geometries on horizons (fig. 6.5c). While the linear chimneys occur above the edge of this syncline basin (fig. 6.5a) they are associated with seismic pull-up columns (fig. 6.2a). Also in this syncline, linear features that are aligned with lowest tips of polygonal faults have similar lengths, and are paralleled with the upper tips of neighbouring polygonal faults (fig. 6.2a).

The polygonal faults in this study have atypical geometries in that they do not always define a perfectly isotropic (polygonal) pattern but instead define anisotropic patterns with strongly preferred alignments. Linear venting systems tend to be aligned parallel to these aligned arrays of polygonal faults of which there are three types (fig. 6.6a-d).

The first type occurs within, and surrounding salt withdrawal synclines and are parallel to larger, tectonic faults which formed during deepening of the withdrawal basin. They have a preferred NW-SE orientation intersecting the NE and SW flank of the two diapirs (fig. 6.6b). The second type of anisotropic polygonal fault network is aligned orthogonal to the salt contact of Diapir 2 defining a radial fault pattern. These radial arrays are similar to those documented by Davison et al., 2000; Stewart, 2006 and Carruthers et al., 2013 in the North Sea (fig. 6.6c). On the flanks of the diapirs which border the withdrawal basin, radial faults deflect with distance and curve around the edge of the basin. The third type of anisotropic polygonal fault network is found inside the area bounded by the concentrically aligned polygonal faults. Here, they form a uni-directional NE-SW aligned array (fig. 6.6c). As mentioned above, linear conduits within polygonal faulted intervals frequently follow the trends of first-order (dominant trending), polygonal faults. In contrast to the examples described above, linear conduits show no preferred orientation off the NNE flank of Diapir 1 and at the intersection between concentric and uni-directional PF arrays. At this location polygonal faults are more isotropically arranged (fig. 6.5a).

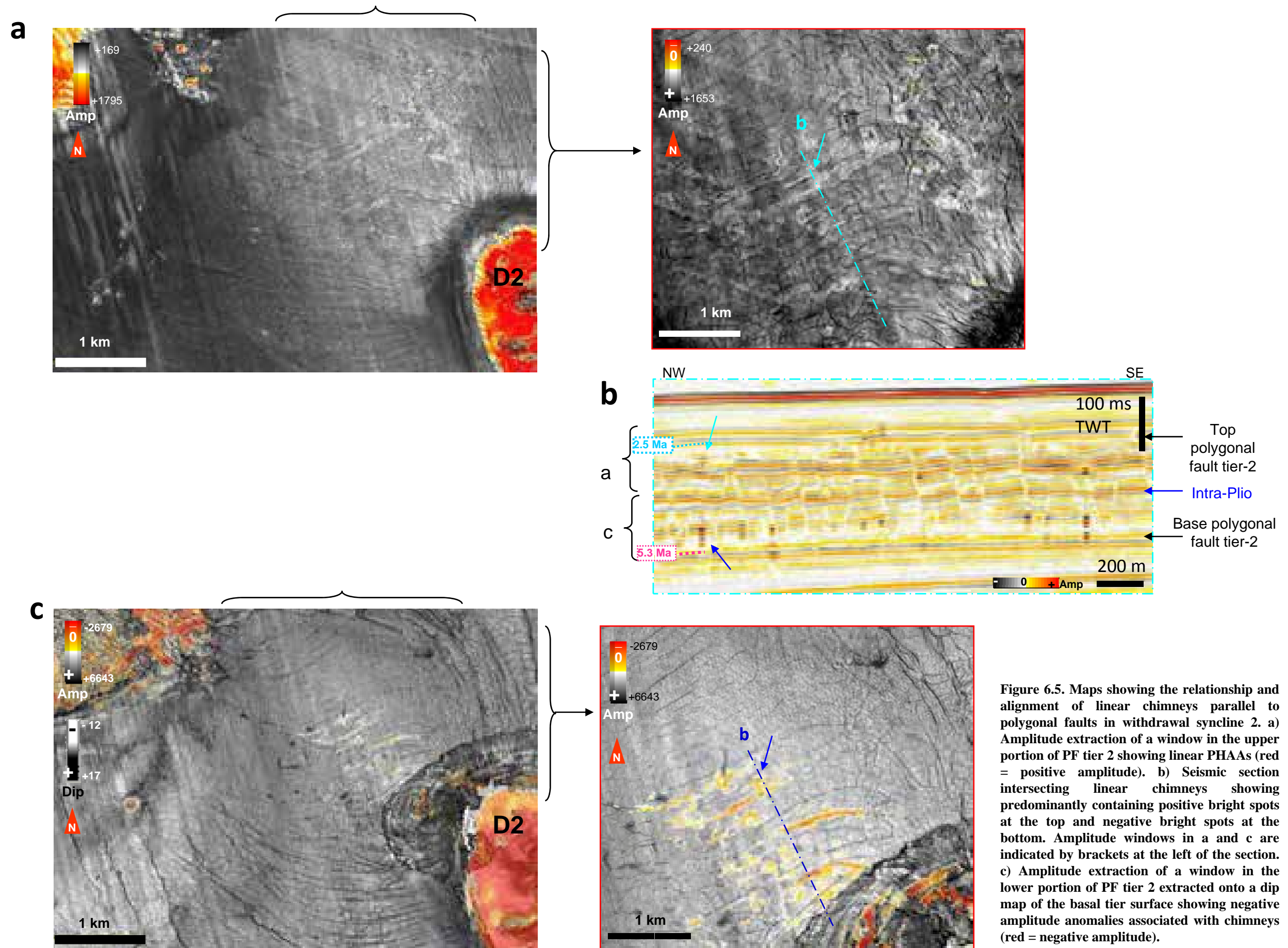


Figure 6.5. Maps showing the relationship and alignment of linear chimneys parallel to polygonal faults in withdrawal syncline 2. a) Amplitude extraction of a window in the upper portion of PF tier 2 showing linear PHAAs (red = positive amplitude). b) Seismic section intersecting linear chimneys showing predominantly containing positive bright spots at the top and negative bright spots at the bottom. Amplitude windows in a and c are indicated by brackets at the left of the section. c) Amplitude extraction of a window in the lower portion of PF tier 2 extracted onto a dip map of the basal tier 2 surface showing negative amplitude anomalies associated with chimneys (red = negative amplitude).

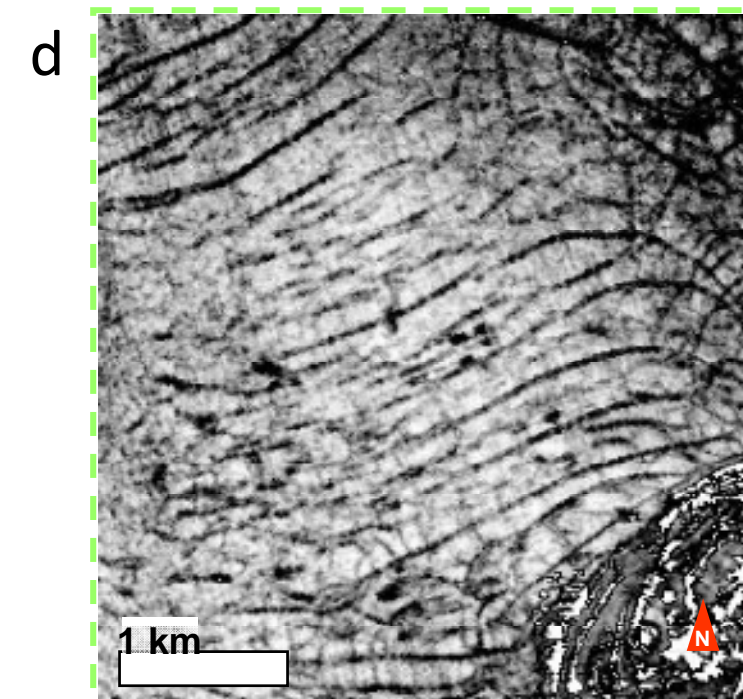
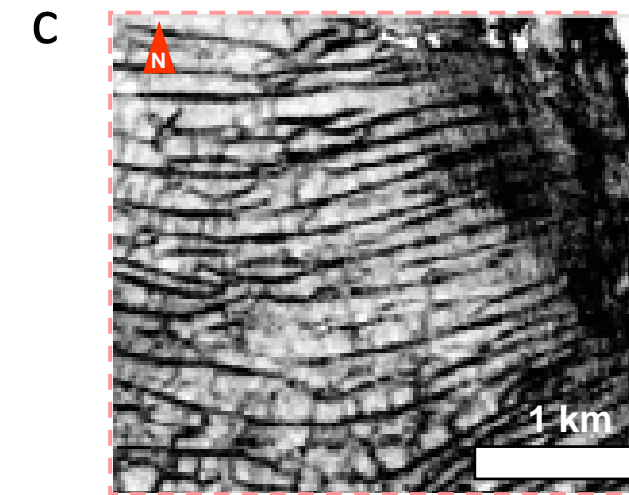
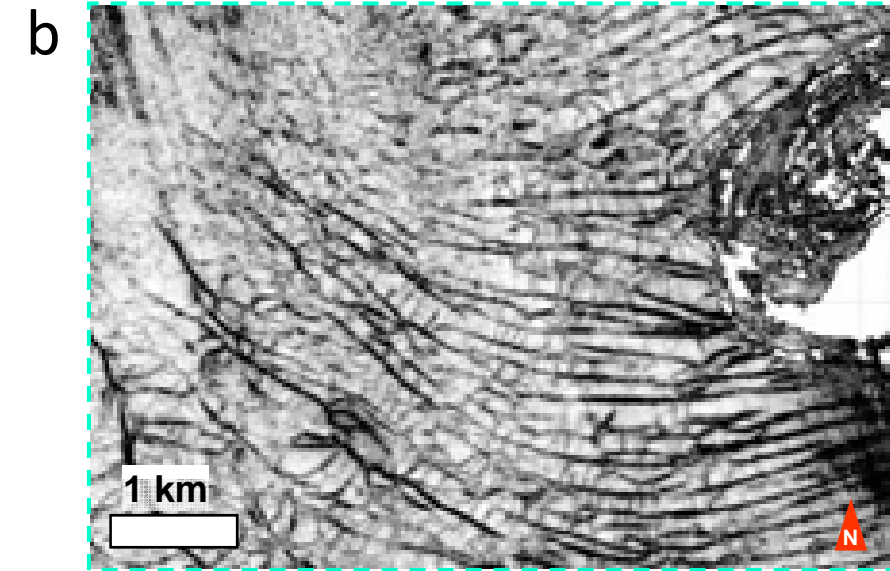
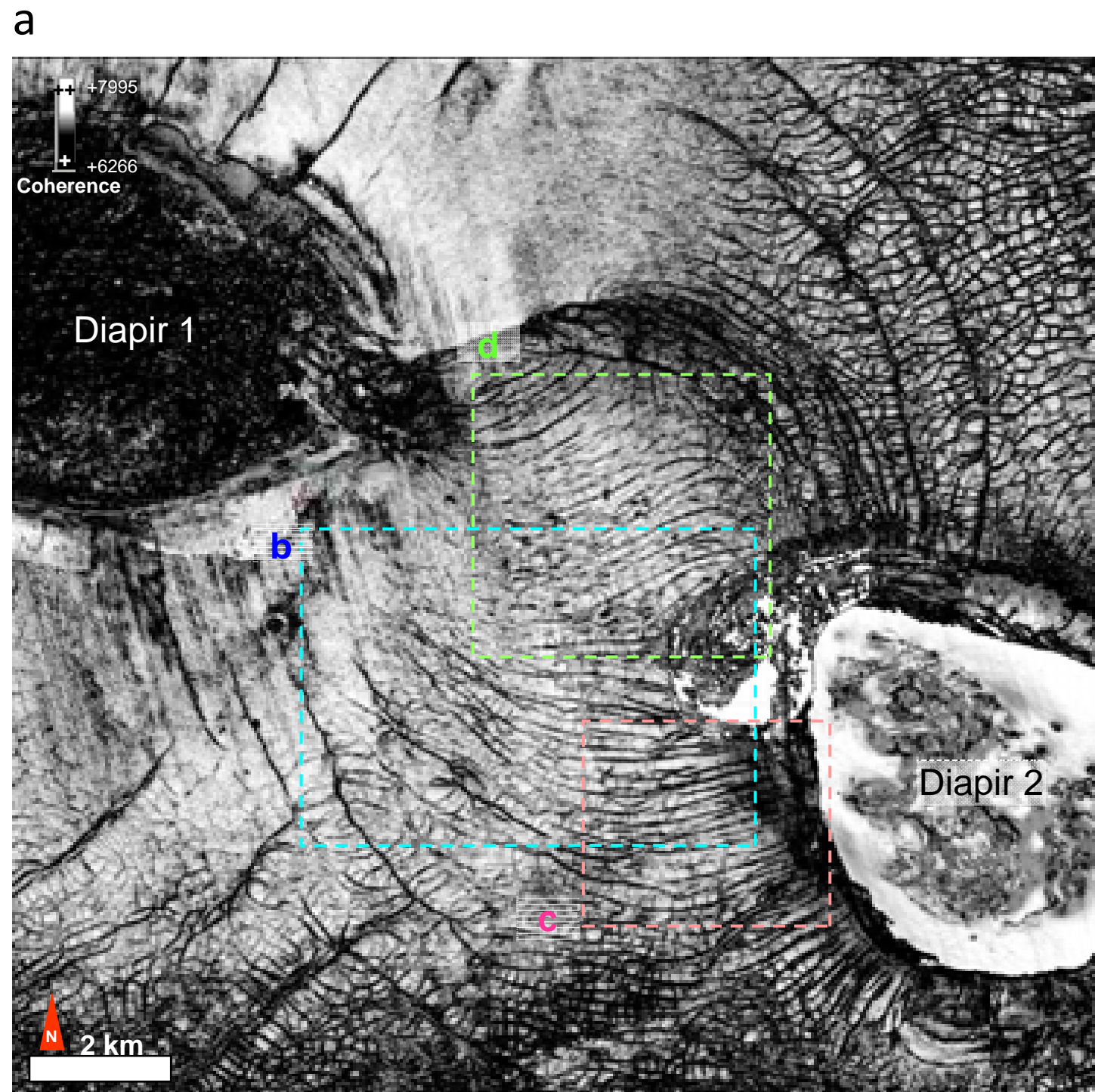


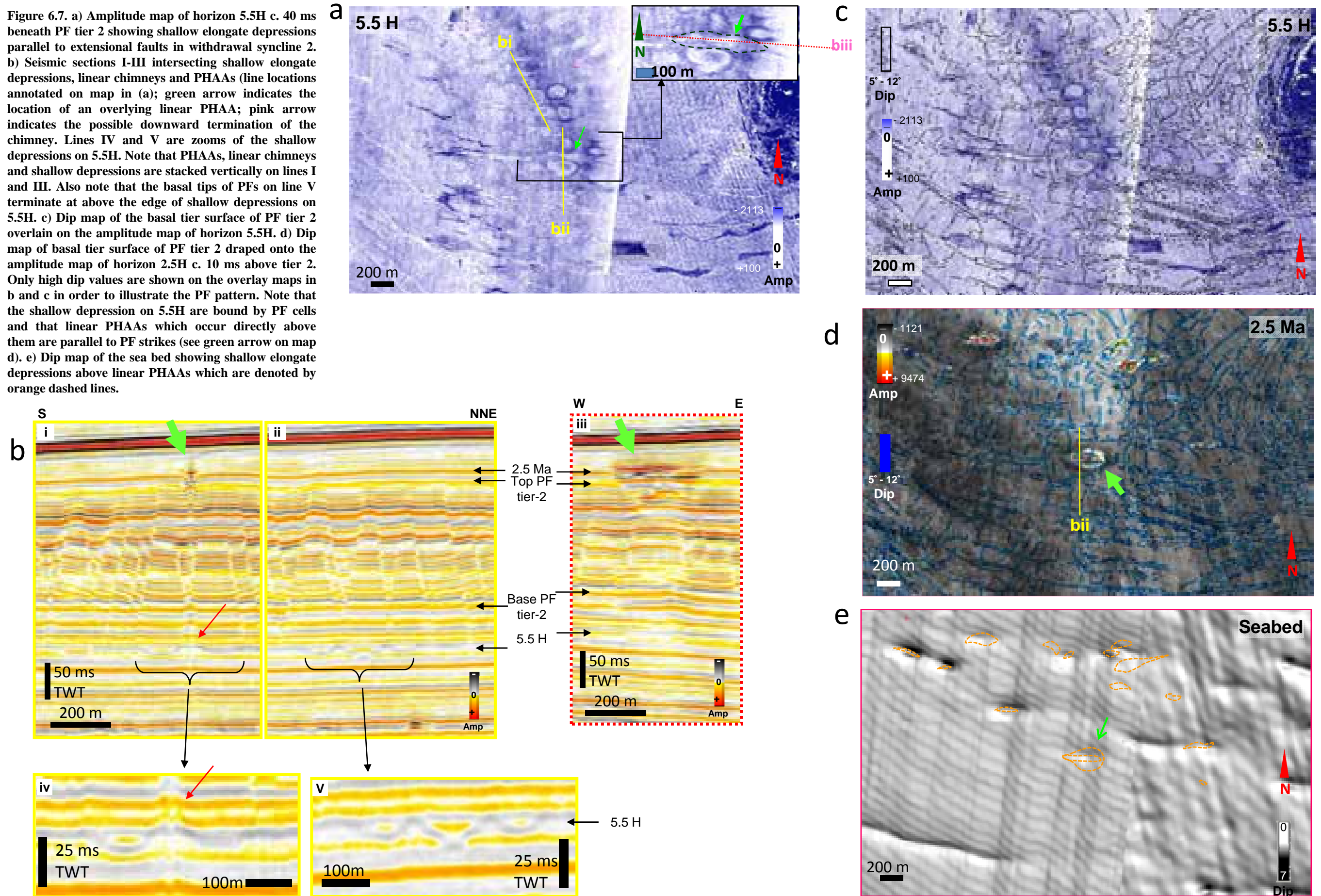
Figure 6.6. a) Coherence attribute extracted onto the basal surface of PF tier 2 showing the geometry and preferential alignment of PF's in withdrawal syncline 2 and around Diapirs 1 and 2. b-d) Zooms of map in (a). Locations of maps are shown by color squares.

A series of elongate, shallow depressions have been observed above the SW edge of Syncline 2 at the level of an Upper Miocene horizon (fig. 6.7a) which is 40 ms TWT below the base of polygonal fault tier-2 (the base of Pliocene). These elongate shallow depressions have depths less than 7-to-11ms (TWT) deep (fig. 6.7b) and have plan form dimensions of tens-to-two hundred meters. Some of them have shallow conical cross sectional geometries. Their long axis is parallel to the strikes of concentrically aligned polygonal faults developed in the overlying stratigraphy (fig. 6.7c). The map in Figure 6.7c shows several smaller faults (second-order PF) which are roughly orthogonal-to-oblique with respect to long (first-order) concentric faults defining a cubic-hexagonal fault network. When the map in Figure 6.7a is superimposed on a dip map of the basal surface of Tier 1 (fig 6.7c) it is interesting to note that the elongate depressions below fit extraordinary well into these cubic-hexagonal fault polygons (fig. 6.7c).

For the minority of elongate depressions that are associated with chimneys the downward termination of the chimney appears to have emanated from the lower part of the PF plane and vertically above the boundary of two neighboring elongate depressions (e.g. fig. 6.7b). Linear PHAAs at the top of these chimneys are aligned parallel to and located directly above the basal tips of PFs (fig. 6.7d). Elongate depressions at the present day seabed occur directly above these linear features (fig. 6.7e). Of the few examples, this trend of fluid venting structures being stacked one above each and aligned parallel to the strikes of polygonal faults is consistently observed.

The shallow depressions described above display various plan form dimensions such as sub-circular, elongate and linear, as defined based on the aspect ratio of the depression plan form. It is interesting to note however that specific depression shapes cluster in specific parts of this hanging wall domain of the study area. On the other hand, these depressions show sub-circular plan form geometries at distance from Syncline-2, e.g. above the crest of the turtle anticline (fig. 6.1; fig.6.8a) and above the ridge in the SE corner of the survey (fig. 6.1). I showed in the preceding paragraphs that the depressions were elongate above the edge of Syncline 2. However, on the SW flank of Diapir 2 shallow depressions have greater aspect ratios and are clearly linear (fig. 6.8b, c).

Figure 6.7. a) Amplitude map of horizon 5.5H c. 40 ms beneath PF tier 2 showing shallow elongate depressions parallel to extensional faults in withdrawal syncline 2. b) Seismic sections I-III intersecting shallow elongate depressions, linear chimneys and PHAAs (line locations annotated on map in (a)); green arrow indicates the location of an overlying linear PHAA; pink arrow indicates the possible downward termination of the chimney. Lines IV and V are zooms of the shallow depressions on 5.5H. Note that PHAAs, linear chimneys and shallow depressions are stacked vertically on lines I and III. Also note that the basal tips of PFs on line V terminate at above the edge of shallow depressions on 5.5H. c) Dip map of the basal tier surface of PF tier 2 overlain on the amplitude map of horizon 5.5H. d) Dip map of basal tier surface of PF tier 2 draped onto the amplitude map of horizon 2.5H c. 10 ms above tier 2. Only high dip values are shown on the overlay maps in b and c in order to illustrate the PF pattern. Note that the shallow depression on 5.5H are bound by PF cells and that linear PHAAs which occur directly above them are parallel to PF strikes (see green arrow on map d). e) Dip map of the sea bed showing shallow elongate depressions above linear PHAAs which are denoted by orange dashed lines.



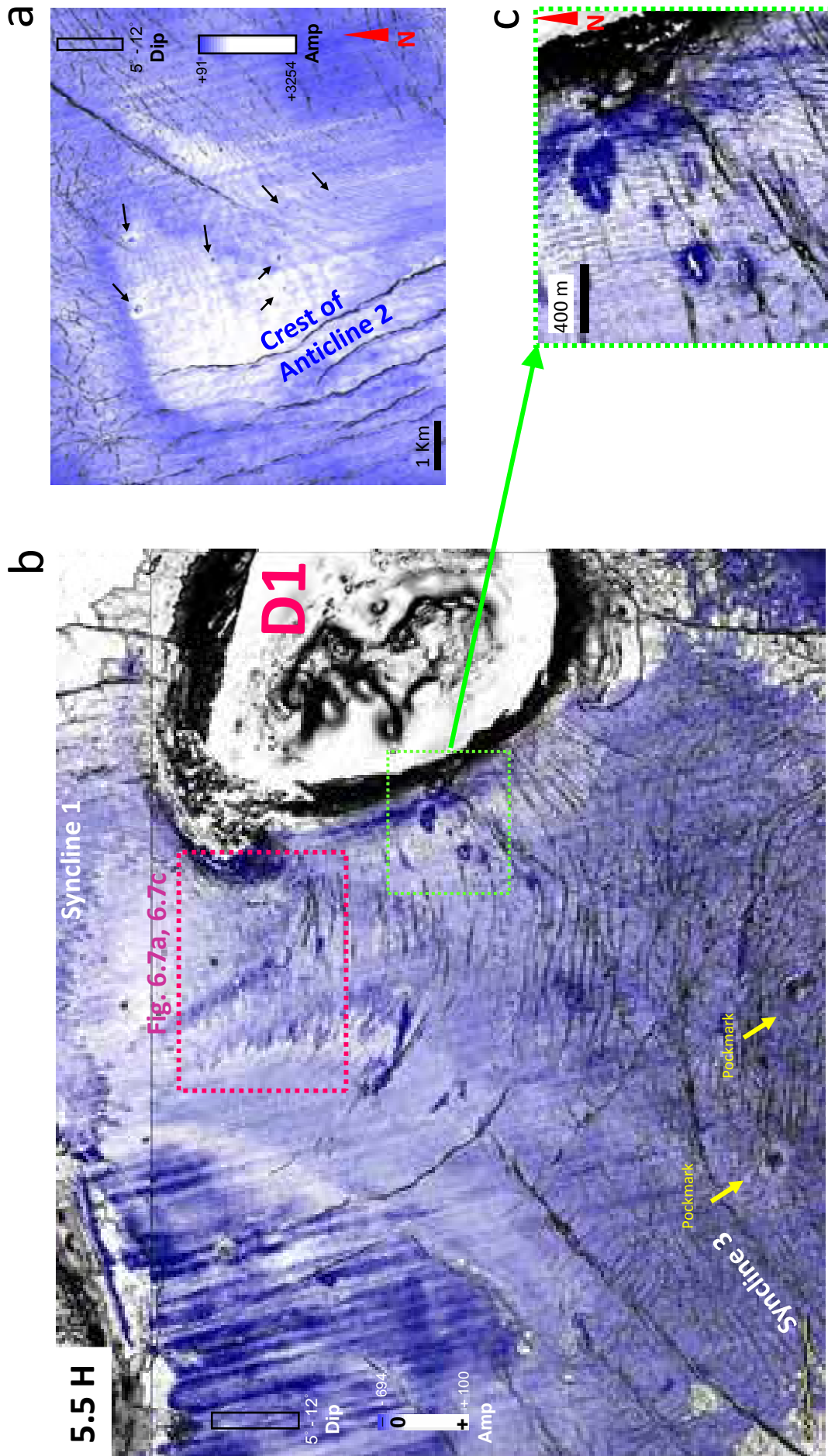


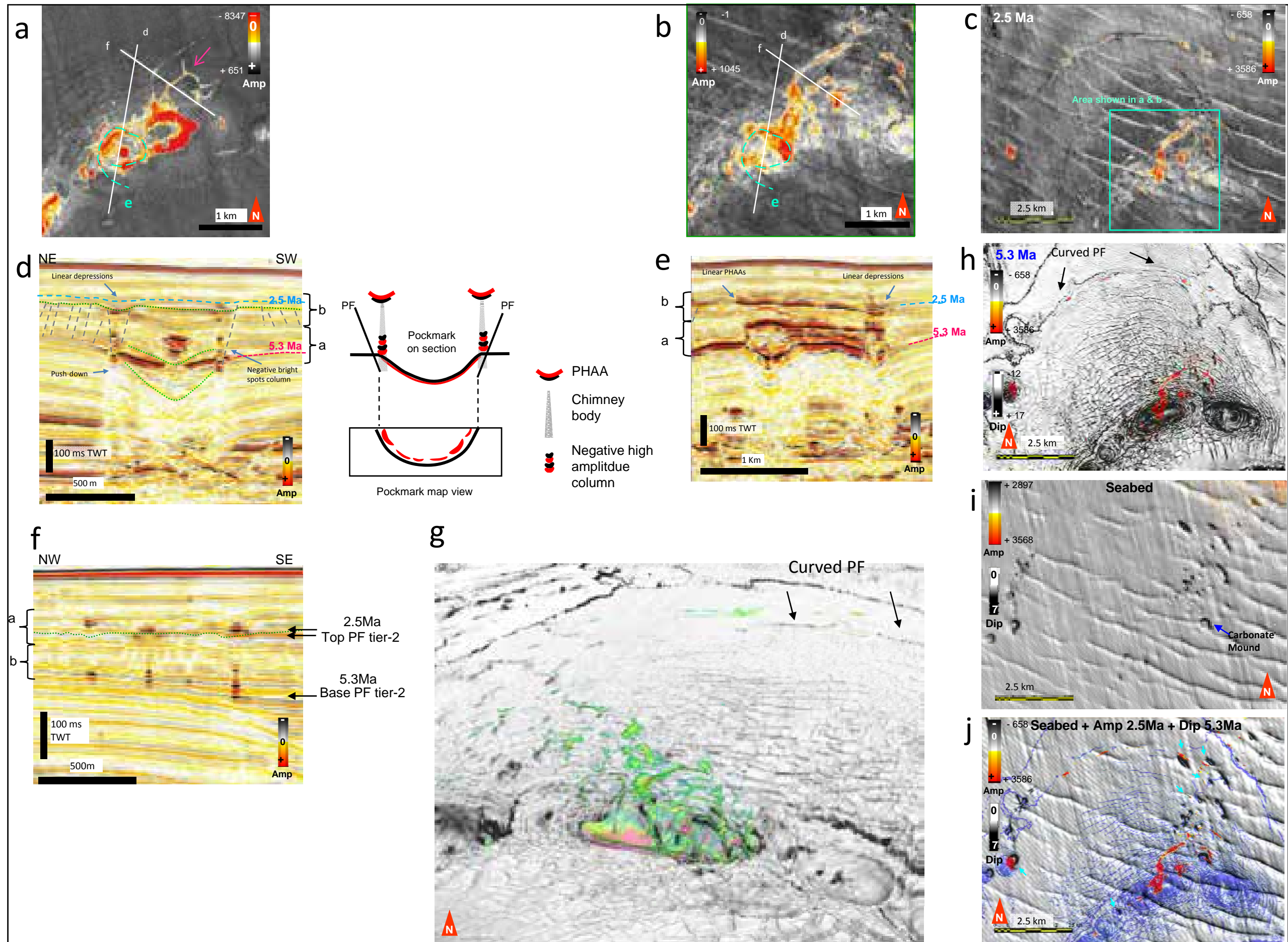
Figure 6.8. Maps showing variations in the aspect ratio of shallow depressions with respect to proximity to salt diapirs and withdrawal basins. a) Amplitude of horizon 5.5H showing circular shallow depressions above Anticline 2 as denoted by black arrows. Strikes of normal faults in the anticline crest indicate the orientation of the fold axis. b) Amplitude map of horizon 5.5H c. 40 ms beneath PF tier 2, c) Zoom of map in map a centred on the SW flank of Diapir 2 showing linear shallow depressions between radial faults.

6.5.1.3.3. Above palaeo-channel complexes and salt-withdrawal Syncline 1 (in hanging wall area)

Linear venting systems located around vertically stacked pockmarks (fig. 6.9a-j) are developed above a hydrocarbon bearing channel complex (Chapter 5). They emanate from the lower tips of first-order PFs which are concentrically aligned around pockmarks (Chopra and Marfurt, 2007; Cartwright, 2011; Imbert et al., 2011) (fig. 6.9a, d). Their downward terminations are characterized by negative high-amplitude bright spots which are located in the lower part of polygonal fault tier-2 (fig. 6.9a, d, f). While their top most terminations are characterized by positive, high-amplitude patches and linear to oval-shaped plan form dimensions (see fig. 6.9b, c, f) occur close to or at the top boundary of polygonal fault tier-2 (fig. 6.9c-e). These linear venting systems are organised into a ring around the pockmarks on horizons (cf. fig. 6.9a, g). They are similar to the linear venting systems described above that they also stem from the basal tip or lower part of the polygonal fault plane, however polygonal faults are concentrically aligned above pockmarks (fig. 6.9a, h). These linear venting systems also terminate downward into the edges of the earliest pockmark craters (fig. 6.9d), and whose infills are expressed by negative high amplitude reflections as shown on Figure 5.7band 5.16b in Chapter 5.

Some individual linear PHAAs extend laterally outward from these ring-shaped amplitude anomalies (fig. 6.9a, b), and follow the trends of individual PF segments (fig. 6.9a, b, h). In particular, note how the intersection between several linear anomalies (see pink arrow on fig. 6.9a) is approximately 120 degrees which is similar to the idealized shape of a polygonal (hexagonal) fault cell. When close to the eastern edge of the syncline, linear features take the direction of secondary polygonal faults that have the same trends as the syncline edge and are parallel to the growth fault (fig. 6.9c, h). In addition, the long curved polygonal fault that developed along the north edge of syncline defines the northern boundary of the polygonally faulted area. The linear features associated with this curved PF has the same trend (fig. 6.9g, h). These linear venting systems which have lengths ranging from a 100-to-several 100's meters are organized into "branching" or "ramification" networks and extend to a distance of 4 km. These networks that are composed of linear, sub-circular and elongate amplitude anomalies which are connected with each other have been reported by Cartwright and Huuse (2006) in the Early Miocene interval in near-by. This type of high-amplitude network has been named previously as "filamental anomalies" (Cartwright and

Figure 6.9 Relationship and geometry between linear PHAAs and chimneys, pockmarks and concentric faults. a) Amplitude extraction from a window of the lower part of PF tier 2. b) Amplitude extraction from a window of the upper part of PF tier 2 (interval used for amplitude extractions are shown on underlying seismic sections d and e). c) Amplitude map of horizon 2.5H, d-e) Zoomed seismic sections across and around the edge of the pockmark craters respectively and showing overlying PHAAs and chimneys. Line locations are shown on map (a) and (b). Cartoon between (d) and (e) shows a simplified cross section and map interpretation showing the concentric alignment of PHAAs parallel to concentrically aligned PF around and above a pockmark crater. f) Zoomed seismic section across linear PHAAs branching away from the pockmark edge. g) 3D view of a dip map of the basal tier surface of Tier 2 (horizon 5.3H). Superimposed are the 3D accumulations of high amplitudes from the pockmark fill sequence and overlying chimneys. h) Plan form view of 3D map in (g). Chimneys defined by regions of high dip show that they are aligned parallel to PHAAs. i) High amplitudes (red patches) from the seabed horizon draped on a dip map of the sea bed. j) Dip map of the sea bed with high amplitudes (red patches) from horizon 5.5H and high dip values (short blue lineaments) from horizon 5.3 H draped on top. Note that PHAAs have the same plan form geometry as overlying shallow depressions.



Huuse, 2006).

Linear venting systems are expressed on the present day seabed as elongate to sub-circular depressions and are quite clearly aligned parallel to the strikes of underlying, first-order polygonal faults around the perimeter of salt withdrawal synclines (fig. 6.9i, j). These present day seafloor depressions are restricted to the polygonally faulted area (fig. 6.9j), and spatially above the salt-withdrawal syncline (fig. 6.9i, j). Linear venting systems are generally absent where polygonal faults are absent with exception to areas locally faulted by salt-related fault systems or above buried channel complexes (see Chapter 5). Notice that these depressions located above linear PHAAs and linear chimneys are all aligned parallel to each other (blue arrows in fig. 6.9j).

6.5.1.3.4. Normal fault set in the footwall domain

Fluid venting structures in the footwall domain (fig. 6.10a, b, c, d), comprise vertically stacked pockmarks (fig. 6.10b, d), linear positive high amplitude anomalies (fig. 6.10a, c), and positive high amplitude carbonate mounds (fig. 6.10a, c). Numerous normal faults occur in the NE corner of the footwall domain (fig. 6.1; fig. 6.10a-d). The polygonal fault system degrades progressively from the footwall area where area behind the two diapirs to the NE where they are completely absent (fig. 3.4b in Chapter 3). All of these venting structures occur within the Pliocene-Quaternary interval with the exception of the vertically stacked shallow pockmarks (fig. 6.11a, b) which are present in the End Miocene and the Lower-to-Middle Pliocene interval. These vertically stacked shallow pockmark successions have heights of about 200 ms TWT. They are composed by individual shallow pockmark and shallow depressions, both of which have relative shallow depths ranging from 5 to 25 ms TWT and have variable diameters from one to several hundreds of metres.

Hook-shaped positive high amplitude anomalies

In the footwall domain, linear PHAAs have unique hook-like plan form geometry (fig. 6.12a). Hook-shaped PHAAs are orthogonal deep-seated fault segments “X” (fig. 6.12a-c) which vary in strike length from 2.5 -to- 10 km and are oriented NE-to-SW on the footwall domain (fig. 6.10c; fig. 6.12a-c). These hook-shaped PHAAs occur within the first 60 ms TWT beneath the present day seafloor or above the stratigraphic levels which correspond to

- 658
+ 3586

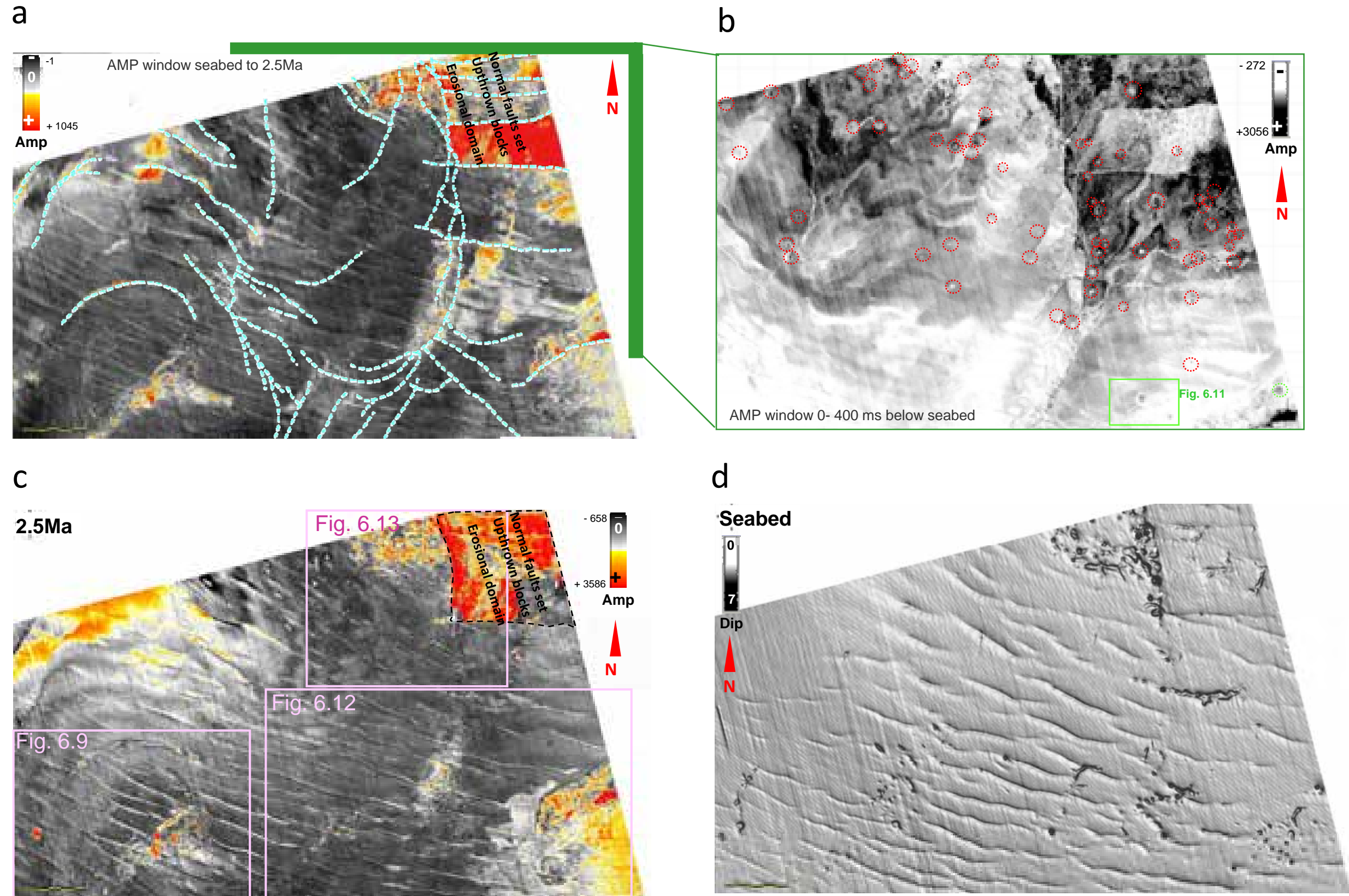


Figure 6.10. Seismic attribute maps showing the spatial distribution of different types of fluid venting structures in the northern corner of the footwall domain (see Fig 6.1 for location of footwall domain). a) Amplitude extraction from a window in the upper part of PF tier 2. The traces of tectonic faults which intersect the interval are shown by light blue dashed lines. b) Amplitude extraction from a window between the seabed to 40 ms below. Red circles show the locations of vertically stacked pockmarks and/or depressions. c) Amplitude map of horizon 2.5H. d) Dip map of the seabed showing shallow depressions above the upper tips of tectonic faults which tip out close to the seafloor.

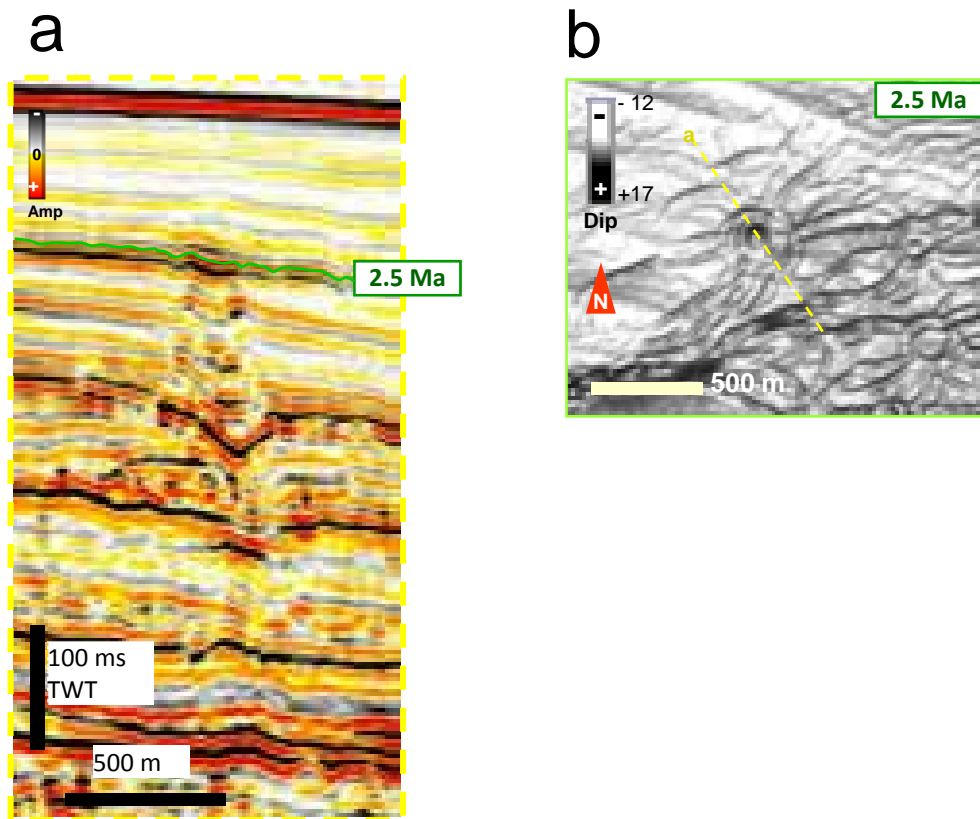
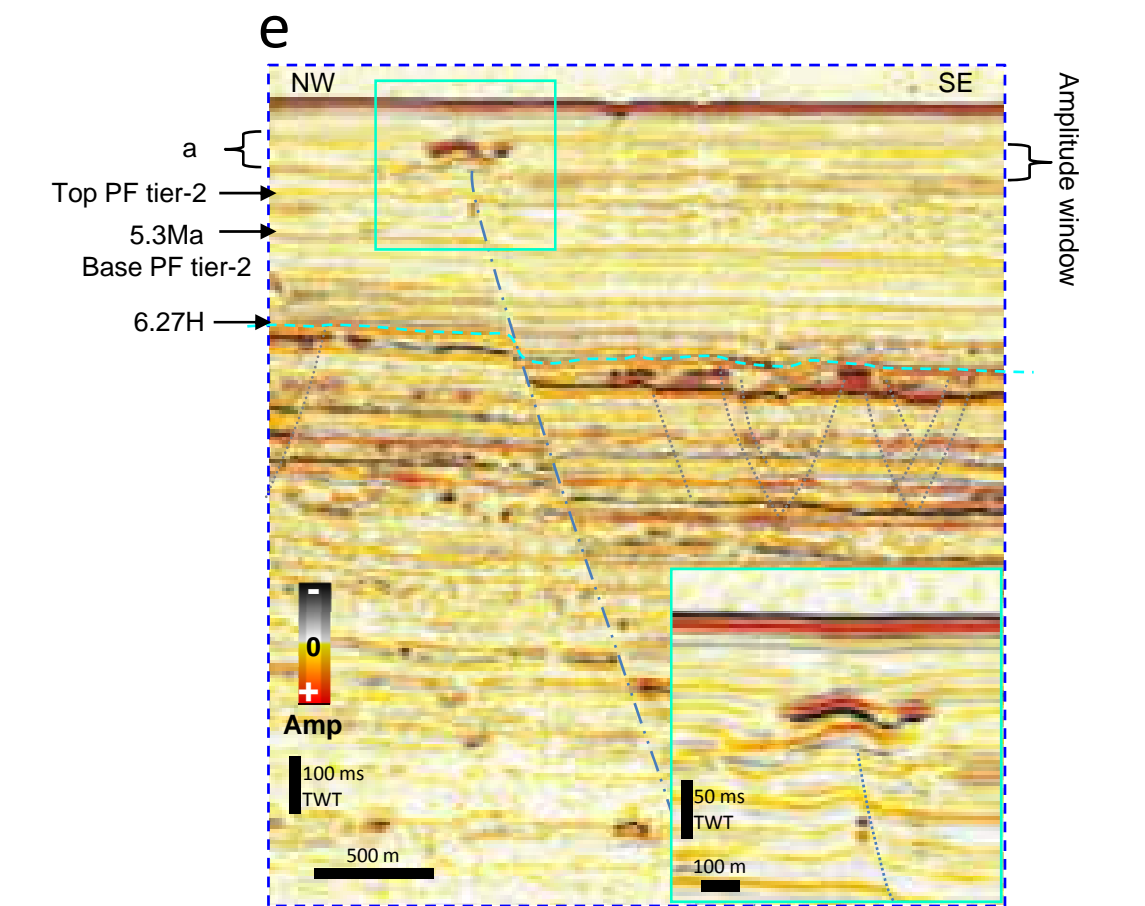
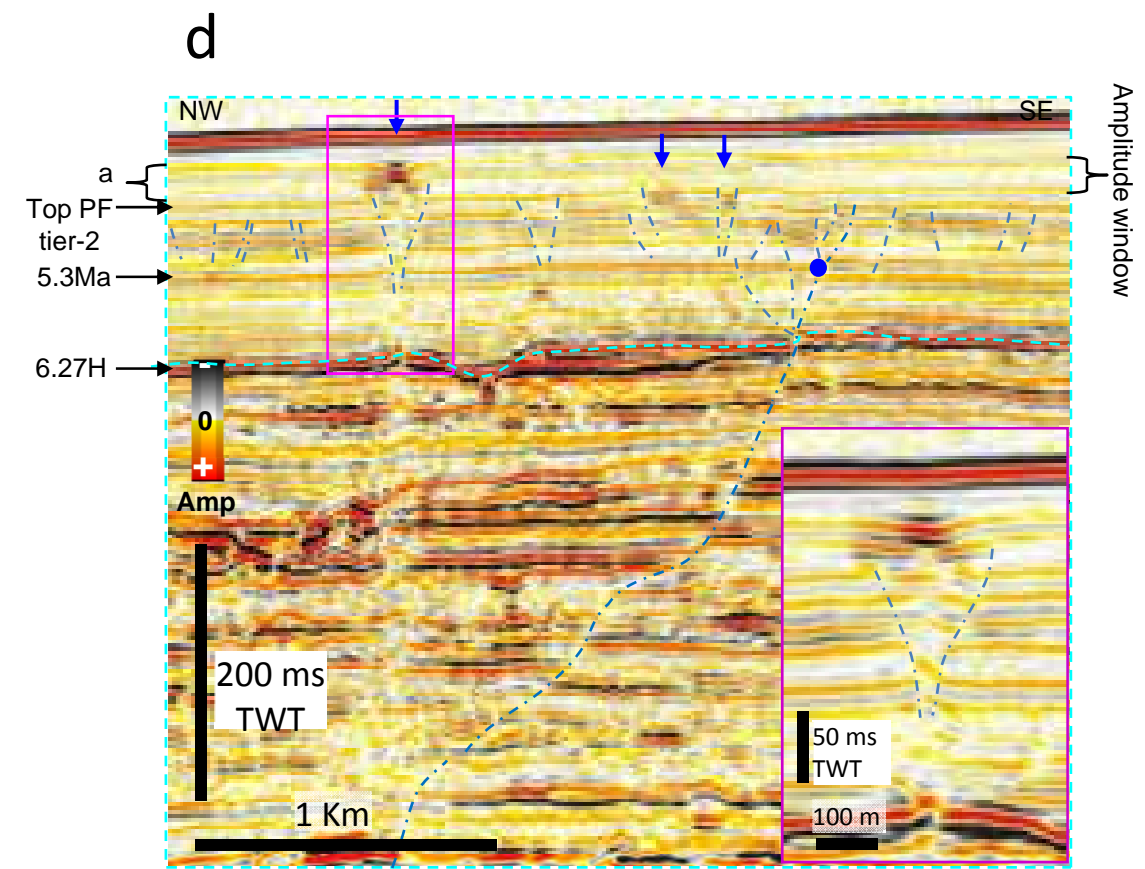
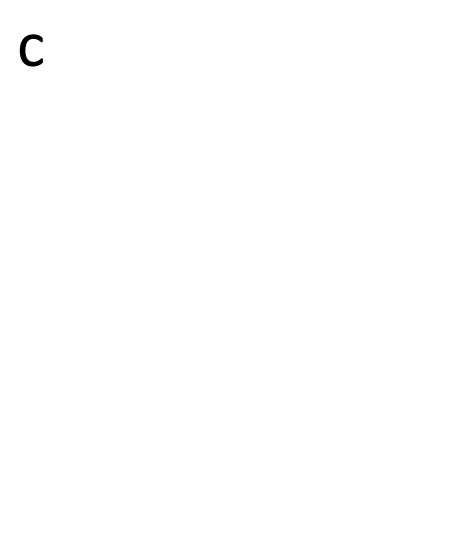
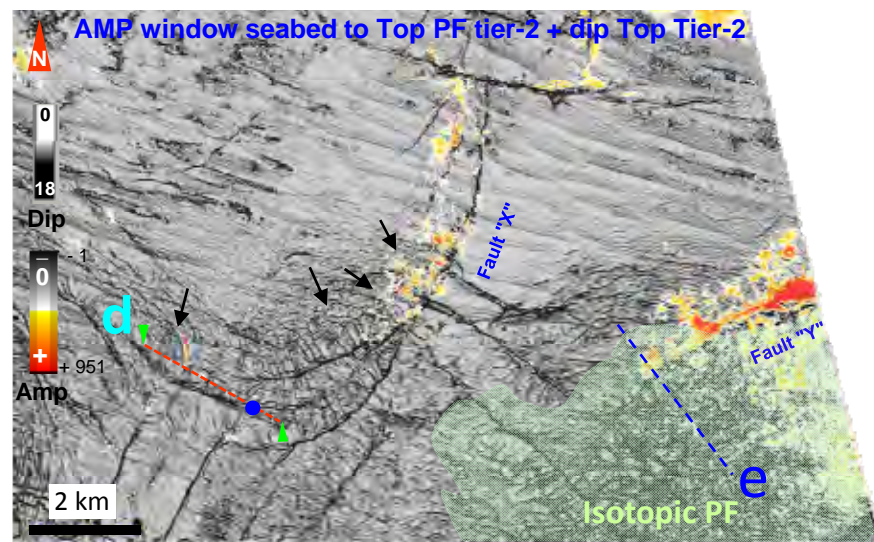
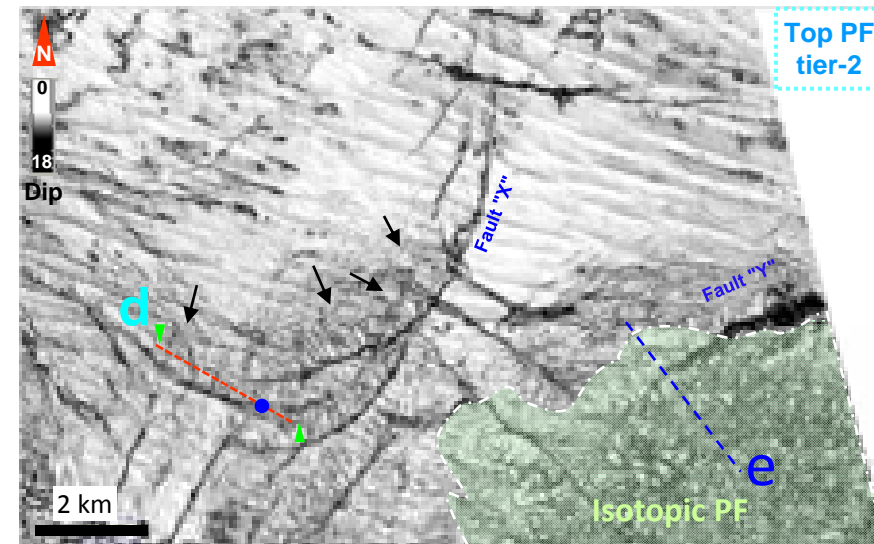
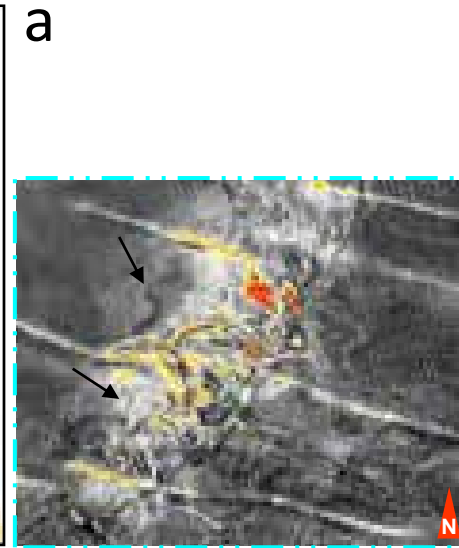
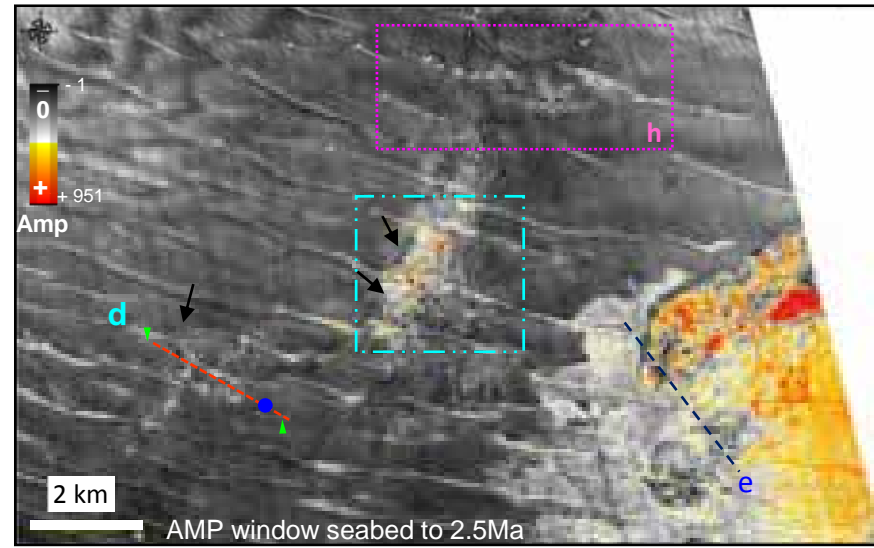
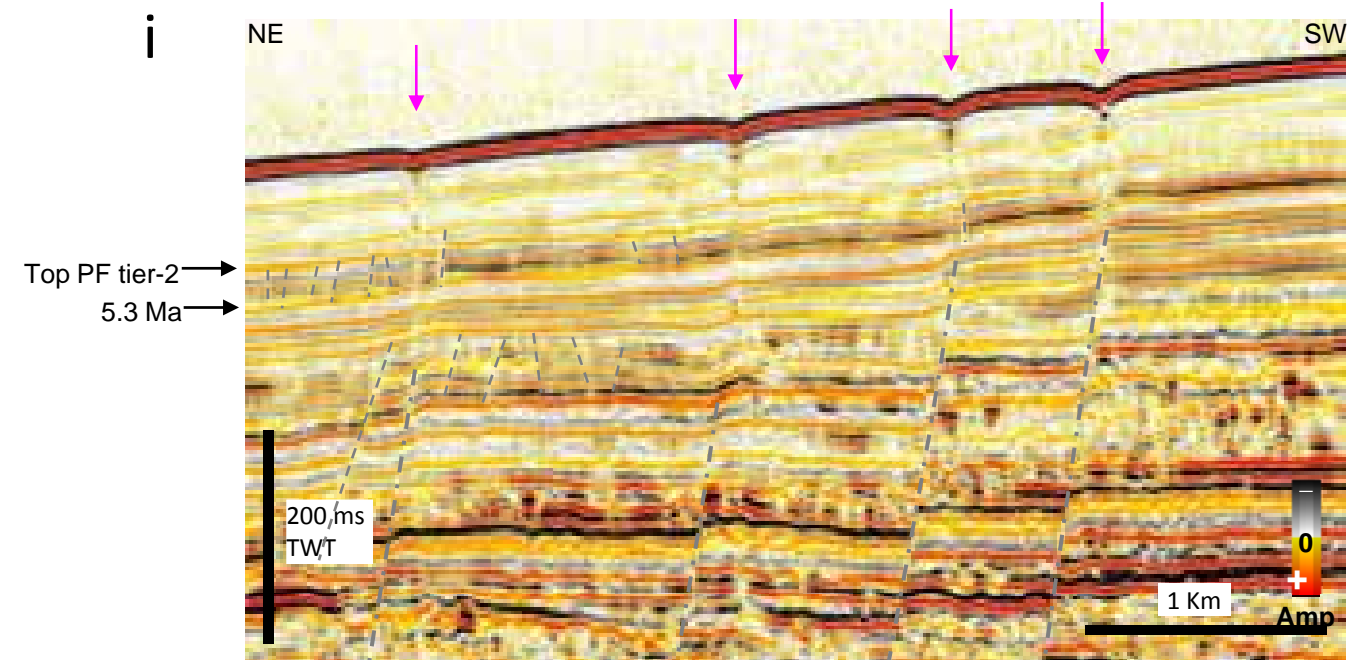
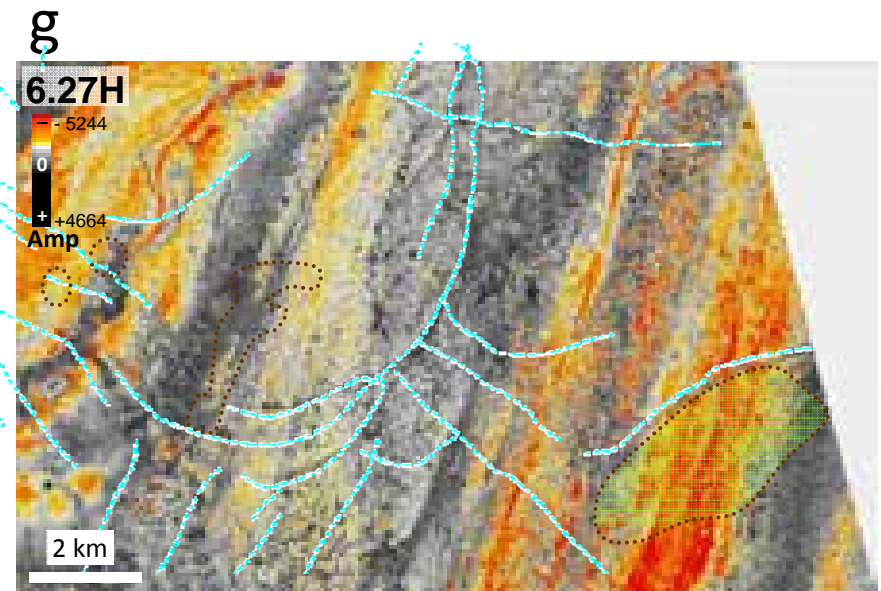
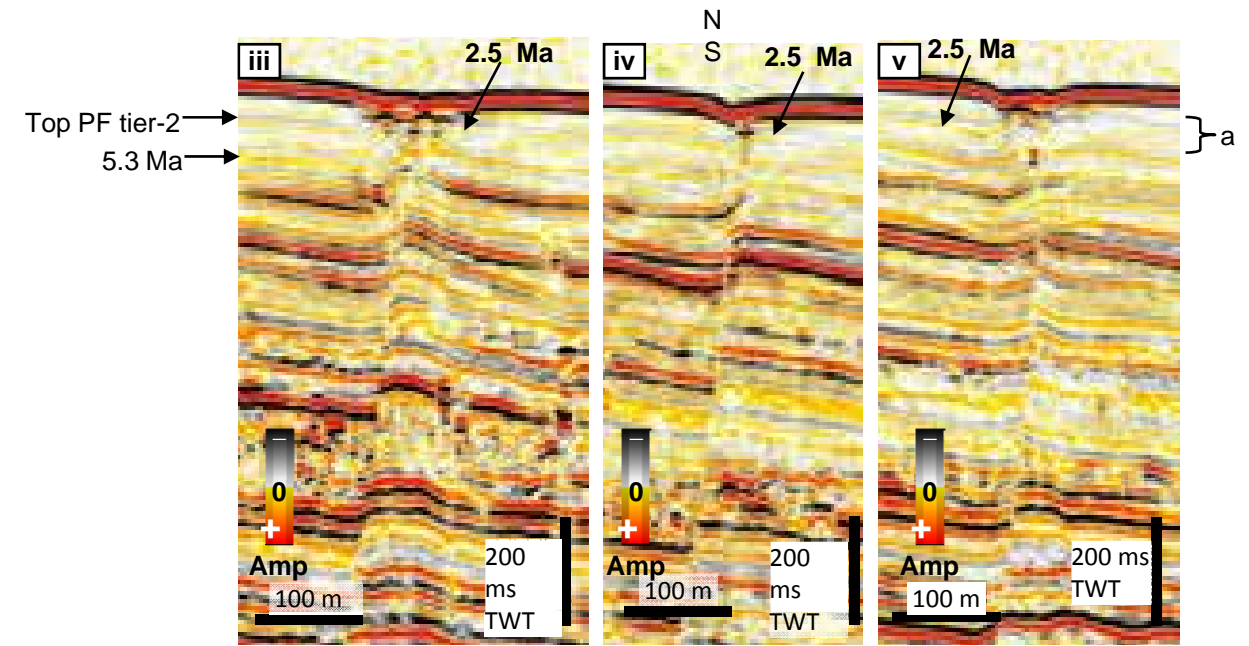
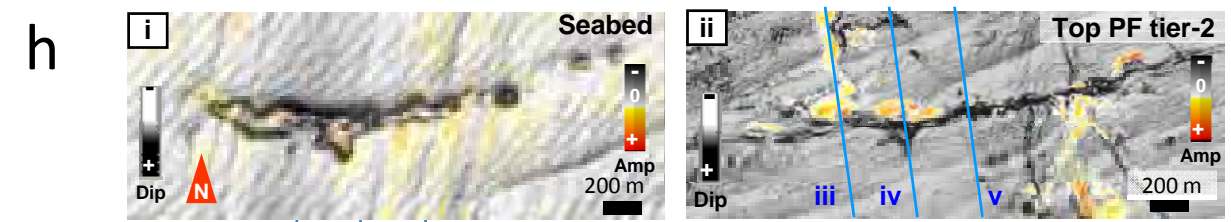
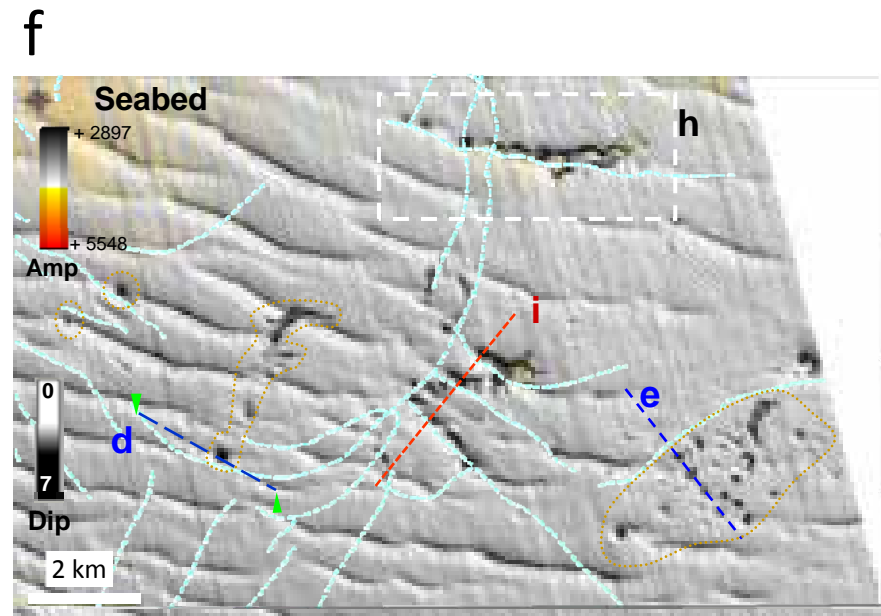


Figure 6.11. a) Seismic section showing vertically stacked pockmarks and depressions in the footwall domain (see line and map location on Figure 6.10b). b) Dip map of horizon 2.5H at the top of PF tier 2.

Figure 6.12. Association of linear PHAAs with tectonic faults in the footwall domain. a) Amplitude extraction from a window between the seabed and the top surface of PF tier 2. The zoomed map shows hook-shaped PHAAs in the hangingwall of a tectonic fault “X”. Note that the anomalies have an orthogonal intersection with the tectonic fault. b) Dip map of the top surface of PF tier 2, c) High amplitude from the amplitude window in a draped over the dip map in b showing PFs and PHAAs perpendicular to a tectonic fault cutting the PF tier (see zoomed map to the right of the figure). The transparent green area on maps in b and c denotes a region of isotropic arrangements of PFs. d) Seismic section intersecting polygonal faults which are in the hangingwall of and orthogonal to a deep-seated tectonic fault. The location of the line is denoted by the red dashed line on maps a-c. The planes of tectonic faults and polygonal faults are interpreted with a light blue dashed line on the section in d. The intersection of the tectonic fault with basal surface of Tier 2 is shown by a dark blue filled circle on map a-d. Vertical blue arrows show the location of PHAAs. The inset and zoomed seismic section shows a PHAA above the graben of a conjugate PF pair. e) Seismic section showing a positive high-amplitude carbonate mound above the upper tip of a deep-seated tectonic fault. f) Dip-amplitude overlay map of the sea bed showing shallow depressions on the sea floor. Some of these depressions occur above PHAAs hosted in the immediately underlying Quaternary sediments (compare maps a and f). g) Amplitude map of horizon 6.27H showing the relationship between burial turbidites and shallow seabed depressions (brown dot contours). h) Elongate zone of coalescence depressions. Maps i & ii are zooms of map f. Cross sections iii – v intersect the seabed depressions and PHAAs and show that they occur above a deep-seated tectonic fault (see line locations on maps i & ii. i) Seismic section across sea bed depressions shown on map f. Note that seabed depressions occur above chimneys which emanate from the upper tips of tectonics faults.





the Pliocene aged polygonal faults tier-2 in hanging wall domain (fig. 6.12d). Their lengths vary from 100-to-700 m and the vast majority strike NE-SW (fig. 6.12a, c). They are aligned parallel to underlying short faults that have same plan form geometries and have lengths ranging from 500-to-700 m and occur within the Pliocene interval (see black arrows on fig. 6.12b). In order to illustrate the relationship between these fractures and distributions of these hook-shaped anomalies an amplitude extraction covering the upper part of Pliocene to lower part Quaternary interval has been calculated and superimposed on the Top PF tier-2 Pliocene dip horizon (fig. 6.12c).

At the outermost limit of the polygonally faulted region as shown by the transparent green area on fig. 6.12b polygonal faults are locally parallel to each other. They strike NW-SE and perpendicular to the adjacent deep-seated fault “X”. Some of the polygonal faults deflect along their strike length becoming slightly oblique to the tectonic faults. Sometimes adjacent polygonal faults deflect towards each other but without intersecting each other (black arrows; fig. 6.12b). The seismic section in Figure 6.12d is sub-parallel to the curved trace of the fault and intersects its southern end (see fig. 6.12b, c). In addition, at the NE-SW striking fault “Y” shown at the eastern side of the map in Figure 6.12b, c. carbonate mounds that are expressed by convex upward positive high amplitude reflections (e.g. fig. 6.12e) are observed above that fault. On the other hand, above the same vertical positions of certain fluid venting structures or above upper tips of deep-seated faults “X” and “Y”, shallow depressions were observed on the present day seabed (fig. 6.12f). In some cases, depressions cluster occur above turbidite deposits rather than deep-seated faults (brown dotted line; fig. 6.12g). But some of these shallow depressions are coalescenced along the underneath tectonic fault to form a long elongate depression, as shown in i and ii in fig. 6.12h. All clustered or individual shallow depressions that occur on the seabed are stacked-up above PHAAs and chimneys which overly tectonic faults (iii to v in fig. 6.12h; fig. 6.12 I).

Interpreted methane-related carbonate mounds

Circular-to-elongated venting structures, methane-related carbonate mounds and pockmarks occur in the NE corner of the survey which is intensively deformed by deep-seated extensional faults (fig. 6.13a-d). Only few linear positive high amplitude anomalies were observed above these normal fault tips (fig. 6.13b). The diameter of carbonate mounds, PHAAs and pockmarks range from 600-800 m, and 100-to-100's ms TWT respectively.

Methane-related carbonate mounds expressed as positive high amplitude reflections

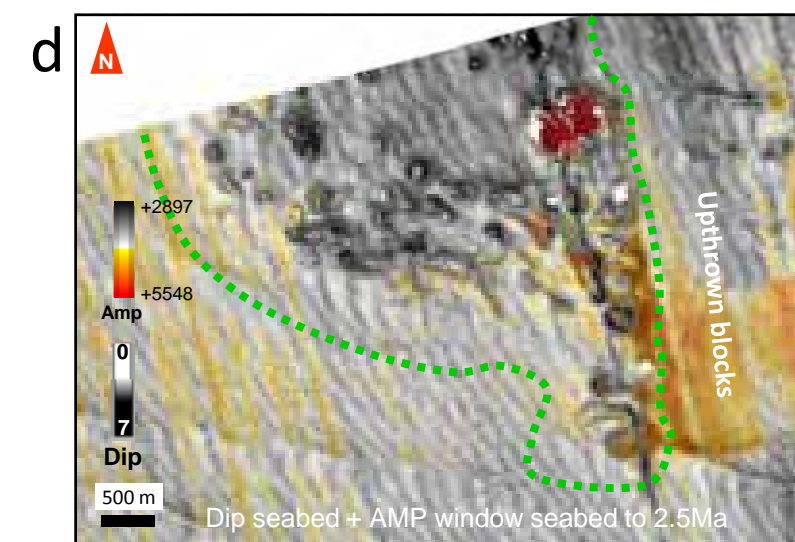
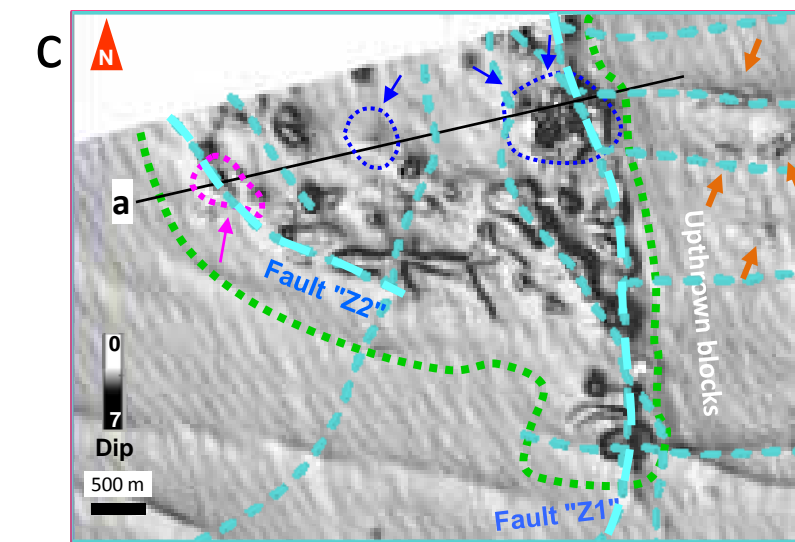
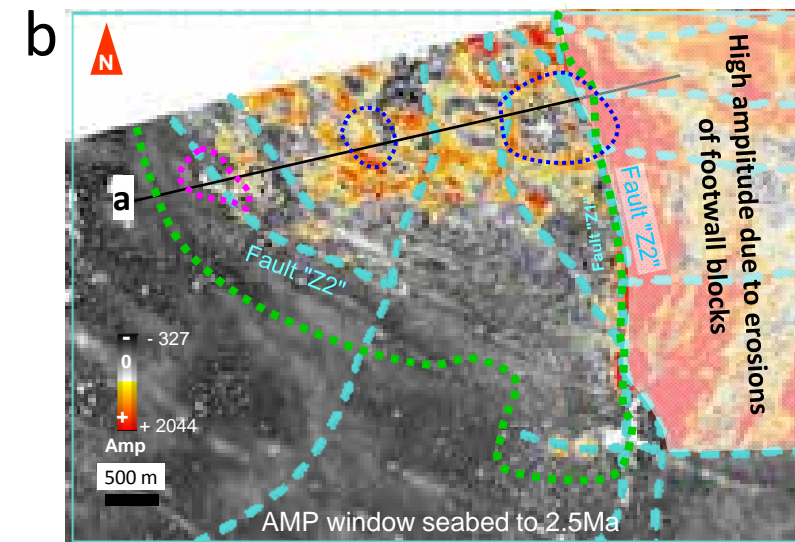
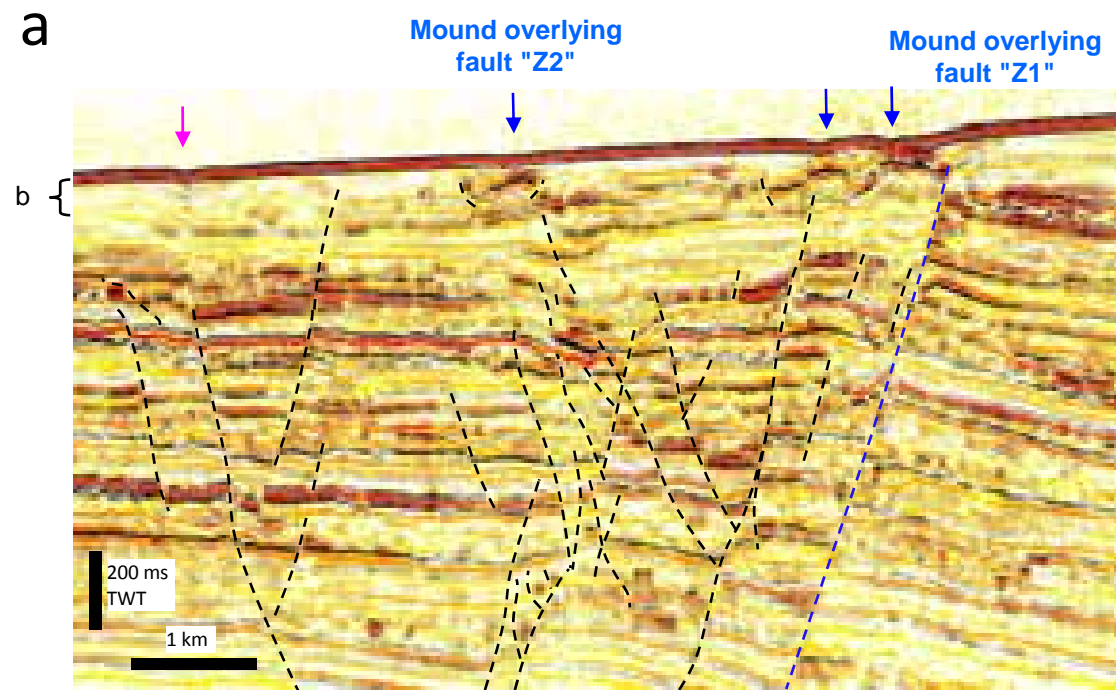


Figure 6.13. Association of carbonate mounds with deep-seated tectonic faults in the NE part of the footwall domain. a) Seismic section showing positive high-amplitude mounds above deep-seated tectonic faults. Mounds are shown by blue arrows. The pink arrows show the location of a shallow seabed depression above a deep-seated tectonic fault. b) Amplitude extraction of the Quaternary sediments showing the distribution of PHAAs. The high amplitude area to the right of the map as defined by the white opaque area is a result of local erosion of a footwall block rather than being related to fluid flow. c) Dip map of the sea bed showing shallow seabed depressions. Note they occur directly above carbonate mounds as indicated by blue arrows. Depressions on the upthrown blocks are indicated by orange arrows and associated with deep root faults. d) High amplitudes from map in (b) draped over the dip map in (c).

(Chapter 4) are developed above the upper tips of extensional faults (fig. 6.13a) and are shown on the horizon of End Pliocene (top boundary of polygonal fault tier-2) (fig. 6.13b). These normal faults are short fault segments of 1.5-2 km long, are bounded by a long fault segments “Z1” striking NNE-SSW and with lengths of 6 km, and by a curved fault “Z2” striking NNW-SSE of a length of 1.5 km (fig. 6.13c; see its location in fig. 6.10a; fig. 3.4b in Chapter 3). These faults define a semi-circular area as highlined by a green dot line in Figure 6.13b – d). Within this area and along these boundary faults, pockmarks, linear-to-sub-circular methane-related carbonates occur and which are expressed by positive high amplitudes reflections (green dot line; fig. 6.13b).

Above some venting structures and on the present day seafloor, sub-circular and elongate depressions which merge together are observed (fig. 6.13c). These present day seabed depressions are often aligned parallel to underlying methane-related carbonated (PHAAs) and have the same sizes (fig. 6.13d). Notice that these seabed depressions mainly occur along these extensional faults (blue dotted lines in fig. 6.13c). This is especially well illustrated in Figure 6.12h and 6.13c, where depressions are aligned with underlying normal faults (orange arrow; fig. 6.13c).

6.5.1.3.5. Complex evolution of a local fluid venting systems above Syncline 0

Development of a complex linear anomalies network within hemipelagic and massive transport complex (MTC)

A more complex venting system defined by linear PHAAs and which terminates upward into pockmarks exhibiting polygonal plan forms has been observed in a deeper interval of Lower Miocene (fig. 6.14a-c; fig. 6.15a-k). This complex venting system is limited by a half-elongate area of approximately 25 kilometres squared with NE – SW orientation and extends to the salt contact of Diapir 1 (fig. 3.5c, Chapter 3). This half-elongate area is located above a gentle withdrawal Syncline 0 (fig. 3.5a, Chapter 3) which is bound by three structures: two crests of the turtle-back antiform and Diapir 1.

MTC's thought to be composed of fine-grained sediments and/or mud-dominated debris flows were deposited during the 11.6 – 16.4 Ma period in this area. The transport direction of MTCs are well illustrated on specific horizons e.g. in Figure 3.5c (in Chapter 3) and Figures 6.15e, f, j. These sediment bodies have all fine-grained matrix as indicated in

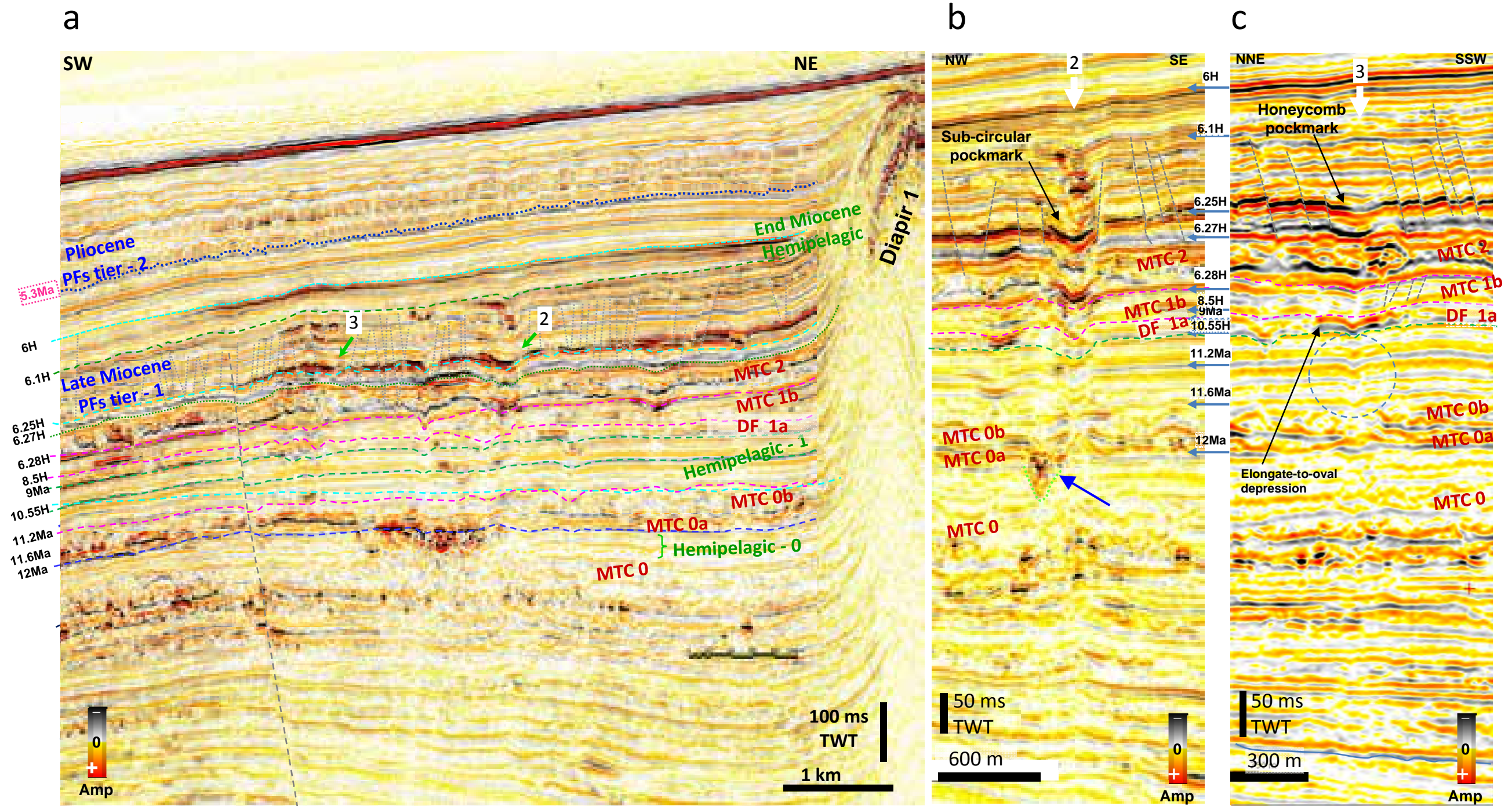


Figure 6.14. Complex venting systems in Syncline 0. a) Seismic section intersecting the West flank of Diapir 1 and Syncline 0 showing vertically stacked pockmarks and shallow depressions (see green arrows). The stacked pockmarks and depressions occur above a kilometre scale negative high amplitude accumulation (see MTC0a). b) Seismic section orthogonal to the stacked pockmark system labelled by the green arrow 3 on section a. The negative high-amplitude anomaly on section b is shown by the blue arrow and is high lined by green dot line. c) Seismic section showing negative reliefs below positive high amplitude shallow depressions; the negative reliefs are surrounding by black dot line.. The location of the line can be found on Figure 6.15e.

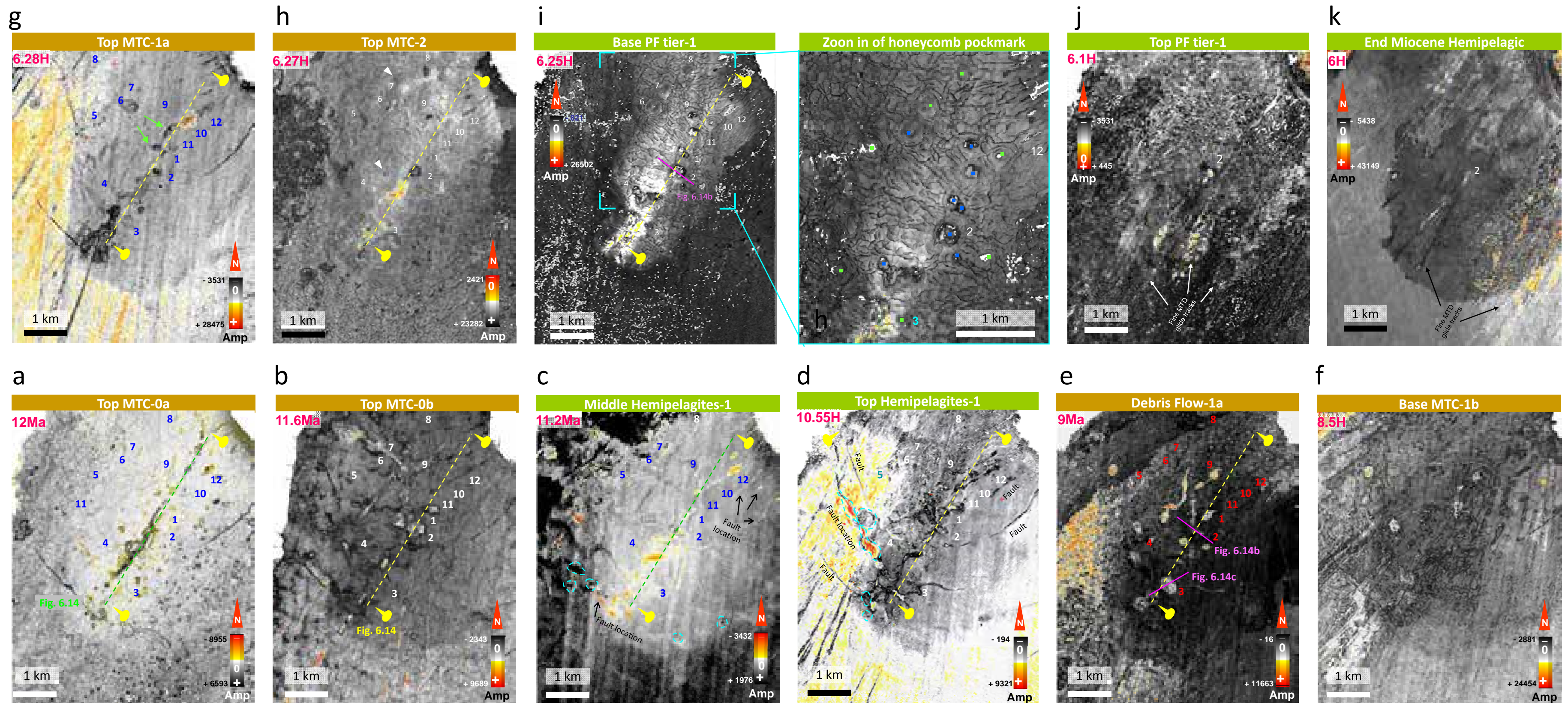


Figure 6.15– Amplitude maps showing variations in the evolution in the distribution and geometry of fluid venting structures during the 6H – 12Ma the Late Miocene. a) Deepest linear negative high amplitude accumulation. b) Grooves on the top of MTC0b. c) PHAA linear network within the hemipelagic unit-1. d) PHAA linear network at the top of hemipelagic unit-1. e) Elongate-to-oval shaped anomalies in the Debris Flow 1a and quasi absent of linear anomalies. f) Quasi absence of high amplitude anomalies at the base of MTC 1b. g) Elongate depressions and few circular craters on the top surface of MTC 1b. h) Circular craters at the top surface of MTC2. i) Honeycomb pockmark field on the basal horizon of PF tier-1, and zone in of the pockmarks. j) The only pockmark remain at the top horizon of PF tier-1. k) The debris flow in End Miocene hemipelagities in syncline 0. Note changes in amplitude polarity on colour scales across figs (a), (c) and (h).

confidential well log reports and generally contain clasts and gravels in this survey. Grooves and glide tracks with same orientation NE – SW are often observed on the surfaces of these sediment bodies (e.g. fig. 6.15a, b, d). In addition, first-order, long concentrically aligned polygonal faults have been observed within the Pliocene sediments above and are parallel to the edge of the subtle Syncline 0 (fig. 3.5b, Chapter 3). Well logs indicate that the sequence hosting networks of linear amplitude anomalies and pockmarks are composed of four MTD units rich in fine-grained sediments. Each of these MTD units is separated by intervals of well-bedded hemipelagites and the shallowest or youngest MTD is overlain by polygonal fault tier-2. In contrast, linear anomalies are primarily observed with hemipelagic beds rather than MTD's.

Fluid venting structures within fine-grained rich MTC-0a

The deepest and earliest linear anomaly occurs on the horizon at the base of MTD unit-0a. It is 4 km long presenting with high, negative amplitudes, negative relief (fig. 6.15a; fig. 6.14a) and is oriented to NE–SW (fig. 6.15a). This earliest linear, high-amplitude anomaly is characterised by a 60 ms thick assemblage of chaotic bright reflections (fig. 6.14a), which extends down into hemipelagic-0 unit. This linear, negative high-amplitude anomaly is overlain by a groove which is hundreds meters long and has the same orientation and occurs on the top surface of MTC 0b above (fig. 6.15b). Similar gouges at the same level are also oriented NE–SW and parallel to the linear negative anomaly previously described. Some irregular-shaped depressions ranging in width and length from several hundred meters and several kilometres respectively were also observed at the upper surface of MTC-0b. The latter two features are associated with positive, high-amplitude anomalies which are interpreted as methane-related carbonates (see Chapter 4).

Linear PHAAs network within hemipelagic-1 interval

Above the high-amplitude features documented above, a complex network of linear high-amplitude anomalies with negative relief occur within an overlying hemipelagic unit (hemipelagic-1). This network is shown on the horizon of 11.2Ma which is located in the centre of the hemipleagic unit (fig. 6.14a; fig. 6.15c). Individual linear anomalies connect with each other and have different lengths and widths which vary from 10s-100s m and 1-10s of m respectively (Chapter 4) (fig. 6.16a). Small elongate/sub-circular shallow depressions with diameters ranging from several tens to a hundred meters are present among the linear

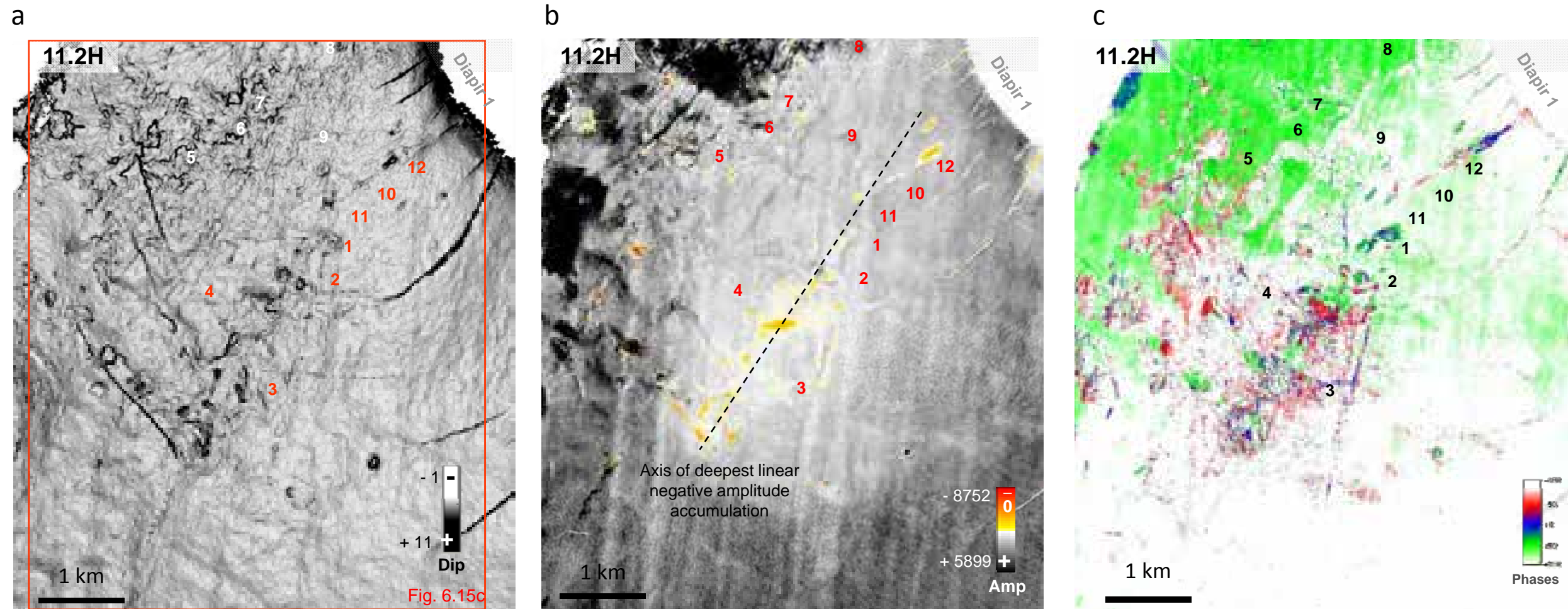


Figure 6.16. Relationship between dominant seismic facies and the geometry of a network of linear high amplitude anomalies in syncline 0. a) Dip map of horizon 11.2H showing morphology of a network of linear anomalies. b) Amplitude map of horizon 11.2H. c) Instantaneous phase map of horizon 11.2H. The map show the degrees of the dominant phase of maximum amplitudes. Different phases correspond to different magnitudes of seismic hardness of the sediments. The blue and red regions on the instantaneous phase map are directly above the deepest and earliest negative high-amplitude accumulations located at horizon MTC0a (primary axis is denoted with a dashed black line).

network or in the adjacent areas (fig. 6.15c; fig. 6.16b). The relief of these depressions is often at below the vertical resolution of the seismic data. Both linear and sub-circular features were spatially linked with each other in some locations.

In contrast to linear PHAAs in the Plio-Quaternary interval (fig. 6.9, 6.12) linear high-amplitude anomalies that occur on horizons have a combination of seismic phases with different hardness's as shown on the instantaneous phase map in Figure 6.16c. This means the polarity of the high amplitude anomalies vary not only vertically but laterally on the same horizon. In such cases, the polarity of high-amplitudes on a given horizon or in a sediment layer can only be distinguished with confidence from instantaneous phase attributes (Paternoster et al., 2011a, b).

The brightest and highest amplitude PHAAs were observed above the earliest linear anomaly. However, some individual linear PHAAs with negative depressions do not have preferred orientations (fig. 6.15a) despite occurring above the NNE-SSW orientated earliest linear anomaly (fig. 6.15a). In contrast, on the SW flank of Diapir 1 PHAAs are parallel to and located above radial faults (Fig 6.15c) and in withdrawal basin 0 some PHAAs are parallel to deep-seated (tectonic) concentric faults. On the top surface of the hemipelagic-1 interval (fig. 6.14a) the configuration of linear, high-amplitude anomalies described above can be observed (fig. 6.15d; fig. 6.17a) but on this horizon the polarity of the linear network is more homogeneous and characterised mainly by positive seismic "hard phases" rather than being multi-phased (fig. 6.17c). Given that depressions at different stratigraphic levels formed at different times, I deduce that changes in their morphology (aspect ratio) and orientation up through hemipelagic-1 unit, until the top of the same unit, occurred gradually during their vertical evolution. Notice that grooves with a SW orientation exist on the top surface of hemipelagic unit-1 (fig. 6.15d; fig. 6.17a) indicating the direction of transported clastic sediments.

Within fine-grained rich Debris flow-1a, MTC-1b, 2

Above the hemipelagic-1 unit, the geometries of high-amplitude anomalies in Debris flow-1a (DF-1a) are different. The Debris flow-1a is expressed by a double reflection with a thickness ranging from 5 to 10 ms TWT (fig. 6.14a) and is close to vertical seismic resolution of the data (5 to 7 ms TWT). Elongate-to-oval shaped anomalies with shallow, negative relief (fig. 6.18a) substitute the linear anomalies underneath at the same vertical location in

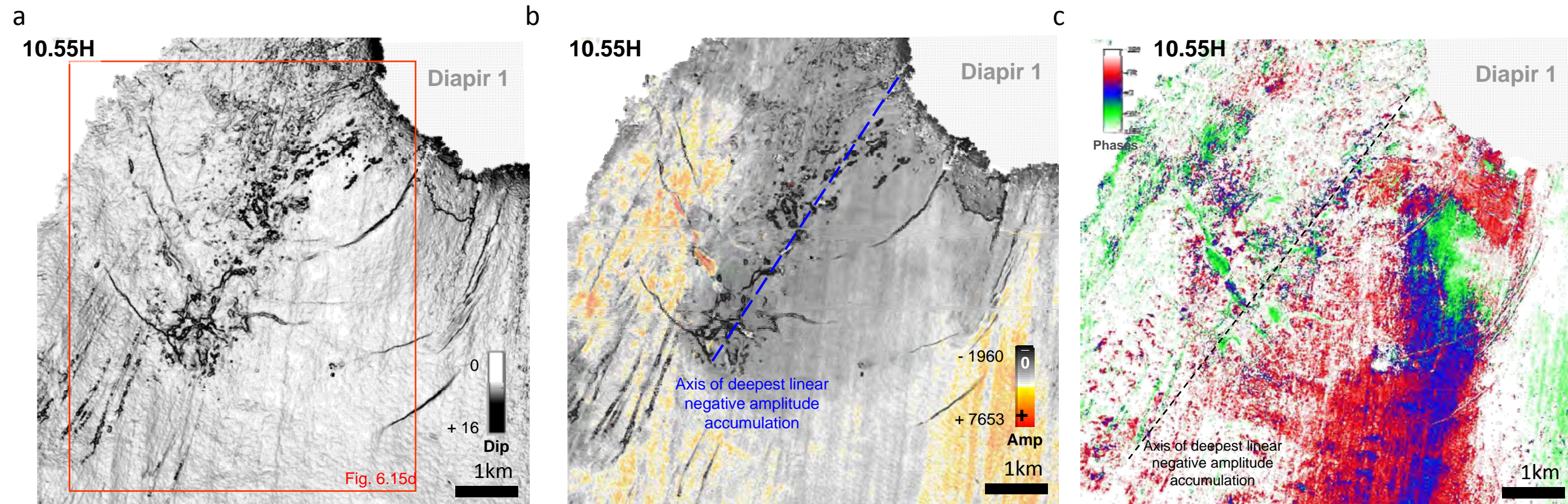


Figure 6.17. Relationship between dominant seismic facies and the geometry of a network of linear high amplitude anomalies in syncline 0. a) Dip map of horizon 10.55 H showing morphology of a network of linear anomalies. b) Amplitude map of horizon 10.55H. c) Instantaneous phase map of horizon 10.55H. The map show the degrees of the dominant phase of maximum amplitudes. Different phases correspond to different magnitudes of seismic hardness of the sediments. The blue and red regions on the instantaneous phase map are directly above the deepest and earliest negative high-amplitude accumulations located at horizon MTC0a (primary axis is denoted with a dashed black line).

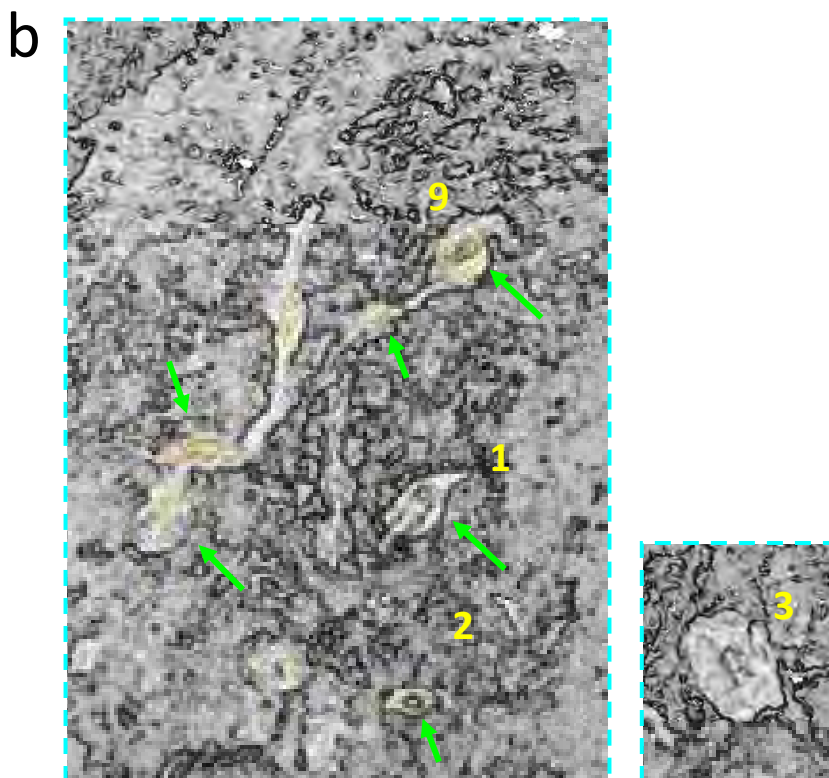
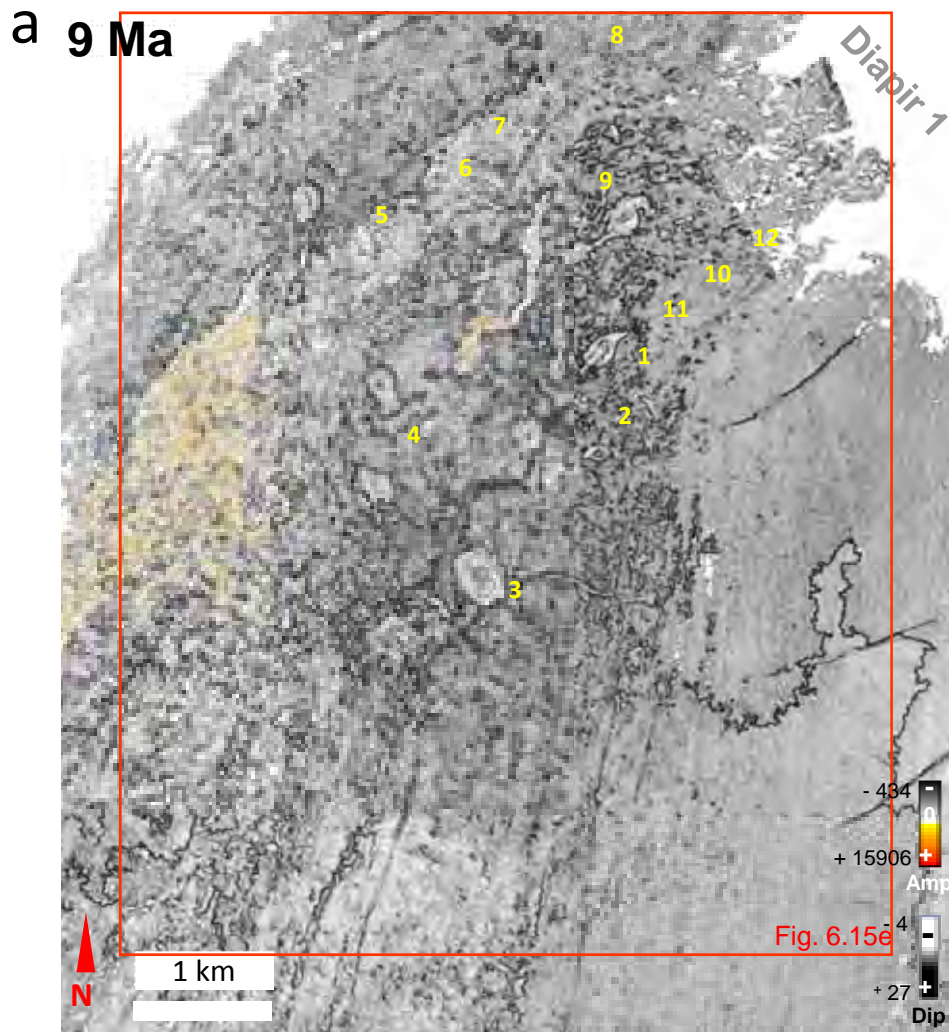


Figure 6.18. Elongate-to-oval depressions occur above linear high amplitude network and are observed in DF-1a in location of syncline 0. a) Dip and amplitude overlay map of horizon Debris Flow-1a showing the morphology of shallow depressions which are indicated by green arrows. The depressions occur above the network of linear anomalies which are hosted in the units beneath horizon hemipelagic 1. b) Zoom section of map in a showing morphology of elongate to oval shaped amplitude anomalies.

hemipelagic-1 unit (fig. 6.15e). Only a few linear anomalies at the top surface of hemipelagic-1 unit remain visible on the horizon of Debris flow-1a (fig. 6.15e). The side walls of some elongate-to-oval depressions terminate abruptly at the ends of the longest axis (fig. 6.18). Within the centre of these depressions there is a second depression with a linear plan form. This linear depression is aligned parallel to the longest axis of the elongate depression. This particular type of depression is restricted to debris flow unit 1a, and which is truncated by these elongate-to-oval shallow depressions (fig. 6.14c).

The vertical evolution in the plan form geometry of these elongate to sub-circular PHAAs within stacked MTCs sequences can be visualized at the interface between each MTC unit. On the basal surface of MTC 1b, PHAAs and depressions are absent (fig. 6.15f). At the interface between MTC units 1b and 2 (fig. 6.15g) only an elongate truncated area of a kilometre-long occur above the southern part of the earliest linear anomaly. While there are a few elongate, high-amplitude depressions can still be observed above the northern and central part of earliest linear anomaly (e.g. indicated by numbers 11, 13 and green arrows in fig. 6.15g). No isolated linear features were observed at the interface or surfaces of MTCs mentioned above. These elongate depressions at the interface of MTCs and the linear features in the underlying hemipelagic-1 unit are aligned parallel to each other above the vertical location of earliest linear anomaly. The vertical distribution of these structures implies a genetic relationship between them and the earliest linear anomaly.

The first conical pockmarks are observed at the top surface of MTC1b (interface MTC1b-2) one of them above the vertical location of earliest linear anomaly (point 2 in fig. 6.15g). These earliest circular pockmarks continued to develop after the deposition of MTC-2 and only occur on the top surface of MTC-2 (point 2 in fig. 6.15h). Few other new depressions occurred afterward above the linear network on the top surface of MTC2 (indicated by white arrows; and points 3, 7, 8, 9 in fig. 6.15h). These new depressions occur at this interface between MTC-2 and middle Miocene polygonal faults tier-1 (white arrows and points 3, 7, 8, 9 in fig. 6.15h) have negative, high amplitudes (e.g. white arrows and points 7 - 9 in fig. 6.15h) in some cases. However, most of these depressions continued to evolve in polygonal fault tier-1 (e.g. points 3, 7, 8, 9 in fig. 6.15i; fig. 6.14a), within an elongate bright amplitude area. This bright-amplitude area at the base of polygonal fault tier-1 (fig. 6.19a) is seismically “soft” as indicated by the instantaneous phase values of -90 degrees (red coloured area; fig. 6.19b). The number of pockmarks within this area decrease steadily toward the top of polygonal fault tier (fig. 6.15j, k). Notice that horizon close to and at the top of polygonal

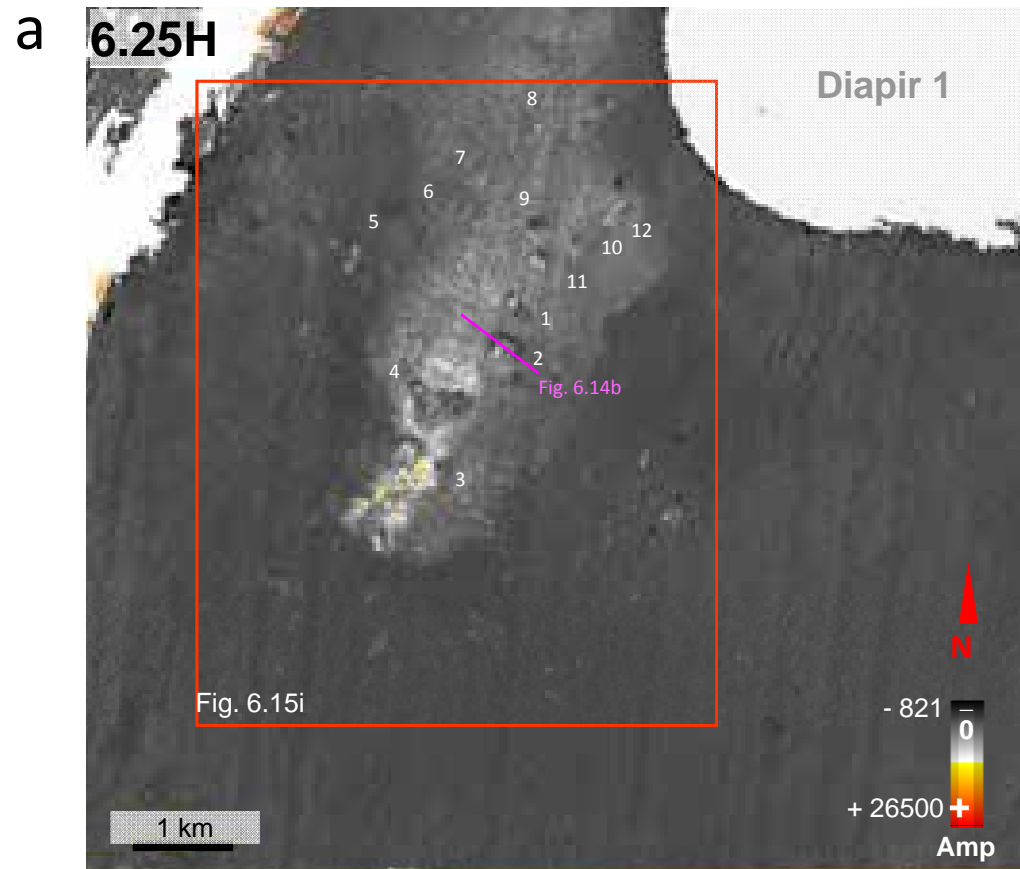
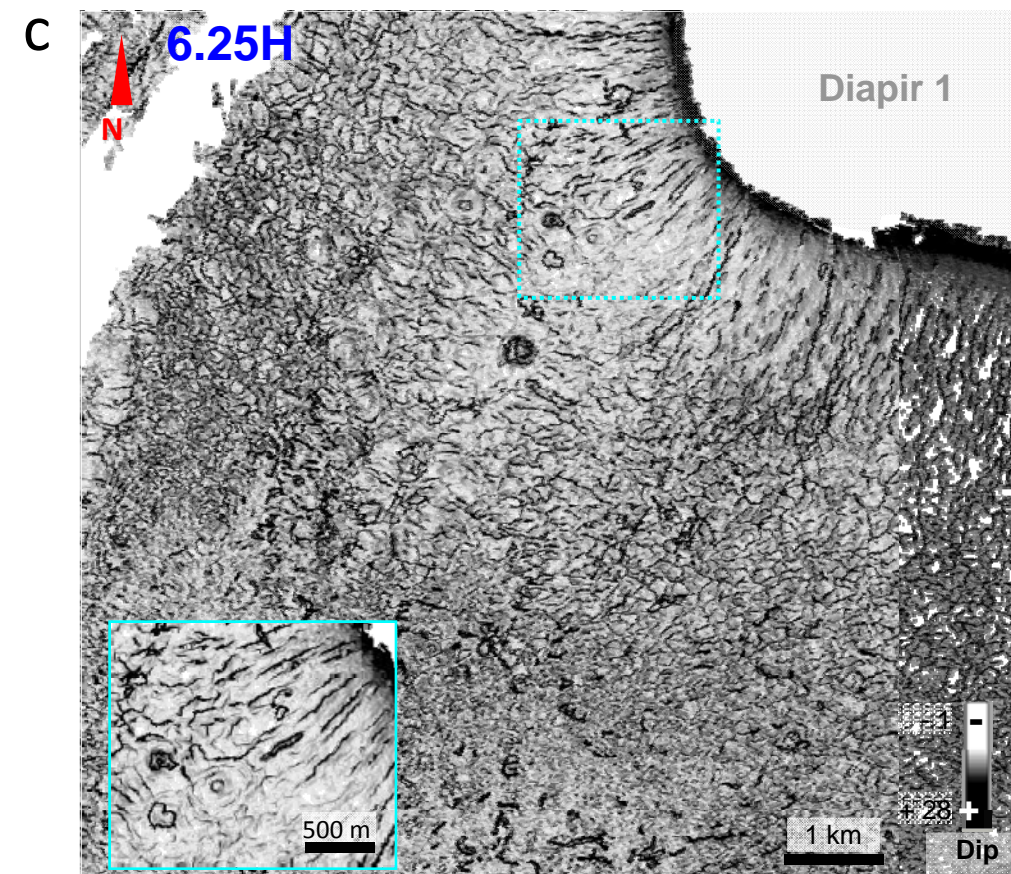
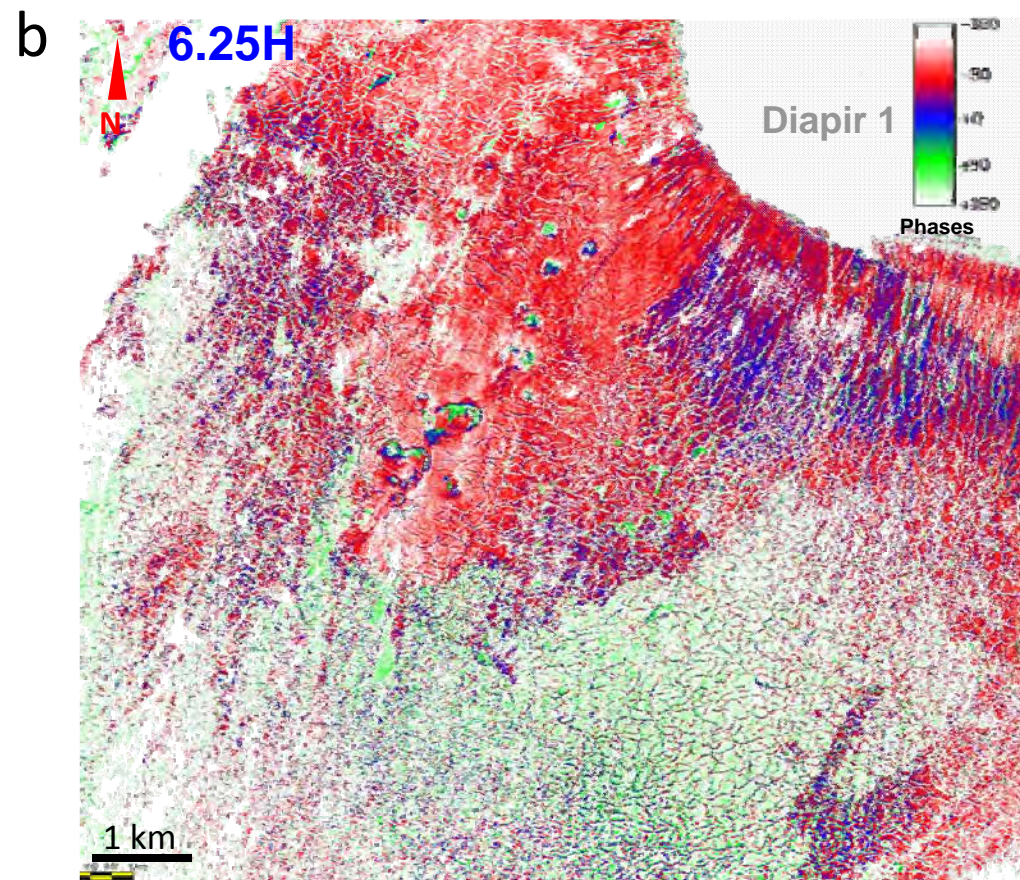


Figure 6.19. Relationship between dominant seismic facies and the distribution of honeycomb pockmarks in syncline 0. a-c) Amplitude, instantaneous phase and dip map of horizon 6.25H respectively. Note that the area containing honeycomb pockmarks corresponds to a red area on the instantaneous phase map which equals -90 degrees. This equates to soft phased horizons. The location of the zoomed inset map on (c) is denoted by the blue box.



fault tier-1 show glide tracks on horizons at the uppermost section of the polygonal fault tier-1 indicates that the sediment transport direction was from NNE toward the SSW (fig. 6.15j, k).

Moreover, linear PHAA networks within hemipelagic-1 unit which are characterized by linear zones of seismic acoustic perturbation on seismic sections switch vertically to elongate-to-oval depressions at the level of debris flow1a (e.g. pockmark-3 in fig. 6.15d, e). Because the earliest anomaly, acoustic perturbation columns and pockmarks are stacked vertically above one another it is suggested that; linear fractures forming above the primary linear, high amplitude anomaly served as fluid conduits for the expulsion of fluid which formed the pockmark craters. This idea is explored more in discussion section.

6.5.1.3.6. Honeycomb pockmarks within polygonal fault tier-1

Above the linear anomalies and within the PF tier-1 several generations of individual shallow pockmarks or flat bottom shallow depressions are stacked vertically (fig. 6.14a). These pockmarks occur intermittently throughout polygonal fault tier-1. These pockmarks (generalized term for describing flat bottom depressions and pockmarks in given vertical successions which composed by both types of features; see section 6.2.2) have been observed to aligned with linear high-amplitude anomalies hosted in the hemipelagic-1 beds and occur mainly along the axis of the earliest, linear negative amplitude accumulation at the base of MTC-0a (fig. 6.15a).

A total of 23 pockmark systems have been found at the lowest boundary of PF tier-1 and inside a pockmark field. The plan form geometry of 15 of the pockmarks and which are less than 12 ms (TWT) deep are particularly well demonstrated by the bottom horizon of the polygonal fault tier-1 (fig. 6.15i; fig. 6.19c).

Instead of being circular- shaped or occurring in the middle of polygonal cells (Imbert, 2009; Andresen and Huuse, 2011), or being surrounded by concentrically aligned polygonal faults (Chopra and Marfurt 2007; Cartwright, 2011; Imbert et al., 2011), these 15 pockmarks appear as same shape as polygonal cells (light green dots in fig. 6.15i; fig. 6.19c). In the other words, the boundaries of these pockmarks depressions in planview on the horizon are cut through by the polygonal faults. These types of pockmarks are referred to as “honeycomb pockmarks” because of their unique crater geometry. The rest of the 8 pockmarks are all sub-circular to circular-shaped and are not affected by polygonal faults (blue dots in fig. 6.15i).

However, the strikes of polygonal faults are still affected by the pockmark crater as can be seen in Figure 6.15i where polygonal faults curve around pockmarks 1 and 2.

The depths and diameters of the lowest individual pockmarks at the lower boundary of PF tier-2-1 have been measured. Because they are the deepest are thus considered being the first to form, and since they are intersected by polygonal faults, so it infer that they preceded polygonal fault growth (fig. 6.14c; fig. 6.19c). The diameter of these pockmarks range from about 100-to-400 meters and varies from 3-to-20 ms (TWT) deep. Furthermore, the fact that polygonal faults deflect around the edge of the pockmark craters implies that crater existed first. In later sections I discuss the relationship between perturbations of the regional stress state around pockmark craters and the alignment of polygonal faults (Chapter 6 in Carruthers, 2013).

6 of the 15 honey comb pockmarks have aspect ratios of more than 1.3 (fig. 6.20a). The remaining 9 honeycomb pockmarks have aspect ratios ranging from 1.04 to 1.2 which is a typical value of the 8 sub-circular pockmarks. Six dip values of the pockmark sidewalls were calculated for each pockmark. Dips were calculated using 3 P-wave velocities (1650; 1750 and 1900 m/s) within the best estimated internal velocity range. This was to establish the degree of error associated with the uncertainty of the true internal velocity of the interval deformed by pockmark craters.

For each P-wave velocity used dips were calculated on the side wall orthogonal to the longest and shortest axis. The studied results show that all of the 8 pockmarks with circular planforms have steepest sidewalls which dip at more than about 4° for both longest and shortest axis (4.6° , 4.9° , 5.3° and 4.8° , 5.1° , 5.6° are minim values respectively obtained by using the three P wave values). While all honeycomb pockmarks have dips less than 4.6° . Interestingly, after comparing the depths of honeycomb and sub-circular pockmarks I found that they former consistently have depths of 3-12 ms while circular pockmark craters are larger and have depths greater than 12 ms (fig. 6.20b). Most of the sub-circular pockmarks within PF tier 1 are stacked vertically above pockmarks depressions on the upper surface of MTC unit -2, MTC unit -1b and debris flow unit-1a. These pockmarks are also aligned above the earliest linear anomaly in the MTC unit-0 implying a genetic relationship exists between all of these venting structures. Notice that there is a 360m long, linear depression with a depth of 13ms TWT (see point 12 in fig. 6.14i) between two radial faults.

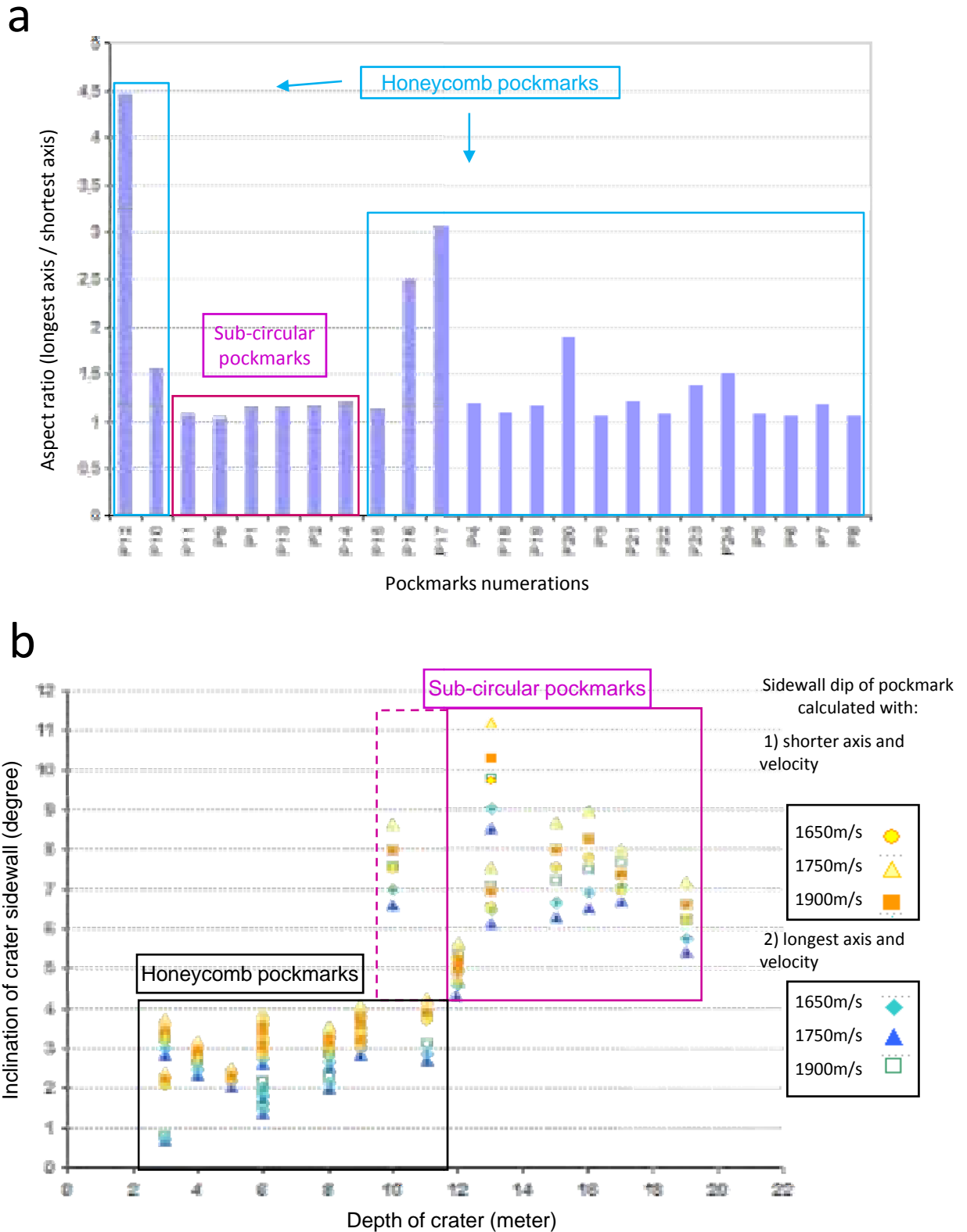


Figure 6.20. Statistical analysis of pockmark dimensions, crater depth and flank inclination. a) Aspect ratio of honeycomb pockmarks (blue square) and sub-circular pockmark depressions (pink square) on horizon 6.25H near the base of PF tier 1. b) Graph showing the relationship between the depth and sidewall inclination of pockmark craters and depressions. Note that honeycomb pockmarks and sub-circular pockmarks fall into two distinct groups.

6.6. Interpretations and discussions

In the preceding sections a detailed analysis and characterisation of the fluid venting structures in the study area, vertical changes in types through stratigraphic intervals with varying lithologies and their proximity and orientation with respect to tectonic structures was presented. The purpose of this section is to expand on these key observations and discuss two main themes, namely; 1) the relationship between the genesis and timing of faults on the evolution of fluid venting structures and their orientation, and 2) outline reasons why vertical variations in lithology through a stratigraphic section may influence the type of fluid venting structure that forms during fluid expulsion. In the former themes, the influence of local stress anisotropy associated with the tectonic structures, of sedimentary propriety associated with depositional models and the resultant formation of linear fractures are investigated.

6.5.1. Significance of linear chimneys within polygonal fault tier-2

6.5.1.1. Formation of linear chimneys at polygonal fault locations

Numerous studies on seismic acoustic chimneys in association with signal perturbations of pull-up, push down or wipe out zone have been investigated over the last decade (Ligtenberg, 2003). Acoustic perturbed columnar zones on seismic are commonly recognized as expressions of fluid conduits (cf. Hegglund, 1997; 2004; Løseth et al., 2001; 2011; Gay et al., 2003; Hustoft et al., 2007; Moss and Cartwright, 2010a, b).

Localised, positive high-amplitude anomalies or stacked reflections associated with seismic chimneys represent seismically hard and fast materials (Hustoft et al., 2007; 2009; 2010; Westbrook et al., 2008, Petersen et al., 2010) and are interpreted here as either methane-related carbonates or potentially having an association with gas hydrates within the gas hydrate stabilisation zones (Chapter 4). On the other hand negative, high-amplitude bright spots (stacked to form columns) or polarities inversions are considered as seismic expressions of free gas accumulations (Coffeen, 1986).

Seismic chimneys which do not terminate upwards into pockmark craters have been classified as “seepage pipes” by Cartwright et al. (2007) and are inferred to form under

relatively slow seepage rates (cf. Roberts, 2001; Roberts et al., 2006; Cartwright 2007; Naudts et al., 2010). On the other hand, vertical chimneys with linear plan forms and which intersect basal-tips of polygonal faults and are associated with methane-related carbonates at the top have been newly reported and interpreted as slow fluid venting structures (Chapter 4). In Chapter 4, I suggested the emplacement of the linear conduits (hydraulic fractures) occurred along the central axis of polygonal fault grabens because fluid pressures exceeded the rock strength and the least principal compressive stress that is orthogonal to the central axis. However, I have not explained why fluid pressures at such location exceeded the least principle stress.

In order to establish if fractures adjacent to polygonal faulting provide the pathways for linear venting systems I first must establish that there is a spatial relationship between the location of PF and linear chimneys (fig. 6.3). Of the 209 number of linear amplitude anomalies I examined what part of the PF plane they emanated from, for example if they consistently occurred in the hanging wall, footwall or at the basal tip. The counting procedure is described in detail in the methodology section. 28 % of linear chimneys stem from the lower part to the basal tips of single PFs, and 8 % stem from the lower part to the basal tips of PFs which is conjugate PF pairs, meaning a majority of linear chimneys (36%) stem from this position on the PF (fig. 6.2c). 19% intersect apparently the bottom tips of paired PF grabens (fig. 6.2a, d). It is possible that the linear chimney also intersected the lower part of PFs but the seismic resolution and acoustic perturbation prevent an accurate determination of the position. 18% of linear chimneys emanate from tectonic faults (fig. 6.2i) whilst 9% of the linear chimneys have migrated through the middle of PFs plane (fig. 6.2h). 7% of linear chimneys have stemmed from the middle of PFs horsts (fig. 6.2e, f). The lower terminations of linear chimneys intersect the upper tips region of PFs (either in footwalls or hanging walls) (Fig 6.3) in 4% of cases. In 3% of cases the upper terminations of linear chimneys are bound by the fault plane of polygonal faults (fig. 6.2g). In 3% of cases it was not possible to determine their exact position. The smallest group of linear chimneys, accounting for 1% of cases, emanate from the topmost tips of polygonal faults (fig 6.3).

The fact that the majority of linear chimneys stem from the lower part of the PF footwall or in the basal tip region surrounding PFs suggests that linear venting systems did not form as a result of fluid migration along or through polygonal fault planes. Instead, it is more likely that fluid initially propagated through the footwall then breached the fault plane and continued migrating vertically up through the hanging wall (fig. 6.21). Only 1% of linear

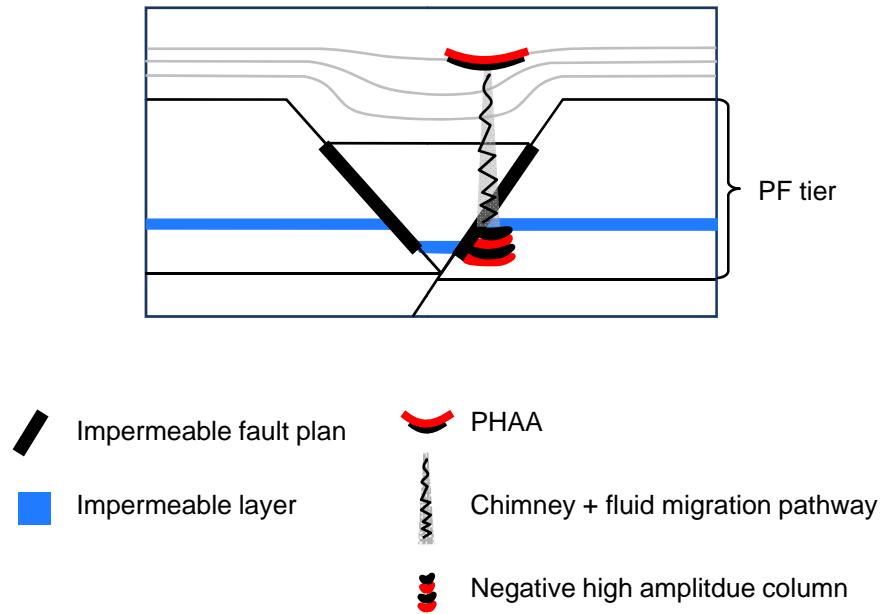


Figure 6.21. A model of fluid migration within polygonal fault tier base on the interpretation of seismic images. Fluid migration via vertical fractures which initiated in the lower part of PF footwall and propagated in PF hanging wall. Cartoon not to scale.

conduits or PHAAs occur at the upper tips of PFs. Of the 36% of linear chimneys that intersect the lowest part of PFs, 48% among the 36% are characterized by free gas columns or accumulations (expressed by negative high amplitude bright spots) in the lower part of footwall or rotated blocks (e.g. fig. 6.2c). These accumulations of free gas are stratigraphically bound by horizon Intra-Plio within the PF tier-2 suggesting that this horizon is impermeable (fig. 6.4f). This structural and stratigraphic configuration forms a fault bound trap. It is especially well illustrated by linear conduits with downward terminations without acoustic perturbations in withdrawal Syncline 2 (fig. 6.2i; fig. 6.5b).

In summary, because the majority of linear chimneys stem from the basal tip region or lower fault block of PF, it suggested that fluid was expelled upward by vertical fracturing from this point rather than opening the upper part of PF plane. This interpretation would be consistent with the results of Nunn (2003) who found that fluid pressure was not great enough to maintain low effective stress in the upper fault zones. Therefore, the lower part of polygonal faults are most likely permeable and critically stressed in their contemporary stress field (cf. Wiprut et al., 2000; Zoback, 2007) while the upper parts are neither permeable nor critically stressed (cf. Wiprut et al., 2000; Zoback, 2007). On the other hand, fluid generated tension in host rocks and propagated new fractures in the hanging wall instead of fully invading the pre-existing PFs plans. This suggests fluid pressure was sufficiently strong to overcome the least compressive stress and the fracture strength of host rocks (Delaney et al., 1986; Kattenhorn et al., 2000). As a result, the stress states of PFs have important role to play in the formation of fluid flow pathways.

6.5.1.2. Gas accumulations in the lowest part of polygonal fault footwall

Preferential accumulation and build-up of gas at the bottom of footwalls of extensional faults (see fig. 6.2i; fig. 6.5b) could occur for following reasons: 1) regimes of fault deformation control on distributions of strains in faulted blocks (Barnett et al., 1987; Zhang et al., 2009) in fault-bounded reservoirs, 2) stratigraphic position of offset permeable layers in fault blocks, 3) permeability of faults relating to fluid pressures. The following hypotheses are proposed by making analogies with studies which have researched fractures around regular normal faults.

1) Strains in extensionally faulted rocks

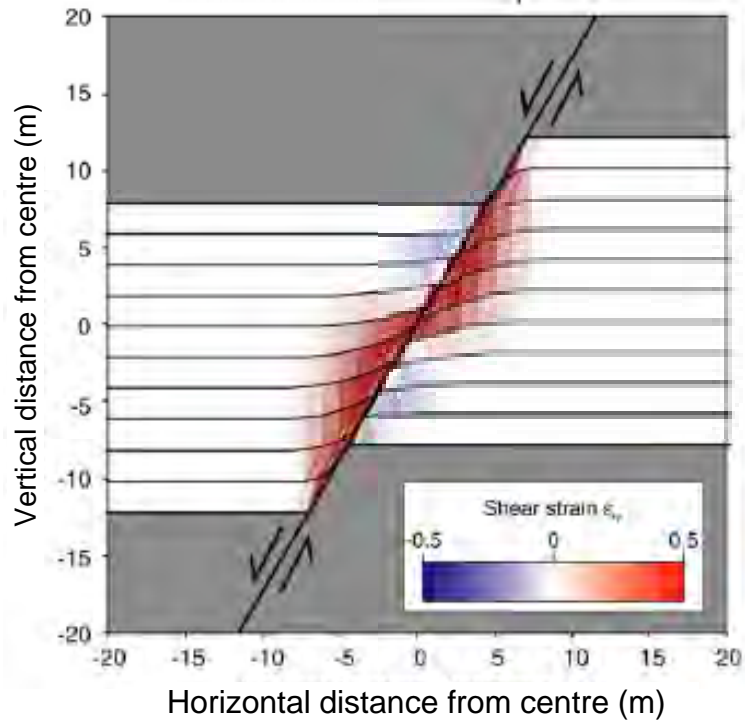
Shear strains resulting from extension and normal faulting affect the hydraulic properties of rocks adjacent to the fault surface (Barnett et al., 1987). Extensional faulting induces significant shear strain and dilatancy (Zhang et al., 2009) which consequently enhances the permeability of the wall rocks. Numerical modelling in Zhang et al. (2009) revealed that lowest shear stresses occurred in the footwall block near the basal fault tips of a normal fault and the greatest shear stresses occurred in the upper part of hanging-wall block. This is consistent with the numerical simulations of Welch et al. (2009) (fig. 6.22a). These numerical models are in accordance with the conceptual model of Barnett et al. (1987) which show that the lower parts of footwalls and upper part of hanging walls were in a state of relative compression compared to the top of the footwall and base of the hanging wall respectively. (fig. 6.22b, c). Variations in the shear strength of the wall rocks can greatly impact their porosity and permeability (Barnett et al., 1987). Given that this stratigraphic interval had only been buried to tens of meters there is a good chance that the sediments are not fully lithified, and thus it is important to understand how this may impact the shear strength in the rocks surrounding normal faults. Barnett et al. (1987) pointed out that unlithified sediments experiencing dilation most likely have a low shear strengths. Therefore, greatest permeability's would be expected in the footwall of a normal fault near the basal fault tip and this is where any fluid migrating into the faulted interval would accumulate (fig. 6.2g, h; fig. 6.5b). This thinking is corroborated by this study as I consistently observe linear chimneys emanating from the lower parts of the footwall, and in which negative high amplitude spots are observed in some cases.

2) Stratigraphic position of permeable layers in footwall compared to hanging wall

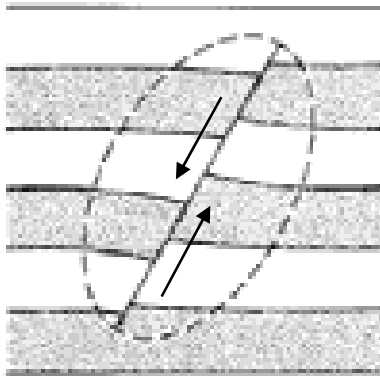
Another possible explanation for preferential accumulation of hydrocarbons in the footwall blocks of normal faults is because beds in the footwall occur at a shallower stratigraphic position compared to the hanging wall. If my suggestion that an impermeable bed (in this case the Intra-Plio horizon) coupled with an impermeable fault plane is the reason for gas being restricted to the lower part of the PF, then any fluid migration below this point would preferentially fill the highest available pore space which for the case of a normal fault is the footwall as illustrated in (fig. 6.23).

a

Numerical modelling of displacement of a normal fault by Welch et al. (2009)



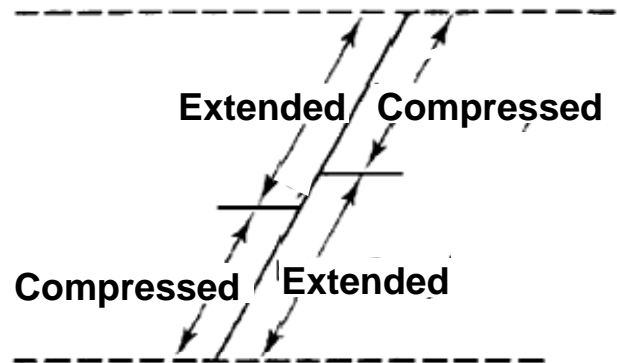
b



Displacement not to scale

(Modified after Barnett et al., 1987)

c



Displacement not to scale

(Modified after Barnett et al., 1987)

Figure 6.22. a) Diagram showing the magnitude of shear straining of the rocks around a normal fault (taken from Welch et al, 2009). b) Displacement of horizontal beds by a normal fault (figure taken from Barnett et al., 1987). c) Regions of relative extension and compression of the rocks around a normal fault (figure taken from Barnett et al., 1987).

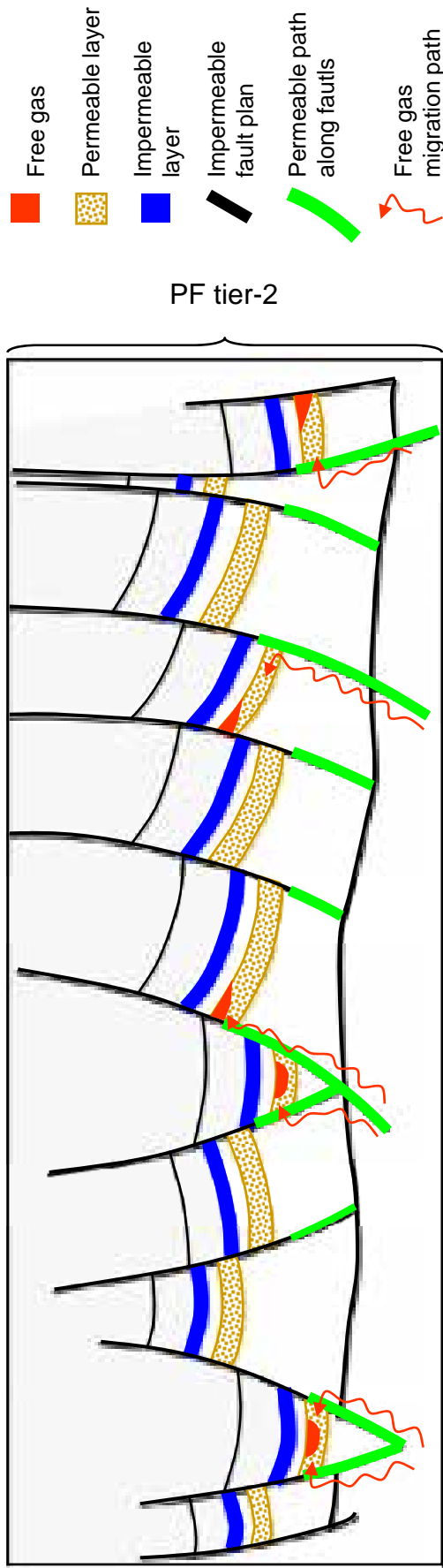


Figure 6.23. Conceptual mode for the migration of free-gas into the permeable layer at the bottom of polygonal fault tier 2. Cartoon not to scale.

3) Permeability of PFs and fluid flow behaviour within PF grabens and horsts

Although the polygonal faults in this study area conform to two discrete stratigraphic intervals i.e. Tiers 1 and 2 close inspection of the stratigraphic position of basal tips show some variation (e.g. fig. 6.2b, g, I; fig. 6.4f, h; fig. 6.5b). Basal tips can terminate at any one of several horizons at the base of the tier. For example, fault maps presented in Figure 6.15h and 6.15i highlight that the lengths of polygonal faults are highly variable.

I propose a conceptual model that; the longest of the polygonal faults which extend to the deepest stratigraphic levels promoted vertical fluid migrations into PF tier-2 from underlying carrier beds. Once fluids migrating laterally reached a polygonal fault surface intersecting the carrier bed, fluid began to migrate vertically along the lower part of PFs footwall until it reached an impermeable barrier. In this study I suggest this barrier was provided either by an Intra-Pliocene impermeable bed as indicated by underlying free gas accumulations that are expressed by negative bright spots (fig. 6.2g, h ; fig. 6.21). Alternatively, the impermeable barrier may be related to the relative stress and strength changes in different fault block domains as predicted by Barnett et al (1987) and explained earlier in this section. Retention of free gas in the lower part of foot walls and the formation of gas chimneys implies that fluid pressure was only sufficient to open hydraulic fractures in the lower part of PFs and below the Intra-Plio horizon. Negative bright spots are lacking in the upper part of PFs and above the Intra-Plio, I suggesting there are no accumulations of gas above this level. Thus, it was likely that no vertical communications between lower part and upper part of PFs blocks in tier-2. However, due to lack of well data, limitations imposed by the vertical resolution of the seismic data, in addition to seismic blanking which obscures the lowest part of the gas chimney further information must be gathers to verify the hypothesis.

The second largest collection of linear gas chimneys (19%) emanate from the intersection of conjugate polygonal fault pairs i.e. from the basal apex of PF graben. Due the acoustic perturbation in the downward termination of the chimneys, it is not possible to confirm the exact positions of the central axis of linear conduits are really at the intersection of conjugate PF pairs. Therefore, I consider two possibilities for the actual position of this population of linear chimneys. Either they emanated from the PF intersection as proposed in Chapter 4 or they emanated from the lower part of the PF plane closing to the basal apex of PF grabens. However, due to acoustic perturbations in the lower part of these chimneys it appears that the chimneys emanate from the basal apex of the PF grabens. Both of these may occur as close inspection of seismic data reveals examples of both (fig. 6.2b, d) e.g. 19% of

linear conduits have central axis align with the apex of graben, 28% of vertical chimneys intersect the bottom tips or the lower part of single PFs plans, and 8% intersect or emitted from the lower part of a PF which was conjugate pair.

Assuming that linear chimneys do in fact emanate from the intersection of conjugate PFs raises further questions about what properties of the wall rock in this setting cause preferential initiation of hydraulic fractures in the apex of PF graben. If beds within the tier have different permeability's this could be explained by migration of fluid into an intra-tier permeable bed, overpressure and breaching of overlying impermeable beds. There are two possible ways in which fluid could migrate into this permeable bed. The first is the stratigraphic position of permeable layers within the grabens. For example, normal fault displacement may be great enough to juxtapose the permeable layer within the graben onto the carrier bed in the adjacent footwalls (fig. 6.24a). Alternatively, the lower part of the polygonal fault plane may be permeable and allow gas to migrate from the carrier bed into the permeable layer in the PF tier (fig. 6.24b). Because the stratigraphic positions of the basal tips of PF's vary, there are second scenarios. The basal tip occurs above the carrier bed (fig. 6.24c), perhaps because of the difference in lithology which is known to influence the vertical confinement of PF's, while the longest PF's, which are thought to be affected by regional or local stress perturbations propagated preferentially in the vertical direction so that the basal tip occurs below the regional basal tier surface (fig. 6.24c). In this scenario the basal tips of some individual faults may occur within the carrier bed (fig. 6.24c). Once the fluid reached the topmost permeable layer which is bound by the impermeable conjugate fault planes and/or impermeable strata free gas was retained inside the bottom of the PF graben. This is evidenced by the negative, high-amplitude anomalies in the lower PF grabens as shown in Figures 6.2d. In this case of hydraulic fractures occur in PF hanging wall, fluid pressure may be stronger than the shear strain in the lower part of hanging wall but not stronger enough to open the impermeable polygonal fault plane, and overpressure fluid may create a new fracture in hanging wall (fig. 6.24d). Therefore, the development and breaching of this fault bound trap thus controls the location of hydraulic fractures and thus the geometry and location of the linear chimneys.

In conclusion, it is statistically more likely based on the downward termination of chimneys locate in the lower part of PF that, the footwall will be the site of local gas retention and resultant overpressure but this does not exclude the possibility of the same

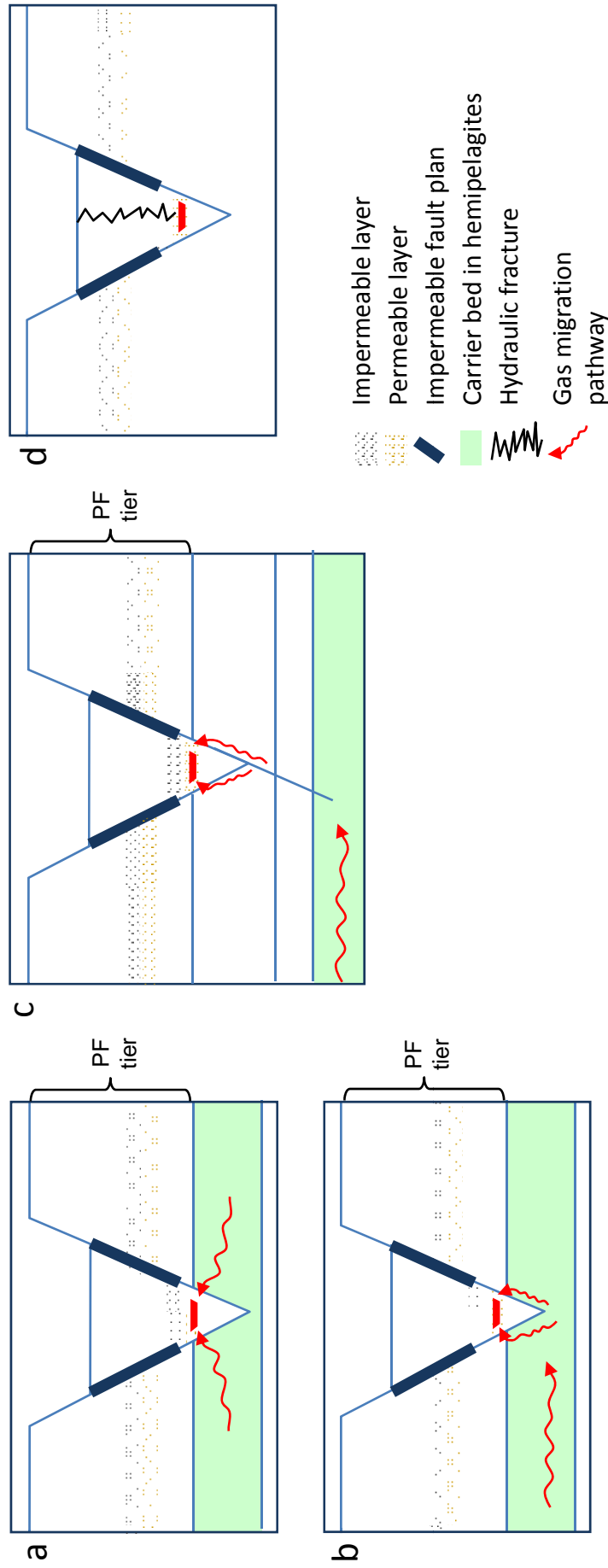


Figure 6.24. Conceptual model illustrating possible mechanism to allow gas migration into an intra-tier permeable bed from an underlying carrier bed. Note that there is an impermeable layer in the PF graben and also that the certain parts of the PF plane are impermeable as shown by the bold blue tracing on the fault plane. a-b) Cases where the carrier bed occurs at the base of a polygonal fault tier. In (a) gas migrates into the overlying permeable layer when it is juxtaposed against the carrier bed. In (b) gas migrated into the permeable layer via a permeable polygonal fault plane. c) Case where the carrier bed occurs beneath the basal tier surface of the PF tier. In C first-order PF's (i.e. those which have propagated under the influence of tectonic stresses) have propagated beneath the regional tier surface and have intersected the carrier bed. d) In the last stage the overpressure increases enough to breach the seal provided by the overlying impermeable layer and gas migrates vertically upward out of the top of the conjugate PF graben.

happening in the hanging wall as evidenced by chimneys emanating from the basal apex of PF grabens. In this minority of cases other subtle differences in the pressure head may influence local retention of gas as explained in paragraph (1) and (2) above.

6.5.1.3. Propagation of linear hydraulic fracture in hanging wall domain

Hydraulic fractures nucleating at the basal tips or in the lower part of polygonal fault footwalls and hanging wall graben could be explained by the permeability of PFs and the accumulation location of overpressure fluids. Nucleation of hydraulic fractures surrounding the basal tip of PFs most likely occurred due to one or more of the following reasons;

1) Initial fluid pressure in the carrier bed below the normal (polygonal) fault is likely low and the effective stress of the faults is likely high as suggested by Nunn (2003) and the pressure of the fluid is insufficient to open the entire fault but only the lower part (Nunn, 2003).

2) On the other hand, the pressure of fluid accumulating below the fault plane and inside the fault bound trap was only sufficient enough to create tension in hanging wall of the normal (polygonal) faults and induced hydraulic fracturing (cf. Løseth et al., 2011). This is demonstrated by the locations of vertical chimneys that occur immediately adjacent to lower parts of footwalls, which suggests that the upper parts of PFs is not likely to be a permeable pathway to migrating fluids (cf. Kattenhorn et al., 2000).

Alternatively, overpressured fluids may open the sub-vertical and pre-existing cracks or fractures in the hanging wall which may intersect the surface of the main fault as proposed by Gaffney et al. (2007; see fig. 2 in Gaffney et al., 2007). Gaffney et al. (2007) also argued that once overpressured fluids passed through sub-vertical cracks intersecting a normal fault surface, fluid filled and pressurized the cracks or fractures in hanging wall (see fig.2 in Gaffney et al., 2007). Moreover, the longer the PFs are that filled with fluid, the greater number of fractures in the hanging wall will be exposed to fluid pressure (Gaffney et al., 2007). Gaffney et al.(2007) emphasised this will only be the case if the pressure required for fluid entering into the hanging wall fractures was less than the pressure that is required to open or flow along the upper PF plane. Hence, hydraulic fractures would propagate vertically in the hanging wall (Delaney et al., 1986; Poland and Ayin, 1988; Cosgrove et al., 1995; Gaffney et

al., 2007). Gaffney et al. (2007) also stressed that; if pre-existing fractures in hanging wall then fluid would flow along the lower part of normal faults until fluid reached one of the pre-existing fractures at which point it would flow vertically upward again through vertical fractures (Gaffney et al., 2007).

Once hydraulic fractures formed pore pressures in the lower part of PF blocks would likely to be reduced and the PFs would be sealed again (cf. Wiprut et al., 2000). Fluid remaining in the footwall would thus be expected re-equilibrate with lithostatic pressure. These interpretations may explain the reason why the seismic expression of free gas, the negative bright spots (columns) that characterised the downward terminations of linear conduits occurred preferentially in the lower part of PFs footwall (fig. 6.2h,). The fluid-related origin of linear hydraulic fractures can be supported by the presence of linear methane-related carbonates at the topmost terminations which are expressed by linear PHAAs with negative reliefs. The occurrence and geometries of methane-related carbonate demonstrates that fluid migrated vertically along the linear conduit allowing the formation of carbonates at the exit point at the palaeo-seabed.

6.5.1.4. Orientation of linear hydraulic fractures in polygonal fault tiers

Orientations of fractures and joints around faults have been investigated by different researchers since the nineteenth century (Pollard and Aydin, 1988). Similar relationships to above of jointing or fractures parallel to adjacent faults have been replicated in analogue models by Andersen E.M. 1951 (see, Kattenhorn et al., 2000). The model of Andersen E.M. 1951 has been investigated in detail by Kattenhorn et al. (2000) who has simulated several numerical models of stress state around normal extensional faults which are based on outcrops of "Rough & Rocky Mesa" in Utah (see Kattenhorn et al., 2000). Kattenhorn et al. (2000) demonstrated that the maximum magnitude of stress occurred in the basal and upper tip of the normal fault and was perpendicular to fault strike. Joints that develop in these locations would thus be parallel to fault strike. Their numerical modelling results were concordant with the predictions of Anderson E.M. 1951 (Kattenhorn et al., 2000).

On the other hand, Vigneresse et al. (1999) proposed a model of planar-shaped magmatic intrusions which define a vertical plane in the hanging wall of extensional faults.

This can be compared to with the vertically orientated fractures planes within the downthrown block of PF's in tier-2. The authors argued that under a tensional regime characterized by normal faulting, the direction of maximum stress was vertical and was induced by lithostatic load. In Vigneresse et al.'s (1999) model, magmatic wedging (compare to fluid intrusion in this case) results in overpressure (Pf) and forces the rock to separate toward the least principle stress direction with the minimum stress (σ_3) increase to $\sigma_3 + Pf$ (Vigneresse et al., 1999). While the intermediate stress (σ_2) increases proportionally to the Poisson's coefficient (ν) and becomes $\sigma_2 + \nu Pf$ (Vigneresse et al., 1999). Vigneresse et al. (1999) stated that the vertical stress component (σ_1) remains constant in the tensional environment as it only depends on the weight of the overburden thus the spatial distributions of stress components cause the magma to be intruded as vertical dikes. This model provides an explanation for the occurrence of linear conduits in the vertical plane within hanging walls of polygonal faults. Now that I have gone some way to understand the role that the state of stress around faults has on controlling fractures orientations. I can now infer the state of stress in areas where linear venting systems occur.

In the absence of tectonic stresses, the stress state is governed by gravitational loading where the vertical stress is the greatest and equal to the weight of the overburden (minus fluid pressure) and the least and intermediate stresses occur in the horizontal plane and are a function of the vertical stress. Under these conditions the least and intermediate principal stresses would be roughly equal at a regional scale. The least principle stress will be equal to the intermediate principle stress and are perpendicular to the maximum principle stress. It has been argued that the random patterns of PFs indicates they formed under this isotropic horizontal stress regime condition (Cartwright, 1998). In the absence of any significant tectonic stresses the local direction of the horizontal principle stresses most likely was maintained after the formation of PFs. Given that the linear venting system (composed by negative bright spot columns or PHAAs and acoustic perturbation columns) are predominantly developed in regions where salt withdrawal and diapirism occur, and where PFs are anisotropic, polygonally faulted units in the tectonically deformed area are exposed to an additional tectonic stresses.

Formations of anisotropic PF networks that are influenced by tectonic faults or salt diapirism have been previously studied by Cartwright (2011). The additional tectonic stresses produce local horizontal stress anisotropy. Polygonal faults nucleating in this anisotropic stress field propagated preferentially in a specific direction which are parallel to the

intermediate principal compressive stress σ_2 (Cartwright, 2009). The fact that linear conduits are aligned with preferentially aligned PFs and the latter are paralleling to the deep-seated tectonic faults and other salt-related fault families the direction of fractures within PF tier-2 are likely affected by the same stress fields as anisotropic PFs are. The fact that linear conduits are parallel to PFs rather than being circular as for the case of pockmarks suggests that the fluid pressure in these locations was initially not strong enough to perturb the local lateral stress field around polygonal faults. Even though, in both cases the fluid pressure was great enough to exceed the minimum principle stress, for the case of pockmarks; the fluid pressure was likely to be significant as a circular crater formed regardless of the locally developed an aligned fractures which formed in the pre-existing local stress field around the PF. It is suggested that in the case of linear fractures, the hydraulic heads in the lower part of PFs are not sufficiently strong enough to exceed the intermediate principal stress even though they are strong enough to overcome the least principle stress. Therefore, the hydraulic fractures propagated into the overlying hanging wall along a vertical plane that is parallel to the intermediate stress direction and first order anisotropy PFs.

In conclusion, the preferred locations of gas accumulations in the fault bound traps and that occur in bottom of PFs footwalls or grabens are bound by impermeable Intra-Plio horizon and the upper portion of PFs. These impermeable barriers and the fault bound traps controlled the future leakage locations of overpressured fluid. Hence nucleation sites of vertical fractures were initiated from the basal tips or lower part of PF footwalls. Moreover, the locations of nucleation sites for linear fractures and PFs may originate from heterogeneities (irregular surfaces) or weakened zones that pre-existing in the sediments (cf. Goult, 2008). This is a supplementary reason for why fluids migrated upward from the basal tips of PFs which may act as weak zones and become a preferential location for hydraulic fracture propagation.

6.5.1.5. Concentrically aligned PHAAs around pockmarks

If the interpretation that; linear fractures nucleated near the basal tips of PFs is correct then I can comment on the origin of concentrically aligned, linear venting systems around pockmarks (fig. 6.9). The presence of high-amplitude columns with reversed phases around the outer edges of advancing pockmarks indicated the presences of free gas chimneys. Free gas probably migrated from the gas-bearing sediments infilling the earliest of the pockmarks

craters underneath these high-amplitude columns (fig. 6b, c; Chapter 5), via the lower part of concentrically aligned PFs which intersecting the edge of the earliest pockmark. Since gas chimneys emanated from the lower part of the polygonal faults, it is suggested that hydraulic fractures propagated upward from the lower portion (or basal tip) of concentric PFs (see section 6.5.1.3.3). Hence, these gas chimneys are concentrically aligned around the pockmark. As a result, methane-related carbonates developed above these linear fractures are also concentrically aligned. Moreover, the different stratigraphic levels of shallow depression and methane-related carbonates (PHAAs) above the fractures (e.g. fig. 6.9e, f), record the timing of seepages at the palaeo-seabed indicating that fluid leakage was diachronous. The presence of shallow depressions and methane-related carbonates alone and above the hydraulic fractures around the pockmark (fig. 6.9e), indicated the regime of fluid migration varied along the location of concentric PFs.

6.5.1.6. Influence of stress regime on geometry and alignment of venting features

In this section I try to establish if the geometry of linear and elongate venting features simply vary as a function of fluid expulsion intensity, or rather by local stress fields, or by both? Stresses have an important impact on the development of fluid venting structures as demonstrated by the elongate shallow depressions above Syncline 2 (fig. 6.8-6.7). Linear PHAAs with shallow negative relief (< 5ms TWT) represent slow venting rates, while circular-to-elongate shallow depressions (< 11ms TWT) represented slow-to-moderate seepage rates (Roberts 2001; Roberts et al., 2006; Naudt et al., 2010). The hypotheses above are in agreement with my observations and results:

- 1) As indicated by the lengths of linear conduits within PF tier-2, fluid pressure should build up sufficiently to overcome the vertical compressive stress that is generated by the overlying sediment column which is at less 100 ms TWT thick. These linear conduit associated with linear shallow depression of < 5ms TWT above them.
- 2) While the overpressured fluid which creates elongate shallow depressions within the sediment layer of <10 ms TWT thick indicates that the fluid venting model was not that fast with respect to conical pockmarks that have more significant depths and diameters (see Appendix II). Therefore, both types of features are unlikely to have

formed by intensive fluid expulsions at the palaeo-seabed.

Assuming that the fluid regime environment in a given time interval is the same everywhere and if the stress regime changed from a state of horizontal stress isotropy to one which is anisotropic because of tectonic processes, the resulting venting features would expect to acquire a geometry that were indicative for the direction of intermediate compressive stress. Under isotropic stress conditions, if fluid pressures are much stronger and overcome σ_2 and σ_3 , then the geometry of venting features should not be affected by addition of local tectonic stresses and should be expected to exhibit circular planar forms. This is well demonstrated by the presence of circular pockmarks craters (with diameter 300m and depth > 100 ms TWT) at a growth fault (fig. 6.8a) on the same horizon above syncline faults in the South of the survey. These examples above point out that the geometry of fluid-related shallow depressions formed by slow and slow-to-moderate fluid regimes which are affected in addition by local stresses. The plan form and orientation of venting features are thus good indicators for distinguishing qualitatively relative strengths and orientations of local stress field.

6.5.1.7. Additional evidence for the timing of polygonal faulting, linear fractures and fluid venting

In the previous sections arguments for the timing of polygonal faulting relative to fluid venting were presented. In addition it was argued that vertical linear fractures formed in response to vertical rise of fluid and local build-up of fluid overpressure in stratigraphy deformed by already present polygonal faults. The presence of these small fractures around PF are purely speculative at this stage given the limitation of seismic resolution and absence of core data, however I argue that their presence is likely on two grounds. 1) Since there is evidence of fluid venting and local trapping of fluid, fluid overpressure and hydraulic fracturing is quite possible. 2) Evidence of purely vertical migration of fluid flow along conduits which are linear in planform suggests their conduit was in some way linked to a fracture or fault. However, pre-existing sub-seismic polygonal faults are probably not vertical but hydraulic fractures forming by overpressure could be.

As mentioned previously methane-related carbonate deposits in the stratigraphy overlying polygonal fault tier 2 are linear and aligned with the same orientation as polygonal

faults directly below them. This strong spatial and geometric relationship between the two implies that the former was in some way influenced by the presence, location and orientation of the pre-existing PF. It is suggested here that the methane-related carbonates formed by methane gas migrating from the underlying linear chimneys which emanated from hydraulic fractures forming parallel to and surrounding the basal tips of PFs (see amplitude map and dip map in fig. 6.2b). Reasons for the common alignment in orientation are still not entirely clear but I suggest that there is a casual link between the general stress state in the Pliocene stratigraphy, which caused local alignments in polygonal fault arrays, nucleation and development of fractures and/or new hydraulic fractures surrounding them as well the formation of fluid related depressions. In following section I comment further on the relative timing and interactions of fluid venting through these proposed vertical and linear hydraulic fractures in PF tier-2 surrounding Diapir 1 and withdrawal Syncline 2.

On the horizon of 5.5H Late Miocene in age (below PF tier 2) the longest axis of the elongate depressions are orientated parallel to the extensional faults in the withdrawal syncline, and these depressions show linear shapes near radial tectonic faults (fig. 6.8a, b). These radial faults are not as abundant as the ones in the polygonally faulted intervals and offset tier boundaries and extend too much deeper stratigraphic levels. Following criteria by Carruthers et al., 2013 they are regarded as tectonic in origin i.e. formed by arching. This radially faulted area is the only location where linear features can be observed outside of polygonally faulted strata. If the aspect ratio of fluid-related depressions varies as a function of the ratio between fluid pressure and local insitu stresses as proposed in section 6.5.1.4. Then I can infer that for the case of these very long depressions that the state of stress around the diapir at the radial faults locations is greater than the fluid pressure. The same would also apply to the edge of Syncline 2 although the depressions here are elongate (i.e. smaller aspect ratio). The greater magnitude of the total stresses and horizontal stress anisotropy in the sediments on the radially faulted flanks of the diapir probably resulted from the presence and movement of the diapir (Carruthers et al., 2013). Several studies have shown that the magnitude of the differential stress increases toward the salt-sediment contact (Fredrich et al, 2003; King et al, 2012; Sanz and Dasari 2010).

Above the polygonal fault tier, the methane-related carbonate deposits have greater aspect ratios and are more linear in the withdrawal syncline whilst those on the radially faulted flanks of the diapir are still linear. Using again the working hypothesis that depression plan form varies as function of magnitude of the insitu stress field versus local overpressure

then there are two possible explanations for the change in depression shape. The first is that the overpressure reduced in the Lower Quaternary sediments when the methane-related carbonate associate depression formed. We discredited this earlier as the crater depths are similar suggesting no significant variation in magnitude of overpressure. The second and preferred explanation is that the magnitude of the total stresses or horizontal stress anisotropy increased in the sediments surrounding polygonal faults and allowed the nucleation of linear chimney which fed overlying methane related carbonate deposits. With local polygonal fault orientations and the local geological setting as the only methods for inferring the general orientation and relative magnitude of the stress state, it is impossible to establish what processes are responsible for this increase. Despite this, it is interesting that linear-shaped depressions are persistently observed in close proximity to faults and in particular densely spaced polygonal faults. Thus, the vertical change in aspect ratio of the fluid features would support the thinking that polygonal faulting and development of hydraulic fractures formed prior to the accumulation of the linear shaped methane-related carbonate deposits.

Finally, in this area I also find additional evidence for the polygonal faulting post dating the formation of the elongate fluid venting anomalies in the Late Miocene reflection beneath the PF tier. Here, the boundaries of polygonal fault cells on the horizon of Base Pliocene age (fig. 6.7c) define with a good fit the outer edge of elongate depressions on horizon of Late Miocene. Some PFs extend below the base of the tier by as much as 30 ms terminate above the depressions edge. For these particular PF's I suggest that they preferentially propagated below the main basal tier surface honored by the majority of PFs due to differential compaction of the tier stratigraphy above these shallow elongate craters. A number of studies have demonstrated that local variations in topographic relief of the basal tier surface of the polygonal fault tier can have quite dramatic influences on their orientation (Andresen and Huuse, 2011; Cartwright, 2011; Ireland et al, 2011). Therefore, it is possible that the local and subtle topography of the crater and overlying compacting tier stratigraphy may have controlled and slightly influenced the lateral propagation of the basal portion of these polygonal faults.

In summary, this local study suggests the following timing interactions of fluid venting, hydraulic fracturing and polygonal faulting.

1. Fluid venting features developed in the Late Miocene and were buried beneath the stratigraphy in Tier 2.
2. During shallow burial of the Pliocene stratigraphy in Tier 2, polygonal faults

formed and locally propagated around shallow depressions immediately below the basal tier surface.

3. Continued fluid flow into the lower stratigraphy of Tier 2 and local sealing of this fluid caused local fluid pressure build-up and reactivation of pre-existing fractures and/or development of new linear and vertical hydraulic fractures.
4. Following this, fluid migrated vertically upward at some point after the formation of polygonal faulting in the Quaternary and invaded the stratigraphy in the very shallow subsurface (Lower Quaternary to seabed). This resulted in the formation of linear-shaped methane-related carbonate deposits.
5. Linear chimneys at these locations are succeeded by shallow elongate depressions at the present day seabed, it is suggested that they remained active until the Holocene (fig. 6.7e).

6.5.2. Relationship between the distribution and orientation of linear venting structures and local tectonic settings

6.5.2.1. Fluid migration pathways in the three salt-withdrawal synclines and in the footwall domain

Linear fluid venting structures are commonly located in areas deformed by anisotropic PF networks. These anisotropic PFs have preferential orientations that are parallel to the tectonic faults in the three salt withdrawal synclines (fig. 3.4) which are considered to be sites of active fluids flow. In areas absent of PFs, linear PHAAs can only be observed above or along traces of tectonic faults (fig. 6.12c, h). The occurrence of venting structures at these locations implies tectonic faults cut through deep interval reservoirs containing gas accumulations and caused leakage. This suggests that tectonic faults served as primary leakage pathways allowing fluids from deep intervals to migrate to shallow depths (fig. 6.25). It is most likely that due to the larger amount of fluid excess the volume of faults. Fluid migrated horizontally into shallow and permeable layers beneath the PF tier-2 and then uses particularly the deep-rooted long PFs as further leakages sites. This may explain why most of

Intense fluid migration at syncline faulted locations from tectonic deep faults via anisotropic PFs

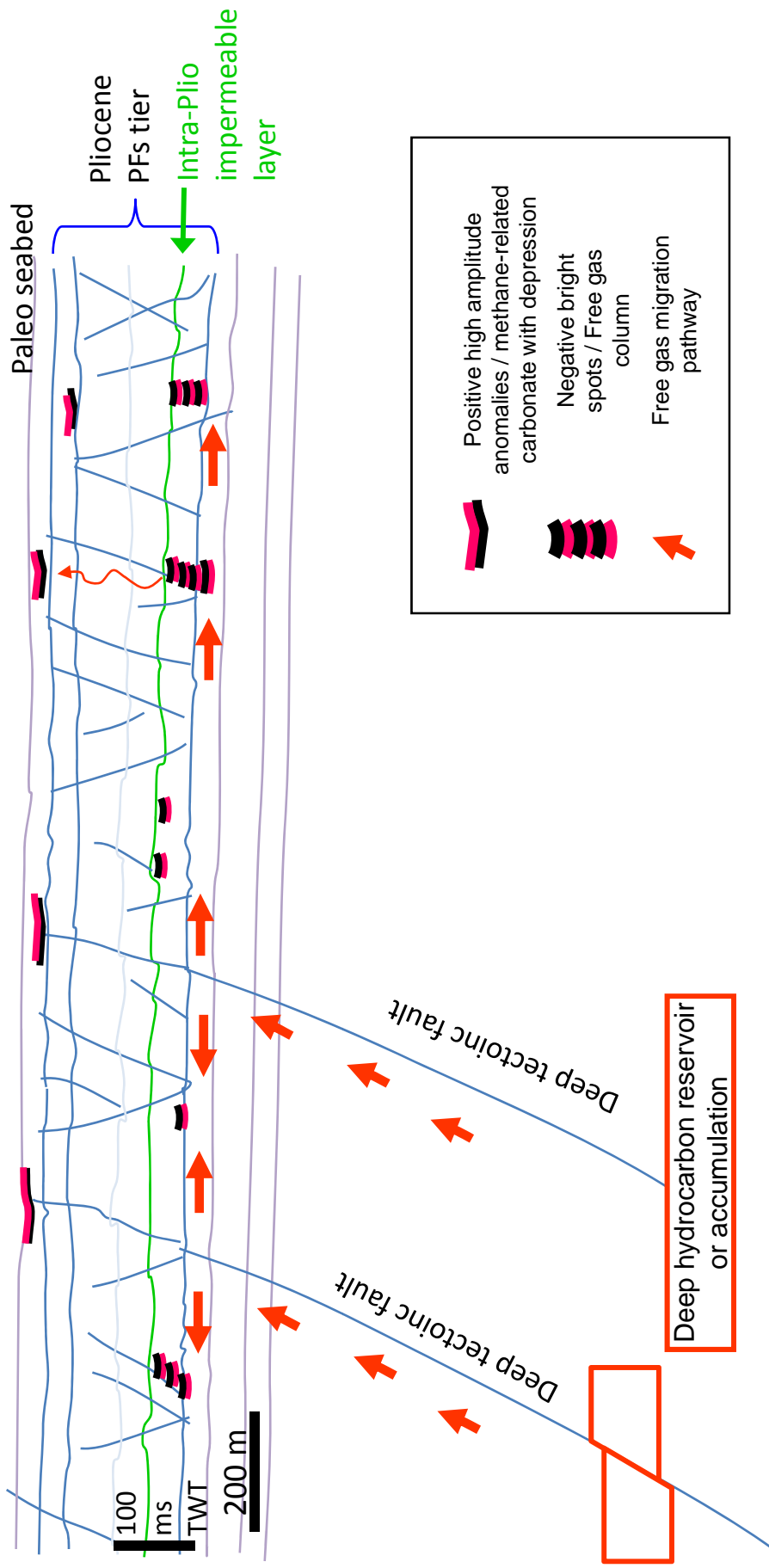


Figure 6.25. Conceptual model showing the migration pathway of methane gas along deep-seated tectonic faults into a shallow interval deformed by a polygonal fault system. Notice that negative bright spots are confined to the interval beneath the Intra-Pliocene horizon and that PHAAs generally occur above the top surface of the polygonal tier. Cartoon not to scale.

gas chimneys emanated from the base of PF tier at the locations of synclines. This may also explain why the gas accumulation occurs within PF tier-2 above the center of Syncline 3 is laterally bounded by deep-seated tectonic faults (fig. 6.4d). The hypothesis above is supported by the absence of linear venting systems in locations where PFs and tectonic faults are absent.

6.5.2.2. Linear venting structures in paralleling to first order anisotropic polygonal faults

Our observations suggest that the local stress state and resultant formation of isotropic or anisotropic PFs play an important role in the formation and geometry of linear venting structures and methane-related carbonates. Following (Cartwright, 2011; Carruthers et al, 2013) the development of anisotropic PF networks can be explained by a regional or local stress regime in which the horizontal stress are not equal i.e. $\sigma_2 \neq \sigma_3$. Such a stress regime is very probable in this study area as the compacting hemipelagic units that undergo polygonal faulting are affected by local tectonic structures such as salt diapirs, salt withdrawal basins, deep-seated normal faults and local fluid venting structures.

6.5.2.3. Linear PHAAs around tectonic faults location in footwall domain

The only venting structures which have linear plan form geometries occur in the footwall domain, is along the array of parallel short faults and the long tectonic faults in Figure 6.12c that these PFs perpendicular with. These fault-orthogonal short faults occur within the sediment interval corresponding PF tier-2 in hanging wall, and located at the horizontal transition boundary between the areas where PFs are absent and present (fig. 3.4a; fig. 6.12b).

Hansen et al. (2004) has argued that PFs had been aligned orthogonal to tectonic faults by the presence of the fault during PFs formation and which were possibly active. The tectonic faults were thus perturbed by the local stress by re-orienting the local maximum tensile stress from perpendicular to parallel to the fault in the surrounding areas (Hansen et al., 2004). Hence, the orthogonal short faults that are observed here are likely perturbed PFs. The

deflection of the PFs strikes (fig. 6.12b), and departure from an aligned array to more polygonal geometries with distance from the tectonic faults may reflect decaying magnitude of local stress anisotropy is associated with the tectonic fault.

PHAAs (methane-related carbonates) that exhibit hook-shaped geometries (fig. 6.12b) like underlying PFs can be explained by hydraulic fractures propagating along the basal tips and lower parts of the PF plane as detailed in previous sections. The magnitude of the near-fault stress field is likely to be most significant near the fault plane and decrease with distance from the fault (Bourne and Willemse, 2001; Kattenhorn et al 2000; Rawnsley et al 1992). The curved nature of the termination of these perturbed polygonal fault traces on horizons probably reflect stress trajectories of the horizontal principle stresses reorienting toward the normal with the first-order polygonal fault plane. Hydraulic fractures are suggested to form parallel to the perturbed PF within the PF tier.

Methane-related carbonates (PHAAs) that occur above these PFs are also curved suggesting that they are fed by similarly aligned hydraulic fractures emanate from the basal tip of these perturbed PFs.

6.5.2.4. Occurrences of sub-circular pockmarks and carbonate mounds at tectonic faults in the footwall domain

The presence of shallow depressions and carbonate mounds (dome-shaped PHAAs) along the trace of deep-seated tectonic faults in the footwall domain (fig. 6.10a, c; fig. 6.12c, e; fig. 6.13), and the vertically stacked shallow pockmark successions (depth < than 25 ms TWT) in faulted areas (fig. 6.10b; fig. 6.11) is likely because of fluid migration along these unique pathways i.e. the tectonic faults. Thus, large amounts of overpressured fluids are likely to channelise only by individual tectonic faults in the footwall domain, and fluid expulsion is thus very focused along the faults.–Shallow depressions and clustered carbonates mounds indicate moderate fluid expulsion along faults in the footwall domain. The vertical succession of shallow pockmarks indicates moderate-to-fast rates of fluid expulsion. Whilst shallow and seabed depressions stacked above these two venting structures (fig. 6.10d) indicate that moderate rates of seepage occurred on the present day seabed and fluid migration along deep-seated faults is still active. Moreover, shallow depressions along tectonic faults merge with

each other and form continuous, long depressions (fig. 6.12h). This aggregation is likely to be caused by repetitive fluid explosions along the fault at different positions.

Abundant circular shallow depressions and shallow pockmarks (fig. 6.10b) in the footwall domain may also be explained by a change in the relative magnitudes of local stress field. The circular depressions and stacked shallow pockmarks are located mainly in the area which are devoid of PF and where anticlines and synclines are absent. These circular, vertically stacked venting structures have same range of diameters (one to two hundred meters) and depths (vary from 5 to 25 ms TWT) as linear depressions and elongate depression do. They are also indicative of the similar flux rates i.e. slow and slow-to-moderate. These shallow pockmark depressions that formed under these fluid regimes have not been affected by conditions of significant horizontal stress anisotropy in the footwall domain, as indicated by their circular plan form geometry. Therefore, the occurrence of circular, shallow venting structures in the footwall domain and where stratigraphy is horizontal or only gently dipping relatively flat, implies that the intensity of fluid venting was significant in comparison the percentage anisotropy of the horizontal principle stresses in the shallow stratigraphy. Given that the stratigraphy is horizontal and there are no tectonic structures underneath these venting structures it may be possible that the regional stress field is isotropic.

6.5.2.5. Orientation of linear fractures above the salt-withdrawal synclines

The influence of local anisotropy of the horizontal stresses on the orientation of polygonal faults and subsequent linear venting systems can also be visualized on the amplitude map of the lower part PF tier-2, which shows local alignments of both in salt-withdrawal Syncline 2 and 3 (fig. 6.5a; fig. 6.4a). Isotropic PFs (fig. 6.5a; fig. 6.6a) occur at the transition zone between anisotropic PFs that are parallel to the edge of Syncline 2 (fig. 6.6b) and the aligned array of PFs in the center of Syncline 2 (fig. 6.6d). The change in fault pattern from anisotropically arranged to isotropically arranged polygonal faults above the salt-related growth fault likely represents the transition to a localized zone in which the horizontal stresses were roughly equal. As a result, the subsequent linear venting features that are occurred in the area containing isotropic PF networks do not show preferred orientations (fig. 6.5a). However, linear venting features those are located above syncline-1 all occur close to and are parallel to the NE inner edge of the syncline (fig. 6.9c, h). These linear features follow

the strikes of second-order PFs which strike NNW and are parallel to the growth fault on the eastern edge. The orientation of first-order PF indicated that the direction of dominant intermediate compressive stress field was initially parallel to the NNW-NE side of Syncline 1 (fig. 6.9h). It seems that when the linear fractures formed the magnitude of stress field along the NE side of syncline-related growth increased. As a result the subsequent linear venting structures are parallel to the eastern edge of Syncline 1 rather than following the strike of first order PFs (fig. 6.9h). The re-orientation of stress fields which controlled the orientation of linear fractures could be attributed to movements on the adjacent extensional faults which strike parallel to the growth fault (fig. 3.6a and fig. 3.4 in Chapter 3). This is evidenced by the upper tips of these extensional faults that are located right below the linear venting features extend to the Quaternary unit. Thus, these tectonic faults were likely active (see Chapter 3) and altered the stress state in the NE side of Syncline 1.

The case above is different from the ones of Syncline 2 and 3 where crestal collapse faults are deep-seated and propagated blind i.e. with the upper tip beneath the seabed. The magnitude of local stresses in sediments above this syncline was likely more homogeneous, as suggested by the widely coverage of linear venting features in this location of Syncline 2 and 3 (fig. 6.4a; fig. 6.5) in comparison to the Syncline 1 (fig. 6.9c, h).

6.5.3. Evolution of a network of linear venting structures to pockmarks fields and the role of varying host lithology

6.5.3.1. Interpretation of linear fracture networks in hemipelagic-1 unit

Linear fractures that are confined to the hemipelagic-1 interval (fig. 6.14a, d, c) are shown by amplitude dim zones on attribute maps (fig. 6.15c, d) and are succeeded by elongate depressions within a stacked MTC sequence (fig. 6.15e, g, h; fig. 6.26). This implies that lithological variations potentially played a role on the geometrical development of fluid venting structures.

The earliest, linear negative high-amplitude accumulation with negative relief (fig.

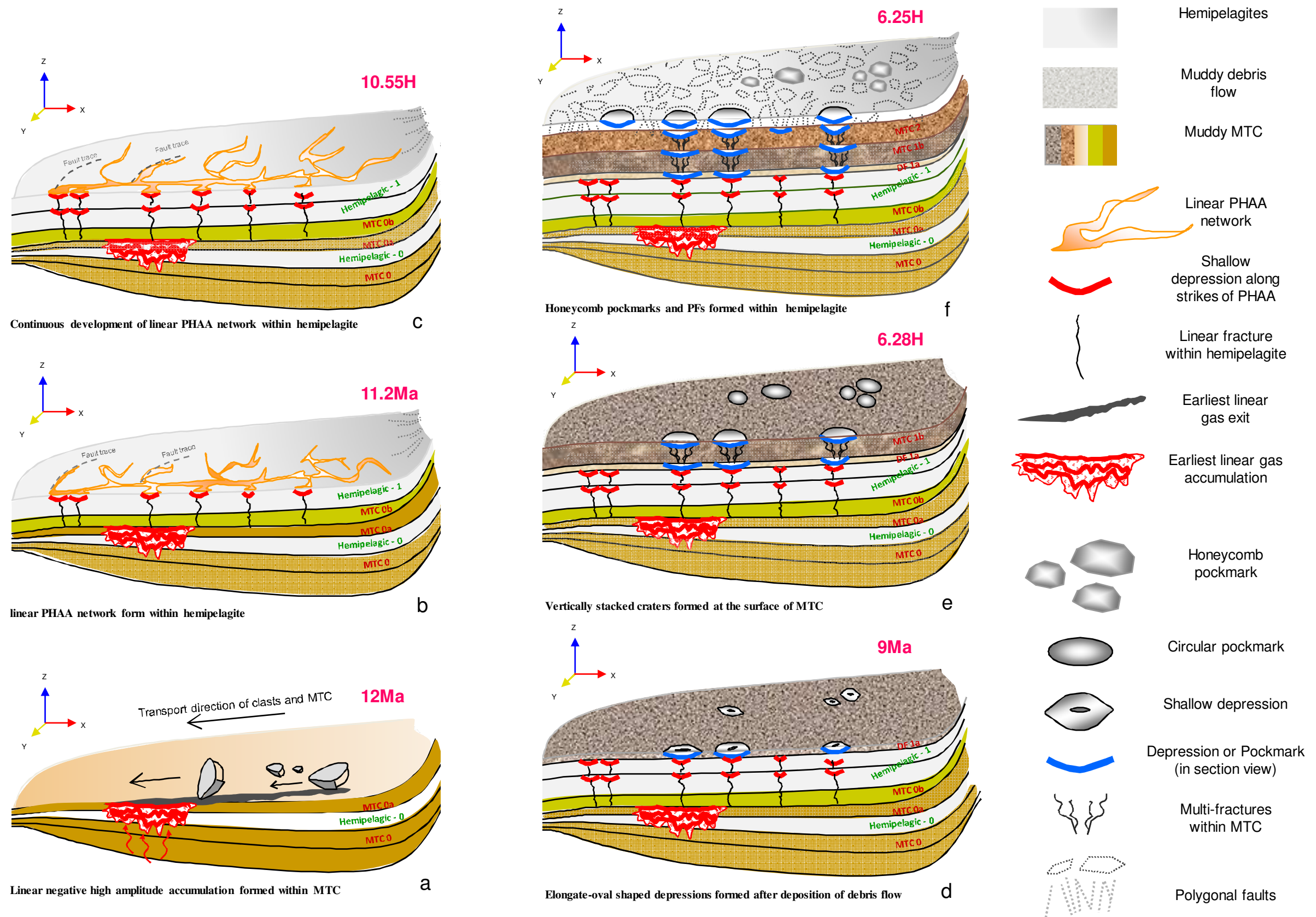


Figure 6.26. Cartoon summarising the evolution of complex venting systems in syncline 0. a is the oldest stage and f is the most recent stage. a) Formation of linear negative high amplitude accumulation. b) Formation of linear PHAA network. c) Development of linear PHAA network. d) Formation of elongate-oval shaped depressions. e) Formation of vertically stacked craters. f) Formation of honeycomb pockmark.

6.14a; fig. 6.15a) most likely corresponds to a long scour mark that is left by scratching of slide blocks or transported materials on the MTC-0a's surface (fig. 6.26a). This is supported by its linear, long and depressed morphology, and its orientation which is the same as the glide tracks in the adjacent area or at the surface of overlying the MTC (fig. 6.15b). Their chaotic, negative high amplitudes are interpreted as gas accumulations (cf. Coffeen, 1986) within the long scour mark. The reduction of local sediment thickness by scouring of the sediments on the palaeo-seabed is suggested to decrease lithostatic pressure which acts to depressurise fluid in this area (cf. Hovland and Judd, 1988). Hence, this promoted the emplacement of linear venting exits for overpressured fluid.

Individual linear fractures that are interconnected to form the complex fracture networks (fig. 6.15c, d) developed above the earliest, linear gas accumulations (fig. 6.15a) and along tectonic faults. This complex linear fracture network is suggested to act as several fluid conduits which fed subsequent venting features such as fluid expulsion depressions, methane-related carbonates (PHAAs) in the sediments above (fig. 6.26a, c). The earliest linear depression (fig. 6.15a) and salt-related-tectonic faults are suggested to be weakened zones that act as pre-existing fluid exits (cf. van Kesteren and van Kessel, 2002). This could explain the reason why the brightest high-amplitude anomalies that are interpreted as subsequent linear venting features (e.g. methane-related carbonates and gas accumulations) occur principally in sediments above the earliest linear accumulation (fig. 6.15a; fig. 6.26a, b) and along these faults (fig. 6.15c, d). High amplitudes that occur along the linear network (fig. 6.15c, d) correspond to phases of different polarities and seismic hardness. Seismically hard or soft phases can be distinguished with confidence by seismic attributes such as instantaneous phase (fig. 6.16c; fig. 6.17c). Therefore, the distribution of soft phases is located above exits of focused fluid vents, i.e. above the earliest gas accumulation at fault locations or within elongate and linear depressions. Soft phases (-90°) are shown in red and are thus favour to be interpreted as free gas rather than soft sediment (cf. Brown, 2004; Paternoster et al., 2011a, b). Hard phases (0°) are shown in blue and are interpreted as carbonate cemented hard grounds (cf. Brown, 2004; Paternoster et al., 2011a, b) under the fine-grained lithological context of this basin (Chapter 3).

The geometry of this complex linear network evolved throughout the deposition of the hemipelgics-1 unit of Late Miocene age. It is shown by the geometric variation of linear depressions on the contemporary palaeo-seabed which is represented by different horizons within this unit (cf. fig. 6.16a; fig. 6.17a). The geometry of this network is especially well

indicated by the instantaneous phase maps that highlight the geometry of carbonate cements and hard pavements which are indicated by green and blue colours (fig. 6.16b; fig. 6.17b). The linear network is suggested to form on the palaeo-seabed. This suggestion is based on 1) the negative reliefs (depths less than 10 ms TWT) that develop along the strikes of the linear network; and 2) the presence of shallow elongate and circular depressions. This is because fluid-related depressions with subsequent draping infill can only be formed by fluid expulsion on their contemporaneous seabed (see Chapter 4). Moreover, a present day linear depression that is associated with linear venting exits has been observed offshore Pakistan by Marum (in ROV video “life under the Deep 1” in <http://www.marum.de/en/marumTV.html>).

The presence and absence of venting structures at the same vertical locations (e.g. blue dot lines in fig. 6.15c, d) at different stratigraphic levels indicated seeping points were not activated all the time at the palaeo-seabed (Cicif et al., 2003; Chapter 4). Seepage intensities could have varied becoming stronger or weaker, as expressed by the morphological variants of linear or circular venting structures at the same location on different horizons. Fluid-related depressions that developed above the earliest linear gas accumulation (fig. 6.15a) in different sediment layers indicate fluid was leaking upward from the earliest gas accumulation and migrated successively upward to the contemporaneous seabed. Furthermore, some individual linear fractures within the linear network have been observed without depressions on each horizon that they intersected but only at the top surface of hemipelagic-1 unit. As fluid expulsion depressions are interpreted to have formed by fluid erosion on seabed sediments (Hovland et Judd, 1987; Roberts et al., 2006; Judd and Hovland, 2007). There it is suggested that these individual fractures formed in one go by gas expulsion on the palaeo-seabed. This contrasts greatly to the case of stacked systems of individual linear depressions and associated linear hydraulic fractures which formed sequentially at different palaeo-sea beds.

6.5.3.2. Influence of lithology on the different types of fluid venting features

6.5.3.2.1. Mechanism of linear fracturing in fine-grained sediments

The linear network that occurs within the hemipelagic sediments does not propagate upward into the overlying debris flow deposits and MTC sequences. The linear network is

succeeded by elongate and oval-shaped negative depressions which occurred in the same location on the top surface of overlying Debris flow-1a (fig. 6.15e; fig. 6.26d). This implies that the variations of sediment properties had impact the development of fluid venting structures. The fact that linear fractures appear principally in hemipelagic sediments but are virtually absent in muddy MTC units suggests methane migration is preferentially aided by linear fractures opening in surficial, soft and cohesive fine-grained sediments (Murdoch, 1992; Boudreau et al., 2005; Boudreau, 2012, Juanes and Bryant, 2006; Jain, 2009; Jain and Juanes, 2009).

Johnson et al. (2002) argued that methane gas migration took place as bubbles growing within unlithified, shallow, cohesive fine-grained sediments by linear elastic fracture mechanism. Hydraulic fractures in fine-grained soft sediments (clay, silty clay) have been widely investigated (cf. Arch et al., 1988; Bruno and Nakagawa, 1991; Murdoch, 1992; Barry et al, 2010) and known to exhibit linear plan form geometries according to various analogue models (e.g. Takada, 1990; Murdoch, 1992; Boudreau et al., 2005; Algar et al., 2011). Hydraulic fracture initiations are due to methane gas high-entry pressures into the sediments and prevent capillary invasions (Algar et al., 2011). A bubble tends to rise because of the large density difference between the gas bubble and its surrounding medium (van Kestern and van Kessel, 2002). Hence, the sediment grains have been forced apart and fractures form (Jain and Juanes, 2009). In Boudreau's (2012) review paper on the formation of gas bubbles in fine-grained sediment, the author proposes that hydraulic fractures are preferentially vertical because of bubbles are not in a uniform vertical stress environment. This is based on the vertical stress that is induced by sediment column and increases with depth, and the bubbles submit less pressures at its topmost extreme than its deepest tips (see fig. 14 in Boudreau, 2012). It means the upper tip of fractures overcome the vertical load of sediment easier than the sediment at any point below the tip (Boudreau, 2012), and thus the fractures propagate upward. Therefore, orientations of vertical/sub-vertical elastic fractures that are induced by bubbles grow can thus be understood in terms of fracturing mechanisms (Boudreau, 2012).

6.5.3.2.2. Fluid migrations and hydraulic fracturing within debris flow and MTCs

In the preceding sections I showed that pockmarks are confined to the surfaces of heterogeneous sediment deposits (fig. 6.14a). It is especially shown by thick MTCs bodies (1b, 2; thickness 40 – 50 ms TWT). The tendency of pockmark depressions to form preferentially

at the upper surface of MTC's but be absent from horizons within could be attributed to one of two parameters; 1) changes in intensity of fluid flow, or 2) changes in the porosity and permeability hence physical proprieties of the rocks in the stratigraphic sections.

Because elongate-to-oval depressions on horizon Debris flow-1a (fig. 6.14c; fig. 6.15d; fig. 6.18) have the same depths as the linear ones, questions must be raised about how the different fluid intensities could produce depressions of contrasting plan form geometries but with the same depth (fig. 6.14c). Also, given that sub-circular depressions have been observed with much greater depths, questions must also be asked why; in this particular case the depressions are restricted to within a 15 ms thick interval defined by the double wavelet of the Debris flow-1a? The reason for these may be because of the fluid pressures causing these elongate depressions were not strong enough to create deeper craters or depressions. Based on the proxy of using crater plan form and size to infer palaeo-fluid flow intensity, elongate depressions form by greater intensities of fluid flow compared to linear ones. However, since both depressions have the same depths regardless of their aspect ratio and have formed in different sediment types. Therefore, I suggest that it is likely that something other than the venting intensity controlled the geometries of venting structures.

6.5.3.2.3. Rheology of debris flows and MTC in the study area and the behaviour of hydraulic fractures

Debris flows and MTC's in this study area are predominantly composed of clay and silt (Total internal report based on confidential well and core data). The rheology of fine-grained debris flows which are supported by sediment and have a variety of clast types and sizes are viscous at the moment of deposition (Philipps, 1988). The debris flows which are characterised by clays, generally follow a plastic or Bingham plastic rheology model as viscosity increases with increasing abundance of fine-grained sediments (Philipps, 1988). Therefore, the muddy debris flows and MTCs in this survey are likely to similar to non-Newtonian Bingham plastic flow at the moment of their depositions on the palaeo-seabed.

The rheology of fine-grained debris flows or MTCs are more complex compared with granular flows and water flooding (Philipps, 1988) as the viscosity of the interstitial fluid (air) that characterised the latter two flows can be neglected. The different rheology of different sediment deposits inspires that, fluid flow behaviour can be affected by variations of physical parameters of the sediment such as: interstitial fluid pressure, volume, concentration of solids,

and water content (cf. Philipps, 1988). Water content is a parameter has greater impact than tensile strengths on the geometry of shear zones in wet and unconsolidated sediments (Arch et al., 1988). Even though it is unsure of the exact magnitudes of these parameters affecting the flow properties of the debris flows, in any case fluids still have to have exceed the internal strength of debris flows including: interstitial fluid pressures; grain-grain interactions forces; cohesion and buoyancy strength which contribute to the flow behaviour (Philipps, 1988). In addition, gas bubbles can also deform the grain matrix of cohesive sediments when the differential pressure between gas bubble and sediment matrix that is required to push aside the matrix-grains is bigger than a specific value (Van Kesteren and van Kessel, 2002). The latter is 4 times the water surface tension divided by the distance between two adjacent grains at gas bubbles surface (Van Kesteren and van Kessel, 2002).

The pressure of fluids which migrated through the hemipelagic-1 unit is suggested to be increased after the deposition of muddy Debris flow-1a and when they reach the base of the the latter, consequently it is likely results in the formation of elongate-to-oval pockmark depressions (fig. 6.18b). However, the build-up of fluid pressure below the base of Debris flow-1a unit still needs to be explained. I recognise the possibility that cohesion strength of fined-grained Debris flow-1a could be an obstacle for slow seepage which generates linear fractures. While relatively intensive seepage was sufficient to overcome the cohesion strength of the Debris flow-1a, thus the fluid was able to attain to the debris flow's surface and created eruptional pockmark craters. As a result, linear depressions, produced by relatively slow fluid expulsion events were not able to form. Nevertheless, if it is the case, the question must be asked; why the migrated fluid pressures that created the linear fractures could overcome the thick hemipelagic-1 unit (several tens ms TWT thickness), but were not able to overcome the cohesion strength of the thin Debris flow-1a unit (< 10 ms TWT)? , even with the fluid pressure that was assumed to increase at the base of DF-1a? This suggests another overriding factor is responsible for the formation of different fluid venting structures. The following are suggested as possible parameters;

1) Cohesion strength see from thin Debris flow-1a:

In the case Debris flow-1a (fig. 6.15e) elongate-to-oval shaped anomalies consisting of a main depression with a secondary linear depression in the centre as described in section 6.5.1.3.5 (fig. 6.18b), the shallow linear relief may have served as the primary venting point of the depressions (fig. 6.27). In concordance with the analogue models of Hori et al. (2002),

the sharp ends of the depressions probably indicated that fluid vertically evaded and laterally expanded the base of the Debris flow-1a (fig. 6.27).

The two sharp ends most likely indicate the maximum lateral hydraulic head thus fluid volume expanded below Debris flow-1a and in the direction of the depressions longest axis (fig. 6.27). As the fluid pressure was initially not strong enough to deform or fracture the overlying sediment (Debris flow-1a) i.e. overcame the internal strengths of a material behaving as a non-Newtonian Bingham plastic fluid before consolidation. Following this, fluid expanded laterally and accumulated under Debris flow-1a until the pressure increased sufficiently to induce migration pathways or fractures within Debris flow-1a. Therefore, elongate depressions formed from fluid expulsion along the linear conduits which are located in the centre of the elongate depression (fig. 6.18b, c). Elongate depressions were relatively long-lived compared to the circular pockmark craters which formed instantaneously and explosively. This may explain why oval-shaped depressions do not extend downward to underlying hemipelagic-1 unit beneath, because of dynamic of fluid expulsion.

2) Heterogeneity of debris flow and MTC:

As debris flows and MTCs are invariably heterogeneous with gravels, rock fragments, and hundred meter-scale clastic blocks, as what have been reported in literatures (e.g. Festa et al., 2012) or observed on seismic sections/horizons (e.g. Riedel et al., 2012). It is suggested that the lithological heterogeneity within the debris flow or MTC units had a great impact on the propagation direction of hydraulic fractures or fluid migration pathways, since defects and planes of weakness inside rocks play a crucial role in the initiation and growth of fractures (Van de Streen et al., 2002).

Fracture propagation is affected by pre-existing defects, discontinuities or planes of weakness in rocks which include: grains boundaries (Howarth, 1987; Bruno and Nakagawa, 1991); pores or voids (Kranz, 1979); cavities (Howarth, 1987); interfaces (Olson et al., 2002; Van de Steen et al., 2002); primary fabrics (Arch et al., 1988); mineral cleavage (Howarth; 1987) and layering (Gomez-Rivas and Grier, 2012) and have been widely agreed and investigated. Planes of weakness or defects are well known as preference sites to release stored strain energy and form preferential directions for fractures growth (Van de Streen et al., 2002) in stressed and unstressed geological materials (Howarth, 1987). Moreover, Howarth (1987) and Van de Streen et al. (2002) point out that, the model of fracture failure is also dependant on the quantity of minerals that contains inside sediments. If minerals are the

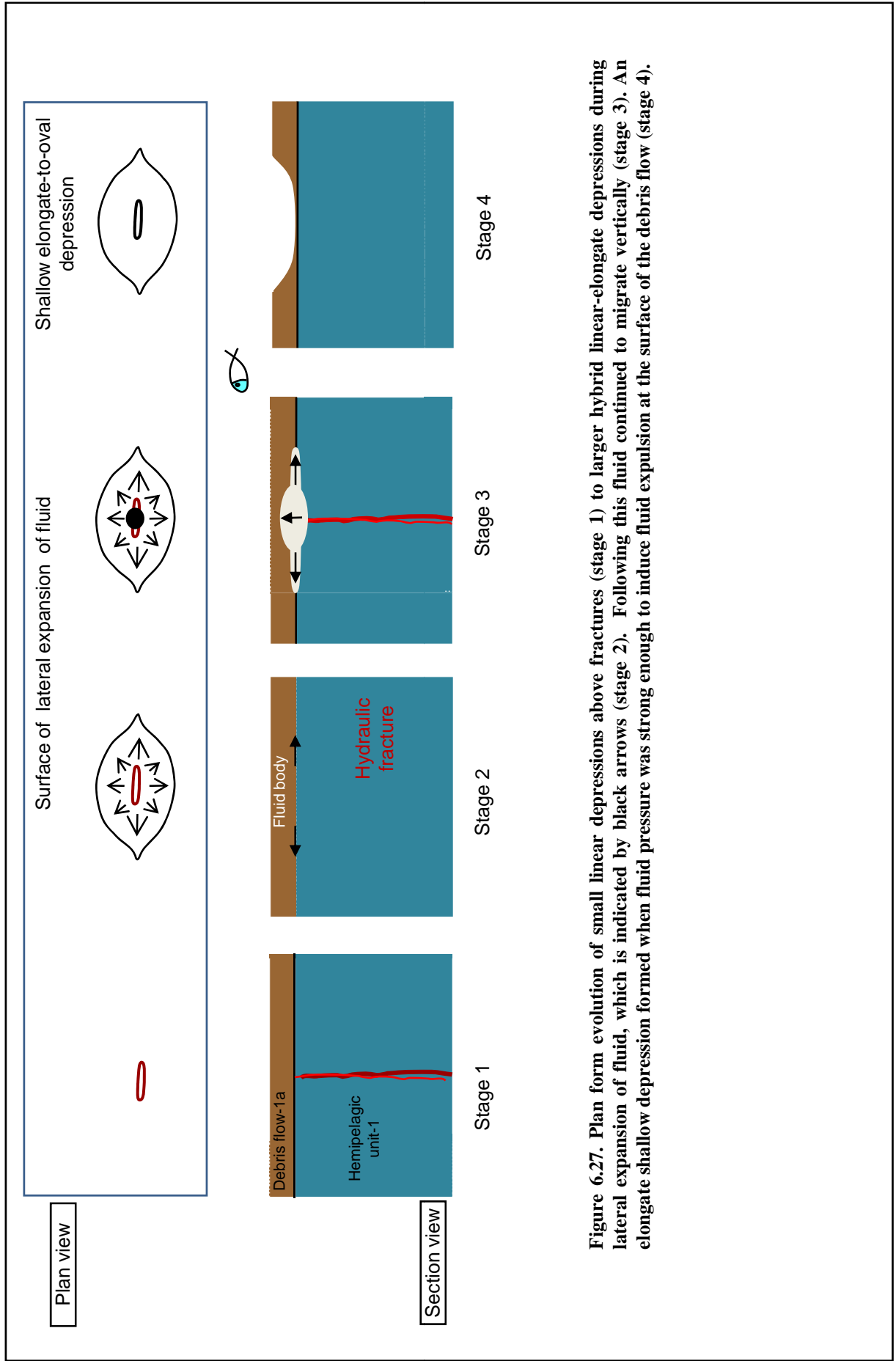


Figure 6.27. Plan form evolution of small linear depressions above fractures (stage 1) to larger hybrid linear-elongate depressions during lateral expansion of fluid, which is indicated by black arrows (stage 2). Following this fluid continued to migrate vertically (stage 3). An elongate shallow depression formed when fluid pressure was strong enough to induce fluid expulsion at the surface of the debris flow (stage 4).

predominant components of the sediment, then the fracturing style will be intra-granular (Howarth, 1987). It is especially true for sediments that contains highly cleaved minerals such as feldspars (Howarth, 1987) or calcites (Van de Streen et al., 2002). In contrast, the fracturing model of low-mineral content sediments will be inter-granular and failure will occur along cement/matrix (Howarth, 1987).

As debris flows and MTCs are composed of clast fragments and reworked rocks which are cemented in a cohesive matrix, clast boundaries are likely to be the principle mechanically weak zones especially in the thickest sections of the MTC-1b and 2 which are likely to contain the most reworked materials. Lateral variations in the magnitude and orientation of the insitu stress state within a debris flow or MTC are attributed to its heterogeneous composition and internal structures. This suggests they affected the direction of fracture propagation. The pressure of fluid that migrated through the underlying linear fractures networks (fig. 6.15d) within the hemipelagic-1 unit are suggested to be initially, insufficiently strong enough to break down the overlying debris flow or MTCs. Thus, fluid accumulation most likely started beneath debris flow or MTC (1 or 2) and migrated into the overlying units when fluid pressure increased enough to exceed the cohesion of the matrix and granular strength of the overlying debris flow or MTCs. Following these fractures nucleated between rocks fragments and along grains boundaries that are paralleled to the maximum principal stress direction (Howarth 1987).

The flow path of migrating fluids is affected by 3-Dimensional variations in permeability of the host sediments which may be enhanced further by fractures. Analogue models of Dawn (2004) demonstrated that flow paths deflected and sub-divided into branches around impermeable barriers within a carrier bed. Hence, migrating fluids likely bypassed impermeable barriers in the form of giant inclusions. Fluid migration bypasses areas of high insitu stress and flows toward the mechanically weak paths in which the matrix strength and inter-granular strength were weak enough to be overcome by the fluid pressure. Once fluids open the weak paths or interfaces between matrix and clasts, hydraulic fractures are suggested to start propagating (fig. 6.28). During fluid migration, different locations inside the debris flow or MTCs would be fractured (fig. 6.28). The segments of fractures grow individually (Van de Streen et al., 2002) either by extensions or by propagation toward the direction of maximum compressive stress (Howarth, 1987). In contrast to the vertical fractures that exist in hemipelagic unit 1, those ones in debris flow or MTC units are likely to have a variety of dips and strikes due to the 3D heterogeneity and 3D geometry of clasts.

Style of fluid migration in fine-grained sediment with clasts inclusions

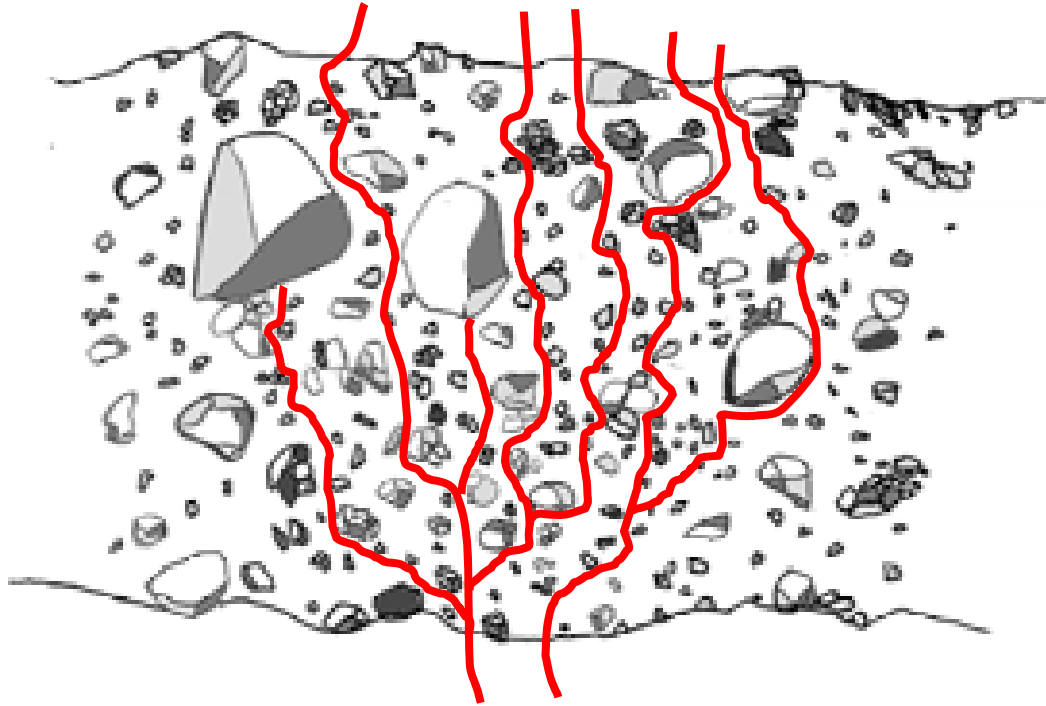


Figure 6.28. Conceptual model for the fluid migration pathway or fracturing within an MTC unit. Fractures or pathways are strongly influenced by clasts and grains. Note that fractures deviated around or stop at grain contacts.

6.5.3.2.4. Formations of pockmarks at the top surface of MTC-1b and 2

Fluid pressure at the strongest seep points above the location of the earliest linear gas exit and on MTCs (1b or 2) surfaces (e.g. point 2, 3, 9 in fig. 6.15g, h) likely persisted, regardless of the thickness of the overlying sediments on the top of the earliest linear exit (fig. 6.26e). The overpressured fluid continued to open the weak paths inside the thick MTC succession. This is suggested based on the occurrence of pockmarks depressions above previous seep points and on the top surface of MTC (point 2 & 3 in fig. 6.15g; 2, 3, 9 in fig. 6.15h). Small fractures within the MTC are probably abundant and concentrated above the major seep points (point 1-3 in fig. 6.15g, h; fig. 6.26f) and are suggested to coalesce to form major fracture zones in these locations (fig. 6.28) (cf. Howrth, 1987; Van de Streen et al., 2002). Overpressured fluids continued to migrate via these (sub-) vertical fractures toward the top surface of the MTC i.e. the palaeo seabed. Once overpressured fluid arrived in the sediment close to the seabed where the lithostatic pressure was less important overpressured fluids underwent volume expansion above these fractures zones (Cathles et al., 2010). As a result, focused fluid venting caused rapid explosions and created pockmarks craters on the surface of MTC (1b or 2; see fig. 6.15g, h) above the major seep points (point 2, 11 in fig. 6.15g; white arrows and point 2, 3, 6, 8, 10 in fig. 6.15h). This explains why there were no obvious pockmarks craters within MTC bodies but only at the surface.

In addition, some venting structures that occurred within hemipelagic-1 unit and beyond the vertical location of the earliest linear gas exit in MTC-0a disappeared toward the top of the MTC sequence (see blue dotted line in fig. 6.15 c & d; also compare with Fig 6.15i). These venting points likely died out because fluid pressures beyond the vertical location of the earliest linear gas exit were not high enough to overcome the in-situ stress or impermeable barriers within MTCs. Thus, the heterogeneous character of debris flows and MTC's has important impact on the style of hydraulic fracturing and fluid migration pathways.

6.5.3.2.5. Pockmarks in the hemipelagic unit above the MTC sequence

The relative dynamic seep points (1 – 12 in fig. 6.15i) that have been active since the burial of MTC-1b and 2 evolved into pockmarks at the base of the hemipelagic unit which

corresponds to PF tier-1 (fig. 6.14a). The least dynamic seep points shown by white arrows on Figure 6.15h most likely became inactive after the deposition of Late Miocene hemipelagic-1 unit on top of MTC-2 as there are no pockmarks above this level. At these long-lived seep points, individual pockmarks within a vertical succession are not continuously developed meaning fluid seepage was intermittent (fig. 6.14a, b; fig. 6.26f). Notice that, sub-circular pockmark craters are deeper (> 12 ms TWT) and their edges are not intersected by polygonal faults (fig. 6.15i). These sub-circular pockmark craters are aligned above the earliest linear gas exit in MTC-0a. The distribution of sub-circular pockmarks with deeper craters suggests again that fluid pressure was stronger along the earliest gas exit which promoted stronger fluid eruptions above.

6.5.3.3. The origin of Honeycomb pockmarks

Pockmarks with circular-shaped craters which are bound by PFs have already been reported by Imbert (2009) and Imbert et al. (2011) and investigated by Andresen and Huuse, (2011). However, in these previous studies, pockmarks did not have the same character as “honeycomb-shaped” pockmarks in this study area. The formation of the honeycomb geometry of pockmark craters (fig. 6.15i; fig. 6.19c) are suggested to be a function of their depths, inclination and the presence of PFs. Measurements of the depth and inclination of the sidewalls (fig. 6.20b) of pockmarks on the lowest horizon of PF tier-1 indicate a relationship exists between the two parameters. The crater depths of honeycomb pockmarks are less than 12 ms (TWT) and the crater sidewalls usually dip less than 4.6° (fig. 6.20b). Variations in the inclination of crater sidewalls have been calculated by considering variations around the pockmark crater i.e. changes at the longest and shortest axis. The inclination of honeycomb pockmark sidewalls contrast to sub-circular pockmarks whose side walls dip at greater than 4.6° from horizontal and have depths ranging from 12 to 20 ms TWT. The shallow depths of honeycomb pockmarks indicate that fluid expulsion rates were slow-to-moderate (Chapter 4) otherwise in cases of more intensive fluid expulsion, venting depressions would be deeper rather than having shallow depths. This is why sub-circular pockmarks with deeper craters all occur above the earliest linear gas exits where fluid pressures are likely to be the most intense and the fluid venting intensity is moderate-to-fast (Chapter 4).

Because pockmarks and their immediately overlying sediments are offset by polygonal

faults it can be deduced that polygonal faults postdate pockmark formation. Similarly, the fact that polygonal fault cells bound and intersect the edge of the crater and are absent from their centre also suggests that the depression formed prior to faulting (e.g. pockmarks 3 in fig. 6.14c and 6.15i). This is most convincing for the case of sub-circular pockmarks (e.g. point 1, 2 in fig. 6.15i) because polygonal faults are clearly arranged into a concentric pattern which is vastly different to the standard hexagonal polygonal plan form. The circular plan form of these pockmarks which are undeformed by PFs and have relatively significant depths (> 12 ms TWT) and sidewall inclinations ($> 4.6^\circ$) imply that the isotropic, local stress state were perturbed in the sediments within, and immediately around and above the pockmark. It is because of this localized perturbation of the local stress field that the orientations of polygonal faults were probably preferentially aligned. Thus, it seems logical to add that the pockmark must pre-date the formation of the concentrically aligned polygonal faults (point 1, 2 in fig. 6.15i and fig. 6.19c) (cf. Cartwright, 2011). In contrast, honeycomb pockmarks have less significant depths and side wall dips. The fact that the isotropic arrangement of polygonal faults is maintained above and around these pockmarks may suggest that the craters are not deep enough to sufficiently perturb the local stress state. Measurements undertaken in this analysis suggest that the critical depth and side wall dips of pockmark craters are required to induce localized stress perturbations great enough to preferentially align polygonal faults into concentric patterns is greater than 12ms TWT and 4.6° respectively. Although the relationship between polygonal fault geometry and the local stress regime is beyond the scope of this study, my results highlight an intriguing relationship between pockmark genesis and morphology, and polygonal fault patterns.

6.6. Conclusions

This study have demonstrated that, subsurface fluid flow and their expression in sediment environment are strongly controlled by the interaction of several factors e.g. fluid venting intensity, basin setting, geological and tectonic structures, sediment depositions. Different examples presented in this study led to the conclusion that fluid flow was tightly linked with the basin evolution. The main conclusions for this chapter are summarized as follows:

1. Linear chimneys and preferentially aligned PFs mainly occur in PF tier 2 which is composed of hemipelagic sediments and is located above salt-withdrawal synclines.
2. Linear chimneys that occur within PF tiers often follow the trends of anisotropic PFs.
3. The majority of linear chimneys occur in the polygonally faulted hemipelagic unit (HD 4) above salt-withdrawal synclines.
4. The majority of linear chimneys emanated from the lower part of the PF plane down to the basal tip.
5. Hydraulic fractures formed preferentially in hangingwall because fluid pressures were not strong enough to open the entire PF planes.
6. The upper part of PFs was impermeable thus sealing any fluid which had migrated into the lower permeable part of the fault plane.
7. For the chimneys which emanated from the basal tip and the lowest part of PFs I suggest;
 - a. Gas accumulated in the lower part of PF footwall as evidenced by negative bright spots.
 - b. Sediment in the lower part of PF footwall was in an extensional regime and underwent dilatation which allowed fluid migration into the lower PF footwall.
 - c. Fluid migrated to the highest point in the permeable layer which was the footwall.
 - d. The impermeable layer was segmented by PFs whose upper portions were impermeable. This created a fault bound trap for fluid within the underlying permeable layer.
 - e. Fluid accumulated in the lower parts of PF footwall either due to the presence of the fault bound trap, or due to the dilatation regime of sediments in the lower part of footwall.
 - f. The presence of polygonal fault bound traps is supported by the occurrence of negative bright spots which are locally confined to strata beneath the Intra-Plio horizon.
 - g. The leakage sites of overpressure fluid are identified by the location of gas accumulations i.e. the PF bound traps.
8. The chimneys which emanate from the intersection of conjugate PFs, and occur along the strikes of PF grabens.

- a. Chimneys may also have emanated from the lower part of PF. However due to seismic resolution and acoustic perturbation in the lower part of chimneys, the exact position of the downward termination is uncertain.
 - b. If gas chimneys emanated from the basal apex of PF grabens, the normally displaced permeable layers within PF graben were not in communication with adjacent footwalls. The intra-tier permeable layer may have been juxtaposed against the stratigraphically older carrier bed by normal displacement. Fluid migrated into the permeable layer from the carrier bed, or migrated along the lower part of PF until reaching a permeable layer in PF graben.
 - c. Further lateral fluid migration into adjacent PF footwalls were prevented because PF grabens were bound by impermeable the PF plane?
9. Fluid migrated along tectonic faults from deeper intervals and was attained into the shallower carrier bed beneath the PF tier.
 10. Fluid migrated horizontally and until it reached basal tips of PF at which point fluid migrated vertically along the lower part of PF planes.
 11. The longest PFs whose basal tips tend to extend to the deepest stratigraphic positions promoted vertical fluid migration.
 12. Linear chimneys within PF tiers are aligned parallel to strikes of PFs. This can be explained by fluid pressure increasing until it exceeded the tensile strength and the least principal compressive stress in the PF blocks. Overpressured fluid was thus able to push aside the host rock toward the direction of least principal stress.
 - a. Anisotropic PFs are parallel and perpendicular to tectonic structures, such as salt-withdrawal basins, salt diapirs and associated fault systems. Their preferential orientation is attributed to a perturbation in the regional stress field due to activity or growth of the structure.
 - b. Shallow and elongate depressions below the chimneys and polygonal faults are also aligned parallel to tectonic structures. This supports the hypothesis of local tectonic stress field affecting the orientations of linear chimneys.
 13. Geometry of fluid venting structures that representing non-fast venting regime not necessary controlled uniquely by fluid venting intensity.
 14. Shallow depressions that representing non-fast venting regime and have same range of depths, form under different state of stress will develop into different geometry.

15. Isotropic, local stress field and development of PF are being affected by presence of pockmark craters.
 - a. Concentric PFs surrounding conical pockmarks were the result of this perturbation.
 - b. Linear chimneys emanated from the lower part or basal tips of concentric PFs and as a result surround the pockmark crater edge.
 - c. Linear PHAAs (methane-related carbonates) formed by migration of methane through linear chimneys surrounding the pockmarks. Thus they are also organized in a ring around the pockmark crater.
16. The following observations indicate that the timing of linear venting structures post-dates the formation of PFs.
 - a. Linear PHAAs (methane-related carbonates) were fed by underlying linear chimneys of similar lengths and orientations.
 - b. Because the majorities of these linear PHAAs occurs above the PF tier but are still aligned parallel to them suggests that the polygonal faults existed before they developed.
 - c. Linear PHAAs are associated with negative and shallow linear depressions. They have comparable depths and lengths as elongate depressions. Both structures formed as a result of slow-to-moderate fluid flux rates rather than rapid flux rates.
 - d. The spectrum of fluid flux rates that produced both types of venting structures was similar. They produced venting structures with the same range of depths but different aspect ratio even though they occur in the same type of sediments with the same thickness. This implies elongate depressions formed before the development of faults in PF tier-2 and were strongly influenced by local tectonic-related stress field. In contrast linear depressions post-date PF formation and were affected by the in-situ field around PFs.
17. A complex fluid venting system occurred in Late Miocene sediment above the inactive and buried syncline 0.
18. Lateral and vertical heterogeneity in the sediments influenced the behavior of fluid flow and style of the resulting venting structures.
19. Linear networks within the hemipelagic-1 unit of Late Miocene age evolved into pockmarks within overlying MTCs sequence.

20. Linear fractures preferentially developed in fined-grained sediment and were caused by ascensions of methane bubbles.
 - a. Methane bubble force the matrix grains apart creating linear and planar fractures.
 - b. Fractures can only be formed in fine-grained sediments when fluid pressure was greater than the cohesion strength and tensile strength of the hosted sediment.
 - c. Linear depressions aligned above linear fractures were produced by slow fluid flow rates.
21. MTCs in the interval of interest were muddy and behaved as a non-Newtonian fluid at the moment of their deposition on the palaeo seabed.
22. Fluid pressures may have exceeded the tensile strength and fractured the MTC units, until fluid was strong enough to overcome the interstitial fluid pressures, grain-grain interactions forces, cohesion and buoyancy strength.
23. The heterogeneous internal structures of MTC induced mechanical weaknesses at clasts interfaces, grains boundaries, surfaces of rock fragments, and through layered clasts.
24. Hydraulic fractures propagated along pre-existing weak zones within MTCs because of heterogeneous distributions of clastic inclusions.
 - a. Overpressured fluid migrated preferentially along mechanically weak zones.
 - b. Hydraulic fractures occur along these mechanically weak zones within MTCs above major seeps points, and coalesced together to form branching fracture zones.
 - c. Overpressured fluid migrated along these branching fractures and caused fluid eruption at the palaeo seabed i.e. the top surface of MTCs.
 - d. Fluid eruption or venting occurred above branching fractured zones within MTCs induced sub-circular depression craters at the surface of MTCs, in contrast to linear geometries of venting structures in fine-grained sediments.
25. Occurrence of pockmarks perturbed the location stress fields
 - a. Pockmarks with sidewall inclinations $> 4^\circ$ and depth > 12 ms TWT were formed by moderate-to-fast fluid venting rates.
 - b. The in-situ stress state in the sediments within and surrounding the rim of the pockmark crater was anisotropic. The degree of anisotropy in the horizontal principal stresses was great enough to cause PF to propagate in specific orientation i.e. parallel to crater edge.

- c. Pockmarks with shallower depths $< 12^\circ$ and inclinations $< 4^\circ$ were formed by slow or slow-to-moderated fluid flux rates.
 - d. PFs growing in the sediments compacting above and around these pockmarks were isotropic.
 - e. These isotropic PFs cut through the edge of pockmarks.
 - f. These shallow pockmark craters whose edges define a polygonal-like plan form geometry are named 'honeycomb pockmarks'.
 - g. Shallow, honeycomb-shaped pockmark craters had insufficient topography to induce enough anisotropy in the horizontal stresses to affect the orientation of PF's.
 - h. The absence of PFs in the center of pockmark craters indicates the shallow honeycomb pockmarks induced only minor anisotropy in the horizontal principal stresses.
26. Most of gas chimneys and PHAAs of Quaternary age are associated with shallow depressions at the present day seabed indicating venting sites are still active.
27. Long depressions in the sediments on the present day seabed are associated with PHAAs and occur above tectonic blind faults.
- a. Long depressions along tectonic faults are composed of several small ones on the present day sea floor. These were induced by episodic fluid expulsion at different position along the tectonic faults
28. Their occurrences on the present day seabed indicate fluids migrated along these blind faults recently and are still going on.

CHAPTER 7

DISCUSSION

7.0. Discussion

7.1. Introduction

The aims of this Chapter are 1) to give a brief summary on the central themes which have been discussed in the core Chapters; 2) to incorporate key results from Chapters 4, 5, 6 into the synthesis of fluid venting intensity in the basin evolution history; 3) to discuss the potential implications of this research; 4) to outline the limitations of this research; and 5) to propose recommendations for future work.

7.2. Summary on discussed topics

Several central topics regarding the vertical evolution of fluid venting structures have already been discussed in detail in the core Chapters: In Chapter 4 and 5, significance of different type of fluid venting structures and their applications; In Chapter 5 and 6, how geometries and types of fluid venting structures that are influenced by geological setting; In Chapter 6, the relationship between distribution and vertical evolution of fluid venting structures, tectonic setting and basin evolution; how regional evolution of geological structures controls fluid migration pathways.

In the next section of this discussion, a reconstruction of the fluid venting history of this study area is given as a synthesis. Stratigraphic distribution and types of venting structures that reflect the ages and dynamics of fluid seeps are used as a proxy for the reconstruction.

7.3. Spatial and temporal evolution of fluid venting structures across different geological settings

The objective of this thesis was to analysis the main factors that control the vertical evolution of fluid venting structures. Six principal influential factors have been examined

individually in detail in Chapters 4, 5, 6. These factors are respectively: seepages intensity (Chapter 4), sedimentation (Chapter 5), bottom currents (Chapter 5), geological setting (Chapter 5), stress regime (Chapter 6) and lithology (Chapter 6).

This section presents a synthesis of fluid flow history at each stage of the basin evolution by integrating influential factors that are listed above, with the purpose of demonstrating how to use fluid leakage phenomena to reconstruct the variation of fluid flux intensity at the palaeo-seabed. Summaries are presented of the temporal and spatial evolution of fluid flow intensity, by joining together the classification of fluid venting dynamics (Chapter 4) and interaction between these controlling factors (Chapters 4-6) using the case study of Offshore Angola. In each case of focused fluid venting, the spatial-temporal distribution and evolution of fluid structures are described and discussed for discrete stratigraphic ages in different geological settings. This reconstruction is especially made by re-establishing the link between the state of stress, lithology, growth of fluid flow features, and by taking into account how the interaction of influential factors impacts on the development of venting feature.

7.3.1 Slow to moderate seepage in Middle Miocene above syncline 0

7.3.1.1. Slow to moderate seepage at 12Ma on the surface of MTC0a

- a. One of the earliest locations for fluid expulsion in the study area likely occurred at 12 Ma in the region of Syncline 0 (fig. 7.1). This structure ceased to develop after Middle Miocene (16.4Ma). Following this time, a series of MTCs were deposited successively in this location alternating with hemipelagic sediment. The fluid flow history in this syncline is the most
- b. Complex in comparison with the rest of fluid migration systems in the survey area.
- c. Local seepages with slow to moderate flux rate are likely to take place at the topmost surface of MTC0a, via the interpreted 4km linear gas feature (fig. 6.15a, Chapter 6) that occurred at the End of Middle Miocene (12 Ma) above Syncline 0 (fig. 7.2). The long and shallow morphology of the depression observed for this linear structure is

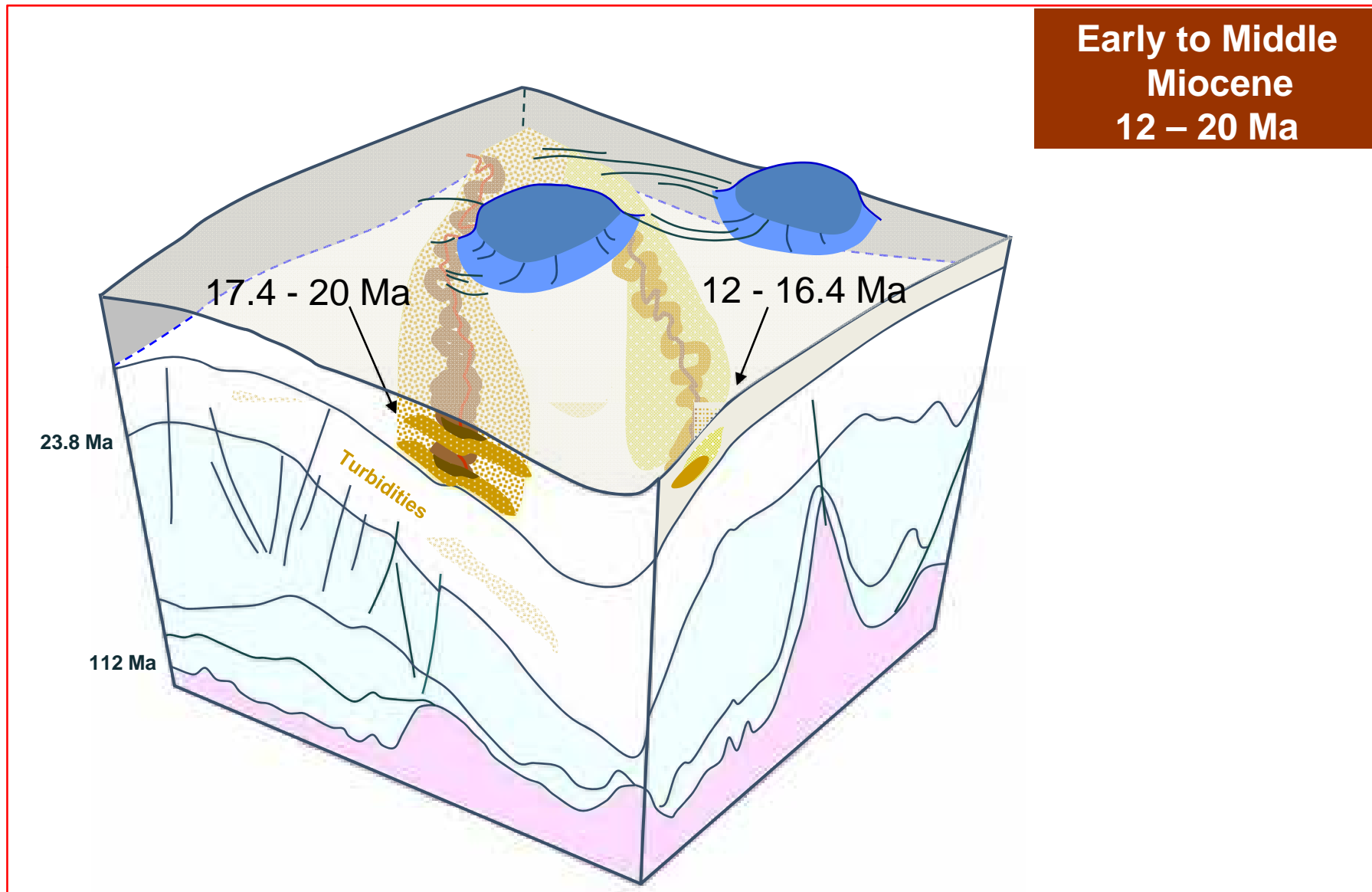


Figure 7.1. Block diagram of the study area showing the situation at the end of the middle Miocene, with the two turbidite channel complexes deposited during the early and middle Miocene (20 to 12 Ma).

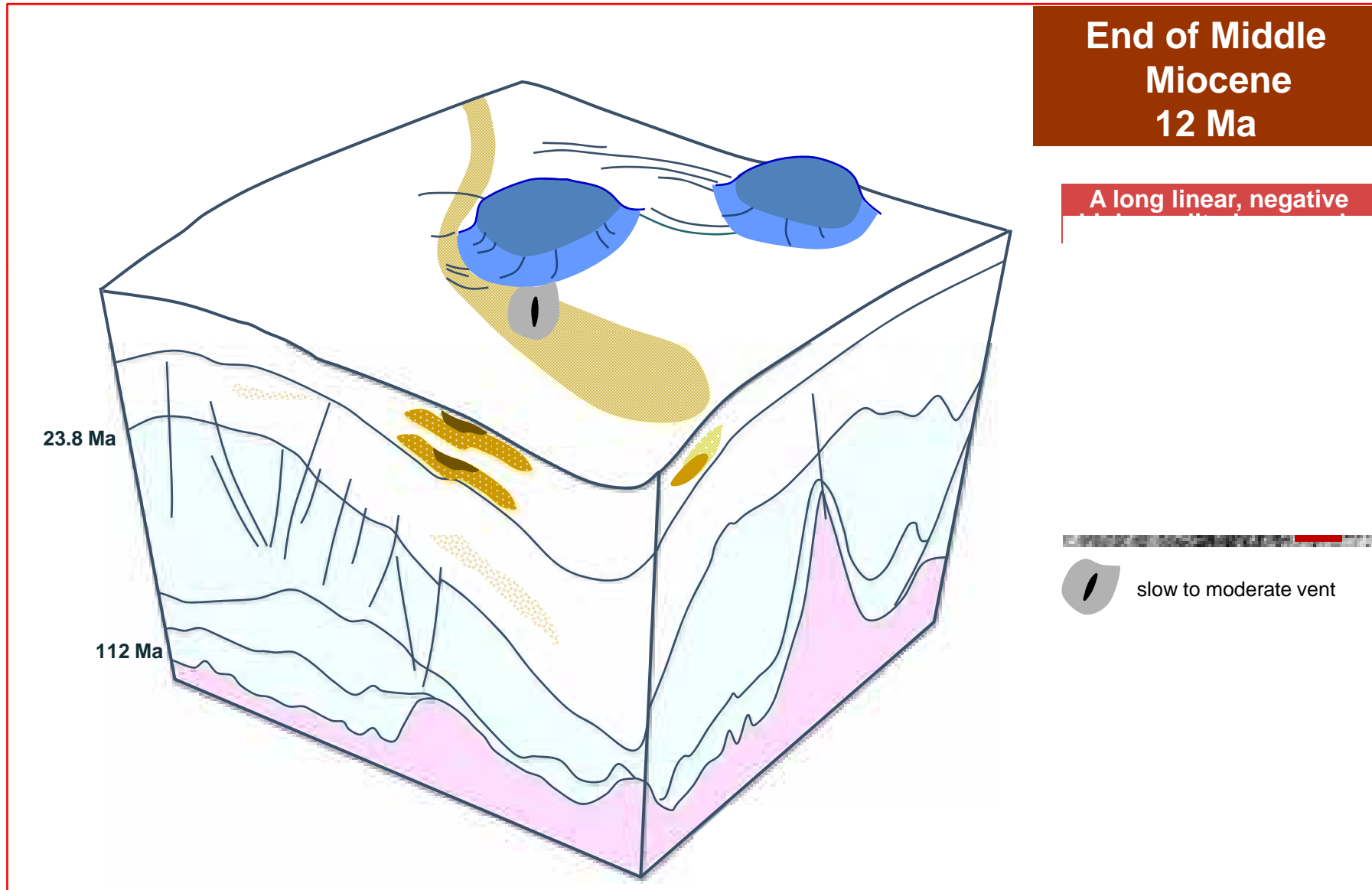


Figure 7.2. Fluid venting structures and venting intensities on the palaeo seafloor at the end of the middle Miocene.

linked to the formation of a MTC. The seepages along this linear depression were likely induced by the erosional action of translated 'glide' blocks entrained in the MTC which triggered local depressurizing within the MTC0. This explanation is suggested by the similarity in orientation of grooves in at this position with those observed on the top surface of overlying MTC0b (fig. 6.15b, Chapter 6). The fluid expulsive origin of this linear feature is also consistent with the accumulation of negative chaotic high amplitude reflections within the depression which are interpreted as small gas accumulations at the same location (fig. 6.14a, b, Chapter 6).

- d. Meanwhile during the same period, Syncline 2 formed between the two diapirs by salt collapse.

7.3.1.2. Slow seepage between 11.2 – 11.6Ma within hemipelagic-1 unit

- a. Successive fine-grained hemipelagic sediments draped on MTC0b directly after 11.6Ma (hemipelagic-1 in fig. 6.15b, Chapter 6). Hydrocarbon leakage is suggested to persist via the primary linear gas exit throughout the Tortonian because subsequent fluid venting features in the overlying stratigraphic layers are observed to be crudely aligned above with the earliest linear exit (fig. 6.15g-i, Chapter 6).
- b. Slow seepages took place at the palaeo seabed at approximately 11.2 Ma by developing linear hydraulic fractures within the fine-grained hemipelagic-1 unit, and cut through the interval between 11.6 – 11.2 Ma (fig. 7.3). These linear fractures principally occur above the vertical location of primary linear gas exit (fig. 6.15c, d, Chapter 6).
- c. This slow venting regime at the palaeo seabed is indicated by the linear geometries of fractures but also the linear shallow depression (5 – 7 ms TWT) at the upper termination of these fractures. These shallow depressions are suggested to have formed at the palaeo seabed and to have originated by suppression of sedimentation or actual physical erosion by fluid seepages. Methane-related carbonates that are expressed by linear PHAAs indicated slow seepages environment in which they are able to precipitate inside these shallow depressions at the palaeo-seabed (Chapter 4).

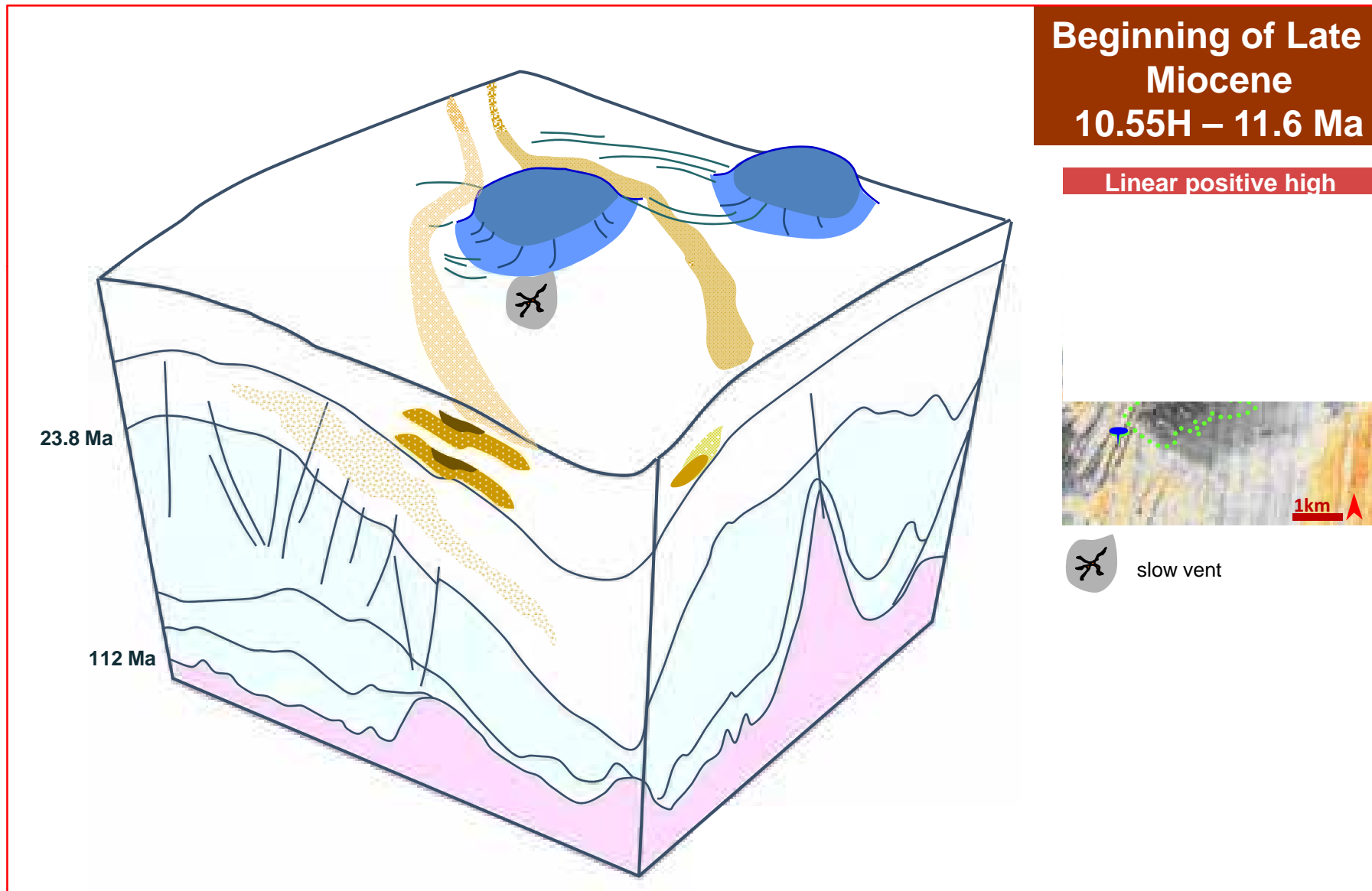


Figure 7.3. Fluid venting structures and venting intensities on the palaeo seafloor at the beginning of the late Miocene.

7.3.1.3. Slow to moderate seepages 6.25H – 10.55H within the interval of debris flow1a, MTC 1b and 2

- a. The gentle Syncline 0 was reactivated at 10.55H (Early Tortonian), while a succession of fine-grained rich MTC (1 & 2) was deposited in this location during 6.25H – 10.55H. The changes of physical property and internal structures of the MTC sediments are suggested to impact fluid flow behaviour. Fluid migration pathways were changed from linear-planar fracturing model to “branching fracturing” model, whereby fluid bypassing mud-dominated MTCs and migrated along the mechanically weakest interfaces (see fig. 6.28, Chapter 6).
- b. During this period, a series of sub-circular shallow depressions that indicate moderate to slow vents developed at the surfaces of MTCs (fig. 6.15g-i, Chapter 6), and above the vertical location of primary gas exit (fig. 6.15a, Chapter 6) ((fig. 7.4). Fluid venting intensities that created these shallow depressions at the MTC surfaces are suggested to only slightly stronger than those responsible for the linear depressions at the top of hemipelagic units. As the depths of both circular depressions (< 12 ms TWT) and the linear depressions (< 7 ms TWT) on the top surface of the MTCs and hemipelagic-1 unit, are similar to typical depths of conical pockmarks (several tens ms TWT; cf. Chapter 4 and 5). The fluid pressure could potentially build up at the base of MTCs, until it became strong enough to overcome the internal strength of the MTCs. However, recalling the explanation given in Chapter 6, the geometries of fluid migration paths were most likely affected by the disorientated planes of mechanical weakness and internal anisotropic fabrics within MTCs, and these heterogeneities potentially played an important role for the geometry of subsequent venting features. Fluid migration is considered to have changed from vertical fracturing into a “branching-fracturing” model, in which fluid conduits/fractures were developed as branching-like organisation within the MTCs and provided clustered fluid exits on the surfaces (fig. 6.28, Chapter 6). This allowed focused fluid expulsion on the upper surfaces of MTCs, and created the sub-circular shallow depressions that are assumed to represent moderate seepage fluxes. The geometries of fluid exits were this grouped into “clustered forms” due to the internal structures of MTCs. It means that, the subsequent venting structures would not be linear in form but their geometries might be were expected to be (sub-) circular.

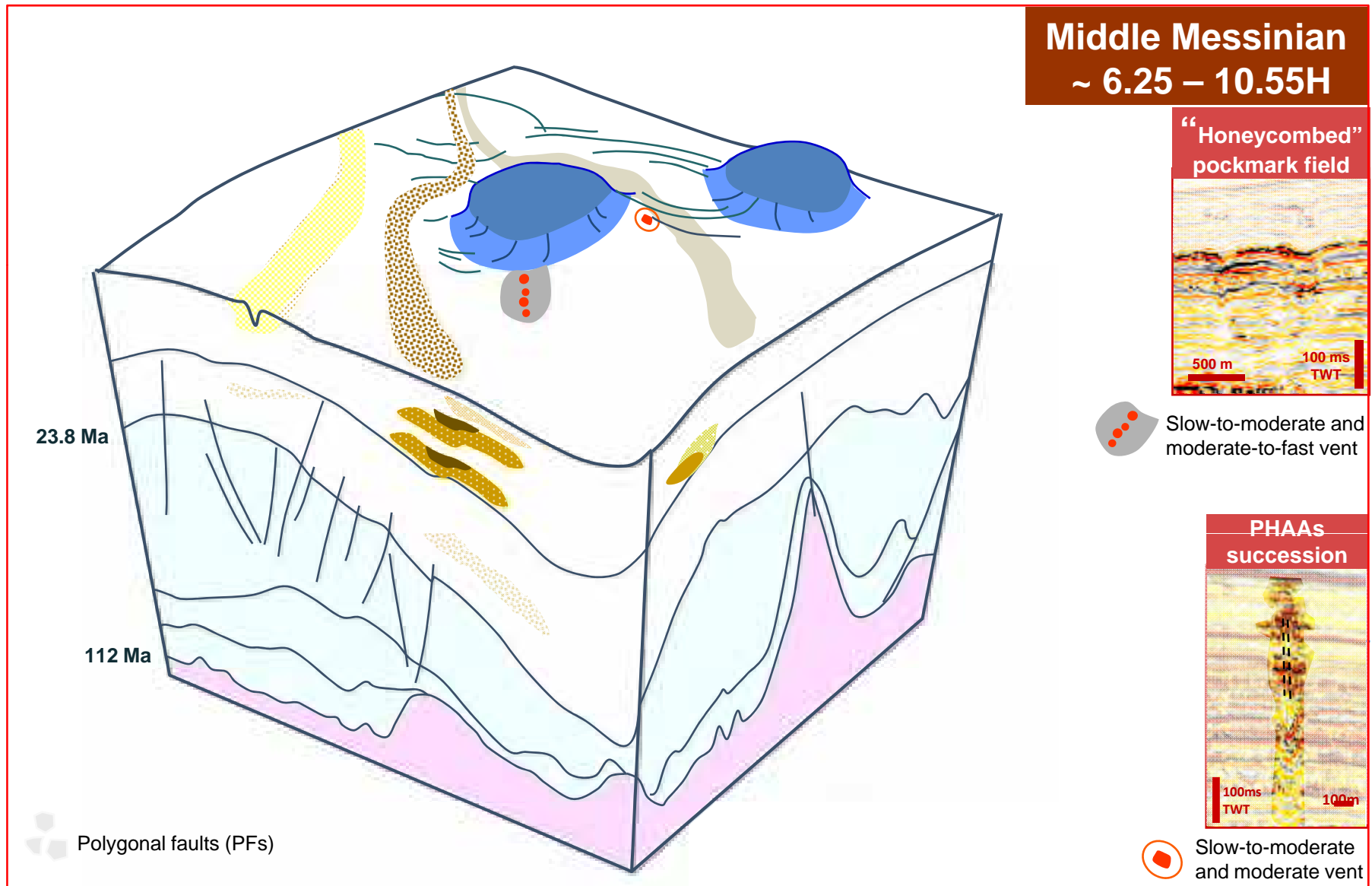


Figure 7.4. Fluid venting structures and venting intensities on the palaeo seafloor of the middle Messinian.

7.3.2. Moderate to fast seepages between 6.05H – 6.25H within the Late Miocene hemipelagic sediments of PF tier-1

- c. Hemipelagic sediments were draped above MTCs after 6.25H in Late Miocene. Fluid leakages were continued throughout the 6.05H – 6.25H interval above the same seeping locations, evidenced by the intermittent occurrences of individual pockmarks/depression within their vertically stacked successions (fig. 6.14a, b, Chapter 6).
- d. The fluid leakages regimes were likely to be moderate to slow and moderate to fast at different seeping points above the vertical location of the primary gas exit in the hemipelagic unit of 6.05H – 6.25H. This is suggested by the depths of shallow sub-circular depressions and pockmarks, which range from 3 – 11 ms TWT and 3 – 20 ms TWT (Chapter 6).
- e. Polygonal faults are suggested to be triggered after the formation of depressions/pockmarks after 6.05H, or once after the occurrence of the lowest pockmarks between the time intervals of 6.05H – 6.25H (fig. 7.5). It is indicated by the isotropic PFs that cutting through the edges of shallow depressions (less than 12 ms TWT), in respecting the central deepest areas. As a result these isotropic PF defined the polygonal plan form of these shallow depressions on horizon, and form the “Honeycomb pockmarks” (see fig. 6.15i; fig. 6.19c; Chapter 6).
- f. In contrast, PFs became anisotropic and deflected around the pockmarks with deeper depths from 12 to 20 ms TWT and sidewall inclination of more than 4°. This deflection occurred because the topography of these pockmarks was enough to perturb the stress field and hence the PF patterns (Chapter 6), although this cannot be the case for honeycomb pockmarks which have shallow depths and gentle inclination (< 4°).
- g. In conclusion, the various leakage phenomena point to an evolution of fluid leakage regimes throughout Tortonian at the Syncline 0. Fluid venting intensities progressively increased over time along the primary linear gas exit of 9.31 Ma, from slow seeps in 10.1H – 12 Ma evolved into slow to moderate in 6.25H – 9H and then moderate to fast thereafter during 6.05 – 6.25H.
- h. Meanwhile started from 6.25H, in the NE corner of footwall domain (see fig. 3.4, Chapter 3) where deformed by tectonic extensional faults, successive slow to

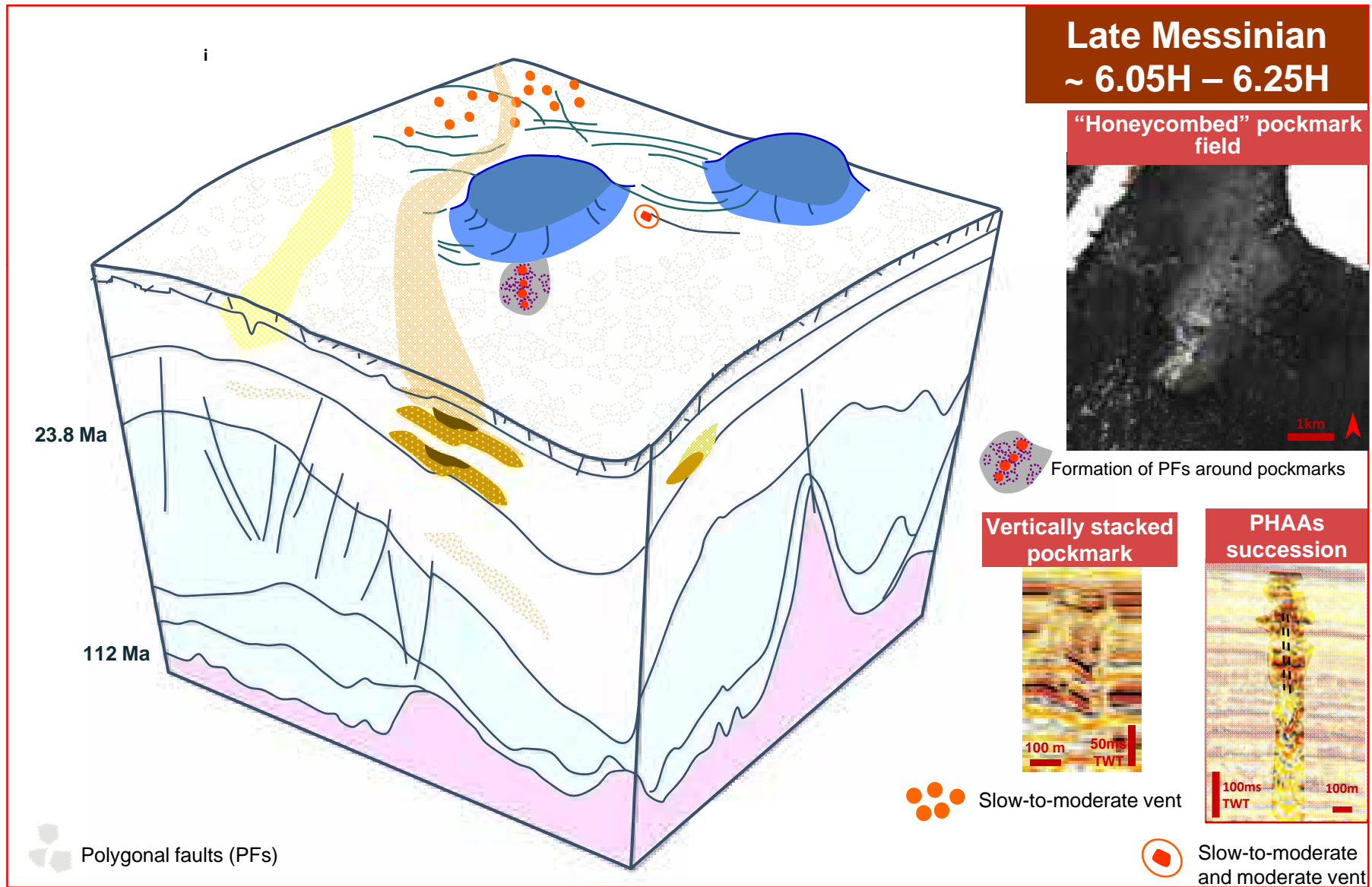


Figure 7.5. Fluid venting structures and venting intensities on the palaeo seafloor at the beginning of the late Messinian.

moderate fluid expulsions were triggered and were expressed by successions of vertically stacked shallow pockmarks with length of 200 ms TWT (fig. 7.5). These pockmark successions were composed by individual pockmarks and shallow depressions (see section 6.2.2 in Chapter 6) and both of which have depths varied from 5 to 25 ms TWT (fig. 6.14a, Chapter 6). These extensional faults are induced by the activities of key-stone grabens and compensation faults in the adjacent area to the studied survey at the end of the Miocene (Total internal report; Philippe, 1999). Moreover, the occurrences of fluid venting structures in the footwall during this period correspond to the timing of hydrocarbon charging in the buried turbidite reservoir upon the basin modelling results (Total internal report; Grauls, 1996; 2000).

- i. In addition, the tectonic event at 6.25H was characterised by the reactivation of Syncline 1 (until the late Pliocene). During the Tortonian, at 6.1H, the channel complex 1 started to develop above the NW shoulder of Syncline 1. At 6H Syncline 0 was completely stable and static, while Syncline 1 began to grow again.
- j. Starting from 6H hemipelagic was draped on the top surfaces of two channel complexes.

7.3.3. Moderate venting at 5.5H above Anticline 1 and 2

- a. A focus hydrocarbon leakages event probably occurred at 5.5H above the two anticlines (fig. 6.1; fig. 6.8c; Chapter 6) and above the ridge in SE corner. This is evidenced by the small fluid expulsion features that developed at this time.
- b. The elongate, shallow conical depressions with depth less than 11 ms TWT indicate slow-to-moderate or very focused small-scale intensive eruptions, which characterise the seepage regime of this venting event (fig. 7.6). The moderate fluid venting event may relate to reactivation of extensional faults adjacent to Syncline 2 at the end of Miocene as seen from seismic (fig. 3.6b in Chapter 3). The extensional faults may have triggered the release of the pore pressures in the reservoirs that they cut through, and facilitated fluid migration to the palaeo seabed.
- c. The geometries of these shallow depressions exhibit elongate shapes above the edge of Syncline 2 (fig. 6.7a, Chapter 6) but linear shape at location of radial

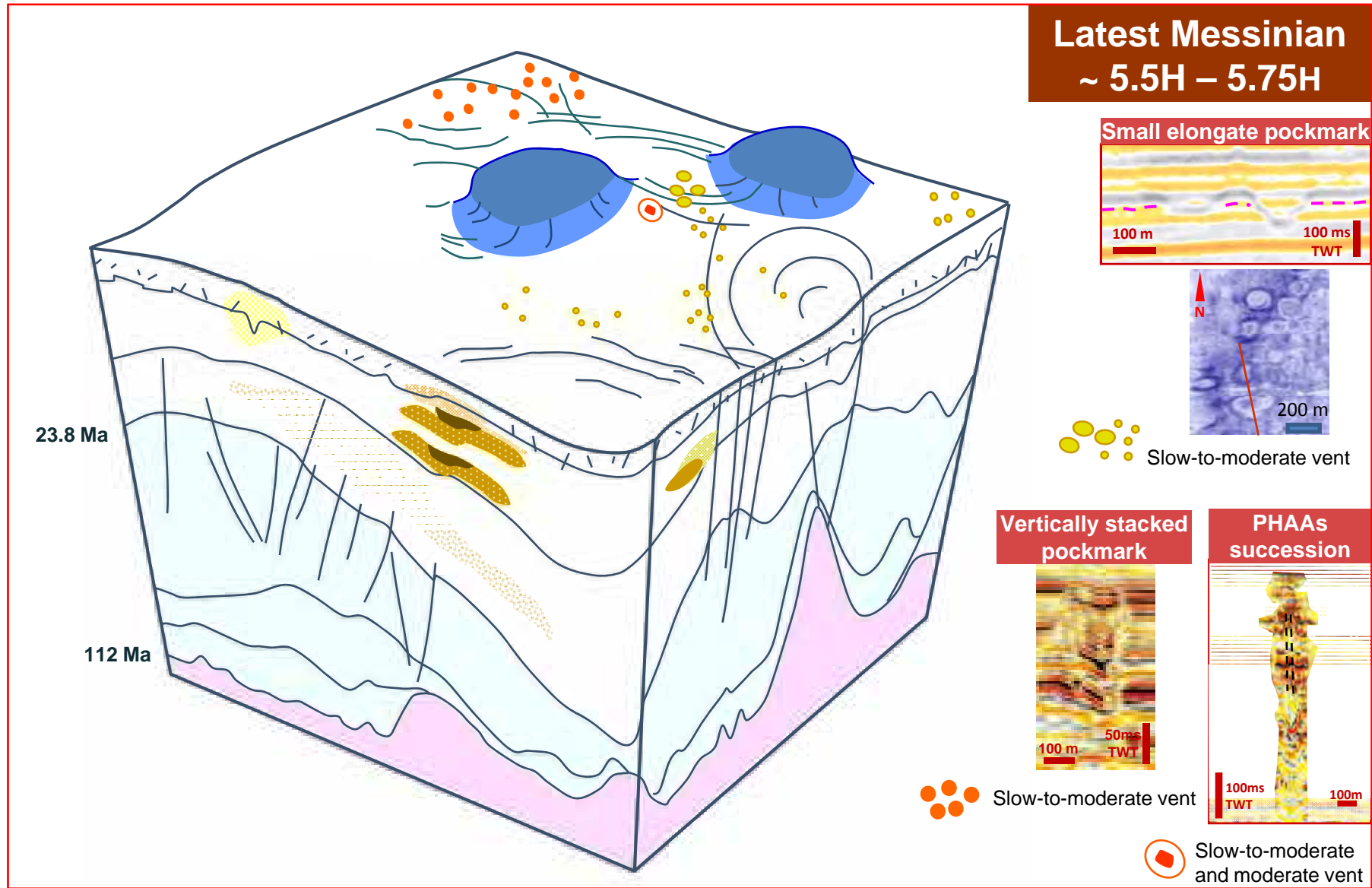


Figure 7.6. Fluid venting structures and venting intensities on the palaeo seafloor in the latest Messinian.

tectonic faults (fig. 6.8b, Chapter 6). The reason for the same type of fluid venting structures but possessing different planforms, was probably because of the state of stress of the underlying tectonic structures. It is likely confirmed by the circular shapes of these depressions (fig. 6.8c, Chapter 6) that occurred outside the syncline location, where seepages are not affected by the local stress field of Syncline 2.

- d. Meanwhile, slow-to-moderate venting was continued in the faulted area in the NE corner of footwall domain. This was indicated by the presence of vertically stacked shallow pockmark successions (fig. 7.6).

7.3.4. Moderate to fast venting at 5.3Ma above Anticline 1 and 2

- a. Certain seep points above the turtle-back anticline continued to be active until the end of Messinian. This is indicated by the circular shallow depressions that occurred above the Anticline 1 evolved into polyphased pockmarks (Chapter 4) (fig. 7.7).
- b. Polyphased pockmark that occurred above the crests anticlines at the End Miocene represent moderate-to-rapid seepages. Their presence indicated the moderate leakages above the anticline since 5.5H changed into moderate-to-rapid seepage at 5.3Ma . The occurrence of the polyphased pockmarks suggests that hydrocarbons continued to leak at these structural high positions at the end of Messinian. The scenario of hydrocarbon leakage above reservoirs and above the turtle-back anticline, within the Miocene to Pliocene interval has also been proposed by the basin modelling results (Total internal report, Grauls, 1996).
- c. Meanwhile, slow-to-moderate venting was continued in the faulted area in the NE corner of footwall domain. This was indicated by the presence of vertically stacked shallow pockmark successions (fig. 7.7).

7.3.5. Fast vents at the end of Messinian above palaeo channel complex 1, 2 and in Syncline 3

- a. Another degassing evening occurred at the end of Messinian in the NE of the survey and in Syncline 3. A series of deep circular pockmarks craters that line up above the

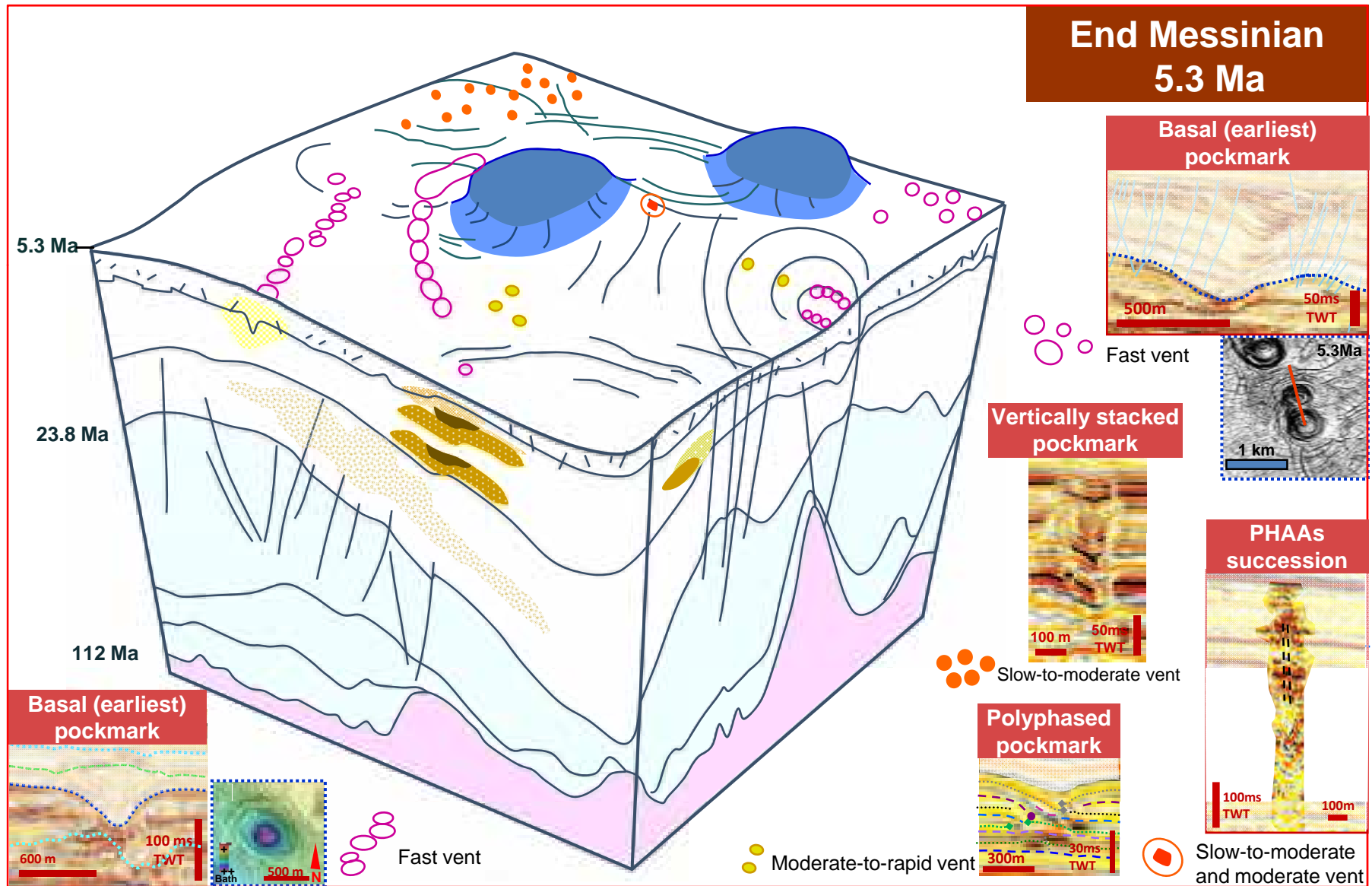


Figure 7.7. Fluid venting structures and venting intensities on the palaeo seafloor at the end of the Messinian.

two palaeo channel complexes indicated intensive fluid explosions (P0 in fig. 5.3a, in Chapter 5) (fig. 7.7).

- b. In the case of palaeo channels complex 1, it was suggested that gas migrated from the hydrocarbon-bearing turbidite channels which stacked vertically above the underlying turbidite reservoirs and from which there must have been direct communication. The presence of methane is indicated by a present day BSR that goes across the deep craters and is located above the channel 1 location (fig. 5.16, Chapter 5).

For the palaeo channel complex 2, gas eruptions are suggested to have occurred above the gas-bearing channel levees above the locations where are cut through by an extensional faults set (fig. 5.11c; fig. 5.20, Chapter 5). The presence of methane gas hosted originally inside the levees and that potentially migrated from deeper intervals, is expressed by reflections with instantaneous phase values of -90° (fig. 5.19a, Chapter 5).

- c. These earliest pockmarks craters above the palaeo channel 1 were almost deactivated afterward, and were sealed possibly by fine-grained turbidites as indicated by the overlapped infills on seismic sections (fig. 5.7, Chapter 5). However, the sediment infilling model of these craters is not the focus of this research, and further study on this topic need to be carried out in the future.
- d. In Syncline 3, the formation of earliest pockmark craters corresponded to the period of activation of Syncline 3 and their extensional faults (fig. 3.6c, Chapter 3). The formation of deep extensional faults cut through the turbidite reservoir and probably guided fluid migrated upward into shallow interval and induced fluid eruption during that period.

7.3.6. Alternation of slow, and moderate to fast venting regime during Pliocene above channel complex 1 and 2

- a. Fluid migration restarted with a slow and moderate-to-fast regime at the beginning of Pliocene above the channel 1 location (fig. 7.8). It is indicated by the presence of subsequent circular craters within advancing pockmark arrays (P3 in fig. 5.3a, in Chapter 5) and occurring above the infill of the earliest pockmarks craters (P0 in fig.

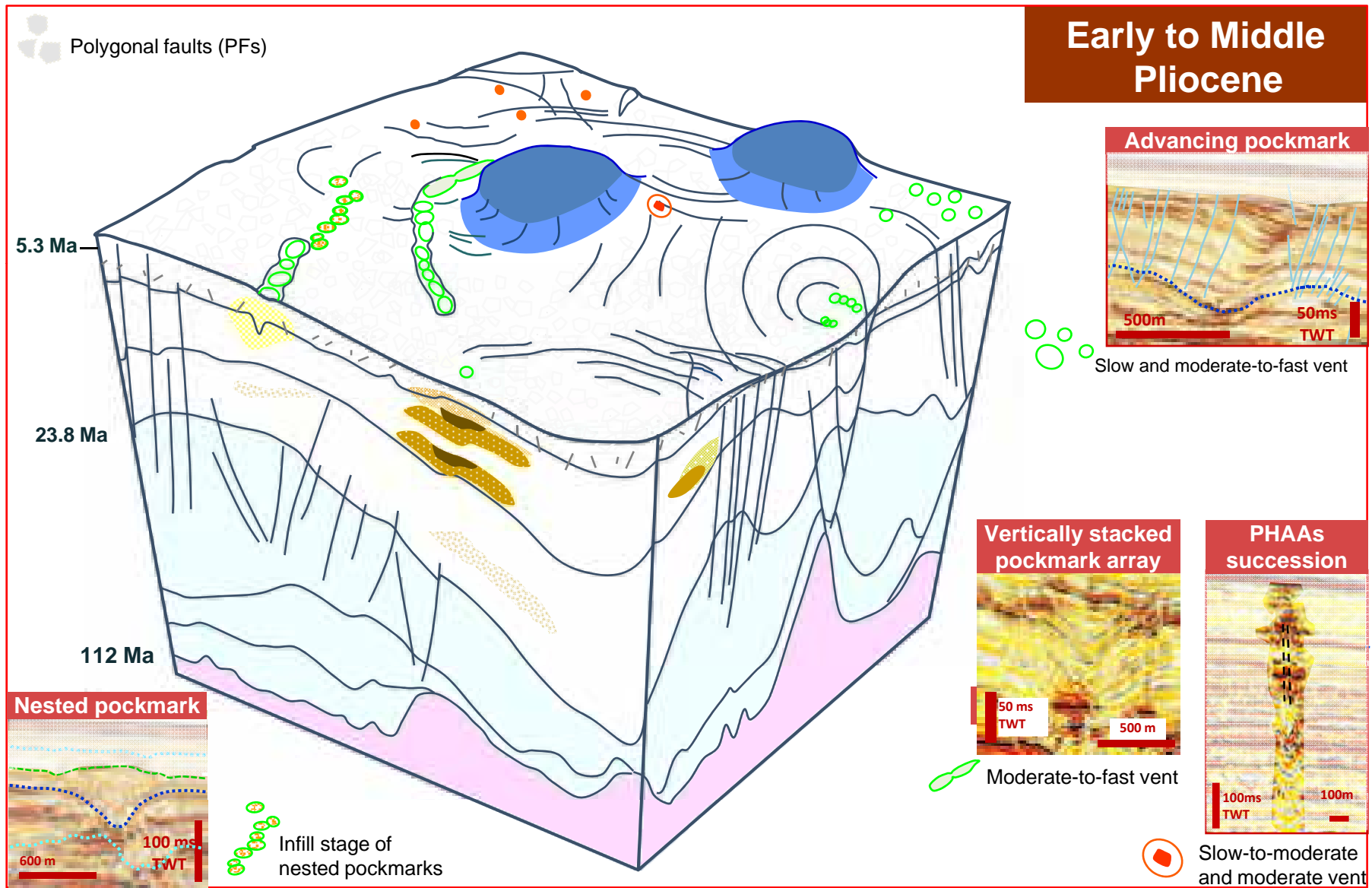


Figure 7.8. Fluid venting structures and venting intensities on the palaeo seafloor during Early to Middle Pliocene.

- 5.3a, in Chapter 5), which provide afterward a foundation for the formation of pockmark arrays.
- b. Moderate-to-fast seepages were expressed through whole of the Pliocene in the upstream part of channel complex 1 by vertically stacked pockmarks craters that developed above the earliest foundational pockmarks, and which are located between crests of sediment undulations within the channel 1 (fig. 5.7b, Chapter 5) (fig. 7.8). The infills of the earliest pockmarks in this upstream part, exhibit negative high amplitudes that are associated with acoustic perturbation columns and are interpreted as being associated with free gas accumulations (see fig. 5.7b, Chapter 5). The upper boundary of the high amplitude infill is characterised by a present day BSR with stacked-up pockmarks developed right above. Whilst in the downstream part, the occurrences of slow seepages alternating with the faster seepages were recorded by the advancing pockmarks arrays (fig. 5.7b, Chapter 5).
 - c. Slow seepage in the downstream part of this channel complex, was suggested by the geometries of venting exits that were represented by the crescent-shaped truncation areas on the downstream sidewalls of hemipelagic drapes (fig. 5.6b, Chapter 5) inside the advancing pockmarks arrays. The crescent-shaped truncated surface was likely caused by re-suspension of unconsolidated sediment, due to vortexes that were generated on downstream sidewalls by backward gravity bottom current, or by episodic seepages that prevented sedimentation (fig. 5.26, Chapter 5). The different generation of truncated areas stacked-up along the downstream side and led to a local weakness zones for overpressured fluid. These weakness zones provided a preferential pathway on the downstream side, for fluid migration and nucleation sites for overpressured fluid eruptions to form younger reactivated pockmark craters. Rapid venting was thus indicated by the reactivated pockmarks which cut through the underlying hemipelagic infills of previous pockmarks.
 - d. The cycle of erosion--sedimentation-fluid eruption regimes at the channel 1 location during the Pliocene, was represented by the truncated surfaces, hemipelagic drapes and reactivated pockmark craters. It was precisely the same case for the advancing pockmarks in downstream area of channel complex 2 during the Pliocene (fig. 5.11b, Chapter 5). However, for the upstream area of channel complex 2, fluid activities were quiescent as there were no obvious seepage expressions (fig. 5.11a, Chapter 5).

- e. During the Quaternary, the fluid migration in the upstream part of the channel complex 2 were reactivated following a lengthy period of quiescence in the Pliocene, as indicated by the occurrence of sub-circular methane-related carbonates (PHAAs) patches above the nesting pockmarks (fig. 5.24a, Chapter 5) (fig. 7.9). These carbonates patches representing slow to moderate seepages were sealed by Holocene sediments (fig. 2d, Chapter 5). A probable carbonate mound is still active at the present day seafloor (fig. 5.17, Chapter 5).
- f. At the same time, fast seepages were likely completely inactive in the footwall, as nearly all vertically stacked pockmarks were sealed (fig. 7.8; fig. 7.9).
- g. Meanwhile, tectonic events that occurred at the end of Miocene/beginning of Pliocene were the cessation of activity of growth faults and salt-collapse faults at the location of Syncline 1 and 2 and the initiation of a third roll over syncline in the southern area in the early Pliocene.

7.3.7. Slow or moderate venting during Quaternary above channel complex 1 and 2

- a. At the end of Pliocene and during the Quaternary, slow and moderate fluid venting regimes in the upstream part of palaeo channel complex 1, were indicated by linear or elongate methane-related carbonates patches (PHAAs) (fig. 7.10; fig. 5.18a-c, Chapter 5; fig. 6.9, Chapter 6). These carbonates were fed by underlying linear chimneys, which emanated from the basal tips of concentrated PFs surrounding the earliest pockmarks and were organised as a ring (fig. 5.18a-c, Chapter 5; fig. 6.9, Chapter 6).
- b. The concentrated polygonal faults developed around the earliest craters below the advancing and nesting pockmark array, most likely because of the fluid pressures were stronger enough to perturb the local stress field.
- c. The stress field of the earliest pockmarks is suggested to contribute their influences directly on the geometry of the linear chimneys and indirectly on the subsequent linear carbonates (PHAAs).
- d. Fluid seepage was almost insignificant in the downstream part of channel complex 1 as no new fluid flow structures were formed within during the Quaternary, and only

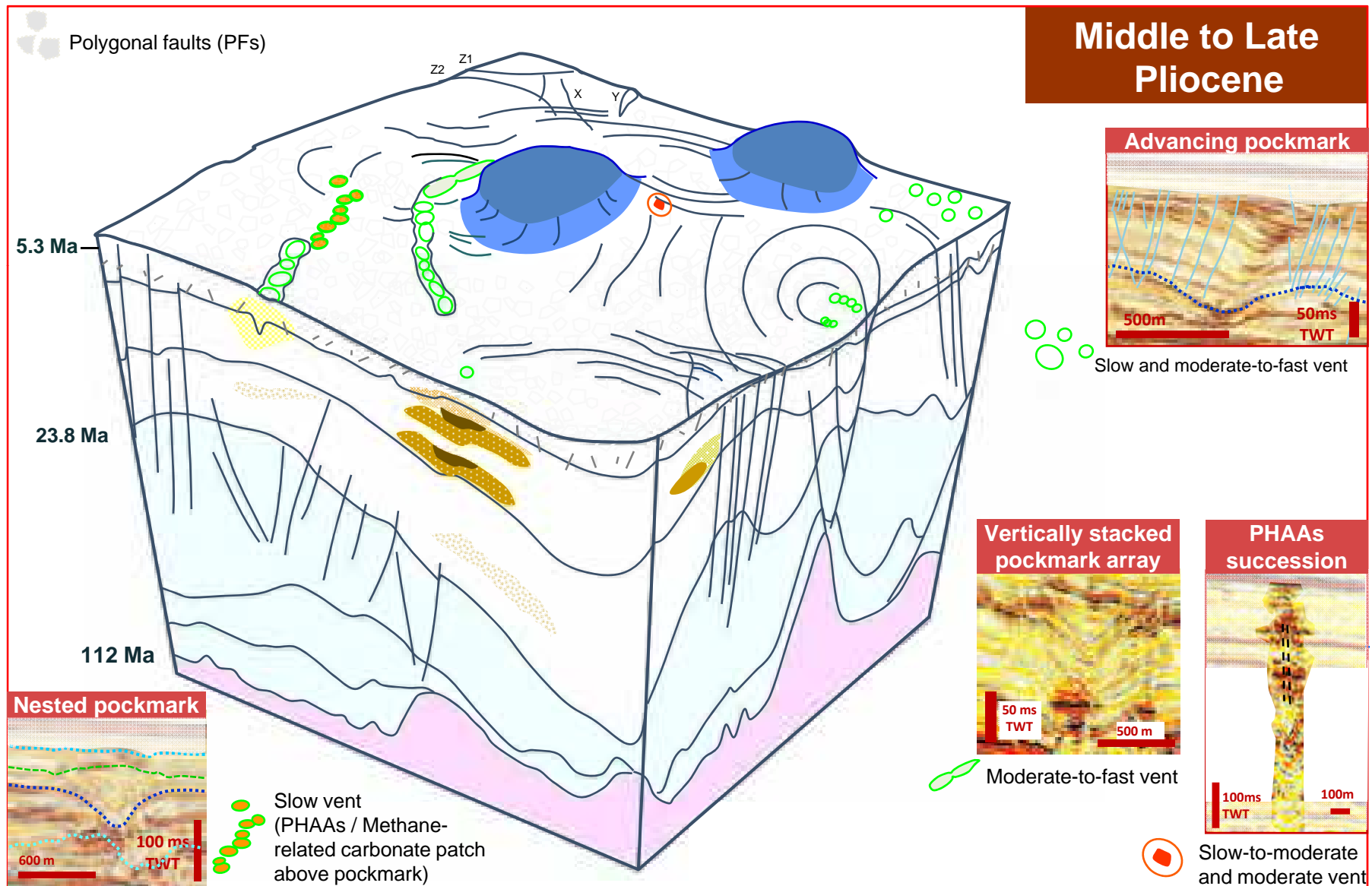


Figure 7.9. Fluid venting structures and venting intensities on the palaeo seafloor during Middle to Late Pliocene.

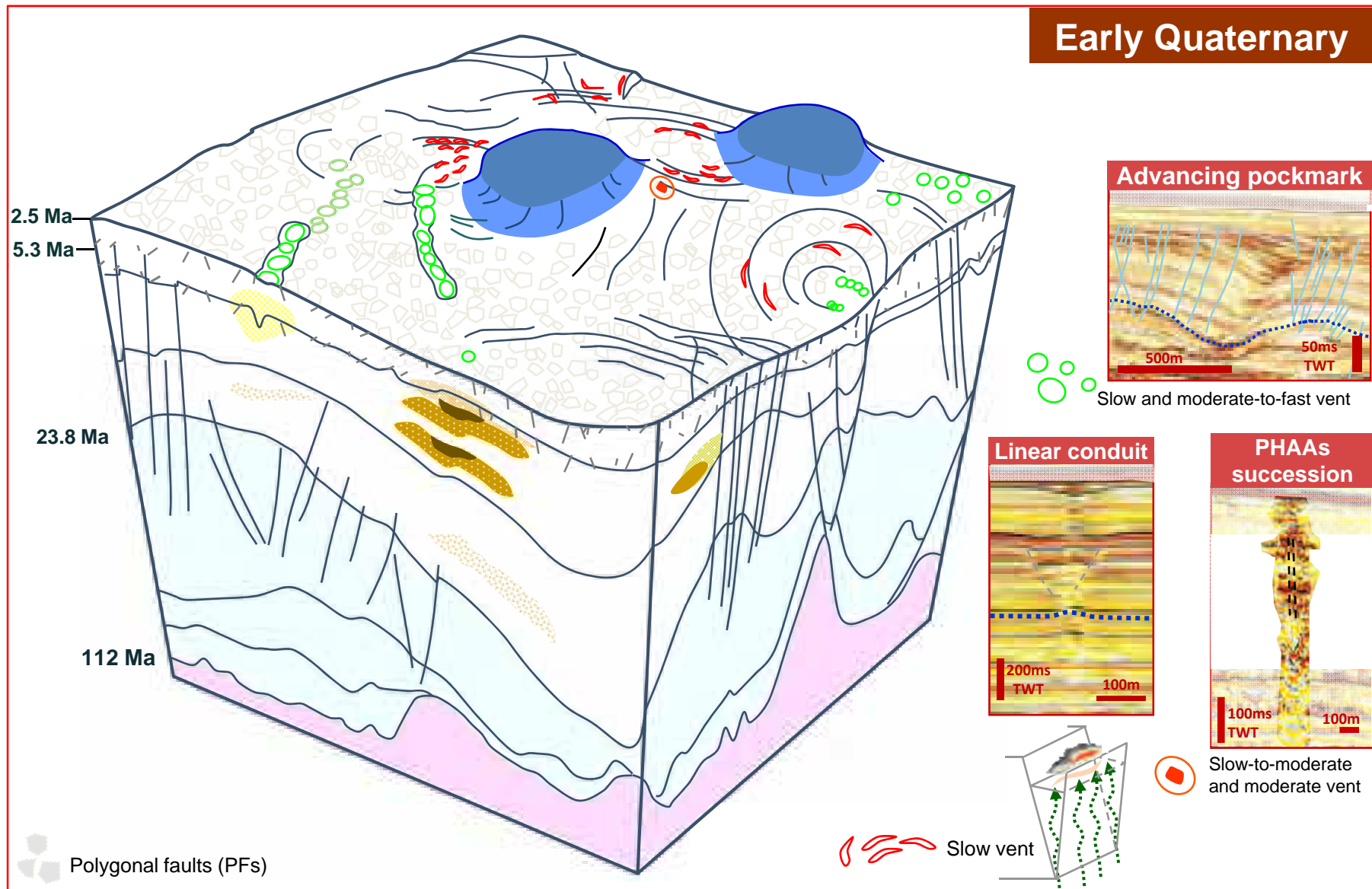


Figure 7.10. Fluid venting structures and venting intensities on the palaeo seafloor during Early Quaternary.

two advancing pockmarks were still active. The upstream part of channel complex 2 was undergoing a slow fluid flow regime as demonstrated by the formation of several linear chimneys emanating from the gas bearing channel levees and terminating upward into linear methane-related carbonates (linear PHAAs).

- e. Few linear chimneys in the upstream location of both channel complexes were also succeeded by elongated depressions on the present day seabed, and which indicated slow to moderate vents (fig. 5.15; fig. 5.18d, Chapter 5).

7.3.8. A regional slow venting event at the transition period from the Late Pliocene to Early Quaternary above synclines 1, 2, 3 and in the footwall domain

- a. At the end of Pliocene/beginning of Quaternary a regional slow venting event occurred principally above the three syncline locations (fig. 6.1, Chapter 6) and above the tectonic faults of the footwall domain. It was the main period in which linear venting structures occurred in the study area (fig. 7.11).
- b. In addition, during these periods, most of the vertically stacked pockmark successions terminated (fig. 6.11) and this is taken to indicate the end of degassing event in footwall domain, particularly where these might be expected at the upper tip locations of deep-cutting tectonic faults.
- c. This regional slow venting event mainly took place above PF tier-2 during Quaternary (fig. 7.11): 1) in the upstream parts of the two pockmarks trails located at Syncline 1 (fig. 5.18a-c, Chapter 5); 2) in Syncline 1 (fig. 6.9i, Chapter 6), 3) in Syncline 2 (fig. 6.5, Chapter 6), 4) in Syncline 3 (fig. 6.4h, Chapter 6), 5) above the orthogonal PF that occurred round the long fault in footwall (fig. 6.12a, Chapter 6).
- d. In the syncline locations, two scenarios are plausible: (1) hydrocarbon-bearing sediments or reservoirs in deeper intervals were likely to be intersected by the extensional faults of synclines, or (2) the balance of lithostatic and pore pressures were destabilized by the vertical movements of synclines at the end of the Miocene/beginning of the Pliocene. Fluids were suggested to migrate along these syncline-related extensional faults (Chapter 6), and it was for this reason that fluid leakage phenomena are thought to occur at the synclinal structures.

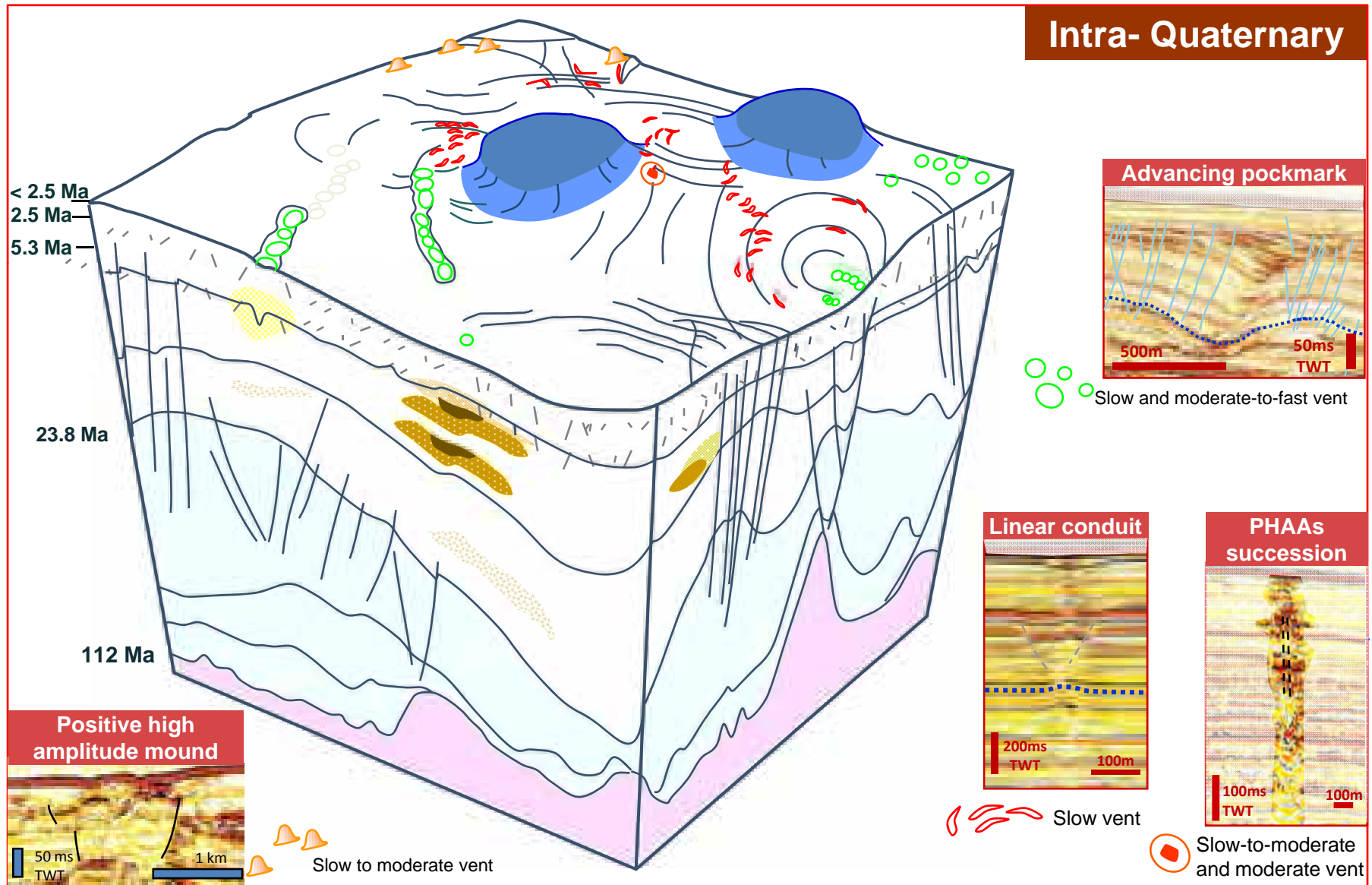


Figure 7.11. Fluid venting structures and venting intensities on the palaeo seafloor in Intra-Quaternary.

- e. In areas affected by local salt movement, either in the form of salt withdrawal basins or rising salt stocks, any polygonal faults or hydraulic fractures will be affected. In particular, polygonal faults or surrounding hydraulic fractures will preferentially propagate in the direction parallel to the intermediate principle stress.
- f. The propagation of hydraulic fractures is influenced by the local stress state which is perturbed around a polygonal fault. Hydraulic fractures probably opened perpendicular to the least principal compressional stress (σ_3) and propagated vertically upwards. Any pre-existing fractures that were slightly oblique to the local stress state during fluid migration may have been reactivated if they were suitably aligned rather than forming new fractures. Both of these scenarios are probable. The mechanism for hydraulic fracturing is valid only if the fluid pressures were not large enough to open the entire pre-existing fault planes (Delaney, 1986). It is considered plausible that the lower part of PFs were critically stressed and that the fault planes were likely more permeable than the surrounding host sediments. Given these conditions and bearing in mind the configuration of the fault-bound trap which is juxtaposed against the adjacent footwall (see Chapter 6), it seems quite possible that fluid migrated upward along the lower part of PFs and accumulated in the lower part of a PF footwall. Hence, the lower part of PF footwall became the loci for fluid pressure build-up, and defines the location for overpressure fluid leakage. It was for these reasons that the majority of vertical chimneys/fractures emanated from the region between the basal tip and lower parts of the PF.

The planforms of these expulsion fractures are thus linear (fig. 6.2, Chapter 6). Methane fluids were likely to migrate along these fractures, and induced linear shallow depressions at the upper fractures tips by slow seepages which eroded/prevented sediment deposition at the palaeo seabed.

Methane-related carbonates were able to precipitate within these linear depressions, under the slow fluid seepage conditions. Thus methane-related carbonates developed the same linear planforms and have directions as the underlying fluid conduits/hydraulic fractures, and aligned with the basal tips of anisotropic PFs and were also parallel to the synclinal margins (fig. 6.5; fig. 6.2j; Chapter 6).

- g. In the footwall dominant the end of Pliocene, slow degassing is interpreted to have occurred along the longer tectonic fault set "X" (see fig. 6.12a-d, Chapter 6). This is indicated by the linear methane-related carbonates (PHAAs) that developed above the

long fault set and above the orthogonally intersecting PFs associated with these faults. These long faults were likely active during the End of Pliocene (fig. 6.12d). These faults reoriented the stress field around it, and thus made the orthogonal PFs perpendicular to them in a manner similar to that demonstrated by Hansen et al. (2004). Given that these faults intersected the deeper hydrocarbon-bearing sediments/reservoirs, it is suggested here that fluids were likely to penetrate fault zones and migrate preferentially upwards along the fault zones (cf. Nunn, 2003; Zhang et al., 2009) and were then redistributed horizontally along the carrier bed below the (orthogonal) PFs interval. Fluid migrated upward through the lower part of PFs into the PFs tier subsequently and formed linear chimneys and linear carbonate (PHAAs) in Quaternary sediments by the same transport mechanism as outlined in the hanging wall (see Chapter 6). However, the reason why these orthogonal PFs occur especially at these tectonic fault locations, in the footwall domain where PFs were absent, still need to be investigated in the future and is not discussed further here.

7.3.9. Slow to moderate seepage during the Quaternary and Holocene above tectonic faults in the footwall domain

- a. During the Quaternary, moderate and intense fluid migrations at only a few active deep faults located in the footwall domain, are evidenced by the occurrence of present day methane-related carbonate mounds (fig. 6.13a, in Chapter 6) and recently pockmarks (fig. 6.12g, in Chapter 6). Their activity in the Holocene can be observed via their association with shallow depressions that occur above them at the present day seabed, and which are taken to indicate a decrease of fluid seepage intensity, from a moderate-fast to a slow-moderate seepage regime (see Chapter 1).
- b. Slow to moderate fluid seepages are especially well indicated by elongate/sub-circular depressions at the present day seabed, in NE area of the studied area (fig. 6.10d, Chapter 6).
- c. In addition, several chimneys of Pliocene-Quaternary age were also active recently during the Holocene, as evidenced by their associated shallow depression at the present day seabed (e.g. fig. 6.17d, e; fig. 6.9h-g, Chapter 6).

7.4. Implications

Implications of each individual type of fluid venting structure have been discussed in detail in Chapter 4, 5 and 6 in particular:

- 1) Usage of vertical successions of venting structures as indicators of variation of fluid seepages intensity over time is emphasised in Chapters 4 and 5
- 2) Geometries and orientation of fluid venting structures are found applicable as indicators of palaeo stress, after an investigation on how the development of venting structures is affected by the stress field in Chapter 6.
- 3) In addition, the previous section has demonstrated how to use fluid venting structure and their vertical succession to reconstruct the variations of leakage intensity at the seabed over time.

It is acknowledged here that the use of fluid venting structures could be broader than presented thus far in the thesis, and their full potential is certainly worthy of further exploration and analysis. In this thesis, the research results presented previously are consistent with concepts developed initially by Roberts (2001) and Roberts et al. (2006) that the vertical evolution of fluid venting structures is dependent on the intensity and frequency of gas flux 'events' which are in turn most probably controlled by pressure fluctuations in a sub seafloor reservoir. Fluctuations themselves are linked to external loading through, for example, sedimentation or changes in stress regime. Pressure cycling in this study area is considered here to be most likely controlled by tectonic activity and potentially sea level fluctuations (see also the views expressed by Andresen and Huus (2011) from a nearby area on the Angolan slope). However, the composition of escaped fluid has not been discussed thus far and neither has the triggering mechanism for leakage events.

In this section two other potential uses of spatial-temporal distribution of fluid venting structures are discussed: 1) as indicators of the origin of the gas component in the migrating fluid i.e. whether it is biogenic or thermogenic; 2) for specifying the triggering of the overpressure 'bleed-off' event and to distinguish whether the event is local or regional. This discussion is based on the examples presented previously in the Chapters 4-6.

7.4.1. Origin of gas: biogenic or thermogenic

Expulsions of methane gas expressed by fluid venting structures are commonly observed on seismic data (Ligtenberg, 2005). However, it is difficult to constrain the provenance of methane gas at seeping locations without chemical analysis and sampling.

The distribution and location of fluid venting structures are generally regarded as proxies that can provide information on the origin of fluid (cf. Ligtenberg, 2003; 2005; Ligtenberg and Connolly, 2003; Heggland, 2005). For example venting structures occur at location of faults, are often associated with salt diapirs, anticlines or deep buried geological features that act as obvious focusing loci for fluid migration, and these can sometimes be used to argue that the migrated fluid is derived and sourced from a deeper interval (Roberts and Carney, 1997; Connolly et al., 2008; Macelloni et al., 2012; Ilg et al., 2012) and hence has a thermogenic origin (i.e. it is derived from below the normal depth and temperature window of active microbes (Shurr and Ridgely, 2002).

Isolated fluid venting structures that are not associated with underlying tectonic structures, are hard to tell if they are formed by fluid of local biogenic gas accumulations or thermogenic gas reservoirs, as they do not give any extra information for fluid migration pathway as these ones that associate with underneath geological structures. Beside these two spatial associative correlations, it is suggested here that the vertical organisation of fluid venting structures is another helpful factor to distinguish the origin of migrating hydrocarbon-bearing fluids.

A good example of this approach is exemplified by the sub-circular PHAAs vertical succession in Chapter 4 (fig. 4.2) which is argued to be a record episodic fluid venting event above a point source. The fact that PHAA stacked up at the same location indicate a quasi continuous gas supply from the Late Miocene to the present day. Such long term gas supply suggests a significant volume of gas in the reservoir, which may not be consistent with the rates of biogenic gas production, unless of course, there is persistent recharge from underlying migration pathways. In addition, this vertical succession local above a tectonic fault which cut across a deeply buried Upper Oligocene and Lower Miocene channel complexes (fig. 3.6; Chapter 3), and the fault is likely to promote fluid migration from deep interval. Therefore, vertical successions of fluid venting structures are likely to point to the thermogenic origin of migrated fluid.

Migrations of thermogenic gas could be well demonstrated by another type of vertical succession of venting structures namely the advancing pockmark arrays that occur above the salt-related extensional faults of Syncline 3 in the southern part of the study area. Several generations of secondary formed pockmarks occurred within these advancing pockmarks arrays throughout late Miocene to present day time, indicated multi-phase and long term fluid migration events.

A similar case is shown by advancing pockmarks which occur above the Miocene channel complexes 1 and 2, are likely connecting with underlying thermogenic gas bearing channels of Eocene-Oligocene age (Total internal report). Gas from deeper channel complex is suggested to migrate upward into shallower Miocene channel complexes (Chapter 5) and induce formations of these pockmark successions. However, biogenic gas may also be generated inside these Miocene channels. A mixture of biogenic and thermogenic gas is thus entirely possible as the gas source for the formation of advancing pockmarks arrays. Thus, it is fair to conclude that using vertical succession of fluid venting structures as an indicator of thermogenic gas should be used with caution unless there is independent geochemical calibration (not available to this study because of confidentiality restrictions).

Another example demonstrates the limitation for the usage of the sequence of vertical venting structures. Such as, an isolated advancing pockmark array with relatively short length has been observed at the surface of a turbidite sheet, which is interpreted to extend laterally from channel complex 1 without connecting vertically with other channels. This isolated advancing pockmark is overlain by several PHAAs that stacked-up vertically below its base (e.g. fig. 4.5, Chapter 4). This advancing pockmark's longevity is reflected by its length and is relative short in compare to those that occur above channel complexes 1 and 2. The relative short duration of fluid expulsion may imply an insufficient gas supply after the formation of the primary crater. This may be due to the slow production of local biogenic gas, or either the fluid pressure of deep migrated thermogenic gas reaches the equilibrium with overburden sediments at the seeping location. The uncertainty on the nature of gas is large in such cases, and the associated geological context needs to be taken into consideration. Geochemical data is recommended in this situation as the key constraint.

Exceptions for these general rules are possible, particularly since this study is based on a single area of one passive margin basin, isolated fluid venting structures do not necessarily originate from biogenesis. For example, most single linear PHAAs that occur in Quaternary sediment and that are associated with linear chimneys in Pliocene sediments, are not

associated with tectonic deep faults. However, their geographical distribution is restricted by deeply rooting extensional faults which define the edge of synclines in three different locations, as well the limit to their occurrences within Quaternary sediment above these synclines. The same spatial-temporal distribution of individual linear PHAA in three different locations is perhaps better explained by a thermogenic source and flux.

In conclusion, when looking at the distribution of fluid venting structures and the geological context in this study area (with its significant number of deeper oil accumulations); it is observed that most of the fluid venting structures are associated with tectonic structures and faults. So the origin of migrated fluid is most likely dominated by thermogenesis. Finally, further study is requested to validate the usage of vertical venting succession as an indicator for the origin of the gas.

7.4.2. Triggering cause of local or regional fluid venting events

The 4D distributions and evolution of fluid venting structures are likely giving indications for the triggering cause of fluid seepages, such as regional overpressures events, tectonic activities or sea level variation.

I test the method for differentiating the regional overpressure events and local degassing in the absence of any well data; by simply using the spatial-temporal distribution of fluid venting structures. This methodology may thus have some merit in future for petroleum exploration in frontier areas, similar to that espoused by Calves et al (2009). In this section, demonstration with examples presented in the core Chapters is provided, and limitation of this method is discussed when encountered.

I start to use a simple case for demonstrating how to identify a local overpressure event, by looking at the complex linear venting system that evolved into honeycomb pockmarks in location of Syncline 0. The occurrence of this system correspond a local venting episode lasting from 12Ma up to 6.1H . Fluid leakage in this complex system is interpreted to be triggered by erosional unloading of slide blocks (Chapter 6), since there was no any other visible venting event during the same time interval in the study area. So fluid seepages at this location are suggested to be an individual venting event, and there is no any other external global parameter being involved (such as tectonic activity or sea level variation).

This contrasts with the vertically stacked pockmarks that are widespread in the NE region of the footwall domain (Chapter 6) which is extensively deformed by tectonic faults. Regional degassing events are likely triggered by fault activity and are registered by these eruptional pockmarks which are vertically stacked-up.

It is suggested to be the same case for shallow elongate depressions and polyphased pockmarks, which occur in the uppermost Miocene 5.5 H to 5.3Ma above the edges of Syncline 2 and above Anticline 1 and 2. The extensional faults of the last three structures were all active during the same period (Chapter 3). Thus, the fluid venting events are suggested to be prompted by the tectonic activity.

Local degassing events without the intervention of tectonic activity can be distinguished by targeting isolated or clustered fluid venting structures in non faulted areas. Good examples are furnished by considering the advancing pockmarks and nested pockmarks, which align above the two channel complexes through the whole of the Pliocene (Chapter 5). Conversely, these palaeo channels are not the only location where this type of individual pockmarks occurs. They are also found above Syncline 3 and occur individually around the flank of Diapir 2 (on slope locations; Chapter 5) in the same time interval. This may imply that the degassing event is not completely local nor is it entirely free of tectonic influences. But the timing of fluid seepages in Syncline 3 location through whole Pliocene corresponds to the timing of the syncline formation. So the activities of syncline related faults are likely linked to the fluid migration, at least in temporal terms.

The precise cause of triggering for fluid seepage cannot be precisely linked to an origin in tectonic activity or to local overpressure build-up. The limitation of using spatial-temporal distribution of fluid venting structures to estimate the cause of leakages is exemplified in this case. Nevertheless, when looking at the triggering time of these pockmarks, 5.3 Ma, it is notable that this age corresponds a global sea level fall. This may explain the possible pressure variations at the contemporary seabed and which induced fluid leakages at certain locations. Further data is required as to local relative sea level excursions in this case for further investigation on this hypothesis.

In addition, regional overpressure event can be confirmed with confidence when fluid venting structures occur within a same stratigraphic interval across a large area in different geological settings. Moss et al. (2010a, b) used this approach when seeking to analyse the formation of fluid expulsion pipes in Namibia. In the Angolan margin study area, the examples of linear PHAAs of Quaternary age which occur both in hanging and footwall

domains across the surveys (Chapter 6) are also informative. The linear PHAAs were all found in Quaternary sediment above the three synclines, between radial faults, and above tectonic faults. Thus the fluid migration at these locations during the Quaternary is most likely to have been facilitated somehow by tectonic faults. However, even though these linear PHAAs occurred above these tectonic structures, most of tectonic structures in the hanging wall domain were inactive from the Quaternary till the present day. Exceptions to this are the tectonic faults sets in the footwall domain, which are still active at present. Therefore, tectonic activity may not be totally the cause of fluid seepage triggering. Given that the Quaternary is characterised by a high frequency of sea level fluctuation, this may be an extra cause to promote fluid leakages in locations where fluid pressure is relative high, and has primed the system for failure.

Examples above demonstrate that, by using the close relationship between spatial-temporal distribution of fluid venting structures and basin evolution, it is possible to track qualitatively the origin of fluid seepage. Nevertheless, this approach is still in its infancy, and further research is required to validate this approach.

7.5. Research limitations

The limitations of the research in this thesis are summarised as follows;

- A data base of in situ measurement of fluid flow from cold seeps would be helpful for validating the assumptions on the signification of fluid venting structures in the fluid flow science. It would be beneficial for a better understanding the relationship between fluid flux intensity and the geological response on the seabed and in the sub surface.
- Ground truthing and core data in the near-seabed sediments would be beneficial for providing detailed compositions of PHAAs. This is essential for confirming the association of methane-related carbonate with hydrate gas within GHSZ, as well for verifying the presence of free gas or oil, and for providing the relative percentage of chemosynthetic communities and MDAC. Ground truthing would also help for

determining the cause of intensity variations of PHAAs and for identifying the cause of seismic pull up and push down.

- Chemical analysis on core sample of fluid venting structures would have benefited from analysing the origin of hydrocarbon phases (thermogenic or biogenetic). Dating on core samples of PHAAs would allow age control on fluid venting events at the palaeo seabed and the duration of venting.
- Well data would have benefited to age calibration in seismic and calculation of sedimentation rates. Porosity and density measurement would provide information on physical characteristics of MTCs and hemipelagic unit. It would give more of an insight into the modes of hydraulic fracture propagation within these units. Pore pressure measurements within polygonal fault tiers, hemipelagic units and MTCs would help for determining the fluid flow behaviour and allow better understanding on the process of hydraulically fracturing in different lithologies. The occurrence of regional seal (Intra-Plio) within polygonal fault tier would be able to confirm by the distribution of pressure in rocks around faults. Ideally, measurement of bottom current velocity and bore hole drilling through advancing pockmarks and nesting pockmarks, would help to confirm the model of water flow on the seabed and provide lithological information for validating the pockmark formational model as proposed in Chapter 5.
- A high resolution seismic survey would be helpful for better illustrating the internal structures of pockmarks and PHAAs, and increase the accuracies of geometrical measurements. It would especially useful for determining the height of gas chimneys, and could have been used to better constrain the contact position between gas chimneys and polygonal faults.

7.6. Future work

Suggested future work is recommended basing on the validity of some hypothesis made in this research. The proposals are in following;

7.6.1. Classification of fluid venting structures with ground truthed flux

Classification of Roberts (2001) and Roberts et al. (2006) as well the model presented in Chapter 4 need to be completed with quantitative ground truth data. For this classification, a data base with the physical measurements of fluid venting dynamic for different type of venting structures need to be established. A study on testing the methodology of using vertical fluid venting structures to identify fluid flux rate in a real case is suggested. This will be consisted an application in an exploration area where venting structures are already present and active, by monitoring the rate of methane ebullitions (as the operation of methane bubble detection at pockmarks or seeps by Torres et al., 2002; Naudts et al., 2010; Schneider vo Deimling et al., 2010; Salmi et al., 2011), by comparing the resulted geological responses and collected data then predict the future type of fluid eruption structures. Establishing a quantitative classification basing on comparison of measured modern flux rate and geometries of venting structures should be the next step of this research.

Investigation on variation of PHAAs intensity by comparing amplitude variations with petrographic proprieties and percentage of calcite contains in cutting samples has not been carried out. Thickness of PHAAs (methane-relate carbonate) on seismic versus dynamics of fluid flux and the duration of methane seepages at palaeo seabed would helpful for revealing the thickness variation of PHAAs. Dating along different vertical points of MDAC sample will be necessary to determine the duration of methane seepages, and thus thickness of MDAC could be used for estimation of longevities of seepages at (palaeo) seabed.

Using vertical successions of fluid venting structures to predict short term fluid flux variation, through analysing fossil seepages and permanent ROV observations on modern seep, could be a preliminary pressure prediction tool in explorations. Testing on the proposed utility of fluid venting structure successions is suggested in a future study.

7.6.2. Analogue modelling on hydraulic fracturing in different sedimentary prosperities

Analogue modelling for simulating the permeability of PF, stress regime of normal faults and flow migration would help to support hypothesis on nucleation of gas chimneys in

extensional fault systems (as the fluid pipe that modelled by Gay et al., 2012). For example, occurrence of gas chimneys in the lower part of PFs is interpreted as fluid pressure built up in fault bound trap of PF footwall, and overpressure fluids created hydraulic fractures in the overlying hanging wall as a hypothesis provided in Chapter 6. This hypothesis is supported by different theories found in literature, but cannot be confirmed by any physical evidence here. Analogue modelling is required and can provide further information on the formation and behaviour of hydraulic fracture in a PF tier.

Moreover, hydraulic fractures propagation changed from linear fracturing style in hemipelagic to branching fracturing model in MTCs, as hypothesis proposed in Chapter 6. This hypothesis is established only basing on separated analogue models on hydraulic fracturing in different types of soft sediment in literatures (e.g. Howarth, 1987; Philippe, 1988; Arch et al., 1988; Hori et al. 2002; Olson et al., 2002; Van de Steen et al., 2002; Dawn 2004; Boudreau et al., 2005; Barry et al., 2010; Algar et al., 2011), but has not been confirmed by a united physical experience. Thus, laboratory analogue modelling could give more of an insight into the hydraulic fracture behaviour when crossing through different lithology.

7.6.3. Numerical record of analogue model compare to seismic modelling

Numerical records issue from analogue modelling on hydraulic fracturing can be compared with seismic modelling results. The experience will help for better interpretation of acoustic chimneys on seismic data, and enhance the comprehension of the genetic mechanisms of gas chimneys.

On the other hand, seismic modelling on MDAC needs to be carried on even the first step of 1D seismic modelling has been done on outcropped MDAC. 1D seismic modelling is benefited for having a clear vision on variations of amplitude intensities that are affected by the vertical thickness of MDAC. 3D seismic modelling on geometries of methane-related carbonates could help to obtain better understand the vertical and spatial organisations of the carbonates on seismic, which cannot be illustrated by seismic reflections because of the limit of vertical seismic resolutions.

CHAPTER 8

CONCLUSION

8.0. Conclusions

The aim of this chapter is to summarize the main results and conclusions drawn throughout this thesis research. The aims and objectives listed in the Introduction (Chapter 1) were tackled sequentially and progressively through each of the core chapters (Chapters 4-6). The main conclusions of these core chapters are listed below.

To the author's knowledge, this research presents the first extended piece of work focusing on the interaction between fluid venting intensity and basin evolution. The core themes of this research have important implications for the wider topic of interaction between fluid flow and geological response.

8.1. Chapter 4 conclusion

In Chapter 4, PHAAs were interpreted as methane-related carbonates based on their seismic character and geometry. This was confirmed later by well log samples and data.

- a. The fluid origin of PHAAs was determined by their association with flat-bottomed shallow depressions, gas chimneys and pockmarks.
- b. PHAAs, i.e. methane-related carbonates, can be used to locate fluid seepage sites and the timing and duration of seepage at these sites.
- c. Methane-related carbonates formed at the palaeo seabed or in shallow sediments down to few meters below the seabed. The seismic horizons on which PHAAs occur thus define the time of fluid seepage at the palaeo seabed.
- d. The morphology of PHAAs is strongly controlled by the intensity of fluid venting.
- e. PHAAs have been classified into two main types; circular and linear.
- f. Circular-shaped PHAAs formed by moderate fluid expulsion and have shallow, flat-bottomed depressions.
- g. Linear-shaped PHAAs formed by slow fluid expulsion and have linear-shaped depressions.
- h. Fluid venting systems comprise stacked PHAAs and combinations of various other venting structures. They contain a record of fluid venting and changes in fluid flux rate.

- i. They can also be used to recover the frequency and style of paleo venting events.
- j. A new type of gas chimney with linear plan form was discovered in the polygonally strata of the study area.
- k. Linear chimneys emanate from the lower part of the PFs and are aligned parallel to first-order PFs.
- l. Linear chimneys formed along hydraulic fractures occurring due to overpressure build-up.
- m. Because linear chimneys and their subsequent linear PHAAs are parallel to PF trends, it suggested that the propagation direction of hydraulic fractures were heavily influenced by the stress state around polygonal faults.
- n. A new type of pockmark “polyphased pockmarks” was documented in Chapter 4. They contain conical-collapse structures which are associated with different types of stacked PHAAs which formed by multiple episodes of fluid venting and various flux rates.

8.2. Chapter 5 conclusion

In Chapter 5, two new types of pockmarks “nested pockmark” and “advancing pockmark arrays” were classified.

- a. Nested pockmarks formed by different generations of sedimentary infill which are organised as vertically-stacked, conically-folded layers where each one is encased within the layer underlying it. The conically-folded and stacked infill layers reflect the reduction in accommodation space in the pockmark crater at each stage of deposition.
- b. Advancing pockmark arrays are composed of a series of downslope-migrating, reactivation craters with progradational infill. Each crater sits above the rupture surface at the downstream sidewall of the underlying and previously deposited infill sequence.
- c. This interrupted surface acted as fluid migration pathway and controlled the future location of reactivation crater for progradating new infill sequences.
- d. The main different between the two types of pockmarks is, nested pockmark is formed by only one episode of fluid expulsion, but advancing pockmark arrays formed by multiple generations of eruptional craters.

- e. Both types of pockmarks formed on inclined topography.
- f. They have infill sequences which migrated laterally and downslope.
- g. The infill sequence migrated laterally due to the local perturbation of down-slope flowing bottom currents by the pockmark craters and vortex erosion.
- h. The geometric evolution of pockmarks was controlled by the interaction between fluid venting, sedimentation, regional topography and bottom currents.
- i. Nested and advancing pockmarks form two pockmark trails above a gas-bearing channel complex and probably occur there due to degassing along these channels.
- j. The alignment and distribution of individual pockmarks were controlled by the morphology of underlying channels and locations of gas accumulations along the channels.

8.3. Chapter 6 conclusion

In Chapter 6, the mechanism of formation were proposed for linear chimneys and newly discovered “honeycomb pockmarks”.

- a. Linear chimneys formed primarily in fine-grained unconsolidated sediments.
- b. The majority of linear chimneys resulted from build-up of fluid overpressure close to the basal tip of PFs or along the lower part of PF planes, which caused hydraulic fracturing.
- c. The location of linear chimneys is controlled also by the distribution of fluid accumulation within PF tier.
- d. Hydraulic fractures formed in PF blocks because the fluid pressure was not strong enough to open the entire PF plane.
- e. Tectonic structures perturbed the regional stress state which controlled the propagation direction of PFs.
- f. Local stress anisotropy around PFs caused hydraulic fractures to propagate parallel to strikes of first order PFs and tectonic structures. This resulted in the linear geometry of hydraulic fractures.
- g. The geometry of fluid venting structures is controlled by two competing factors; the magnitude of stresses around local structures and fluid flux intensity.

- h. If the magnitude of stress and horizontal stress anisotropy was greater than the fluid pressure then fluid-related depressions would develop parallel to the intermediate principal stress.
- i. In an environment free of tectonic stresses the fluid flux rate was the dominant parameter determining the geometry of venting structures.
- j. The geometries of fluid venting structure can thus give some indication of the conditions of the palaeo stress state.
- k. Conical pockmarks locally perturbed the regional stress state.
- l. Honeycomb pockmark formed because hexagonal PF cells cut through their outer edge.
- m. Honey-comb pockmark craters were too shallow to perturb the regional stress state.
- n. Circular craters that have sidewall dip $> 4.6^\circ$ and depths > 12 ms TWT perturbed the local stress field enough to affect the propagation direction of PF propagation. PF's are concentrically arranged around pockmark craters.
- o. Different properties of sediment induced different styles of fluid migration and thus the formation of different types of fluid venting structures.

REFERENCES

- Abelson, A., & Denny, M., 1997. Settlement of marine organisms in flow. *Annual Review of Ecology and Systematics* **28**, 317-339.
- Agirrezabala, L. M., 2009. Mid-Cretaceous hydrothermal vents and authigenic carbonates in a transform margin, Basque-Cantabrian Basin (western Pyrenees): a multidisciplinary study. *Sedimentology* **56**, 969-996.
- Agirrezabala, L. M., Kiel, S., Blumenberg, M., Schäfer, N., and Reitner, J., 2013. Outcrop analogues of pockmarks and associated methane-seep carbonates: A case study from the Lower Cretaceous (Albian) of the Basque-Cantabrian Basin, western Pyrenees. *Palaeogeography, Palaeoclimatology, Palaeoecology* **390**, 94-115.
- Aiello, I., 2005. Fossil seep structures of the Monterey Bay region and tectonic/structural controls on fluid flow in an active transform margin. *Palaeogeography, Palaeoclimatology, Palaeoecology* **227**, 124-142.
- Aiello, I. W., Garrison, R. E., Moore, J. C., Kastner, M., and Stakes, D. S., 2001. Anatomy and origin of carbonate structures in a Miocene cold-seep field. *Geology* **29**, 1111-1114.
- Algar, C. and Boudreau, B., 2009. Transient growth of an isolated bubble in muddy, fine-grained sediments. *Geochimica et Cosmochimica Acta* **73**, 2581-2591.
- Algar, C. K., Boudreau, B. P., and Barry, M. A., 2011. Initial rise of bubbles in cohesive sediments by a process of viscoelastic fracture. *Journal of Geophysical Research: Solid Earth (1978–2012)* **116**.
- Allen, J., 1970. A Quantitative Model Of Climbing Ripples And Their Cross-Laminated Deposits. *Sedimentology* **14**, 5-26.
- Aminzadeh, F., Connolly, D., Hegglund, R., Meldahl, P., and de Groot, P., 2002. Geohazard detection and other applications of chimney cubes. *The Leading Edge* **21**, 681-685.
- Anderson, J., Cartwright, J., Drysdall, S., and Vivian, N., 2000. Controls on turbidite sand deposition during gravity-driven extension of a passive margin: examples from Miocene sediments in Block 4, Angola. *Marine and Petroleum Geology* **17**, 1165-1203.
- Andresen, K. J., Huuse, M., and Clausen, O., 2008. Morphology and distribution of Oligocene and Miocene pockmarks in the Danish North Sea—implications for bottom current activity and fluid migration. *Basin Research* **20**, 445-466.
- Andresen, K. J. and Huuse, M., 2011. ‘Bulls-eye’ pockmarks and polygonal faulting in the Lower Congo Basin: Relative timing and implications for fluid expulsion during shallow burial. *Marine Geology* **279**, 111-127.
- Andresen, K.J., Huuse, M., Schodt, N.H., Clausen, L. F. and Seidler, L., 2011. Hydrocarbon plumbing systems of salt minibasins offshore Angola revealed by three-dimensional seismic analysis. *AAPG Bulletin* **95**, 1039–65.
- Andresen, K. J., 2012. Fluid flow features in hydrocarbon plumbing systems: What do they tell us about the basin evolution? *Marine Geology* **332**, 89-108.
- Anka, Z. and Séranne, M., 2004. Reconnaissance study of the ancient Zaire (Congo) deep-sea fan. (ZaiAngo Project). *Marine Geology* **209**, 223-244.
- Anka, Z., Seranne, M., Lopez, M., Scheck-Wenderoth, M., and Savoye, B., 2009. The long-term evolution of the Congo deep-sea fan: a basin-wide view of the interaction between a giant submarine fan and a mature passive margin (ZaiAngo project). *Tectonophysics* **470**, 42-56.

References

- Anstey, N. A. 1970. Signal characteristics and instrument specifications. In *Seismic Prospecting Instruments*, vol. I. *Berlin: Gebruder Borntraeger*.
- Arch, J., Maltman, A., and Knipe, R., 1988. Shear-zone geometries in experimentally deformed clays: the influence of water content, strain rate and primary fabric. *Journal of Structural Geology* **10**, 91-99.
- Arntsen, B., Wensaas, L., Løseth, H., & Hermanrud, C., 2007. Seismic modeling of gas chimneys. *Geophysics* **72**, SM251-SM259.
- Ashley, G. M., Southard, J. B., and Boothroyd, J. C., 1982. Deposition of climbing-ripple beds: a flume simulation. *Sedimentology* **29**, 67-79.
- Ashton, C. P., Bacon, B., Mann, A., Moldoveanu, N., Déplanté, C., Aquitaine, E., Sinclair, T., Redekop, G., and AS, M. O. Q., 1994. 3D seismic survey design. *Oilfield Review* **6**, 19-32.

– B

- Bacon, M., Simm, R., Redshaw, T., 2003. *Three-D Seismic Interpretation*. *Cambridge University Press*.
- Bajorich, M. and Farmer, S., 1995. 3-D seismic discontinuity for faults and stratigraphic features: The coherence cube. *The Leading Edge* **14**, 1053-1058.
- Barbieri, R., & Cavalazzi, B., 2005. Microbial fabrics from Neogene cold seep carbonates, Northern Apennine, Italy. *Palaeogeography, Palaeoclimatology, Palaeoecology* **227**, 143-155.
- Barnes, A. E., 1998. The complex seismic trace made simple. *The Leading Edge* **17**, 473-473.
- Barnett, J. A., Mortimer, J., Rippon, J. H., Walsh, J. J., and Watterson, J., 1987. Displacement geometry in the volume containing a single normal fault. *AAPG Bulletin* **71**, 925-937.
- Barry, M., Boudreau, B., Johnson, B., and Reed, A., 2010. First-order description of the mechanical fracture behavior of fine-grained surficial marine sediments during gas bubble growth. *Journal of Geophysical Research: Earth Surface (2003–2012)* **115**.
- Barry, M. A., Boudreau, B. P., and Johnson, B. D., 2012. Gas domes in soft cohesive sediments. *Geology* **40**, 379-382.
- Bayon, G., Pierre, C., Etoubleau, J., Voisset, M., Cauquil, E., Marsset, T., Sultan, N., Le Drezen, E., and Fouquet, Y., 2007. Sr/Ca and Mg/Ca ratios in Niger Delta sediments: Implications for authigenic carbonate genesis in cold seep environments. *Marine Geology* **241**, 93-109.
- Beck, A. E., 1981. *Physical principles of exploration methods: an introductory text for geology and geophysics students*. *John Wiley & Sons, Incorporated*.
- Berger, W. H., Lange, C. B., and Wefer, G., 2002. Upwelling history of the Benguela-Namibia system: A synthesis of Leg 175 results. *Proc. Ocean Drill. Program Sci. Results*.
- Berggren, W.A., Kent, D.V., Swisher, C.C., III, and Aubry, M.-P., 1995. A revised Cenozoic geochronology and chronostratigraphy. In Berggren, W.A., Kent, D.V., Aubry, M.-P., and Hardenbol, J. (Eds.), *Geochronology, Time Scales and Global Stratigraphic Correlation*. Special Publication 0151, *Society of Economy Paleontology and Mineral (Society of Sedimentology and Geology)* **54**, 129-212.
- Berndt, C., Bünz, S., & Mienert, J. 2003. Polygonal fault systems on the mid-Norwegian margin: a long-term source for fluid flow. *Geological Society, London, Special Publications* **216**, 283-290.

References

- Berndt, C., 2005. Focused fluid flow in passive continental margins. *Philosophical Transactions of the Royal Society A: Mathematical, Physical and Engineering Sciences* **363**, 2855-2871.
- Blouet, J., Imbert, P., Ho, S., 2012. Morphology Variations Of Methanogenic Carbonates In Relation Ship With Their Genesis Mechanisms, Vocontian Basin, France: A Multidisciplinary Study. Abstract. In *proceeding of: 11th Conference of Gas in Marine Sediments*, 21-22.
- Bøe, R., Rise, L., and Ottesen, D., 1998. Elongate depressions on the southern slope of the Norwegian Trench (Skagerrak): morphology and evolution. *Marine Geology* **146**, 191-203.
- Boehm, A. and Moore, J., 2002. Fluidized sandstone intrusions as an indicator of paleostress orientation, Santa Cruz, California. *Geofluids* **2**, 147-161.
- Boersma, A., 1984. Pliocene planktonic and benthic foraminifers from the southeastern Atlantic Angola margin-leg 75, site 532, deep-sea drilling project. *Initial reports of the deep sea drilling project*, **75**, 657-669.
- Bohlooli, B. and De Pater, C., 2006. Experimental study on hydraulic fracturing of soft rocks: influence of fluid rheology and confining stress. *Journal of Petroleum Science and Engineering* **53**, 1-12.
- Boudreau, B. P., Algar, C., Johnson, B. D., Croudace, I., Reed, A., Furukawa, Y., Dorgan, K. M., Jumars, P. A., Grader, A. S., and Gardiner, B. S., 2005. Bubble growth and rise in soft sediments. *Geology* **33**, 517-520.
- Boudreau, B. P., 2012. The physics of bubbles in surficial, soft, cohesive sediments. *Marine and Petroleum Geology* **38**, 1-18.
- Borowski, W. S., Paull, C. K., and Ussler, W., 1996. Marine pore-water sulfate profiles indicate in situ methane flux from underlying gas hydrate. *Geology* **24**, 655-658.
- Bouriak, S., Vanneste, M., and Saoutkine, A., 2000. Inferred gas hydrates and clay diapirs near the Storegga Slide on the southern edge of the Vøring Plateau, offshore Norway. *Marine Geology* **163**, 125-148.
- Bourne, S. J. and Willemsse, E. J., 2001. Elastic stress control on the pattern of tensile fracturing around a small fault network at Nash Point, UK. *Journal of Structural Geology* **23**, 1753-1770.
- Bres, G. A., & Colonius, T., 2007. Direct numerical simulations of three-dimensional cavity flows. *AIAA Paper* **3405**.
- Brothers, L. L., Kelley, J. T., Belknap, D. F., Barnhardt, W. A., Andrews, B. D., & Maynard, M. L., 2011. More than a century of bathymetric observations and present-day shallow sediment characterization in Belfast Bay, Maine, USA: implications for pockmark field longevity. *Geo-Marine Letters* **31**, 237-248.
- Broucke, O., Temple, F., Rouby, D., Robin, C., Calassou, S., Nalpas, T., & Guillocheau, F., 2004. The role of deformation processes on the geometry of mud-dominated turbiditic systems, Oligocene and Lower–Middle Miocene of the Lower Congo basin (West African Margin). *Marine and Petroleum Geology* **21**, 327-348.
- Brown, A. R., 1999. Interpretation of three-dimensional seismic data. *AAPG and SEG*.
- Bruno, M. S., & Nakagawa, F. M., 1991. Pore pressure influence on tensile fracture propagation in sedimentary rock. In *International Journal Of Rock Mechanics And Mining Sciences & Geomechanics Abstracts* **28**, 261-273. Pergamon.
- Bünz, S., Mienert, J., & Berndt, C. , 2003. Geological controls on the Storegga gas-hydrate system of the mid-Norwegian continental margin. *Earth and Planetary Science Letters* **209**, 291-307.

- Bussmann, I., & Suess, E., 1998. Groundwater seepage in Eckernförde Bay (Western Baltic Sea): Effect on methane and salinity distribution of the water column. *Continental Shelf Research* **18**, 1795-1806.

– C

- Camacho, R. G. R., & Barbosa, J. R., 2005. The boundary element method applied to incompressible viscous fluid flow. *Journal of the Brazilian Society of Mechanical Sciences and Engineering* **27**, 456-462.
- Campbell, K. A., & Bottjer, D. J., 1993. Fossil cold seeps. *Research & Exploration* **9**, 326-343.
- Calvès, G., Huuse, M., Schwab, A., and Clift, P., 2008. Three-dimensional seismic analysis of high-amplitude anomalies in the shallow subsurface of the Northern Indus Fan: Sedimentary and/or fluid origin. *Journal of Geophysical Research: Solid Earth (1978–2012)* **113**.
- Carruthers, T., D., 2013. Interaction Of Polygonal Fulat Systems With Salt Diapirs. Phd Thesis. *Cardiff University*.
- Carruthers, D., Cartwright, J., Jackson, M., & Schutjens, P., 2013. Origin and timing of layer-bound radial faulting around North Sea salt stocks: New insights into the evolving stress state around rising diapirs. *Marine and Petroleum Geology* **48**, 130-148.
- Cartwright, J. A., & Dewhurst, D. N., 1998. Layer-bound compaction faults in fine-grained sediments. *Geological Society of America Bulletin* **110**, 1242-1257.
- Cartwright, J., Huuse, M., 2006. Case study A: Seismic facies analysis of ‘waste zone’ and ‘regional seals’. Internal research publication, *Total S.A. France*.
- Cartwright, J., Huuse, M., & Aplin, A., 2007. Seal bypass systems. *AAPG bulletin* **91**, 1141-1166.
- Cartwright, J. A., 2009. Palaeostress reconstruction using polygonal faults. In *AGU Fall Meeting Abstracts*, 01.
- Cartwright, J., 2011. Diagenetically induced shear failure of fine-grained sediments and the development of polygonal fault systems. *Marine and Petroleum Geology* **28**, 1593-1610.
- Cathles, L., Su, Z., and Chen, D., 2010. The physics of gas chimney and pockmark formation, with implications for assessment of seafloor hazards and gas sequestration. *Marine and Petroleum Geology* **27**, 82-91.
- Cattaneo, A., Correggiari, A., Marsset, T., Thomas, Y., Marsset, B., and Trincardi, F., 2004. Seafloor undulation pattern on the Adriatic shelf and comparison to deep-water sediment waves. *Marine Geology* **213**, 121-148.
- Cauquil, E. and Adamy, J., 2008. Seabed imagery and chemosynthetic communities: examples from deep offshore West Africa. *Offshore Technology Conference*, OTC-19352.
- Cauquil, E., Stephane, L., George, R., and Shyu, J.-P., 2003. High-resolution autonomous underwater vehicle (AUV) geophysical survey of a large, deep water pockmark offshore Nigeria. *65th EAGE Conference & Exhibition*, 56-59.
- Chadwick, R., Arts, R., Bentham, M., Eiken, O., Holloway, S., Kirby, G., Pearce, J., Williamson, J., and Zweigel, P., 2009. Review of monitoring issues and technologies associated with the long-term underground storage of carbon dioxide. *Geological Society, London, Special Publications* **313**, 257-275.

References

- Chand, S., Rise, L., Ottesen, D., Dolan, M., Bellec, V., and Bøe, R., 2009. Pockmark-like depressions near the Goliat hydrocarbon field, Barents Sea: morphology and genesis. *Marine and Petroleum Geology* **26**, 1035-1042.
- Charlou, J., Donval, J., Fouquet, Y., Ondreas, H., Knoery, J., Cochonat, P., Levaché, D., Poirier, Y., Jean-Baptiste, P., and Fourré, E., 2004. Physical and chemical characterization of gas hydrates and associated methane plumes in the Congo–Angola Basin. *Chemical Geology* **205**, 405-425.
- Chopra, S. and Marfurt, K. J., 2007. Volumetric curvature attributes add value to 3D seismic data interpretation. *The Leading Edge* **26**, 856-867.
- Çifçi, G., Dondurur, D., and Ergün, M., 2003. Deep and shallow structures of large pockmarks in the Turkish shelf, Eastern Black Sea. *Geo-Marine Letters* **23**, 311-322.
- Clari, P., Cavagna, S., Martire, L., and Hunziker, J., 2004. A Miocene mud volcano and its plumbing system: a chaotic complex revisited (Monferrato, NW Italy). *Journal of Sedimentary Research* **74**, 662-676.
- Coffeen, J. A., 1986. Seismic exploration fundamentals. *Pennwell Books*.
- Connolly, D. L., & Aminzadeh, F., 2003. Geo-hazard detection with chimney cubes. *Offshore Technology Conference*, OTC-15114.
- Connolly, D. L., Brouwer, F., and Walraven, D., 2008. Detecting fault-related hydrocarbon migration pathways in seismic data: implications for fault-seal, pressure, and charge prediction. *Gulf Coast Association of Geological Societies Transactions* **58**, 191-203.
- Cosgrove, J., 1995. The expression of hydraulic fracturing in rocks and sediments. *Special Publication-Geological Society Of London* **92**, 187-187.
- Cosgrove, J., 1997. Hydraulic fractures and their implications regarding the state of stress in a sedimentary sequence during burial. *Evolution of Geological Structures in Micro-to Macro-scales*, 11-25.
- Coterill, K., Tari, G., Valasek, D., and Van Dyke, S., 2005. 3D Gulf of Guinea seismic images offer useful comparisons with offshore Morocco. *World oil* **226**, 43.
- Cramez, C. and Jackson, M., 2000. Superposed deformation straddling the continental-oceanic transition in deep-water Angola. *Marine and Petroleum Geology* **17**, 1095-1109.

– D

- Davies, R. and Cartwright, J., 2002. A fossilized Opal A to Opal C/T transformation on the northeast Atlantic margin: support for a significantly elevated Palaeogeothermal gradient during the Neogene? *Basin Research* **14**, 467-486.
- Davies, R. J., 2003. Kilometer-scale fluidization structures formed during early burial of a deep-water slope channel on the Niger Delta. *Geology* **31**, 949-952.
- Davies, R. J., Mathias, S. A., Moss, J., Hustoft, S., and Newport, L., 2012. Hydraulic fractures: How far can they go? *Marine and Petroleum Geology* **37**, 1-6.
- Davison, I., Alsop, I., Birch, P., Elders, C., Evans, N., Nicholson, H., Rorison, P., Wade, D., Woodward, J., and Young, M., 2000. Geometry and late-stage structural evolution of Central Graben salt diapirs, North Sea. *Marine and Petroleum Geology* **17**, 499-522.
- Dawe, R. A., 2004. Miscible Displacement In Heterogeneous Porous Media. Invited Session Leturer. *The Sixth Caribbean Congress Of Fluid Dynamics, Uwi*, 1-12.
- De Boever, E., Swennen, R., and Dimitrov, L., 2006. Lower Eocene carbonate cemented chimneys (Varna, NE Bulgaria): Formation mechanisms and the (a) biological mediation of chimney growth? *Sedimentary Geology* **185**, 159-173.

References

- de Vries, M. H., Svano, G., and Tjelta, T. I., 2007. Small scale model testing of gas migration in a soft seabed as a basis for developing a mechanical model for gas migration. *Proceeding of Offshore Site Investigation and Geotechnics Confronting New Challenges and Sharing Knowledge. Society for Underwater Technology, London.*
- de Vries, M. H., Svanø, G., Tjelta, T. I., and Emdal, A. J., 2007. Pockmarks: Created by Reduced Sedimentation or a Sudden Blow-out? *Proceeding of The Seventeenth International Offshore and Polar Engineering Conference. International Society of Offshore and Polar Engineers.*
- DiLeonardo, C. G., Moore, J. C., Nissen, S., & Bangs, N., 2002. Control of internal structure and fluid-migration pathways within the Barbados Ridge décollement zone by strike-slip faulting: Evidence from coherence and three-dimensional seismic amplitude imaging. *Geological Society of America Bulletin* **114**, 51-63.
- Delaney, P. T., Pollard, D. D., Ziony, J. I., and McKee, E. H., 1986. Field relations between dikes and joints: Emplacement processes and paleostress analysis. *Journal of Geophysical Research: Solid Earth (1978–2012)* **91**, 4920-4938.
- Dimitrov, L. and Woodside, J., 2003. Deep sea pockmark environments in the eastern Mediterranean. *Marine Geology* **195**, 263-276.
- Droz, L., Rigaut, F., Cochonat, P., and Tofani, R., 1996. Morphology and recent evolution of the Zaire turbidite system (Gulf of Guinea). *Geological Society of America Bulletin* **108**, 253-269.
- Dudley, J., and Ukeiley, L., 2011. Detached Eddy Simulation of a Supersonic Cavity flow with and without Passive flow Control. *AIAA Paper* **3844**.
- Dupre, S., Bertotti, G., and Cloetingh, S., 2007. Tectonic history along the South Gabon Basin: Anomalous early post-rift subsidence. *Marine and Petroleum Geology* **24**, 151-172.
- Duranti, D. and Mazzini, A., 2005. Large-scale hydrocarbon-driven sand injection in the Paleogene of the North Sea. *Earth and Planetary Science Letters* **239**, 327-335.
- Duval, B., Cramez, C., and Jackson, M., 1992. Raft tectonics in the Kwanza basin, Angola. *Marine and Petroleum Geology* **9**, 389-404.

– E

- Ecker, C., Dvorkin, J., and Nur, A., 1998. Sediments with gas hydrates: Internal structure from seismic AVO. *Geophysics* **63**, 1659-1669.
- Eichhubl, P., Greene, H., Naehr, T., and Maher, N., 2000. Structural control of fluid flow: offshore fluid seepage in the Santa Barbara Basin, California. *Journal of Geochemical Exploration* **69**, 545-549.
- Eichhubl, P., & Aydin, A., 2003. Ductile opening-mode fracture by pore growth and coalescence during combustion alteration of siliceous mudstone. *Journal of Structural Geology* **25**, 121-134.
- Ellis, J. P. and McGuinness, W. T., 1986. Pockmarks of the northwestern Arabian Gulf. *Oceanology* **6**, 353-367.
- Ewen, S.M., 2010. Diagenetic Evolution Of Some Modern And Ancient Cold Seep-Carbonates From East Coast Basin, New Zealand. Master Thesis. *The Univerity of Waiko.*

– F

References

- Fader, G. B., 1991. Gas-related sedimentary features from the eastern Canadian continental shelf. *Continental Shelf Research* **11**, 1123-1153.
- Fang, L., Nicolaou, D., and Cleaver, J., 1999. Transient removal of a contaminated fluid from a cavity. *International journal of heat and fluid flow* **20**, 605-613.
- Festa, A., Dilek, Y., Pini, G., Codegone, G., and Ogata, K., 2012. Mechanisms and processes of stratal disruption and mixing in the development of mélanges and broken formations: redefining and classifying mélanges. *Tectonophysics* **568**, 7-24.
- Fisher, C., 1997. Penn State Science, 1997. Scientists Discover Methane Ice Worms On Gulf Of Mexico Sea Floor. Website: [Http://www.Science.Psu.Edu/News-And-Events/1997-News/Iceworms.Htm](http://www.Science.Psu.Edu/News-And-Events/1997-News/Iceworms.Htm).
- Flodén, T. and Söderberg, P., 1988. Pockmarks and related seabed structures in some areas of Precambrian bedrock in Sweden. *Geological Survey of Finland, Special Paper* **6**, 163-169.
- Foucher, J. P., Westbrook, G., Boetius, A., Ceramicola, S., Dupré, S., Mascle, J., Mienert, J., Pfannkuche, O., Pierre, C., and Praeg, D., 2009. Structure and drivers of cold seep ecosystems. *Oceanography* **22**, 92-109.
- Frerichs, W. E., & Shive, P. N., 1971. Tectonic implications of variations in sea floor spreading rates. *Earth and Planetary Science Letters* **12**, 406-410.
- Fredrich, J. T., Coblenz, D., Fossum, A. F., and Thorne, B. J., 2003. Stress perturbations adjacent to salt bodies in the deepwater Gulf of Mexico. *SPE Annual Technical Conference and Exhibition*, SPE paper 84554. Society of Petroleum Engineers.

– G

- Gaffney, E. S., Damjanac, B., and Valentine, G. A., 2007. Localization of volcanic activity: 2. Effects of pre-existing structure. *Earth and Planetary Science Letters* **263**, 323-338.
- García-García, A., Vilas, F., and García-Gil, S., 1999. A seeping sea-floor in a Ria environment: Ria de Vigo (NW Spain). *Environmental Geology* **38**, 296-300.
- Gartrell, A., Zhang, Y., Lisk, M., and Dewhurst, D., 2004. Fault intersections as critical hydrocarbon leakage zones: integrated field study and numerical modelling of an example from the Timor Sea, Australia. *Marine and Petroleum Geology* **21**, 1165-1179.
- Gay, A., 2002. Les marqueurs géologiques de la migration et de l'expulsion des fluides sédimentaires sur le plancher des marges passives matures: exemples dans le bassin du Congo. PhD Thesis. University of Lille I.
- Gay, A., Lopez, M., Cochonat, P., Sultan, N., Cauquil, E., and Brigaud, F., 2003. Sinuous pockmark belt as indicator of a shallow buried turbiditic channel on the lower slope of the Congo Basin, West African Margin. *Geological Society, London, Special Publications* **216**, 173-189.
- Gay, A., Lopez, M., Cochonat, P., and Sermondadaz, G., 2004. Polygonal faults-furrows system related to early stages of compaction–upper Miocene to recent sediments of the Lower Congo Basin. *Basin Research* **16**, 101-116.
- Gay, A., Lopez, M., Cochonat, P., Séranne, M., Levaché, D., and Sermondadaz, G., 2006a. Isolated seafloor pockmarks linked to BSRs, fluid chimneys, polygonal faults and stacked Oligocene–Miocene turbiditic palaeochannels in the Lower Congo Basin. *Marine Geology* **226**, 25-40.

References

- Gay, A., Lopez, M., Ondreas, H., Charlou, J.-L., Sermondadaz, G., and Cochonat, P., 2006b. Seafloor facies related to upward methane flux within a Giant Pockmark of the Lower Congo Basin. *Marine Geology* **226**, 81-95.
- Gay, A., Lopez, M., Berndt, C., and Seranne, M., 2007. Geological controls on focused fluid flow associated with seafloor seeps in the Lower Congo Basin. *Marine Geology* **244**, 68-92.
- Gay, A., Mourgues, R., Berndt, C., Bureau, D., Planke, S., Laurent, D., Gautier, S., Lauer, C., and Loggia, D., 2012. Anatomy of a fluid pipe in the Norway Basin: Initiation, propagation and 3D shape. *Marine Geology* **332**, 75-88.
- Gibson, R., Atkinson, R., and Gordon, J., 2005. Ecology of cold seep sediments: interactions of fauna with flow, chemistry and microbes. *Oceanography and Marine Biology: An Annual Review* **43**, 1-46.
- Gomez-Rivas, E. and Griera, A., 2012. Shear fractures in anisotropic ductile materials: an experimental approach. *Journal of Structural Geology* **34**, 61-76.
- Goult, N., 2008. Geomechanics of polygonal fault systems: a review. *Petroleum Geoscience* **14**, 389-397.
- Grauls, D., 1996. Angola – Block 17 Hydrocarbon Evaluation Study Using 2d Numerical Modeling. Internal Report. *Elf Exploration*, 1-19.
- Grauls, D., 2000. Angola Block 17 Offshore Angola Petroleum Evaluation Using 3d Basin Modelling. Internal Report. *Elf Exploration*, 1-35.

– H

- Haigermoser, C., Vesely, L., Novara, M., Zuzio, D., & Onorato, M., 2007. Time-resolved PIV applied to cavity unsteady flows. *AIAA Paper* **3432**.
- Hamed, A., Basu, D., and Das, K., 2003. Detached eddy simulations of supersonic flow over cavity. *AIAA paper* **549**.
- Hamlin, H. S., 2009. Ozona sandstone, Val Verde Basin, Texas: Synorogenic stratigraphy and depositional history in a Permian foredeep basin. *AAPG Bulletin* **93**, 573-594.
- Hammer, Ø., Webb, K. E., and Depreiter, D., 2009. Numerical simulation of upwelling currents in pockmarks, and data from the Inner Oslofjord, Norway. *Geo-Marine Letters* **29**, 269-275.
- Hanneman, D. L., Wideman, C. J., and Halvorson, J., 1994. Calcic paleosols: their use in subsurface stratigraphy. *AAPG Bulletin* **78**, 1360-1371.
- Hansen, D. M., Shimeld, J. W., Williamson, M. A., and Lykke-Andersen, H., 2004. Development of a major polygonal fault system in Upper Cretaceous chalk and Cenozoic mudrocks of the Sable Subbasin, Canadian Atlantic margin. *Marine and Petroleum Geology* **21**, 1205-1219.
- Haq, B. U., Hardenbol, J., and Vail, P. R., 1987. Chronology of fluctuating sea levels since the Triassic. *Science* **235**, 1156-1167.
- Haskell, N., Nissen, S., Whitman, D., and Antrim, L., 1997. Structural features on the West African continental slope delineated by 3D seismic coherency. Abstract. *AAPG Bulletin* **81**, 1382.
- Hathaway, J. C. and Degens, E. T., 1969. Methane-derived marine carbonates of Pleistocene age. *Science* **165**, 690-692.
- Heezen, B. C., Hollister, C. D., and Ruddiman, W. F., 1966. Shaping of the continental rise by deep geostrophic contour currents. *Science* **152**, 502-508.

References

- Heggland, R., 1997. Detection of gas migration from a deep source by the use of exploration 3D seismic data. *Marine Geology* **137**, 41-47.
- Heggland, R., 1998. Gas seepage as an indicator of deeper prospective reservoirs. A study based on exploration 3D seismic data. *Marine and Petroleum Geology* **15**, 1-9.
- Heggland, R., 2005. Using gas chimneys in seal integrity analysis: A discussion based on case histories. In Boulton, P. and Kaldi, J. (Eds.), *Evaluating fault and cap rock seals. AAPG Hedberg Series* **2**, 237 – 245.
- Hein, J. R., O'NEIL, J. R., and Jones, M. G., 1979. Origin of authigenic carbonates in sediment from the deep Bering Sea. *Sedimentology* **26**, 681-705.
- Heiniö, P. and Davies, R. J., 2009. Trails of depressions and sediment waves along submarine channels on the continental margin of Espirito Santo Basin, Brazil. *Geological Society of America Bulletin* **121**, 698-711.
- Higdon, J. J., 1985. Stokes flow in arbitrary two-dimensional domains: shear flow over ridges and cavities. *Journal of Fluid Mechanics* **159**, 195-226.
- Hill, J., Halka, J., Conkwright, R., Koczot, K., and Coleman, S., 1992. Distribution and effects of shallow gas on bulk estuarine sediment properties. *Continental Shelf Research* **12**, 1219-1229.
- Hill, J. C., Driscoll, N. W., Weissel, J. K., and Goff, J. A., 2004. Large-scale elongated gas blowouts along the US Atlantic margin. *Journal of Geophysical Research: Solid Earth (1978–2012)* **109**.
- Hjelstuen, B. O., Haflidason, H., Sejrup, H. P., and Nygård, A., 2010. Sedimentary and structural control on pockmark development—evidence from the Nyegga pockmark field, NW European margin. *Geo-Marine Letters* **30**, 221-230.
- Ho, S., Blouet, J. p., Imbert, P., 2012. Seep carbonates: seismic expression vs. outcrop observations. Abstract. *Proceeding of 11th Conference of Gas in Marine Sediments*, 111-112.
- Holbrook, W., Gorman, A., Hornbach, M., Hackwith, K., Nealon, J., Lizarralde, D., and Pecher, I., 2002. Seismic detection of marine methane hydrate. *The Leading Edge* **21**, 686-689.
- Hori, T., Mohri, Y., Matsushima, K., & Aoyama, S., 2002. Features Of Crack Propagation By Hydraulic Fracturing. In *Cohesive Soil-Experimental Study On Seepage Failure Of Small Earth Dams. Transactions-Japanese Society Of Irrigation Drainage And Reclamation Engineering*, 89-98.
- Hovland, M., 1981. A classification of pockmark related features in the Norwegian Trench. *Continental Shelf Institute, Iku., Publication* **106**, 28.
- Hovland, M., 1982. Pockmarks and the recent geology of the central section of the Norwegian Trench. *Marine Geology* **47**, 283-301.
- Hovland, M. and Gudmestad, O. T., 1984. Potential influence of gas-induced erosion on seabed installations. *Seabed Mechanics*, 255-263.
- Hovland, M., Judd, A. G., and King, L. H., 1984. Characteristic features of pockmarks on the North Sea Floor and Scotian Shelf. *Sedimentology* **31**, 471-480.
- Hovland, M., 1985. Seabed Features Caused By Shallow Gas In North Sea. Abstract. *AAPG Bulletin* **69**, 267.
- Hovland, M. and Sommerville, J. H., 1985. Characteristics of two natural gas seepages in the North Sea. *Marine and Petroleum Geology* **2**, 319-326.
- Hovland, M., Talbot, M., Olausson, S., and Aasberg, L., 1985. Recently formed methane-derived carbonates from the North Sea floor. In: Thomas, B.M. (Ed.). *Petroleum*

- Geochemistry in Exploration of the Norwegian Shelf. Norwegian Petroleum Society. *Graham & Trotman*, 263-266.
- Hovland, M. and Judd, A., 1988. Seabed pockmarks and seepages: impact on geology, biology, and the marine environment. *Graham & Trotman, London*.
 - Hovland, M., Talbot, M. R., Qvale, H., Olaussen, S., and Aasberg, L., 1987. Methane-related carbonate cements in pockmarks of the North Sea. *Journal of Sedimentary Research* **57**, 230.
 - Hovland, M., 1989. The formation of pockmarks and their potential influence on offshore construction. *Quarterly Journal of Engineering Geology and Hydrogeology* **22**, 131-138.
 - Hovland, M. and Thomsen, E., 1989. Hydrocarbon-based communities in the North Sea? *Sarsia* **74**, 29-42.
 - Hovland, M., 1992. Hydrocarbon seeps in northern marine waters—their occurrence and effects. *Palaios* **7**, 376-382.
 - Hovland, M. and Irwin, H., 1992. Habitat of methanogenic carbonate cemented sediments in the North Sea. *Bacterial Gas, Technip, Paris*, 157-172.
 - Hovland, M., Croker, P. F., and Martin, M., 1994. Fault-associated seabed mounds (carbonate knolls?) off western Ireland and north-west Australia. *Marine and Petroleum Geology* **11**, 232-246.
 - Hovland, M., Gardner, J., and Judd, A., 2002. The significance of pockmarks to understanding fluid flow processes and geohazards. *Geofluids* **2**, 127-136.
 - Hovland, M. and Svensen, H., 2006. Submarine pingoes: Indicators of shallow gas hydrates in a pockmark at Nyegga, Norwegian Sea. *Marine Geology* **228**, 15-23.
 - Hovland, M., 2007. Discovery of prolific natural methane seeps at Gullfaks, northern North Sea. *Geo-Marine Letters* **27**, 197-201.
 - Hovland, M., 2008. Deep-Water Coral Reefs. Unique Biodiversity Hot-Spots. *Praxis Publishing, UK*.
 - Howarth, D. F., 1987. The Effect Of Pre-Existing Microcavities On Mechanical Rock Performance In Sedimentary And Crystalline Rocks. *International Journal Of Rock Mechanics And Mining Sciences & Geomechanics Abstracts* **24**, 223-233. Pergamon.
 - Hurst, A. and Cartwright, J., 2007. Relevance of sand injectites to hydrocarbon exploration and production. *AAPG Memoir* **87**, 1–20.
 - Hustoft, S., Mienert, J., Bünz, S., and Nouzé, H., 2007. High-resolution 3D-seismic data indicate focussed fluid migration pathways above polygonal fault systems of the mid-Norwegian margin. *Marine Geology* **245**, 89-106.
 - Hustoft, S., Bünz, S., Mienert, J., and Chand, S., 2009. Gas hydrate reservoir and active methane-venting province in sediments on < 20 Ma young oceanic crust in the Fram Strait, offshore NW-Svalbard. *Earth and Planetary Science Letters* **284**, 12-24.
 - Hustoft, S., Bünz, S., and Mienert, J., 2010. Three-dimensional seismic analysis of the morphology and spatial distribution of chimneys beneath the Nyegga pockmark field, offshore mid-Norway. *Basin Research* **22**, 465-480.
- I
- Imbert, P., Ho, S., Le, Q.P., 2008. Funnel-Shaped Seismic Anomalies: Characterization And Emplacement Processes. Abstract. AAPG International Conference And Exhibition 2008.
 - Imbert, P., 2009. Seismic-scale Expression of Fluid Sourcing Circulation and Expulsion in Sedimentary Series. *International Petroleum Technology Conference*.

- Imbert, P., Gay, A., Ho, S., Nahan, S., 2011. Polygonal Fault Networks In Conjugate Pairs And Pockmarks In Fine-Grained Series: Timing Of Initiation And Mutual Relationships. *Submitted to Marine Geology*.
- Imbert, P. and Ho, S., 2012. Seismic-scale funnel-shaped collapse features from the Paleocene–Eocene of the North West Shelf of Australia. *Marine Geology* **332**, 198-221.
- Ireland, M. T., Davies, R. J., Goult, N. R., and Moy, D. J., 2011. Thick slides dominated by regular-wavelength folds and thrusts in biosiliceous sediments on the Vema Dome offshore of Norway. *Marine Geology* **289**, 34-45.
- Ilg, B. R., Hemmings-Sykes, S., Nicol, A., Baur, J., Fohrmann, M., Funnell, R., & Milner, M., 2012. Normal Faults And Gas Migration In An Active Plate Boundary, Southern Taranaki Basin, Offshore New Zealand. *AAPG Bulletin* **96**, 1733-1756.

– J

- Jain, A. K. 2009. Preferential Mode Of Gas Invasion In Sediments: Grain-Scale Mechanistic Model Of Coupled Multiphase Fluid Flow And Sediment Mechanics. Master Thesis, *Massachusetts Institutge of Techology*.
- Jain, A. and Juanes, R., 2009. Preferential Mode of gas invasion in sediments: Grain-scale mechanistic model of coupled multiphase fluid flow and sediment mechanics. *Journal of Geophysical Research: Solid Earth (1978–2012)* **114**.
- Jansen, J., 1990. Glacial-interglacial oceanography of the southeastern atlantic Ocean and the paleoclinlate of west central Africa. In Lanfranchi, R., Schwartz, D. (Eds.), *Paysages Quaternaires de l’Afrique centrale atlantique*, *ORSTOM*, 110–123.
- Jansen, J., Van Weering, T., Gieles, R., and Van Iperen, J., 1984. Middle and late Quaternary oceanography and climatology of the Zaire-Congo fan and the adjacent eastern Angola Basin. *Netherlands Journal of Sea Research* **17**, 201-249.
- Jobe, Z. R., Lowe, D. R., and Uchtyl, S. J., 2011. Two fundamentally different types of submarine canyons along the continental margin of Equatorial Guinea. *Marine and Petroleum Geology* **28**, 843-860.
- Johnson, B. D., Boudreau, B. P., Gardiner, B. S., and Maass, R., 2002. Mechanical response of sediments to bubble growth. *Marine Geology* **187**, 347-363.
- Johnson, B. D., Barry, M. A., Boudreau, B. P., Jumars, P. A., and Dorgan, K. M., 2012. In situ tensile fracture toughness of surficial cohesive marine sediments. *Geo-Marine Letters* **32**, 39-48.
- Johnson, J. E., Goldfinger, C., and Suess, E., 2003. Geophysical constraints on the surface distribution of authigenic carbonates across the Hydrate Ridge region, Cascadia margin. *Marine Geology* **202**, 79-120.
- Jopling, A. V., 1964. Interpreting the concept of the sedimentation unit. *Journal of Sedimentary Research* **34**.
- Jopling, A. V. and Walker, R. G., 1968. Morphology and origin of ripple-drift cross-lamination, with examples from the Pleistocene of Massachusetts. *Journal of Sedimentary Research* **38**.
- Josenhans, H. W., King, L. H., and Fader, G. B., 1978. A side-scan sonar mosaic of pockmarks on the Scotian Shelf. *Canadian Journal of Earth Sciences* **15**, 831-840.
- Juanes, R., Bryant, S. L., 2006. Mechanisms Leading to Co-existence of Gas and Hydrate. *Ocean Sediments, National Energy Technology Laboratory, U.S. Department of Energy*.

References

- Juanes R. and Bryant, S. L., 2011. Mechanisms Leading to Co-Existence of Gas and Hydrate in Ocean Sediments, Quarterly Progress Report, University of Texas.
- Judd, A. G. and Hovland, M., 2007. Seabed fluid flow: the impact of geology, biology and the marine environment. *Cambridge University Press*.

– K

- Kallweit, R. and Wood, L., 1982. The limits of resolution of zero-phase wavelets. *Geophysics* **47**, 1035-1046.
- Karisiddaiah, S. and Veerayya, M., 1994. Methane-bearing shallow gas-charged sediments in the eastern Arabian Sea: a probable source for greenhouse gas. *Continental Shelf Research* **14**, 1361-1370.
- Kastner, M., Keene, J.B., Gieskes, J.M., 1977. Diagenesis Of Siliceous Oozes—I. Chemical Controls On The Rate Of Opal-A To Opal-Ct Transformation—An Experimental Study. *Geochimica Et Cosmochimica Acta* **41**, 1041–1059.
- Kattenhorn, S. A., Aydin, A., and Pollard, D. D., 2000. Joints at high angles to normal fault strike: an explanation using 3-D numerical models of fault-perturbed stress fields. *Journal of Structural Geology* **22**, 1-23.
- Kelley, J. T., Dickson, S. M., Belknap, D. F., Barnhardt, W. A., and Henderson, M., 1994. Giant sea-bed pockmarks: evidence for gas escape from Belfast Bay, Maine. *Geology* **22**, 59-62.
- Kelly, C. A., Rudd, J. W., St Louis, V. L., and Moore, T., 1994. Turning attention to reservoir surfaces, a neglected area in greenhouse studies. *Eos, Transactions American Geophysical Union* **75**, 332-333.
- Kesteren, W. v. and Kessel, T. v., 2002. Gas bubble nucleation and growth in cohesive sediments. *Proceedings in Marine Science* **5**, 329-341.
- King, L. H. and MacLEAN, B., 1970. Pockmarks on the Scotian shelf. *Geological Society of America Bulletin* **81**, 3141-3148.
- King, R., Backé, G., Tingay, M., Hillis, R., and Mildren, S., 2012. Stress deflections around salt diapirs in the Gulf of Mexico. *Geological Society, London, Special Publications* **367**, 141-153.
- Kranz, R. L., 1979. Crack-crack and crack-pore interactions in stressed granite. *International Journal of Rock Mechanics and Mining Sciences & Geomechanics Abstracts* **16**. 37-47. Pergamon.
- Kulsri, S., Jaroensutasinee, M., and Jaroensutasinee, K., 2007. Simulation of Lid Cavity Flow in Rectangular, Half-Circular and Beer Bucket Shapes using Quasi-Molecular Modeling. *Proceedings Of World Academy Of Science, Engineering And Technology* **19**, 401-406.

– L

- Larson, R. L. and Ladd, J. W., 1973. Evidence for the opening of the South Atlantic in the Early Cretaceous. *Nature* **246**, 209–212.
- Lavier, L. L., Steckler, M. S., and Brigaud, F., 2001. Climatic and tectonic control on the Cenozoic evolution of the West African margin. *Marine Geology* **178**, 63-80.
- Lawson, S. and Barakos, G., 2009. Assessment of passive flow control for transonic cavity flow using detached-eddy simulation. *Journal of Aircraft* **46**, 1009-1029.

References

- Lein, A. Y., 2004. Authigenic carbonate formation in the ocean. *Lithology and Mineral Resources* **39**, 1-30.
- León, R., Somoza, L., Medialdea, T., González, F., Díaz-del-Río, V., Fernández-Puga, M., Maestro, A., and Mata, M., 2007. Sea-floor features related to hydrocarbon seeps in deepwater carbonate-mud mounds of the Gulf of Cádiz: from mud flows to carbonate precipitates. *Geo-Marine Letters* **27**, 237-247.
- Levin, L. A., 2005. Ecology of cold seep sediments: Interactions of fauna with flow, chemistry and microbes. *Oceanography and Marine Biology - an Annual Review* **43**, 1-46. CRC Press.
- Licari, L. and Mackensen, A., 2005. Benthic foraminifera off West Africa (1 N to 32 S): do live assemblages from the topmost sediment reliably record environmental variability? *Marine Micropaleontology* **55**, 205-233.
- Lindsey, J. P., 1989. The Fresnel zone and its interpretive significance. *The Leading Edge* **10**, 33-39.
- Ligtenberg, J., 2003. Unravelling the petroleum system by enhancing fluid migration paths in seismic data using a neural network based pattern recognition technique. *Geofluids* **3**, 255-261.
- Ligtenberg, H. and Connolly, D., 2003. Chimney detection and interpretation, revealing sealing quality of faults, geohazards, charge of and leakage from reservoirs. *Journal of Geochemical Exploration* **78**, 385-387.
- Ligtenberg, J., 2005. Detection of fluid migration pathways in seismic data: implications for fault seal analysis. *Basin Research* **17**, 141-153.
- Liro, L.M., Dawson, W.C., 2000. Reservoir Systems Of Selected Basins Of The South Atlantic. In: Mello, M.R., Katz, B.J., (Eds.), *Petroleum Systems Of South Atlantic Margins. AAPG Memoir* **73**, 77-92.
- Lister, J. R. and Kerr, R. C., 1991. Fluid-mechanical models of crack propagation and their application to magma transport in dykes. *Journal of Geophysical Research: Solid Earth (1978-2012)* **96**, 10049-10077.
- Loncke, L., Mascle, J., and Parties, F. S., 2004. Mud volcanoes, gas chimneys, pockmarks and mounds in the Nile deep-sea fan (Eastern Mediterranean): geophysical evidences. *Marine and Petroleum Geology* **21**, 669-689.
- Løseth, H., Wensaas, L., Arntsen, B., Hanken, N., Basire, C., and Graue, K., 2001. 1000 m long gas blow-out pipes. *63rd EAGE Conference & Exhibition*.
- Løseth, H., Gading, M., and Wensaas, L., 2009. Hydrocarbon leakage interpreted on seismic data. *Marine and Petroleum Geology* **26**, 1304-1319.
- Løseth, H., Wensaas, L., Arntsen, B., Hanken, N.-M., Basire, C., and Graue, K., 2011. 1000 m long gas blow-out pipes. *Marine and Petroleum Geology* **28**, 1047-1060.
- Lutjeharms, J. and Meeuwis, J., 1987. The extent and variability of south-east Atlantic upwelling. *South African Journal of Marine Science* **5**, 51-62.

– M

- Macelloni, L., Simonetti, A., Knapp, J. H., Knapp, C. C., Lutken, C. B., and Lapham, L. L., 2012. Multiple resolution seismic imaging of a shallow hydrocarbon plumbing system, Woolsey Mound, Northern Gulf of Mexico. *Marine and Petroleum Geology* **38**, 128-142.
- Macelloni, L., Brunner, C. A., Caruso, S., Lutken, C. B., D'Emidio, M., and Lapham, L. L., 2013. Spatial distribution of seafloor bio-geological and geochemical processes as

- proxies of fluid flux regime and evolution of a carbonate/hydrates mound, northern Gulf of Mexico. *Deep Sea Research Part I: Oceanographic Research Papers* **74**, 25-38.
- Maisey, G., Rokoengen, K., and Raaen, K., 1980. Pockmarks formed by seep of petrogenic gas in the southern part of the Norwegian Trench. *IKU Rep. P-258*.
 - Manley, P. L., Manley, T., Watzin, M. C., and Gutierrez, J., 2004. Lakebed pockmarks in Burlington Bay, Lake Champlain: I. Hydrodynamics and implications of origin. *Lake Champlain: Partnerships and Research in the New Millennium*, 299-329.
 - Mascle, J. and Phillips, J. D., 1972. Magnetic smooth zones in the South Atlantic. *Nature* **240**, 80–84.
 - Mazeika, P., 1967. Thermal domes in the eastern tropical Atlantic Ocean. *Limnology Oceanography* **12**, 537-539.
 - Mazzini, A., Svensen, H., Hovland, M., and Planke, S., 2006. Comparison and implications from strikingly different authigenic carbonates in a Nyegga complex pockmark, G11, Norwegian Sea. *Marine Geology* **231**, 89-102.
 - Mazzini, A., Ivanov, M. K., Neramoen, A., Bahr, A., Bohrmann, G., Svensen, H., and Planke, S., 2008. Complex plumbing systems in the near subsurface: geometries of authigenic carbonates from Dolgovskoy Mound (Black Sea) constrained by analogue experiments. *Marine and Petroleum Geology* **25**, 457-472.
 - McCaffrey, W. and Kneller, B., 2001. Process controls on the development of stratigraphic trap potential on the margins of confined turbidite systems and aids to reservoir evaluation. *AAPG Bulletin* **85**, 971-988.
 - McQuillin, R., Bacon, M., and Barclay, W., 1984. An introduction to seismic interpretation-Reflection seismics in petroleum exploration. Graham & Trotman, London.
 - Meldahl, P., Heggland, R., Bril, B., and de Groot, P., 2001. Identifying faults and gas chimneys using multiattributes and neural networks. *The Leading Edge* **20**, 474-482.
 - Menand, T. and Tait, S. R., 2002. The propagation of a buoyant liquid-filled fissure from a source under constant pressure: An experimental approach. *Journal of Geophysical Research: Solid Earth (1978–2012)* **107**, ECV 16-1-ECV 16-14.
 - Mienert, J., Posewang, J., and Baumann, M., 1998. Gas hydrates along the northeastern Atlantic margin: possible hydrate-bound margin instabilities and possible release of methane. *Geological Society, London, Special Publications* **137**, 275-291.
 - Mitchum Jr, R., Vail, P., and Thompson III, S., 1977. Seismic stratigraphy and global changes of sea level: Part 2. The depositional sequence as a basic unit for stratigraphic analysis: Section 2. In Payton, C. E., (Eds.), *Seismic stratigraphy: Application to Hydrocarbon Exploration. AAPG Memoir* **26**, 53-62.
 - Moore, J. C., Orange, D., and Kulm, L. D., 1990. Interrelationship of fluid venting and structural evolution: Alvin observations from the frontal accretionary prism, Oregon. *Journal of Geophysical Research: Solid Earth (1978–2012)* **95**, 8795-8808.
 - Moore, J. C., Iturrino, G. J., Flemings, P. B., Hull, I., and Gay, A., 2007. Fluid Migration and State of Stress Above the Blue Unit Ursa Basin: Relationship to the Geometry of Injectites. *Offshore Technology Conference. OTC-18812*.
 - Moss, J. and Cartwright, J., 2010a. 3D seismic expression of km-scale fluid escape pipes from offshore Namibia. *Basin Research* **22**, 481-501.
 - Moss, J. and Cartwright, J., 2010b. The spatial and temporal distribution of pipe formation, offshore Namibia. *Marine and Petroleum Geology* **27**, 1216-1234.
 - Moss, J.L., 2011. The spatial and temporal distribution of pipe and pockmark formation. Phd Thesis. *Cardiff University*.

References

- Murdoch, L., 1993. Hydraulic fracturing of soil during laboratory experiments Part 3. Theoretical analysis. *Geotechnique* **43**, 277-287.

– N

- Naudts, L., Greinert, J., Artemov, Y., Staelens, P., Poort, J., Van Rensbergen, P., and De Batist, M., 2006. Geological and morphological setting of 2778 methane seeps in the Dnepr paleo-delta, northwestern Black Sea. *Marine Geology* **227**, 177-199.
- Naudts, L., Greinert, J., Artemov, Y., Beaubien, S. E., Borowski, C., and Batist, M. D., 2008. Anomalous sea-floor backscatter patterns in methane venting areas, Dnepr paleo-delta, NW Black Sea. *Marine Geology* **251**, 253-267.
- Naudts, L., Greinert, J., Poort, J., Belza, J., Vangampelaere, E., Boone, D., Linke, P., Henriot, J.-P., and De Batist, M., 2010. Active venting sites on the gas-hydrate-bearing Hikurangi Margin, off New Zealand: Diffusive-versus bubble-released methane. *Marine Geology* **272**, 233-250.
- Nelson, H., Thor, D., Sandstrom, M., and Kvenvolden, K., 1979. Modern biogenic gas-generated craters (sea-floor “pockmarks”) on the Bering Shelf, Alaska. *Geological Society of America Bulletin* **90**, 1144-1152.
- Newton, R. S., Cunningham, R. C., and Schubert, C. E., 1980. Mud volcanoes and pockmarks: seafloor engineering hazards or geological curiosities? *Offshore Technology Conference*. OTC-3729 .
- Nowell, A. and Jumars, P., 1984. Flow environments of aquatic benthos. *Annual review of ecology and systematics*, 303-328.
- Nunn, J. A. and Meulbroek, P., 2002. Kilometer-scale upward migration of hydrocarbons in geopressed sediments by buoyancy-driven propagation of methane-filled fractures. *AAPG Bulletin* **86**, 907-918.
- Nunn, J. A., 2003. Pore-pressure-dependent fracture permeability in fault zones: implications for cross-formational fluid flow. *Multidimensional Basin Modeling, American Association of Petroleum Geologists/Datapages Discovery Series*, 89-103.

– O

- Olson, J. E., Holder, J., and Rijken, P., 2002. Quantifying the fracture mechanics properties of rock for fractured reservoir characterization. *SPE/ISRM Rock Mechanics Conference*. Society of Petroleum Engineers.
- Olu-Le Roy, K., Caprais, J.C., Fi fis, A., Fabri, M.C., Galéron, J., Budzinsky, H., Le Ménach, K., Khripounoff, A., Ondréas, H., Sibuet, M., 2007. Cold-seep assemblages on a giant pockmark off West Africa: spatial patterns and environmental control. *Marine Ecology* **28**, 115-130.
- Olu, K., Caprais, J.-C., Galeron, J., Causse, R., Von Cosel, R., Budzinski, H., Ménach, K. L., Roux, C. L., Levaché, D., and Khripounoff, A., 2009. Influence of seep emission on the non-symbiont-bearing fauna and vagrant species at an active giant pockmark in the Gulf of Guinea (Congo–Angola margin). *Deep Sea Research Part II: Topical Studies in Oceanography* **56**, 2380-2393.
- Orange, D. L., Yun, J., Maher, N., Barry, J., and Greene, G., 2002. Tracking California seafloor seeps with bathymetry, backscatter and ROVs. *Continental Shelf Research* **22**, 2273-2290.

- Osborne, M. J. and Swarbrick, R. E., 1997. Mechanisms for generating overpressure in sedimentary basins: a reevaluation. *AAPG Bulletin* **81**, 1023-1041.

- P

- Pantin, H.M., 1980. Late Devensian And Flandrian Sequence In The Northern Irish Sea. *Proceeding of The Quaternary Research Association Discussion Meeting, "Offshore And Onshore Quaternary Of Northwest Europe–The Scope For Correlation"*, Edinburgh.
- Papatheodorou, G., Lavrentaki, M., Mourelatos, P., Voutsinas, K., and Xenos, K., 2001. Pockmarks on the seabed of the Aetoliko Lagoon, Greece. *Alieftika Nea (Fishing News)* **238**, 73-87.
- Partyka, G. A., 2000. Seismic Attribute Sensitivity to Energy Bandwidth Phase And Thickness. Expanded Abstracts. *70st Annual International Meeting of the Society of Exploration Geophysicists*, 503-506.
- Paternoster, B. J., Cauquil, E. C., and Saint-Andre, C., 2011a. How Good Seismic Resolution Needs To Be For Detecting Thin Beds? *Proceeding of Offshore Technology Conference*, OTC-21537.
- Paternoster, B., Cooper, R., Brahim, L.B., 2011b. Careful Use Of Seismic Amplitudes To Derive Net-Pay, Geophysical Seminar – PESGB.
- Paull, C. K., Ussler, W., Borowski, W. S., and Spiess, F. N., 1995. Methane-rich plumes on the Carolina continental rise: associations with gas hydrates. *Geology* **23**, 89-92.
- Paull, C. K. and Ussler III, W., 2008. Re-evaluating the significance of seafloor accumulations of methane-derived carbonates: seepage or erosion indicators? *Proceedings of the 6th International Conference on Gas Hydrates (ICGH 2008)*. Paper 5581.
- Pedersen, T. and Bjørlykke, K., 1994. Fluid flow in sedimentary basins: model of pore water flow in a vertical fracture. *Basin Research* **6**, 1-16.
- Petersen, C. J., Bünz, S., Hustoft, S., Mienert, J., and Klaeschen, D., 2010. High-resolution P-Cable 3D seismic imaging of gas chimney structures in gas hydrated sediments of an Arctic sediment drift. *Marine and Petroleum Geology* **27**, 1981-1994.
- Phillips, W. J., 1972. Hydraulic fracturing and mineralization. *Journal of the Geological Society* **128**, 337-359.
- Phillips, C. J., 1988. Rheological investigations of debris flow materials. PhD Thesis. *University of Canterbury*.
- Philippe, Y., 1999. Angola-Block 17 Outer Trend, Regional Structural Synthesis . Internal Report. *Elf Exploration*.
- Philippe, Y., 2000. Angola-Block 17 Se Corner, Central Area And SW Corner : Tertiary Regional Structural Synthesis. Internal Report. *Elf Exploration*.
- Pickrill, R., 1993. Shallow seismic stratigraphy and pockmarks of a hydrothermally influenced lake, Lake Rotoiti, New Zealand. *Sedimentology* **40**, 813-828.
- Pierre, C. and Fouquet, Y., 2007. Authigenic carbonates from methane seeps of the Congo deep-sea fan. *Geo-Marine Letters* **27**, 249-257.
- Pilcher, R. and Argent, J., 2007. Mega-pockmarks and linear pockmark trains on the West African continental margin. *Marine Geology* **244**, 15-32.
- Plaza-Faverola, A., Bünz, S., and Mienert, J., 2010. Fluid distributions inferred from P-wave velocity and reflection seismic amplitude anomalies beneath the Nyegga pockmark field of the mid-Norwegian margin. *Marine and Petroleum Geology* **27**, 46-60.

References

- Plaza-Faverola, A., Bünz, S., and Mienert, J., 2011. Repeated fluid expulsion through sub-seabed chimneys offshore Norway in response to glacial cycles. *Earth and Planetary Science Letters* **305**, 297-308.
- Plaza-Faverola, A., Bünz, S., and Mienert, J., 2012. The free gas zone beneath gas hydrate bearing sediments and its link to fluid flow: 3-D seismic imaging offshore mid-Norway. *Marine Geology* **291**, 211-226.
- Podvin, B., Fraigneau, Y., Lusseyran, F., and Gougat, P., 2006. A reconstruction method for the flow past an open cavity. *Journal of fluids engineering* **128**, 531-540.
- Pollard, D. D. and Aydin, A., 1988. Progress in understanding jointing over the past century. *Geological Society of America Bulletin* **100**, 1181-1204.

– R

- Rawnsley, K., Rives, T., Petti, J.-P., Hencher, S., and Lumsden, A., 1992. Joint development in perturbed stress fields near faults. *Journal of Structural Geology* **14**, 939-951.
- Regnier, P., Dale, A. W., Arndt, S., LaRowe, D., Mogollón, J., and Van Cappellen, P., 2011. Quantitative analysis of anaerobic oxidation of methane (AOM) in marine sediments: a modeling perspective. *Earth-Science Reviews* **106**, 105-130.
- Reynolds, O., 1883. An experimental investigation of the circumstances which determine whether the motion of water shall be direct or sinuous, and of the law of resistance in parallel channels. *Proceedings of the royal society of London* **35**, 84-99.
- Riedel, M., Novosel, I., Spence, G. D., Hyndman, R. D., Chapman, R. N., Solem, R. C., and Lewis, T., 2006. Geophysical and geochemical signatures associated with gas hydrate-related venting in the northern Cascadia margin. *Geological Society of America Bulletin* **118**, 23-38.
- Riedel, M., Bahk, J.-J., Scholz, N., Ryu, B.-J., Yoo, D.-G., Kim, W., and Kim, G., 2012. Mass-transport deposits and gas hydrate occurrences in the Ulleung Basin, East Sea—part 2: gas hydrate content and fracture-induced anisotropy. *Marine and Petroleum Geology* **35**, 75-90.
- Rise, L., Sættem, J., Fanavoll, S., Thorsnes, T., Ottesen, D., and Bøe, R., 1999. Sea-bed pockmarks related to fluid migration from Mesozoic bedrock strata in the Skagerrak offshore Norway. *Marine and Petroleum Geology* **16**, 619-631.
- Ritger, S., Carson, B., and Suess, E., 1987. Methane-derived authigenic carbonates formed by subduction-induced pore-water expulsion along the Oregon/Washington margin. *Geological Society of America Bulletin* **98**, 147-156.
- Robein, E., 2003. Velocities, Time-imaging, and Depth-imaging in Reflection Seismics: Principles and Methods. EAGE publications.
- Roberts, S. J. and Nunn, J. A., 1995. Episodic fluid expulsion from geopressed sediments. *Marine and Petroleum Geology* **12**, 195-204.
- Roberts, H. H. and Carney, R. S., 1997. Evidence of episodic fluid, gas, and sediment venting on the northern Gulf of Mexico continental slope. *Economic Geology* **92**, 863-879.
- Roberts, H. H., 2001. Fluid and Gas Expulsion on the Northern Gulf of Mexico Continental Slope: Mud-Prone to Mineral-Prone Responses. *Natural gas hydrates*, 145-161.
- Roberts, H. H., Hardage, B. A., Shedd, W. W., and Hunt Jr, J., 2006. Seafloor reflectivity—an important seismic property for interpreting fluid/gas expulsion geology and the presence of gas hydrate. *The Leading Edge* **25**, 620-628.

References

- Rowley, C. W., Colonius, T., & Basu, A. J., 2002. On self-sustained oscillations in two-dimensional compressible flow over rectangular cavities. *Journal of Fluid Mechanics* **455**, 315-346.
- S
- Sahling, H., Bohrmann, G., Spiess, V., Bialas, J., Breitzke, M., Ivanov, M., Kasten, S., Krastel, S., and Schneider, R., 2008. Pockmarks in the Northern Congo Fan area, SW Africa: Complex seafloor features shaped by fluid flow. *Marine Geology* **249**, 206-225.
- Salmi, M. S., Johnson, H. P., Leifer, I., and Keister, J. E., 2011. Behavior of methane seep bubbles over a pockmark on the Cascadia continental margin. *Geosphere* **7**, 1273-1283.
- Sangree, J. and Widmier, J., 1978. Seismic stratigraphy and global changes of sea level, part 9: seismic interpretation of clastic depositional facies. *AAPG Bulletin* **62**, 752-771.
- Sangree, J., Waylett, D., Frazier, D., Amery, G., and Fennessy, W., 1978. Recognition of Continental-Slope Seismic Facies, Offshore Texas-Louisiana: 2. The Concepts.
- Sanz, P. and Dasari, G., 2010. Controls on in situ stresses around salt bodies. *ARM* **10-169**, 1-12.
- Sathar, S., Reeves, H., Cuss, R., and Harrington, J., 2012. The role of stress history on the flow of fluids through fractures. *Mineralogical Magazine* **76**, 3165-3177.
- Savoye, B., Babonneau, N., Dennielou, B., and Bez, M., 2009. Geological overview of the Angola–Congo margin, the Congo deep-sea fan and its submarine valleys. *Deep Sea Research Part II: Topical Studies in Oceanography* **56**, 2169-2182.
- Scanlon, K. M. and Knebel, H. J., 1989. Pockmarks in the floor of Penobscot Bay, Maine. *Geo-Marine Letters* **9**, 53-58.
- Schmale, O., Schneider von Deimling, J., Gülzow, W., Nausch, G., Waniek, J., and Rehder, G., 2010. Distribution of methane in the water column of the Baltic Sea. *Geophysical Research Letters* **37**, L12604.
- Schwab, W. C. and Lee, H. J., 1988. Causes of two slope-failure types in continental-shelf sediment, northeastern Gulf of Alaska. *Journal of Sedimentary Research* **58**.
- Séranne, M. and Nzé Abeigne, C.-R., 1999. Oligocene to Holocene sediment drifts and bottom currents on the slope of Gabon continental margin (West Africa): Consequences for sedimentation and southeast Atlantic upwelling. *Sedimentary Geology* **128**, 179-199.
- Séranne, M. and Anka, Z., 2005. South Atlantic continental margins of Africa: a comparison of the tectonic vs climate interplay on the evolution of equatorial west Africa and SW Africa margins. *Journal of African Earth Sciences* **43**, 283-300.
- Shannon, L.V., 2009. Benguela Current. In: Steele, J.H., Thorpe, S.A., Turekian, K.K. (Eds), Encyclopedia of Ocean Sciences. *Academic Press*, 255 – 267.
- Sheriff, R. E., 1996. Understanding the Fresnel zone. *AAPG Explorer October 1996*, 18-19.
- Shin, H. and Santamarina, J. C., 2010. Fluid-driven fractures in uncemented sediments: Underlying particle-level processes. *Earth and Planetary Science Letters* **299**, 180-189.
- Shurr, G. W. and Ridgley, J. L., 2002. Unconventional shallow biogenic gas systems. *AAPG Bulletin* **86**, 1939-1969.
- Sibuet, M. and Olu, K., 1998. Biogeography, biodiversity and fluid dependence of deep-sea cold-seep communities at active and passive margins. *Deep-Sea Research Part II* **45**, 517-567.
- Sieck, H. C., 1975. High-resolution geophysical studies for resource development and environmental protection. *Offshore Technology Conference*. OTC-2179 .

References

- Sinclair, H., 2000. Delta-fed turbidites infilling topographically complex basins: a new depositional model for the Annot Sandstones, SE France. *Journal of Sedimentary Research* **70**.
- Sinha, S., Gupta, A., and Oberai, M., 1981. Laminar separating flow over backsteps and cavities. I-Backsteps. *AIAA journal* **19**, 1527-1530.
- Snyder, G. T., Hiruta, A., Matsumoto, R., Dickens, G. R., Tomaru, H., Takeuchi, R., Komatsubara, J., Ishida, Y., and Yu, H., 2007. Pore water profiles and authigenic mineralization in shallow marine sediments above the methane-charged system on Umitaka Spur, Japan Sea. *Deep Sea Research Part II: Topical Studies in Oceanography* **54**, 1216-1239.
- Solheim, A. and Elverhøi, A., 1985. A pockmark field in the Central Barents Sea; gas from a petrogenic source? *Polar Research* **3**, 11-19.
- Soter, S., 1999. Macroscopic seismic anomalies and submarine pockmarks in the Corinth-Patras rift, Greece. *Tectonophysics* **308**, 275-290.
- Stewart, S., 2006. Implications of passive salt diapir kinematics for reservoir segmentation by radial and concentric faults. *Marine and Petroleum Geology* **23**, 843-853.
- Sultan, N., Marsset, B., Ker, S., Marsset, T., Voisset, M., Vernant, A.-M., Bayon, G., Cauquil, E., Adamy, J., and Colliat, J., 2010. Hydrate dissolution as a potential mechanism for pockmark formation in the Niger delta. *Journal of Geophysical Research: Solid Earth (1978–2012)* **115**.
- Swarbrick, R. E. and Osborne, M. J., 1998. Chapter 2: Mechanisms that Generate Abnormal Pressures: an Overview. *AAPG Memoir* **70**, 13 – 32.
- Syvitski, J. P. and Praeg, D. B., 1989. Quaternary sedimentation in the St. Lawrence Estuary and adjoining areas, eastern Canada: an overview based on high-resolution seismo-stratigraphy. *Géographie physique et Quaternaire* **43**, 291-310.

– T

- Takada, A., 1990. Experimental study on propagation of liquid-filled crack in gelatin: Shape and velocity in hydrostatic stress condition. *Journal of Geophysical Research: Solid Earth (1978–2012)* **95**, 8471-8481.
- Takamatsu, T., & Sawada, T., 1966. On Mixing Models of Continuous Stirred Tank. *Chemical Engineering* **30**, 1032-1925.
- Taneda, S., 1979. Visualization of separating Stokes flows. *Journal of the Physical Society of Japan* **46**, 1935-1942.
- Taner, M. T., Koehler, F., and Sheriff, R., 1979. Complex seismic trace analysis. *Geophysics* **44**, 1041-1063.
- Taylor, D., 1992. Nearshore shallow gas around the UK coast. *Continental Shelf Research* **12**, 1135-1144.
- Thrasher, J., Fleet, A. J., Hay, S. J., Hovland, M., and Düppenbecker, S., 1996. Understanding geology as the key to using seepage in exploration: the spectrum of seepage styles. In D. Schumacher and M.A. Abrams (Eds.), *Hydrocarbon Migration and Its Near-Surface Expression*. *AAPG Memoir* **66**, 223–241.
- Tony-George, R. A. and Cauquil, E., 2007. AUV Ultrahigh-Resolution 3D Seismic Technique for Detailed Subsurface Investigations. *Offshore Technology Conference*. OTC-18784 .
- Torres, M., McManus, J., Hammond, D., De Angelis, M., Heeschen, K., Colbert, S., Tryon, M., Brown, K., and Suess, E., 2002. Fluid and chemical fluxes in and out of

References

sediments hosting methane hydrate deposits on Hydrate Ridge, OR, I: Hydrological provinces. *Earth and Planetary Science Letters* **201**, 525-540.

– V

- Van Bennekom, A. and Berger, G., 1984. Hydrography and silica budget of the Angola Basin. *Netherlands Journal of Sea Research* **17**, 149-200.
- Van de Steen, B., Vervoort, A., and Sahin, K., 2002. Influence of internal structure of crinoidal limestone on fracture paths. *Engineering geology* **67**, 109-125.
- Van Kessel, T. & Van Kesteren, W., 2002. Gas production and transport in artificial sludge depots. *Waste management* **22**, 19-28.
- Van Kesteren, W. & Kessel, T. v., 2002. Gas bubble nucleation and growth in cohesive sediments. *Proceedings in Marine Science* **5**, 329-341.
- Van Rensbergen, P., Hillis, R. R., Maltman, A. J., and Morley, C. K., 2003. Subsurface sediment mobilization: introduction. *Geological Society, London, Special Publications* **216**, 1-8.
- Vignau, S., Deharbe, J.M., Ros, J.B., Boutet, C., Masse, P., Jaffuel, F., Walgenwitz, F., Gerard, J., Martin, R., Blake, B., 2000. Well Study Report: Sedimentology-Inorganic Geochemistry-Structural Analysis-Biostratigraphy. Internal Report. *Total S.A. France*.
- Vignerresse, J.-L., Tikoff, B., and Améglio, L., 1999. Modification of the regional stress field by magma intrusion and formation of tabular granitic plutons. *Tectonophysics* **302**, 203-224.

– W

- Walgenwitz, F., Pagel, M., Meyer, A., Maluski, H., and Monie, P., 1990. Thermo-Chronological Approach to Reservoir Diagenesis in the Offshore Angola Basin: a Fluid Inclusion, {40} Ar-{39} Ar and K-Ar Investigation (1). *AAPG Bulletin* **74**, 547-563.
- Watanabe, T., Masuyama, T., Nagaoka, K., and Tahara, T., 2002. Analog experiments on magma-filled cracks: Competition between external stresses and internal pressure. *Earth Planets and Space* **54**, 1247-1262.
- Watzin, M. C., Manley, P. L., Manley, T. O., & Kyriakeas, S. A., 2004. Lakebed Pockmarks In Burlington Bay, Lake Champlain Ii. Habitat Characteristics And Biological Patterns. In *Lake Champlain: Partnerships And Research In The New Millennium*, 331-348. Springer US.
- Wauthy, B., 1977. Revision de 1a classification des eaux de surface du Golfe de Guinee (Berrit 1961). *Cahiers O.R.S.T.O.M., serié Océanographie* **12**, 279-295.
- Webster, M., Keshtiban, I., and Belblidia, F., 2004. Computation of weakly-compressible highly-viscous liquid flows. *Engineering computations* **21**, 777-804.
- Wefer, G., Berger, W.H., Richter, C., Shipboard Scientific Party, 1998. Initial Reports 175, site 1077 – 1079. *Proceedings Ocean Drilling Program*, College Station. 115 – 199.
- Welch, M. J., Knipe, R. J., Souque, C., and Davies, R. K., 2009. A Quadshear kinematic model for folding and clay smear development in fault zones. *Tectonophysics* **471**, 186-202.
- Westbrook, G. K., Exley, R., Minshull, T., Nouzé, H., Gailler, A., Jose, T., Ker, S., and Plaza, A., 2008. High-resolution 3D seismic investigations of hydrate-bearing fluid-escape chimneys in the Nyegga region of the Vøring plateau, Norway. *Proceedings Of The 6th International Conferenceon Gas Hydrates Vancouver*, 1-12.

References

- Widess, M., 1973. How thin is a thin bed? *Geophysics* **38**, 1176-1180.
- Wiprut, D. and Zoback, M. D., 2000. Fault reactivation and fluid flow along a previously dormant normal fault in the northern North Sea. *Geology* **28**, 595-598.
- Wood, J. and Boles, J., 1991. Evidence for episodic cementation and diagenetic recording of seismic pumping events, North Coles Levee, California, USA. *Applied geochemistry* **6**, 509-521.
- Wood, W., Gettrust, J., Chapman, N., Spence, G., and Hyndman, R., 2002. Decreased stability of methane hydrates in marine sediments owing to phase-boundary roughness. *Nature* **420**, 656-660.
- Woods, E., 1991. Eocene seismic velocity anomalies from the Timor Sea. *Exploration Geophysics* **22**, 461-464.
- Worzel, J. L. and Watkins, J. S., 1974. Location of a lost drilling platform. *Offshore Technology Conference*. OTC-2016.

– Y

- Yager, P. L., Nowell, A. R., and Jumars, P. A., 1993. Enhanced deposition to pits: a local food source for benthos. *Journal of Marine Research* **51**, 209-236.
- Yao, H., Cooper, R., and Raghunathan, S., 2000. Simulation of three-dimensional incompressible cavity flows. *Proceeding of 22nd International Congress of Aeronautical Sciences*, 296.

– Z

- Zdanski, P., Ortega, M., and Fico Jr, N. G., 2003. Numerical study of the flow over shallow cavities. *Computers & fluids* **32**, 953-974.
- Zhang, X. and Jeffrey, R. G., 2006. The role of friction and secondary flaws on deflection and re-initiation of hydraulic fractures at orthogonal pre-existing fractures. *Geophysical Journal International* **166**, 1454-1465.
- Zhang, Y., Gartrell, A., Underschultz, J., and Dewhurst, D., 2009. Numerical modelling of strain localisation and fluid flow during extensional fault reactivation: Implications for hydrocarbon preservation. *Journal of Structural Geology* **31**, 315-327.
- Zoback, M. D., 2010. Reservoir geomechanics. *Cambridge University Press*.

Appendix I

Additional material: Chapter 1

Patchy high-amplitude seismic anomalies in the Lower Congo Basin: an insight into their subsurface morphology from analogue outcrops of SE France

Ho, Sutieng^{1*}, Blouet, J-P², Imbert, P³, Tampilang, F⁴, Podia, J⁵, Cartwright, J. A.⁶

*Earth Sciences School, Cardiff University, Park Place, CF103YE, UK

Sutieng.ho@gmail.com; HoS2@cardiff.ac.uk

Patches of positive high-amplitude anomalies (PHAAs) are commonly observed on seismic data in mud-dominated deep-water siliciclastic series, like mud-rich turbidite systems along passive continental margins. They are generally interpreted as methane-derived carbonates 1) in the absence of any other convincing mechanism to produce such local anomalies and 2) by reference to present-day seafloor observations of seep carbonates. The absence of direct physical calibration however leaves some uncertainty on this interpretation. Better characterization would help interpreting the conditions of their formation, itself related to the understanding of the evolution of seepage vs. time in buried series.

Two occurrences of PHAAs were recently drilled, providing the first direct calibration of these anomalies. One of the boreholes recovered a 10 cm-scale sample from an isolated slightly depressed PHAA “thanks to” borehole caving (fig. A.1); the other drilled through a series of stacked subcircular PHAAs forming depressions up to 7 m deep with a maximum diameter of 300 m. The logs recorded show that the corresponding sediment bodies are characterized by a high sonic velocity and a high resistivity (fig. A.1), along with a local decrease in the rate of penetration indicating harder material.

Sampling in the second case is limited to ditch cuttings recovered every 10 m. About 10% of carbonate cuttings were observed in the interval where the amplitude anomalies develop, whereas none were seen above or below. This suggests that carbonates occur as relatively thin beds or scattered nodules rather than making a continuous, thick layer.

Examination of the cuttings from the second borehole show that the ca. 10 % of limestone fragments in the interval of PHAAs consist of dark gray micrite with several generations of calcitic cement including sparite and botryoidal calcite, while the encasing muds contain foraminifera and abundant pyrite framboids indicating a reducing environment of emplacement.

On the other hand, methane-derived carbonates at the outcrop have been observed in the Vocontian basin, SE France (fig. A.2). The role of methane in their formation is evidenced by the depletion in $\delta^{13}\text{C}$ isotope with respect to normal marine values, while continuous carbonate layers in the same series show normal marine isotopic signatures. Methane-derived carbonates occur as nodules, tubes and irregular concretions a few cm to a few m in diameter. They are typically clustered in preferential layers a few meters thick, where individual concretions make from a few % to ca.20 % of the interval. Petrographic examination shows the same lithological and diagenetic characteristics as in the boreholes.

Put together, these observations allow proposing a geometric model for the positive high-amplitude anomalies observed in the Lower Congo Basin: they are likely to correspond mainly to a local enrichment in subseismic-scale nodules, tubes and concretions, many of them potentially emplaced below seafloor, in the sulphate-methane transition zone. The seismic response would thus result from the averaging effect of the seismic signal over a domain locally enriched in carbonate nodules and concretions.

Appendix II

Additional material: Chapter 5

Table A2.1 – Geometrical parameters of earliest pockmarks (basal craters). Yellow filled boxes indicate basal pockmarks below the location of Advancing pockmarks, Pale yellow boxes indicate Nesting pockmarks, White filled boxes indicate normal pockmarks. In the location column S = Syncline, C = Channel complex, D = Diapir, TSE = Topographic high in SE.

Location	Horizontal offset between topmost and lowest depression apexes (in meter)	Pockmark array length(unit)	Longest axis (meter)	Shortest axis (meter)	Average diameter (meter)
C2-7b	238	130	650	575	612.5
C2-11	88	122	425	325	375
C1-13	375	267	650	563	606.5
C1-14	288	178	550	537	543.5
C1-16	226	204	600	562	581
C1-17	200	203	550	488	519
C1-18	263	250	750	488	619
C1-19	80	60	250	230	240
C1-20	350	200	250	230	240
S3-1	350	135	562	425	493.5
S3-1b	225	134	562	425	493.5
S3-3	262	183	350	312	331
S3-4	300	300	413	387	400
S3-5	200	271	388	363	375.5
S3-6	100	153	N/A	N/A	N/A
S3-7	75	90	425	413	419
TSE-1	100	97	338	313	325.5
TSE-2	187	100	500	450	475
TSE-3	110	100	400	350	375
TSE-4	162	44	388	238	313
TSE-5	161	48	450	450	450
TSE-6	60	110	463	425	444
D2NE-1	100	166	425	400	412.5
D2NE-5	150	65	550	525	537.5
D2NE-8	137	68	375	350	362.5
D2NE-9	287	180	612	500	556
S3-2	30	160	462	450	456
C2-1	150	90	650	525	587.5
C2-2	160	90	587	550	568.5
C2-3	150	80	550	537	543.5
C2-3b	88	64	515	500	507.5
C2-4	75	70	537	480	508.5
C2-5	75	100	512	462	487
C2-6	100	150	600	525	562.5
C2-7	43	90	587	525	556
D1SW	0	60	337	337	337

Appendix II

C1-1b	0	86	430	275	352.5
C1-1'	0	86	375	325	350
C1-1"	0	99	562	463	512.5
C1-4	50	116	600	600	600
C1-5	0	101	875	775	825
C1-6	63	156	N/A	520	N/A
C1-7	0	141	850	813	831.5
C1-8	63	139	550	540	545
C1-9	0	103	650	638	644
C1-10	0	79	838	762	800
C1-10'	0	113	450	373	411.5
C1-10"	0	141	338	338	338
C1-15	0	40	463	375	419
D2NE-2	0	96	537	475	506
D2NE-3	0	38	475	462	468.5
D2NE-4	0	63	500	350	425
D2NE-6	0	20	512	437	474.5
D2NE-7	0	75	1275	962	1118.5
D2NE-10	0	60	1312	1275	1293.5
D2NE-11	0	60	762	650	706
D2NE-12	0	120	300	225	262.5
D2NE-13	0	120	362	200	281
D2NE-14	0	100	500	362	431
D2NNE	0	100	230	220	225
D2NW-1	0	100	400	337	368.5
D2NW-2	0	180	400	325	362.5
D2NW-3	0	120	612	380	496
D2NW-4	0	111	625	537	581

Appendix III

Additional material: Chapter 6

Table A3.1 – Measurements of the aspect ratio (column 5) and inclinations of honeycomb pockmark or circular pockmark sidewalls along short (Columns 6-9) and long (columns 10-12) plan form axes. Blue filled boxes indicate circular pockmarks L_s = Short axis, L_L = Long axis. The inclination measurements were based on 3 different velocity values as indicated in row 2. LD = Linear Depression

(P): pockmark n° in fig. 6.15	Diameters and depths of pockmarks				Side wall inclination along L_L axis			Side wall inclination along L_s axis		
	TWT (ms)	Long axis	Short axis	L/S	V/S = 1650	V/S = 1750	V/S = 1900	V/S = 1650	V/S = 1750	V/S = 1900
P12 (LD)	13	362	81	4,469	3,391	3,596	3,903	14,832	15,688	16,958
P10	8	380	246	1,545	1,989	2,110	2,291	3,071	3,257	3,536
P11	13	200	187	1,070	6,122	6,490	7,040	6,544	6,936	7,524
P9	17	240	230	1,043	6,666	7,066	7,665	6,953	7,370	7,994
P1	13	143	125	1,144	8,531	9,039	9,800	9,737	10,315	11,178
P13	10	143	125	1,144	6,582	6,977	7,568	7,520	7,970	8,643
P2	19	331	287	1,153	5,411	5,736	6,224	6,234	6,608	7,169
P14	16	231	193	1,197	6,520	6,911	7,497	7,789	8,255	8,951
P15	6	218	193	1,130	2,600	2,758	2,993	2,936	3,114	3,380
P16	6	418	168	2,488	1,357	1,439	1,562	3,372	3,576	3,882
P17	3	418	137	3,051	0,678	0,720	0,781	2,069	2,195	2,382
P4	4	162	137	1,182	2,333	2,474	2,686	2,758	2,925	3,175
P18	9	270	250	1,080	3,148	3,338	3,624	3,399	3,605	3,913
P19	3	100	87	1,149	2,834	3,005	3,262	3,256	3,453	3,749
P20	6	331	175	1,891	1,713	1,817	1,973	3,238	3,434	3,727
P3	9	237	225	1,053	3,585	3,802	4,127	3,776	4,004	4,346
P21	15	225	187	1,203	6,277	6,654	7,219	7,539	7,991	8,666
P22	9	256	240	1,067	3,320	3,521	3,822	3,541	3,755	4,075
P23	11	386	281	1,374	2,692	2,855	3,099	3,696	3,919	4,254
P24	6	300	200	1,500	1,890	2,005	2,176	2,834	3,005	3,262
P5	9	300	281	1,068	2,834	3,005	3,262	3,025	3,208	3,482
P6	12	243	231	1,052	4,658	4,939	5,360	4,899	5,194	5,637
P7	8	300	256	1,172	2,519	2,672	2,901	2,952	3,130	3,398
P8	5	231	218	1,060	2,045	2,169	2,355	2,167	2,298	2,495

Table A3.2 – Number of chimneys which emanate or intersect different parts of polygonal and tectonic faults in different parts of the study area.

Inclusion of tectonic faults						
	Flank of Diapir 2	Syncline 1 and 2	Flank Diapir 1	Syncline 3	SE corner of survey	Total
Intersection with apex of PF graben	5	13	4	6	12	40
Intersection with the basal portion of a conjugate PF (Single PF)	10	14	5	29	17	75
Emanating from deep-seated tectonic fault	2	8	7	14	7	38
Intersection with PF horst block (Centre of a rotated fault block)	3	3	4	2	2	14
Intersection with central portion of PF	3	14	0	2	0	19
Intersection with upper PF tip	2	5	0	1	0	8
Emanating from upper PF tip	1	0	1	1	0	3
No determinable	1	3	0	2	0	6
Terminating abruptly upwards against PF plane	0	0	0	0	6	6
						209
Exclusion of tectonic faults						
	Flank of Diapir 2	Syncline 1 and 2	Flank Diapir 1	Syncline 3	SE corner of survey	Total
Intersection with apex of PF graben	5	13	4	6	12	40
Intersection with the basal portion of a conjugate PF (Single PF)	10	14	5	29	17	75
Emanating from deep-seated tectonic fault	3	3	4	2	2	14
Intersection with central portion of PF	3	14	0	2	0	19
Intersection with upper PF tip	2	5	0	1	0	8
Emanating from upper PF tip	1	0	1	1	0	3
No determinable	1	3	0	2	0	6
Terminating abruptly upwards against PF plane	0	0	0	0	6	6
						171

